National Technical University of Athens
School of Electrical and Computer Engineering
Division of Communication, Electronic and Information Engineering

Image Reconstruction Approaches and Circuit Modeling in Electrical Impedance Tomography

PhD Thesis

Christos G. Dimas

Circuits & Systems Group

Athens, December 2021

Εθνικό Μετσόβιο Πολυτεχνείο
Σχολή Ηλεκτρολόγων Μηχανικών & Μηχανικών Υπολογιστών
Τομέας Επικοινωνιών, Ηλεκτρονικής & Συστημάτων Πληροφορικής

Μέθοδοι Ανακατασκευής Εικόνας και Μοντελοποίησης Κυκλωμάτων σε Τομογραφική Απεικόνιση Ηλεκτρικής Εμπέδησης

Διδακτορική Διατριβή

Χρήστος Γ. Δήμας

Circuits & Systems Group
Αθήνα, Δεκέμβριος 2021

National Technical University of Athens
School of Electrical and Computer Engineering
Division of Communication, Electronic and Information Engineering

Image Reconstruction Approaches and Circuit Modeling in Electrical Impedance Tomography

PhD Thesis

Christos G. Dimas

Advisory Committee:

Paul - Peter Sotiriadis	Nikolaos Uzunoglu	Konstantina Nikita
Professor, NTUA	Professor Emeritus, NTUA	Professor, NTUA

Approved by the seven-member examination committee on 12/01/2022.

.....	.....	.....	.....
Paul - Peter Sotiriadis	Nikolaos Uzunoglu	Konstantina Nikita	Georgios Matsopoulos
Professor, NTUA	Professor Emeritus, NTUA	Professor, NTUA	Professor, NTUA

.....	.....	.....
Georgios Kyriakou	Irene Karanasiou	Andreas Demosthenous
Professor, DUT	Professor, Hellenic Military Academy	Professor, UCL

Circuits & Systems Group

Athens, December 2021

.....

Χρήστος Γ. Δήμας
Διπλωματούχος Ηλεκτρολόγος Μηχανικός και Μηχανικός Υπολογιστών Ε.Μ.Π.

Copyright © Χρήστος Δήμας, 2021
Με επιφύλαξη παντός δικαιώματος. All rights reserved.

Απαγορεύεται η αντιγραφή, αποθήκευση και διανομή της παρούσας εργασίας, εξ ολοκλήρου ή τμήματος αυτής, για εμπορικό σκοπό. Επιτρέπεται η ανατύπωση, αποθήκευση και διανομή για σκοπό μη κερδοσκοπικό, εκπαιδευτικής ή ερευνητικής φύσης, υπό την προϋπόθεση να αναφέρεται η πηγή προέλευσης και να διατηρείται το παρόν μήνυμα. Ερωτήματα που αφορούν τη χρήση της εργασίας για κερδοσκοπικό σκοπό πρέπει να απευθύνονται προς το συγγραφέα.

Οι απόψεις και τα συμπεράσματα που περιέχονται σε αυτό το έγγραφο εκφράζουν το συγγραφέα και δεν πρέπει να ερμηνευθεί ότι αντιπροσωπεύουν τις επίσημες θέσεις του Εθνικού Μετσόβιου Πολυτεχνείου.

Abstract

This PhD thesis presents novel inverse problem formulation and image reconstruction approaches as well as hardware design and simulation methodologies in Electrical Impedance Tomography. Evaluation of the proposed algorithms has been performed via extensive simulations, experimental and in-vivo data. A simulation interface was also developed to observe the performance of different hardware and electrode configurations.

In the first chapter (1), a brief introduction in the definition of Electrical Impedance Tomography as well as a historical review is performed.

The second chapter (2) describes the problem's mathematical formulation, the current and measurement patterns, the forward and the inverse problems. The non-linear, ill-posed and ill-conditioned inverse problem is treated as a regularized least-square optimization problem. In this chapter, a description of the state-of-the-art as well as the more recent approaches on the solution of the inverse problem is performed. It includes linear and non-linear requlrarization approaches, the non-linear inverse scattering Fourier transform-based D-Bar method, as well as machine learning ones.

In the third chapter (3), a novel efficient method-of-moment approach using Green's functions and modified radial basis functions for the representation of the conductivity logarithm is described. The inverse problem is treated with L^1-norm or L^2-norm regularization methods. The main advantage of this approach is that it uses a more accurate expression of the relationship between the electrode boundary voltages and the conductivity distribution than the typical weak-linearized one. This limits the effects of the problem's non-linearity and leads to faster convergence of the solution, even if conductivity perturbations are intense. The approach is also tested in 3D cylindrical setups, while fine-remeshing (dual reconstruction) can be also applied. Its effectiveness is verified both qualitatively and quantitatively, through numerous simulation examples with the signal noise considered, as well as experimental and in-vivo cases.

The fourth chapter (4) presents an approach which combines the method-of-moment described in the third chapter with a sparse Bayesian learning algorithm, based on the EM-algorithm. It offers noise robustness and decreases the effect of hyperparameter values to the reconstruction spatial performance. The method is applied on dynamic lung imaging. For its qualitative and quantitative evaluation, a number of three-dimensional thoracic simulated models were built, based on CT images of 3 adult male subjects and considering five breath-cycle discrete states: from the expiration-end to the inspiration-end. An image registration method for the extraction of the reference (true) images was performed and a number of quantitative metrics was used for the evaluation. Both simulation and in-vivo results showed improved

performance at most of the figures of merit compared to state-of-the-art methods.

The fifth chapter (5) performs an extensive review of the EIT hardware typical characteristics. Firstly, the basic system's architecture is described. Secondly, common topologies of current sources for bioimpedance measurement, with their advantages and disadvantages are described. The effect of reduced output impedance, mismatch between source and sink and common signal is discussed. Then, a description of the voltage recording circuitry configuration is performed, followed by SNR estimation models. In addition, the demodulation process and possible digital control methods are described.

In the sixth chapter (6) an extensive simulation interface for EIT hardware, developed with MATLAB and LT SPICE is presented. Apart from signal noise, the impact of important effects (common signal, parasitic capacitances, electrode contact impedance, sampling rate and resolution, number of samples per measurement, e.t.c.) in the reconstruction quality is researched. For many of them, accurate mathematical models do not exist, hence a direct simulation approach prior to the design process is essential. The signal noise is added to transient simulations, that are transferred in MATLAB to simulate the digital process. The subject under test is also merged in the simulation setup using frequency-dependent multiport equivalent circuits.

In the seventh chapter (7), the content of three research papers about miscellaneous bioimpedance modeling applications is included. In the first part (7.1), a highly tunable two-dimensional time-variant thoracic model is presented, focusing on the impact of the boundary and tissues' movement during the measurement process on the reconstructed image. In second part (7.3), the skin-electrode contact during tetrapolar bioimpedance measurement is simulated using Cole model analog realization. A post-layout implementation and simulation on IC analog circuit evaluates the model's accuracy. Finally, in the third part (7.4), healthy and cancerous lung cells are realized as Cole model-based analog IC circuits using current feedback amplifiers.

In the nineth chapter (8), the conclusions of the research conducted are drawn. Finally, the appendices (9 and 10) include basic parts of the MATLAB code used as well as mathematical proofs for the second Green theorem integral equation formulation and the Neumann Green's function on a circular domain.

Index Terms Electrical Impedance Tomography, image reconstruction, forward problem, inverse problem, regularization, method-of-moment, Sparse Bayesian Learning, hardware, current source, analog front-end, noise, evaluation.

Περίληψη

Στη διδακτορική αυτή διατριβή περιλαμβάνεται μια εκτεταμένη βιβλιογραφική έρευνα, καθώς και την ανάπτυξη νέων μεθοδολογιών που αφορούν τόσο τους αλγορίθμους απεικόνισης όσο και την σχεδίαση και προσομοίωση του υλικού σχετικά με την Ηλεκτρική Τομογραφία Σύνθετης Εμπέδησης. Τα αποτελέσματα της έρευνας παρατίθενται μέσω εκτεταμένων προσομοίωσεων καθώς και πειραματικών και ιατρικών δεδομένων.

Στο 1ο κεφάλαιο της διδακτορικής διατριβής πραγματοποιείται μια σύντομη εισαγωγή στην έννοια της ηλεκτρικής τομογραφίας σύνθετης εμπέδησης καθώς και μια ιστορική αναδρομή.

Στο 2ο κεφάλαιο πραγματοποιείται μια εκτεταμένη περιγραφή του μαθηματικού μοντέλου του προβλήματος, των χρησιμοποιούμενων στρατηγικών μέτρησης, του ορθού (forward) προβλήματος καθώς και του αντίστροφου προβλήματος (inverse problem). Η επίλυση του μη γραμμικού (non-linear) και κακώς ορισμένου (ill-posed and ill-conditioned) αντίστροφου προβλήματος ανάγεται στην συγκρότηση ενός προβλήματος βελτιστοποίησης με έναν όρο ελαχίστων τετραγώνων μεταξύ των προσομοιούμενων και των μετρηθέντων τάσεων των ηλεκτροδίων υπό δεδομένη κατανομή αγωγιμότητας και έναν ή περισσότερους όρους κανονικοποίησης. Στο κεφάλαιο αυτό περιγράφονται οι κλασσικές και οι πιο σύγχρονες μέθοδοι επίλυσης αυτού του προβλήματος ελαχιστοποίησης, περιλαμβανομένων των γραμμικών και μη γραμμικών μεθόδων κανονικοποίησης (regularization), μη γραμμικών αντίστροφων μετασχηματισμών Fourier (D-Bar) καθώς και μεθόδων που χρησιμοποιούν τη μηχανική μάθηση (machine learning).

Στο 3ο κεφάλαιο μελετάται μια νέα μέθοδος αντιμετώπισης του προβλήματος απεικόνισης (reconstruction problem), με χρήση συναρτήσεων Green, μεθόδου των στιγμών (method of moments) και τροποποιημένων Γκαουσιανών συναρτήσεων βάσης (modified radial basis functions). Η μέθοδος ανάγεται σε ένα πρόβλημα ελαχιστοποίησης που αντιμετωπίζεται με κλασικές μεθόδους κανονικοποίησης χρησιμοποιώντας όρους νόρμας L1 ή L2. Βασικό πλεονέκτημα της μεθόδου είναι η ακριβέστερη θεώρηση της εξάρτησης των τάσεων των ηλεκτροδίων από της κατανομή της αγωγιμότητας, κάτι το οποίο βελτιώνει τις επιπτώσεις της μη γραμμικότητας (non-linearity) του προβλήματος οδηγώντας σε ταχύτερη σύγκλιση ακόμα και όταν οι διαταρραχές της αγωγιμότητας (conductivity perturbations) στη διάταξη μέτρησης είναι έντονες. Η μέθοδος επίσης μπορεί να προσαρμοστεί σε τριδιάστατα προβλήματα καθώς και δυικές διακριτοποιήσεις του χώρου απεικόνισης (fine remeshing). Η αποτελεσματικότητά της εξετάζεται τόσο ποιοτικά όσο και ποσοτικά μέσω πολλαπλών παραδειγμάτων διδιάστατης και τριδιάστατης προσομοίωσης θεωρώντας θορυβώδη σήματα τάσης, μέσω πειραματικών διατάξεων καθώς και δεδομένων από ασθενείς (in-vivo data).

Στο 4ο κεφάλαιο, μια μέθοδος αραιής Μπαεζιανής μάθησης (Sparse Bayesian Learning-SBL) εν-

σωματώνεται στη μέθοδο των στιγμών που περιγράφεται στο 3ο κεφάλαιο, προσφέροντας βελτιωμένη ποιότητα απεικόνισης και αντίσταση στο θόρυβο (noise robustness). Η εφαρμογή της μεθόδου εξειδικεύεται σε δυναμική απεικόνιση θώρακα και πνευμονικής λειτουργίας (dynamic thoracic imaging, lung impedance changes, lung functioning). Για την ποσοτική επαλήθευση της αποτελεσματικότητάς της, κατασκευάστηκαν τριδιάστατα μοντέλα τομής θώρακα βασιμένα σε 3 αξονικές τομογραφίες ασθενών από ανοικτή βάση δεδομένων. Ακολουθήθηκε μια μέθοδος εξαγωγής εικόνας αναφοράς καθώς και πολλαπλά κριτήρια ποσοτικής αξιολόγησης. Τα αποτελέσματα έδειξαν σημαντική βελτίωση στα περισσότερα αυτά κριτήρια απεικόνισης.

Στο 5ο κεφάλαιο πραγματοποιείται μια εκτεταμένη περιγραφή των τυπικών χαρακτηριστικών του υλικού (hardware) ενός συστήματος ηλεκτρικής τομογραφίας σύνθετης εμπέδησης. Αρχικά γίνεται αναφορά στην βασική δομή ενός τέτοιου συστήματος. Στη συνέχεια, περιγράφονται οι πιθανές διατάξεις και τοπολογίες πηγών ρεύματος για μέτρηση βιοαντίστασης, καθώς και τα πλεονεκτήματα-μειονεκτήματα της καθεμίας. Ιδιαίτερη αναφορά γίνεται στο ζήτημα της μειωμένης αντίστασης εξόδου, της αναντιστοιχίας συμμετρικών τμημάτων του κυκλώματος καθώς και την ύπαρξη κοινού σήματος. Έπειτα, μια αντίστοιχη περιγραφή πραγματοποιείται σχετικά με το κύκλωμα μέτρησης τάσης, συνοδευόμενη από βασικά μαθηματικοποιημένα μοντέλα εκτίμησης θορύβου. Τέλος περιγράφεται η διαδικασία της αποδιαμόρφωσης (demodulation) και πιθανοί τρόποι άσκησης ψηφιακού ελέγχου στο σύστημα.

Στο 6ο κεφάλαιο μελετάται μια εκτεταμένη μέθοδος προσομοίωσης συστημάτων ηλεκτρικής τομογραφίας. Για τις προσομοιώσεις χρησιμοποιείται μια διεπαφή μεταξύ του LT SPICE (για το αναλογικό μέρος) και του MATLAB (για το ψηφιακό μέρος). Μελετάται η απευθείας επίδραση στην ποιότητα της απεικόνισης παραγόντων πέραν του θορύβου, για τους οποίους δεν είναι εύκολο να εκτιμηθεί με αυστηρά μαθηματικά μοντέλα. Τέτοιοι παράγοντες είναι το κοινό σήμα, η επίδραση των παρασιτικών χωρητικοτήτων, των αντιστάσεων επαφής των ηλεκτροδίων, του αριθμού των δειγμάτων του φίλτρου αποδιαμόρφωσης καθώς και της ποιότητας της δειγματοληψίας. Για την ενσωμάτωση του θορύβου στα χρονικά προσομοιούμενα σήματα, χρησιμοποιούνται πέραν της προσομοίωσης θορύβου μέσω LT SPICE και μαθηματικά μοντέλα για την εκτίμησή του. Παράλληλα, η εκάστοτε εξεταζόμενη διάταξη μετατρέπεται σε ένα ισοδύναμο παθητικό πολύθυρο κύκλωμα, εξαρτώμενο από τη συχνότητα του σήματος εισόδου.

Στο 7ο κεφάλαιο παρατίθεται το περιεχόμενο τριών εργασιών που αφορούν σε διάφορα θέματα μοντελοποίησης. Στο πρώτο κομμάτι, περιγράφεται η παραμετρική μοντελοποίησης ενός διδιάστατου μοντέλου θώρακα πραγματικού χρόνου, που έχει σαν σκοπό τη μελέτη της επίδρασης της κίνησης των οργάνων κατά τη διάρκεια της ίδιας της διαδικασίας της μέτρησης. Στο 2ο κομμάτι, πραγματοποιείται η μοντελοποίηση της επαφής δέρματος-ηλεκτροδίου σε τετραπολική μέτρηση, χρησιμοποιώντας μοντέλα τύπου Cole-Cole και υλοποίηση σε διάταξη αναλογικού ολοκληρωμένου κυκλώματος. Τέλος στο 3ο μέρος, μοντελοποιείται ο πνευμονικός ιστός με χρήση Cole-Cole σε αναλογικό κύκλωμα. Στόχος είναι η μελέτη και ο διαχωρισμός των υγιών από τους καρκινικούς ιστούς, βάσει της συμπεριφοράς του μοντέλου βιοαντίστασης.

Στο 8ο κεφάλαιο γίνεται η αποτίμηση της διεξαχθείσας έρευνας και η σύνοψη των συμπερασμάτων της. Τέλος, στο 9ο κεφάλαιο (παραρτήματα) περιέχονται ορισμένες μαθηματικές αποδείξεις χρησιμοποιούμενων εξισώσεων καθώς και βασικά τμήματα κώδικα που χρησιμοποιήθηκαν για την εξαγωγή αποτελεσμάτων.

Λέξεις Κλειδιά Ηλεκτρική Τομογραφία Σύνθετης Εμπέδησης, απεικόνιση, ορθό πρόβλημα, αντίστροφο πρόβλημα, κανονικοποίηση, μέθοδος των στιγμών, αραιή Μπαεζιανή μάθηση, υλικό, πηγή ρεύματος, αναλογική διάταξη, θόρυβος, εκτίμηση.

Εκτεταμένη Περίληψη

Η παρούσα διατριβή πραγματεύεται την απεικόνιση (imaging) της κατανομής της σχετικής αγωγιμότητας (relative conductivity distribution) σε ιστούς και υλικά σώματα με χρήση Ηλεκτρικής Τομογραφίας Σύνθετης Εμπέδησης (Electrical Impedance Tomography-EIT).

Η Ηλεκτρική Τομογραφία Σύνθετης Εμπέδησης είναι μια τεχνική κατά την οποία ένα εναλασσόμενο ρεύμα διαχέεται μέσω ενός πίνακα ηλεκτροδίων σε ένα εξεταζόμενο σώμα, ιστό ή αντικείμενο με σκοπό την εκτίμηση της κατανομής της σχετικής αγωγιμότητάς του. Για να πραγματοποιηθεί η ανακατασκευή της εικόνας (image reconstruction), μετράται ένας συνδυασμός δυναμικών μεταξύ των ηλεκτροδίων. Τα δυναμικά αυτά χρησιμοποιούνται σαν πληροφορία (μέτρηση-raw data measurements) για τη διαδικασία της ανακατασκευής που επιτυγχάνεται μέσω μιας σύνθετης μαθηματικής διαδικασίας.

Η Ηλεκτρική Τομογραφία Σύνθετης Εμπέδησης βρίσκει εφαρμογή κυρίως σε ιατρική απεικόνιση (medical imaging), αλλά και στη βιομηχανία (industrial process tomography), την γεωλογία και την αρχαιολογία. Συγκεκριμένα, στον ιατρικό κλάδο, η πιο δημοφιλής εφαρμογή εντοπίζεται στην θωρακική απεικόνιση συνεχούς χρόνου (dynamic thoracic imaging). Αυτή έχει στόχο την παρακολούθηση της διαδικασίας της αναπνοής (breathing) μέσω της συνεχούς μεταβολής της ηλεκτρικής εμπέδησης των πνευμόνων (lung conductivity change) λόγω της μεταβολής του όγκου του περιλαμβανόμενου αέρα (air volume). Μια άλλη σημαντική χρήση της μεθόδου στην ιατρική απεικόνιση είναι η παρακολούθηση της ηλεκτρικής εμπέδησης του εγκεφάλου, ορισμένες φορές σε συνδυασμό με την παρακολούθηση της ηλεκτρικής του δραστηριότητας μέσω Ηλεκτροεγκεφαλογραφήματος (EEG), με σκοπό τον εντοπισμό ισχαιμικών (ischaimic stroke) ή αιμοραγικών επεισοδίων (hemorrhage). Επιπλέον, ο εντοπισμός καρκινικών όγκων (cancerous tissues), ειδικότερα στο μαστό ή τον προστάτη αποτελεί μια ακόμα σημαντική εφαρμογή της μεθόδου στον κλάδο. Στη βιομηχανία, η Ηλεκτρική Τομογραφία Σύνθετης Εμπέδησης έχει εφαρμογή στον εντοπισμό μεταλλικών ελασμάτων καθώς και στο μη καταστροφικό έλεγχο (non-destructive control). Τέλος, στην γεωλογία και την αρχαιολογία η μέθοδος είναι περισσότερο γνωστή σαν Ηλεκτρική Τομογραφία (Electrical Resistivity Tomography-ERT).

Η εξεταζόμενη μέθοδος έχει ορισμένα σημαντικά πλεονεκτήματα σε σχέση με τις συμβατικές ιατρικές μεθόδους απεικόνισης. Συγκεκριμένα, η χρήση ενός πολύ χαμηλής έντασης ηλεκτρικού ρεύματος (συνήθως $100\mu A - 6mA$, ανάλογα την εφαρμογή-application και την συχνότητα-frequency), εγγυάται την απουσία ιοντίζουσας ακτινοβολίας (ionizing radiation), σε αντίθεση με την Αξονική Τομογραφία (Computed Tomography-CT) και την Τομογραφία Εκπομπής Ποζιτρονίου (Positron Emission Tomography-PET). Επιπλέον, το κόστος υλικού είναι ιδιαίτερα χαμηλό (low-cost), ενώ είναι και μικρό σε έκταση, παρέχοντας τη δυνατότητα εύκολης μεταφοράς (portability). Πρόσφατα μάλιστα, έχουν α-

ναπτυχθεί πειραματικές διατάξεις οι οποίες διακρίνονται από χαμηλή κατανάλωση ισχύος (low-power consumption) και μπορούν να ”φορεθούν” από τον ίδιο τον ασθενή (wearable systems). Παράλληλα, η ταχύτητα λήψης των μετρήσεων και της ανακατασκευής εικόνας είναι υψηλή, επιτρέποντας έτσι την απεικόνιση σε συνεχή χρόνο, με αυξημένη χρονική ανάλυση (high temporal resolution). Το τελευταίο αυτό χαρακτηριστικό δίνει τη δυνατότητα στη μέθοδο να χρησιμοποιηθεί στην παρακολούθηση της αναπνευστικής λειτουργίας των ασθενών με αξιόλογη αποτελεσματικότητα. Μια ειδική περίπτωση όπου η Ηλεκτρική Τομογραφία Σύνθετης Εμπέδησης αποτελεί αποκλειστική επιλογή για τον παραπάνω σκοπό είναι η παρακολούθηση νεογνών (neonates) με οξύ αναπνευστικό σύνδρομο (Respiratory Distress Syndrome). Πρέπει εδώ να σημειωθεί ότι τα νεογνά δεν θα πρέπει να εκτίθενται οποιασδήποτε μορφής ακτινοβολία. Τέλος, το τελευταίο πλεονέκτημα της μεθόδου σε συνδυασμό με τη φορητότητα και τη χαμηλή κατανάλωση ισχύος ενός συστήματος που την υλοποιεί θα μπορούσε να αξιοποιηθεί σαν εργαλείο παρακολούθησης ασθενών του γενικού πληθυσμού που αναπτύσσουν οξύ αναπνευστικό σύνδρομο εξαιτίας της ασθένειας COVID-19. Οι πρώτες σχετικές μελέτες έχουν ήδη πραγματοποιηθεί και παρατίθενται στη βιβλιογραφία.

Παρά τα παραπάνω πλεονεκτήματα της Ηλεκτρικής Τομογραφίας Σύνθετης Εμπέδησης, υπάρχουν ορισμένα σοβαρά ζητήματα, εξαιτίας των οποίων η μέθοδος δεν έχει ακόμα χρησιμοποιηθεί σε ευρεία κλίμακα, παρότι προτάθηκε για πρώτη φορά ήδη από το 1978. Το σημαντικότερο μειονέκτημα, συγκρίνοντας με άλλες τομογραφικές μεθόδους, είναι η χαμηλή ανάλυση εικόνας (spatial resolution). Δυστυχώς, μια αυτοτελής εικόνα δεν παρέχει επαρκή οπτική πληροφορία για λεπτομέρειες της δομής των ιστών ή του περιεχομένου ενός σώματος, πέραν ορισμένων πολύ βασικών χαρακτηριστικών. Επομένως, για την εξαγωγή κάποιων ασφαλών συμπερασμάτων, θα πρέπει να χρησιμοποιηθεί το πλεονέκτημα της υψηλής χρονικής ανάλυσης, μέσω της λήψης πολλών συνεχόμενων πλαισίων (time-difference EIT, td-EIT) αν πρόκειται για απεικόνιση συνεχούς χρόνου. Αντίστοιχα, σε στατικές λήψεις (για την ανίχνευση παραδείγματος χάρην καρκινικών ιστών) συνηθίζεται η χρήση πολλών συχνοτήτων στο ρεύμα διέγερσης (frequency-difference EIT, fd-EIT).

Ένα ακόμα πρόβλημα που τίθεται κατά την εφαρμογή της μεθόδου είναι η αξιοσημείωτη ευαισθησία της εικόνας σε σήματα θορύβου (noise signals). Αυτό οφείλεται σε ένα φαινόμενο που ονομάζεται soft-field effect. Συγκεκριμένα, όταν ρεύμα εκχέεται σε ένα σώμα μέσω ενός ζεύγους ηλεκτροδίων, η κατανομή (πυκνότητά) του μέσα σε αυτό δεν είναι ομοιόμορφη. Αντιθέτως, η πυκνότητα του ρεύματος είναι υψηλή κοντά στα ηλεκτρόδια ρεύματος και πολλές τάξεις μεγέθους χαμηλότερη μακριά από αυτά (current diffusion). Αυτό έχει σαν αποτέλεσμα να μετρώνται δυναμικά πολύ χαμηλού πλάτους στα ηλεκτρόδια που βρίσκονται σε απόσταση από την πηγή. Δεδομένου ότι η πυκνότητα του ρεύματος υποδηλώνει την ευαισθησία του πεδίου σε μεταβολές της αγωγιμότητας, η μειωμένη ευαισθησία του δυναμικού των απομακρυσμένων ηλεκτρόδιων υποβαθμίζει σημαντικά την ουσιαστική πληροφορία που λαμβάνεται από τις μετρήσεις. Αυτό σημαίνει ουσιαστικά ότι το μαθηματικό πρόβλημα που περιλαμβάνει την πληροφορία (μετρήσεις) είναι κακώς ορισμένο (ill-conditioned). Από μαθηματική σκοπιά, αυτό σημαίνει ότι υπάρχουν γραμμικές εξαρτήσεις (linear dependance) μεταξύ των εξισώσεων. Το γεγονός αυτό σε συνδυασμό με το ότι τις περισσότερες φορές οι μετρήσεις είναι λιγότερες από τα διακριτά χωρία στα οποία θέλουμε να ανακατασκευάσουμε την εικόνα (ill-posed problem) δημιουργεί ένα μοτίβο ενός προβλήματος που είναι ιδιαίτερα ευαίσθητο σε διαταρραχές των μετρήσεων (θόρυβο).

Πέραν του θορύβου στις μετρήσεις, ένας άλλος παράγοντας που δημιουργεί σφάλμα στην απεικόνιση (reconstruction error) είναι η αναντιστοιχία που υπάρχει στη γεωμετρία μεταξύ του πραγματικού (ή προσομοιωτικού) μοντέλου και της γεωμετρίας στην οποία ανακατασκευάζουμε την εικόνα (reconstruction domain). Η αναντιστοιχία αυτή είναι πιθανό να παρουσιάζεται είτε στο σύνορο, είτε στις θέσεις/γεωμετρία των ηλεκτροδίων είτε στις διαστάσεις τους. Ωστόσο, συνηθίζεται παρότι το πραγματικό αντικείμενο προς εξέταση είναι τρισδιάστατο, η απεικόνιση να γίνεται σε δυο διαστάσεις λόγω μειωμένης πολυπλοκότητας αλλά και του γεγονότος ότι μειώνεται το χάσμα μεταξύ των μετρήσεων και των χωρίων που περιλαμβάνονται στη γεωμετρία που πραγματοποιείται η απεικόνιση (reconstruction domain) (reduced ill-posedness). Επιπλέον, για να μειωθεί αισθητά η επίδραση των περιγραφόμενων σφαλμάτων στην ποιότητα της απεικόνισης, είναι αρκετά σύνηθες να εφαρμόζεται διαφορική Ηλεκτρική Τομογραφία Σύνθετης Εμπέδησης (difference-EIT, td-EIT ή fd-EIT), όπου λαμβάνεται η διαφορά μεταξύ δυο πλαισίων μετρήσεων (measurement frames) αντί της απόλυτης (absolute EIT) που χρησιμοποιεί μόνο ένα πλαίσιο.

Ακολούθως, περιγράφονται συνοπτικά οι μεθοδολογίες που ακολουθούνται για τη διαδικασία της απεικόνισης, καθώς επίσης και η προσέγγιση που μελετάται στα πλαίσια της διδακτορικής αυτής διατριβής.

Μέθοδοι Ανακατασκευής Εικόνας με Ηλεκτρική Τομογραφία Σύνθετης Εμπέδησης

Από μαθηματικής-πεδιακής σκοπιάς, το πρόβλημα που τίθεται σύμφωνα με τη μέθοδο αυτή, ακολουθεί την εξίσωση έκχυσης ρεύματος μέσα σε μια κατανομή αγωγιμοτήτων:

$$\nabla(\sigma(\boldsymbol{r})\nabla u(\boldsymbol{r})) = 0 \tag{1}$$

όπου το διάνυσμα $\boldsymbol{r} \in \Omega$, όπου Ω είναι το διδιάστατο ή τρισδιάστατο χωρίο στο οποίο εξετάζεται το πρόβλημα. Επίσης σ και u είναι η αγωγιμότητα και το δυναμικό στο χώρο αντίστοιχα. Οι συνοριακές συνθήκες εξαρτώνται από το μοντέλο των ηλεκτροδίων που θεωρούμε κατά την ανάλυσή μας. Τα πιο δημοφιλή είναι το σημειακό μοντέλο ηλεκτροδίων (point electrode model-PEM) και το πλήρες μοντέλο ηλεκτροδίων (complete electrode model-CEM).

Αν θεωρήσουμε το PEM, τότε η (1) τροποποιείται ως ακολούθως:

$$\nabla(\sigma(\boldsymbol{r})\nabla u(\boldsymbol{r};\boldsymbol{r}_+,\boldsymbol{r}_-)) = Ik\big(\delta(\boldsymbol{r}-\boldsymbol{r}_+) - \delta(\boldsymbol{r}-\boldsymbol{r}_-)\big) \tag{2}$$

όπου I είναι το πλάτος του εκχεόμενου ρεύματος, $k = 1/\text{meter}^n$ μια σταθερά και $\boldsymbol{r}_+$, $\boldsymbol{r}_-$ οι θέσεις των ηλεκτροδίων έκχυσης ρεύματος (source and sink). Η συνοριακή συνθήκη ορίζει ότι το ρεύμα δεν διαπερνάει το σύνορο $\partial\Omega$ σε κανένα σημείο (υπό την προϋπόθεση ότι τα σημειακά ηλεκτρόδια από μαθηματικής σκοπιάς θα θεωρηθούν ότι βρίσκονται λίγο εντός του συνόρου):

$$\frac{\partial u(\boldsymbol{r};\boldsymbol{r}_+,\boldsymbol{r}_-)}{\partial \boldsymbol{n}} = 0 \tag{3}$$

όπου $\boldsymbol{n}$ ένα μοναδιαίο κάθετο στο σύνορο διάνυσμα.

Το πλήρες μοντέλο ηλεκτροδίου (CEM) ορίζεται από την (1) και τις ακόλουθες συνοριακές συνθήκες:

$$u(\boldsymbol{r}) + z_l \sigma(\boldsymbol{r}) \frac{\partial u(\boldsymbol{r})}{\partial \boldsymbol{n}} = U_l, \quad \boldsymbol{r} \in e_l,\ l = 1, ..., N \tag{4}$$

$$\int_{e_l} \sigma(\boldsymbol{r}) \frac{\partial u(\boldsymbol{r})}{\partial \boldsymbol{n}} dS = I_l, \quad l = 1, ..., N \tag{5}$$

$$\sigma(\boldsymbol{r}) \frac{\partial u(\boldsymbol{r})}{\partial \boldsymbol{n}} = 0, \quad \boldsymbol{r} \in \partial\Omega \backslash \bigcup_{l=1}^{N} e_l \tag{6}$$

όπου z_l η αντίσταση επαφής (contact impedance) του l-οστού ηλεκτροδίου και N ο συνολικός αριθμός των ηλεκτροδίων. Για την μαθηματική διαδικασία της απεικόνισης, ορίζεται το ορθό πρόβλημα (forward problem) και το αντίστροφο (inverse problem).

Το ορθό πρόβλημα (forward problem) θεωρεί γνωστή την κατανομή της αγωγιμότητας σε ένα χώρο-/δομή (domain/structure) και ασχολείται με την εύρεση του δυναμικού, σύμφωνα με τις εξισώσεις του μοντέλου που έχει οριστεί (PEM, CEM, κ.ο.κ.). Για την επίλυσή του χρησιμοποιείται συνηθέστερα η μέθοδος των Πεπερασμένων Στοιχείων (Finite Element Method-FEM) όπου το χωρίο διαχωρίζεται σε μικρότερα διακριτά γεωμετρικά χωρία που ακολουθούν ένα συγκεκριμένο κανόνα συναρτήσεων βάσης (base functions). Η παραδοχή που συνήθως γίνεται είναι ότι η κατανομή της αγωγιμότητας είναι ομογενής (homogeneous), εκτός αν υπάρχει κάποια πρότερη γνωστή πληροφορία (a-priori).

Στο αντίστροφο πρόβλημα (inverse problem), λαμβάνεται υπόψη η κατανομή του δυναμικού που ευρίσκεται κατά τη μελέτη του ορθού προβλήματος (forward problem) ώστε γίνει μια προσέγγιση της κατανομής της αγωγιμότητας (conductivity distribution). Παρότι το πρόβλημα που περιγράφεται από τις εξισώσεις του PEM και του CEM είναι μη γραμμικό (non-linear), όταν ακολουθείται η μέθοδος των Πεπερασμένων Στοιχείων (FEM) συνηθίζεται να γράφεται σε διγραμμική (bilinear), ασθενή ολοκληρωτική μορφή. Στην περίπτωση του PEM (που είναι το απλούστερο μοντέλο) και του διαφορικού EIT μπορούμε να γράψουμε την ακόλουθη ασθενή μορφή:

$$\delta U_{dm} = -\int_{\Omega} \delta\sigma \nabla u(I^d) \cdot \nabla u(I^m) dA \tag{7}$$

όπου δU_{dm} είναι η υπολογιζόμενη τάση μεταξύ 2 ηλεκτροδίων, όταν παρουσιάζεται μια μικρή μεταβολή αγωγιμότητας $\delta\sigma$. Επίσης το ρεύμα εκχέεται στο m-οστό ζεύγος ηλεκτροδίων και μετράται στο d-οστό ζεύγος. Σημειώνεται επίσης ότι το $\nabla u(I^d)$ είναι το ηλεκτρικό πεδίο που υπολογίζεται στο ορθό πρόβλημα θεωρώντας ότι το ρεύμα εκχέεται στο d-οστό ζεύγος ηλεκτροδίων και $\nabla u(I^m)$ είναι το ηλεκτρικό πεδίο όταν θεωρούμε το ρεύμα το m-οστό ζεύγος.

Θεωρώντας μικρές τις διαταρραχές της αγωγιμότητας (small conductivity inclusions), μπορούμε να υπολογίσουμε την ευαισθησία (sensitivity) ως ακολούθως:

$$J^i_{dm} = \frac{\partial \delta U_{dm}}{\partial \delta\sigma} = -\int_{\Omega_i} \nabla u(I^d) \cdot \nabla u(I^m) dA \tag{8}$$

Η ευαισθησία αυτή υπολογίζεται για όλους τους χρησιμοποιούμενους συνδυασμούς ζευγών ηλεκτροδίων ρεύματος-τάσης (συνήθως τετραπολικές μετρήσεις-tetrapolar measurements). Έτσι, συμπληρώνεται ο Ιακωβιανός πίνακας $\boldsymbol{J}$ (Jacobian matrix). Με χρήση του $\boldsymbol{J}$ μπορεί να ακολουθηθεί η παρακάτω προσέγγιση για μικρές διαταρραχές της αγωγιμότητας (γύρω από μια τιμή $\boldsymbol{\sigma_o}$)

$$\boldsymbol{\delta U} = \frac{\partial \boldsymbol{\delta U}}{\partial \boldsymbol{\delta \sigma}}|_{\sigma_o} \boldsymbol{\delta \sigma} + O(\|\boldsymbol{\delta \sigma}\|^2) \simeq \boldsymbol{J \delta \sigma} \tag{9}$$

Το αντίστροφο πρόβλημα (inverse problem) μπορεί να αποτυπωθεί πρωτογενώς σαν ένα πρόβλημα εύρεσης της βέλτιστης κατανομής αγωγιμότητας ούτως ώστε οι υπολογισθείσες τάσεις $\boldsymbol{\delta U} \in \mathbb{R}^{Nh}$ στα ηλεκτρόδια μέσω της εξίσωσης της ασθενούς μορφής (7) να έχουν την ελάχιστη απόκλιση από τις μετρηθήσες $\boldsymbol{\delta V} \in \mathbb{R}^{Nh}$. Αν θεωρήσουμε ότι το μοντέλο παρουσιάζει Γκαουσιανό θόρυβο μηδενικής μέσης τιμής $\boldsymbol{e_n}$ (Gaussian noise), τότε μπορούμε να γράψουμε την ακόλουθη έκφραση:

$$\boldsymbol{\delta V} = \boldsymbol{\delta U} + \boldsymbol{e_n} \tag{10}$$

Λόγω της ασθενούς ορισμένης φύσης του προβλήματος (ill-conditioned), θεωρούμε ένα πρόβλημα ελαχιστοποίησης (minimization problem) με έναν όρο ελαχίστων τετραγώνων για τις τάσεις και έναν (ή περισσότερους) όρους κανονικοποίησης (penalty or regulariztion terms P):

$$F(\boldsymbol{\delta \sigma}) = \|\boldsymbol{J \delta \sigma} - \boldsymbol{\delta V}\|^2_{\boldsymbol{W}} + \lambda^2 P(\boldsymbol{\delta \sigma}). \tag{11}$$

Όπου $\boldsymbol{W} \in \mathbb{R}^{Nh}$ είναι ένας διαγώνιος πίνακας που καθορίζει το βάρος κάθε μέτρησης και h ο αριθμός των διαφορικών μετρήσεων που λαμβάνεται για κάθε ζεύγος ηλεκτροδίων έκχυσης ρεύματος. Ο όρος κανονικοποίησης P μπορεί να εκφράζει μια L^2 ή μια L^1 νόρμα.

Οι συχνότερες φόρμουλες που χρησιμοποιούνται με L^2 νόρμα είναι η κανονικοποίηση Tikhonov, με μοναδιαίο πίνακα ή με διακριτά φίλτρα τύπου Laplace, NOSER ή Γκαους (Gaussian high-pass filter). Τότε έχουμε

$$P(\boldsymbol{\delta \sigma}) = \|\boldsymbol{\delta \sigma}\|^2_{\boldsymbol{Q}} \tag{12}$$

Όπου $\mathbf{Q} \in \mathbb{R}^{L \times L}$ είναι ο πίνακας διακριτού φίλτρου (prior matrix) και L τα διακριτά χωρία στα οποία χωρίζεται ο χώρος Ω. Η λύση που δίνεται είναι κλειστού τύπου (closed form solution):

$$\boldsymbol{\delta \sigma_*} = \left(\boldsymbol{J^T W J} + \lambda^2 \boldsymbol{Q}\right)^{-1} \boldsymbol{J^T W \delta V} \tag{13}$$

Η προσθήκη όρων L^2 νόρμας βελτιώνουν σημαντικά την ασθενώς ορισμένη φύση του προβλήματος, ωστόσο προσδίδει υπερβολική ομαλότητα (smoothness) στην εκτιμηθείσα κατανομή των αγωγιμοτήτων (estimated conductivity distribution), μειώνοντας τη χωρική ανάλυση (spatial resolution). Επιπλέον, η μη γραμμικότητα (non-linearity) του προβλήματος που δυσχαιρένει όταν παρουσιάζονται εντονότερες μεταβολές στην αγωγιμότητα, επιβάλλει ορισμένες φορές τη χρήση επαναληπτικού σχήματος (iterative scheme) για το αντίστροφο πρόβλημα βελτιστοποίησης (11). Αυτό επιτυγχάνεται μέσω πολλαπλών επιλύσεων του ορθού και του αντιστρόφου προβλήματος, με νέες εκτιμήσεις της αγωγιμότητας και του πεδίου σε κάθε επανάληψη. Για το σκοπό αυτό μπορεί να χρησιμοποιηθεί η μέθοδος Gauss-Newton (ή

Newton-Raphson) ή η μέθοδος Landweber. Είναι γεγονός ότι η επαναληπτικότητα αυτή αυξάνει σημαντικά τη συνολική πολυπλοκότητα (complexity) του προβλήματος, επηρρεάζοντας τους χρόνους εκτέλεσης. Η επίδραση σε εφαρμογές που απαιτούν απεικόνιση συνεχούς χρόνου, όπως η παρακολούθηση της αναπνοής, είναι σημαντική.

Πέρα από τις φόρμουλες που χρησιμοποιούν L^2 νόρμες, συχνά χρησιμοποιούνται φόρμουλες με L^1 νόρμες, γνωστές ως μέθοδος των ολικών μεταβολών (Total Variation-TV). Στην περίπτωση αυτή ισχύει

$$P(\boldsymbol{\delta\sigma}) = \|\boldsymbol{\delta\sigma}\|_1 \tag{14}$$

όπου η διαδικασία της ελαχιστοποίησης του (11) είναι πλήρως μη γραμμική και απαιτεί επαναλήψεις (iterations). Η αντιμετώπιση αυτή προσφέρει τη δυνατότητα απεικόνισης εντονότερων μεταβολών της αγωγιμότητας (steep conductivity changes) μεταξύ των περιοχών του χωρίου. Δημοφιλείς μέθοδοι TV είναι η Primal-Dual Interior Point (PD-IPM), η Bregman distance, καθώς και υβριδικές μέθοδοι που ενδεχομένως να χρησιμοποιούν τόσο L^1 όσο L^2 όρους στην (11). Παρά την πρόοδο των τελευταίων ετών, βασικό μειονέκτημα των μεθόδων αυτών είναι η αυξημένη πολυπλοκότητα (complexity) καθώς και το συχνά μεγάλό πλήθος παραμέτρων που απαιτούν καθορισμό, μέσω μη προφανών διαδικασιών. Περισσότερες λεπτομέρειες σχετικά με τις εν λόγω μεθόδους παρατίθενται στα κύρια κεφάλαια της διδακτορικής διατριβής.

Αξίζει να σημειωθεί ότι την τελευταία τριετία έχει αρχίσει να μελετάται η εφαρμογή μεθόδων μάθησης (learning approaches) στο EIT, κάτι το οποίο αναμένεται να πάρει σημαντικές διαστάσεις με την ανάπτυξη της Μηχανικής Μάθησης (Machine Learning). Οι βασικότεροι άξονες-προσεγγίσεις στους οποίους έχουν μελετηθεί οι εν λόγω μέθοδοι είναι οι Μέθοδοι Στατιστικής-Μπαεζιανής Μάθησης (Statistical Bayesian Learning-SBL) καθώς και Μέθοδοι Βαθιάς Μάθησης (Deep Learning-DL) που χρησιμοποιούν Συνελικτικά Νευρωνικά Δίκτυα (Convolutional Neural Networks-CNN).

Πέρα από τις μεθόδους εκτίμησης της κατανομής αγωγιμότητας που αναφέρθηκαν, τα τελευταία χρόνια έχουν μελετηθεί και ορισμένες μέθοδοι ανακατασκευής των σχημάτων των διαταρραχών της αγωγιμότητας σε ένα σώμα. Οι μέθοδοι αυτές καλούνται Μέθοδοι Ανακατασκευής Σχήματος (Shape Reconstruction). Βασικό τους χαρακτηριστικό είναι η χρήση περιοριστικών όρων στην (11) που αφορούν αποκλειστικά τα σχήματα-σύνορα των διαταρραχών (inclusions). Οι μέθοδοι αυτές επιτυγχάνουν αξιόλογα αποτελέσματα στην ανίχνευση των σχημάτων, ωστόσο απαιτούν πρότερη γνώση (a-priori knowledge) του πλήθους και της τάξης μεγέθους και θέσης της έκτασης των εξεταζόμενων διαταρραχών.

Στην παρούσα διατριβή, αναπτύσσεται μια νέα μέθοδος κατάστρωσης του προβλήματος απεικόνισης, με τη χρήση συναρτήσεων Green (Green's functions) και τροποποιημένες Γκαουσιανές συναρτήσεις (Modified Gaussian functions or Radial Basis functions-RBFs). Η αντιμετώπιση αυτή βασίζεται στη Μέθοδο των Στιγμών (Method of Moments-MoM).

Θεωρώντας το μοντέλο PEM (ωστόσο μπορεί να γίνει επέκταση και στο CEM) και την εξίσωση (2), και θεωρώντας μη ασυνεχείς μεταβολές της αγωγιμότητας και μια σταθερή αγωγιμότητα κοντά στην περιοχή των ηλεκτροδίων, μπορεί να χρησιμοποιηθεί το θεώρημα του Green (Green's Second Identity) για να γράψουμε την ακόλουθη ολοκληρωτική μορφή:

$$u(\boldsymbol{r};\boldsymbol{r}_+,\boldsymbol{r}_-)=\int_\Omega G(\boldsymbol{r},\boldsymbol{r'})\nabla\left(\ln\sigma(\boldsymbol{r'})\right)\cdot\nabla u_o(\boldsymbol{r'};\boldsymbol{r}_+,\boldsymbol{r}_-)dA+u_o(\boldsymbol{r};\boldsymbol{r}_+,\boldsymbol{r}_-) \tag{15}$$

Όπου με $G(\boldsymbol{r},\boldsymbol{r'})$ υποδηλώνεται η συνάρτηση Green μεταξύ ενός σημείου παρατήρησης (observation point) $\boldsymbol{r}$ και σημείου πηγής (source point) $\boldsymbol{r'}$. Επιπλέον, οι μεταβλητές $\boldsymbol{r}_+$, $\boldsymbol{r}_-$ υποδηλώνουν τις συντεταγμένες των ηλεκτροδίων από όπου εισέρχεται και εξέρχεται το ρεύμα αντίστοιχα (source and sink). Έπειτα, εκφράζουμε το λογάριθμο της ειδικής αγωγιμότητας ως εξής:

$$\ln\sigma(\boldsymbol{r'})\triangleq\ln(\sigma_o)+\sum_{j=1}^{L}c_j\theta(\boldsymbol{r'},\boldsymbol{r_j}) \tag{16}$$

Η συνάρτηση βάσης RBF επιλέγεται ως ακολούθως:

$$\theta(\boldsymbol{r'},\boldsymbol{r_j})\triangleq exp\left(-\frac{\|\boldsymbol{r'}-\boldsymbol{r_j}\|_{p_1}^{p_1/p_2}}{2D^2}\right) \tag{17}$$

όπου η μεταβλητή D υποδηλώνει το εύρος της συνάρτησης.

Διακριτοποιώντας την ολοκληρωτική εξίσωση (15) και αντικαθιστώντας το λογάριθμο της αγωγιμότητας με την έκφραση (16), και λαμβάνοντας τις διαφορικές μετρήσεις των ηλεκτροδίων, ανάλογα με τη στρατηγική μέτρησης που ακολουθείται, οδηγούμαστε στο ακόλουθο σύστημα γραμμικών εξισώσεων (linear equation system)

$$\boldsymbol{M^o c}=\boldsymbol{\delta U}. \tag{18}$$

όπου $\boldsymbol{M^o}\in\mathbb{R}^{Nh\times L}$ είναι ο πίνακας του συστήματος, $\boldsymbol{c}=[c_j]_{j=1}^{L}\in\mathbb{R}^{L\times 1}$ είναι ο πίνακας των (αγνώστων) συντελεστών της (16) και $\boldsymbol{\delta U}\in\mathbb{R}^{Nh\times 1}$ είναι οι πεδιακά υπολογισμένες τάσεις των ηλεκτροδίων. Ακολουθώντας το μοντέλο μέτρησης που περιγράφεται από την σχέση (10), θεωρούμε το ακόλουθο πρόβλημα βελτιστοποίησης

$$F(\boldsymbol{c})=\|\boldsymbol{M^o c}-\boldsymbol{\delta V}\|_{\boldsymbol{W}}^2+\lambda^2 P(\boldsymbol{c}). \tag{19}$$

Το πρόβλημα αυτό μπορεί να επιλυθεί με τη μέθοδο Gauss-Newton ή TV, αναλόγως αν θα επιλεχθεί όρος κανονικοποίησης $P(\boldsymbol{c})$ l^2 ή l^1 νόρμας. Ωστόσο, σε αντίθεση με την ασθενή μορφή που ακολουθείται κατά την εφαρμογή της Μεθόδου των Πεπερασμένων Στοιχείων (FEM), η ολοκληρωτική μορφή (15) ισχύει για σημαντικά μεγαλύτερο εύρος διαταρραχών της αγωγιμότητας γύρω από το σημείο αναφοράς-γραμμικοποίησης (linearization point) σ_o. Αυτό μειώνει σημαντικά τη μη γραμμικότητα (non-linearity) του προβλήματος με αποτέλεσμα να απαιτείται μόνο μια επανάληψη (iteration) για τη σύγκλιση όταν χρησιμοποιείται κανονικοποίηση (regularization) τύπου νόρμας L^2. Παράλληλα, ο αριθμός των επαναλήψεων που απαιτούνται όταν επιλέγεται κανονικοποίηση με νόρμα τύπο L^1 (TV) είναι αισθητά μειωμένος σε σχέση με τη συμβατική μέθοδο.

Η μέθοδος αυτή, που περιγράφεται αναλυτικότερα εντός της παρούσας διατριβής, αποδεικνύεται ταχεία και αποδοτική (efficient). Προσομοιώσεις έχουν πραγματοποιηθεί σε κυκλινδρικά μοντέλα τόσο για διδιάστατη, όσο και για τρισδιάστατη απεικόνιση. Επίσης δοκιμάζεται σε πραγματικές μετρήσεις που έχουν πραγματοποιηθεί σε κυλινδρικές διατάξεις που περιλαμβάνουν αλατόνερο, καθώς και μεταλλικά και

πλαστικά δοκίμια στο εσωτερικό τους, ως διαταρραχές της αγωγιμότητας. Τέλος η μέθοδος δοκιμάζεται και σε κλινικές συνθήκες (in-vivo), με την απεικόνιση ενός πλήρους αναπνευστικού κύκλου ασθενούς.

Συστήματα Κυκλωμάτων Τομογραφικής Απεικόνισης Ηλεκτρικής Εμπέδησης

Η ευαισθησία της εικόνας που παράγεται κατά την Ηλεκτρική Τομογραφία Σύνθετης Εμπέδησης (EIT) στο θόρυβο και γενικότερα σε οποιεσδήποτε διαταρραχές του σήματος, καταδεικνύουν τη βαρύτητα που έχει ο σχεδιασμός ενός συστήματος EIT με προδιαγραφές οι οποίες να περιορίζουν στο ελάχιστο τις διαταρραχές αυτές.

Ένα κυκλωματικό σύστημα EIT γενικά περιλαμβάνει το κύκλωμα διέγερσης (όπου παράγεται το ρεύμα που εισέρχεται στο σώμα προς εξέταση), τα ηλεκτρόδια, το κύκλωμα λήψης μετρήσεων (διαφορικών τάσεων μεταξύ των ηλεκτροδίων) και έναν ψηφιακό έλεγχο (digital control). Φυσικά, κατά τη διάρκεια των τεσσάρων περίπου δεκαετιών έρευνας της μεθόδου, αναπτύχθηκε μεγάλο πλήθος διαφορετικών τοπολογιών-αρχιτεκτονικών καθώς και μεθόδων λήψης-επεξεργασίας σήματος τόσο στο αναλογικό όσο και στο ψηφιακό κομμάτι.

Στον τομέα της έρευνας τα γνωστότερα συστήματα γενικής χρήσης που αναπτύχθηκαν είναι το Sheffield MK (v1 1987, v3.5 2001), το ACT 3 και ACT 4 (1994, 2005) και το KHU Mark 2.5 (2014). Για τον εντοπισμό κακοηθών όγκων στο μαστό αναπτύχθηκε το σύστημα του πανεπιστημίου Dartmouth (1998, 2001, 2008), ενώ για την απεικόνιση θώρακα συνεχούς χρόνου το Swisstom (2012) και το ACE1 (2019). Επιπλέον, συστήματα για την απεικόνιση του εγκεφάλου με σκοπό την ανίχνευση και παρακολούθηση ισχαιμικών επεισοδίων ή και της λειτουργία του εγκεφάλου (σε συνδυασμό με EEG) έχουν αναπτυχθεί από ρο Fourth Military Medical University της Κίνας καθώς και από το UCL του Λονδίνου. Πρόσφατα επίσης αναπτύχθηκαν ολοκληρωμένα κυκλώματα ειδικά προσανατολισμένα σε εφαρμογές της τομογραφικής απεικόνισης ηλεκτρικής εμπέδησης. Συγκεκριμένα, το πανεπιστήμιο του Dartmouth έχει αναπτύξει ολοκληρωμένο κύκλωμα λήψης μετρήσεων στοχευμένο στην ανίχνευση καρκινικών όγκων του προστάτη (2020), ενώ το UCL έχει αναπτύξει ολοκληρωμένο κύκλωμα διέγερσης και λήψης σήματος με σκοπό την θωρακική απεικόνιση υψηλής ταχύτητας (100fps) (CRADL project 2018-2020).

Στα περισσότερα συστήματα που έχουν αναπτυχθεί το κύκλωμα διέγερσης αποτελείται κυρίως από ένα στάδιο ενίσχυσης και έναν μετατροπέα τάσης σε ρεύμα (πηγή ρεύματος-current source ή Voltage Controlled Current Source-VCCS). Οι μετατροπείς αυτοί υλοποιούνται είτε με διακριτά εξαρτήματα (Howland Current Source με τελεστικούς ενισχυτές-Opamps), είτε σε επίπεδο ολοκληρωμένου κυκλώματος (συνήθως με ενισχυτές διαγωγιμότητας-Operational Transconductance Amplifier-OTA). Τα επιθυμητά χαρακτηριστικά (desired specifications) μιας πηγής ρεύματος είναι η χαμηλή αντίσταση εξόδου, το μεγάλο γραμμικό εύρος λειτουργίας, η αποφυγή κοινών σημάτων (common signals) και ο χαμηλός θόρυβος.

Το σήμα εισόδου του κυκλώματος διέγερσης συνήθως παράγεται ψηφιακά μέσω ενός Direct Digital Synthesizer (DDS) που μετατρέπεται σε αναλογικό σήμα μέσω ενός Digital-to-Analog Converter (DAC). Είναι αρκετά σημαντικό το παραγόμενο σήμα εισόδου να έχει ικανοποιητική ανάλυση και χαμηλό κβαντικό θόρυβο (quantization noise). Επίσης, θα πρέπει να παράγονται οι επιθυμητές συχνότητες του σήματος διέγερσης, οι οποίες εξαρτώνται από το είδος της εφαρμογής.

Το ρεύμα εξόδου του κυκλώματος διέγερσης οδηγείται προς τα ηλεκτρόδια που βρίσκονται σε επαφή με την επιφάνεια του σώματος που εξετάζεται. Τα ηλεκτρόδια στα οποία θα οδηγηθεί το ρεύμα επιλέγονται συνήθως με ένα σύστημα διακοπτών/ πολυπλεκτών (multiplexers) που ελέγχονται ψηφιακά. Τα ηλεκτρόδια αυτά σε κάποιες διατάξεις βρίσκονται σε πολύ μικρή απόσταση από το κύκλωμα διέγερσης ή το κύκλωμα λήψης (ή και τα δυο) (ενεργό ηλεκτρόδιο-active electrode) ή σε μεγαλύτερη απόσταση (παθητικό ηλεκτρόδιο-passive electrode).

Το κύκλωμα λήψης (analog readout front-end) ή διαφορετικά κύκλωμα μέτρησης οδηγεί τα διαφορικά σήματα τάσεων μεταξύ των ηλεκτροδίων στο δειγματολήπτη (Analog-to-Digital Converter-ADC), μέσω διαδοχικών σταδίων ενίσχυσης (amplification) και φιλτραρίσματος (filtering). Τα σήματα τάσης μεταξύ των ηλεκτροδίων χαρακτηρίζονται από μικρό πλάτος (της τάξης των $\mu V - mV$), το οποίο όσο απομακρυνόμαστε από τα ηλεκτρόδια διέγερσης μειώνεται. Επομένως το πλάτος ακολουθεί ένα μεγάλο εύρος σε μικρής τάξης τιμές, με αποτέλεσμα ο τυχόν θόρυβος να το παραμορφώνει σημαντικά.

Τα σήματα τάσεων των ηλεκτροδίων διακρίνονται από μεγάλο κοινό σήμα (common signal), που δημιουργείται λόγω των αναντιστοιχιών μεταξύ των καναλιών μέτρησης (channel missmatches) καθώς και των αντιστάσεων επαφών των ηλεκτροδίων (contact impedances). Το φαινόμενο είναι ακόμα εντονότερο σε εφαρμογές όπου η επιφάνεια στην οποία τοποθετούνται τα ηλεκτρόδια είναι σκληρή και μη αγώγιμη (απεικόνιση εγκεφάλου), καθώς οι αντιστάσεις επαφών ηλεκτροδίων-επιφάνειας είναι μεγάλες. Το κοινό σήμα είναι μια από τις βασικότερες αιτίες προβλημάτων στην απεικόνιση EIT, καθώς μπορεί να ενισχυθεί μαζί με το διαφορικό, παραμορφώνοντας το σήμα τάσης. Για την αντιμετώπισή του, χρησιμοποιείται μια βαθμίδα ενισχυτή οργάνου (instrumentation amplifier) που να χαρακτηρίζεται από μεγάλο λόγο απόρριψης κοινού σήματος (Common Mode Rejection Ratio-CMRR) σε όσο το δυνατό μεγαλύτερο εύρος συχνοτήτων (frequency range).

Οι ενισχυτικές βαθμίδες του κυκλώματος λήψης έχουν σαν σκοπό να ενισχύσουν το σήμα που λαμβάνεται από τα ηλεκτρόδια τόσο ώστε να αξιοποιηθεί το μέγιστο δυνατό δυναμικό εύρος του ADC. Με τον τρόπο αυτό θα λαμβάνεται η μέγιστη δυνατή ανάλυση στο σήμα (maximum resolution). Δεδομένου του μεγάλου εύρους του πλάτους των σημάτων, η χρήση ενός ή περισσότερων ενισχυτών προγραμματιζόμενου κέρδους (Programmable Gain Amplifiers-PGAs) παρουσιάζεται σε μεγάλο αριθμό συστημάτων EIT.

Τα σήματα τάσης χαρακτηρίζονται επίσης από θόρυβο και η επίδρασή του όσο μικραίνει το πλάτος τους είναι όλο και πιο καταλυτική. Οι ενισχυτικές βαθμίδες, συμπεριλαμβανομένου του ενισχυτή οργάνου(instrumentation amplifier), τυχόν απομονωτών (buffers), τελεστικών ενισχυτών (Opamps) και PGA ενισχύουν και το θόρυβο παράλληλα με το σήμα, ενώ από μόνες τους προσθέτουν θόρυβο απόσβεσης (flicker noise-$1/f$). Έτσι μετά την τελευταία ενισχυτική βαθμίδα το σήμα έχει επιβαρυνθεί σημαντικά από άποψη θορύβου. Ο θόρυβος μπορεί να μειωθεί με τη χρήση αναλογικών ζωνοπερατών φίλτρων, ωστόσο, η βασικότερη μέθοδος αποθορυβοποίησης σε ένα σύστημα EIT είναι η αποδιαμόρφωση (demodulation).

Η αποδιαμόρφωση (demodulation), είναι μια σημαντική διαδικασία που σκοπό έχει πέρα από την ελαχιστοποίηση του θορύβου, τον εντοπισμό του πλάτους και της φάσης του σήματος προς μέτρηση. Ο πιο χαρακτηριστικός τύπος αποδιαμόρφωσης είναι η In phase-Quadrature (IQ) αποδιαμόρφωση (IQ demodulation). Αυτή επιτυγχάνεται με τον πολλαπλασιασμό του σήματος τάσης με το σήμα διέγερσης

και το σήμα διέγερσης μετατοπισμένο κατά 90 μοίρες. Τα γινόμενα των παραπάνω σημάτων διέρχονται από 2 αντιστοιχισμένα χαμηλοπερατά φίλτρα-ολοκληρωτές (matched low-pass filters, integrators), ενώ σαν αποτέλεσμα λαμβάνονται 2 DC σήματα που αντιπροσωπεύουν το In Phase και το Quadrature στοιχείο του σήματος αντίστοιχα. Οι τιμές των σημάτων I,Q στέλνονται στον υπολογιστή ως στοιχεία που χαρακτηρίζουν την τάση στο κανάλι ηλεκτροδίων που πραγματοποιείται η μέτρηση τη δεδομένη στιγμή. Η συλλογή ενός συνόλου I,Q τιμών που αντιστοιχούν σε όλους τους συνδυασμούς των ηλεκτροδίων, δεδομένης της στρατηγικής μέτρησης (measurement pattern), μας δίνει ένα πλαίσιο μέτρησης (measurement frame) που χρησιμοποιείται σαν πληροφορία (raw data) για την διαδικασία της απεικόνισης (image reconstruction).

Η διαδικασία της αποδιαμόρφωσης μπορεί να επιτευχθεί είτε με αναλογικό (analog demodulation), είτε με ψηφιακό (digital demodulation) τρόπο. Στην πρώτη περίπτωση, οι πολλαπλασιασμοί και το φιλτράρισμα των σημάτων πραγματοποιούνται αναλογικά, ενώ έπεται η λήψη των I,Q σημάτων με χρήση ADC, συνήθως τύπου Σ-Δ (sigma-delta). Σύμφωνα με ορισμένες μελέτες (οι πηγές κατονομάζονται στο κύριο μέρος της διατριβής), στην περίπτωση αυτή απαιτείται αναλογικό φίλτρο υψηλής τάξης (≥ 8) αλλά και μεγαλύτερος ρυθμός λήψης (sampling rate) και ανάλυση (resolution bits) από τον ADC. Στην περίπτωση του ψηφιακού IQ demodulation, το σήμα δειγματοληπτείται από έναν SAR ADC πριν από τη διαδικασία της αποδιαμόρφωσης. Η περίπτωση αυτή είναι και η πιο συνηθισμένη καθώς οι απαιτήσεις για τον ADC και το φίλτρο είναι χαμηλότερες, ωστόσο το σήμα διέγερσης και το σήμα λήψης θα πρέπει να είναι μόνιμα συγχρονισμένα μέσω του ψηφιακού ελέγχου.

Σύμφωνα με τη βιβλιογραφία, ο σηματοθορυβικός λόγος (Signal-to-Noise Ratio-SNR) του πλάτους (amplitude) και της φάσης (phase) του τελικού σήματος στην περίπτωση της αναλογικής αποδιαμόρφωσης, μπορεί να προσσεγγιστεί σύμφωνα με τις ακόλουθες εκφράσεις

$$SNR_A = 10\log_{10}\left[\frac{A^2}{\frac{LSB^2}{12} + 2\sigma_n^2 \cdot \frac{N \cdot BW_F}{BW_n}}\right] \tag{20}$$

και

$$SNR_\phi = 10\log_{10}\left[\frac{A^2\phi^2}{\frac{LSB^2}{12} + 2\sigma_n^2 \cdot \frac{N \cdot BW_F}{BW_n}}\right] \tag{21}$$

όπου είναι το πλάτος του σήματος, LSB η τάση που αντιπροσωπεύεται από ένα bit (η ελάχιστη δυνατή τάση που μπορεί να ανιχνευτεί κατά τη δειγματοληψία), σ_n ο Γκαουσιανός θόρυβος του σήματος τάσης στην αρχή της αλυσίδας του κυκλώματος λήψης, N ο αριθμός των δειγμάτων (samples-taps) που δειγματοληπτείται ανά κανάλι μέτρησης, BW_n το εύρος ζώνης θορύβου (equivalent noise bandwidth) που οφείλεται στο filtering effect των ενισχυτών της αλυσίδας και BW_F το εύρος ζώνης θορύβου του αναλογικού φίλτρου.

Αντίστοιχα, στην περίπτωση της ψηφιακής αποδιαμόρφωσης έχουμε τις ακόλουθες εκφράσεις για το SNR

$$SNR_A = 10\log_{10}\left[\frac{A^2\frac{N}{2}}{\frac{LSB^2}{12} + \sigma_n^2}\right] \tag{22}$$

και

$$SNR_{\phi} = 10\log_{10}\left[\frac{A^2\frac{N}{2}\phi^2}{\frac{LSB^2}{12}+\sigma_n^2}\right] \tag{23}$$

Το ψηφιακό μέρος μιας υλοποίησης EIT είναι απαραίτητο για την παραγωγή και τον έλεγχο του σήματος διέγερσης (DDS-DAC), τον προγραμματισμό και τον έλεγχο του ADC, την επιλογή των καναλιών των ηλεκτροδίων στα οποία θα περνάει το ρεύμα διέγερσης ή θα μετράται η τάση μέσω των πολυπλεκτών (multiplexers), την επιλογή του κέρδους των PGAs, καθώς και το συγχρονισμό των διαδικασιών αυτών. Μπορεί να υλοποιηθεί είτε σε μικροελεκτή (Microcontroller Processing Unit-MCU) είτε σε Field Programmable Gate Array (FPGA), ανάλογα με τις απαιτήσεις τους συστήματος.

Προηγουμένως έγινε μια συντομευμένη αναφορά στις αλγοριθμικές προσεγγίσεις που ακολουθούνται για την ανακατασκευή της εικόνας EIT. Η ποιοτική και τελική αξιολόγησή των μεθόδων πραγματοποιείται εν μέσω πειραμάτων με χρήση του υλικού (experimental validation). Ωστόσο, η αποκλειστική επαλήθευση και αξιολόγηση των αλγορίθμων μέσω του πειραματικού μέρους είναι ιδιαίτερα δαπανηρή, δεν προσφέρει καμία δυνατότητα ποσοτικής εκτίμησης της επίδοσης της απεικόνισης, ειδικά σε πραγματικές (π.χ. ιατρικές) εφαρμογές. Γι αυτό το λόγο το πρώτο στάδιο της επαλήθευσης περιλαμβάνει ηλεκτρομαγνητική προσομοίωση του μοντέλου προς απεικόνιση, όπου γίνεται αριθμητικός υπολογισμός των τάσεων των ηλεκτροδίων. Ωστόσο, το υλικό δεν συμπεριλαμβάνεται στις προσομοιώσεις αυτού του τύπου. Αντί αυτού, για να επαληθευτεί η αντοχή/συμπεριφορά μιας μεθόδου ανακατασκευής εικόνας στις διαταρραχές του σήματος, συνήθως προστίθεται ένας ”τεχνητός” λευκός θόρυβος στις μετρήσεις που έχουν προσομοιωθεί. Αυτό όμως, δεν αντικατοπτρίζει όλες τις διαταρραχές που παρουσιάζονται στα σήματα μέτρησης, όπως το κοινό σήμα ή πιθανές αποσυνδέσεις ηλεκτροδίων. Έτσι, οδηγούμαστε στην αναγκαιότητα συνυπολογισμού των παραμέτρων του υλικού στην ποιότητα των μετρήσεων και κατ’ επέκταση της εξαγόμενης εικόνας.

Στην παρούσα διατριβή πραγματοποιείται μια εκτεταμένη προσέγγιση προσομοίωσης του υλικού (hardware), συμπεριλαμβανομένου του αναλογικού μέρους, του ψηφιακού μέρους καθώς και ισοδυνάμων πολύθυρων κυκλωμάτων του σώματος προς εξέταση (Subject Under Test-SUT). Για τις προσομοιώσεις χρησιμοποιούνται το πρόγραμμα LT SPICE (Analog Devices) και το MATLAB (Mathworks). Κατά την προσέγγιση αυτή εξετάζεται η επίδραση διαφόρων παραμέτρων του υλικού στην ποιότητα της απεικόνισης. Τέτοιες παράμετροι αποτελούν ο παραγόμενος θόρυβος, τα χαρακτηριστικά των ηλεκτροδίων (αντιστάσεις και επιφάνεια επαφής), το κοινό σήμα, η ανάλυση σε bit και η ταχύτητα δειγματοληψίας του ADC καθώς και τα χαρακτηριστικά του σώματος προς εξέταση.

Βασικό επίσης χαρακτηριστικό της προσέγγισης αυτής είναι ότι οι προσομοιώσεις του αναλογικού μέρους πραγματοποιούνται στο πεδίο του χρόνου (transient), λαμβάνοντας υπόψη μεταβατικά φαινόμενα λόγω των ανοιγοκλεισίματος των διακοπτών για την επιλογή των ηλεκτροδίων. Οι χρονικές αποκρίσεις μεταφέρονται στο MATLAB όπου προσομοιώνεται όλο το ψηφιακό κομμάτι και η πραγματοποιείται η διαδικασία της απεικόνισης.

Στο αναλογικό τμήμα γίνεται μια συνοπτική σύγκριση της επίδρασης των πηγών ρεύματος διέγερσης με μικρή και με μεγαλύτερη αντίσταση εξόδου στην ποιότητα της απεικόνισης. Επίσης εξετάζεται η παράμετρος του μεγέθους των ηλεκτροδίων, της αντίστασης επαφής τους, και η επίδραση τυχόν αποσύνδεσής τους στην απεικόνιση.

Το ισοδύναμο κύκλωμα του σώματος προς εξέταση σχηματίζεται με χρήση ενός μαθηματικού μοντέλου που περιγράφεται εκτενώς στο κύριο μέρος της διατριβής. Εξετάζονται αρχικά διδιάστατες διατάξεις, στη συνέχεια κυλινδρικές διατάξεις και τέλος εφαρμογές σε θωρακικά μοντέλα. Στα τελευταία, αναπτύσσεται μια μέθοδος ποσοτικής αξιολόγησης της εικόνας στις περιπτώσεις που το μοντέλο προσομοίωσης των μετρήσεων έχει διαφορετική (και στην πραγματικότητα άγνωστη) γεωμετρία (boundary missmatches) σε σχέση με τη γεωμετρία στην οποία πραγματοποιείται η απεικόνιση. Επιπλέον, στην προσομοίωση των θωρακικών μοντέλων εξετάζεται και ο τύπος των ηλεκτροδίων με κριτήριο την απόστασή τους από το υπόλοιπο κύκλωμα (παθητικά-passive, ενεργά-active).

Στο ψηφιακό μέρος που πραγματοποιείται στο MATLAB, προσομοιώνεται η διαδικασία της δειγματοληψίας (sampling) (μέσω μιας μαθηματικής διαδικασίας επιλογής πλησιέστερων χρονικών σημείων), της κβαντοποίησης (quantization) και της ψηφιακής αποδιαμόρφωσης (digital demodulation) των σημάτων. Οι παράμετροι που αλλάζουν ώστε να εξεταστεί η επίδρασή τους στην απεικόνιση είναι η ανάλυση του ADC (resolution), ο ρυθμός δειγματοληψίας (sampling rate) και ο συνολικός αριθμός των δειγμάτων που εξετάζονται σε κάθε μέτρηση καναλιού (filter taps).

Το πλεονέκτημα της χρήσης των ενεργών ηλεκτροδίων σε σχέση με τις κλασικές διατάξεις που χρησιμοποιούν παθητικά ηλεκτρόδια είναι ότι περιορίζονται οι παρασιτικές χωρητικότητες (strain capacitances) των καναλιών που περιορίζουν την αντίσταση εξόδου των πηγών ρεύματος, δημιουργούν κοινά σήματα στα κανάλια μέτρησης τάσης και μειώνουν το εύρος συχνοτήτων λειτουργίας του συστήματος. Ωστόσο, η χρήση πολλαπλών ενεργών ολοκληρωμένων κυκλωμάτων για την υλοποίηση των πηγών ρεύματος και των ενισχυτών οργάνου, αυξάνει σημαντικά την κατανάλωση ισχύος του συστήματος. Παράλληλα, ιδιαίτερη προσοχή πρέπει να επιδειχθεί στο ζήτημα των αναντιστοιχιών μεταξύ των πηγών ρεύματος (source και sink), το οποίο μπορεί επίσης να προκαλέσει τη δημιουργία κοινού σήματος. Τα ζητήματα αυτά είναι αντικείμενα έρευνας στο χώρο της βελτίωσης των συστημάτων Ηλεκτρικής Τομογραφίας Σύνθετης Εμπέδησης.

Δομή της Διδακτορικής Διατριβής

Η δομή της παρούσας διδακτορικής διατριβής είναι η ακόλουθη. Αρχικά, πραγματοποιείται μια γενική εισαγωγή στην ιστορία, τα πλεονεκτήματα και τα μειονεκτήματα της μεθόδου, καθώς και μια αναφορά σε βασικές εφαρμογές τόσο στον ιατρικό όσο και σε άλλους κλάδους. Το δεύτερο κεφάλαιο αναφέρεται αναλυτικά στη μαθηματική διατύπωση του προβλήματος απεικόνισης καθώς και τις μεθόδους που ακολουθούνται από τη βιβλιογραφία για την επίλυσή του. Το τρίτο κεφάλαιο αναφέρεται σε μια μέθοδο απεικόνισης που αναπτύσσεται στα πλαίσια της διατριβής και χρησιμοποιεί τη Μέθοδο των Στιγμών (Method of Moments) με χρήση τροποποιημένων Γκαουσιανών συναρτήσεων. Το τέταρτο κεφάλαιο αναφέρεται στην εφαρμογή του παραπάνω μεθόδου με ένα Μπαεζυανό αλγόριθμο μηχανικής μάθησης, σε απεικόνιση θώρακα, όπου πραγματοποιείται ποιοτική, ποσοτική αξιολόγηση βάσει συγκεκριμένων δεικτών αλλά και σύγκρισή της με τις υπόλοιπες μεθόδους. Το πέμπτο κεφάλαιο περιγράφει αναλυτικά τις μεθόδους και τοπολογίες σχεδιασμού του υλικού των συστημάτων Ηλεκτρικής Τομογραφία Σύνθετης Εμπέδησης που αναπτύσσονται στη βιβλιογραφία. Στο έκτο κεφάλαιο παρουσιάζεται μια νέα προσέγγιση προσομοίωσης με στόχο την εκτίμηση της επίδοσης και το σχεδιασμό των συστημάτων που υλοποιούν Ηλεκτρική Τομογραφία Σύνθετης Εμπέδησης. Εξετάζονται εφαρμογές σε τριδιάστατα κυλινδρικά και

θωρακικά μοντέλα. Στο έβδομο κεφάλαιο παρατίθεται το περιεχόμενο τριών εργασιών που αφορούν σε διάφορα θέματα μοντελοποίησης (παραμετρική μοντελοποίηση ενός διδιάστατου μοντέλου θώρακα πραγματικού χρόνου, μοντελοποίηση της επαφής δέρματος-ηλεκτροδίου σε τετραπολική μέτρηση και μοντελοποίηση πνευμονικού ιστού με χρήση Cole-Cole σε αναλογικό κύκλωμα, με στόχο το διαχωρισμό υγειών και καρκινικών όγκων). Στο όγδοο κεφάλαιο, γίνεται η αποτίμηση της διεξαχθείσας έρευνας και η σύνοψη των συμπερασμάτων της, ενώ στα παραρτήματα διατίθενται αναλυτικές μαθηματικές αποδείξεις καθώς τμήματα του κώδικα MATLAB που χρησιμοποιήθηκε για την εξαγωγή των αποτελεσμάτων.

Acknowledgements

Through the completion of this PhD dissertation, I would like to extend my graditude to my supervisor Prof. Paul Peter Sotiriadis for the assignment of this research topic, his supportive supervision and his valuable advice during the five years of my PhD study. I would also like to extend my graditude to emeritus Prof. Nikolaos Uzunoglu for his invaluable guidance and helpful instruction during the whole period of my study. I express my thanks to my collaborate member and friend Vassilis Alimisis for the flawless collaboration, his assistance and support during the last two years. I also express my thanks to my collaborate member and friend Ioannis Georgakopoulos whose assistance during all the years of my study was priceless. Furthermore I thank all of the members and collaborators in the circuits and systems electronics lab of National Technical University of Athens and especially Konstantinos Papafotis, Konstantinos Touloupas, Nikolaos Temenos, Konstantinos Asimakopoulos, Dimitris Baxevanakis and Neoklis Chatzigeorgiou for their support, assistance and collaboration. Finally I express my thanks to my parents and friends for their priceless support all over the years.

This research is co-financed by Greece and the European Union (European Social Fund- ESF) through the Operational Programme ”Human +Resources Development, Education and Lifelong Learning” in the context of the project ”Strengthening Human Resources Research Potential via Doctorate Research” (MIS-5000432), implemented by the State Scholarships Foundation (IKY).

List of Author's Publications

0.1 Relevant Publications

0.1.1 Journals

1. C. Dimas, N. Uzunoglu, P.P. Sotiriadis, "An efficient Point-Matching Method-of-Moments for 2D and 3D Electrical Impedance Tomography Using Radial Basis functions", IEEE Transactions on Biomedical Engineering, 2021 (Early Access).
   doi: 10.1109/TBME.2021.3105056

2. C. Dimas, V. Alimisis, N. Uzunoglu, P.P. Sotiriadis, "A Point-Matching Method of Moment with Sparse Bayesian Learning Applied and Evaluated in Dynamic Lung Electrical Impedance Tomography", Bioengineering 2021, 8, 191.
   doi: `https://doi.org/10.3390/bioengineering8120191`

3. C. Dimas, V. Alimisis, I. Georgakopoulos, N. Voudoukis, N. Uzunoglu, P.P. Sotiriadis, "Analysis, Simulation, and Development of a Low-Cost Fully Active-Electrode Bioimpedance Measurement Module", Technologies 2021, 9, 59.
   doi: `https://doi.org/10.3390/technologies9030059`

4. C. Dimas, V. Alimisis, I. Georgakopoulos, N. Voudoukis, N. Uzunoglu, P.P. Sotiriadis, "Evaluation of Thoracic Equivalent Multiport Circuits Using an Electrical Impedance Tomography Hardware Simulation Interface", Technologies 2021, 9, 58.
   doi: `https://doi.org/10.3390/technologies9030058`

5. V. Alimisis, C. Dimas, G. Pappas, P.P. Sotiriadis, "Analog Realization of Fractional-Order Skin-Electrode Model for Tetrapolar Bio-Impedance Measurements". Technologies 2020, 8, 61.
   doi: `https://doi.org/10.3390/technologies8040061`

6. C. Dimas, N. Uzunoglu, P.P. Sotiriadis, "A parametric EIT system Spice simulation with phantom equivalent circuits", Technologies 2020, 8, 13.
   doi: `https://doi.org/10.3390/technologies8010013`

0.1.2 Conferences

1. C. Dimas, V. Alimisis, N. Uzunoglu, P. P. Sotiriadis, “Evaluation of 3D Thoracic Equivalent Circuit Models using Co-simulation with EIT Hardware”, 21stInternational Conference on Biomedical Applications of Electrical Impedance Tomography (EIT 2021), Galway, Ireland, 2021
   doi: 10.5281/zenodo.4635480

2. V. Alimisis, C. Dimas, P.P. Sotiriadis, ”Analogue Realization of Fractional-Order Healthy and Cancerous Lung Cell Models for Electrical Impedance Spectroscopy”, IEEE International Conference on Microelectronics (ICM), Aqaba Jordan, 2020. (**Best Paper Award**)
   doi:10.1109/ICM50269.2020.9331793

3. C. Dimas, K. Asimakopoulos, P.P. Sotiriadis, ”A highly tunable dynamic thoracic model for Electrical Impedance Tomography”, IEEE International Conference on BioInformatics And BioEngineering, USA, 2020.
   doi: 10.1109/BIBE50027.2020.00163

4. C. Dimas, V. Alimisis, P.P. Sotiriadis, ”SPICE and MATLAB simulation and evaluation of Electrical Impedance Tomography readout chain using phantom equivalents”, European Conference on Circuit Theory and Design, Sofia, Bulgaria, 2020.
   doi: 10.1109/ECCTD49232.2020.9218384

5. C. Dimas, N. Uzunoglu, P. P. Sotiriadis, “3D EIT imaging with Green’s functions”, 20st International Conference on Biomedical Applications of Electrical Impedance Tomography (EIT 2019), London, UK, 2019
   doi: 10.5281/zenodo.2691705

6. C. Dimas, N. Uzunoglu, P. Sotiriadis, ”Electrical Impedance Tomography Image Reconstruction: Impact of Hardware Noise and Errors”, IEEE International Conference on Modern Circuits and Systems Technologies, Thessaloniki, Greece, 2019.
   doi: 10.1109/MOCAST.2019.8741913

7. C. Dimas, P. Sotiriadis, ”Electrical Impedance Tomography Image Reconstruction for Adjacent and Opposite Strategy using FEMM and EIDORS Simulation Models”, IEEE International Conference on Modern Circuits and Systems Technologies, 2018.
   doi: 10.1109/MOCAST.2018.8376604

8. C. Dimas, N. Uzunoglu, P. P. Sotiriadis, “A Field Theory Approach in EIT with Green’s Functions”, 19th International Conference on Biomedical Applications of Electrical Impedance Tomography (EIT 2018), Edinburgh, Scotland, UK, 2018
   doi: 10.5281/zenodo.1210246

9. C. Dimas, P. Sotiriadis, ”Conductivity Distribution Measurement at Different Low Frequencies Using a Modular 64 Electrode Electrical Impedance Tomography System”, IEEE 4th PAnhellenic Conference on Electronics and Telecommunications, 2017.
   doi: 10.1109/PACET.2017.8259973

10. C. Dimas, P. Tsampas, N. Ouzounoglou, P. P. Sotiriadis, “Development of a Modular 64-Electrodes Electrical Impedance Tomography System”, IEEE International Conference on Modern Circuits and Systems Technologies, 2017.
    doi: 10.1109/MOCAST.2017.7937666

0.2 Other Publications

0.2.1 Journals

1. V. Alimisis, M. Gourdouparis, G. Gennis, C. Dimas, P.P. Sotiriadis, ”Analog Gaussian Function Circuit: Architectures, Operating Principles and Applications”. Electronics, 2021, 10, 20, 2530.
   doi: `https://doi.org/10.3390/electronics10202530`

2. M. Gourdouparis, V. Alimisis, C. Dimas, P.P. Sotiriadis ”An ultra-low power, ± 0.3 V supply, fully-tunable Gaussian function circuit architecture for radial-basis functions analog hardware implementation”, AEU-International Journal of Electronics and Communications, 136, 153755.
   doi: `https://doi.org/10.1016/j.aeue.2021.153755`

3. N. Voudoukis, C. Dimas, K. Asimakopoulos, D. Baxevanakis, K. Papafotis, K. Oustoglou, P.P. Sotiriadis, ”The Importance of Introducing the OCTC Method to Undergraduate Students as a Tool for Circuit Analysis and Amplifier Design”, Technologies, 2020, 8, 1, 7.
   doi: `https://doi.org/10.3390/technologies8010007`

0.2.2 Conferences

1. V. Alimisis, M. Gourdouparis, C. Dimas, P.P. Sotiriadis, ”Implementation of fractional-order model of nickel-cadmium cell using current feedback operational amplifiers”. IEEE European Conference on Circuit Theory and Design (ECCTD), 2020.
   doi: 10.1109/ECCTD49232.2020.9218311

2. M. Gourdouparis, V. Alimisis, C. Dimas, P.P. Sotiriadis, ”Ultra-Low Power (4nW), 0.6V Fully-Tunable Bump Circuit operating in Sub-threshold regime” IEEE International Conference on Design & Test of Integrated Micro & Nano-Systems (DTS), 2021, pp. 1-6
   doi: 10.1109/DTS52014.2021.9498044

3. V. Alimisis, M. Gourdouparis, C. Dimas, P.P. Sotiriadis, ”Ultra-Low Power, Low-Voltage, Fully-Tunable, Bulk-Controlled Bump Circuit”, IEEE 10th International Conference on Modern Circuits and Systems Technologies (MOCAST), 2021, pp. 1-4
   doi: 10.1109/MOCAST52088.2021.9493363

4. V. Alimisis, M. Gourdouparis, C. Dimas, P. P. Sotiriadis, ”A 0.6 V, 3.3 nW, Adjustable Gaussian Circuit for Tunable Kernel Functions,” 34th SBC/SBMicro/IEEE/ACM Symposium on Integrated Circuits and Systems Design (SBCCI), 2021, pp. 1-6, [**Best Paper Award**]
   doi: 10.1109/SBCCI53441.2021.9529988.

5. G. Pappas, V. Alimisis, C. Dimas, P.P. Sotiriadis, ”Analogue Realization of a Fully Tunable Fractional-Order PID Controller for a DC Motor,” IEEE 32nd International Conference on Microelectronics (ICM), 2020, pp. 1-4,
   doi: 10.1109/ICM50269.2020.9331798.

6. V. Alimisis, G. Gennis, C. Dimas, P.P. Sotiriadis, ”An Analog Bayesian Classifier Implementation, for Thyroid Disease Detection, based on a Low-Power, Current-Mode Gaussian Function Circuit,” IEEE International Conference on Microelectronics (ICM), 2021, pp. 153-156, [**Best Paper Award**],
   doi: 10.1109/ICM52667.2021.9664939.

Contents

List of Figures

List of Tables

List of Algorithms

Abbreviations

ANN	Artificial Neural Network
ADC	Analog-to-Digital Converter
ADMM	Alternating Direction Method of Multipliers
AFE	Analogue Front-End
AMP	Approximate Message Passing
ARDS	Acute Respiratory Distress Syndrome
ASIC	Application-Specific Integrated Circuit
AU	Arbitrary Units
BEM	Boundary Element Method
BE-SOM	Bases-Expansion Subspace Optimization Method
BioZ	Bioimpedance
BP	Blood Pressure
BPF	Band-Pass Filter
CC	Correlation Coefficient
CCII	Current Conveyor
CEM	Complete Electrode Model
CFE	Constant Phase Element
CFOA	Current Feedback Operation Amplifier
CMRR	Common Mode Rejection Ration
CNN	Convolutional Neural Network
CPE	Constant Phase Element
CT	Computed Tomography
DAC	Digital-to-Analog Converter

DC-DLS	Dominant-Current Deep Learning Scheme
DCP	Diametric Conductivity Plots
DDS	Direct Digital Synthesizer
DDTA	Differential Difference Tranconductance Amplifier
DL	Deep Learning
DL	Dirichlet-to-Neumann
DO-CCII	Double Output Current Conveyor
DSP	Digital Signal Processing
ECG	Electrocardiogram
EEG	Electroencephalogram
ECT	Electrical Capacitance Tomography
EIDORS	Electrical Impedance Tomography and Diffuse Optical Tomography Reconstruction Software
EIS	Electrical Impedance Spectroscopy
EIT	Electrical Impedance Tomography
EM	Expectation Maximization
EMG	Electromyography
ENOB	Effective number of Bits
FC	Fully Connected
Fd-EIT	Frequency-Difference Electrical Impedance Tomography
FDM	Finite Difference Method
FDM	Frequency Division Multiplexing
FE	Finite Element
FE	Front-End
FEM	Finite Element Method
FoM	Figure of Merit
FPGA	Field Programmable Gate Array
FPS	Frames per Second
FR	Full Reference
FSM	Finite State Machine

GIC	Generalized Impedance Converter
GN	Gauss Newton
GFR	Global Full Reference
GREIT	Graz consensus Reconstruction algorithm for EIT
GS	Group Sparsity
GTR	Generalized Tikhonov Regularization
HCP	Howland Current Pump
HR	Heart Beat Rate
HPF	High-Pass Filter
IA	Instrumentation Amplifier
IC	Integrated Circuit
ICC	Induced Contrast Current
IFLF	Inverse Follow the Leader
IQ	In-Phase/Quadrature
LARS	Least-Angle Regression
LPF	Low-Pass Filter
LS	Least Squares
LSB	Least Significant Bit
LSTM	Long Short-Term Memory
LT	Linear Technologies
LUT	Look Up Table
MCU	Microprocessor Unit
MAP	Maximum A-Posteriori
MAPE	Mean Absolute Percentage Error
ML	Machine Learning
MMC	Moving Morphable Components
MMV	Multiple Measurement Vector
MoM	Method of Moment
MRI	Magnetic Resonance Imaging
MSB	Most Significant Bit
MSE	Mean Square Error

MSFCF	Multi-Scale Feature Cross Function Network
ND	Neumann-to-Dirichlet
NF	Noise Figure
NIRS	Near-Infrared Spectroscopy
NLD	Non-Linear Difference
NN	Neural Network
NOSER	Newton's One-Step Error Reconstructor
OPAMP	Operational Amplifier
OTA	Operational Transconductance Amplifier
PCA	Principal Component Analysis
PDE	Partial Differential Equation
PD-IPM	Primal-Dual Interior Point
PE	Position Error
PEM	Point Electrode Model
PGA	Programmable Gain Amplifier
PLS	Parametric Level Set
PM-MoM	Point Matching Method of Moment
PPT	Pulse Transit Time
PSD	Phase Sensitive Detector
PSD	Power Spectral Density
PWL	Piece-Wise Linear
RBF	Radial Basis Function
RCR	Relative Coverage Ratio
RE	Reciprocity Error
RES	Resolution
RGB	Red Green Blue
RNG	Ringing
RRE	Relative Reconstruction Error
SADB	Structure Aware Dual-Branch
SAR	Successive Approximation Register
SA-SBL	Structure Aware Sparse Bayesian Learning

SBL	Sparse Bayesian Learning
SD	Shape Deformation
SE	Single-Ended
SiPMs	photomultipliers
SNR	Signal to Noise Ratio
SVD	Singular Value Decomposition
SVM	Support Vector Machine
SS	Steady State
SSIM	Structural Similarity Index
STR	Standard Tikhonov Regularization
SUT	Subject Under Test
TA	Target Amplitude
TLS	Traditional Level Set
THD	Total Harmonic Distortion
Td-EIT	Time-Difference Electrical Impedance Tomography
TSDL	Two-Stage Deep Learning
TSVD	Truncated Singular Value Decomposition
TLS	Traditional Level Set
TV	Total Variation
VCCS	Voltage Controlled Current Source
V/I	Voltage-to-Current

Glossary

Admittance	Σύνθετη Αγωγιμότητα
Algorithm	Αλγόριθμος
Alternating	Εναλασσόμενο
Alternating	Εναλασσόμενο
Amplification	Ενίσχυση
Analog	Αναλογικός
Capacitance	Χωρητικότητα
Circuit	Κύκλωμα
Conductivity	Αγωγιμότητα
Current	Ρεύμα
Demodulation	Αποδιαμόρφωση
Diagonal	Διαγώνιος
Differential Amplifier	Διαφορικός Ενισχυτής
Diffusion	Διάχυση
Digital	Ψηφιακός
Dimension	Διάσταση
Direct Current	Συνεχές Ρεύμα
Discretization	Διακριτοποίηση
Domain	Χωρίο
Electrical Impedance Tomography	Ηλεκτρική Τομογραφία Σύνθετης Εμπέδησης
Electrode	Ηλεκτρόδιο
Equation	Εξίσωση
Field	Πεδίο

Filter	Φίλτρο
Finite Difference Method	Μέθοδος Πεπερασμένων Διαφορών
Finite Element Method	Μέθοδος Πεπερασμένων Στοιχείων
Frequency	Συχνότητα
Hardware	Υλικό
High-Pass	Υψιπερατό
Hyperparameter	Υπερπαράμετρος
Image	Εικόνα
Imaging	Απεικόνιση
Impedance	Σύνθετη Αντίσταση (Εμπέδηση)
Injection	Έγχυση
Integration	Ολοκλήρωση
Instrumentation Amplifier	Ενισχυτής Οργάνου
Linear	Γραμμικός
Linearity	Γραμμικότητα
Low-Pass	Βαθυπερατό
Machine Learning	Μηχανική Μάθηση
Matrix	Πίνακας
Microcontroller	Μικροελεκτής
Modeling	Μοντελοποίηση
Neural Network	Νευρωνικό Δίκτυο
Noise	Θόρυβος
Non-Linear	Μη-Γραμμικός
Parameter	Παράμετρος
Processor	Επεξεργαστής
Reconstruction	Ανακατασκευή
Reference	Αναφορά
Regularization	Κανονικοποίηση
Sinusoidal	Ημιτονοειδής
Software	Λογισμικό
Source	Πηγή

Sparse	Αραιός
Subject	Αντικείμενο
System	Σύστημα
Total Variation	Ολική Μεταβολή
Unit	Μονάδα
Variable	Μεταβλητή
Vector	Διάνυσμα
Voltage	Τάση

1 Introduction

Electrical impedance tomography (EIT) is a continuously developing imaging modality that provides an image of the relative conductivity distribution of the application domain. In EIT, a small amplitude ($0.1 - 6$ mA) alternating current spanning a frequency range of 1 kHz-1 MHz is injected in the subject under test (SUT) through a cluster of electrodes. The electrodes are usually attached on the SUT surface, while the exact current and frequency values depend on the application. At the same time, voltages are measured between a specific combination of electrode pairs, depending on the measurement strategy adopted. The voltage data is then used for the image reconstruction process.

Although the concept of electrical resistivity tomography (ERT), which provides estimation for the SUT electrical resistivity distribution, had been already researched and applied for the 1940s, EIT was officialy first researched in 1978 by Henderson and Webster [1]. In this particular work, the authors attached a rectangular array of 100 electrodes on one side of the chest earthed with a single large electrode on the other side. By applying voltage and measuring the output current, a transmission image of the tissues was produced. Since then, remarkable progress has been made in EIT research, in both the hardware and the image reconstruction methods.

EIT finds wide application in the medical field, considering it as a medical imaging technique. Contemporary medical applications of EIT include real-time breath and cardio-ventricular function display [2], [3], [4], [5], [6], [7], [8], breast cancer detection [9], brain or neural activity imaging [10], [11], [12] and skin-relevant disturbances investigation. EIT is also applicable to geology, non-destructive evaluation and industrial process tomography (non-destructive evaluation) [13, 14, 15, 16, 17]. In the industrial field, a similar method is used, called electrical capacitance tomography (ECT) [18].

Contrary to other medical imaging techniques that employ harmful radiation or intense magnetic fields (such as Computed Tomography-CT and Magnetic Resonance Tomography-MRI), in EIT is a radiation free technique which implies a low amplitude current within the patient safety standards. Furthermore, EIT is low-cost; its hardware cost is about ten to hundred orders lower than a CT-scanner's and has the prospect of portability and wearability. Another important advantage of EIT is that it offers the capability of real-time imaging and continuous monitoring of a patient's physiological conditions, since the data collection and imaging speed can be optimized to sufficiently high levels. Some recent EIT hardware systems, applied mainly in dynamic lung imaging, have the capability to reconstruct over 50 image

frames per second (fps) [19], [20], [21]. Hence, the method's temporal resolution can be exceptionally high, capturing some effects in real time that are difficult to be monitored with conventional imaging modalities.

Despite the advantages above, EIT suffers from limited spatial resolution and high sensitivity to signal noise and distortion. This effect is caused due to the highly ill-posed (under-determined), ill-conditioned and non-linear nature of the EIT reconstruction problem. The ill-posed behavior of the problem is related to the fact that the total number of independent measurements is lower than the unknown discrete-domain conductivities. In addition, the ill-conditioned behavior is caused by the soft-field effect of the current distribution.

During the last 3 decades, a lot of research has been performed in the following two directions. Firstly, to design high performance, low-noise and low signal distortion EIT systems, and, secondly, to establish and optimize noise robust reconstruction approaches, in order to improve the spatial resolution.

This thesis focuses on the research in both these directions. It introduces a Method-of-Moment (MoM) technique, where the logarithm of conductivity is expressed by Radial Basis functions (RBFs), in order to decrease the non-linearity effect in the image reconstruction. From simulations on 2D and 3D cases, as well as experimental validation, it is shown that the MoM method leads to improved solution convergence. In vivo results also show that MoM is efficient in real-time EIT imaging. Furthermore, MoM is combined with a Sparse Bayesian Learning (SBL) approach to provide robustness to the inverse problem in noise. The method is extensively tested on 3D thoracic structures both qualitatively and quantitatively and it is shown to outperform the traditional and more advanced regularization based methods, as well as the regularized MoM.

In addition, hardware design approaches are researched and an extensive simulation approach, combining EIT system analog and digital hardware as well as SUT equivalent circuits is proposed. A SPICE-MATLAB interface is established for the simulations, while the impact of many hardware configurations, such as active/passive electrodes, electrode dimensions, signal frequency, Analog-to-Digital converter resolution, sampling frequency and number of filter taps, on the imaging signal quality and imaging performance has been examined. The potential advantages of an active electrode configuration are discussed, including the elimination of signal distortion, caused by the stray capacitances and the channel mismatches. The latter is crucial for an EIT system, since, unlike noise, distortion caused by common signals cannot be filtered.

The remainder of this thesis is organized as follows. In chapter 2, a presentation of the EIT mathematical principle and state-of-the-art reconstruction approaches is performed. In chapter 3, a novel problem formulation and efficient reconstruction approach, based on the Point matching Method of Moments (MoM) is described and evaluated. In chapter 4, the Method of Moment presented in chapter 3, is combined with a Sparse Bayesian Learning approach to enhance robustness to the inverse problem, and evaluated in dynamic thoracic imaging. Chapter 5 includes an extensive description of the state-of-the-art methodologies and topologies used in existing EIT hardware systems, either generic or application targeted. Chapter 6 presents a hardware simulation interface, which targets to the estimation of hardware's configurations impact on the signal and imaging performance. Chapter 7 includes content from 3 research works related with miscellaneous modeling and simulation approaches, applications and considerations.

In chapter 8, the conclusions of the conducted research are written. Finally, the appendices provide the mathematical proofs as well as basic parts of the code used for the result extraction.

2 Image Reconstruction Approaches in Electrical Impedance Tomography

This chapter performs an extensive description of the EIT mathematical formulation, as well as the existing methods that treat the forward and the inverse reconstruction problem.

2.1 The EIT Problem

Assume a 2 or 3-dimensional compact, Lipschitz domain Ω, where the image reconstruction takes place. The boundary is attached with a number of N electrodes e_n, $n = \{1, ..., N\}$, and an alternating current I is source and sinked via a pair of electrodes e_k and e_l respectively. According to the Maxwell's electrostatic theory, the voltage $u \subseteq H^1(\Omega)$ satisfies the Laplace equation:

$$\nabla \left(\gamma(\boldsymbol{r})\nabla u(\boldsymbol{r})\right) = 0, \qquad \boldsymbol{r} \in \Omega \tag{2.1}$$

where $\gamma(\boldsymbol{r}) \in C^1$ is the domain's permittivity distribution. In the literature, instead of the permittivity γ, only the conductivity σ is often considered, and (2.1) is written accordingly:

$$\nabla \left(\sigma(\boldsymbol{r})\nabla u(\boldsymbol{r})\right) = 0, \qquad \boldsymbol{r} \in \Omega \tag{2.2}$$

The exact form of the Neumann boundary conditions that formulate the problem (2.1) or (2.2) depend on the electrode model adopted.

2.1.1 Electrode Models

A brief description of the electrode models [22], [23] that define the boundary conditions for the Laplace-Neumann EIT problem is performed.

Point Electrode Model (PEM)

This is the simplest electrode model, which assumes dimensionless electrodes, expressed with dirac delta functions. It is described by the following boundary condition [24]:

$$\boldsymbol{n} \cdot \sigma(\boldsymbol{r})\nabla u(\boldsymbol{r}) = \Sigma_{l=1}^{N} I_l \delta(\boldsymbol{r} - \boldsymbol{e_l}), \qquad \boldsymbol{r} \in \partial\Omega \tag{2.3}$$

where $\boldsymbol{n}$ is the normalized outward pointing vector, I^l is the total current injected (sourced or sinked) for the l^{th} electrode and $\boldsymbol{e_l}$ is the position vector of the l^{th} electrode.

Continuum (Gap) Model

Assume a current injecting electrode e_k, of an area A, located at an angle $k\theta = 2\pi/(N-1)$. Then, the current density on the electrode is given by [22]:

$$j^k(\theta) = \frac{5\cos(k\theta)}{A} \tag{2.4}$$

and the Neumann boundary condition which is applied in (2.2) is [22]:

$$\sigma(\boldsymbol{r})\frac{\partial u(\boldsymbol{r})}{\partial \boldsymbol{n}} = j^k(\theta), \qquad \boldsymbol{r} \in \partial\Omega \tag{2.5}$$

The GAP model was firstly researched for the circular domain case, where $\boldsymbol{r} = (r, \theta)$, but since then it has been extended to non-canonical geometry domains [25].

Discretization Effect

This model assumes the same boundary conditions as the GAP one, however the angle of each injecting electrode k ranges between a $\theta - \Delta\theta/2$ and a $\theta + \Delta\theta/2$ value. In the recent literature, the GAP model often includes the discretization effect.

Perfectly Conducting (No Contact Impedance-Pure Shunting)

This model assumes the following boundary conditions:

$$\sigma(\boldsymbol{r})\frac{\partial u(\boldsymbol{r})}{\partial \boldsymbol{n}} = 0, \quad \boldsymbol{r} \in \partial\Omega \backslash \bigcup_{l=1}^{N} e_l \tag{2.6}$$

and

$$\int_{e_l} \sigma(\boldsymbol{r})\frac{\partial u(\boldsymbol{r})}{\partial \boldsymbol{n}} dS = I_l, \quad l = 1, ..., N \tag{2.7}$$

It assumes that each electrode is a perfect conductor with zero contact impedance.

Complete Electrode Model (CEM)

This model accounts for the electrode's dimensions, shunt effect and conduct impedances. It implies the following boundary conditions [23]:

$$u(\boldsymbol{r}) + z_l \sigma(\boldsymbol{r}) \frac{\partial u(\boldsymbol{r})}{\partial \boldsymbol{n}} = U_l, \quad \boldsymbol{r} \in e_l,\ l = 1, ..., N \tag{2.8}$$

$$\int_{e_l} \sigma(\boldsymbol{r}) \frac{\partial u(\boldsymbol{r})}{\partial \boldsymbol{n}} dS = I_l, \quad l = 1, ..., N \tag{2.9}$$

$$\sigma(\boldsymbol{r}) \frac{\partial u(\boldsymbol{r})}{\partial \boldsymbol{n}} = 0, \quad \boldsymbol{r} \in \partial\Omega \backslash \bigcup_{l=1}^{N} e_l \tag{2.10}$$

where z_l refers to the l^{th} electrode's contact impedance and U_l to the l^{th} electrode's voltage. It is known to be the most accurate model, which is essential to be applied in voltage measurement simulation cases or in cases when the distance between the electrodes is comparable with their dimensions.

The EIT problem poses that for known boundary measurements and from (2.2) and the boundary conditions, the Ω domain's conductivity σ (or admittance γ) distribution has to be found. The problem is divided in two main stages: the *forward problem* and the *inverse* one. Briefly, the forward problem assumes a known conductivity distribution and the electric potential and field distributions are computed from the Laplace Neumann equations in Ω. In the inverse problem, it is assumed that the potential and field distributions in Ω are known, while we have to solve for the conductivity distribution.

2.1.2 EIT measurement patterns

Although different types of measuring techniques have been developed, the most conventionally used is the current skip-m, voltage skip-n protocol [26]. In a N-electrode EIT system, a bipolar AC current source is applied to two electrodes with a gap of m electrodes between them, while differential voltages are acquired from two other electrodes, at a distance of n electrodes between each other (tetrapolar measurement). After the voltage measurements are taken, the bipolar source is shifted to the next electrode pair and potentials are collected in a serial or parallel way. The process described above continues for all N current electrode pairs and is briefly demontrated in Fig. 2.1.

For each current electrode pair injection, $h = N - 3$ voltage measurements are acquired when $m = n$ or $h = N - 4$, in case $m \neq n$. Therefore, for all current source positions, a total number of $N \cdot h$ voltage measurements is taken, which together create a single EIT measurement frame and are utilized in order to extract a static image through an inverse reconstruction algorithm.

In the special case that $m = 0$ and $n = 0$, the pattern is known as "adjacent" or "pairwise" [27], [28], which is the first adopted and still widely used in practice, due to its relatively simple implementation and that it provides a relatively high number of independent measurements ($N(N-3)/2$). Another non-skip type widely applicable current pattern is the trigonometric one [29], [30]. However, it has been shown that the adjacent current pattern better tolerates any modeling errors [31]. Another study in 2005, showed that the trigonometric current pattern belongs to a set of optimal current patterns that reduce the total variance of the estimation for the resistance or conductance matrix [32].

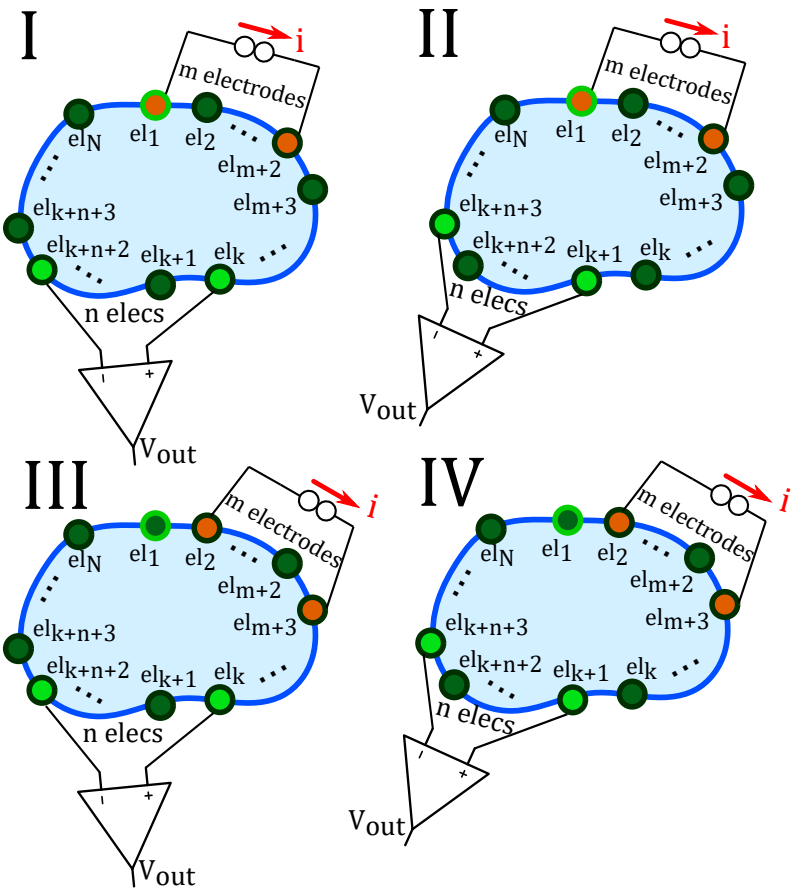

Figure 2.1: Explanatory schematic of the current skip-m, voltage skip-n pattern. I: 1st current injection, voltage measurement between the k-th and $(k+n+2)$-th electrodes (leaving a gap of n electrodes). II: Same current injection and next voltage measurement (between the $(k+1)$-th and $(k+n+3)$-th electrodes). III: Next current injection (source on 2nd and $(m+3)$-th electrodes), voltage measurement between the k-th and $(k+n+2)$-th electrodes. IV: Same current injection, next voltage measurement (between the $(k+1)$-th and $(k+n+3)$-th electrodes).

2.2 The Finite Element Method (FEM)

For canonical geometries and when applying the Point Electrode Model (PEM), the problem sometimes can stand an analytical solution. However, in most cases the geometry of Ω is non-regular and proper discretization is required to treat the problem. The finite element method (FEM) is one of the most popular discretization techniques for solving partial differential equation (PDE) problems, widely applied in solid and fluid mechanics and electromagnetic fields. FEM is also very popular in EIT since it is used in the strong majority of the EIT literature. The two discretization formulations implied by the FEM is the Galerkin and the Riesz method.

The Galerkin method assumes a weak problem formulation. In our case, we assume that the domain Ω is properly discretized into a number of L elements and N_e vertices (nodes). Furthermore, let us assume u_h as the weak solution of the forward problem defined above. We expand it at an orthonormal basis

functions scheme:

$$u_h = \Sigma_{i=1}^{N_e} u_i \phi_i \tag{2.11}$$

where u_i is the potential on the i^{th} node (weight coefficient) and ϕ_i are polynomial basis functions, that satisfy the following condition:

$$\phi_i(\boldsymbol{r}) = \left\{ \begin{array}{ll} 1, & \text{if } \boldsymbol{r} \text{ on } i \text{ node} \\ 0, & \text{if } \boldsymbol{r} \text{ not on } i \text{ node} \end{array} \right\}.$$

The most simple and usual case is to use piecewise linear basis function for the potential [33], [34]. In a similar manner, the conductivity is usually expressed with piecewise constant basis functions on the elements:

$$\psi_e(\boldsymbol{r}) = \left\{ \begin{array}{ll} 1, & \text{if } \boldsymbol{r} \text{ on } e \text{ element} \\ 0, & \text{if } \boldsymbol{r} \text{ not on } e \text{ element} \end{array} \right\}.$$

Calderon (1980) [35] showed that a proper integral equation weak form of the problem (2.2) is the following:

$$\int_{\Omega_e} \left(\sigma(\boldsymbol{r}) \left\| \nabla u(\boldsymbol{r}) \right\|^2 \right) dA = 0, \qquad \boldsymbol{r} \in \Omega \tag{2.12}$$

where Ω_e is the e^{th} element domain.

Using the Green's second identity, expanding u according to (2.11) and applying the CEM boundary conditions (2.8) we get:

$$\iint_{\Omega_e} \psi_e \left(u_j \frac{\partial \phi_i}{\partial x} \frac{\partial \phi_j}{\partial x} + u_j \frac{\partial \phi_i}{\partial y} \frac{\partial \phi_j}{\partial y} \right) dA = \oint_{\partial \Omega_e} \phi_i \frac{1}{z_l} \left(u_j \phi_j - U_l \right) dS \tag{2.13}$$

in case Ω is two-dimensional. The formulation is similar for the three-dimensional case.

To numerically solve the forward problem, we set the following matrices [36], [37]:

$$A_m(i,j) = \iint_{\Omega_e} \psi_e \left(u_j \frac{\partial \phi_i}{\partial x} \frac{\partial \phi_j}{\partial x} + u_j \frac{\partial \phi_i}{\partial y} \frac{\partial \phi_j}{\partial y} \right) dA, \tag{2.14}$$

$$A_z(i,j) = \oint_{\partial \Omega_e} \frac{1}{z_l} \phi_i \phi_j dS, \tag{2.15}$$

$$A_u(i,j) = - \oint_{\partial \Omega_e} \frac{1}{z_l} \phi_i dS, \tag{2.16}$$

$$A_D(i,j) = \left\{ \begin{array}{ll} \left(\frac{1}{z_l} \right)_j |E_l|, & \text{if } i = j \\ 0, & \text{otherwise} \end{array} \right\} \tag{2.17}$$

for $i, j = \{1, ..., L\}$ ($|E_l|$ refers to the l^th electrode's surface area) and

$$I_l = \frac{1}{z_l}|E_l|U_l - \sum_{l=1}^{N} \frac{1}{z_l} u_j \oint_{\partial\Omega_e} \phi_j dS \tag{2.18}$$

Then, the following linear equation system is constructed:

$$\begin{bmatrix} \boldsymbol{A_m} + \boldsymbol{A_z} & \boldsymbol{A_v} \\ \boldsymbol{A_v^*} & \boldsymbol{A_D} \end{bmatrix} \begin{bmatrix} \boldsymbol{u} \\ \boldsymbol{U} \end{bmatrix} = \begin{bmatrix} \boldsymbol{0} \\ \boldsymbol{I^d} \end{bmatrix} \tag{2.19}$$

where $\boldsymbol{u} = [u_i]_{i=1}^{N_e}$, $\boldsymbol{U} = [U_l]_{l=1}^{N}$ and I^d is finite set of current patterns (see 2.1.2, 3.1.5 and [26] for further information on the current patterns).

Eq. (6.9) demonstrates the forward problem in numerical form, which, has to be solved for all the possible current electrode pairs according to the particular current pattern used.

Instead of the conventional high-complexity cost Gauss method, the system is resolved with iterative numerical methods. In the past, the Cholesky method was used to treat this problem [36], [38]. However, the Conjugate-Gradient (CG) method is mostly used in recent applications [38]. In addition, in order to further reduce the complexity cost, the system matrix in (6.9) is often re-assembled in a sparse form.

As mentioned, for the voltage representation, the most usual case is to use piecewise linear base functions. Increasing the basis function polynomial order leads to better accuracy at an extra computational cost [39].

Furthermore, it is also worth to mention that apart from the FEM, another popular discretization method is the iterative Boundary Element Method (BEM). BEM solves the problem by discretizing the boundary, singnificantly reducing ill-posedness [40], [41], [42]. However, BEM does not always apply to non-linear problems, employing non-symmetric and inhomogeneous forward operators [43].

2.3 Formulation of the Sensitivity Matrix

Calderon (1980) [35] and later research works [44], [45], [46] have shown that the conductivity is uniquely determined by the complete knowledge of the Dirichlet-to-Neumann (DL) map on bounded domains. The operator which maps to conductivity σ to the boundary (electrode) voltages U_l is actually non-linear. However when the problem is in weak form, and assuming small conductivity perturbations $\delta\sigma = \sigma - \sigma_o$ around a reference conductivity σ_o, the expression is written as follows [37]:

$$\delta U_{dm} = -\int_{\Omega} \delta\sigma \nabla u(I^d) \cdot \nabla u(I^m) dA \tag{2.20}$$

where δU_{dm} is the calculated voltage between two electrodes when a small $\delta\sigma$ conductivity change occurs and $\Omega \subset \mathbb{R}^n$, $n \in \{2, 3\}$ is a two or three-dimensional domain of interest. Furthermore, $\nabla u(I^d)$ and $\nabla u(I^m)$ are the calculated electric fields due to the lead (d^{th} pair) and the measurement (m^{th} current injection pair) electrodes respectively [37].

From this point, we assume that conductivity is a discrete vector $\boldsymbol{\sigma} = [\sigma_i]_{i=1}^{L}$, representing the constant conductivity values on the set of elements that comprise the reconstruction domain Ω. Assume a

non-linear operator $F(\boldsymbol{\sigma}) : \boldsymbol{\delta\sigma} \rightarrow \boldsymbol{\delta U}$, which maps the conductivity (or admittance) distribution perturbations to the electrode (boundary) voltages. In principle, the Jacobian matrix is the (first) discrete Frechet derivative of the non-linear operator $F(\boldsymbol{\sigma})$ with respect to the perturbations $\boldsymbol{\delta\sigma}$. For a particular lead d and measurement m electrode pair, as well as a particular element i, the Jacobian matrix is computed as follows [37]:

$$J^i_{dm} = \frac{\partial \delta U_{dm}}{\partial \delta \sigma_i} = -\int_{\Omega_i} \nabla u(I^d) \cdot \nabla u(I^m) dA \tag{2.21}$$

around a reference conductivity σ_o. The problem is then linearized around σ_o as follows:

$$\boldsymbol{\delta U} = \frac{\partial \boldsymbol{\delta U}}{\partial \boldsymbol{\delta\sigma}}\Big|_{\boldsymbol{\sigma_o}} \boldsymbol{\delta\sigma} + \mathcal{O}(\|\boldsymbol{\delta\sigma}\|^2) \simeq \boldsymbol{J\delta\sigma} \tag{2.22}$$

where $\boldsymbol{J} \in \mathbb{R}^{M\times L}$ is the Jacobian matrix and M the total number of measurements (depended on the electrodes number N and the measurement pattern). In earlier years, the perturbation method was used to be popular for the Jacobian matrix computation [47], [48]. However, in more recent research and applications the adjoint method is preferred [37].

The Jacobian matrix is also called sensitivity matrix and actually demonstrates the influence of each local conductivity perturbation to the electrode voltages measured. In the case the F.E.M. mesh grid is non-uniform, the following normalization is needed to estimate the total sensitivity S_i of voltage data to conductivity changes in each element i:

$$S_i = \frac{1}{A_i}\sqrt{\sum_{j=1}^{Nh} J^2_{j,i}} \tag{2.23}$$

where A_i is the i^{th} element's area or volume.

Fig. 2.2 demonstrates the voltage measurement sensitivity when acting the adjacent current and voltage pattern at a simple circular domain, attached from 16 electrodes. The domain is discretized into $L = 1215$ triangular elements and $N_e = 663$ nodes. As shown, the sensitivity is higher near the current injecting pair (electrodes 1-2) while it decreases as the distance from the current electrodes is increased.

From the sensitivity matrix behavior it is obvious that internal conductivity perturbations that are relatively far from the boundary electrodes do not cause significant changes to the boundary voltages. In actual, this is caused by the fact that EIT is a current diffusion problem; the current is dense only near the injecting electrodes, while current density drops significantly while distance from them increases. This is called "soft-field" effect.

The above observations demonstrate the weakness of EIT in detecting small conductivity perturbations near the examined medium's center. The change in boundary measurements is weak, and ofter even smaller than the signal noise. This outcomes the importance of minimizing EIT signal noise. In other words, the more the signal noise is, the less measurements (from a set of Nh measurements) provide valuable information about the conductivity distribution. In mathematical terms, the so called "soft-field" effect means that the Jacobian system matrix is singular. Its determinant reaches almost zero, i.e. the larger singular values of $\boldsymbol{J}$ are many orders of magnitude higher than the lower ones (see Fig. 2.3). It is finally

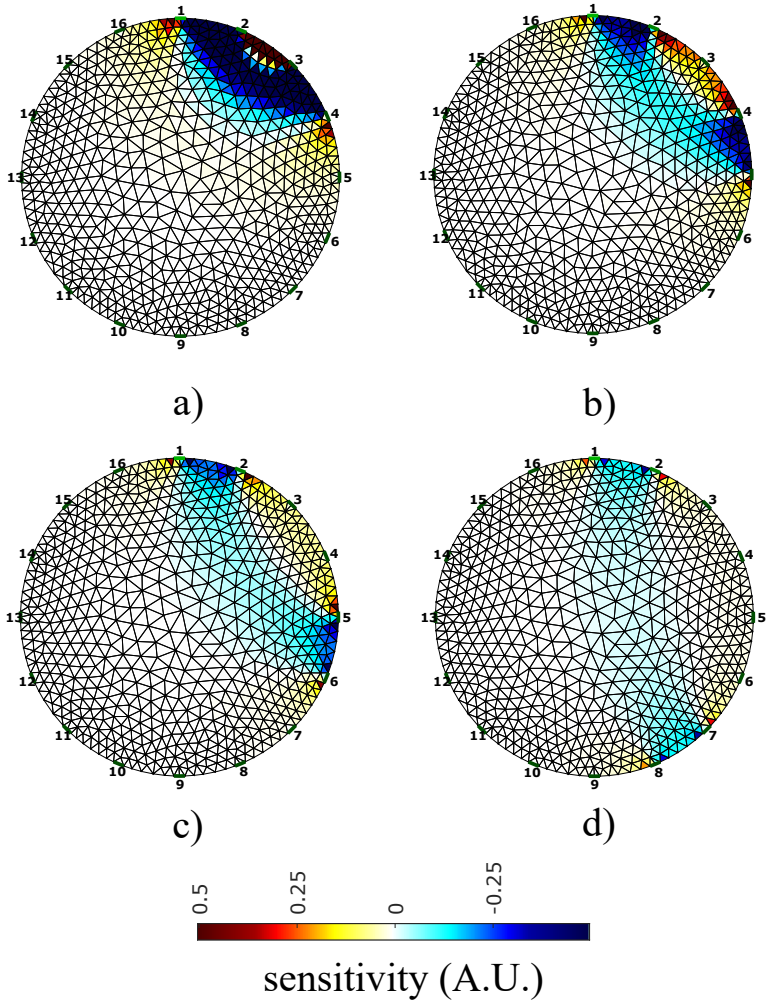

Figure 2.2: EIT field sensitivity when current is injected from the 1^{st} and the 2^{nd} electrodes in a circular 16-electrode domain (adjacent current pattern). a)Voltage measurement between the 3^{rd} and the 4^{th} electrode. b) Voltage measurement between the 4^{th} and the 5^{th} electrode. c) Voltage measurement between the 5^{th} and the 6^{th} electrode. d) Voltage measurement between the 7^{th} and the 8^{th} electrode.

worth to mention that the singular value behavior is moderately affected from the current-voltage pattern selection.

The treatment of Jacobian matrix singularity as well as the non-linear problem of revealing the conductivity distribution are parts of the *inverse problem*, described in the next subsection.

2.4 Inverse Problem

The inverse problem is defined by the process of finding the conductivity distribution that corresponds to a specific boundary voltage (measurement) set. Thus, a trivial form of the inverse problem would be the following Least Squares (LS) Problem:

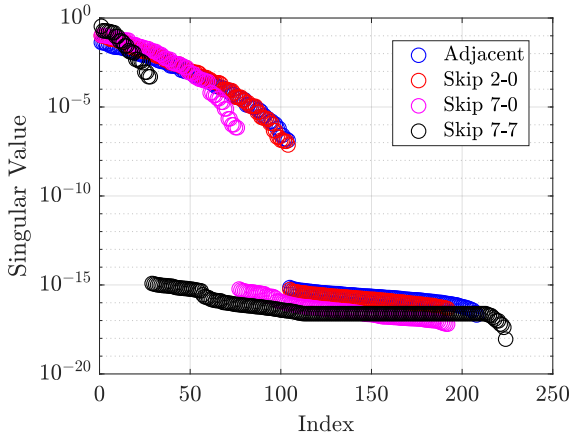

Figure 2.3: Current-Voltage measurement pattern influence on the Jacobian matrix singular value spectrum of a 16-electrode circular domain EIT setup for adjacent current and voltage pattern, skip-2 current pattern with adjacent voltage measurement, opposite current pattern with adjacent voltage measurement and opposite current pattern with opposite voltage measurement.

$$\boldsymbol{\sigma}_* = \underset{\boldsymbol{\sigma}\in\mathbb{R}^L}{\operatorname{argmin}} \Big\{ \|\boldsymbol{U}(\boldsymbol{\sigma}) - \boldsymbol{V}\|^2 \Big\} \tag{2.24}$$

If difference (time or frequency) EIT (td-EIT or fd-EIT respectively), (2.24) is written as follows:

$$\boldsymbol{\delta\sigma}_* = \underset{\boldsymbol{\delta\sigma}\in\mathbb{R}^L}{\operatorname{argmin}} \Big\{ \|\boldsymbol{\delta U}(\boldsymbol{\delta\sigma}) - \boldsymbol{\delta V}\|^2 \Big\} \tag{2.25}$$

For sake of simplicity, in this particular section we will use the variables $\boldsymbol{\sigma}$, $\boldsymbol{U}$ and $\boldsymbol{V}$ either for absolute or difference EIT.

Following the previously defined linearization $\boldsymbol{U} \simeq \boldsymbol{J\sigma}$ in order to treat the non-linear dependence of $\boldsymbol{U}$ from $\boldsymbol{\sigma}$, (2.24) takes the form of a simple linear equation system:

$$\boldsymbol{J\sigma} = \boldsymbol{V} \tag{2.26}$$

Since $\boldsymbol{J} \in \mathbb{R}^{Nh\times 1}$, $\boldsymbol{\sigma} \in \mathbb{R}^{L\times 1}$ and usually $L >> Nh$, the problem is ill-posed. It would be trivial to treat the problem as follows:

$$\boldsymbol{J^T J\sigma} = \boldsymbol{J^T V} \tag{2.27}$$

and hence to invert $\boldsymbol{J^T J}$. However, due to the soft-field effect, as described in the previous subsection, $\boldsymbol{J}$ is almost singular and therefore $\boldsymbol{J^T J}$ cannot be inverted.

In the earlier years, some X-ray, CT and ultrasound tomography reconstruction imaging techniques, such as the back-projection (BP) [49], [50] and the algebraic reconstruction technique (ART) method [51], [52], were applied to treat the EIT inverse problem. The truncated Singular Value Decomposition (TSVD), which performs SVD to the linearized Jacobian matrix $\boldsymbol{J}$ sets a threshold to keep the higher (most significant) singular values was also a dominant method during 90s [53], [54].

2.5 Regularization Approaches

From the mid-90s, regularization techniques began to gain popularity, and remain one of the most popular methods for EIT image reconstruction till nowadays. Many regularization techniques have been proposed and combined over these years. Among them, the main concept is to stabilize the LS (fidelity) term in (2.27) by adding a regularization term $P(\boldsymbol{\sigma})$ to the objective function [54]:

$$\boldsymbol{\sigma}_* = \underset{\boldsymbol{\sigma}\in\mathbb{R}^L}{\operatorname{argmin}}\Big\{ \|\boldsymbol{U}(\boldsymbol{\sigma}) - \boldsymbol{V}\|^2_{\boldsymbol{W}} + \lambda^2 P(\boldsymbol{\sigma})\Big\} \tag{2.28}$$

where $\boldsymbol{W} \in \mathbb{R}^{Nh\times Nh}$ is diagonal, noise covariance matrix and λ the regularization hyperparameter which balances the problem between overfitting and underfitting.

2.5.1 Tikhonov Regularization

The most straightforward way to solve this problem to linearize it near the reference σ_o and act standard Tikhonov regularization (STD), [54], by setting $P(\boldsymbol{\sigma}) = \|\boldsymbol{\sigma}\|_2^2$:

$$\boldsymbol{\sigma}_* = \underset{\boldsymbol{\sigma}\in\mathbb{R}^L}{\operatorname{argmin}}\Big\{ \|\boldsymbol{J\sigma} - \boldsymbol{V}\|^2_{\boldsymbol{W}} + \lambda^2 \|\boldsymbol{\sigma}\|_2^2 \Big\} \tag{2.29}$$

The single step solution is acquired from the following expression:

$$\boldsymbol{\sigma_*} = \boldsymbol{\sigma_o} + \Big(\boldsymbol{J^T W J} + \lambda^2 \boldsymbol{I}_{L\times L}\Big)^{-1} \boldsymbol{J^T W V} \tag{2.30}$$

where $\boldsymbol{I}$ is the identity matrix and $\boldsymbol{\sigma_o} = [\sigma_o, ..., \sigma_o]^T \in \mathbb{R}^{L\times 1}$. In the case of difference EIT, the term $\boldsymbol{\sigma_o}$ is neglected. In practical terms, the STR increases the $\boldsymbol{J^T J}$ main diagonal terms in order to deal with the system matrix singularity. It assumes that all the elements conductivity values follow a uniform behavior, without actually adding any specific prior information. Such information is implied by using the generalized Tikhonov regularization (GTR), where we set a prior filter matrix $\boldsymbol{Q} \in \mathbb{R}^{L\times L}$ the to regularization term:

$$\boldsymbol{\sigma}_* = \underset{\boldsymbol{\sigma}\in\mathbb{R}^L}{\operatorname{argmin}}\Big\{ \|\boldsymbol{J\sigma} - \boldsymbol{V}\|^2_{\boldsymbol{W}} + \lambda^2 \|\boldsymbol{\sigma}\|^2_{\boldsymbol{Q}} \Big\}. \tag{2.31}$$

The linearized (single-step) solution is:

$$\boldsymbol{\sigma_*} = \boldsymbol{\sigma_o} + \Big(\boldsymbol{J^T W J} + \lambda^2 \boldsymbol{Q}\Big)^{-1} \boldsymbol{J^T W V} \tag{2.32}$$

The $\boldsymbol{Q}$ matrix can be either implemented as a discrete Laplace, a NOSER ($\boldsymbol{Q} = \operatorname{diag}(\boldsymbol{J^T J})$) or a Gaussian discrete filter [30], [54], [55]. The STR and GTR (Tikhonov) regularization techniques are characterized by the use of L^2-norm priors for the term $P(\boldsymbol{\sigma})$.

Since the EIT reconstruction problem is non-linear, the system sensitivity (Jacobian) matrix $\boldsymbol{J}$ just assists in the approximation demonstrated in (2.22). This approximation holds for small $\boldsymbol{\delta\sigma}$ perturbations

around σ_o. However, in many practical applications such an assumption does not often hold. Therefore, in such cases, the minimization problem (2.28) needs to be treated iteratively. In particular, in each step, the $\boldsymbol{J}$ matrix is computed according to a previous $\boldsymbol{\sigma}$ estimation. Then, a new estimation of $\boldsymbol{\sigma}$ is performed by solving (2.31) via the iterative Gauss-Newton (GN or Newton-Raphson) formula [4]:

$$\boldsymbol{\sigma}^{\kappa+1} = \boldsymbol{\sigma}^{\kappa} + \alpha\Big((\boldsymbol{J}^{\boldsymbol{\kappa}})^T \boldsymbol{W} \boldsymbol{J}^{\boldsymbol{\kappa}} + \lambda^2 \boldsymbol{Q}\Big)^{-1}\Big((\boldsymbol{J}^{\boldsymbol{\kappa}})^T \boldsymbol{W}\big(\boldsymbol{V} - \boldsymbol{U}(\boldsymbol{\sigma}^{\kappa})\big) + \lambda^2 \boldsymbol{Q}(\boldsymbol{\sigma_o} - \boldsymbol{\sigma}^{\kappa})\Big) \tag{2.33}$$

where $\boldsymbol{\sigma}^{\kappa}$ is the estimated conductivity (or conductivity change if difference EIT is applied) from the previous iteration, $\boldsymbol{\sigma}^{\kappa+1}$ is the new conductivity estimation and $\alpha > 0$ is a step estimated via linesearch in order to that the objective function is properly minimized [4].

An alternative approach to iterative (non-linear) GN, is the Levenberg–Marquardt method, [56], [57], where the conductivity update is given from the following formula [58]:

$$\boldsymbol{\sigma}^{\kappa+1} = \boldsymbol{\sigma}^{\kappa} + \Big((\boldsymbol{J}^{\boldsymbol{\kappa}})^T \boldsymbol{W} \boldsymbol{J}^{\boldsymbol{\kappa}} + \lambda_{\kappa}^2 \boldsymbol{I}_{L\times L}\Big)^{-1}\Big((\boldsymbol{J}^{\boldsymbol{\kappa}})^T \boldsymbol{W}\big(\boldsymbol{V} - \boldsymbol{U}(\boldsymbol{\sigma}^{\kappa})\big) + \lambda_{\kappa}^2 \boldsymbol{I}_{L\times L}(\boldsymbol{\sigma_o} - \boldsymbol{\sigma}^{\kappa})\Big) \tag{2.34}$$

while, contrary to the GN method, the hyperparameter λ (which here has the damping factor's role) is updated on each iteration as follows:

$$\lambda_{\kappa+1} = A_{\kappa}\lambda_0 \tag{2.35}$$

where λ_0 is the initial hyperparameter choice and $A_{\kappa} > 0$ a properly selected coefficient such as (2.31) is minimized.

2.5.2 Total Variation Regularization

The GTR techniques might be a good choice for conductivity distribution imaging in the case that change between neighboring pixels'/elements' conductivity is non-significant. However, since GTR tends to smooth the solution, it might result in poor performance in capturing steep conductivity changes. To overcome this possible issue, L^1-norm regularization techniques (also called as Total Variation-TV) are implied to the EIT inverse problem. The objective function takes the following general form:

$$\boldsymbol{\sigma}_* = \underset{\boldsymbol{\sigma}\in\mathbb{R}^L}{\operatorname{argmin}}\Big\{ \|\boldsymbol{U}(\boldsymbol{\sigma}) - \boldsymbol{V}\|_{\boldsymbol{W}}^2 + \lambda^2 \|\boldsymbol{\sigma}\|_1 \Big\}. \tag{2.36}$$

The regularization term is written as:

$$P_{TV}(\boldsymbol{\sigma}) = \sum_{i=1}^{N_{ed}} \sqrt{\|\boldsymbol{L_i}\boldsymbol{\sigma}\|^2 + \beta} \tag{2.37}$$

where N_{ed} is the total number of the edges between the reconstruction domain's elements, $\boldsymbol{L_i}$ denotes the i^{th} line of the $\boldsymbol{L}$ matrix which quantifies the relation between the elements and their edges. Furthermore, $\beta > 0$ is a term that prevents the TV term from reaching zero and become non-differentiable. The optimization problem defined from (2.36) and (2.37) is non-linear, and, contrary to the L^2-norm

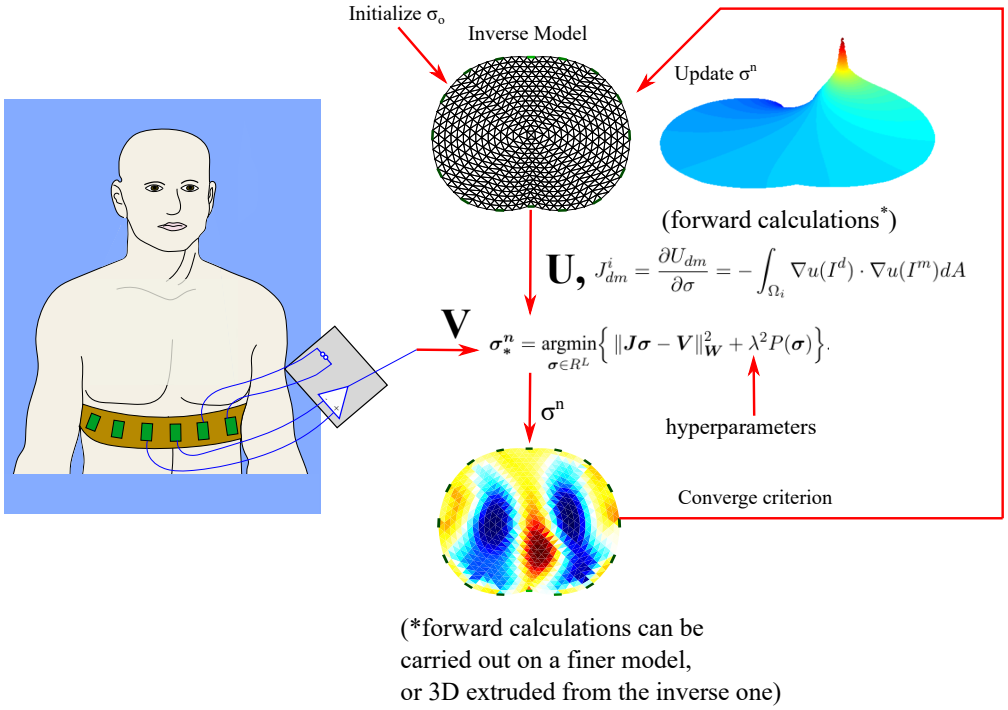

Figure 2.4: Simplified illustration of the EIT forward and inverse problem procedure.

regularization cases, it does not have a closed-form solution. To solve the TV problem, some particular approaches have been proposed in the literature [4], [59], [60], [61]. The most well-known ones are the Primal-Dual Interior Point (PD-IPM) [60] and the split-Bregman distance TV [61], [62], [63]. Another popular TV method is also the ADMM, [61], [64], which applies an augmented Lagrangian function to the regularization term.

Primal-Dual Interior Point (PD-IPM)

The PD-IPM method is based on the primal-dual theory [65], introducing a dual variable $\boldsymbol{\chi} \in \mathbb{R}^{N_{ed}\times 1}$ to the primal TV problem according to the Cauchy–Schwartz inequality [61]. The problem is solved using the multi-variable GN method, with the following updates per iteration:

$$\begin{aligned}\boldsymbol{\delta\sigma^{\kappa}} &= \left((\boldsymbol{J^{\kappa}})^T\boldsymbol{W}\boldsymbol{J^{\kappa}} + \lambda^2\boldsymbol{L^T}\left(\boldsymbol{E^{\kappa}}\right)^{-1}\boldsymbol{K^{\kappa}}\boldsymbol{L}\right)^{-1}\cdot \\ &\quad \left((\boldsymbol{J^{\kappa}})^T\boldsymbol{W}\left(\boldsymbol{V}-\boldsymbol{U}(\boldsymbol{\sigma^{\kappa}})\right) - \lambda^2\boldsymbol{L^T}\left(\boldsymbol{E^{\kappa}}\right)^{-1}\boldsymbol{L\sigma^{\kappa}}\right), \\ \boldsymbol{\delta\chi^{\kappa}} &= -\boldsymbol{\chi^{\kappa}} + \left(\boldsymbol{E^{\kappa}}\right)^{-1}\boldsymbol{L\sigma^{\kappa}} + \left(\boldsymbol{E^{\kappa}}\right)^{-1}\boldsymbol{K^{\kappa}}\boldsymbol{L\delta\sigma^{\kappa}}\end{aligned} \tag{2.38}$$

where

$$\begin{aligned} \boldsymbol{E}^{\boldsymbol{\kappa}} &= \operatorname{diag}\Big(\Big[\sqrt{\|\boldsymbol{L_i}\boldsymbol{\sigma}^{\boldsymbol{\kappa}}\|^2+\beta}\Big]_{i=1}^{N_{ed}}\Big), \\ \boldsymbol{K}^{\boldsymbol{\kappa}} &= \operatorname{diag}\left(\left[1-\frac{\boldsymbol{\chi_i}\boldsymbol{L_i}\boldsymbol{\sigma}^{\boldsymbol{\kappa}}}{\sqrt{\|\boldsymbol{L_i}\boldsymbol{\sigma}^{\boldsymbol{\kappa}}\|^2+\beta}}\right]_{i=1}^{N_{ed}}\right) \end{aligned} \tag{2.39}$$

then we get the new primal and dual variables' values as follows:

$$\boldsymbol{\sigma}^{\boldsymbol{\kappa+1}} = \boldsymbol{\sigma}^{\boldsymbol{\kappa}} + \alpha_1 \boldsymbol{\delta\sigma}^{\boldsymbol{\kappa}} \tag{2.40}$$

and

$$\boldsymbol{\chi}^{\boldsymbol{\kappa+1}} = \boldsymbol{\chi}^{\boldsymbol{\kappa}} + \alpha_2 \boldsymbol{\delta\chi}^{\boldsymbol{\kappa}} \tag{2.41}$$

respectively, where $a_1 > 0$ can be found via linesearch and $a_2 > 0$ can be found via the scaling rule [4]. The conductivity is initialized to a homogeneous or a-priori known distribution, while the dual variable $\boldsymbol{\chi}$ can be initialized to a zero vector.

It is important to note that choice of β value is crucial for the problem's behavior. A small β may cause divergence and non-differentiability of the objective function (2.36), while a large β leads to a smooth solution and decreased convergence speed.

Split Bregman Distance

This method makes use of an auxiliary variable $\boldsymbol{d}$ and the Bregman distance definition [66]. The general form of the objective function, where both $\boldsymbol{\sigma}$ and $\boldsymbol{d}$ have to be estimated, is the following:

$$(\boldsymbol{\sigma}_*, \boldsymbol{d}_*) = \underset{\boldsymbol{\sigma}\in\mathbb{R}^L, \boldsymbol{d}\in\mathbb{R}^L}{\operatorname{argmin}} \Big\{ \|\boldsymbol{U}(\boldsymbol{\sigma}) - \boldsymbol{V}\|_{\boldsymbol{W}}^2 + \lambda_1^2 \|\boldsymbol{\sigma} - \boldsymbol{d}\|_{\boldsymbol{Q}}^2 + \lambda_2^2 \|\boldsymbol{d}\|_1 \Big\}. \tag{2.42}$$

The problem is split in two minimization problems for $\boldsymbol{\sigma}$ and $\boldsymbol{d}$, respectively and each iteration κ as follows:

$$\boldsymbol{\sigma}_*^{\boldsymbol{\kappa}} = \underset{\boldsymbol{\sigma}\in\mathbb{R}^L, \boldsymbol{d}\in\mathbb{R}^L}{\operatorname{argmin}} \Big\{ \big\|\boldsymbol{J}^{\boldsymbol{\kappa-1}}\boldsymbol{\sigma} - \boldsymbol{V}\big\|_{\boldsymbol{W}}^2 + \lambda_1^2 \big\|\boldsymbol{\sigma} - \boldsymbol{d}^{\boldsymbol{\kappa-1}}\big\|_{\boldsymbol{Q}}^2 \Big\} \tag{2.43}$$

and

$$\boldsymbol{d}_*^{\boldsymbol{\kappa}} = \underset{\boldsymbol{d}\in\mathbb{R}^L}{\operatorname{argmin}} \Big\{ \|\boldsymbol{\sigma}^{\boldsymbol{\kappa}} - \boldsymbol{d}\|_{\boldsymbol{Q}}^2 + \lambda_2^2 \|\boldsymbol{d}\|_1 \Big\} \tag{2.44}$$

where $\boldsymbol{d}^{\boldsymbol{\kappa-1}}$ is known from the previous iteration update (or initialization if $\kappa = 1$) and $\boldsymbol{\sigma}^{\boldsymbol{\kappa}}$ which is needed to minimize (2.44) is previously estimated from the minimization problem (2.43).

The first sub-problem (2.33) can be treated using the traditional GN method as follows:

$$\boldsymbol{\sigma}^{\kappa} = \boldsymbol{\sigma}^{\kappa-1} + \alpha\Big((\boldsymbol{J}^{\boldsymbol{\kappa-1}})^T\boldsymbol{W}\boldsymbol{J}^{\boldsymbol{\kappa-1}} + \lambda_1^2\boldsymbol{Q}\Big)^{-1}\Big((\boldsymbol{J}^{\boldsymbol{\kappa-1}})^T\boldsymbol{W}\big(\boldsymbol{V} - \boldsymbol{U}(\boldsymbol{\sigma}^{\kappa-1})\big) + \lambda_1^2\boldsymbol{Q}(\boldsymbol{d}^{\boldsymbol{\kappa-1}} + \boldsymbol{\sigma_o} - \boldsymbol{\sigma}^{\kappa-1})\Big) \tag{2.45}$$

The second sub-problem (2.44), an approach proposed in [63] is to add a field variable $\boldsymbol{w} \in \mathbb{R}^{\boldsymbol{L\times n}}$

(n is the domain's dimensions) through a penalty term as follows:

$$(\boldsymbol{d}_*^{\boldsymbol{\kappa}}, \boldsymbol{w}_*^{\boldsymbol{\kappa}}) = \underset{\boldsymbol{d}\in\mathbb{R}^L, \boldsymbol{w}\in\mathbb{R}^{L\times n}}{\operatorname{argmin}} \Big\{ \|\boldsymbol{\sigma}^{\boldsymbol{\kappa}} - \boldsymbol{d}\|_{\boldsymbol{Q}}^2 + \lambda_2^2 \|\boldsymbol{d}\|_1 + \lambda_3^2 \|\boldsymbol{w} - \nabla \boldsymbol{d}\|_2^2 \Big\}. \tag{2.46}$$

To solve it, a $\boldsymbol{b} \in \mathbb{R}^{L\times n}$ auxiliary variable is also introduced [67], [68], [69] and the problem is treated using the Bregman iteration approach:

$$(\boldsymbol{d}_*^{\boldsymbol{\kappa}}, \boldsymbol{w}_*^{\boldsymbol{\kappa}}) = \underset{\boldsymbol{d}\in\mathbb{R}^L, \boldsymbol{w}\in\mathbb{R}^{L\times n}}{\operatorname{argmin}} \Big\{ \|\boldsymbol{\sigma}^{\boldsymbol{\kappa}} - \boldsymbol{d}\|_{\boldsymbol{Q}}^2 + \lambda_2^2 \|\boldsymbol{d}\|_1 + \lambda_3^2 \left\|\boldsymbol{w} - \nabla \boldsymbol{d} - \boldsymbol{b}^{\boldsymbol{\kappa-1}}\right\|_2^2 \Big\} \tag{2.47}$$

and

$$\boldsymbol{b}^{\boldsymbol{\kappa}} = \boldsymbol{b}^{\boldsymbol{\kappa-1}} + (\nabla \boldsymbol{u}^{\boldsymbol{\kappa}} - \boldsymbol{w}^{\boldsymbol{\kappa}}) \tag{2.48}$$

where initialization is performed as follows $\boldsymbol{b}^{\boldsymbol{0}} = \boldsymbol{0}$.

The problem (2.47), (2.48) can be solved by further splitting the L^2-norm and L^1-norm regularization terms. Therefore, we get the two following corresponding minimization sub-problems:

$$\boldsymbol{d}_*^{\boldsymbol{\kappa}} = \underset{\boldsymbol{d}\in\mathbb{R}^L}{\operatorname{argmin}} \Big\{ \|\boldsymbol{\sigma}^{\boldsymbol{\kappa}} - \boldsymbol{d}\|_{\boldsymbol{Q}}^2 + \lambda_3^2 \left\|\boldsymbol{w}^{\boldsymbol{\kappa-1}} - \nabla \boldsymbol{d} - \boldsymbol{b}^{\boldsymbol{\kappa-1}}\right\|_2^2 \Big\} \tag{2.49}$$

and

$$\boldsymbol{w}_*^{\boldsymbol{\kappa}} = \underset{\boldsymbol{w}\in\mathbb{R}^{L\times n}}{\operatorname{argmin}} \Big\{ \lambda_2^2 \|\boldsymbol{d}^{\boldsymbol{\kappa}}\|_1 + \lambda_3^2 \left\|\boldsymbol{w} - \nabla \boldsymbol{d}^{\boldsymbol{\kappa}} - \boldsymbol{b}^{\boldsymbol{\kappa-1}}\right\|_2^2 \Big\} \tag{2.50}$$

The problem (2.49) has the following closed-form solution:

$$\boldsymbol{d}_*^{\boldsymbol{\kappa}} = (\boldsymbol{Q} - \lambda_3 \boldsymbol{\Delta})^{-1} \left(\boldsymbol{\sigma}^{\boldsymbol{\kappa}} + \lambda_3 \nabla (\boldsymbol{w}^{\boldsymbol{\kappa-1}} - \boldsymbol{b}^{\boldsymbol{\kappa-1}})^T\right) \tag{2.51}$$

where $\boldsymbol{\Delta} = \nabla^2$ is the Laplacian operator.

The problem (2.50) is solved using the shrinkage function [70]:

$$\boldsymbol{w}_*^{\boldsymbol{\kappa}} = \frac{1}{D^{\kappa}} \max\Big\{ D^{\kappa} - \frac{\lambda_2}{2\lambda_3}, 0 \Big\} \cdot \left(\nabla \boldsymbol{d}^{\boldsymbol{\kappa}} + \boldsymbol{b}^{\boldsymbol{\kappa-1}}\right) \tag{2.52}$$

where

$$D^{\kappa} = \left\|\nabla \boldsymbol{d}^{\boldsymbol{\kappa}} + \boldsymbol{b}^{\boldsymbol{\kappa-1}}\right\|_2 \tag{2.53}$$

It has been shown that the split Bregman method provides increased robustness to the reconstruction problem, while there is no need for the parameter β.

2.6 Graz consensus Reconstruction algorithm for EIT (GREIT)

The GREIT approach performs linear EIT reconstruction and is based on a Wiener filter form reconstruction matrix, as well as a number of Figures of Merit (FoM) that are briefly described in chapter 4. The GREIT uses ”training” sets of measurements and conductivity inclusion targets at a fine model, performing the reconstructions at a coarse model. Instead of the regularization hyperparameter λ, the *Noise Figure* (NF), which is used as a FoM, is a-priori set at a desired level. In actual, NF defines the desired spatial resolution, in trade-off with image artefacts. A reconstruction matrix **R** is calculated and used, which minimizes the following quantity

$$F = \sum_{k=1}^{K} ||\tilde{\boldsymbol{x}}^{(\boldsymbol{k})} - \boldsymbol{R}\boldsymbol{y}^{(\boldsymbol{k})}|| \tag{2.54}$$

where K is the total number of training samples, $\tilde{\boldsymbol{x}}^{(\boldsymbol{k})}$ is the ”desired position” of the k^{th} training sample inclusion and $\boldsymbol{y}^{(\boldsymbol{k})}$ is the difference of the measurement frames between the homogeneous and the k^{th} inclusion states. The $\boldsymbol{R}$ matrix is computed as follows

$$\boldsymbol{R} = \tilde{\boldsymbol{X}}_{\boldsymbol{t}}\boldsymbol{Y}_{\boldsymbol{t}}^{\boldsymbol{T}}\left(\boldsymbol{J}\boldsymbol{\Sigma}_{\boldsymbol{x}}\boldsymbol{J}^{\boldsymbol{T}} + \boldsymbol{\Sigma}_{\boldsymbol{n}}\right)^{-1} \tag{2.55}$$

where $\tilde{\boldsymbol{X}}_{\boldsymbol{t}}$ is the normalized matrix that contains the ”desired positions” vectors of the training samples, $\tilde{\boldsymbol{Y}}_{\boldsymbol{t}}$ is the normalized matrix that contains the $\boldsymbol{y}^{(\boldsymbol{k})}$ measurement frame differences, $\boldsymbol{\Sigma}_{\boldsymbol{x}}$ is the covariance matrix of the distribution from which the training targets set is drawn and $\boldsymbol{\Sigma}_{\boldsymbol{n}}$ is the covariance matrix of the distribution from which the signal noise of the measurements is taken. The estimated conductivity change is

$$\boldsymbol{\sigma}_{*} = \boldsymbol{R}\boldsymbol{V} \tag{2.56}$$

GREIT takes data from the training sets and the desired NF, optimizes the parameters and performs a single-step EIT reconstruction. It is widely used in thoracic EIT imaging, due to its great performance. However, it can be often computationally expensive, due to the need of a fine, usually $3D$ model for the forward calculations ($2.5D$ imaging) and the training. A detailed description of the GREIT algorithm can be found in [71].

A popular MATLAB-based library tool for the L^2-norm regularization, the PD-IPM TV and the GREIT approach which supports both 2D and 3D imaging and provides several online measurement datasets is the Electrical Impedance Tomography and Diffuse Optical Tomography Reconstruction Software (EIDORS) [72]: `http://eidors3d.sourceforge.net/`. In Figs. 2.5 and 2.6, a simple simulated EIT reconstruction is demonstrated, using the EIDORS tool. The code used for the simulated model and the image reconstructions is provided in Chapter 9 (Appendix A).

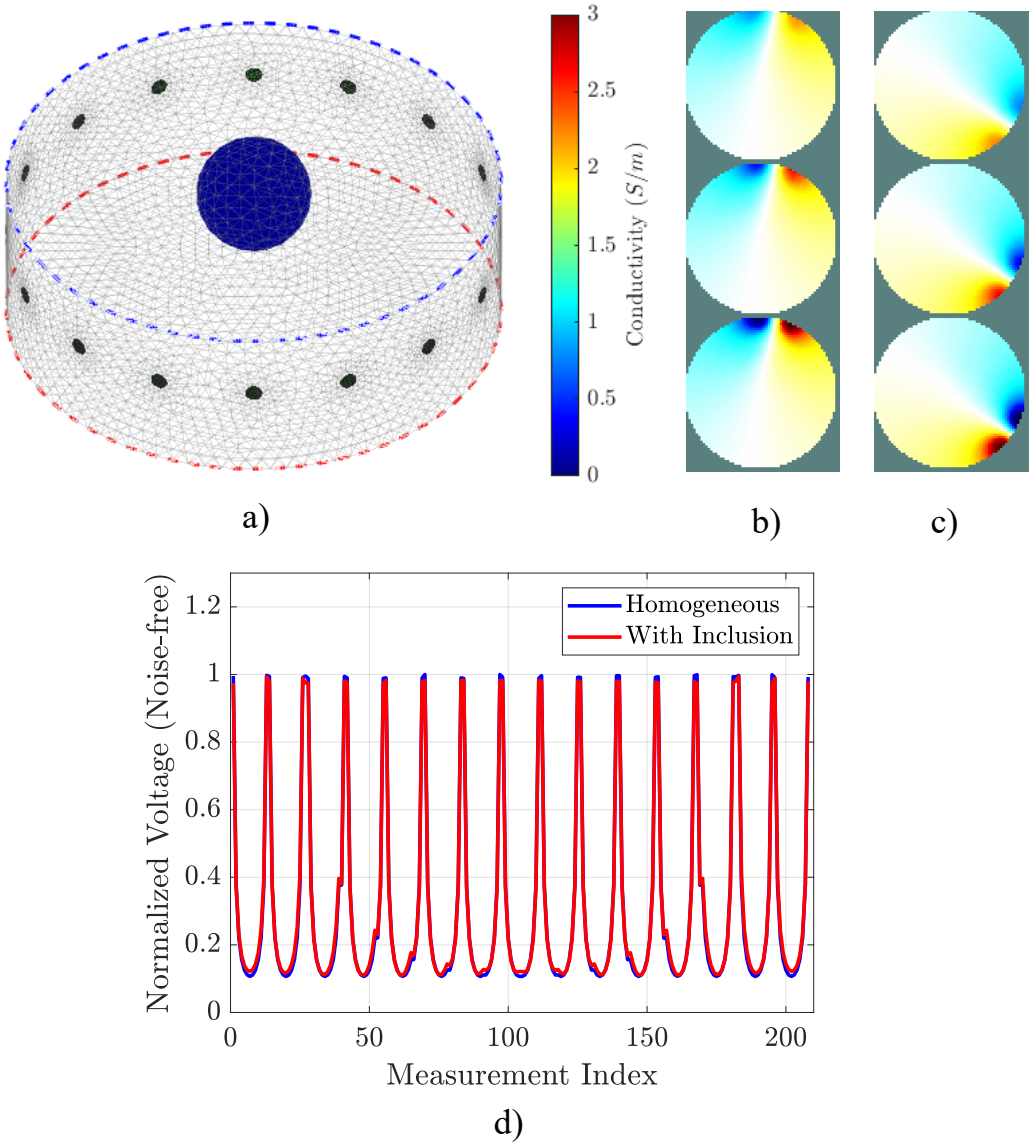

Figure 2.5: Simulated EIT setup: a) Simulation cylindrical model (radius 1.5 AU, height 1 AU) with spherical non-conductive inclusion of radius 0.35 AU centered the position $r_i = (0, 0.5, 0.5)$. b) Voltage distribution (non-quantified) on various z-levels for adjacent current pattern when current is injected from the 1^{st} and the 2^{nd} electrodes. c) Voltage distribution (non-quantified) on various z-levels for adjacent current pattern when current is injected from the 6^{th} and the 7^{th} electrodes. d) Homogeneous and non-homogeneous normalized electrode voltage measurements for adjacent current pattern.

2.7 D-Bar Reconstruction

The D-Bar is a direct non-linear EIT reconstruction method [73, 74, 75, 76, 77], which is based on a nonlinear scattering Fourier transformation [46] of the measured boundary current-to-voltage data. Low-pass filtering is performed to the transformed data which acts as regularization.

This method models the measurement data as a current-to-voltage Neumann-to-Dirichlet (ND) map

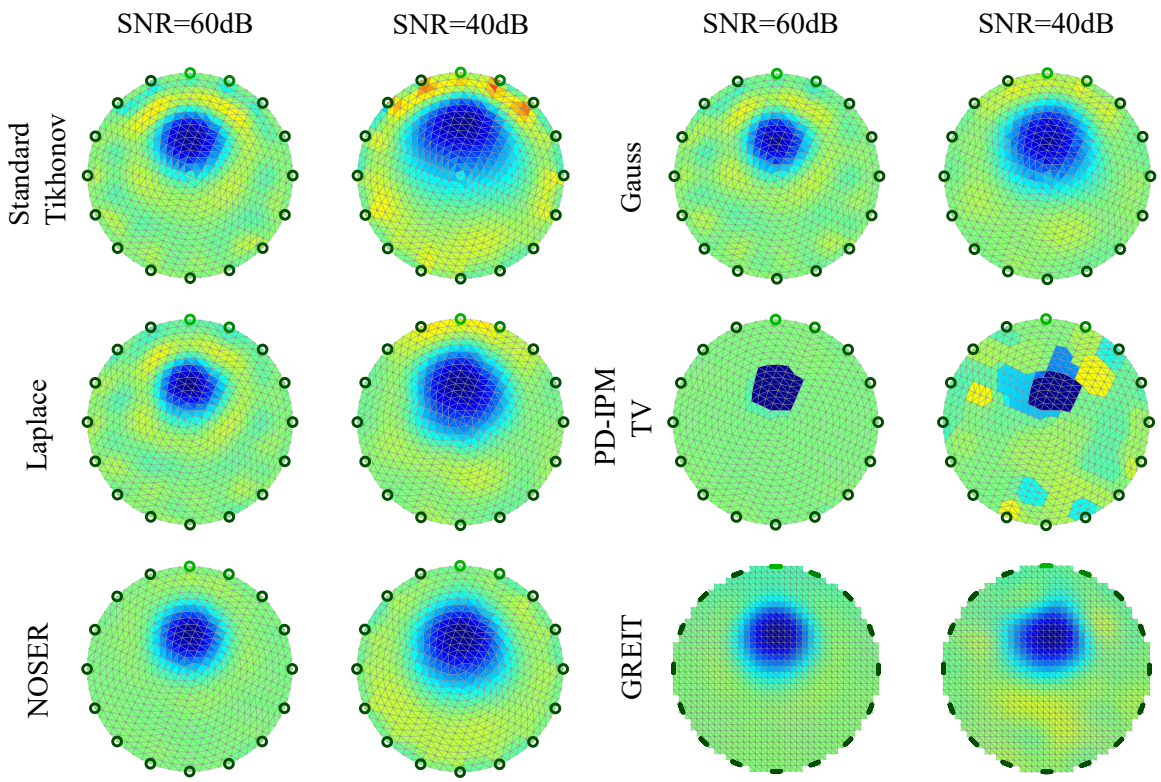

Figure 2.6: Qualitative EIT reconstructions for the setup in Fig. 2.5 using various approaches and priors and signal SNR of a) 60dB and b) 40dB. For the regularized approaches, the hyperparameter values have been heuristically selected, while for the GREIT reconstruction the NF value was set to 0.5. The reconstruction is performed a point-electrode 1024-triangular element and 545-node domain for the regularized cases and on a 965-pixel domain for GREIT. The training procedure for the GREIT reconstruction was performed on an extruded 3D fine cylindrical domain, containing 39710 elements and 8905 nodes. The MATLAB-EIDORS code used for the reconstructions is provided in Chapter 9 (Appendix A).

R_σ:

$$R_\sigma \phi = u|_{\partial\Omega} \tag{2.57}$$

where ϕ applied mean-free current on the EIT problem Neumann boundary condition. The ND map expresses the boundary voltage for current pattern utilized. The Dirichlet-to-Neumann (DN) map is also defined as follows:

$$\Lambda_\sigma = (R_\sigma)^{-1} \tag{2.58}$$

To perform the scattering transform of the data, the EIT Laplace equation (2.2) is transformed to a Schrodinger one, by substituting:

$$\tilde{u} = \sqrt{\sigma} u \tag{2.59}$$

and

$$q(z) = \sigma^{-1/2}(z) \Delta \sigma^{1/2}(z). \tag{2.60}$$

Using the special solution form

$$\tilde{u} = \psi(z,k) \tag{2.61}$$

the following Schrodinger equation is formulated:

$$[-\Delta + q(z)]\psi(z,k) = 0, \qquad z \in \mathbb{C}, \quad k \in \mathbb{C} \setminus \{0\} \tag{2.62}$$

By mapping

$$kz = (k1 + ik2)(z1 + iz2), \tag{2.63}$$

defining

$$e(z,k) \triangleq exp\{i(kz + \bar{k}\bar{z})\} \tag{2.64}$$

and

$$\mu(z,k) = e^{-ikz}\psi(z,k) \sim 1 \tag{2.65}$$

and using the following nonlinear scattering transform:

$$\boldsymbol{t}(k) = \int_{\mathbb{C}} e(z,k)q(z)\mu(z,k)dz \tag{2.66}$$

as well as the Alessandrini's identity [78], we are led to the following data transformation:

$$\boldsymbol{t^{exp}}(k) = \left\{ \begin{array}{l} \int_{\partial\Omega} e^{i\bar{k}\bar{z}}(\Lambda_\sigma - \Lambda_1)e^{ikz}dS(z), \quad 0 \leq |k| \leq R \\ 0, \quad \text{else} \end{array} \right\} \tag{2.67}$$

where R acts as a regularization low-pass filter threshold.

The following D-Bar equation:

$$\bar{\partial}_k \mu(z,k) = \frac{1}{4\pi\bar{k}} \boldsymbol{t}(k) e(z,-k) \overline{\mu(z,k)} \tag{2.68}$$

is then solved for each $z \in \Omega$ using the following formula:

$$\mu^{exp}(z,\kappa) = 1 + \frac{1}{4\pi^2} \int_{\mathbb{C}} \frac{\boldsymbol{t^{exp}}(k) e(z,-k)}{(\kappa - k)\bar{k}} \overline{\mu^{exp}(z,k)} d\kappa_1 d\kappa_2. \tag{2.69}$$

Finally, the conductivity distribution is estimated as follows:

$$\sigma^{exp}(z) = \left[\mu^{exp}(z,0)\right]^2, \quad z \in \Omega. \tag{2.70}$$

Contrary to the iterative regularization approaches, the D-Bar method has been proven robust to modeling errors [79]. A detailed comparison of the image reconstruction performance between the D-Bar and the regularized methods can be found in [80]. Finally, a MATLAB-based code tutorial for D-Bar method EIT imaging can be found in the following website: `https://blog.fips.fi/tomography/eit/the-d-bar-method-for-electrical-impedance-tomography-simulated-data/`.

2.8 Shape-Based Reconstruction

In the methods described above, the main purpose is to estimate the conductivity distribution of an examined subject through the inverse problem. However, this general approach does not provide reliable quantitative information about the inclusions' exact conductivity values and does not accurately recover their shapes. A main source of these inaccuracies is the the fact that the inverse problem has almost always an extremely large number of unknowns compared to the actual data provided from the measurements.

To overcome this issue, a general research approach is to recover the inclusions' shapes instead of the conductivity distribution. This can be performed by adding specific constraints to the regularization terms in the objective function and assuming that: A) The examined domain has a uniform background conductivity and B) Each inclusion has also a uniform conductivity. In this way, the number of inverse problem's unknowns is significantly reduced and the problem becomes well-posed. Such problems are called *shape-based* ones.

2.8.1 Traditional Level Set (TLS)

The level set is a common used approach for shape-based inverse scattering problems. It was firstly introduced in [81] and applied in EIT in [82], [83], [84] and [85]. The traditional level set approach, models the conductivity distribution as a linear combination of two piece-wise constant conductivities; the background's and the inclusion's one:

$$\sigma(\boldsymbol{r}) = \sigma_o \left(1 - H_\epsilon(f(\boldsymbol{r}))\right) + \sigma_1 H_\epsilon(f(\boldsymbol{r})), \quad \boldsymbol{r} \in \Omega. \tag{2.71}$$

where $H_\epsilon(x)$ is a smoothed Heaviside function [86]:

$$H_\epsilon(x) = \left\{ \begin{array}{ll} 1, & x > \epsilon \\ 0, & x < -\epsilon \\ \frac{1}{2}\Big[1 + \frac{x}{\epsilon} + \frac{1}{\pi}\sin\big(\frac{\pi x}{\epsilon}\big)\Big], & \text{else} \end{array} \right\} \tag{2.72}$$

where $\epsilon > 0$ is a sufficiently small value. Assuming $D \subset \Omega$ the inclusion's subdomain, the level set function $f(\boldsymbol{r})$ satisfies the following conditions:

$$\left\{ \begin{array}{ll} f(\boldsymbol{r}) > 0, & \boldsymbol{r} \in D \\ f(\boldsymbol{r}) = 0, & \boldsymbol{r} \in \partial D \\ f(\boldsymbol{r}) < 0, & \boldsymbol{r} \in \Omega \setminus D \end{array} \right\} \tag{2.73}$$

and is expressed as a signed distance function [84]. The objective function is the following:

$$(\sigma_{o*}, \sigma_{1*}, \boldsymbol{f}_*) = \underset{\boldsymbol{f} \in \mathbb{R}^{N_e}, \sigma_o \in \mathbb{R}, \sigma_1 \in \mathbb{R}}{\operatorname{argmin}} \left\{ \|\boldsymbol{U}(\boldsymbol{\sigma}) - \boldsymbol{V}\|_{\boldsymbol{W}}^2 + \left\|\boldsymbol{f} - \overline{\boldsymbol{f}}\right\|_Q^2 + \|\sigma_o - \overline{\sigma_o}\|_2^2 + \|\sigma_1 - \overline{\sigma_1}\|_2^2 \right\} \tag{2.74}$$

where $\boldsymbol{f}$ is the discretized form of f, calculated on each node $i \in \{1, ..., N_e\}$ and $\overline{\boldsymbol{f}}$, $\overline{\sigma_o}$ and $\overline{\sigma_1}$ are predefined values [84].

2.8.2 Parametric Level Set (PLS)

A more recent work [87], introduces the parametric level set (PLS) approach in EIT, where the level set function $f(\boldsymbol{r})$ is written as a linear combination of radial basis functions (RBFs):

$$f(\boldsymbol{r}) = \sum_{i=1}^{N_b} \mu_i \cdot p_i(\boldsymbol{r}) \tag{2.75}$$

where N_b denotes the number of basis functions used, $\boldsymbol{\mu} = [\mu_1, ..., \mu_{N_b}] \in \mathbb{R}^{N_b}$ denotes the PLS coefficients vector and $p_i(\boldsymbol{r})$, for $i = \{1, ...N_b\}$ are the RBFs. In [87], Gaussian RBFs are implied and the level set function becomes parametric to a small positive threshold value $c > 0$:

$$\left\{ \begin{array}{ll} f(\boldsymbol{r}, \boldsymbol{\mu}) > c, & \boldsymbol{r} \in D \\ f(\boldsymbol{r}, \boldsymbol{\mu}) = c, & \boldsymbol{r} \in \partial D \\ f(\boldsymbol{r}, \boldsymbol{\mu}) < c, & \boldsymbol{r} \in \Omega \setminus D \end{array} \right\} \tag{2.76}$$

Therefore, the conductivity expression (2.71) is modified as follows:

$$\sigma(\boldsymbol{r}) = \sigma_o \left(1 - H_\epsilon(f(\boldsymbol{r}, \boldsymbol{\mu})) - c\right) + \sigma_1 \left(H_\epsilon(f(\boldsymbol{r}, \boldsymbol{\mu})) - c\right), \quad \boldsymbol{r} \in \Omega. \tag{2.77}$$

The objective function is expressed as follows [87]:

$$(\sigma_{o*}, \sigma_{1*}, \boldsymbol{\mu}_*) = \underset{\boldsymbol{\mu} \in \mathbb{R}^{N_b}, \sigma_o \in \mathbb{R}, \sigma_1 \in \mathbb{R}}{\operatorname{argmin}} \left\{ \|\boldsymbol{U}(\boldsymbol{\sigma}) - \boldsymbol{V}\|^2_{\boldsymbol{W}} + \|\boldsymbol{\mu} - \overline{\boldsymbol{\mu}}\|_2^2 + \|\sigma_o - \overline{\sigma_o}\|_2^2 + \|\sigma_1 - \overline{\sigma_1}\|_2^2 \right\} \tag{2.78}$$

where $\overline{\boldsymbol{\mu}}$, $\overline{\sigma_o}$ and $\overline{\sigma_1}$ are reference, a-priori determined values. The optimization problem (2.78) can be solved using the GN iterative method. To linearize the problem, the following Jacobian matrices are computed in each iteration, using the chain rule:

$$\boldsymbol{J}_U(\boldsymbol{\mu}) = \frac{\partial \boldsymbol{U}(\boldsymbol{\sigma})}{\partial \boldsymbol{\sigma}} \cdot \frac{\partial \boldsymbol{\sigma}}{\partial \boldsymbol{f}} \cdot \frac{\partial \boldsymbol{f}}{\partial \boldsymbol{\mu}} = \ = \boldsymbol{J}_U(\boldsymbol{\sigma})(\sigma_1 - \sigma_o)(\delta(\boldsymbol{f} - c)) \frac{\partial \boldsymbol{f}}{\partial \boldsymbol{\mu}}, \tag{2.79}$$

$$\boldsymbol{J}_U(\sigma_o) = \frac{\partial \boldsymbol{U}(\boldsymbol{\sigma})}{\partial \boldsymbol{\sigma}} \cdot \frac{\partial \boldsymbol{\sigma}}{\partial \sigma_o} = \boldsymbol{J}_U(\boldsymbol{\sigma})(1 - H(\boldsymbol{f} - c)), \tag{2.80}$$

and

$$\boldsymbol{J}_U(\sigma_1) = \frac{\partial \boldsymbol{U}(\boldsymbol{\sigma})}{\partial \boldsymbol{\sigma}} \cdot \frac{\partial \boldsymbol{\sigma}}{\partial \sigma_1} = \boldsymbol{J}_U(\boldsymbol{\sigma}) H(\boldsymbol{f} - c), \tag{2.81}$$

where $\boldsymbol{\sigma} = [\sigma_o, \ \sigma_1]^T$.

The PLS method has shown significantly improved performance in reconstructing the conductivity inclusions' shapes compared to the traditional one, while the method was extended to difference-EIT imaging in [88] and multi-phase [89] conductivity distributions.

2.8.3 Geometrically Constrained Boundary Reconstructor (GCBR)

Another shape-reconstruction proposed in [90], where the local boundary parameterization model is penalized by the geometric constraints defined in the boundary integral equations. The problem is formulated as an energy minimization objective function, where the energy dependence from boundary perturbations is expressed:

$$\mathcal{E}(\boldsymbol{x}) = \frac{1}{2}\left\|\boldsymbol{U}(\boldsymbol{x}) - \boldsymbol{V}\right\|_2^2 + \frac{\alpha}{2}\oint_{\Gamma}|\boldsymbol{x'}(\boldsymbol{s})|^2 ds + \frac{\beta}{2}\oint_{\Gamma}|\boldsymbol{x''}(\boldsymbol{s})|^2 ds \tag{2.82}$$

where Γ is the target inclusion boundary, $\boldsymbol{x} = [\boldsymbol{x}(s_1), ..., \boldsymbol{x}(s_{N_b})] \in \Gamma$ denotes the set of points on Γ and $\boldsymbol{s} \in [0, 1]$ is a local arc-length parameter. The 1^{st} term of $\mathcal{E}$ is the fidelity one, the 2^{nd} expresses the tension and the 3^{rd} the stiffness, while α and β are properly selected hyperparameters [90].

Using the Boundary Element Method (B.E.M.) as well as the Euler–Lagrange equation and proper discretization, the problem is led to the following equation system:

$$\boldsymbol{A}\boldsymbol{u} + \boldsymbol{N}\boldsymbol{J}^T(\boldsymbol{U}(\boldsymbol{x}) - \boldsymbol{V}) = \boldsymbol{A}\boldsymbol{u} + \boldsymbol{N}\boldsymbol{r} = 0 \tag{2.83}$$

where $\boldsymbol{N} \in \mathbb{R}^{N_b \times N_b}$ is a diagonal matrix which includes the components of the normal outward vector to the inclusions' boundary Γ, $\boldsymbol{A} \in \mathbb{R}^{N_b \times N_b}$ is a cyclic pentadiagonal banded matrix:

$$\boldsymbol{A} \triangleq \begin{bmatrix} d & c & b & ... & c & b \\ c & d & c & ... & 0 & b \\ ... & ... & ... & ... & ... & \\ c & b & 0 & ... & c & d \end{bmatrix} \tag{2.84}$$

where $a = \alpha/(\delta s^2)$, $b = \beta/(\delta s^4)$, $c = -a - 4b$ and $d = 2a + 6b$, while δs is a sample of the local arc length parameter $\boldsymbol{s}$. Furthermore, the inclusion boundary points' components $\boldsymbol{x}(s_j) = [x(s_j), y(s_j)]$ are separately denoted with u_j. Hence $\boldsymbol{u} = [u_1, ..., u_{N_b}]^T \in \mathbb{R}^{N_b \times 1}$. The first term in (2.83) expresses the (2.82) fidelity term, while the second one is conducted from the (2.82) penalizing terms [90]. Adopting the semi-implicate method for image segmentation [91], [92], three assumptions are made: A) the right-hand side term in (2.83) is set to one time step and the left-hand side terms are derived with negative time, B) $\boldsymbol{r}$ is constant and equals $\boldsymbol{r}^{t-1}$ during each iteration, and, C) $\boldsymbol{A}$ is specified at time step t. Hence the following boundary time-variant equation is derived:

$$\boldsymbol{A}\boldsymbol{u}^t + \boldsymbol{N}^{t-1}\boldsymbol{r}^{t-1} = -\frac{\boldsymbol{u}^t - \boldsymbol{u}^{t-1}}{\delta t} \tag{2.85}$$

where δt denotes the selected time step. The system (2.85) is solved iteratively as follows [90]:

$$\left\{ \begin{array}{l} \boldsymbol{r}^{t-1} = \boldsymbol{J}^T\boldsymbol{x}^{t-1}(\boldsymbol{U}(\boldsymbol{x}^{t-1}) - \boldsymbol{V}) \\ \boldsymbol{u}^t = \boldsymbol{S}^{-1}(\boldsymbol{u}^{t-1} - \delta t\boldsymbol{N}^{t-1}\boldsymbol{r}^{t-1}) \end{array} \right\} \tag{2.86}$$

where $\boldsymbol{S} = \delta t\boldsymbol{A} + \boldsymbol{I}_{N_b \times N_b}$.

An energy minimization approach, combined with a Statistical Shape Constrained Reconstruction (SSCR) and applied in chest phantoms and noisy simulated data was presented in [93].

2.8.4 Moving Morphable Components (MMC) based reconstruction

The PLS method, described in 2.8.2 offers such an good imaging performance of the inclusions' boundaries. However, it makes use of RBFs for the representation of the level set function, that has some potential disadvantages, such as the difficulty of center initialization and the absence of physical interpretation. An improved level set representation has been performed in [94], using Moving Morphable Components (MMC). To this end, the TLS level set function identity expressed in (2.73) is used with the following level set functions:

$$f_i(x,y) = 1 = \left(\frac{x'}{L_i}\right)^m - \left(\frac{y'}{g_i(x')}\right)^m \tag{2.87}$$

where m is an even number called the exponent, L_i denotes the half length of the i^{th} component, $g_i(x')$ describes the component's thickness profile [94], [95], [96] and

$$\begin{bmatrix} x' \\ y' \end{bmatrix} = \begin{bmatrix} \cos(\theta_i) & \sin(\theta_i) \\ -\sin(\theta_i) & \cos(\theta_i) \end{bmatrix} \cdot \begin{bmatrix} x - x_o^i \\ y - y_o^i \end{bmatrix} \tag{2.88}$$

where θ_i s the inclined angle of the component measured from the horizontal axis counter-clockwisely and (x_o^i, y_o^i) the coordinates of the i^{th} component's center. Each component is also characterized by its thickness parameters $\boldsymbol{w}^i = [w_1^i,\ w_2^i,\ w_3^i]$. Hence, the shape design variable is defined as follows:

$$\boldsymbol{\gamma}^i = [x_o^i,\ y_o^i,\ L_i,\ \theta_i,\ w_1^i,\ w_2^i,\ w_3^i]. \tag{2.89}$$

and the vector $\boldsymbol{\gamma} = [\boldsymbol{\gamma}^1, ..., \boldsymbol{\gamma}^{N_c}]$, where N_c is the total number of components.

The objective function is formulated as [94]:

$$(\sigma_{o*}, \sigma_{1*}, \boldsymbol{\gamma}_*) = \underset{\boldsymbol{\gamma}\in\mathbb{R}^{7N_c\times 1}, \sigma_o\in\mathbb{R}, \sigma_1\in\mathbb{R}}{\operatorname{argmin}} \left\{ \|\boldsymbol{U}(\boldsymbol{\sigma}) - \boldsymbol{V}\|_{\boldsymbol{W}}^2 + \|\boldsymbol{\gamma} - \overline{\boldsymbol{\gamma}}\|_2^2 + \|\sigma_o - \overline{\sigma_o}\|_2^2 + \|\sigma_1 - \overline{\sigma_1}\|_2^2 \right\} \tag{2.90}$$

and is solved with the GN method, similarly to the PLS case. The MMC method was also extended to difference-EIT imaging in [97].

2.8.5 B-spline level set method

Another level set function representation for EIT shape reconstruction, based on B-spline curves, is discussed in [98]. The tensor-product expression used is the following:

$$f(x,y) = \sum_{i=1}^{m}\sum_{j=1}^{n} N_{i,k}(x) N_{j,l}(y) q_{i,j} \tag{2.91}$$

where a 2D model with $(m+1)(n+1)$ control points $P_{i,j} \in \mathbb{R}^3$ has been assumed, $q_{i,j}$ is the z-axis coordinate of $P_{i,j}$ and $N_{i,k}$, $N_{j,l}$ are the i^{th} and j^{th} B-spline basis function of degree k (x-direction) and l (y-direction), respectively. The basis function N is defined as:

$$N_{i,0}(x) = \left\{ \begin{array}{ll} 1, & x_i \leq x \leq x_i + 1 \\ 0, & \text{else} \end{array} \right\} \tag{2.92}$$

and

$$N_{i,k}(x) = \frac{x - x_i}{x_{i+k} - x_i} N_{i,k-1}(x) + \frac{x_{i+k+1} - x}{x_{i+k+1} - x_{i+1}} N_{i+1,k-1}(x) \tag{2.93}$$

where $\{x_i\}_{i=0}^{b}$ is a uniform knot vector, expressed as:

$$x_i = \left\{ \begin{array}{ll} 0, & i = 0, 1, ..., k \\ \frac{i-k}{m-k+1}, & i = k+1, k+2, ..., m \\ 1, & i = m+1, m+2, m+k+1 \end{array} \right\} \tag{2.94}$$

and $b = m + k + 1$.

The level set conditions are defined suchlike in (2.73), while the objective function is formulated as [98]:

$$(\sigma_{o*}, \sigma_{1*}, \boldsymbol{q}_*) = \underset{\boldsymbol{q} \in \mathbb{R}^{(m+1)\cdot(n+1)\times 1}, \sigma_o \in \mathbb{R}, \sigma_1 \in \mathbb{R}}{\operatorname{argmin}} \left\{ \|\boldsymbol{U}(\boldsymbol{\sigma}) - \boldsymbol{V}\|_{\boldsymbol{W}}^2 + \|\boldsymbol{q} - \overline{\boldsymbol{q}}\|_2^2 + \|\sigma_o - \overline{\sigma_o}\|_2^2 + \|\sigma_1 - \overline{\sigma_1}\|_2^2 \right\} \tag{2.95}$$

and treated as in the PLS and MMC described above.

The B-Spline curve based method offers the capability of easy boundary shape demonstration with limited number of control points $(m+1)(n+1)$, while it preserves the inclusions' sharp properties. However, it is necessary to have an a-priori knowledge of the exact number of inclusions and topological changes cannot be easily handled [99]. In [99] a Boolean operation framework coupled with B-spline curves is applied for EIT shape reconstruction, where special care has been taken for overlapping, merging, and separation of different shapes. Finally, the Boolean operation shape reconstruction approach mentioned above has been combined with Fourier-based parameterization, eliminating the requirement for a-priori information about the number of inclusions [100]. This approach also offers increased ability to preserve sharp boundary shapes in the reconstructed images.

2.9 Learning Methods for EIT Reconstruction

Machine Learning (ML) is a continuously growing research field, offering a surplus variety of applications in all the areas. Its application in EIT actually begins from the early 90s, with the implementation of a simple Neural Network (NN) [101], based on Adaptive Linear Element (ADALINE). Many other works have applied ML techniques in EIT, which can be considered as a regression problem, since then. In [102] (1998), two Artificial NN (ANN) reconstruction methods were presented for reconstructing conductivity distribution in simple square pixel domains. In [103], principal component analysis (PCA) and

an ANN are used, employing multi-region BEM with a quadratic interpolation function for the surface elements. Application of BEM leads to dimensionality reduction, while the method showed noise robustness and allowed real-time result acquisition. In addition, [104] used an RBF neural network for the image reconstruction of the Electrical Capacitance Tomography (ECT). An adaptive genetic algorithm was used to optimize the RBF networks' hidden units parameters. Furthermore, gradient boosting machine approaches [105], principal component and partial least square regression methods [106], least absolute shrinkage and selection operator (Lasso) [107] and convolutional NN (CNN) [108] have also been applied. In [109], an extensive comparison has been performed, where Elastic net, least-angle regression (LARS) [89] and multiply ANN are applied to reconstruct EIT images from simulated and phantom setup cases.

Recently, the evolution of hardware computational capabilities offered considerably large area for the application of more complex ML approaches. In EIT there has been a significant turn in ML methods during the last years. Overall, recent research in learning techniques applied in EIT can be separated into two main categories: Deep Learning applications and Sparse Bayesian Learning (SBL).

2.9.1 Deep Learning Applications in EIT

The concept of employing Deep Convolutional Neural Networks in inverse scattering and imaging problems has been extensively discussed in [110]. Training multilayer networks has proven such a sufficient method to deal with the EIT's problem non-linearity. Overall, three main DL approaches can be found in image reconstruction [111], [112].

In the first, a classic linear or non-linear reconstruction method is applied to obtain an initial image which may suffer from noise or artefacts. Then NN are applied to perform image post-processing. For instance, in [113] a linear GN solver is applied to produce 3D EIT images, while the reconstructed images are further processed from an ANN, providing a strong measurement noise resistance. This is the most common approach used.

The second category relies on iterative model-based techniques, where at each iteration, a NN is applied to perform an updated image reconstruction. This NN acquires information from both the measurement data and the forward model (see 2.1, 2.2 and 2.3). Related medical imaging related paradigms can be found in [114] and [115].

In the third category, a NN is applied to reconstruct the images directly from the measurement data [116]. This approach needs larger amount of training data, may issue instabilities during the training process and the may images suffer from noise or artefacts. In EIT such methods are applied in [109] while [113] compares a post-reconstruction method with a direct ANN-based measurement processing one.

A very widely used CNN for post-processing EIT image reconstruction is the commonly known U-Net [117]. Its general architecture is demonstrated in Fig. 2.7 The U-net has been applied for post-processing of images acquired via the D-Bar method (see 2.7) in [118], introducing the Deep D-Bar method for absolute EIT imaging. In particular, the U-net has been properly modified to achieve a 64×64 pixel D-Bar reconstructed EIT image $\boldsymbol{\sigma}^{exp}$ as input, providing an output segmentation map $\tilde{\boldsymbol{\sigma}}$. The Deep

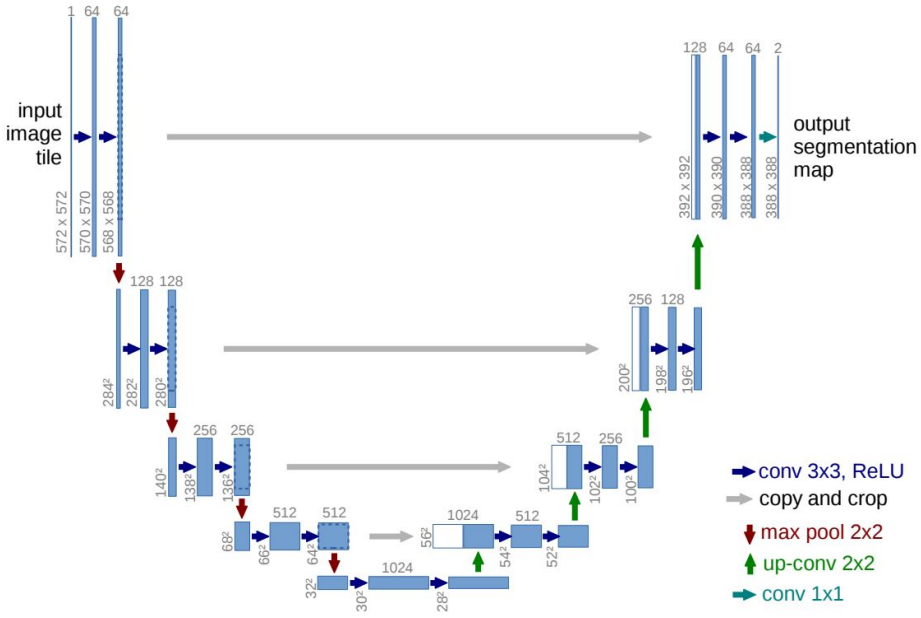

Figure 2.7: U-net architecture (32x32 pixel example). Each blue box corresponds to a multi-channel feature map. The number of channels is denoted on top of the box. The dimensions are provided at the lower left edge of the box. White boxes represent copied feature maps. [117]

D-Bar network $\mathcal{D}_\theta$ is trained using a dataset $\{\boldsymbol{\sigma_i}, \boldsymbol{\sigma}_i^{exp}\}_i$ ($\boldsymbol{\sigma_i}$ denotes the "true" conductivity distribution of the training sample i) demonstrating a number of simulated circular setups with metallic and plastic inclusions as well as agar/graphite targets simulating chest phantoms. The L^2-norm loss function applied is the following:

$$\text{loss}(\tilde{\boldsymbol{\sigma}}) = \|\tilde{\boldsymbol{\sigma}} - \boldsymbol{\sigma}\|_2^2 \tag{2.96}$$

The post-imaging results showed a significant artefact reduction as well as an increase in the Structural Similarity Indices (SSIMs) of the images [118]. The Deep D-Bar approach was extended in [119] where the Beltrami equation formulation was employed in the D-Bar method, managing a domain-independent data training.

The U-net has also been utilized in a Dominant-Current Deep Learning Scheme (DC-DLS) [120]. Firstly, the bases-expansion subspace optimization method (BE-SOM) [121] is applied, keeping the dominant parts of induced contrast current (ICC). Secondly, the dominant parts are utilized to generate multi-channel inputs of the U-net (Fig. 2.8). The method is compared to the traditional iterative BE-SOM one, showing improved performance and noise robustness. [122] performs EIT using an artifcial skin through super-sensing method data from conductive fabric. The U-net NN is used for image denoising.

In [123], a Fully-Connect (FC) and a ReLU layer are added before the typical U-net network, consisting the FC-UNet architecture. The FC layer performs an initial reconstruction directly using measured data for Cell EIT imaging. Then, the U-net is applied to denoise the image. The overall concept is shown in Fig. 2.9.

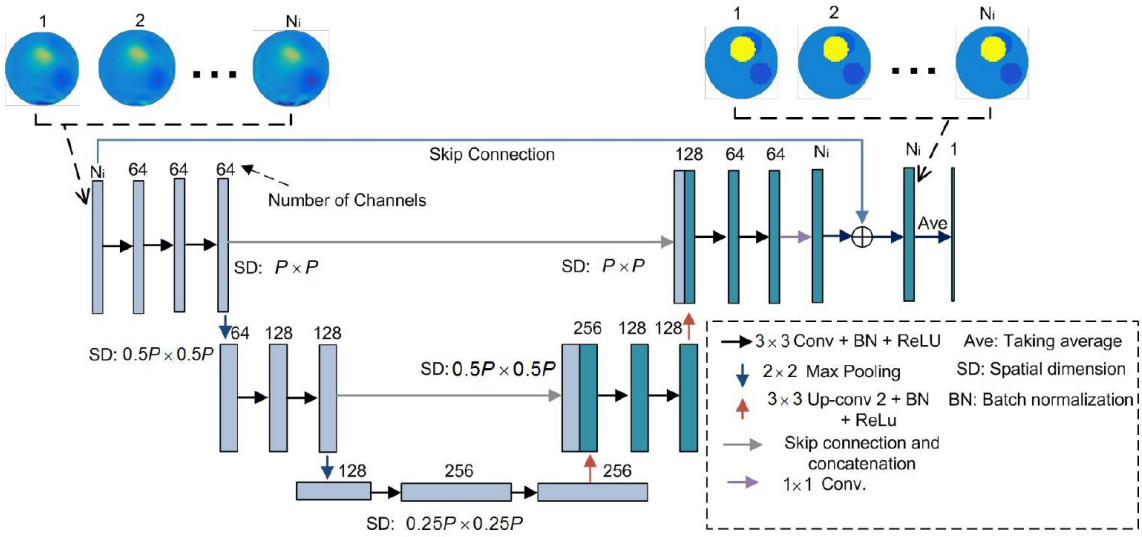

Figure 2.8: Modified multi-channel U-net architecture for the DC-DLS. [120]

The FC-UNet application in EIT Cell imaging was expanded in the terms of a Deep Learning Group Sparsity (DL-GS) framework in [124], consisting of a hybrid learning-based cell aggregate EIT imaging technique. In principle, the FC-UNet identifies binary structural information of each inclusion, which is encoded into group sparsity (GS) regularization (Fig. 2.10). Furthermore, in [125], a structure-aware dual-branch network has been implemented (SADB-Net) for Cell imaging. It consists of two branches to learn the structural and conductivity representations in the first place, respectively. The FC-UNet is included in the structure branch, as a mask generator. Then, the multibranch features are fused by two fully connected layers. In addition, an impedance-optical dual-modal imaging framework, which aims to 3D cell culture imaging is presented in [126]. The framework consists of three parts: A) An impedance-optical dual-modal sensor, B) A guidance image processing algorithm and C) A two input multi-scale feature cross fusion network (MSFCF-Net). The network inputs consist of the measurement data and a binary mask generated from B).

Apart from the above, U-net/ FC-UNet based works, in [127], inspired from the DC-DLS method, the authors employed a cascaded end-to-end CNN (CE-CNN) architecture to apply the post-processing Induced-Current Learning Method (ICLM), also based in the BE-SOM approach.

[128] proposes the Fista-Net CNN, a fast iterative shrinkage thresholding network for imaging prob-

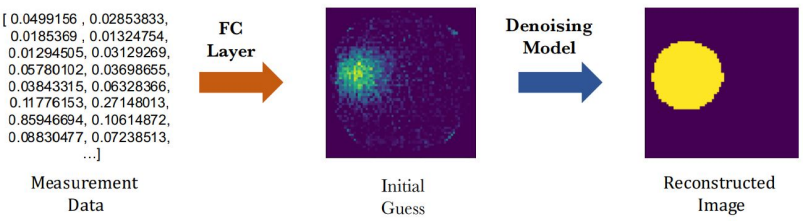

Figure 2.9: The Processing Pipeline of FC-UNet. [123]

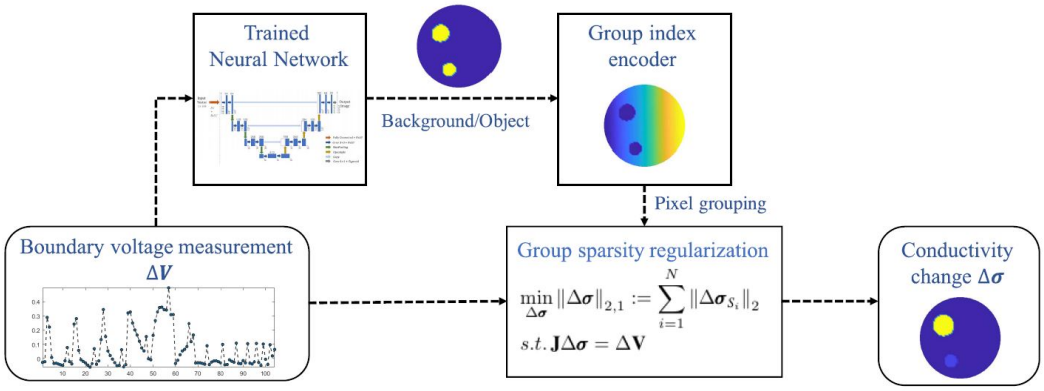

Figure 2.10: DL-GS framework principle [124].

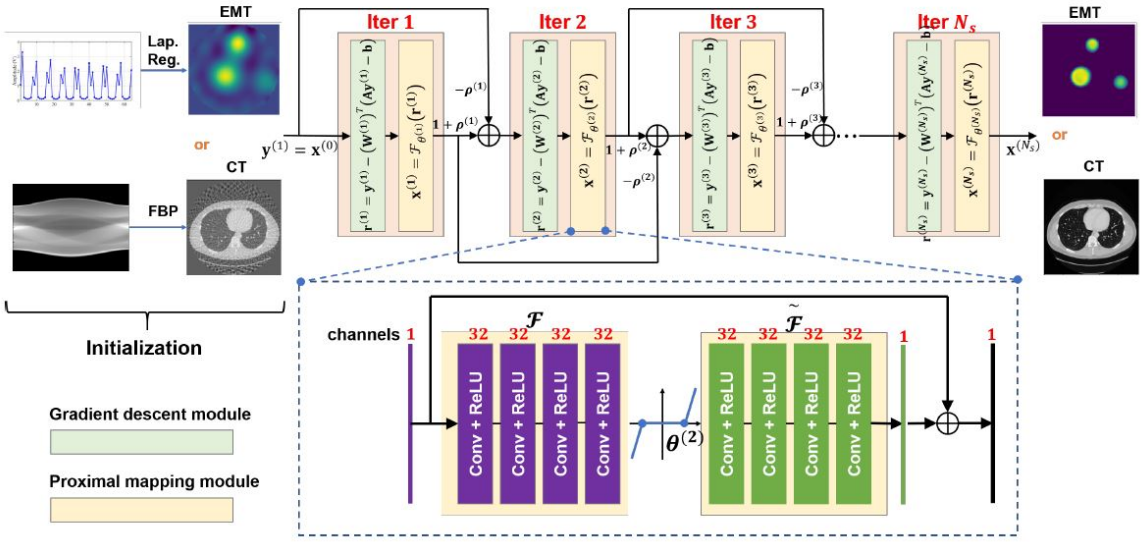

Figure 2.11: Fista-Net architecture [128].

lems (Fig. 2.11). It comprises three cascaded stages: multiple gradient descent, proximal mapping, and momentum modules. In each iteration, the gradient matrix is updated and a proximal operator network is developed for nonlinear thresholding which can be learned through end-to-end training.

Another architecture developed for frequency-difference EIT, is the multiple measurement vector network (MMV-Net) [129]. It is based on the Alternating Direction Method of Multipliers (ADMM) [130] and uses a non-linear shrinkage regularization operator with a Spatial Self-Attention module and a convolutional long short-term memory (ConvLSTM) module to reveal any frequency correlations. The network along with the algorithm summary is demonstrated in Fig. 2.12.

A two-stage deep learning (TSDL) method for robust shape reconstruction with EIT is presented in [131]. It consists of a pre-reconstruction block and a CNN. The pre-reconstruction block learns the regularization pattern from the training data set and provides a rough reconstruction of the target. The CNN post-processes the pre-reconstruction result in a multi-level feature analysis strategy, and eliminates

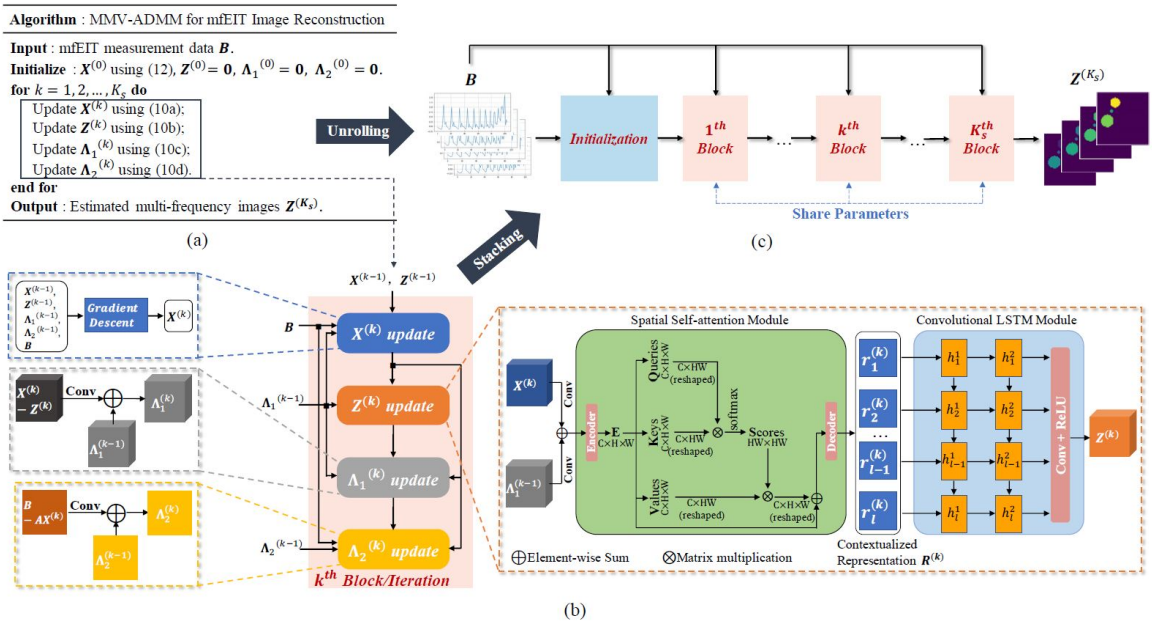

Figure 2.12: (a) The iterative MMV-ADMM algorithm. (b)-(c) Illustration of MMV-Net architecture and process flow [129].

the modelling errors with prior information of the observation domain shape. Both blocks are trained by using a minimum square approach.

In [132] a 2 hidden layer custom NN, trained with backpropagation method according to the Fletcher–Reeves updates [133] is implemented for electrode position optimization, while in [134] optimal pattern selection approach based on the implementation of a support vector machine (SVM) is proposed.

Finally, some unsupervised methods have been applied in EIT reconstruction imaging. In [135], a fuzzy C-means clustering algorithm is proposed for the evaluation of reconstructed EIT images without the need of any prior information or reference images. The method is further expanded in[136]. Overall, an extensive review on DL algorithms for resolving inverse scattering problems (before 2020) can be found in [137].

2.9.2 Sparse Bayesian Learning (SBL)

The Sparse Bayesian Learning (SBL) is an unsupervised machine learning technique, introduced in the signal processing field in [138], [139], [140] and [141]. It assumes the conductivity distribution of an examined object as a set of clusters, lying in a homogeneous background, and, therefore, the conductivity is represented at a sparse form. Furthermore structure-aware SBL (SA-SBL), applied in EIT in [142], considers both for the clustered sparsity and intra-cluster correlation (via pattern coupling) to achieve improved reconstruction accuracy.

The SBL belongs in the second learning approach category defined in 2.9.1, where measurement data and information about the forward model (sensitivity matrix) are needed. Assuming Gaussian noise

$\boldsymbol{e_n} \in \mathbb{R}^{Nh\times 1}$ in the measurement data $\boldsymbol{V}$, we get the following linearized model:

$$\boldsymbol{J\sigma} + \boldsymbol{e_n} \simeq \boldsymbol{V} \tag{2.97}$$

Instead of the general objective function form defined in (2.28), SBL assumes a Bayes-form log-likelihood one:

$$\boldsymbol{\sigma}_* = \underset{\boldsymbol{\sigma}\in\mathbb{R}^L}{\operatorname{argmin}}\Big\{ \ln p(\boldsymbol{V}|\boldsymbol{\sigma}) + \lambda \ln p(\boldsymbol{\sigma};\boldsymbol{\Theta})\Big\} \tag{2.98}$$

where $\boldsymbol{\Theta}$ is a set of hyperparameters and $\boldsymbol{\sigma}$ is considered as a cluster superposition. The first term demonstrates the least-squares (fidelity) one, while the second one represents the regularization terms. Assuming that the clusters overlap each other with an equal size of H, we get a total number of $g = L - H + 1$ clusters. The conductivity $\boldsymbol{\sigma}$ is factorized as follows:

$$\boldsymbol{\sigma} = \boldsymbol{\Psi x} = [\boldsymbol{\Psi_1}, ..., \boldsymbol{\Psi_g}][\boldsymbol{x_1}^T, ..., \boldsymbol{x_g}^T]^T \tag{2.99}$$

where $\boldsymbol{x_i} \in \mathbb{R}^{H\times 1}$ and $\boldsymbol{\Psi_i} = \begin{bmatrix}\mathbf{0}^T_{(i-1)\times H} & \boldsymbol{I}_{H\times H} & \mathbf{0}^T_{(L-i-H+1)\times H}\end{bmatrix}^T \in \mathbb{R}^{L\times H}$. The model (2.97) is now written as:

$$\boldsymbol{V} = \boldsymbol{J\sigma} + \boldsymbol{e_n} = \boldsymbol{J\Psi x} + \boldsymbol{e_n}. \tag{2.100}$$

The following matrix is also defined $\boldsymbol{\Phi} = \boldsymbol{J\Psi} \in \mathbb{R}^{Nh\times gH}$. According to the SBL theory, the weight vector $\boldsymbol{x} \in \mathbb{R}^{gH\times 1}$ obeys the following Gaussian distribution

$$p\left(\boldsymbol{x}; \{\gamma_i, \boldsymbol{B_i}\}_{i=1}^g\right) = \mathcal{N}\left(0, \boldsymbol{\Sigma_0}\right) \tag{2.101}$$

with zero mean value and $\boldsymbol{\Sigma_0} \in \mathbb{R}^{gH\times gH}$ stretched covariance matrix:

$$\boldsymbol{\Sigma_0} = \begin{bmatrix} \gamma_1\boldsymbol{B_1} & ... & \mathbf{0}_{\boldsymbol{H\times H}} \\ ... & ... & ... \\ \mathbf{0}_{\boldsymbol{H\times H}} & ... & \gamma_g\boldsymbol{B_g} \end{bmatrix} \tag{2.102}$$

The hyperparameters are then expressed as $\boldsymbol{\Theta} = \{\gamma_o, \{\gamma_i, \boldsymbol{B_i}\}_{i=1}^g\}$. Assuming zero mean value and covariance proportional to γ_o for the noise $\boldsymbol{e_n}$, we get a maximum a-posteriori (MAP) expression for the weight vector $\boldsymbol{x}$:

$$p\left(\boldsymbol{x}|\boldsymbol{v};\boldsymbol{\Theta}\right) = \mathcal{N}(\boldsymbol{\mu_x}, \boldsymbol{\Sigma_x}) \tag{2.103}$$

The mean values vector can be estimated as follows [142]:

$$\boldsymbol{\mu_x} = \boldsymbol{\Sigma_o \Phi^T \Sigma_u^{-1}} \tag{2.104}$$

while the covariance matrix is given by the following expression:

$$\boldsymbol{\Sigma_x} = \boldsymbol{\Sigma_0} - \boldsymbol{\Sigma_0 \Phi^T \Sigma_u^{-1} \Phi \Sigma_0} \tag{2.105}$$

where $\boldsymbol{\Sigma_u} = \gamma_o \boldsymbol{I}_{Nh\times Nh} + \boldsymbol{\Phi}\boldsymbol{\Sigma_o}\boldsymbol{\Phi}^{\boldsymbol{T}}$.

The hyperparameter γ_o is updated as follows:

$$\gamma_o^{new} = \frac{1}{Nh}\left(\|\boldsymbol{V} - \boldsymbol{\Phi}\boldsymbol{\mu_x}\|_2^2 + \sum_{i=1}^{g} tr\left(\boldsymbol{\Sigma}_{\boldsymbol{x}}^i \boldsymbol{\Phi}_i^T \boldsymbol{\Phi}_i\right)\right) \tag{2.106}$$

If pattern-coupling is applied (see [142]), the γ_i coefficients are also updated according to the following expression:

$$\gamma_i^{new} = \left[\gamma_i + \beta(\gamma_{i+} + \gamma_{i-})\right] \cdot \frac{\left\|\sqrt{\boldsymbol{B_i}}\boldsymbol{\Phi}_i^T \boldsymbol{\Sigma_u}^{-1}\boldsymbol{V}\right\|_2}{\sqrt{tr\left(\boldsymbol{\Phi}_i^T \boldsymbol{\Sigma_u}^{-1}\boldsymbol{\Phi}_i \boldsymbol{B_i}\right)}} \tag{2.107}$$

for each cluster $i \in \{1, ..., g\}$. Furthermore, γ_{i+}, γ_{i-} denote the neighboring clusters to γ_i, establishing a correlation between them in the $\boldsymbol{\gamma}$ updating rule, and controlling it with a parameter β.

The correlation structure matrix $\boldsymbol{B_i}$ is initialized as $\boldsymbol{B_i} = Toeplitz\left(\left[0.9^0, ..., 0.9^{h-1}\right]\right)$ and updated as

$$\boldsymbol{B}_{\boldsymbol{i}}^{new} = Toeplitz\left(\left[r_i^0, ..., r_i^{h-1}\right]\right) \tag{2.108}$$

where

$$r_i = sign(\tilde{r}_i) \cdot \min\{|\tilde{r}_i|,\ 0.99\}, \tag{2.109}$$

$$r_i = \tilde{r}_i = \frac{\overline{diag\left(\tilde{\boldsymbol{B}}_{\boldsymbol{i}}, 1\right)}}{\overline{diag\left(\tilde{\boldsymbol{B}}_{\boldsymbol{i}}\right)}}, \tag{2.110}$$

for each cluster $i \in \{1, ..., g\}$ and

$$\tilde{\boldsymbol{B}}_{\boldsymbol{i}}^{new} = \tilde{\boldsymbol{B}}_{\boldsymbol{i}} + \frac{1}{\gamma_i}\left(\boldsymbol{\Sigma}_{\boldsymbol{x}}^i + \boldsymbol{\mu}_{\boldsymbol{x}}^i \left(\boldsymbol{\mu}_{\boldsymbol{x}}^i\right)^T\right). \tag{2.111}$$

The covariance matrices $\boldsymbol{\Sigma_o}$ and $\boldsymbol{\Sigma_v}$ need to be updated in each iteration according to (2.102) and (2.105) respectively. When the convergence criterion is satisfied, the final conductivity estimation is given by: $\boldsymbol{\sigma_*} = \boldsymbol{\Psi}\boldsymbol{\mu_x}$.

The process and the SA-SBL algorithm's properties are detailed in [142], while a simple SBL approach is applied along with a Method-of-Moment (MoM) technique for lung imaging in Chapter 4. The SBL approach provides noise robustness to the EIT reconstruction procedure, eliminating artefacts that are present with traditional regularization methods at the cost of high complexity, which is $\mathcal{O}(N^2h^2gH)$ per iteration.

To overcome the complexity issue, an accelerated SA-SBL algorithm has been proposed for 3D EIT reconstructions in [143]. To improve the computation speed, an approximate message passing (AMP) [144] accelerated expectation maximization (EM) technique is proposed. The AMP gives a MAP estimation for $\boldsymbol{\mu_x}$ and $\boldsymbol{\Sigma_x}$ per each iteration. This approach is also adopted in [145] in an effort to improve complexity with time-sequence learning in real-time EIT applications. Finally, SA-SBL has also been applied in frequency-difference EIT [146].

3 An efficient Point-Matching Method-of-Moments for 2D and 3D Electrical Impedance Tomography Using Radial Basis functions

In this section, an integral equation approach for difference-EIT imaging, based on the point-matching Method of Moments (M.o.M.) is presented. The expression of the electrode voltages is a non-linear (logarithmic) function of the conductivity, derived from Green's second identity. This differs from the formulation in (2.20), where the relation between conductivity change and electrode voltages is linearly approximated and applies only for small conductivity changes. Furthermore, the logarithm of conductivity is expressed using Gaussian or modified Radial Basis Functions (RBFs), instead of the conventional piecewise linear or polynomial basis functions utilized in the weak linearized formulation (2.20). In addition, the voltage and field distributions are demonstrated as differences of Green's functions and their derivatives, depending on the measurement pattern adopted.

A system matrix is formulated, which presents an improved singular value spectrum compared to the F.E.M. piecewise linear approaches. L^1 and L^2-norm regularization techniques are applied to solve the linear system of equations. Simulations and experimental test-cases on 2D reconstruction domains show improved qualitative and quantitative results obtained using single-step (direct) reconstruction with L^2-norm regularization, even for strong conductivity variations. In contrast, the conventional approach needed a number of iterations to produce an acceptable result when such variations apply. Moreover, the proposed method when using L^1-norm regularization, also provided good reconstruction quality with a lower number of iterations than the corresponding conventional approach. Simulations performed over a 3D cylindrical geometry, in the presence of minor modeling errors, show superior conductivity inclusion reconstruction results at the electrode-height area. Finally, the proposed method is tested on in-vivo thoracic data, where fast reconstruction is crucial for high frame rate time-difference EIT. The corresponding images, reconstructed on thoracic-shape geometries, show successful detection of the lung's air-content related conductivity changes over time.

The method is straightforward to apply, providing that the Green function in the reconstruction domain is analytically or numerically computed. This formulation allows us to embed the boundary conditions into the integral equation. Contrary to the iterative F.E.M. solution, the proposed method results in a linear system of equations which can be solved in a single step, when L^2-norm regularization is used.

Furthermore, for standard geometries, the system and prior matrices can be precomputed and stored, resulting in fast image reconstruction.

3.1 Methods

In EIT, low frequency currents are injected into the, two or three-dimensional, domain of interest $\Omega \subset \mathbb{R}^n$, $n \in \{2, 3\}$, rendering an electromagnetic problem of quasi-static nature. We consider N electrodes located at the points $\{\boldsymbol{e_m}\}_1^N$. Throughout this work, we assume that $\{\boldsymbol{e_m}\}_1^N$ are internal points of Ω, yet close to the boundary $\partial\Omega$. The Point Electrode Model (PEM) is considered for simplicity [24], since this work focuses on difference-EIT imaging, where the electrode effects are eliminated [147]. However the forward problem formulation can be extended in order to include the electrodes' effects.

3.1.1 EIT Integral Equation Formulation

Assume current I is sourced and sinked via the injecting electrodes at points $\boldsymbol{r}_+$ and $\boldsymbol{r}_-$, respectively. The theory of electrostatics implies that voltage U, considered in the Sobolev space $H^1(\Omega)$, satisfies the Poisson-Neumann problem [24], is parameterized on $\boldsymbol{r}_+$ and $\boldsymbol{r}_-$, i.e. $U(\cdot; \boldsymbol{r}_+, \boldsymbol{r}_-)$, and therefore

$$\nabla\big(\sigma(\boldsymbol{r})\nabla U(\boldsymbol{r}; \boldsymbol{r}_+, \boldsymbol{r}_-)\big) = Ik\big(\delta(\boldsymbol{r} - \boldsymbol{r}_+) - \delta(\boldsymbol{r} - \boldsymbol{r}_-)\big) \tag{3.1}$$

for $\boldsymbol{r} \in \Omega$ and $\boldsymbol{r}_+, \boldsymbol{r}_- \in \{\boldsymbol{e_m}\}_1^N$. In addition we have the boundary condition

$$\frac{\partial U(\boldsymbol{r}; \boldsymbol{r}_+, \boldsymbol{r}_-)}{\partial \boldsymbol{n}} = 0 \tag{3.2}$$

for $\boldsymbol{r} \in \partial\Omega$. Moreover $\sigma : \Omega \to \mathbb{R}$ is the conductivity function, $k = 1/\text{meter}^n$ is a constant, $\boldsymbol{r} \in \Omega$ is the observation point, δ is the Dirac delta function and $\boldsymbol{n}$ is the normal outward-pointing vector (Fig. 3.1α′).

The model described by (3.1) and (3.2) will be converted to integral form. To this end, we define the following Poisson's problem with Neumann boundary conditions and use it to generate a convenient Green's function. We have

$$\nabla^2 G(\boldsymbol{r}, \boldsymbol{r'}) = -\delta(\boldsymbol{r} - \boldsymbol{r'}), \quad \boldsymbol{r}, \boldsymbol{r'} \in \Omega \tag{3.3}$$

$$\frac{\partial G(\boldsymbol{r}, \boldsymbol{r'})}{\partial \boldsymbol{n}} = -\frac{1}{S}, \quad \boldsymbol{r} \in \Omega,\ \boldsymbol{r'} \in \partial\Omega \tag{3.4}$$

where the differentiation[1] is with respect to $\boldsymbol{r'}$ and S is the perimeter or surface of $\partial\Omega$, required for the divergence Theorem to hold [148].

The solution of (3.3)-(3.4) is inserted into Green's second identity along with the voltage function $U(\boldsymbol{r}; \boldsymbol{r}_+, \boldsymbol{r}_-)$. Then, for any observation point $\boldsymbol{r} \in \Omega$ and any pair $\boldsymbol{r}_+, \boldsymbol{r}_- \in \{\boldsymbol{e_m}\}_1^N$, integration with

[1] Differentiation in (3.3) can be done in terms of $\boldsymbol{r}$ or $\boldsymbol{r'}$, due to the symmetry of the Green's function

respect to $\boldsymbol{r'}$ gives

$$\begin{aligned}&\int_{\Omega}\Big(G(\boldsymbol{r},\boldsymbol{r'})\nabla^2 U(\boldsymbol{r'};\boldsymbol{r}_+,\boldsymbol{r}_-)-U(\boldsymbol{r'};\boldsymbol{r}_+,\boldsymbol{r}_-)\nabla^2 G(\boldsymbol{r},\boldsymbol{r'})\Big)dA\\&=\oint_{\partial\Omega}\left(G(\boldsymbol{r},\boldsymbol{r'})\frac{\partial U(\boldsymbol{r'};\boldsymbol{r}_+,\boldsymbol{r}_-)}{\partial \boldsymbol{n}}-U(\boldsymbol{r'};\boldsymbol{r}_+,\boldsymbol{r}_-)\frac{\partial G(\boldsymbol{r},\boldsymbol{r'})}{\partial \boldsymbol{n}}\right)dS\end{aligned} \tag{3.5}$$

where again all derivatives are with respect to $\boldsymbol{r'}$. Since the integration at the right hand side of (3.5) is done with $\boldsymbol{r'}\in\partial\Omega$, (3.2) implies

$$\oint_{\partial\Omega} G(\boldsymbol{r},\boldsymbol{r'})\frac{\partial U(\boldsymbol{r'};\boldsymbol{r}_+,\boldsymbol{r}_-)}{\partial \boldsymbol{n}}dS=0 \tag{3.6}$$

Furthermore, for the second part of the right hand side of (3.5), from (3.4) we get

$$\oint_{\partial\Omega} U(\boldsymbol{r'};\boldsymbol{r}_+,\boldsymbol{r}_-)\frac{\partial G(\boldsymbol{r},\boldsymbol{r'})}{\partial \boldsymbol{n}}dS=C(\boldsymbol{r}_+,\boldsymbol{r}_-) \tag{3.7}$$

where we have defined

$$C(\boldsymbol{r}_+,\boldsymbol{r}_-)\triangleq-\frac{1}{S}\oint_{\partial\Omega} U(\boldsymbol{r'};\boldsymbol{r}_+,\boldsymbol{r}_-)dS. \tag{3.8}$$

Note that $C(\boldsymbol{r}_+,\boldsymbol{r}_-)$ is independent of the observation point $\boldsymbol{r}$ but depends on our selection of the voltage reference node.

To proceed we assume that *The $\sigma(\boldsymbol{r})$ function is constant and equal to some value σ_o in neighborhoods of the electrode points* $\{\boldsymbol{e_m}\}_1^N$. Based on this assumption and the previous development, the EIT Green integral equation is given by (3.9)

$$\begin{aligned}U(\boldsymbol{r};\boldsymbol{r}_+,\boldsymbol{r}_-)=&\int_{\Omega} G(\boldsymbol{r},\boldsymbol{r'})\nabla\left(\ln\sigma(\boldsymbol{r'})\right)\cdot\nabla U(\boldsymbol{r'};\boldsymbol{r}_+,\boldsymbol{r}_-)dA\\&+U_o(\boldsymbol{r};\boldsymbol{r}_+,\boldsymbol{r}_-)\end{aligned} \tag{3.9}$$

where we have used $\nabla\left(\ln\sigma(\boldsymbol{r'})\right)=\nabla\left(\sigma(\boldsymbol{r'})\right)/\sigma(\boldsymbol{r'})$ and We have also defined

$$U_o(\boldsymbol{r};\boldsymbol{r}_+,\boldsymbol{r}_-)\triangleq\frac{Ik}{\sigma_o}\big(G(\boldsymbol{r},\boldsymbol{r}_-)-G(\boldsymbol{r},\boldsymbol{r}_+)\big)+C(\boldsymbol{r}_+,\boldsymbol{r}_-) \tag{3.10}$$

is the (homogeneous) voltage when the conductivity is σ_o (constant) within the whole domain Ω.

Equation (3.9) gives the potential U at the observation point $\boldsymbol{r}$, when current is injected at $\boldsymbol{r}_+$ and $\boldsymbol{r}_-$ (Fig. 2). The integral in (3.9) captures the voltage deviation $U-U_o$ as a non-linear function of the inhomogeneity $\Delta\sigma=\sigma-\sigma_o$ and σ_o.

This formulation differs from the traditional difference-EIT forward one which performs linearization for small conductivity changes [149]. It also differs from the B.E.M. formulation since the latter one discretizes the boundary integral equation (i.e. the right term in (3.5)), [14], [33].

3.1.2 Initial Approximation and Refinement

In the definition of the EIT's Green integral equation (3.9), the Green's function $G(\boldsymbol{r}, \boldsymbol{r'})$ and the homogeneous voltage distribution $U_o(\boldsymbol{r'}; \boldsymbol{r}_+, \boldsymbol{r}_-)$ are known (analytically or numerically), whereas the inhomogeneous field ∇U and the conductivity function $\sigma(\boldsymbol{r})$ are unknown. The product of these two unknowns makes (3.9) a nonlinear (bilinear) problem. To proceed, we simplify (3.9) by approximating ∇U by ∇U_o, which is known, reducing the problem to

$$U(\boldsymbol{r}; \boldsymbol{r}_+, \boldsymbol{r}_-) = \int_\Omega G(\boldsymbol{r}, \boldsymbol{r'}) \nabla \left(\ln \sigma(\boldsymbol{r'}) \right) \cdot \nabla U_o(\boldsymbol{r'}; \boldsymbol{r}_+, \boldsymbol{r}_-) dA + U_o(\boldsymbol{r}; \boldsymbol{r}_+, \boldsymbol{r}_-) \tag{3.11}$$

This approximation is used to get an initial solution for the conductivity. It differs from the conventional forward approach [35], [149], where the product of the conductivity and the electric field is linearized around σ_o and U_o.

It is noted that the Green's function as well as the homogeneous reference voltage distribution and field can be derived either analytically when reconstructing on canonical geometries or numerically (via the F.E.M. or F.D.M.) when reconstructing on non-canonical shapes.

From (3.11) and assuming sufficient smoothness and compactness of Ω, the electric field at any observation point $\boldsymbol{r} \in \Omega$ can be derived by taking the gradient with respect to $\boldsymbol{r}$, i.e.,

$$\nabla_{\boldsymbol{r}} U(\boldsymbol{r}; \boldsymbol{r}_+, \boldsymbol{r}_-) = \int_\Omega \nabla_r G(\boldsymbol{r}, \boldsymbol{r'}) \nabla \left(\ln \sigma(\boldsymbol{r'}) \right) \cdot \nabla U_o(\boldsymbol{r'}; \boldsymbol{r}_+, \boldsymbol{r}_-) dA + \nabla_{\boldsymbol{r}} U_o(\boldsymbol{r}; \boldsymbol{r}_+, \boldsymbol{r}_-). \tag{3.12}$$

3.1.3 Domain and Equations Discretization

To proceed with the discretization of the point-matching M.o.M. problem and the conversion of it into a system of linear equations, we start with the domain Ω. We assume a partition of Ω into L subdomains (2D or 3D depending on Ω), e.g. as shown in Fig. 3.1β′, with center points $\boldsymbol{r_i}$, $i \in \{1, 2, ..., L\}$ and areas (or volumes) $\boldsymbol{A_i}$, $i \in \{1, 2, ..., L\}$, respectively.

Since the voltage measurements in EIT take place at the electrodes, the observation point $\boldsymbol{r}$ in (3.11) should be such that $\boldsymbol{r} = \boldsymbol{e_m}$, for some $m \in \{1, 2, ..., N\}$. Similarly the current is injected at $\boldsymbol{r}_+ = \boldsymbol{e_k}$ and $\boldsymbol{r}_- = \boldsymbol{e_l}$ for some $k, l \in \{1, 2, ..., N\}$.

To discretize equation (3.11) we define the following

$$\begin{aligned} U_{k,l,m} &\triangleq U(\boldsymbol{e_m}; \boldsymbol{e_k}, \boldsymbol{e_l}), \quad U^o_{k,l,m} \triangleq U_o(\boldsymbol{e_m}; \boldsymbol{e_k}, \boldsymbol{e_l}) \\ E^o_{k,l,i} &\triangleq -\nabla U_o(\boldsymbol{r'}; \boldsymbol{e_k}, \boldsymbol{e_l})|_{\boldsymbol{r'}=\boldsymbol{r_i}} \\ g_{m,i} &\triangleq G(\boldsymbol{e_m}, \boldsymbol{r_i}) \\ K_i &\triangleq \nabla \left(\ln \sigma(\boldsymbol{r'}) \right) |_{\boldsymbol{r'}=\boldsymbol{r_i}} \end{aligned} \tag{3.13}$$

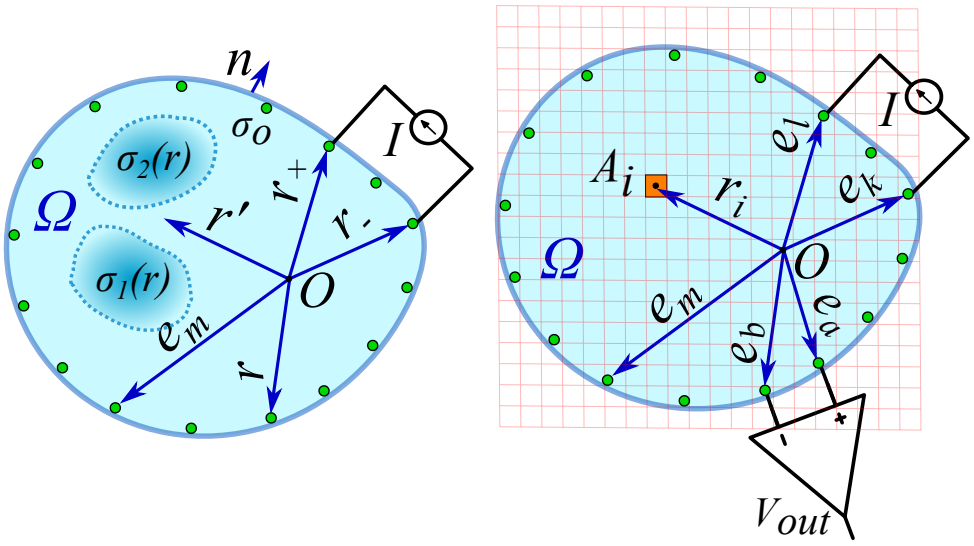

(α′) (β′)

Figure 3.1: a) Description of the EIT concept on a random geometry Ω area. b) Discretization of a random geometry Ω area.

to get

$$U_{k,l,m} = -\sum_{i=1}^{L} g_{m,i} E^{o}_{k,l,i} \cdot K_i A_i + U^{o}_{k,l,m}. \tag{3.14}$$

3.1.4 Radial Basis Functions for Conductivity Logarithm

We approximately express $\ln \sigma(\boldsymbol{r'})$ in (3.11) as a weighted sum of translated versions of one of the following two RBFs

$$\theta_1(\boldsymbol{r'}, \boldsymbol{r_j}) \triangleq exp\left(-\frac{\|\boldsymbol{r'} - \boldsymbol{r_j}\|^2}{2D^2}\right) \tag{3.15}$$

and the generalization of it,

$$\theta_2(\boldsymbol{r'}, \boldsymbol{r_j}) \triangleq exp\left(-\frac{\|\boldsymbol{r'} - \boldsymbol{r_j}\|_{p_1}^{p_1/p_2}}{2D^2}\right) \tag{3.16}$$

where $\boldsymbol{r_j}$ is the j^{th} subdomain's central point, $j \in \{1, 2, ..., L\}$. Also, D is a width-adjustment parameter of the RBFs, p_1 and p_2 are properly selected positive integers (p_1 is even), and, $\|.\|_{p_1}$ is the p_1-norm. Using the RBFs the conductivity logarithm is expressed as

$$\ln \sigma(\boldsymbol{r'}) \triangleq \ln \sigma_o + \sum_{j=1}^{L} c_j \theta(\boldsymbol{r'}, \boldsymbol{r_j}) \tag{3.17}$$

where $\{c_j\}_1^N$ are real constants and θ is either θ_1 or θ_2. Then, the gradient of $\ln \sigma(\boldsymbol{r'})$ is written as

$$\nabla \left(\ln \sigma(\boldsymbol{r'}) \right) = \sum_{j=1}^{L} c_j \bar{\theta}(\boldsymbol{r'}, \boldsymbol{r_j}) \tag{3.18}$$

where $\bar{\theta} = [\bar{\theta}_x, \bar{\theta}_y]$ with $\bar{\theta}_x \triangleq \frac{\partial \theta}{\partial x'}$ and $\bar{\theta}_y \triangleq \frac{\partial \theta}{\partial y'}$ (likewise for the 3D case). It can be shown that

$$\bar{\theta}_1(\boldsymbol{r'}, \boldsymbol{r_j}) = -\frac{1}{D^2}(\boldsymbol{r'} - \boldsymbol{r_j}) exp\left(-\frac{\|\boldsymbol{r'} - \boldsymbol{r_j}\|^2}{2D^2} \right) \tag{3.19}$$

as well as that

$$\begin{aligned} \bar{\theta}_2(\boldsymbol{r'}, \boldsymbol{r_j}) = -\frac{p_1}{2p_2 D^2} \left\| \boldsymbol{r'} - \boldsymbol{r_j} \right\|_{p_1}^{(1-p_2)p_1/p_2} \\ \cdot exp\left(-\frac{\|\boldsymbol{r'} - \boldsymbol{r_j}\|_{p_1}^{p_1/p_2}}{2D^2} \right) \cdot \ (\boldsymbol{r'} - \boldsymbol{r_j})^{\bullet(p_1-1)} \end{aligned} \tag{3.20}$$

for $\boldsymbol{r'} \neq \boldsymbol{r_j}$, where $\bullet$ is the Hadammard power [150].

The Gaussian base function $\theta_1(\boldsymbol{r'}, \boldsymbol{r_j})$ is smooth while the generalized one $\theta_2(\boldsymbol{r'}, \boldsymbol{r_j})$ is not, when $p_1 < p_2$. The singularity at $\boldsymbol{r'} = \boldsymbol{r_j}$ and the particular shape of the gradient of the last one can be used to improve the contrast of the final image. It requires certain care however when it is used numerically.

Using the above definitions, vectors K_i in (3.13) admit the following expression

$$K_i = \sum_{j=1}^{L} c_j \bar{\theta}_{i,j} \tag{3.21}$$

where we have set $\bar{\theta}_{i,j} = \bar{\theta}(\boldsymbol{r_i}, \boldsymbol{r_j})$.

3.1.5 Linear System Formulation

Replacing (3.21) into (3.14) gives

$$U_{k,l,m} = -\sum_{j=1}^{L} c_j \sum_{i=1}^{L} g_{m,i} E^o_{k,l,i} \cdot \bar{\theta}_{i,j} A_i + U^o_{k,l,m} \tag{3.22}$$

For the rest of this work we assume that the current skip-s and voltage skip-t pattern is utilized [26]. Since the current is injected in electrodes k and l, as captured in (3.14) and (3.22), they should satisfy $l = (k+s) \mod N+1$. Moreover, let differential voltage measurement be taken from b to a electrodes. Then it must be $b = (a+t) \mod N+1$.

Given s, t and k, the value of l is defined and the pair (a, b) can take a certain number, say h, of vector values. Formally we can define the set function $S : \{1, 2, ..., N\} \to 2^{\{1,2,...,N\} \times \{1,2,...,N\}}$ such as $S(k; s, t, N) = \{\text{all feasible pairs } (a, b) \mid \text{given } s, t \text{ and } k\}$. Hence $h = |S(k; s, t, N)|$. Particularly, if

tetrapolar measurement is used, we have

$$h = \left\{ \begin{array}{ll} N-3, & s = t \\ N-4, & s \neq t \end{array} \right\}.$$

From hereon we assume tetrapolar measurement and for a, b, k and l satisfying the above we define the following voltage and Green function values' differences

$$\begin{aligned} \delta U_{k,l}^{a,b} &\triangleq U_{k,l,a} - U_{k,l,b}, \quad \delta U_{k,l}^{o,a,b} \triangleq U_{k,l,a}^{o} - U_{k,l,b}^{o} \\ \text{and } \delta g_i^{a,b} &\triangleq g_{a,i} - g_{b,i} \end{aligned} \tag{3.23}$$

Then, the forward solver (3.22) is written in difference form

$$\delta U_{k,l}^{a,b} = -\sum_{j=1}^{L} c_j \sum_{i=1}^{L} \delta g_i^{a,b} E_{k,l,i}^{o} \cdot \bar{\theta}_{i,j} A_i + \delta U_{k,l}^{o,a,b}. \tag{3.24}$$

To proceed with the definitions of the matrices and the vectors involved in the discrete problem formulation, we need to order the elements of the set $S(k; s, t, N)$. To this end we assume two functions (among the many possible ones and parameterized on k as well as on s, t and N - not shown for convenience)

$$\hat{a}(.;k), \hat{b}(.;k) : \{1, 2, ..., h\} \rightarrow \{1, 2, ..., N\} \tag{3.25}$$

such that $S(k; s, t, N) = \left\{ \left(\hat{a}(n;k), \hat{b}(n;k) \right) |_{n=1}^{h} \right\}$.

For example, when using the adjacent current pattern (current and voltage skip-0), $N = 16$ electrodes and current flows through the 1^{st} and the 2^{nd} electrodes, we get

$$S(1; 0, 0, 16) = \{[3, 4, ..., 15], [4, 5, ..., 16]\} \tag{3.26}$$

Following the above, for a given value of k (and thus of l) we define

$$\begin{aligned} \boldsymbol{\delta U_k} &\triangleq \left[\delta U_{k,l}^{\hat{a}(n;k),\hat{b}(n;k)} \right]_{n=1}^{h} \quad \boldsymbol{\delta U_k^o} \triangleq \left[\delta U_{k,l}^{o,\hat{a}(n;k),\hat{b}(n;k)} \right]_{n=1}^{h} \\ \boldsymbol{\delta G_k^o} &\triangleq \left[\delta g_i^{\hat{a}(n;k),\hat{b}(n;k)} \right]_{\substack{n=1,2,...,h \\ i=1,2,...,L}} \\ \boldsymbol{\Psi_k^o} &\triangleq \left[\text{diag}([E_{k,l,i,x}^{o}]_{i=1}^{L}),\ \text{diag}([E_{k,l,i,y}^{o}]_{i=1}^{L}) \right] \\ \bar{\boldsymbol{\Theta}} &\triangleq \left[\begin{array}{cc} \left[\bar{\theta}_{i,j,x})\right]_{\substack{i=1,2,...,L \\ j=1,2,...,L}}^{T}, & \left[\bar{\theta}_{i,j,y}\right]_{\substack{i=1,2,...,L \\ j=1,2,...,L}}^{T} \end{array} \right]^T \\ \boldsymbol{I_A} &\triangleq \text{diag}([A_i]_{i=1}^{L}), \quad \boldsymbol{c} \triangleq \left[c_j\right]_{j=1}^{L} \end{aligned} \tag{3.27}$$

where $\boldsymbol{\delta U_k} \in \mathbb{R}^{h \times 1}$, $\boldsymbol{\delta U_k^o} \in \mathbb{R}^{h \times 1}$, $\boldsymbol{\delta G_k^o} \in \mathbb{R}^{h \times L}$, $\boldsymbol{\Psi_k^o} \in \mathbb{R}^{L \times 2L}$, $\bar{\boldsymbol{\Theta}} \in \mathbb{R}^{2L \times L}$, $\boldsymbol{I_A} \in \mathbb{R}^{L \times L}$ and $\boldsymbol{c} \in \mathbb{R}^{L \times 1}$. It is noted that most entries in every row of $\bar{\boldsymbol{\Theta}}$ are very close to zero, due to the RBF's

degradation. Values below a selected threshold can be set to zero making $\bar{\boldsymbol{\Theta}}$ a sparse matrix, significantly accelerating the computations in (3.28) without any essential degradation of the results' quality. Indeed, MATLAB simulations showed that for a threshold of 10^{-2} (or lower) and for D equal to each pixel's length, the image reconstruction quality is not essentially affected. Finally, the matrices and vectors are defined accordingly for the 3D case.

With the above definitions, the forward solver (3.24) is written in the following vectorized form

$$\boldsymbol{\delta U_k} = -\boldsymbol{\delta G_k^o} \cdot \boldsymbol{I_A} \cdot \boldsymbol{\Psi_k^o} \cdot \bar{\boldsymbol{\Theta}} \cdot \boldsymbol{c} + \boldsymbol{\delta U_k^o}. \tag{3.28}$$

Furthermore, grouping (3.28) for all N current injection pairs (k, l) we get the following linear system of equations

$$\boldsymbol{\delta U} = -\boldsymbol{T^o} \cdot \bar{\boldsymbol{\Theta}} \cdot \boldsymbol{c} + \boldsymbol{\delta U^o} \tag{3.29}$$

where matrix $\boldsymbol{T^o} \in \mathbb{R}^{(Nh)\times(2L)}$, and vectors $\boldsymbol{\delta U} \in \mathbb{R}^{(Nh)\times 1}$, and $\boldsymbol{\delta U^o} \in \mathbb{R}^{(Nh)\times 1}$ are defined respectively as

$$\boldsymbol{T^o} \triangleq \begin{bmatrix} \boldsymbol{\delta G_1^o} \cdot \boldsymbol{I_A} \cdot \boldsymbol{\Psi_1^o} \\ \boldsymbol{\delta G_2^o} \cdot \boldsymbol{I_A} \cdot \boldsymbol{\Psi_2^o} \\ \cdots \\ \boldsymbol{\delta G_N^o} \cdot \boldsymbol{I_A} \cdot \boldsymbol{\Psi_N^o} \end{bmatrix}, \boldsymbol{\delta U} \triangleq \begin{bmatrix} \boldsymbol{\delta U_1} \\ \boldsymbol{\delta U_2} \\ \cdots \\ \boldsymbol{\delta U_N} \end{bmatrix}, \boldsymbol{\delta U^o} \triangleq \begin{bmatrix} \boldsymbol{\delta U_1^o} \\ \boldsymbol{\delta U_2^o} \\ \cdots \\ \boldsymbol{\delta U_N^o} \end{bmatrix} \tag{3.30}$$

Finally, setting

$$\boldsymbol{\delta \tilde{U}} = \boldsymbol{\delta U} - \boldsymbol{\delta U^o} \tag{3.31}$$

and

$$\boldsymbol{M^o} \triangleq \frac{\partial \boldsymbol{\delta U}}{\partial \boldsymbol{c}^T} = -\boldsymbol{T^o} \cdot \bar{\boldsymbol{\Theta}} \tag{3.32}$$

where $\boldsymbol{M^o} \in \mathbb{R}^{(Nh)\times L}$, the linear system is written as

$$\boldsymbol{M^o c} = \boldsymbol{\delta \tilde{U}}. \tag{3.33}$$

Note that matrix $\boldsymbol{M^o}$ is known and typically $Nh < L$ making the problem ill-posed.

Recall that $\boldsymbol{\delta \tilde{U}} \in \mathbb{R}^{(Nh)\times 1}$ in (3.31) is the vector of the differences between the differential voltages $\boldsymbol{\delta U} \in \mathbb{R}^{(Nh)\times 1}$, of the inhomogeneous solution, and those, $\boldsymbol{\delta U^o}$, of the homogeneous one. Since both have to be measured using the EIT hardware setup, in order to be used in solving (3.33), let $\boldsymbol{\delta V}$ and $\boldsymbol{\delta V^o}$ in $\mathbb{R}^{(Nh)\times 1}$ be the *measurements* of $\boldsymbol{\delta U}$ and $\boldsymbol{\delta U^o}$ respectively and define

$$\boldsymbol{\delta \tilde{V}} = \boldsymbol{\delta V} - \boldsymbol{\delta V^o}. \tag{3.34}$$

To account for measurement errors and noise we assume that

$$\boldsymbol{\delta \tilde{U}} = \boldsymbol{\delta \tilde{V}} + \boldsymbol{e_n} \tag{3.35}$$

where $\boldsymbol{e_n}$ is zero-mean Gaussian random vector [151]. Replacing in (3.33) we conclude that

$$\boldsymbol{M^o c} = \boldsymbol{\delta \tilde{V}} + \boldsymbol{e_n}. \tag{3.36}$$

We solve (3.36) for $\boldsymbol{c}$ as a weighted (W) Least-Squares problem adding a regularization cost function $P(.)$ since the problem is otherwise ill-conditioned, therefore,

$$\boldsymbol{c_*} = \underset{\boldsymbol{c} \in R^L}{\operatorname{argmin}} \Big\{ F(\boldsymbol{c}) \Big\} \tag{3.37}$$

where

$$F(\boldsymbol{c}) = \left\| \boldsymbol{M^o c} - \boldsymbol{\delta \tilde{V}} \right\|_{\boldsymbol{W}}^2 + \lambda^2 P(\boldsymbol{c}). \tag{3.38}$$

The (symmetric positive defininte) weighting matrix $\boldsymbol{W} \in \mathbb{R}^{(Nh)\times(Nh)}$ is often selected to be the noise $\boldsymbol{e_n}$ covariance matrix, typically diagonal. Parameter (hyperparameter) λ balances the weighting between the terms for regularization.

Finally, we note that in order to derive $\boldsymbol{M^o}$ and use it in (3.38), we need the value of the reference (homogeneous) conductivity distribution σ_o in (3.10). We follow [149] to derive an estimate of σ_o. To this end we define vectors $\boldsymbol{\delta Y_k} \in \mathbb{R}^{h\times 1}$, $k = 1, 2, \ldots, N$ and $\boldsymbol{\delta Y} \in \mathbb{R}^{(Nh)\times 1}$ as

$$\begin{aligned} Y_{m,k,l} &\triangleq G(\boldsymbol{e_m}, \boldsymbol{e_k}) - G(\boldsymbol{e_m}, \boldsymbol{e_l}),\ \delta Y_{k,l}^{a,b} \triangleq Y_{a,k,l} - Y_{b,k,l} \\ \boldsymbol{\delta Y_k} &\triangleq \left[\delta Y_{k,l}^{\hat{a}(n;k),\hat{b}(n;k)} \right]_{n=1}^{h} \\ \boldsymbol{\delta Y} &\triangleq \left[\left(\boldsymbol{\delta Y_1}\right)^T, \left(\boldsymbol{\delta Y_2}\right)^T, \ldots \left(\boldsymbol{\delta Y_N}\right)^T \right]^T. \end{aligned} \tag{3.39}$$

Then

$$\sigma_o = \frac{I \cdot \|\boldsymbol{\delta Y}\|_2^2}{(\boldsymbol{\delta Y})^T \cdot \boldsymbol{\delta V^o}}. \tag{3.40}$$

3.1.6 Solution of the Inverse Problem

The problem (3.37)-(3.38) can be solved with the Gauss-Newton single-step or iterative approach [30],[55]. The regularization function P it typically the L^2-norm, when expecting smooth conductivity variation, or the L^1-norm, if more steep variation is expected [151].

L^2-Norm Regularization

In this case, the $P(\boldsymbol{c})$ term is written in the following quadratic form

$$P(\boldsymbol{c}) = \|\boldsymbol{c}\|_{\boldsymbol{Q}}^2 \tag{3.41}$$

where (symmetric positive defininte) $\boldsymbol{Q} \in \mathbb{R}^{L\times L}$ is a smooth prior filter matrix (e.g. Laplace prior, NOSER, Gaussian, e.t.c.) [28], [30], [54], [55] or the identity matrix (Tikhonov regularization). The exact

solution of (3.37)-(3.38), is given in closed form

$$\boldsymbol{c} = \left((\boldsymbol{M^o})^T \boldsymbol{W} \boldsymbol{M^o} + \lambda^2 \boldsymbol{Q}\right)^{-1} (\boldsymbol{M^o})^T \boldsymbol{W} \boldsymbol{\delta \tilde{V}}. \tag{3.42}$$

Contrary to the conventional linearizing approach [37],[149], there is no need for iterations when solving with an L^2 prior, since the conductivity is not approximated by its first Taylor-series term in the governing equation (3.11).

L^1-Norm Regularization

If the expected conductivity distribution has sharp changes, L^1-norm regularization approaches may be preferred, such as the Total Variation (TV) [59],[152]. In this case, the discretized form of the TV regularization prior is expressed as

$$P(\boldsymbol{c}) = \sum_{i=1}^{N_{ed}} \sqrt{\|\boldsymbol{L_i c}\|^2 + \beta} \tag{3.43}$$

where N_{ed} is the total number of edges between the subdomains, $\boldsymbol{L} \in \mathbb{R}^{N_{ed} \times L}$ is a sparse matrix capturing the relationship between the subdomains and their edges [60] and $\beta > 0$ is a parameter essential for the differentiability of P when $\|\boldsymbol{L_i c}\| = 0$ [59], [60]. Here $\boldsymbol{L_i}$ is the i^{th} row of matrix $\boldsymbol{L}$ which corresponds to the i^{th} edge.

To proceed we follow the Primal-Dual Interior Point (PD-IPM) TV method [4], [59], [60], [61]. The solution of (3.38) is approached via iterations, where parameter β is carefully reduced while λ remains constant. For the updates of the solution, we have the following equations

$$\begin{aligned} \boldsymbol{\delta c^\kappa} &= \Big((\boldsymbol{M^\kappa})^T \boldsymbol{W} \boldsymbol{M^\kappa} + \lambda^2 \boldsymbol{L^T} \big(\boldsymbol{E^\kappa}\big)^{-1} \boldsymbol{K^\kappa} \boldsymbol{L}\Big)^{-1} \cdot \\ &\quad \Big((\boldsymbol{M^\kappa})^T \boldsymbol{W} \big(\boldsymbol{\delta \tilde{V}} - \boldsymbol{\delta \tilde{U}^\kappa}\big) - \lambda^2 \boldsymbol{L^T} \big(\boldsymbol{E^\kappa}\big)^{-1} \boldsymbol{L c^\kappa}\Big), \\ \boldsymbol{\delta \chi^\kappa} &= -\boldsymbol{\chi^\kappa} + \big(\boldsymbol{E^\kappa}\big)^{-1} \boldsymbol{L c^\kappa} + \big(\boldsymbol{E^\kappa}\big)^{-1} \boldsymbol{K^\kappa} \boldsymbol{L \delta c^\kappa} \end{aligned} \tag{3.44}$$

where

$$\begin{aligned} \boldsymbol{E^\kappa} &= \operatorname{diag}\Big(\Big[\sqrt{\|\boldsymbol{L_i c^\kappa}\|^2 + \beta}\Big]_{i=1}^{N_{ed}}\Big), \\ \boldsymbol{K^\kappa} &= \operatorname{diag}\left(\left[1 - \frac{\boldsymbol{\chi_i L_i c^\kappa}}{\sqrt{\|\boldsymbol{L_i c^\kappa}\|^2 + \beta}}\right]_{i=1}^{N_{ed}}\right) \end{aligned} \tag{3.45}$$

and $\boldsymbol{\chi} \in \mathbb{R}^{N_{ed} \times 1}$ is the dual variable. A linesearch is needed at every step to find a $\gamma > 0$ to update $\boldsymbol{c^{\kappa+1}} = \boldsymbol{c^\kappa} + \gamma \boldsymbol{\delta c^\kappa}$ in such a way that F in (3.38) is minimized [4]. The update of $\boldsymbol{\chi}$ can be performed with the scaling rule [4]. Furthermore, $\boldsymbol{c}$ and $\boldsymbol{\chi}$ are initialized to zero vectors. Thus, the first iteration is performed as a standard Tikhonov regularization step (see L^2-norm regularization). Finally, $\boldsymbol{M}$ is updated

as follows

$$\boldsymbol{M^{\kappa}} = -\boldsymbol{T^{\kappa}} \cdot \bar{\boldsymbol{\Theta}}, \quad \boldsymbol{T^{\kappa}} = \begin{bmatrix} \boldsymbol{\delta G_1^{\kappa}} \cdot \boldsymbol{I_A} \cdot \boldsymbol{\Psi_1^{\kappa}} \\ \boldsymbol{\delta G_2^{\kappa}} \cdot \boldsymbol{I_A} \cdot \boldsymbol{\Psi_2^{\kappa}} \\ \cdots \\ \boldsymbol{\delta G_N^{\kappa}} \cdot \boldsymbol{I_A} \cdot \boldsymbol{\Psi_N^{\kappa}} \end{bmatrix} \tag{3.46}$$

where $\boldsymbol{\delta G_k^{\kappa}}$ is the updated voltage distribution (Green functions' difference) and $\boldsymbol{\Psi_k^{\kappa}}$ is the updated electric field matrix for the k^{th} current injection after the κ^{th} iteration. The voltage distribution $\boldsymbol{\delta G_k^{\kappa}}$ is updated using the discretized form of (3.11), replacing $\boldsymbol{r_+}$ and $\boldsymbol{r_-}$ with $\boldsymbol{e_a}$ and $\boldsymbol{e_b}$ correspondingly (i.e. the drive with the lead electodes). In addition, the electric field can be updated using the discretized form of (3.12) for $\boldsymbol{r} \in \Omega$ and $\boldsymbol{r'} \in \Omega$. Accuracy can be further improved by mesh refining.

Mesh Refining: To perform the updates (3.44)-(3.45), it is essential to perform accurate numerical integration of (3.11), (3.12). To this end, fine-meshing of Ω can be used. This is done here by pixel refinement, i.e, a number of nodes is uniformly added between every neighbouring pair of central pixels on the regular grid. This results in a fine-pixel mesh of L_f subdomains and their corresponding central points, from which the L central points of the coarse mesh can be sampled.

An interpolation matrix $\boldsymbol{f} \in \mathbb{R}^{L_f \times L}$ is used to get the interpolated coefficients vector $\boldsymbol{c_f} = \boldsymbol{f} \cdot \boldsymbol{c}$, where $\boldsymbol{c_f} \in \mathbb{R}^{L_f \times 1}$. Furthermore, to discretize the integral in (3.11) at L_f subdomains, we define the following matrices

$$\begin{aligned} \boldsymbol{G_f} &\triangleq \Big[G(\boldsymbol{r_{fi}}, \boldsymbol{r_{fj}})\Big]_{\substack{i=1,2,...,L_f \\ j=1,2,...,L_f}}, \boldsymbol{I_{Af}} \triangleq \text{diag}([A_i]_{i=1}^{L_f}) \\ \boldsymbol{\Psi_{f}^{\kappa}}_k &\triangleq \Big[\text{diag}([E_{k,l,i,x}^{\kappa}]_{i=1}^{L_f}),\ \text{diag}([E_{k,l,i,y}^{\kappa}]_{i=1}^{L_f})\Big] \\ \bar{\boldsymbol{\Theta}}_{\boldsymbol{f}} &\triangleq \begin{bmatrix} \big[\bar{\theta}_{i,j,x}\big]^T_{\substack{i=1,2,...,L_f \\ j=1,2,...,L_f}}, \big[\bar{\theta}_{i,j,y}\big]^T_{\substack{i=1,2,...,L_f \\ j=1,2,...,L_f}} \end{bmatrix}^T \end{aligned} \tag{3.47}$$

where $\boldsymbol{G_f} \in \mathbb{R}^{L_f \times L_f}$, $\boldsymbol{\Psi_{k,f}^{\kappa}} \in \mathbb{R}^{L_f \times 2L_f}$, $\bar{\boldsymbol{\Theta}}_{\boldsymbol{f}} \in \mathbb{R}^{2L_f \times L_f}$ and $\boldsymbol{I_{Af}} \in \mathbb{R}^{L_f \times L_f}$. Based on the above and (3.11), the update of the voltage distribution is derived from

$$\boldsymbol{\delta G_k^{\kappa}} = -(\boldsymbol{f^T} \cdot \boldsymbol{f})^{-1} \cdot \boldsymbol{f^T} \cdot \boldsymbol{G_f} \cdot \boldsymbol{I_{Af}} \cdot \boldsymbol{\Psi_{k,f}^{\kappa-1}} \cdot \bar{\boldsymbol{\Theta}}_{\boldsymbol{f}} \cdot \boldsymbol{c_f^{\kappa}} + \boldsymbol{\delta G_k^o} \tag{3.48}$$

To update the electric field using (3.12) we need the Green's function gradient at all L_f central points of the refined mesh. To this end we define

$$\begin{aligned} \bar{\boldsymbol{G}}_{\boldsymbol{f}} &\triangleq \Big[\nabla_r G(\boldsymbol{r}, \boldsymbol{r'})\Big]_{\substack{\boldsymbol{r}=\boldsymbol{r_{fi}}, i=1,2,...,L_f \\ \boldsymbol{r'}=\boldsymbol{r_{fj}}, j=1,2,...,L_f}} \\ \boldsymbol{E_k^o} &\triangleq \Big[[E_{k,l,i,x}^o]_{i=1}^{L},\ [E_{k,l,i,y}^o]_{i=1}^{L}\Big]^T \end{aligned} \tag{3.49}$$

where $\bar{\boldsymbol{G}}_{\boldsymbol{f}} \in \mathbb{R}^{2L_f \times L_f}$ and $\boldsymbol{E_k^o} \in \mathbb{R}^{2L \times 1}$. Again, from (3.12) and (3.15), the κ^{th} update of the electric

field is given by

$$\boldsymbol{E_k^\kappa} = -(\boldsymbol{f^T}\cdot\boldsymbol{f})^{-1}\cdot\boldsymbol{f^T}\cdot\bar{\boldsymbol{G}}_{\boldsymbol{f}}\cdot\boldsymbol{I_{Af}}\cdot\boldsymbol{\Psi_{k,f}^{\kappa-1}}\cdot\bar{\boldsymbol{\Theta}}_{\boldsymbol{f}}\cdot\boldsymbol{c_f^\kappa} + \boldsymbol{E_k^o} \tag{3.50}$$

where $\boldsymbol{E_k^\kappa} \in \mathbb{R}^{2L\times 1}$ is the updated electric field when current injects from the k^{th} electrode pair. Using (3.48) and (3.50) for every voltage and current electrode pair respectively, we update (3.46) to find $\boldsymbol{M^\kappa}$. Then, we can update $\boldsymbol{\delta\tilde{U}^\kappa}$ as follows:

$$\boldsymbol{\delta\tilde{U}^\kappa} = \boldsymbol{M^\kappa c^{\kappa+1}} \tag{3.51}$$

Finally, the updated $\boldsymbol{M^\kappa}$ and $\boldsymbol{\delta\tilde{U}^\kappa}$ are used in (3.44).

Finally note that the mesh refining method described can also be properly applied for dual-mesh reconstruction, where the forward model is finer than the reconstruction one [153]. Hence the system matrix can be computed more accurately with a minor computational cost.

3.2 Simulation and Experimental Validation

The performance of the proposed approach is verified through simulation, experimental and in-vivo cases. In the simulation and the experimental cases, the validation is performed both visually and quantitatively. For the quantitative evaluation, the following three metrics have been used.

1) The Correlation Coefficient (CC) quantifies the similarity between the true model and the reconstructed image

$$CC = \frac{\text{Cov}(\sigma_{true}, \hat{\sigma})}{\text{Std}(\sigma_{true})\text{Std}(\hat{\sigma})} \tag{3.52}$$

where σ_{true} is the ground truth conductivity, $\hat{\sigma}$ is the estimated conductivity and Cov is the covariance between true and estimated values. The value of CC is between 0 and 1 and higher CC indicates a more accurate reconstruction. Finally, due to the different discretization of the simulated and the reconstruction models, a decimation of the conductivity to set the true (ideal) image is performed.

2) The Relative size Coverage Ratio (RCR) shows the ratio between percentage of coverage of the reconstructed inclusions (CR) and the true conductivity perturbations (CR_{true}) [151]

$$RCR = \frac{CR}{CR_{true}} \tag{3.53}$$

It can take any positive value and ideally is 1. However, RCR strongly depends on the threshold selected for each pixel to be categorized as inclusion. Thus for the comparisons, it is essential to use a common threshold. In this work, a threshold of 25% for inclusion's maximum value was used.

3) The Structural Similarity Index (SSIM), image assessment quantity [154], with the same value range as CC.

Each testcase's result is qualitatively and quantitatively compared with the corresponding reconstruction achieved using the standard Gauss-Newton iteration with the linearized F.E.M. approach and piecewise linear basis functions. For the image reconstructions with the F.E.M., the EIDORS library tool [72] along with MATLAB were used.

3.2.1 Simulated Reconstructions on Circular Domains

Overall, EIT reconstruction is characterized by high susceptibility to *inverse crime* [155]. To avoid this effect in the simulated reconstructions on circular domain, a 3D Finite-Element cylindrical model, of radius $R_o = 1.5$ in Arbitrary Units (AU), and height $H = 1$ AU, was used to precisely simulate the measurements. This fine model includes $N_e = 52452$ elements and $N = 16$ electrodes of 0.1 AU radius are placed perimetrically at a height of $H_e = 0.6$ AU. Furthermore, $\sigma_o = 1$ S/m and the injected ac current I has amplitude 1mA.

Three cases of inclusions have been simulated:

I) Two symmetrical spherical inclusions, centered at the positions $\boldsymbol{h_1} = (-0.45, -0.45, 0.6)$ and $\boldsymbol{h_2} = (0.45, 0.45, 0.6)$, of equal radius $R_{1,2} = 0.35$, all in AU, and equal relative conductivity of $\sigma_{1,2} = 5$ mS/m.

II) A very simple thoracic model consisted of i) a 'right lung' equivalent inclusion: a semi-spherical volume centered at $\boldsymbol{h_3} = (-0.375, 0, 0.7)$ with a radius of $R_3 = 0.9$ AU and $\sigma_3 = 0.75$ S/m, ii) a 'left lung' inclusion: a smaller semi-spherical volume centered at $\boldsymbol{h_4} = (0.375, 0, 0.7)$ with a radius $R_4 = 0.675$ AU and $\sigma_4 = 0.75$ S/m and iii) a "heart" inclusion: a small sphere centered at $\boldsymbol{h_5} = (0, 0, 0.7)$, with a radius of $R_5 = 0.375$ AU and relative conductivity of $\sigma_5 = 1.25$ S/m.

III) A structure including two opposite-ordered hemispherical cavities of radius $R_{6,7} = 0.45$ AU positioned at $\boldsymbol{h_6} = (-0.525, 0, 0.7)$ and $\boldsymbol{h_7} = (0.525, 0, 0.7)$ (AU) with relative conductivity of $\sigma_6 = 1.5$ S/m and $\sigma_7 = 0.5$ S/m respectively.

In each case, the F.E. simulation model was built in MATLAB with the NETGEN tool. Two levels of Gaussian noise have been added to all the measurements, resulting in signal-amplitude SNR of 70 dB and 40 dB, which correspond to high-performance and moderate-performance clinical EIT hardware systems respectively, [156], [157], [158]. For these simulations (A,B and C), the current skip-3 pattern and adjacent voltage measurement were used ($\boldsymbol{\delta \tilde{V}} \in \mathbb{R}^{192\times 1}$) [26].

The 2D reconstruction domain is a unit radius circular disk which contains $N'_e = 1024$ equally sized triangular elements for the F.E.M. and $L = 1009$ uniformly distributed square subdomains (pixels) for the M.o.M. Both reconstruction models assume dimensionless electrodes. The Green function was calculated using the analytic expression

$$G(\boldsymbol{r}, \boldsymbol{r'}) = -\frac{1}{2\pi}\ln|\boldsymbol{r} - \boldsymbol{r'}| - \frac{1}{2\pi}\ln\sqrt{1 + \frac{(r \cdot r')^2}{R_o^4} - 2\frac{r \cdot r'}{R_o^2}\cos(\phi - \phi')} \tag{3.54}$$

where $\boldsymbol{r} = (r'\cos\phi, r'\sin\phi)$ and $\boldsymbol{r'} = (r'\cos\phi', r'\sin\phi')$ are the observation and the source vectors, respectively, R_o is the domain's radius and $|.|$ denotes the Euclidean norm.

It is empirically verified that the Gaussian RBF gives better results when using L^1-norm regularization, while the modified RBF should be preferred when using NOSER L^2 regularization. For Laplace L^2 regularization, the performance of the two RBFs is almost identical. Both RBFs are used in our experiments and their D-parameter, in (3.15) and (3.16), was heuristically selected equal to the pixels' width. This was done to optimize the distribution of the system's matrix singular values and to avoid significant aliasing between neighboring pixels. Note that simulation indicates similar singular value distribution for

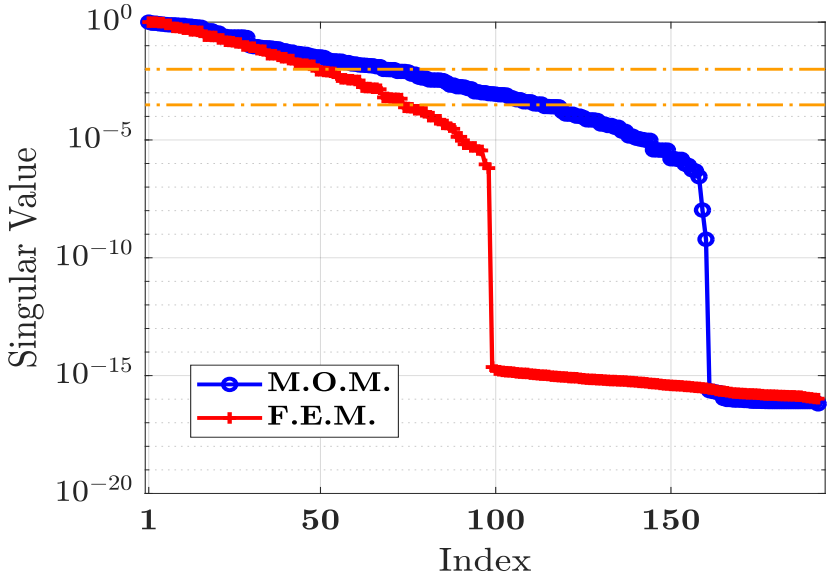

Figure 3.2: Singular value spectrum of the M and the F.E.M. Jacobian matrices utilized for the reconstructions on the $2D$ circular domain.

the two RBFs for the same D value.

Fig. 3.2 presents i) the singular value distribution of $\boldsymbol{J}$ (Jacobian matrix built using the F.E.M. linearized approach, as in (2.21) [33],[37],[54]), at the first iteration, and ii) that of $\boldsymbol{M^o}$ (system's matrix with Gaussian RBF).

Fig. 3.2 shows that the $\boldsymbol{J}$ matrix has 48 singular values larger than 10^{-2} (-40 dB, upper dashed-dotted line) and 73 values larger than $3.16 \cdot 10^{-4}$ (-70 dB, lower line). At the same time, the $\boldsymbol{M^o}$ matrix has 67 singular values larger than 10^{-2} and 113 singular values larger than $3.16 \cdot 10^{-4}$. This potentially indicates an improved robustness of image reconstruction of the proposed M.o.M. method when the EIT signal noise is -40 dB or lower for these common, uniform reconstruction meshes. However, since discretization potentially affects the SVD spectrum, several mesh-refinement methods can be adopted to improve it, such as adaptive sensitivity methods [159] and weighted element volumes methods [160] in the case of F.E.M. In the M.o.M. case, non-uniform subunits can be used, adding resolution locally near the electrodes, where increased sensitivity occurs. Despite the potential benefits of these methods, the complexity and computational cost should be considered, which is proportional to the number of iterations. Hence single-step reconstruction approaches, such as the L^2 M.o.M. are proved advantageous for real-time applications.

The image reconstructions have been performed using the Laplace and NOSER priors (L^2-norm) [28],[30] for the 70 dB measurements, and, the Laplace, NOSER and TV priors (L^2 and L^1-norm) for the 40 dB measurements. For the NOSER prior parameter values $(p_1, p_2) = (4, 6)$, in (3.16), are empirically chosen for the modified RBF. The λ hyperparameter values have been also chosen heuristically at the value where the corresponding EIT image CC is maximized. The effect of hyperparameter's λ selection is shown explicitly for case I using L^2 regularization (where λ_0 is the "optimal" value). For the TV

Table 3.1: Case I: Reconstruction parameters and quantitative results.

Testcase	SNR	λ	**Iters.**	CC	RCR	$SSIM$
Laplace F.E.M.	70dB	$9\cdot10^{-4}$	2	0.854	1.29	0.618
Laplace M.o.M.	70dB	$8\cdot10^{-6}$	1	0.862	1.25	0.638
NOSER F.E.M.	70dB	10^{-2}	2	0.890	1.11	0.633
NOSER M.o.M.	70dB	$15\cdot10^{-2}$	1	0.898	1.17	0.724
Laplace F.E.M.	40dB	$25\cdot10^{-4}$	2	0.759	1.76	0.606
Laplace M.o.M.	40dB	$25\cdot10^{-6}$	1	0.770	1.76	0.611
NOSER F.E.M.	40dB	$3\cdot10^{-2}$	2	0.822	1.55	0.626
NOSER M.o.M.	40dB	$5\cdot10^{-1}$	1	0.853	1.47	0.716
TV F.E.M.	40dB	$5\cdot10^{-8}$	25	0.769	1.76	0.630
TV M.o.M.	40dB	$5\cdot10^{-6}$	25	0.828	1.52	0.675
TSVD F.E.M.	70dB	$4\cdot10^{-1}$	1	0.871	1.31	0.640
TSVD F.E.M.	40dB	$8\cdot10^{-1}$	1	0.719	1.92	0.598

Table 3.2: Case II: Reconstruction parameters & quantitative results

Testcase	SNR	λ	**Iters.**	CC	RCR	$SSIM$
Laplace F.E.M.	70dB	10^{-3}	2	0.849	0.72	0.714
Laplace M.o.M.	70dB	$6\cdot10^{-6}$	1	0.851	0.70	0.720
NOSER F.E.M.	70dB	10^{-2}	2	0.845	0.59	0.706
NOSER M.o.M.	70dB	$2\cdot10^{-1}$	1	0.863	0.62	0.726
Laplace F.E.M.	40dB	$9\cdot10^{-3}$	2	0.807	0.61	0.644
Laplace M.o.M.	40dB	$3\cdot10^{-5}$	1	0.842	0.54	0.675
NOSER F.E.M.	40dB	10^{-1}	2	0.717	0.49	0.659
NOSER M.o.M.	40dB	$9\cdot10^{-1}$	1	0.807	0.64	0.680
TV F.E.M.	40dB	10^{-7}	25	0.73	0.64	0.656
TV M.o.M.	40dB	$4\cdot10^{-6}$	25	0.758	0.76	0.653

prior, β is also chosen heuristically between 10^{-4} and 10^{-8} to balance the convergence speed with the image quality. For TV reconstruction we used 25 iterations. Finally, for case I, reconstructions using the Truncated SVD (TSVD) single-step algorithm [53] have been included for comparison.

The simulation reconstructions are shown in Fig. 3.3 for case I, in Fig. 3.4 for case II and in Fig. 3.5 for the case III. The λ and β values chosen, the number of iterations needed to obtain the images, as well as the CC and RCR values are shown in Tables 3.1,3.2 and 3.3 for cases I, II and III respectively. For the proposed method, the σ values are estimated directly from (3.17), while for the F.E.M. the reference value σ_o estimation was added to the difference $\Delta\sigma$.

A visual inspection of the simulation results shows that the proposed method succesfully tracks the inclusions under both noise signal SNRs for all the three testcases and priors (except from the case II TV where none of the approaches detects the ”heart” inclusion). At 70 dB EIT signals, the reconstruction is slightly improved both qualitatively and quantitatively (according to Tables 3.1, 3.2 and 3.3), compared to the conventional F.E.M. approach. For 40 dB simulated EIT data, the images’ quality is significantly

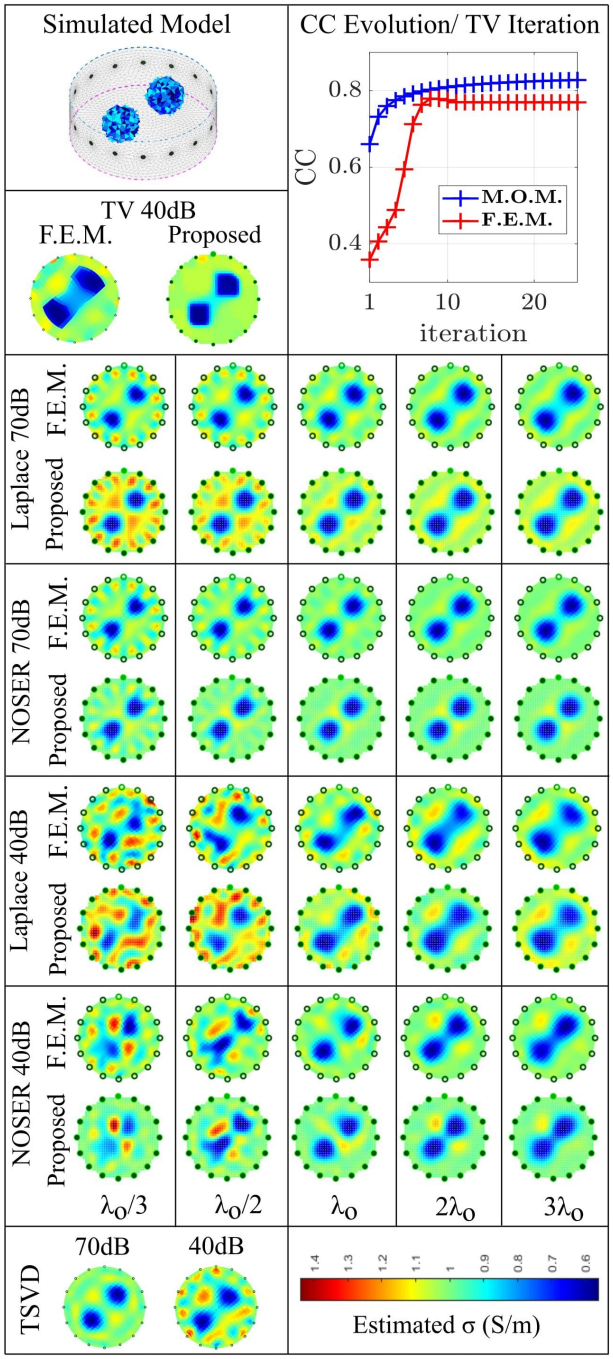

Figure 3.3: EIT image reconstructions for the simulated case I, under various conditions and priors. The corresponding inverse problem parameters selected and the quantitative results are shown in Table 3.1.

better than that of F.E.M., especially in cases II and III. In addition to the images' visual quality, the CC improvement ranges from 1.1% to 9% (except cases II and III TV) and RCR is also closer to 1. The $SSIM$ also shows improvement when using the M.o.M. method, varying from 0.6% to 8% (except from case II TV). In addition, the TSVD approach for both 70dB and 40dB signals in case I has lower performance than both the iterative F.E.M. and the L^2 and L^1 M.o.M. approaches.

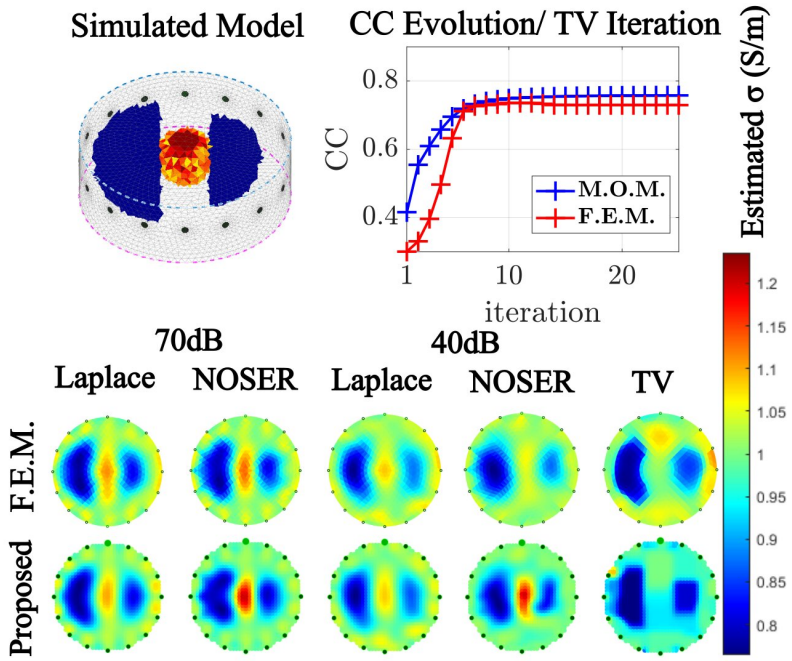

Figure 3.4: EIT images for the simulated case II, under various conditions and priors. The corresponding inverse problem parameters selected with the quantitative results are shown in Table 3.2.

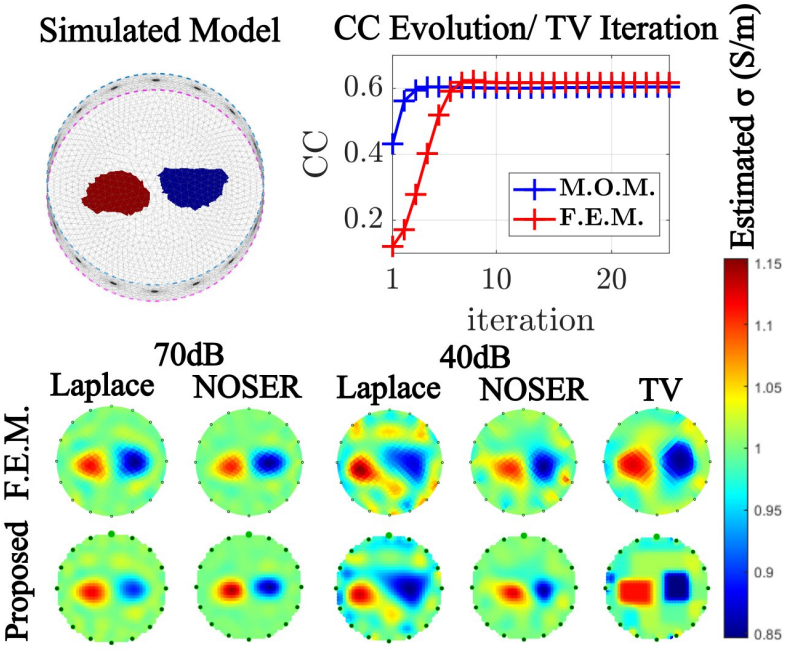

Figure 3.5: EIT images for the simulated case III, under various conditions and priors. The corresponding inverse problem parameters selected with the quantitative results are shown in Table 3.3.

Furthermore, in all the L^2-norm reconstruction cases, the proposed approach requires only one iteration to reconstruct the images. Consider for example case (I) and residual error metric $\left\| \boldsymbol{M^o c} - \boldsymbol{\delta \tilde{V}} \right\|_{\boldsymbol{W}}^2$

Table 3.3: Case III Reconstruction parameters & quantitative results

Testcase	SNR	λ	**Iters.**	CC	RCR	$SSIM$
Laplace F.E.M.	70dB	10^{-3}	2	0.769	1.95	0.728
Laplace M.o.M.	70dB	$2\cdot10^{-6}$	1	0.806	1.96	0.758
NOSER F.E.M.	70dB	10^{-2}	2	0.815	1.74	0.753
NOSER M.o.M.	70dB	$2\cdot10^{-1}$	1	0.839	1.71	0.798
Laplace F.E.M.	40dB	10^{-2}	2	0.530	3.48	0.697
Laplace M.o.M.	40dB	$4\cdot10^{-5}$	1	0.559	3.86	0.769
NOSER F.E.M.	40dB	$8\cdot10^{-2}$	2	0.685	2.33	0.721
NOSER M.o.M.	40dB	1.2	1	0.748	1.73	0.773
TV F.E.M.	40dB	10^{-7}	25	0.617	3.04	0.699
TV M.o.M.	40dB	$4\cdot10^{-6}$	25	0.604	2.90	0.707

for the M.o.M. and $\left\|\boldsymbol{J\delta\sigma}-\boldsymbol{\delta\tilde{V}}\right\|_{\boldsymbol{W}}^{2}$ for the F.E.M respectively. Using the Laplace prior reconstruction, the F.E.M. resulted in residual error of $2.45\cdot10^{-8}$ and $9\cdot10^{-13}$ at the 1st iteration and the 2nd iterations respectively. While the proposed method results in residual error of $5.22\cdot10^{-13}$ with a single-step reconstruction.

When using the TV prior, the corresponding images' CC values per iteration are demonstrated in Figs. 3.3, 3.4 and 3.5. It is shown that a near maximum CC is achieved faster by the proposed method. Furthermore, in cases I and II the final CC is better in the proposed method. In case III, the CC that was achieved with the proposed method is slightly lower (1.3%) than the CC that was achieved with the F.E.M., however, the convergence is much faster and the RCR is better.

Finally, with the system matrices and priors precomputed, when using single-step M.o.M., each reconstruction takes about 30ms for the NOSER and 50ms for the Laplace prior. The corresponding times for the F.E.M. approach depend on the number of iterations. For 2 iterations, each reconstruction takes about 1.5 seconds. For the TV method, both approaches take about 4 to 6 seconds. All the recorded times have been achieved using an AMD Ryzen 5 3600 system.

3.2.2 Experimental Validation on a Circular Domain

In addition to the simulations above, the findings of three experiments with circular tanks (vertically uniform cylindrical structures) are discussed. The measurements have been acquired using the KIT4 EIT system from the University of Eastern Finland (UEF) [157], [161]. The circular tank has been filled with saline water of $\sigma_o = 0.03$ S/m up to a height of 7 cm [118], [161] and $N = 16$, 2.5cm width rectangular electrodes were attached. Conductive metal rings or/and highly resistive solid plastic objects were selectively placed in the tank for the three experiments. A 2 mA amplitude, 1 kHz AC current was induced and the skip-3 current pattern with adjacent measurement was adopted.

The Laplace, NOSER and TV priors have been used in both F.E.M. and M.o.M. (proposed) image reconstructions. The hyperparameter λ has been heuristically selected as shown in Table 3.4 while β is selected at 10^{-3} for the F.E.M. and 10^{-16} for the M.o.M. TV reconstructions. The *CC* (6.40), the *RCR*

(3.53) and the *SSIM* quantitative metrics are recorded assuming that the metallic and plastic inclusions have $\sigma = 10$ S/m and $\sigma = 0.01$ S/m respectively (σ approaches infinity and zero respectively). Note that it has been shown that for extremely low or high conductivity, the reconstruction images saturate (due to the non-linearity of the EIT problem [55]). For every experimental case setup, an RGB color conductivity representative image has been created, named "σ pattern" (Fig. 3.6 1st row): Red represents the metallic conductivity, blue the plastic's one and green the saline water background. The "σ pattern" images' pixels are mapped to the Finite Elements and the proposed reconstruction domain pixels.

From the reconstructed images in Fig. 3.6, it is observed that the proposed approach achieves an overall better performance. It is also observed that the F.E.M. method underestimates the conductive inclusions, while the proposed one results on piecewise constant and more accurate σ values that demonstrate the metallic rings. These visual inspections are confirmed by the CC values in Table 3.4, where an $0.6\% - 9.4\%$ improvement is shown. In some of the testcases, however, the proposed method's RCR is higher, since the corresponding reconstructed conductive inclusions get higher and more constant values. In addition, the $SSIM$ varies between 0.565 and 0.69 for the F.E.M. and between 0.565 and 0.753 for the M.o.M. Furthermore, only one iteration needed for the L^2 prior reconstructions with the proposed method, while the F.E.M. formulation images needed $3 - 9$ iterations (Table 3.4).

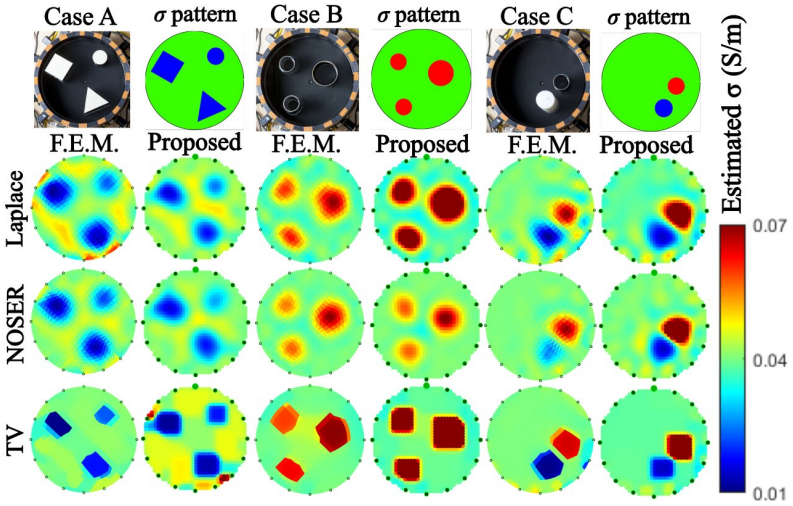

Figure 3.6: EIT image reconstructions for the experimental cases. The corresponding inverse problem parameters selected with the quantitative results are shown in Table 3.4.

3.2.3 Simulated Reconstruction on Cylindrical Domains

A number of 3D simulations have been performed based on a cylindrical tank and a multilayer electrode distribution. To simulate the measurements, a fine F.E.M. cylinder model of a $R_o = 1$ AU radius and $H = 2$ AU height, attached with 3 layers of a total of $N = 48$ electrodes (16 electrodes per layer), has been created. The electrodes' radius is 0.05 AU. The model contains $N_e = 376033$ elements and $N_o = 70153$ nodes. The electrode layers are set at $z_{l1} = 0.6$, $z_{l2} = 1.05$ and $z_{l3} = 1.45$ AU. Background conductivity and measurement SNR are set to $\sigma_o = 1$ S/m and 70 dB. The current skip-3 and adjacent

Table 3.4: Reconstruction parameters and quantitative results for the experimental cases

Testcase	λ	**Iters.**	CC	RCR	$SSIM$
A Laplace F.E.M.	$2\cdot10^{-2}$	4	0.750	1.68	0.565
A Laplace M.o.M.	10^{-1}	1	0.763	1.52	0.571
A NOSER F.E.M.	$4\cdot10^{-2}$	6	0.765	1.63	0.569
A NOSER M.o.M.	1	1	0.779	1.65	0.574
A TV F.E.M.	$3\cdot10^{-7}$	25	0.757	1.37	0.568
A TV M.o.M.	$6\cdot10^{-6}$	25	0.777	1.83	0.565
B Laplace F.E.M.	$2\cdot10^{-3}$	6	0.792	1.78	0.612
B Laplace M.o.M.	$8\cdot10^{-6}$	1	0.839	1.85	0.651
B NOSER F.E.M.	$4\cdot10^{-2}$	4	0.801	1.65	0.629
B NOSER M.o.M.	$15\cdot10^{-2}$	1	0.807	1.49	0.707
B TV F.E.M.	10^{-7}	25	0.792	1.82	0.617
B TV M.o.M.	$3\cdot10^{-6}$	25	0.866	2.18	0.720
C Laplace F.E.M.	$8\cdot10^{-4}$	3	0.677	2.07	0.688
C Laplace M.o.M.	$8\cdot10^{-6}$	1	0.771	2.46	0.753
C NOSER F.E.M.	$4\cdot10^{-2}$	9	0.720	2.14	0.645
C NOSER M.o.M.	$15\cdot10^{-1}$	1	0.740	2.68	0.675
C TV F.E.M.	10^{-7}	25	0.767	2.25	0.690
C TV M.o.M.	10^{-6}	25	0.783	2.07	0.694

voltage (skip-0) pattern is used and a $I = 1$ mA amplitude current is injected.

The reconstruction model is also a $R_o = 1$ AU radius, $H = 2$ AU height cylinder, but with deliberately slightly shifted $N = 48$ electrodes, placed at layers $z'_{l1} = 0.5$, $z'_{l2} = 1$ and $z'_{l3} = 1.5$ AU. The electrodes shift was introduced to capture the impact of modeling error to the reconstructed image, in real world EIT experiments where the exact model parameters are rarely known. The F.E.M. reconstruction is performed using the coarse mesh with $N'_e = 26320$ elements and $N'_o = 5424$ nodes, while the M.o.M. was applied using a $L = 21150$ uniform voxel mesh. Finally, the Green's function is computed using the following analytical expression [162]

$$\begin{aligned} G(\boldsymbol{r},\boldsymbol{r'}) = &-\frac{1}{2\pi\cdot H}\ln\left(R\cdot R'\right)+\frac{2}{\pi\cdot H}\sum_{p=1}^{\infty}\cos\left(\frac{p\pi z}{H}\right)\cos\left(\frac{p\pi z'}{H}\right) \\ &\cdot\sum_{m=1}^{\infty}\left\|\frac{I_m\left(\frac{p\pi r'}{H}\right)}{I'_m\left(\frac{p\pi R_o}{H}\right)}\cdot\{A(r)-B(r)\}\right\|_{r',r}\cdot\cos(m(\phi-\phi')) \end{aligned} \tag{3.55}$$

where I_m and K_m are the modified 1st and 2nd kind Bessel functions, $\|F\|_{r',r} \triangleq \min\{F(r',r), F(r,r')\}$ and

$$
\begin{aligned}
R &= \sqrt{r^2 + r'^2 - 2rr'\cos(\phi - \phi')} \\
R' &= \sqrt{r^2 + \frac{R_o^4}{r'^2} - 2r\frac{R_o^2}{r'}cos(\phi - \phi')} \\
A(r) &= I'_m\left(\frac{p\pi R_o}{H}\right)K_m\left(\frac{p\pi r}{H}\right),\ B(r) = I_m\left(\frac{p\pi r}{H}\right)K'_m\left(\frac{p\pi R_o}{H}\right)
\end{aligned}
\tag{3.56}
$$

The Green's function gradient is approximated from the free-space electrical field in the Cartesian coordinates

$$
\nabla_{\boldsymbol{r}} G(\boldsymbol{r}, \boldsymbol{r'}) \approx -\frac{1}{4\pi}\left[\frac{x - x'}{Q^2}\hat{x} + \frac{y - y'}{Q^2}\hat{y} + \frac{z - z'}{Q^2}\hat{z}\right] \tag{3.57}
$$

where $Q = \sqrt{(x - x')^2 + (y - y')^2 + (z - z')^2}$,
$(x, y) = (r\cos\phi, r\sin\phi)$ and $(x', y') = (r'\cos\phi', r'\sin\phi')$.

Two particular cases are simulated. In the first one, 4 spherical inclusions of radius $R = 0.2$ AU and $\sigma = 0.9$ S/m are introduced at the following positions: $\boldsymbol{r_i} = \big(0, (-0.5)^i, 0.6\big)$ for $i = \{1, 2\}$ and $\boldsymbol{r_i} = \big(0, (-0.5)^i, 1.3\big)$ for $i = \{3, 4\}$. In the second case, one more spherical inclusion of radius $R = 0.15$ AU and $\sigma = 0.9$ S/m is added at $\boldsymbol{r_5} = (0.5, 0.5, 1.3)$.

The NOSER inverse prior is used [30] for both the F.E.M. and the proposed M.o.M approaches. Contrary to the $2D$ cases, single-step Gauss-Newton inversion is applied here to maintain reasonable computational complexity when using the fine mesh. The θ_2 RBF is utilized with $p_1 = 2$ and $p_2 = 3$. Moreover, (3.42) is evaluated using the Woodbury's inversion formula [163], significantly limiting the computational cost. Indeed, with the system matrix, the Jacobian and prior ones precomputed, the M.o.M. approach takes 4.5 seconds while F.E.M. takes about 9.5 seconds. For the quantitative evaluation, only the CC metric is estimated. The hyperparameters are heuristically chosen in each case in order to maximize the resulting reconstructions' CC.

The resulting 3D reconstructions are shown in Fig. 3.7 and the reconstructions' parameters with the CC metrics are presented in Table 3.5. Only the elements/voxels that have σ values more than 25% of the corresponding case's maximum $\Delta\sigma$ are shown for clarity. The inclusions are more clearly reconstructed and separated from the proposed M.o.M. reconstruction, as verified both from the illustrations and the CC. However, the inclusions appear closer to the z-axis than they actually are in the simulated model. Furthermore, some artifacts appear at the cylinder's bases (mainly the upper one) due to the approximated field from (3.57) that does not take into account the Neumann boundary conditions on the bases.

3.2.4 In-Vivo Thoracic Dynamic Imaging

A representative application of difference-EIT is dynamic thoracic imaging. It provides valuable information for the lung-state condition in real time, which cannot be easily accessed by traditional imaging methods (e.g. mechanical ventilation for patients with acute respiratory distress syndrome-ARDS, neonates, etc.). We test the applicability of the proposed method on continuous thoracic imaging.

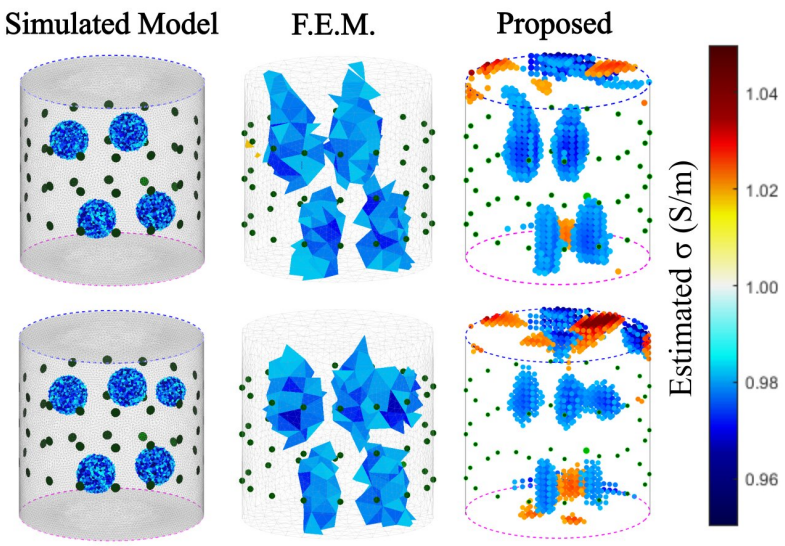

Figure 3.7: EIT image reconstructions for the 3D cases with NOSER prior (25% threshold). The corresponding problem parameters selected with the quantitative results are shown in Table 3.5.

Table 3.5: Reconstruction parameters and CC of the 3D cases.

Testcase	λ	SNR	CC
4 inclusions F.E.M.	$4 \cdot 10^{-2}$	70dB	0.443
4 inclusions M.o.M.	$9 \cdot 10^{-1}$	$70dB$	0.502
5 inclusions F.E.M.	$4 \cdot 10^{-2}$	70dB	0.427
5 inclusions M.o.M.	$9 \cdot 10^{-1}$	70dB	0.443

For this purpose we use a 2D thoracic-shape coarse mesh with $L = 1060$ pixels involving $N = 16$ electrodes. Thirty four (34) data frames of a single breath cycle were captured by the EIT SCANNER in [164, 165], using online data from [72] and the adjacent current and voltage measurement pattern. Difference- EIT was performed with the 1-st frame as the reference one, resulting in 33 images.

To compute the Green's function differences, a voltage distribution simulation was performed on a 48 times interpolated $L_f = 612341$-node fine square-element mesh. The electric field was computed with the Finite Differences Method using the resulted voltage distributions. The fine mesh voltages and field distributions were sampled to get the coarse structure's distributions. The reconstruction was done with the NOSER algorithm, with $\lambda = 0.4$, $D = \sqrt{A}$, $p_1 = 4$ and $p_2 = 6$.

The image reconstructions in Fig. 3.8 reveal the air-related conductivity changes during a single breath cycle, with significant temporal resolution. However, the blood cycle related changes are not clearly visible. Their detection may be achievable using hardware $SNR \geq 75$dB, higher frame rate, or post-reconstruction processing methods [6], [166].

In thoracic imaging, electrodes with non-negligible dimensions are typically attached on the patient. Although the proposed method assumes dimensionless electrodes, it can be accurate enough if the distance from the boundary is small relative to the subject's size and if the electrodes' dimensions are also relatively

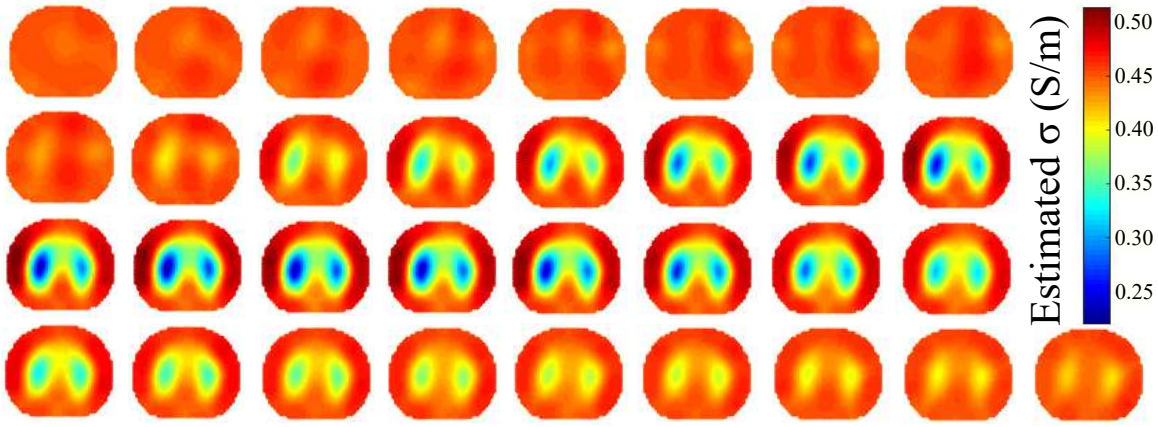

Figure 3.8: Dynamic EIT reconstruction for a single breath cycle, using the proposed approach.

small. For large electrode dimensions, an extension of the method to include the CEM can compensate any field effects resulting from the electrodes.

4 Evaluation of the Point Matching Method-of-Moment using Sparse Bayesian Learning in Dynamic Lung Electrical Impedance Tomography

4.1 Introduction

Electrical impedance tomography (EIT) is a medical imaging technique which reveals the conductivity or admittance distribution of a subject under test (SUT) [4]. In EIT, an alternating, low-amplitude current usually up to 1MHz is induced into a cluster of electrodes, while the measured electrode potentials are used as raw data for the image reconstruction. Unlike other medical imaging modalities, EIT is characterized by the absence of ionizing radiation, its low cost and its notable temporal resolution. This makes EIT a useful tool for real-time lung function monitoring. Many studies have shown the importance of EIT for revealing vital signs related to ventilation properties, such as tidal volume (TV) [167], or pathological situations, such as acute respiratory distress syndrome (ARDS) [168].

Despite its potential advantages, EIT is lacking in spatial resolution, something that still keeps its application in medical equipment limited. In addition, EIT images often present artefacts that, in some cases, may degrade their clinical value and diagnostic efficacy. Such artefacts are related to the highly ill-posed and ill-conditioned nature of the EIT inverse reconstruction problem. This means that the image quality presents with high sensitivity to voltage signal noise. In real-time EIT imaging, the signal-to-noise ratio (SNR) is often limited, because higher frequency currents need to be injected in order to achieve a high temporal resolution [169, 170]. Indeed, in practice, lower frame rate EIT hardware systems [156, 171] usually present better voltage SNR levels than higher frame rate systems [20, 21].

Furthermore, EIT is susceptible to modeling errors. Particularly in dynamic thoracic imaging, the lack of a homogeneous background, the patient's unknown chest boundary shape, as well as its changes over time due to the patient's breathing cycles and the high chance of the electrodes' displacement during signal acquisition also introduce significant modeling errors [151, 172, 173]. Despite the fact that a percentage of modeling errors can be compensated when time-difference EIT is applied, their impact on image quality may be still noticeable. Moreover, EIT is a highly non-linear problem, which means that highly inhomogeneous admittance inclusions cannot be accurately estimated with simple linear methods [151]. The variations in the lungs' admittance due to the continuous change in air volume is a typical

case [174].

Over the years, many approaches have been proposed for EIT image reconstruction. The most simple approaches assume small conductivity or admittance inclusions and linearize the problem around a predefined homogeneous value. Then, the problem is treated directly using either truncated singular value decomposition (TSVD) or standard Tikhonov regularization (STR), where an identity matrix prior is considered. Generalized Tikhonov regularization (GTR) schemes [54] such as the Laplace prior, the NOSER prior [30] and the high-pass filter Gaussian prior [55] can be also applied, improving the image reconstruction performance compared to TSVD and STR. To compensate boundary movement effects, [175, 176] introduced electrode movement priors, combining them with the previous schemes. Another single-step approach which makes use of a figure-of-merit (FoM) framework to optimize both parameters and performance is the Graz consensus reconstruction algorithm for EIT (GREIT) [71]. GREIT uses dual-mesh schemes, i.e., a coarse 2D domain for the admittance reconstruction and a fine 3D domain, extruded from the coarse 2D one, for accurate forward calculations. This greatly improves accuracy, but at the cost of additional time and complexity.

Despite the benefits of single-step approaches in dynamic EIT imaging speed, EIT is a non-linear problem. Therefore, most linear approaches cannot accurately capture significant conductivity changes. In such cases, iterative approaches have been developed to deal with the non-linearity. A common iterative framework is based on the Gauss–Newton (GN) algorithm, which makes use of the GTR schemes mentioned above (L^2-norm regularization) [28]. Another popular iterative approach is the total variation (TV) approach, where L^1-norm regularization priors are used [59, 60, 61]. A hybrid non-linear difference EIT imaging approach was proposed in [85, 151] in an effort to effectively deal with both the models' mismatches and the problem's non-linearity. Another L^1-norm approach uses the Bregman distance scheme, showing improved performance in lung imaging compared to the traditional TV scheme [63].

Sparse Bayesian learning (SBL) was firstly proposed as a mathematical formulation in [138, 139, 177] but was only recently applied in EIT [142, 143, 145, 178]. Instead of the traditional regularization schemes, it treats the inverse problem as a log-likelihood optimization procedure, assuming a sparse conductivity distribution. SBL approaches show robustness to signal noise, while the non-trivial hyper-parameter selection needed in regularization techniques is avoided. Although some SBL methods, such as structure-aware SBL (SA-SBL) [142] and time-sequence learning SBL [145] have been proposed for EIT, their evaluation is limited to simple circular and cylindrical structures. Hence, SBL has not been applied in dynamic thoracic imaging, where the structures have more complex geometries, usually unknown, and are highly non-homogeneous.

The point-matching method of moment (PM-MoM) for EIT was also recently proposed in [179]. It uses a global integral equation approach with Green's functions. The logarithm of conductivity is expressed as a linear combination of modified radial basis functions (RBFs). Contrary to the traditional finite element (F.E.) approach, which treats the problem as a weak form that does not hold for significant conductivity changes, the PM-MoM is formulated globally, decreasing the problem's non-linearity. The PM-MoM has therefore shown to converge faster than the traditional F.E. approaches both in L^1 and L^2-norm inverse problem schemes. Despite the fact that PM-MoM has been tested on circular and cylindrical structures, it has not been quantitatively evaluated in dynamic thoracic imaging.

Motivated by the benefits of the PM-MoM and the SBL optimization scheme, in this work we introduce an approach that combines these two methods. In particular, the proposed PM-MoM SBL approach undertakes the image reconstruction problem's non-linearity, offering robustness to noise and reduced susceptibility in modeling errors. To evaluate the PM-MoM SBL approach, we apply it to 3D F.E. thoracic structures (cases) based on 3 male subjects' CT images, available online. For each case, five sub-structures are built, considering five corresponding breath-cycle states from expiration to the end-inspiration. Each structure includes the lungs, heart, vertebrae, muscle and skin tissues to avoid the assumption of a uniform background [173]. It is noted that most previous studies for EIT approaches in dynamic thoracic imaging consider only the inspiration and expiration ends and only the lung tissues in their models for quantitative evaluation. The proposed approach is compared with traditional (GN, TV, difference of absolute images) and more advanced (prior movement, hybrid non-linear imaging) F.E.-based regularization approaches, as well as the regularized MoM approach, showing increased noise robustness and improved performance both qualitatively and quantitatively. Finally, the proposed method is tested in in vivo human breath data which is available online, verifying its proper applicability.

The rest of this paper is organized as follows. In Section 4.2, the EIT problem's principle, as well as state-of-the-art regularization-based methods, are outlined. In Section 4.3, the proposed PM-MoM SBL approach is presented, while in Section 4.4, the 3D thoracic structures, the evaluation FoM, the method adopted to extract the reference images and the in vivo data are described. In Section 4.5, the image reconstruction results, as well as the quantitative results, are demonstrated and discussed.

4.2 Background

In this section, a brief review of the EIT mathematical formulation and the state-of-the-art inverse reconstruction approaches used for the comparisons is performed.

4.2.1 EIT Principle

Assume a N-electrode EIT setup and a d-dimensional domain ($d \in \{2, 3\}$) Ω, where the current is injected. The problem can be described according to the following Laplace equation:

$$\nabla\big(\boldsymbol{\sigma}(\boldsymbol{r})\nabla u(\boldsymbol{r})\big) = 0, \quad \boldsymbol{r} \in \Omega \tag{4.1}$$

that implies the following boundary conditions, according to the complete electrode model (CEM) [23]:

$$u(\boldsymbol{r}) + z_l\sigma(\boldsymbol{r})\frac{\partial u(\boldsymbol{r})}{\partial \boldsymbol{n}} = U_l, \quad \boldsymbol{r} \in e_l,\ l = 1, ..., N \tag{4.2}$$

$$\int_{e_l} \sigma(\boldsymbol{r})\frac{\partial u(\boldsymbol{r})}{\partial \boldsymbol{n}} dS = I_l, \quad l = 1, ..., N \tag{4.3}$$

$$\sigma(\boldsymbol{r})\frac{\partial u(\boldsymbol{r})}{\partial \boldsymbol{n}} = 0, \quad \boldsymbol{r} \in \partial\Omega \backslash \bigcup_{l=1}^{N} e_l \tag{4.4}$$

where $\boldsymbol{r} \in \mathbb{R}^d$ is the position vector, $\sigma(\boldsymbol{r})$ is the conductivity, $u(\boldsymbol{r})$ is the potential, $\boldsymbol{n}$ is the normal outward-pointing vector, e_l is the electrodes' positions set, z_l is the electrodes' contact impedances, U_l is the lth electrode voltage and I_l is the current injected on the lth electrode.

4.2.2 Time-Difference EIT

In time-difference (dynamic) EIT imaging, we assume two consecutive states. The corresponding computed boundary voltages' vectors can be written as follows:

$$\boldsymbol{U^{(1)}} = [U_1^1 \, U_2^1 \, ... \, U_{Nm}^1] \in \mathbb{R}^{Nm \times 1} \tag{4.5}$$

and

$$\boldsymbol{U^{(2)}} = [U_1^2 \, U_2^2 \, ... \, U_{Nm}^2] \in R^{Nm \times 1}, \tag{4.6}$$

where m is the total voltage measurements acquired for each current injection electrode pair, according to the selected measurement pattern [26]. Accordingly, we assume that two voltage data measurement frames $\boldsymbol{V^{(1)}} \in \mathbb{R}^{Nm \times 1}$ and $\boldsymbol{V^{(2)}} \in \mathbb{R}^{Nm \times 1}$ are acquired from the EIT system. We then set the differential voltage frames

$$\boldsymbol{\delta U} = \boldsymbol{U^{(2)}} - \boldsymbol{U^{(1)}} \tag{4.7}$$

and

$$\boldsymbol{\delta V} = \boldsymbol{V^{(2)}} - \boldsymbol{V^{(1)}}. \tag{4.8}$$

Considering Gaussian noise $\boldsymbol{e_n} \in \mathbb{R}^{Nm \times 1}$ between the simulated boundary voltages and the measurements, we have

$$\boldsymbol{\delta V} = \boldsymbol{\delta U} + \boldsymbol{e_n}. \tag{4.9}$$

Furthermore, we assume $\sigma^{(1)}(\boldsymbol{r})$ and $\sigma^{(2)}(\boldsymbol{r})$ as the corresponding conductivity distributions, setting the difference

$$\boldsymbol{\delta\sigma}(\boldsymbol{r}) = \sigma^{(2)}(\boldsymbol{r}) - \sigma^{(1)}(\boldsymbol{r}). \tag{4.10}$$

If the finite element method (F.E.M.) discretization scheme is applied in Ω, we assume a number of L elements and that each element i presents a constant conductivity σ_i.

Hence, we can write the following conductivity vectors:

$$\boldsymbol{\sigma^{(1)}} = [\sigma_i^{(1)}]_{i=1}^L \in \mathbb{R}^{L \times 1} \tag{4.11}$$

$$\boldsymbol{\sigma^{(2)}} = [\sigma_i^{(2)}]_{i=1}^L \in \mathbb{R}^{L \times 1} \tag{4.12}$$

$$\boldsymbol{\delta\sigma} = [\delta\sigma_i]_{i=1}^L \in \mathbb{R}^{L \times 1}. \tag{4.13}$$

The general approach is to formulate the inverse problem as a weighted-least squares (WLS) minimization problem between $\boldsymbol{\delta V}$ and $\boldsymbol{\delta U}$, adding a regularization term $P(\boldsymbol{\delta\sigma})$ to stabilize the problem's

ill-conditioned nature, such that

$$F(\boldsymbol{\delta\sigma}) = \|\boldsymbol{\delta U} - \boldsymbol{\delta V}\|^2_{\boldsymbol{W}} + \lambda^2 P(\boldsymbol{\delta\sigma}). \tag{4.14}$$

$$\boldsymbol{\delta\sigma_*} = \underset{\boldsymbol{\delta\sigma}\in\mathbb{R}^L}{\operatorname{argmin}}\Big\{F(\boldsymbol{\delta\sigma})\Big\}, \tag{4.15}$$

where $\boldsymbol{W} \in \mathbb{R}^{Nm\times Nm}$ is a diagonal, noise covariance matrix and λ is the regularization hyperparameter. The problem is to find the optimal $\boldsymbol{\delta\sigma}$ that minimizes $F(\boldsymbol{\delta\sigma})$ in (4.14). From hereon, we assume that all the measurement channels have the same noise; hence, $\boldsymbol{W} = \boldsymbol{I_{Nm}}$.

4.2.3 Single-Step Linear Reconstruction

As mentioned in the introduction, EIT image reconstruction is a non-linear problem, i.e., the relation between $\boldsymbol{U}$ and $\sigma(\boldsymbol{r})$ is non-linear. However, assuming relatively small conductivity changes, and using Taylor approximation around a linearization point σ_o, we can write

$$\boldsymbol{\delta U} = \frac{\partial \boldsymbol{\delta U}}{\partial \boldsymbol{\delta\sigma}}\Big|_{\boldsymbol{\sigma_o}} \boldsymbol{\delta\sigma} + O(\|\boldsymbol{\delta\sigma}\|^2) \simeq \boldsymbol{J\delta\sigma}, \tag{4.16}$$

where $\boldsymbol{J} \in \mathbb{R}^{Nm\times L}$ is the Jacobian matrix around σ_o. In the simplest case (dimensionless electrodes), $\boldsymbol{J}$ is computed according to the following formula [180]:

$$J^i_{dm} = \frac{\partial \delta U_{dm}}{\partial \delta\sigma} = -\int_{\Omega_i} \nabla u(I^d)\cdot\nabla u(I^m) dA, \tag{4.17}$$

where Ω_i denotes the i-th element's domain, d denotes the current injection differential channel and m denotes the voltage measurement differential channel. The minimization function is then written according to the following form:

$$F(\boldsymbol{\delta\sigma}) = \|\boldsymbol{J\delta\sigma} - \boldsymbol{\delta V}\|^2_{\boldsymbol{W}} + \lambda^2 P(\boldsymbol{\delta\sigma}). \tag{4.18}$$

In this case, smooth L^2 priors, such as the standard Tikhonov, the Laplace, the NOSER or the Gaussian priors, are commonly utilized [30, 54, 55]. Hence, we can write

$$P(\boldsymbol{\delta\sigma}) = \|\boldsymbol{\delta\sigma}\|^2_{\boldsymbol{Q}}, \tag{4.19}$$

where $\boldsymbol{Q} \in \mathbb{R}^{L\times L}$ is the prior matrix. The linearized problem has the following closed-form solution:

$$\boldsymbol{\delta\sigma_*} = \Big(\boldsymbol{J^T W J} + \lambda^2 \boldsymbol{Q}\Big)^{-1} \boldsymbol{J^T W \delta V}. \tag{4.20}$$

This is the most commonly used linear EIT scheme.

4.2.4 Regularized Reconstruction Approaches

In this section, we perform a brief review of the regularization-based linear and non-linear approaches used for the comparisons.

(I) *Non-Linear Gauss–Newton (GN):* The traditional non-linear GN approach makes an iterative estimation of conductivity change distribution to optimize

$$F(\boldsymbol{\delta\sigma}) = \|\boldsymbol{\delta U} - \boldsymbol{\delta V}\|_{\boldsymbol{W}}^2 + \lambda^2 \|\boldsymbol{\delta\sigma}\|_{\boldsymbol{Q}}^2 . \tag{4.21}$$

An initial solution is taken from (4.20). Then, $\boldsymbol{J}$, as well as $\boldsymbol{\delta\sigma}$, are re-estimated in each iteration until convergence.

(II) *Total Variation (TV):* This non-linear, iterative approach assumes that intense conductivity changes occur between neighboring elements of Ω by applying L^1-norm priors. The functional to be minimized is written as follows:

$$F(\boldsymbol{\delta\sigma}) = \|\boldsymbol{\delta U} - \boldsymbol{\delta V}\|_{\boldsymbol{W}}^2 + \lambda^2 \sum_{i=1}^{N_{ed}} \sqrt{\|\boldsymbol{L_i}\boldsymbol{\delta\sigma}\|^2 + \beta}, \tag{4.22}$$

where N_{ed} is the total number of edges between the domain's elements, and $\boldsymbol{L} \in \mathbb{R}^{N_{ed}\times L}$ is a sparse matrix which shows the relation between the elements and their edges. $\boldsymbol{L_i}$ refers to the ith row of the matrix $\mathbf{L}$, and $\beta > 0$ is a parameter that prevents the non-differentiability of the regularization term [60]. In terms of this paper, the primal-dual interior point (PD-IPM) TV method is adopted [59, 60, 61].

(III) *Movement Prior:* This approach, which was firstly proposed by [175] and furtherly developed in [176], performs linear difference-EIT reconstruction while considering the electrodes' movement effect. The electrode movement $\boldsymbol{\delta x} \in \mathbb{R}^{dN\times 1}$ is also estimated along with the conductivity change. To this end, Tikhonov and Laplace priors have been proposed for the simultaneous estimation of $\boldsymbol{\delta\sigma}$ and $\boldsymbol{\delta x}$, properly modifying the Jacobian matrix $\boldsymbol{J}$ and the prior matrix $\boldsymbol{Q}$ [175, 176]. Apart from λ, a $\mu > 0$ regularization hyperparameter for the electrode movement prior is needed. In terms of this paper, both $\boldsymbol{\delta\sigma}$ and $\boldsymbol{\delta x}$ estimations are performed using the Laplace prior, in the way described in [176]. This approach has proven to reduce the artefacts caused by the electrodes' movement and boundary changes and has been exclusively developed for applications in dynamic lung imaging.

(IV) *Difference of Absolute Images:* In this approach, absolute, instead of difference, EIT reconstruction is applied particularly for each measurement frame [181]. The problem's objective functions are the following:

$$F_1(\boldsymbol{\sigma^{(1)}}) = \left\|\boldsymbol{U^{(1)}} - \boldsymbol{V^{(1)}}\right\|_{\boldsymbol{W}}^2 + \lambda^2 \left\|\boldsymbol{\sigma^{(1)}}\right\|_{\boldsymbol{Q}}^2 . \tag{4.23}$$

and

$$F_2(\boldsymbol{\sigma^{(2)}}) = \left\|\boldsymbol{U^{(2)}} - \boldsymbol{V^{(2)}}\right\|_{\boldsymbol{W}}^2 + \lambda^2 \left\|\boldsymbol{\sigma^{(2)}}\right\|_{\boldsymbol{Q}}^2 . \tag{4.24}$$

Defining $\boldsymbol{\sigma_*^{(1)}} \in \mathbb{R}^L$ and $\boldsymbol{\sigma_*^{(2)}} \in \mathbb{R}^L$ as the obtained solutions from (4.23) and (4.24), respectively, the final estimated conductivity change is simply obtained by

$$\boldsymbol{\delta\sigma_*} = \boldsymbol{\sigma_*^{(2)}} - \boldsymbol{\sigma_*^{(1)}} \tag{4.25}$$

In this paper's reconstructions, the minimization of F_1 and F_2 is performed by using the absolute GN

non-linear approach with a Laplace prior.

(V) *Multiple Priors (Non-Linear Difference Imaging—N.L.D.):* This approach, proposed in [85, 151], concatenates the voltage data measurement frames as follows:

$$\overline{\boldsymbol{V}} = [\boldsymbol{V^{(1)T}} \quad \boldsymbol{V^{(2)T}}]^T \in \mathbb{R}^{2Nm\times 1}, \tag{4.26}$$

and the computed boundary voltages as follows:

$$\overline{\boldsymbol{U}} = [\boldsymbol{U^{(1)T}} \quad \boldsymbol{U^{(2)T}}]^T \in \mathbb{R}^{2Nm\times 1}, \tag{4.27}$$

while it is assumed that conductivity changes occur in a particular region of interest ($\Omega_{ROI} \subseteq \Omega$), which is discretized in $L_{ROI} \leq L$ elements, such that

$$\boldsymbol{\sigma^{(2)}} = \boldsymbol{\sigma^{(1)}} + \boldsymbol{M\delta\sigma_{ROI}}, \tag{4.28}$$

where $\boldsymbol{M}$ is an operator that maps $\boldsymbol{\delta\sigma_{ROI}}$ with the domain's elements. The following optimization problem is defined:

$$F(\overline{\boldsymbol{\sigma}}) = \left\|\overline{\boldsymbol{U}} - \overline{\boldsymbol{V}}\right\|^2_{\boldsymbol{W}} + \lambda_1^2 \left\|\boldsymbol{\sigma^{(1)}}\right\|^2_{\boldsymbol{Q_1}} + \lambda_2^2 \sum_{i=1}^{N_{ed,ROI}} \sqrt{\left\|\boldsymbol{L_{i,ROI}\delta\sigma_{ROI}}\right\|^2 + \beta}, \tag{4.29}$$

where λ_1 and λ_2 are regularization hyperparameters, $N_{ed,ROI}$ is the total number of edges between the ROI elements and $\boldsymbol{L_{i,ROI}} \in \mathbb{R}^{N_{ed,ROI}\times L_{ROI}}$ shows the relation between the ROI's elements and their edges. A smooth L^2-norm prior (prior matrix $\boldsymbol{Q_1}$) is used to estimate $\boldsymbol{\sigma^{(1)}}$, while a L^1-norm prior is used to estimate the local conductivity change $\boldsymbol{\delta\sigma_{ROI}}$. The solution $\overline{\boldsymbol{\sigma}}_*$ that minimizes (4.29) is achieved via an iterational process. A linesearch to perform the updates is essential due to the problem's high non-linearity.

It is worthwhile to mention that apart from these methods, many other approaches have been developed for difference-EIT imaging. For example, the TSVD, a traditional linear approach, gives similar results to (4.20) by performing thresholding SVD instead of regularization. Finally, a very well-known single-step approach is the D-Bar, which uses a non-linear scattering transform and low-pass filtering [77, 182, 183]. A comparison between D-Bar and regularized methods can be found in [80].

4.3 Method-of-Moment with Sparse Bayesian Learning (Pm-Mom SBL)

This section presents the proposed method as a combination of the PM-MoM system matrix formulation and an SBL approach for the occurring inverse problem.

The PM-MoM formulates a global integral equation (holding in the whole Ω) instead of using the weak form of (4.1). It expresses the voltages and fields as Green's functions and their gradients, respectively. The conductivity is non-linearized in the integral equation, and, unlike the conventional F.E.M. formulation, is not assumed to be a piecewise constant at each element. Instead, its logarithm is expressed

as a summary of radial basis functions (RBFs) [179].

The governing integral equation takes the following form:

$$u(\boldsymbol{r};\boldsymbol{r}_+,\boldsymbol{r}_-)=\int_\Omega G(\boldsymbol{r},\boldsymbol{r'})\nabla\left(\ln\sigma(\boldsymbol{r'})\right)\cdot\nabla u_o(\boldsymbol{r'};\boldsymbol{r}_+,\boldsymbol{r}_-)dA+u_o(\boldsymbol{r};\boldsymbol{r}_+,\boldsymbol{r}_-), \tag{4.30}$$

where $G(\boldsymbol{r},\boldsymbol{r'})$ denotes the Green's function set between an observation point $\boldsymbol{r}$ and a source point $\boldsymbol{r'}$, u_o denotes the domain's voltage distribution when the conductivity is constant (homogeneous with a value σ_o) and $\boldsymbol{r}_+$, $\boldsymbol{r}_-$ denote the electrode coordinates from where the current is sourced and sinked, respectively. It is also found that

$$u_o(\boldsymbol{r'};\boldsymbol{r}_+,\boldsymbol{r}_-)=\frac{I}{\sigma_o}\left[G(\boldsymbol{r},\boldsymbol{r}_+)-G(\boldsymbol{r},\boldsymbol{r}_-)\right]. \tag{4.31}$$

We then express the logarithm of conductivity as follows:

$$\ln\sigma(\boldsymbol{r'})=\ln(\sigma_o)+\sum_{j=1}^{L}c_j\theta(\boldsymbol{r'},\boldsymbol{r_j}), \tag{4.32}$$

where $\boldsymbol{r_j}$ is the jth pixel's center point. The RBF θ is selected according to the following generalized form:

$$\theta(\boldsymbol{r'},\boldsymbol{r_j})=exp\left(-\frac{\|\boldsymbol{r'}-\boldsymbol{r_j}\|_{p_1}^{p_1/p_2}}{2D^2}\right), \tag{4.33}$$

where $p_1>0$ and $p_2>0$ are integers (p_1 even), and D is a parameter which adjusts the RBF's width. By discretizing (4.30), replacing the conductivity logarithm with (3.17) and taking the electrodes voltages' differences, according to the measurement pattern adopted and the method described in [179], we are led to a linear system of equations

$$\boldsymbol{M^o c}=\boldsymbol{\delta U}, \tag{4.34}$$

where $\boldsymbol{M^o}\in\mathbb{R}^{Nm\times L}$ is the system matrix, $\boldsymbol{c}=[c_j]_{j=1}^{L}\in\mathbb{R}^{L\times 1}$ is the weighting coefficients' vector and $\boldsymbol{\delta U}\in\mathbb{R}^{Nm\times 1}$ denotes the numerically expected electrode potentials' differences. Adopting the measurement model described by (4.9), we treat the inverse problem as a minimization of the following WLS objective function:

$$F(\boldsymbol{c})=\|\boldsymbol{M^o c}-\boldsymbol{\delta V}\|_{\boldsymbol{W}}^2+\lambda^2 P(\boldsymbol{c}). \tag{4.35}$$

The minimization of (4.35) can be performed with the traditional L^2 or L^1-norm regularized approaches [179]. Unlike $\boldsymbol{J}$, the matrix $\boldsymbol{M^o}$ occurs directly from the discretization of (4.30) without the assumption of $\ln(\sigma(\boldsymbol{r'}))\simeq\sigma(\boldsymbol{r'})-1$ near σ_o. Hence, the expression of the boundary voltages as a function of conductivity is more accurate, leading to a faster convergence of the inverse solution. We note that the Green's function G and its gradient can be separately precomputed either analytically for canonical geometries or by using the F.E.M. or the finite difference method (F.D.M.) (at the same discretization mesh as MoM) to solve the Laplace equation for the potential and the field for non-canonical geometries.

In this particular work, we make use of an SBL formulation [142] to minimize (4.35). To this point,

we interpret the objective function in a Bayes log-likelihood context

$$F_B(\boldsymbol{c}) = \ln p(\boldsymbol{\delta V}|\boldsymbol{c}) + \lambda \ln p(\boldsymbol{c};\boldsymbol{\Theta}), \tag{4.36}$$

where $\boldsymbol{\Theta}$ is a set of hyperparameters. Considering that $\boldsymbol{c}$ is a superposition of some clusters overlapping each other with an equal size h, and $g = L - h + 1$ is the total number of clusters, the following factorization is performed:

$$\boldsymbol{c} = \boldsymbol{\Psi x} = [\boldsymbol{\Psi_1}, ..., \boldsymbol{\Psi_g}][\boldsymbol{x_1}^T, ..., \boldsymbol{x_g}^T]^T, \tag{4.37}$$

where $\boldsymbol{x_i} \in \mathbb{R}^{h\times 1}$ and $\boldsymbol{\Psi_i} = \left[\mathbf{0}^T_{(i-1)\times h}\ \boldsymbol{I}_{h\times h}\ \mathbf{0}^T_{(L-i-h+1)\times h}\right]^T \in \mathbb{R}^{L\times h}$. The Gaussian noise model (4.9) is approximated as

$$\boldsymbol{\delta V} = \boldsymbol{M^o c} + \boldsymbol{e_n} = \boldsymbol{M^o \Psi x} + \boldsymbol{e_n}. \tag{4.38}$$

We also define $\boldsymbol{\Phi} = \boldsymbol{M^o \Psi} \in \mathbb{R}^{Nm\times gh}$. Furthermore, we assume that the weight vector $\boldsymbol{x} \in \mathbb{R}^{gh\times 1}$ obeys the following Gaussian distribution:

$$p\left(\boldsymbol{x}; \{\gamma_i, \boldsymbol{B_i}\}_{i=1}^g\right) = \mathcal{N}\left(0, \boldsymbol{\Sigma_0}\right) \tag{4.39}$$

with zero mean value and $\boldsymbol{\Sigma_0} \in \mathbb{R}^{gh\times gh}$ covariance matrix.

Considering the hyperparameters $\boldsymbol{\Theta} = \{\gamma_o, \{\gamma_i, \boldsymbol{B_i}\}_{i=1}^g\}$ and adopting the expectation-minimization (EM) method, as in [142], we get an a posteriori estimation of the weight vector's $\boldsymbol{x}$ mean values vector $\boldsymbol{\mu_x} \in \mathbb{R}^{gh\times 1}$ and covariance matrix $\boldsymbol{\Sigma_x} \in \mathbb{R}^{gh\times gh}$. Hence, we get a maximum a posteriori (MAP) estimation of $\boldsymbol{x}$. For clarity, we summarize the SBL process in Algorithm 1.

The updating rule for γ_i is based on the majoration-minimization method [138, 184]. In addition, instead of the linearized Jacobian matrix, we use the PM-MoM $\boldsymbol{M^o}$ system matrix as an input in order to limit the problem's non-linearity effect and avoid the necessity of recalculating $\boldsymbol{J}$.

The SBL method shows increased robustness to noise and modeling errors, while the reconstruction artefacts are minimized. Furthermore, unlike the traditional regularized schemes, the choice of the hyperparameter h (number of clusters) slightly affects the reconstruction quality [142]. Hence, the cumbersome and non-trivial process of hyperparameter selection is avoided. Moreover, the regular "moment" grids used in PM-MoM are suitable for performing sparse-based reconstructions. However, despite recent developments, the SBL methods are overall characterized by high complexity. For instance, the SBL approach applied presents a complexity of $\mathcal{O}(N^2m^2gh)$ per iteration. Nevertheless, avoiding the search process for optimal hyperparameters partially reduces the increased complexity effects. A simplified flow chart of the whole PM-MoM SBL, as well as an example of a domain's clustering, are depicted in Figure 4.1. The SBL approach adopted in this particular paper is in the form used in [142]. However, some modified SBL approaches using approximate message passing (AMP) to accelerate the E-step of the algorithm have been researched for $3D$ imaging [143], frequency-difference EIT [146] and multiple measurement vector (MMV) time-sequence measurements [145]. Such techniques can also be appropriately combined with the PM-MoM in a similar manner.

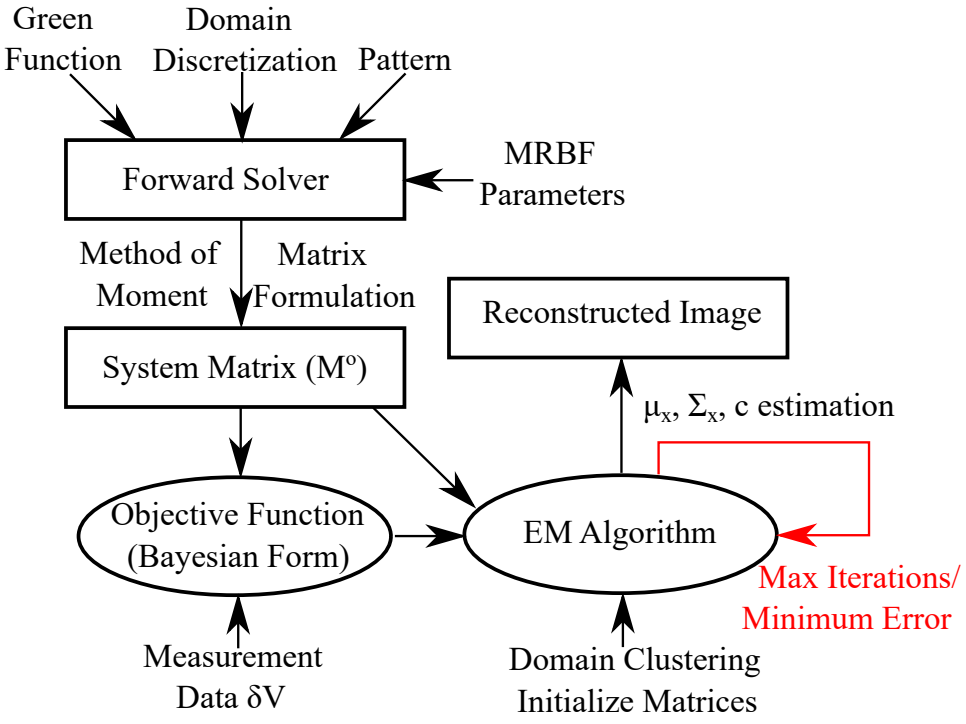

(a)

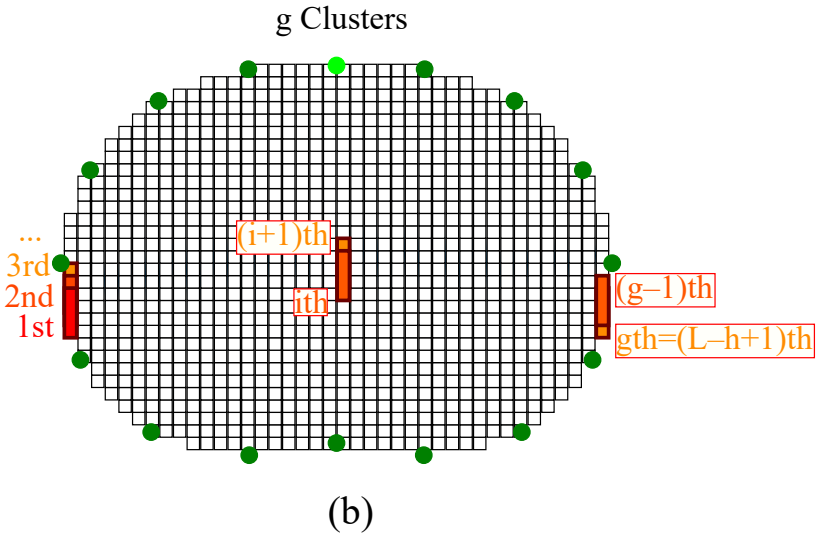

(b)

Figure 4.1: (**a**) Simplified demonstration of the PM-MoM SBL method process. (**b**) Illustrative example of a thoracic pixelized domain's clustering structure

.

Algorithm 1: Sparse Bayesian learning (SBL).

Inputs: $\boldsymbol{M^o},\ \boldsymbol{\delta V},\ h,\ \epsilon_{min},\ i_{max}$

Initialize: $\epsilon = 1,\ \kappa = 0,\ \boldsymbol{\mu_x = 0}_{gh\times 1},\ \boldsymbol{\Sigma_x = 0_{gh\times gh}},\ \boldsymbol{\gamma} = diag(\boldsymbol{I}_{g\times g}) \in \mathbb{R}^{g\times 1}$,

$\gamma_o = 0.01 \times \sqrt{\frac{1}{Nm-1}\sum_{j=1}^{Nm}|\delta V_j - \overline{\boldsymbol{\delta V}}|^2},\ \boldsymbol{B_i} = Toeplitz\left(\left[1, \zeta^1, ..., \zeta^{h-1}\right]\right), \zeta = 0.9,\ \boldsymbol{\Psi}$,

$\boldsymbol{\Sigma_0} = \begin{bmatrix} \gamma_1\boldsymbol{B_1} & ... & \boldsymbol{0_{h\times h}} \\ ... & ... & ... \\ \boldsymbol{0_{h\times h}} & ... & \gamma_g\boldsymbol{B_g} \end{bmatrix},\ \boldsymbol{\Phi = M^o\Psi},\ \boldsymbol{\Sigma_u} = \gamma_o\boldsymbol{I}_{Nm\times Nm} + \boldsymbol{\Phi\Sigma_o\Phi^T},\ \tilde{\boldsymbol{B}}_{\boldsymbol{i}} = \boldsymbol{B_i}.$

LOOP:

While $\epsilon > \epsilon_{min}$ and $\kappa \leq \kappa_{max}$ **do**

1. $\boldsymbol{\mu_x} := \boldsymbol{\Sigma_o\Phi^T\Sigma_u^{-1}}$
2. $\boldsymbol{\Sigma_x} := \boldsymbol{\Sigma_0 - \Sigma_0\Phi^T\Sigma_u^{-1}\Phi\Sigma_0}$
3. $\gamma_o := \frac{1}{Nm}\left(\|\boldsymbol{\delta V - \Phi\mu_x}\|_2^2 + \sum_{i=1}^{g} tr\left(\boldsymbol{\Sigma_x^i\Phi_i^T\Phi}_i\right)\right)$
4. $\gamma_i := \gamma_i \cdot \frac{\left\|\sqrt{\boldsymbol{B_i}}\boldsymbol{\Phi}_i^T\boldsymbol{\Sigma_u^{-1}\delta V}\right\|_2}{\sqrt{tr\left(\boldsymbol{\Phi}_i^T\boldsymbol{\Sigma_u^{-1}\Phi}_i\boldsymbol{B_i}\right)}}$, for each cluster $i \in \{1, ..., g\}$.
5. $\tilde{\boldsymbol{B}}_{\boldsymbol{i}} := \tilde{\boldsymbol{B}}_{\boldsymbol{i}} + \frac{1}{\gamma_i}\left(\boldsymbol{\Sigma_x^i} + \boldsymbol{\mu_x^i}\left(\boldsymbol{\mu_x^i}\right)^T\right)$, for each cluster $i \in \{1, ..., g\}$.
6. $\tilde{r}_i := \frac{\overline{diag\left(\tilde{\boldsymbol{B}}_{\boldsymbol{i}}, 1\right)}}{\overline{diag\left(\tilde{\boldsymbol{B}}_{\boldsymbol{i}}\right)}}$, for each cluster $i \in \{1, ..., g\}$.
7. $r_i := sign(\tilde{r}_i) \cdot \min\{|\tilde{r}_i|,\ 0.99\}$, for each cluster $i \in \{1, ..., g\}$.
8. $\boldsymbol{B_i} := Toeplitz\left(\left[r_i^0, ..., r_i^{h-1}\right]\right)$, for each cluster $i \in \{1, ..., g\}$.
9. Update $\boldsymbol{\Sigma_0}$ and $\boldsymbol{\Sigma_u}$.
10. $\epsilon = \frac{\|\boldsymbol{\mu_x^{new} - \mu_x^{prev}}\|_2}{\|\boldsymbol{\mu_x^{new}}\|_2}$
11. $\kappa := \kappa + 1$

End

Output: $\boldsymbol{c_* = \Psi\mu_x}$

Estimate $\sigma(\boldsymbol{r})$ using (3.17) and (3.16).

4.4 Evaluation Methods

In this section, the thoracic structures' extraction and the corresponding tissues' electrical properties are demonstrated. In addition, the evaluation metrics, including GREIT FoMs with minor modifications, the Pearson CC, the $RMSE$ and the recently proposed FR are briefly explained. Finally, an in vivo online available dataset demonstrating a subject's full-breath cycle is briefly described.

4.4.1 Thoracic Structures

To examine and compare the previously described algorithms' performance in dynamic imaging, we have created 3 $3D$ fine F.E. thoracic structures based on 3 CT-images of 3 corresponding different healthy adult male subjects. The CT images were taken between the third and the fourth intercostal levels and are included in a large medical database which is available online in [185]. The $3D$ models have been created in MATLAB using the EIDORS and the NETGEN software [72, 186] and include the following tissues: left lung, right lung, heart, vertebra and skin, while muscle is assumed to be the background.

For each structure, 5 breath-cycle states have been considered from end-expiration (deflated) to end-inspiration (inflated). Hence, a total number of 15 F.E. models have been created, demonstrating 3 subjects' cases in 5 breath-cycle states. Each state presents chest boundary changes (a total change of 5–8% of the chest's width) and lung shape changes (total expansion 10–15% of the lungs' width at the inflated state) [151]. The lungs' admittance changes between the states have also been considered.

The tissues' admittance values are loaded from an open-source database, demonstrated in [187, 188, 189]. All admittance values depend on the selected current signal frequency f in which the EIT measurements are performed, while the lungs' admittances also depend on the breathing state. For this particular work, we assume $f = 100$ kHz, which is in the range of the current frequencies used for dynamic lung imaging. This is actually a common frequency choice for such applications [171, 190, 191]. Nevertheless, higher frequencies, such as those applied in high-performance modern EIT systems [21, 171], can be also considered. Furthermore, to take into account each tissue's inhomogeneity, the following standard deviations (std) of the admittance values assigned to each tissues' elements have been taken into account: 1% for the skin, 2% for the heart and the muscle background and 3% for both lungs. These values fall within the range depicted in the mentioned database.

The conductivity and permittivity values assigned to each tissue at 100 kHz, as well as their std are shown in Table 4.1. For the lungs, the deflated and inflated states' values were taken from [187, 188, 189]. To find the intermediate states' values, we firstly assumed that the lungs' volumes increase linearly over time during the inhalation process [192]. A relative (arbitrary unit—A.U.) volume has been defined as follows:

$$F_i = \frac{3}{P+1} i + \frac{3}{P-1} + 4, \quad \textit{for} \quad 1 \leq i \leq P, \tag{4.40}$$

where P is the total number of states from end-expiration to the end-inspiration. In our case, $P = 5$. In actuality, the lungs' volume change is more complex and heavily depends on each particular breath. The main changes in the lungs' admittance occur due to the air-flow. The lungs' conductivity as a function of their volume can be expressed by [192, 193]

$$\sigma_l = K_1 \left(\frac{0.85 s_b}{w} + 0.03 s_i \right) \frac{32F + 4.5}{(32F + 9)^2} + K_2, \tag{4.41}$$

where s_b, w and s_i are lung morphological parameters described in [193], with their values selected to be $s_b = 0.5$, $w = 1.5$ and $s_i = 2$. In addition, K_1 and K_2 are coefficients used to scale the lungs' conductivity between the known values and end-inspiration and end-expiration. The permittivity of the

lungs is correspondingly defined as [193]

$$\epsilon_l = L_1 \left(\frac{0.85 e_{rb}}{w} + 780 F^{1/3} e_{rm} \right) \frac{32F + 4.5}{(32F + 9)^2} + L_2, \tag{4.42}$$

where e_{rb} and e_{rm} are also lung morphological parameters described in [193], with their values selected at $e_{rb} = 10^4$ and 10, respectively. Furthermore, L_1 and L_2 are scaling coefficients. We note that blood-cycle related changes have not been taken into consideration, since the HR frequency is 3–6 times higher than the breath frequency.

Table 4.1: Assigned conductivity and permittivity values to the thoracic models' tissues for $f = 100$kHz, according to [187, 188, 189], and (4.41)-(4.42). The admittance is estimated as $\gamma = \sigma + j\omega\epsilon\epsilon_o$.

Tissue	σ **at** 100**kHz** (S/m)	$\omega\epsilon\epsilon_o$ **at** 100**kHz** $(F \cdot Hz/m)$
Heart	0.215 ± 0.004	0.0548 ± 0.001
Deflated Lung	0.272 ± 0.003	0.029 ± 0.001
Lung State 2	0.225 ± 0.003	0.019 ± 0.001
Lung State 3	0.179 ± 0.003	0.017 ± 0.000
Lung State 4	0.145 ± 0.002	0.029 ± 0.001
Inflated Lung	0.107 ± 0.002	0.014 ± 0.000
Bones	0.021 ± 0.000	0.001 ± 0.000
Skin & Fat	0.045 ± 0.000	0.043 ± 0.000
Muscle (backrgound)	0.380 ± 0.008	0.024 ± 0.001

In each case (1–3), the boundary extracted from the corresponding CT image is used as a cross-section to create the $3D$ F.E. structure. For each structure, a height of $h = 1$ A.U. has been considered, while the x-axis limits have been normalized between -1 and 1 A.U. A number of $N = 16$ circular electrodes of radius $R_{el} = 0.05$ A.U. have been placed at the $z = 1/2$ A.U. level. In addition, an electrode position error has been added: 5% height std and 3% angle std, since this is a more realistic case.

The thoracic structures are demonstrated in Figures 4.2–4.4. Their boundary and lungs' shape changes are demonstrated at the cross-section level in Figure 4.5. Finally, the numbers of each model's tetrahedral elements and nodes are shown in Table 4.2.

To simulate the measurements, the adjacent (skip-0) current and voltage measurement pattern was considered [26, 27], while a Gaussian noise of -50dB SNR was added to the extracted raw signals. The EIDORS library tool in MATLAB was used to perform the simulations [72].

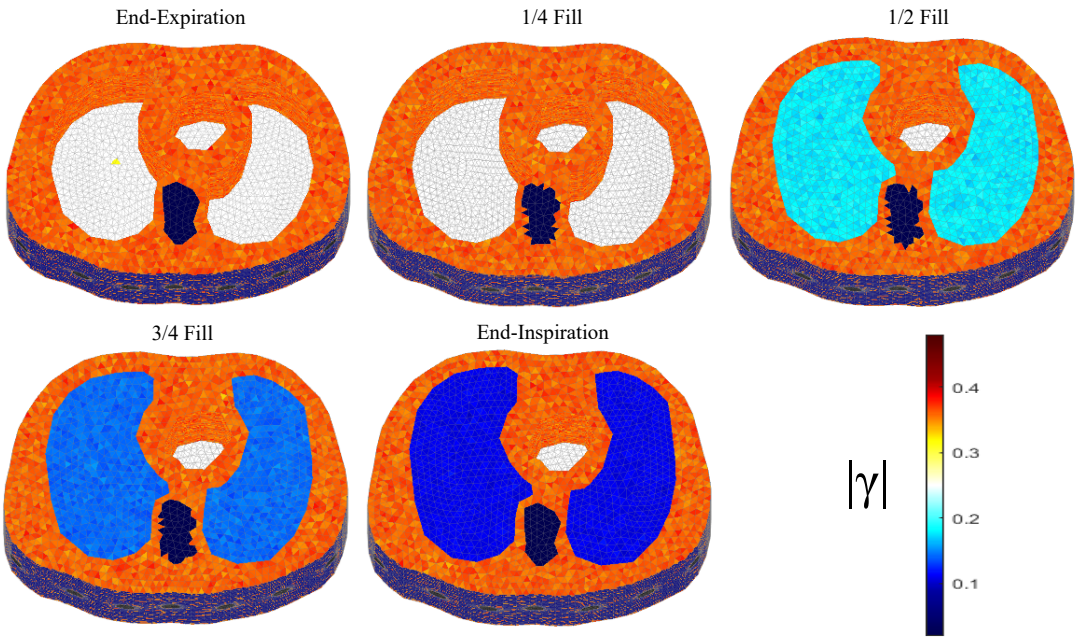

Figure 4.2: The 3D F.E. structure for the 1st subject case in 5 breath cycle states.

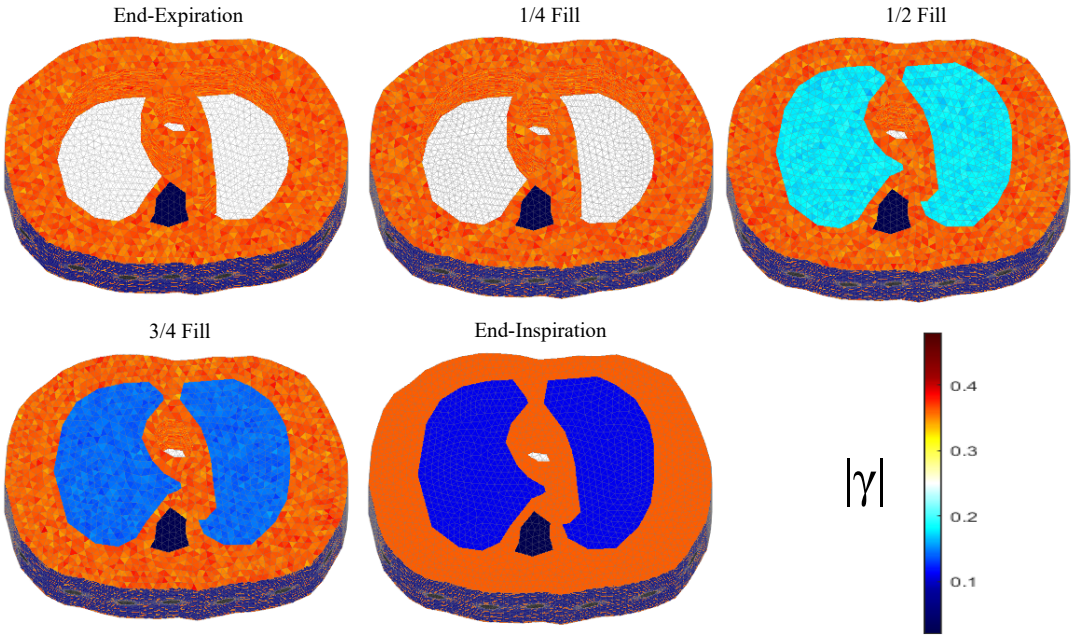

Figure 4.3: The 3D structure for the 2nd subject case in 5 breath cycle states.

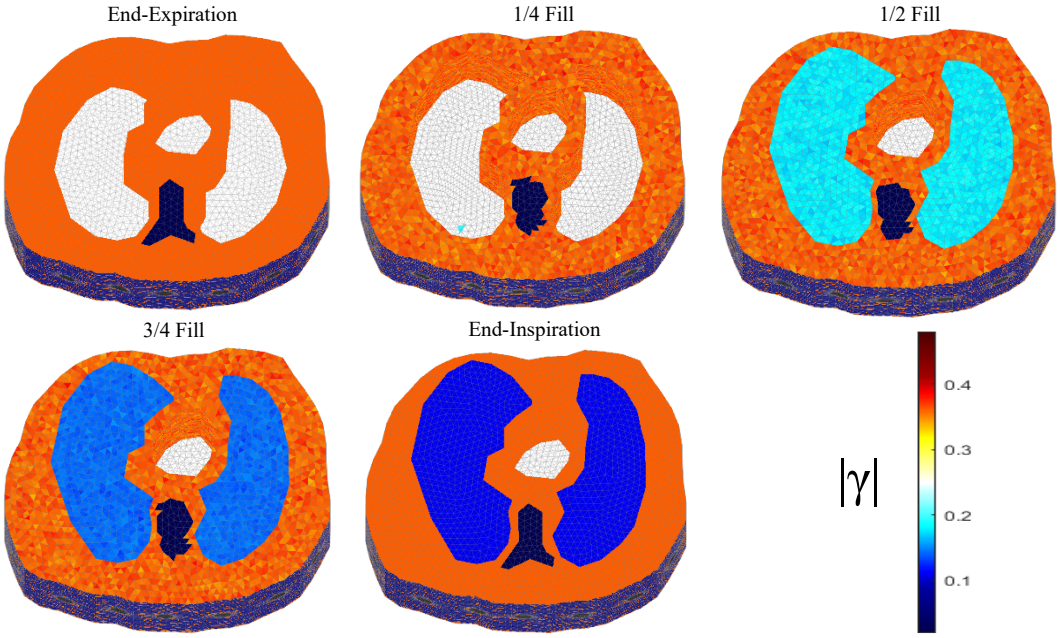

Figure 4.4: The 3D structure for the 3rd subject case in 5 breath cycle states.

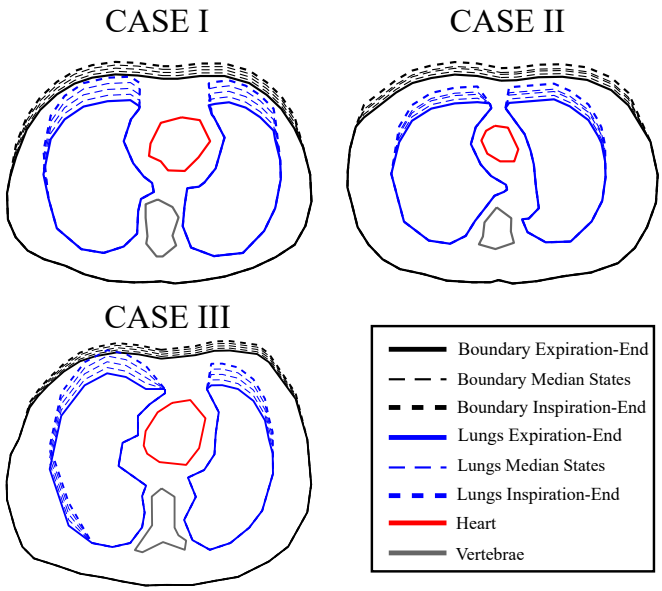

Figure 4.5: Cross-sectional boundary and lung shape changes from the end-expiration to the end-inspiration states. The extracted shapes were used to create extruded $3D$ models using NETGEN.

Table 4.2: Number of tetrahedral elements and nodes per each $3D$ thoracic F.E. model.

Model	**No of Elements (L_e)**	**No of Nodes (n_e)**
Case I, deflated state	133529	27328
Case I, state 2	139486	28374
Case I, state 3	139798	28433
Case I, state 4	142070	28814
Case I, inflated state	146000	29542
Case II, deflated state	144329	29125
Case II, state 2	147838	29815
Case II, state 3	146871	29688
Case II, state 4	149887	30219
Case II, inflated state	150775	30359
Case III, deflated state	158855	31791
Case III, state 2	158392	31768
Case III, state 3	159185	31937
Case III, state 4	159550	31984
Case III, inflated state	160349	32159

4.4.2 Reconstruction Domain

When the EIT image reconstruction is performed using simulated models, we need to avoid *inverse crime.* This occurs when the simulated model's and the reconstruction domain's mesh or boundary is equal [155]. Instead, the reconstruction needs to be performed on a significantly different mesh, usually coarser than the simulated model's one.

In this work, all the image reconstructions are performed on a $2D$ coarse thoracic-shaped domain, called Ω, which presents a different boundary than any of the original model's boundaries. For the FEM-based reconstruction approaches, the domain contains $L = 1024$ triangular elements and $n_e = 545$ nodes. The shunt electrode model has been assumed to simulate the electrodes' effects [22, 23]. Furthermore, for the PM-MoM reconstructions, a $L = 1060$ uniform pixel grid has been used, considering the electrodes as points [24]. The reconstruction domain for the two discretizations is shown in Figure 4.6.

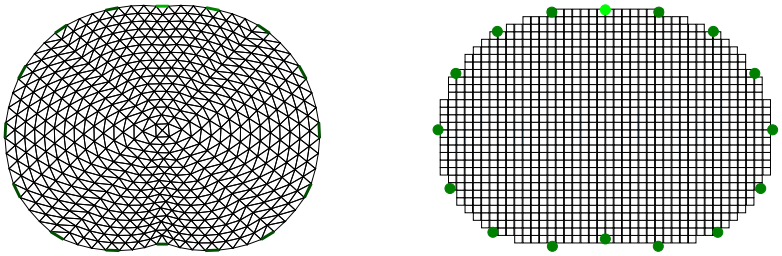

Figure 4.6: Reconstruction domain Ω used for the EIT imaging. **Left**: F.E. mesh. **Right**: MoM mesh.

4.4.3 Reference Image Extraction

In order to perform a quantitative evaluation of EIT imaging, a corresponding "ground truth" reference image has to be defined on the reconstruction domain Ω. However, the simulated models have completely different shapes and discretization meshes compared to Ω in both the standard FEM and MoM reconstruction cases. In order to "match" the simulated models with the reconstruction domain, the approach presented in [194] is adopted.

This approach considers that the simulated models' shape in all three cases is not constant, as well as that difference-EIT imaging is performed. Hence, we firstly get five absolute reference images, each one representing a particular state. Then we take the differences between the 2nd–5th images and the 1st "reference frame", resulting in 4 reference images.

Each "true boundary" domain $\tilde{\Omega}_{k,l}$, $k = \{1, 2, 3\}$, $l = \{1, 2, ..., 5\}$ is extracted from the $3D$ models' electrodes' cross-section plane. Then, we scale Ω and each $\tilde{\Omega}_{i,j}$ in the x-axis by normalizing its limits between -1 and 1. We secondly define A_i as the Ω ith-element's/pixel's area, with $i = \{1, 2, ..., L\}$. Then, the percentage of A_i which is within the curves defined by the following six tissues, left lung, right lung, vertebra, heart, skin and muscle, is expressed as a weight vector,

$$\boldsymbol{w^i_{k,l}} = [w^i_{j,k,l}]^6_{j=1} \in \mathbb{R}^{6\times 1}_+, \tag{4.43}$$

for the kth case and lth state. At this point, we define the vector

$$\boldsymbol{\gamma_{t,l}} = [\gamma_{j,l}]_{j=1}^{6} \in \mathbb{C}^{1\times 6}, \tag{4.44}$$

which represents the mean admittances for each one of the 6 mentioned tissues at the lth state. Then, the ith element's or pixel's reference admittance is estimated as follows:

$$\gamma_{r,k,l,i} = \boldsymbol{\gamma_{t,l}} \cdot \boldsymbol{w_{k,l}^{i}} \in \mathbb{C}. \tag{4.45}$$

The kth case, lth state (absolute) reference admittance vector is then defined as

$$\boldsymbol{\gamma_{r,k,l}} = [\gamma_{r,k,l,i}]_{i=1}^{L} \in \mathbb{C}^{L\times 1}. \tag{4.46}$$

For each image frame, we get the following difference reference admittance vector:

$$\boldsymbol{\delta\gamma_{r,k,l+1}} = \boldsymbol{\gamma_{r,k,l+1}} - \boldsymbol{\gamma_{r,k,1}}, \tag{4.47}$$

where $\boldsymbol{\delta\gamma_{r,k,l+1}} \in \mathbb{C}^{L\times 1}$ for $l = \{1, 2, 3, 4\}$, assuming the kth case.

A simple example of this process and the F.E.M. reference images for $k = 1$ are demonstrated in Figure 4.7.

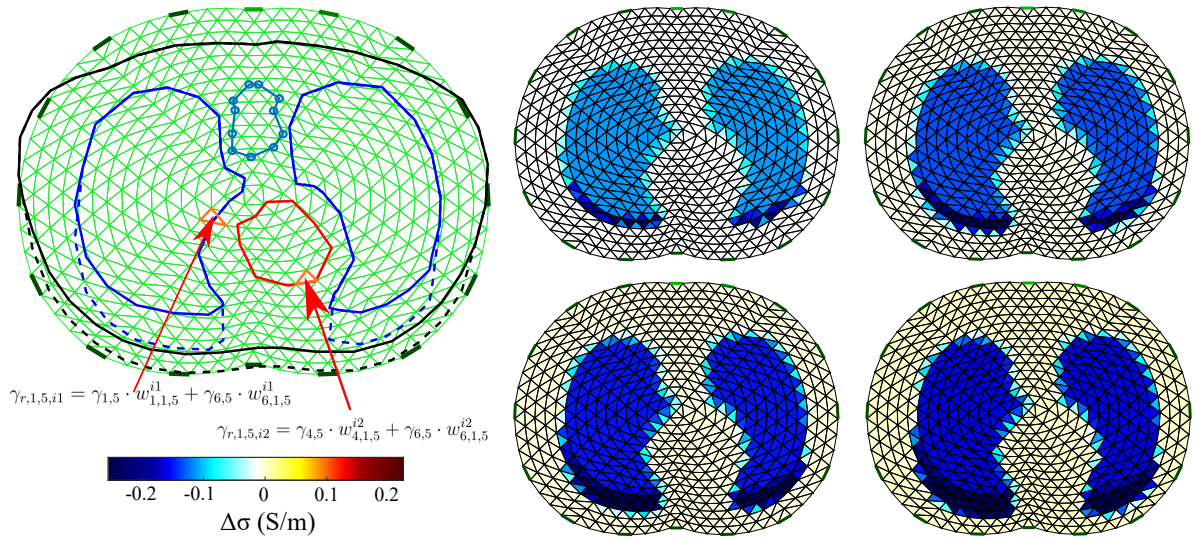

Figure 4.7: Visual example of the reference images' extraction for the 1st thoracic case ($k = 1$). **Left**: example of the absolute admittance extraction of the i_1th and i_2th elements when in an inflated case ($l = 5$). **Right**: the difference image reference frames for case $k = 1$ when F.E.M. is applied. Only the conductivity difference (real values) is expressed in the legend.

4.4.4 Figures of Merit

To quantitatively evaluate the EIT reconstructions, we use the following five GREIT FoM: target amplitude—TA, position error—PE, shape deformation—SD, resolution—RES and ringing—RNG [71]. These have been properly adapted to the examined thoracic cases. Furthermore, the CC, the $RMSE$ and the FR metrics are applied.

Target Amplitude—TA

Assume $\boldsymbol{\delta\sigma_*} \in \mathbb{R}^{L\times 1}$ isthe conductivity difference estimated from the EIT reconstructions. The TA can be defined as the normalized summary of elements'/pixels' amplitudes in the image,

$$TA = \frac{\sum_{i=1}^{L} \delta\sigma_{*,i}}{\max\{|\delta\sigma_{*,i}|\}}. \tag{4.48}$$

TA is a FoM similar to the amplitude response—AR, which is considered to be the most important GREIT FoM [71]. Its absolute value should be relatively low and stable during the breath process. When admittance values are reconstructed, TA can be estimated by taking only the real values.

Position Error—PE

The position error—PE—shows the precision of the reconstructed inclusions' center of gravity. In our case, we define the right and the left lung as the corresponding inclusions. Then, we get two PE values:

$$PE_{LL} = |\boldsymbol{r_{tLL}} - \boldsymbol{r_{iLL}}|, \tag{4.49}$$

for the left lung, where $\boldsymbol{r_{tLL}}$ is the true center of the left lung and $\boldsymbol{r_{iLL}}$ is the reconstucted left lung's center, and

$$PE_{RL} = |\boldsymbol{r_{tRL}} - \boldsymbol{r_{iRL}}| \tag{4.50}$$

for the right lung, where $\boldsymbol{r_{tRL}}$ is the true center of the right lung, and $\boldsymbol{r_{iRL}}$ is the reconstucted right lung's center. The total PE is given by

$$PE = PE_{LL} + PE_{RL}. \tag{4.51}$$

To detect an inclusion as "lung", we first filter the reconstructed image, setting all the elements'/pixels' absolute values that are below a selected threshold ($-1/4$ of the maximum absolute value) to zero and all non-zero values to 1. We denote $\boldsymbol{x_f} \in \mathbb{R}^{L\times 1}$ as the filtered image conductivity distribution, where

$$x_{f_i} = \begin{cases} 1 & \text{if } \delta\sigma_{*,i} \leq -1/4 \max\{|\boldsymbol{\delta\sigma_*}|\} \\ 0 & \text{otherwise} \end{cases} \tag{4.52}$$

Secondly, the left and right lung inclusions are separated in the reconstructed image with a y-axis line, as shown in Figure 4.8.

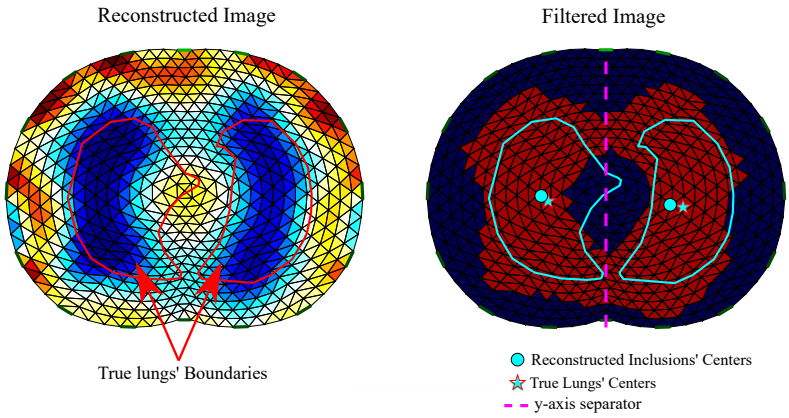

Figure 4.8: Reconstructed EIT image filtering and detection of PE. **Left**: raw reconstructed image including the true lungs' boundaries (for the corresponding $3D$ model's cross-section). **Right**: filtered image including true and reconstructed lungs' centers.

Shape Deformation—SD

Shape deformation—SD—denotes the percentage of the reconstructed and filtered inclusion which is not within the "true lung's" boundary. Assume LL and RL are the "true" left and right lungs' domains, respectively. If $\boldsymbol{x_f}$ is the filtered reconstructed image conductivity distribution, we get

$$SD_{LL} = \frac{\sum_{i\notin LL} x_{f_{i,left}} A_i}{\sum_{i\in LL} x_{f_{i,left}} A_i} \tag{4.53}$$

for the left lung and for each element/pixel left from the y-axis with an area A_i (see Figure 4.8). For the right lung we have

$$SD_{RL} = \frac{\sum_{i \notin RL} x_{f_{i,right}} A_i}{\sum_{i \in RL} x_{f_{i,right}} A_i} \tag{4.54}$$

for each element/pixel right from the y-axis with an area A_i.

The total SD is given by

$$SD = \frac{\sum_{i \notin LL} x_{f_{i,left}} A_i + \sum_{i \notin RL} x_{f_{i,right}} A_i}{\sum_{i \in LL} x_{f_{i,left}} A_i + \sum_{i \in RL} x_{f_{i,right}} A_i}. \tag{4.55}$$

SD should also be low and stable.

Resolution—RES

If A_{LL} represents the reconstructed left lung inclusion's area, A_{RL} is the reconstructed right lung inclusion's area and A_o is the Ω area, the resolution—RES—is given by

$$RES = \sqrt{\frac{A_{LL} + A_{RL}}{A_o}}. \tag{4.56}$$

We can estimate A_{LL} and A_{RL} from the following expressions

$$A_{LL} = \sum_{i \in LL} x_{f_{i,left}} A_i \tag{4.57}$$

and

$$A_{RL} = \sum_{i \in RL} x_{f_{i,right}} A_i, \tag{4.58}$$

RES should be low and uniform [71].

Ringing—RNG

Ringing—RNG—demonstrates whether the reconstructed inclusion causes areas of opposite sign near the target inclusion. It is given by

$$RNG = \frac{\sum_{i \notin LL \& i \notin RL \& \delta\sigma_{*,i} < 0} \delta\sigma_{*,i}}{\sum_{i \in LL} \delta\sigma_i + \sum_{i \in RL} \delta\sigma_{*,i}}. \tag{4.59}$$

RNG is an important GREIT FoM, since in dynamic lung image reconstructions, conductive areas often appear between the lungs that are sometimes wrongly recognized as "heart" [71]. It should also be low and as stable as possible.

Apart from the above GREIT parameters, we also apply the following FoM.

Pearson Correlation Coefficient—CC

The Pearson correlation coefficient—CC—is one of the most common metrics that quantify an image's quality. It indicates the similarity between a "ground truth" reference image and the reconstructed image. It is given by

$$CC = \frac{\text{Cov}(\boldsymbol{\delta\sigma_*}, \boldsymbol{\delta\sigma_r})}{\text{std}(\boldsymbol{\delta\sigma_*})\text{std}(\boldsymbol{\delta\sigma_r})}, \tag{4.60}$$

where $\boldsymbol{\delta\sigma_r} = Re\{\boldsymbol{\delta\gamma_r}\}$ for each particular case k and state l.

Root Mean Square Error—$RMSE$

An additional FoM used for the image evaluation is the well-known $RMSE$, which is estimated according to the following formula:

$$RMSE = \sqrt{\frac{\sum_{i=1}^{L} \left(\delta\sigma_{r,i} - \delta\sigma_{*,i}\right)^2}{L}}. \tag{4.61}$$

Full Reference—FR

This metric was recently proposed as a universal FoM for EIT systems' evaluation on the reconstructed images [195]. It has been extensively presented and applied in phantom experimental setups. However, this is the first time that FR is applied in dynamic thoracic models.

To estimate FR, the normalization of the reference images $\boldsymbol{\delta\sigma_r}$ and the reconstructed images $\boldsymbol{\delta\sigma_*}$ (element/pixel) data between -1 and 1 needs to be performed. We define as $\boldsymbol{EDref} \in \mathbb{R}^{L\times 1}$ the normalized reference image data and $\boldsymbol{EDtest} \in \mathbb{R}^{L\times 1}$ the normalized reconstructed image data.The global FR (GFR) is defined as follows:

$$GFR = 0.5 \cdot \sum_{i=1}^{L} |EDref_i - EDtest_i|. \tag{4.62}$$

We also define the local FRs for the left and the right lungs, respectively, as

$$FR_{LL} = 0.5 \cdot \sum_{i\in LL} |EDref_i - EDtest_i| \tag{4.63}$$

and

$$FR_{RL} = 0.5 \cdot \sum_{i\in RL} |EDref_i - EDtest_i| \tag{4.64}$$

Both local and global FR indicate a high-quality reconstruction when they take low values.

4.4.5 In Vivo Data

A qualitative comparison is attempted using online available in vivo EIT data [72]. This data consists of 34 data frames of a single breath cycle captured by the 16-electrode serial-data EIT Scanner [196]

using the adjacent current and voltage measurement pattern. This system performs demodulation of the input signal with an AM signal of a higher order of magnitude frequency than that of the electrode voltage signal. The injected current frequency (carrier) signal was set at 65 kHz. Since difference-EIT imaging is performed, the first frame is used as reference, resulting in 33 image reconstructions.

4.5 Results and Discussion

Image reconstructions were performed for the 3 structures presented in 4.4.1, considering each one of the 5 mentioned breathing states and resulting 4 images per structure. Reconstructions were also performed for the in vivo data described in 4.4.5, resulting in 33 EIT images. The regularization scheme-based approaches described in Section 4.2.4, the MoM-regularized approach, as well as the proposed MoM SBL approach described in Section 4.3 were used. Particularly for the multiple priors difference non-linear approach (N.L.D.), we consider that the ROI where $\delta\sigma_{ROI}$ occurs is equal to Ω, since the "lungs" area covers a significant part of Ω [151].

For all cases, the reconstruction hyperparameter λ value, as well as the μ, β and h parameters' values (for the movement-prior, TV and PM-MoM SBL reconstructions, respectively) were heuristically selected, as shown in Table 4.3. The selection of λ was performed in such a way that CC is maximized. Although some methods for the λ selection, such as the L-curve, the noise figure (NF) and the BestRes calibration methods [71, 197], have been proposed, this process is beyond this work's scope. Finally, for the PM-MoM SBL, we set the maximum number of iterations κ_{max} to 5 and the minimum tolerance ϵ_{min} to 10^{-5}.

Table 4.3: Selection of reconstruction parameters per algorithm

Algorithm	λ	μ	β	h
Movement Prior	$8 \cdot 10^{-3}$	1.42	–	–
Gauss-Newton (GN)	$8 \cdot 10^{-3}$	–	–	–
Total Variation (TV)	10^{-6}	–	10^{-3}	–
Difference of Absolute Images	$5 \cdot 10^{-2}$	–	–	–
Multiple Prior (N.L.D.)	$\lambda_1 : 5 \cdot 10^{-5}$ $\lambda_{ROI} : 8 \cdot 10^{-5}$	–	10^{-3}	–
PM-MoM Laplace	0.2	–	–	–
PM-MoM SBL	–	–	–	4

4.5.1 Simulation Results

The resulting image reconstructions and the FoM values demonstrating the simulated cases are depicted in Figures 4.9–4.14. Specifically, the image reconstructions that represent each one of the structures

1–3 are shown in Figures 4.9, 4.11 and 4.13, respectively. We define the reference image extracted according to the process described in 4.4.3 as the ”true” image. Furthermore, the corresponding FoM values obtained are demonstrated in Figures 4.10, 4.12 and 4.14, respectively.

A visual inspection of the images which resulted from the 1st structure (Figure 4.9) shows that the air-filled lungs are successfully detected from all the approaches. However, the lungs' shape and area is deformed, while “pseudo-heart” and boundary artefacts often appear. Such effects are less intense in the MoM Laplace and the MoM SBL cases. As we proceed to the full-inhalation state, the conductivity contrast increases, resulting overall in increased absolute TA, PE and sometimes RNG (Figure 4.10). At the same time, both local and global FR decrease, while non-significant changes occur at the RES, SD and CC. The $RMSE$ value remains almost constant for all the approaches, except for the TV, where it decreases. Comparing the metric values for each algorithm, better results are obtained by the PM-MoM SBL approach, which shows the lowest and most uniform absolute TA, the lowest PE, RES, SD, $RMSE$ and GFR and the highest CC, followed by the PM-MoM regularization approach.

The images obtained from the simulations of the second structure (Figure 4.11), which is characterized by closer distance between the lungs, show almost all the artefacts near the boundary instead of between the lungs. The PM-MoM SBL method also shows less intense artefacts, while, along with the regularized PM-MoM and the multiple priors N.L.D. approach, achieving the best CC and lower $RMSE$, local and GFR values (Figure 4.12). The proposed method also achieves the lowest absolute and most constant TA, RES and SD. However, the best local FR levels are extracted from the N.L.D, while the PM-MoM shows an increased RNG metric.

The third case results in Figure 4.13 are characterized by overestimation of the air-related conductivity change near the chest. This occurs due to the presence of lung tissue very close to the chest boundary, as the EIT measurements are sensitive to conductivity changes near the boundary [198]. A visual comparison of the images in Figure 4.13 indicates that the PM-MoM SBL method has the best performance, an absence of “positive conductivity change” artefacts and less lung deformation. Considering the quantitative results, the PM-MoM SBL approach achieves the lowest PE, RES, SD and $RMSE$ (Figure 4.14). Although the best TA, RNG, CC and GFR are demonstrated by the GN, N.L.D, N.L.D. and the regularized PM-MoM methods, respectively, the PM-MoM SBL shows the most constant TA, acceptable levels of RNG, a CC which is close to the best one, and the second-lowest GFR.

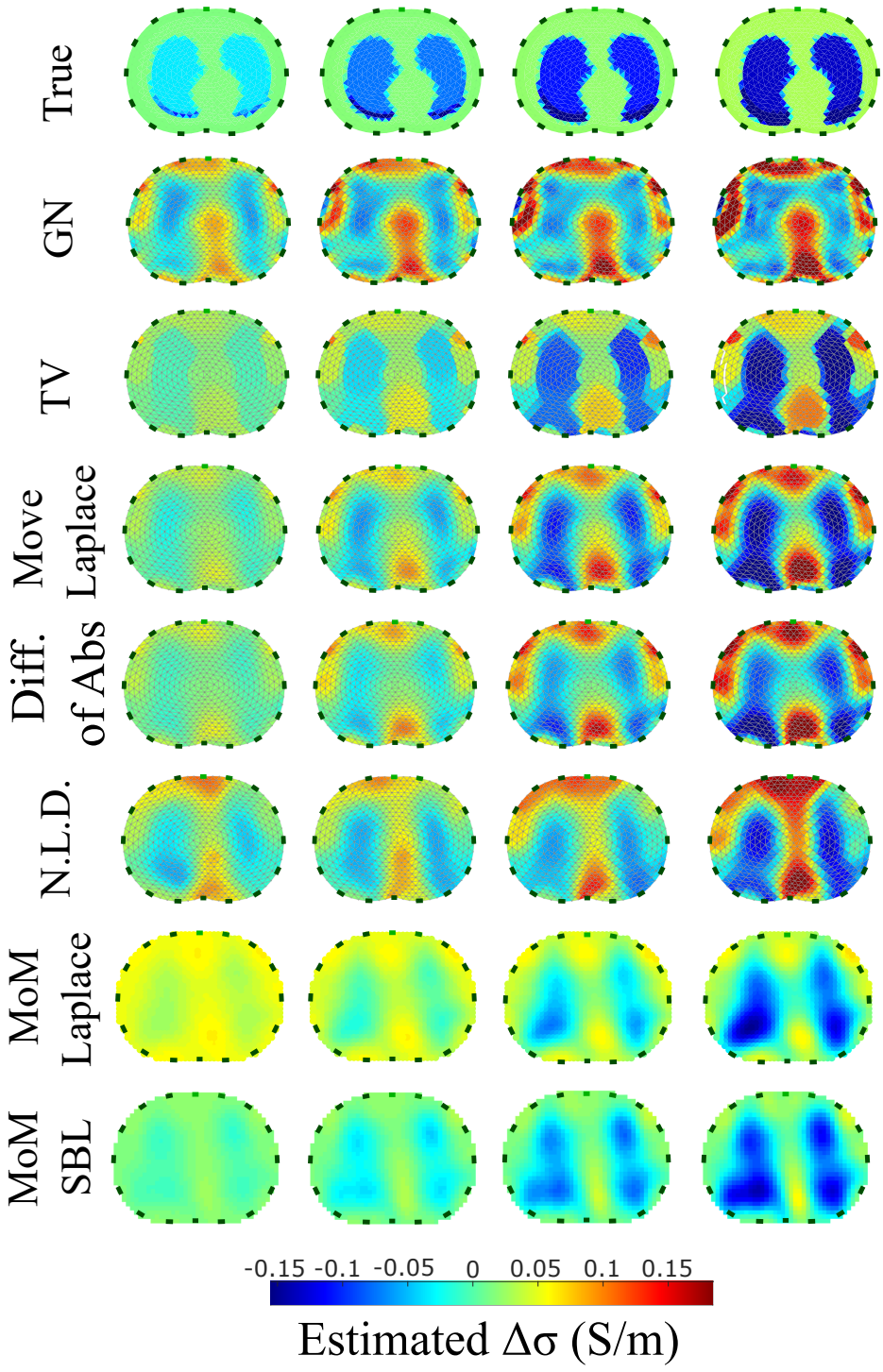

Figure 4.9: Reconstructed EIT images (conductivity differences) for the first case.

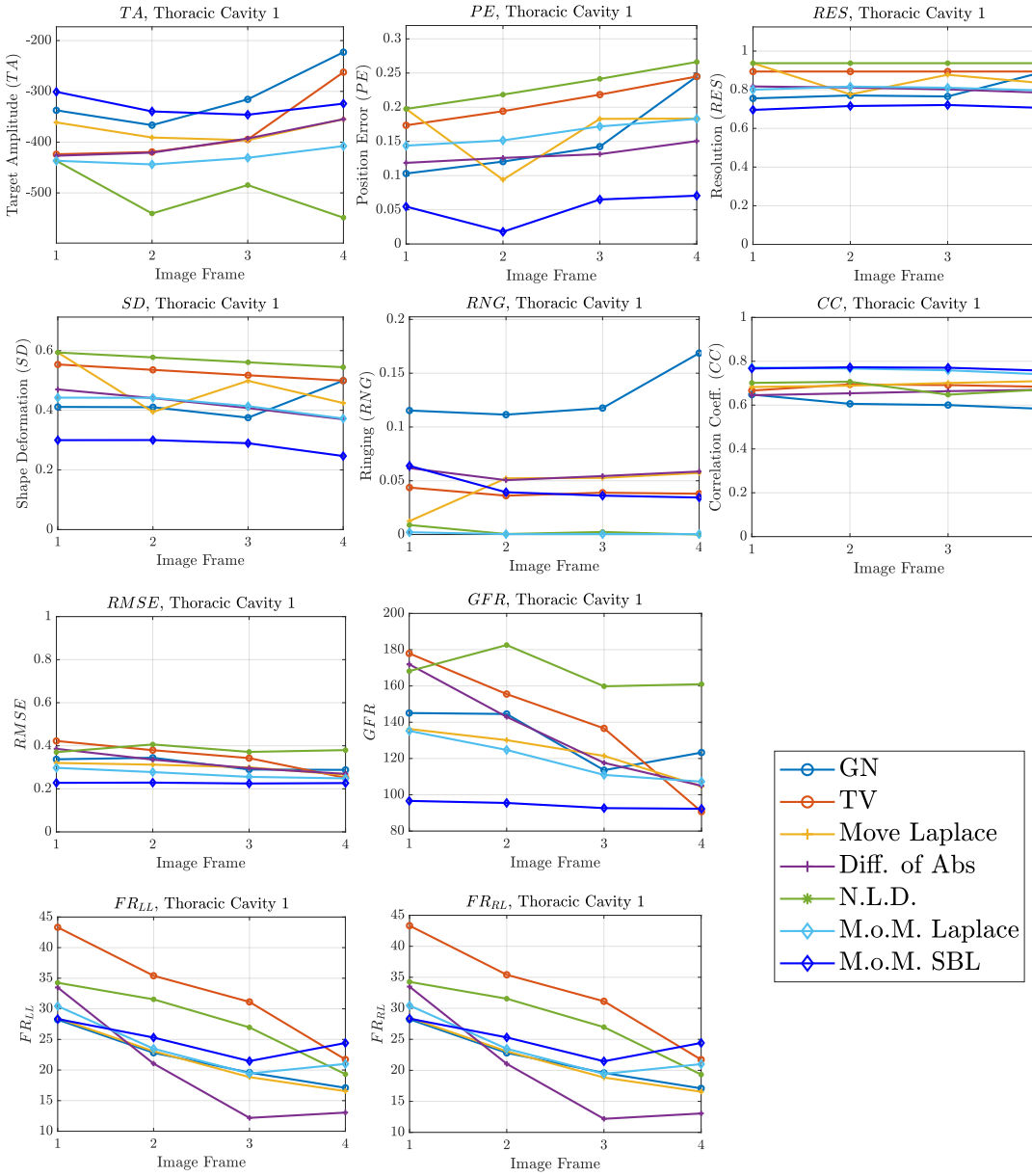

Figure 4.10: FoM results for the first case.

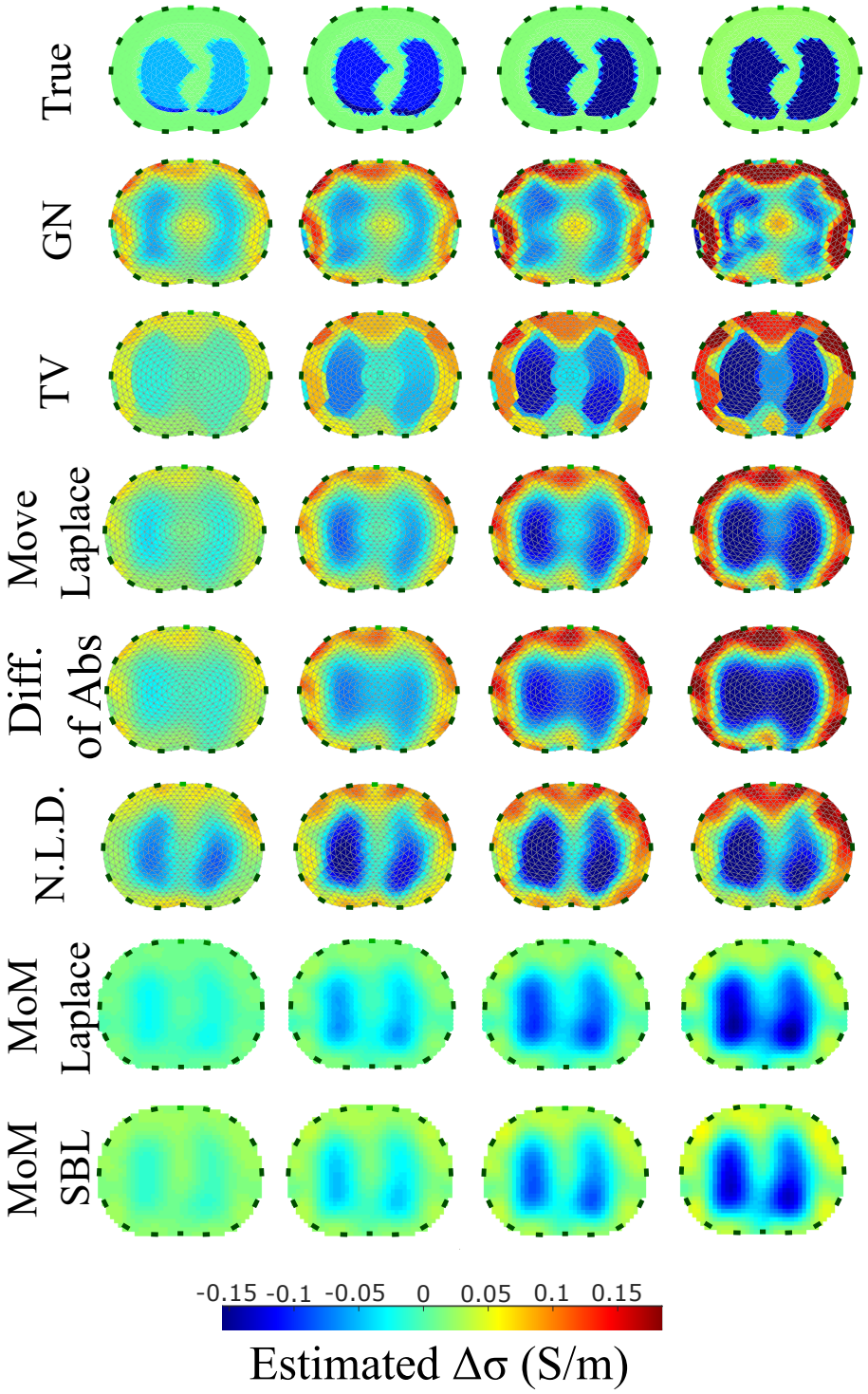

Figure 4.11: Reconstructed EIT images (conductivity differences) for the second case.

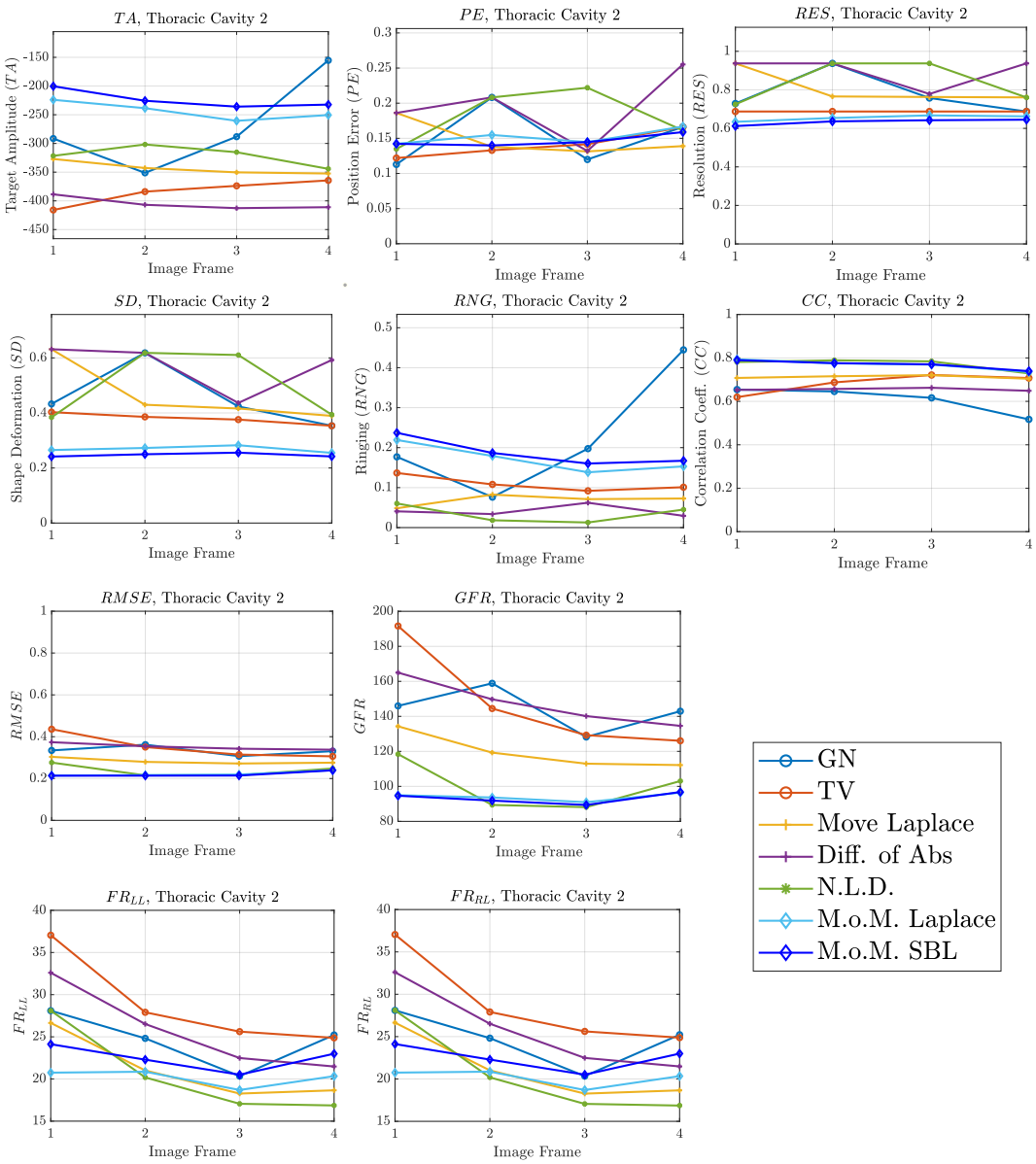

Figure 4.12: FoM results for the second case.

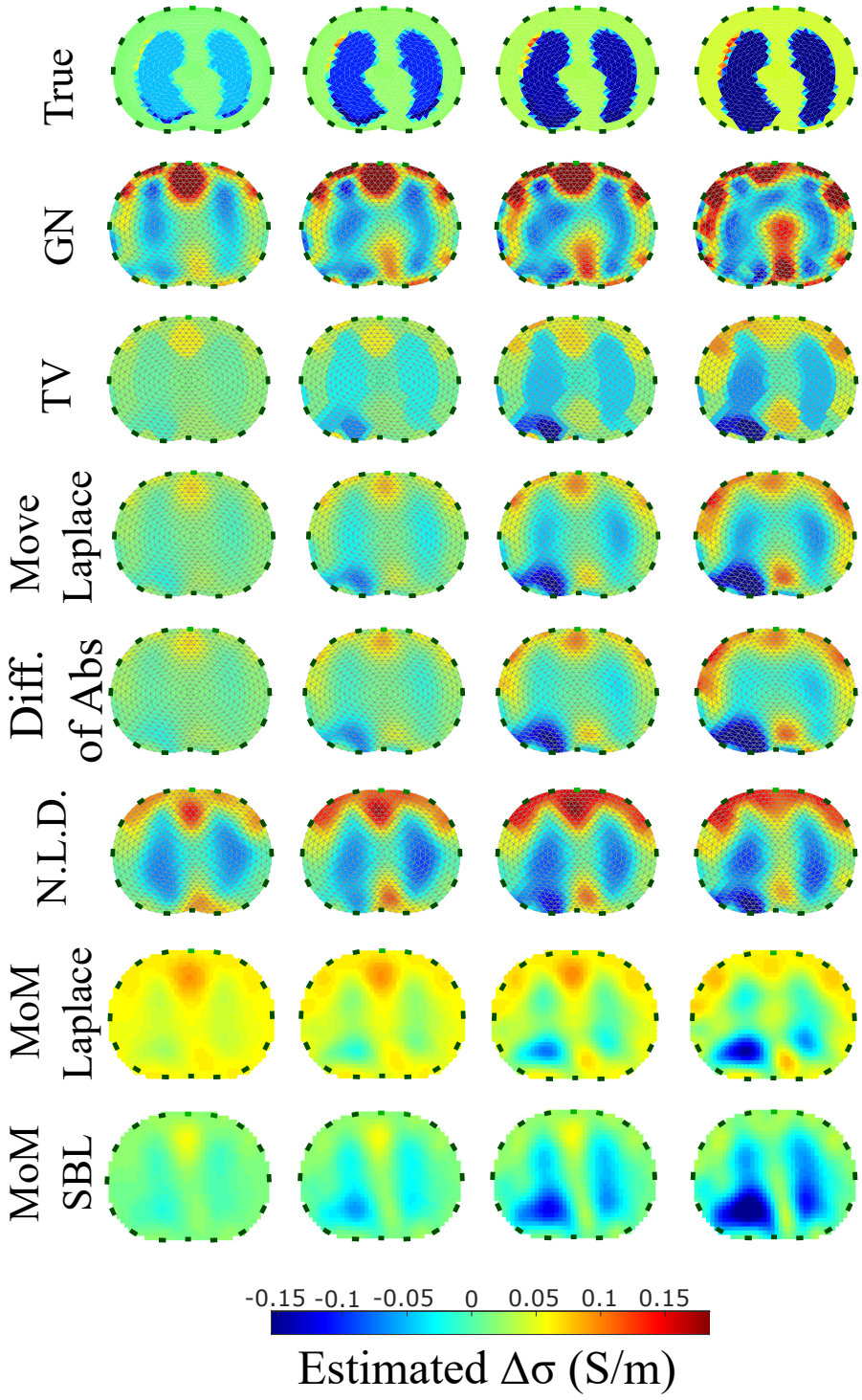

Figure 4.13: Reconstructed EIT images (conductivity differences) for the third case.

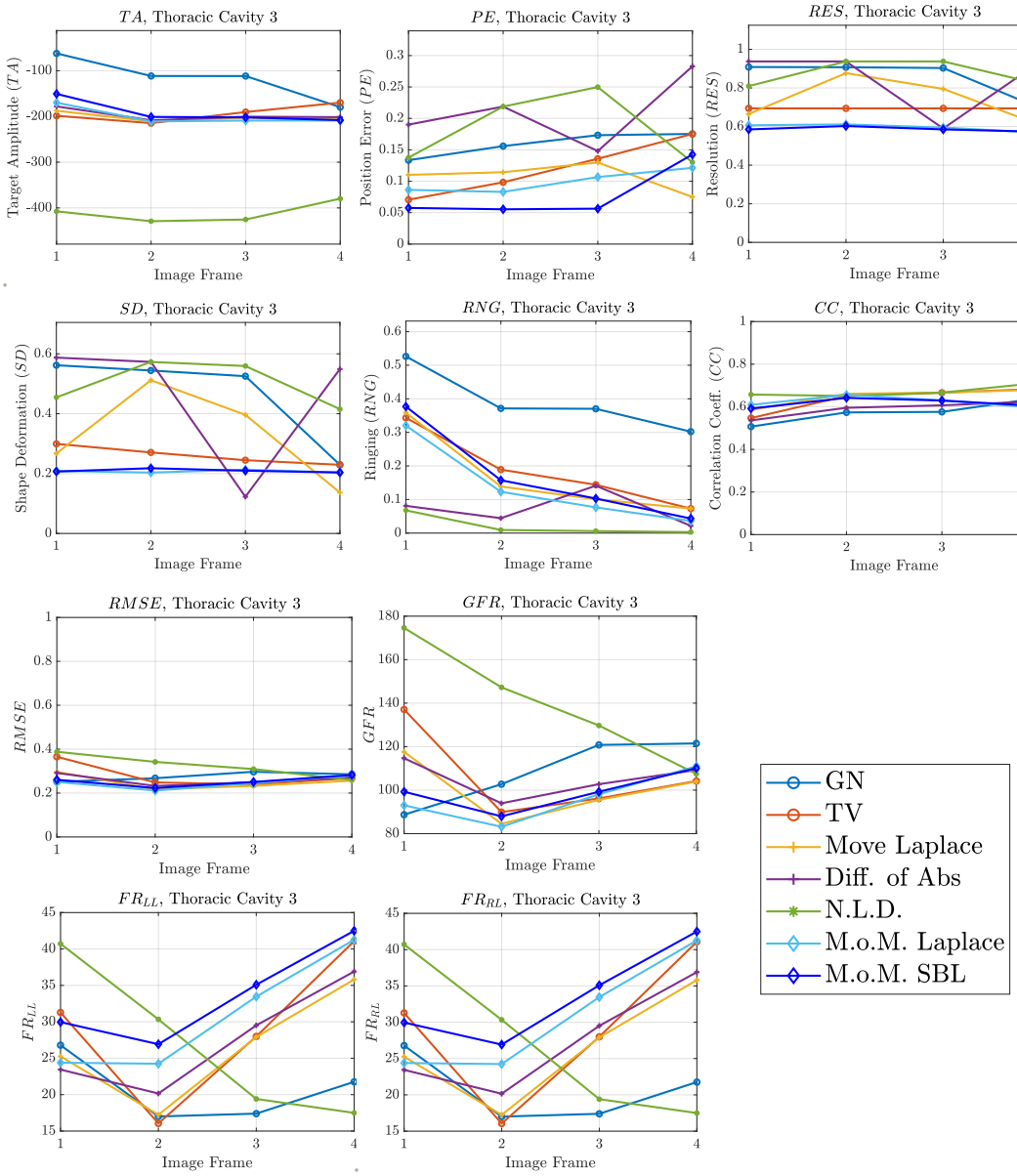

Figure 4.14: FoM results for the third case.

4.5.2 In Vivo Results

The in vivo EIT reconstructed images that demonstrate a subject's single breath, as described in 4.4.5, are shown in Figures 4.15–4.18. In particular, Figure 4.15 shows the reconstructed images using the GN and TV approaches, reviewed in 4.2.4. Figure 4.16 shows the reconstructed images using the movement prior linear approach, Figure 4.17 depicts the reconstructed images using the difference of absolute images and the multiple priors non-linear difference imaging (N.L.D.) approaches and Figure 4.18 demonstrates the regularized and SBL PM-MoM reconstructed images.

A qualitative observation of the images leads to the outcome that all the approaches, except for GN, are able to detect the full-inspiration state. However, the presence of ringing is significant near the centre

(between the lungs) in the movement prior, GN and N.L.D. approaches. This might lead to misleading conclusions about the presence of "heart" tissue between the lungs, as mentioned above. In fact, the heart tissue is not directly detectable in difference EIT imaging, since its conductivity does not significantly change during the breath cycle. In addition, any blood-cycle-related conductivity changes are synchronized with the heart rate HR, while the "pseudo-heart" inclusion is synchronized with the breath cycle. Meanwhile, the TV, difference of absolute images and both PM-MoM approaches demonstrate boundary "positive conductivity change" artefacts which are related to the mismatch between the patients' thoracic shape and $\partial\Omega$. This effect is less intensive in the regularized PM-MoM, PM-MoM SBL, the difference of absolute images and the TV methods, which overall perform better than GN, N.L.D. and movement prior. However, the TV method appears to underestimate the lungs' area in relation to the total thoracic area. We also observe that the inequality between the lungs' volumes is successfully detected by most of the approaches (except for TV), but is more clear when enacting PM-MoM (regularized or SBL), difference of absolute images and N.L.D.

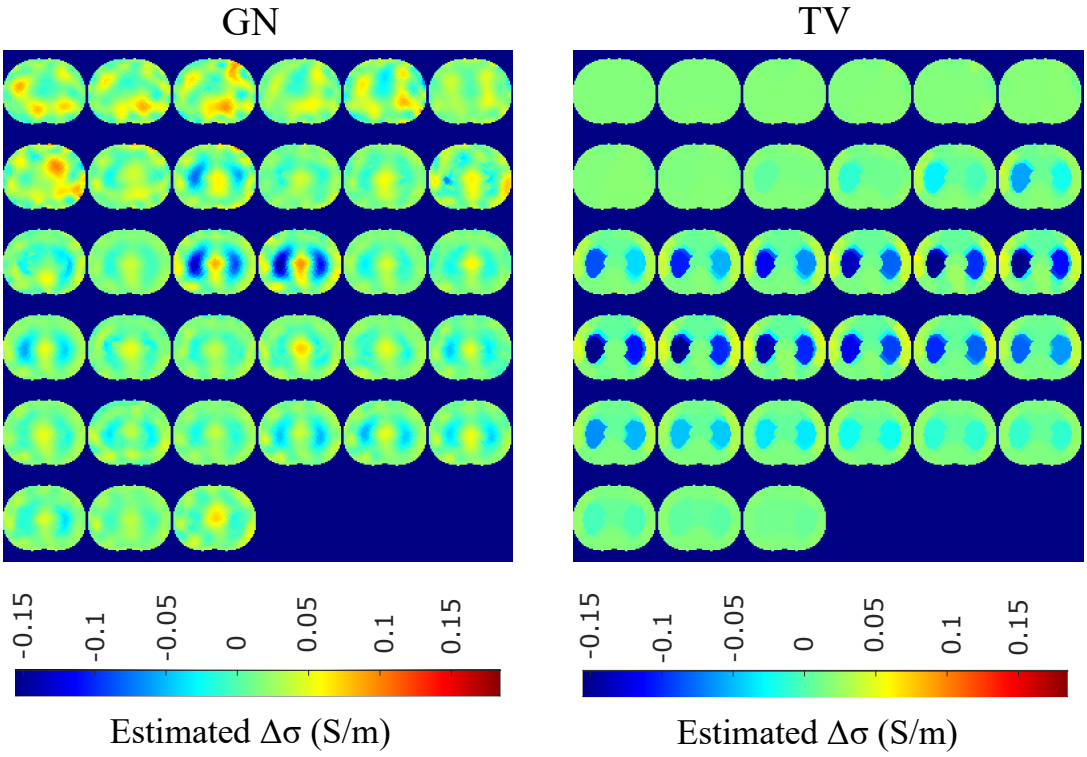

Figure 4.15: Single–breath in vivo results using the GN and TV approaches.

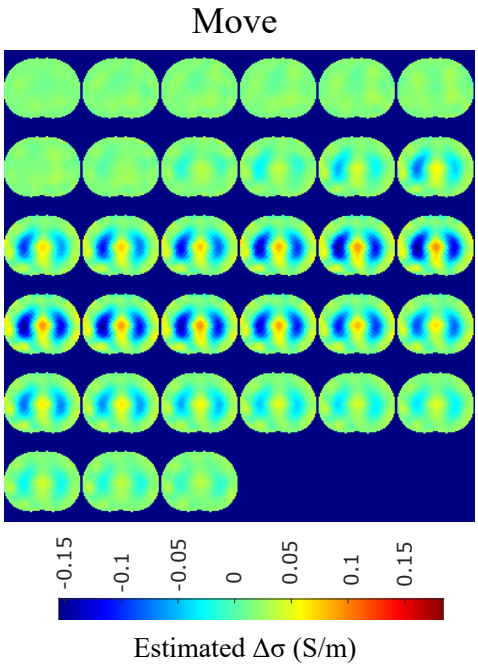

Figure 4.16: Single–breath in-vivo results using the movement Laplace prior approach.

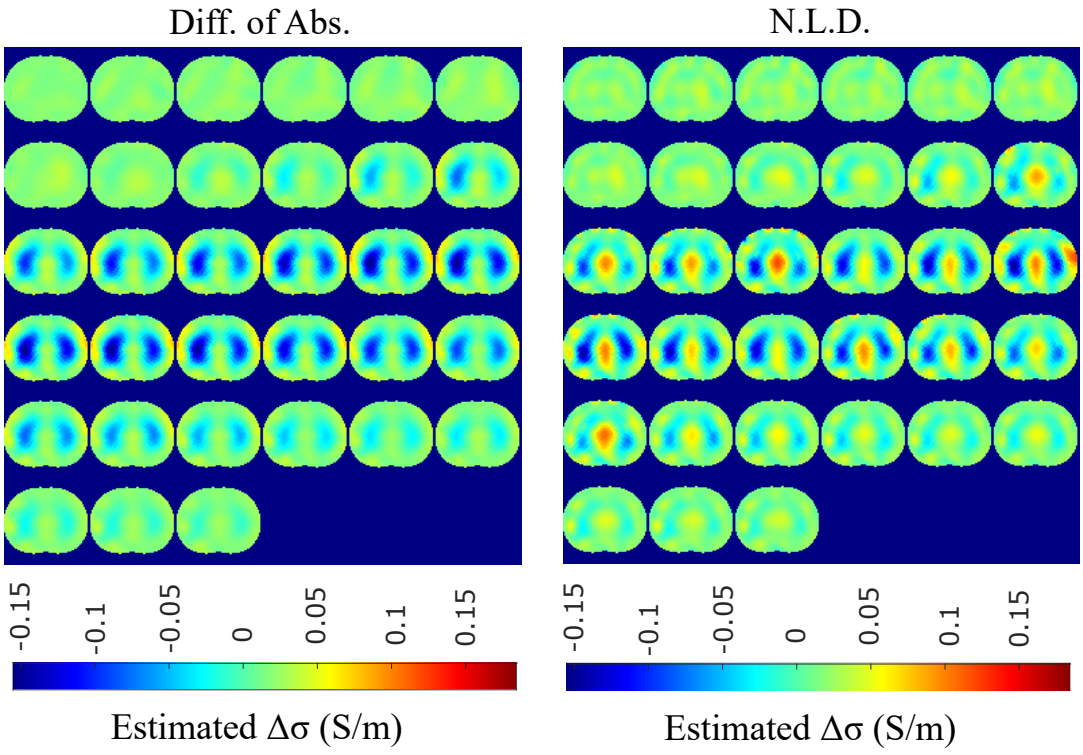

Figure 4.17: Single–breath in vivo results using the difference of absolute images and multiple priors non-linear difference imaging approaches.

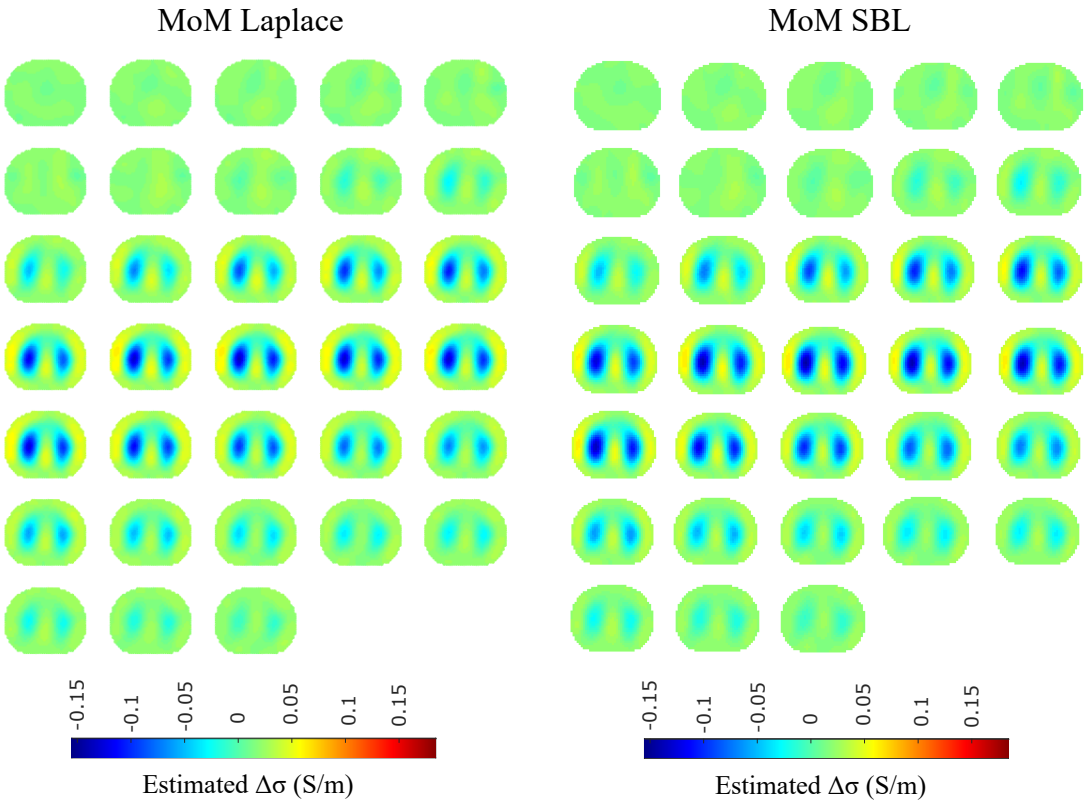

Figure 4.18: Single–breath in vivo results using the PM-MoM with Laplace regularization prior and the PM-MoM SBL approaches.

4.5.3 Discussion

In this work, a proposed EIT reconstruction method, which combines PM-MoM for the system matrix formulation and SBL for the inverse problem solution, is applied to dynamic thoracic imaging. A number of evaluation criteria is adopted, and an extensive comparison is performed with numerous state-of-the art approaches. Qualitative and quantitative studies have been performed on 3D time-variant non-homogeneous thoracic models. In vivo imaging of a patient's full-breath cycle has also been applied.

The qualitative results both in the simulation (Figures 4.9, 4.11 and 4.13) and the in vivo studies (Figures 4.15–4.18) reveal that, overall, the proposed PM-MoM SBL approach shows a better spatial resolution than both the traditional and some more advanced linear and non-linear EIT reconstruction methods, as well as the regularized PM-MoM method. This is confirmed quantitatively in Figures 4.10, 4.12 and 4.14 for the simulated cases. In all three subject-cases, the PM-MoM SBL outperforms the other approaches in most of the FoMs.

It is worthwhile to mention that, of the other approaches, the regularized PM-MoM appears to be the most efficient. In addition, the more recently proposed movement prior, difference of absolute images and multiple priors N.L.D. apaproaches appear to outperform the traditional GN and TV methods.

Considering the time needed for the reconstructions, the best performance (about 50 ms per frame) is achieved by the regularized PM-MoM when using the Laplace L^2-norm prior with a single step. The

movement prior linear approach needs about the same amount of time per reconstruction, while the non-linear GN and TV methods need significantly more time (about 4 to 6 seconds, depending on the number of iterations needed). Due to the relatively high complexity of SBL ($\mathcal{O}(N^2m^2gh)$ per iteration), the PM-MoM SBL approach needs, on average, 5.6 s per image frame reconstruction, when $h = 4$, $N = 16$, $m = 13$, $g = 1055$ and the number of iterations is 5. However, despite the time needed for PM-MoM SBL, the hyperparameter selection process, which is usually time-consuming, is avoided, contrary to the regularization approaches. Finally, the difference of absolute images as well as the multiple priors N.L.D. approaches require significantly longer times to reconstruct the images. The times mentioned above have been achieved using an AMD Ryzen 5 3600 system.

In conclusion, the PM-MoM SBL approach outperforms the regularized MoM one regarding the images' quality and spatial resolution. Additionally, there is no need for hyperparameter selection, which partially reduces the SBL process complexity effect on execution time. The PM-MoM SBL can be directly applied either for offline imaging (after collecting the measurements) or online on particular breath states where the lung conductivity change is significant. Another choice for faster online imaging is to reduce either the maximum number of iterations κ_{max} or tolerance ϵ_{min} (see Algorithm 1). It is worthwhile to mention that further research on optimizing the SBL approaches' complexity, as well as evolution in hardware, might improve the total time needed per image reconstruction.

5 Hardware Design Methodology for Electrical Impedance Tomography and Its Applications

EIT is an imaging technique which in the mathematical point of view faces an ill-conditioned inverse problem. This means that image reconstruction is sensitive to any signal noise or distortion. Therefore, it is obvious that a properly functioning hardware setup, characterized by appropriate specifications is essential for a successful EIT imaging. However, the design and implementation of such a system is not a simple process; many requirements and trade-offs presented make this process challenging. In fact, the specific requirements of an EIT system are depended on the application targeted to. For instance, lung air-flow related impedance change monitoring, or the imaging of cardiac blood-cycle related impedance variations require high frame rate time-difference EIT systems, while the detection of malignant tissues requires wide-band, high-SNR frequency-difference EIT setups. This chapter reviews EIT hardware design methodologies, implemented generic and application targeted EIT systems.

5.1 Basic EIT Hardware Principle

In EIT an alternating current is injected in a SUT through an electrode array, while electrode voltages are measured at the same time. The measurements are usually performed in a tetrapolar way, while the current inject and voltage measurement channel sequence depends on the measurement pattern adopted (see 2.1.2, [26] and [27]). From the above, it is obvious that the fundamental parts of an EIT hardware setup include the current source, one or more voltage amplifiers, a multiplexing system for channel/electrode selection and a digital control unit. Specifically, the current source usually produces one or more sinusoidal signals; which frequency and amplitude are digitally controlled from a direct digital synthesizer (DDS). The DDS in a simple consideration includes a phase accumulator [199] and a digital-to-analog converter (DAC). The analog multiplexing system is also digitally controlled, and each time, at least two electrode pairs are selected: one for the current sourcing and sinking and one for the differential voltage measurement. The voltage recording circuitry overall includes one or more instrumentation amplifiers and buffers, a programmable gain amplifier (PGA) and some usually wide-band filters. For a proper EIT reconstruction, the voltage data should contain information about both the channels potentials' amplitudes and phases. The in-phase (I) and quadrature (Q) voltage output components are obtained through

$I - Q$ demodulation and a matched low pass filter. This part can be either implemented in the analog or in the digital domain. In all cases, an analog-to-digital converter samples the output voltages either non-demodulated or demodulated and the raw sampled data is processed in the digital domain. The final data is sent to a PC processor for the image reconstruction process. A brief block diagram of a typical EIT system, with the demodulation process performed in the analog and the digital domain respectively is shown in Fig. 5.1. It is noted that many changes in the stages' structure are observed between different EIT implementations and applications.

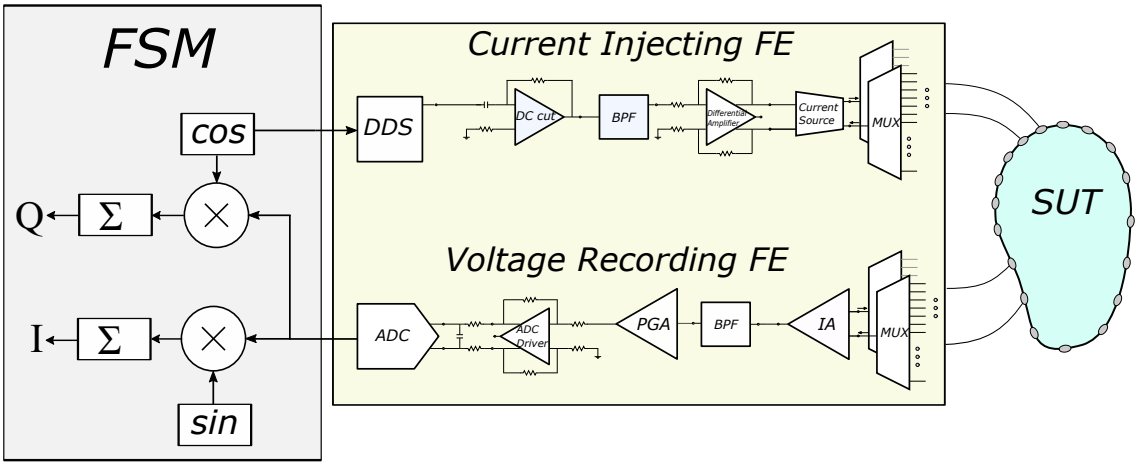

(α′)

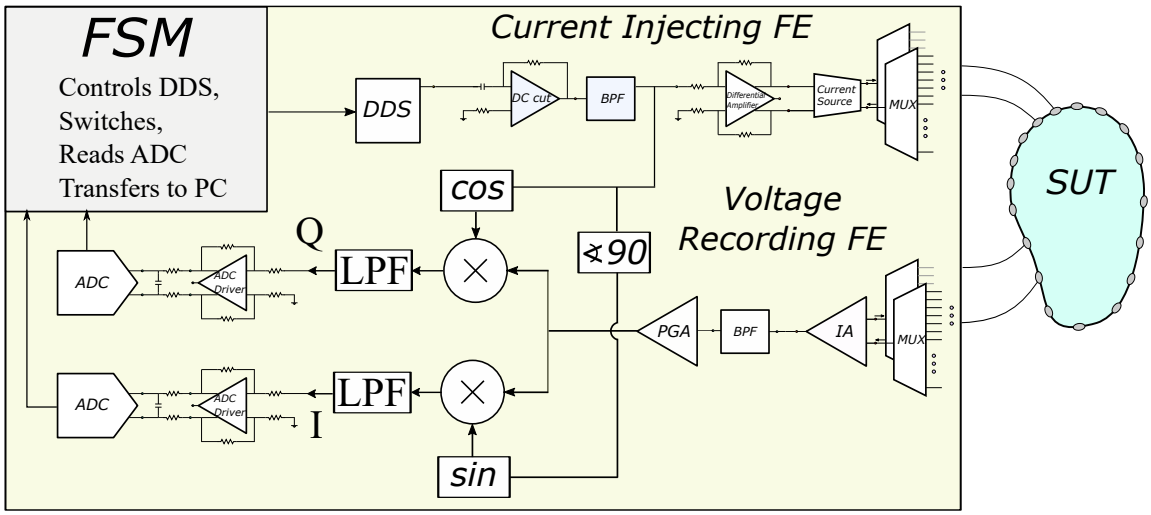

(β′)

Figure 5.1: Typical EIT hardware setups with: a) digital demodulation b) analog demodulation

5.2 Current Source

The current source is a fundamental EIT system circuitry part, since it implies an appropriate alternating current to the electrodes in order to perform tetrapolar measurements. This current should satisfy three conditions: A) to be safe for the patient (in case of medical applications), B) to carry as low noise as possible and C) not to suffer from distortion, e.g. due to common signal effects. The necessity for fulfillment of such constraints induces that the design and implementation of a properly functioning current source is not a strain-forward process.

5.2.1 General Properties

As mentioned above, first of all, the alternating current amplitude should be safe for the patients. The maximum current amplitude permitted, according to the IEC 60601-1 standards, depends on the selected frequency and is defined as follows [200]:

$$I_{max}(A_{rms}) = \left\{ \begin{array}{ll} 100\mu & f < 1kHz \\ \frac{100f \cdot 10^{-6}}{1kHz} & 1kHz \leq f \leq 100kHz \\ 10m & f \geq 100kHz \end{array} \right\} \tag{5.1}$$

The presence of noise in a current source is unavoidable, since all the possible topologies used consist of active and resistive components, causing flicker and thermal noise respectively. Very little particular analysis on current drivers' noise exists (i.e. [201], [202]), since the produced noise, along with the biological sources' noise, is considered as an input one in the voltage acquisition chain analysis part [169],[170] and can properly be filtered.

However, any signal distortion caused by other sources is crucial in this part, since it cannot be fully compensated in the voltage recording circuit. The common mode voltage is a fundamental source of signal distortion which needs to be minimized in the current source stage. To this end, EIT systems' current drivers have to be characterized by fully differential outputs. In this case, common-mode voltage tends to be rejected during voltage measurements [200], [203]. Indeed, the common-mode voltage presents significantly higher amplitudes when single-ended output current drivers are employed.

However, it is difficult to compensate any mismatches between the source and sink output of of a fully-differential current driver. These mismatches also cause significant common voltages, proportional to the current mismatch and the current source's output impedance. A visual demonstration of such effect is shown i Fig. 5.2. We assume that a ΔI current mismatch between the source and the sink is present. The current ΔI flows to the ground through the current source's output impedance (Z_{o1} and Z_{o2}) and through the instrumentation amplifier's input impedance or the multiplexers' stray capacitances (Z_{c1} and Z_{c2}). Note that Z_{L1}, Z_{L2}, Z_{L3} denote the load impedances for the tetrapolar measurement and Z_{e1}, Z_{e2}, Z_{e3} and Z_{e4} denote the electrodes' contact impedances. The current ΔI results at a common signal between the instrumentation amplifiers' inputs which is not totally rejected, especially at higher frequencies, causing signal distortion. It the simple case of a bipolar measurement the common signal generated is $V_{cm} = \Delta I r_o/2$.

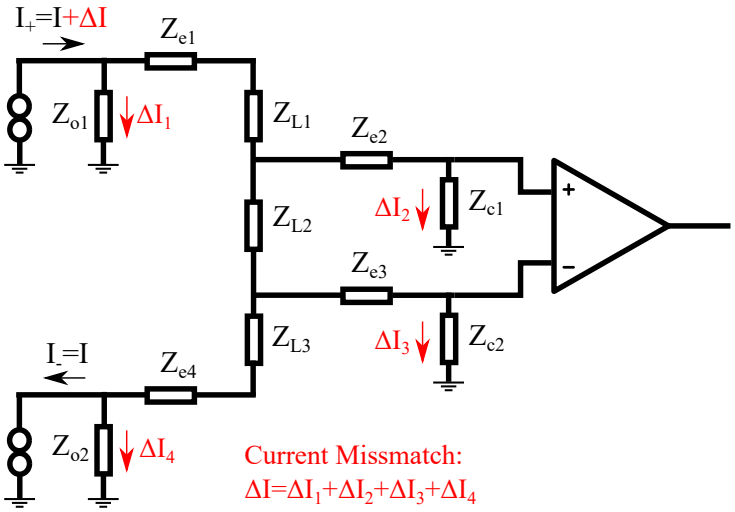

Figure 5.2: Tetrapolar measurement principle and current mismatch effect.

In some custom bioimpedance current driver designs, ultra low tolerance resistors (see Howland current pumps below) and a passive ground electrode on the object's surface are used in the setup to reduce the common signal effects. However, a more systematic solution is to employ a common mode feedback circuit. This can actually be applied as a slave circuit at the sink part of the current driver. Some implementation examples presented in recent literature are described in the next subsection.

5.2.2 Current Source Implementations

The current sources applied in EIT systems can be categorized as voltage-mode and current-mode ones [204]. The voltage-mode approach is characterized by the current generation through the voltage in one or more of the active circuit's nodes. Such topologies include the well-known Howland current pump (HCP) [204, 205, 206, 207, 208, 209], the Tietze topology [210], the load-in-the-loop topology [211], and differential-difference topologies [212, 213, 214]. Current-mode approach makes use of operational transconductance amplifiers (OTAs) [20, 200, 215, 216] or current conveyors (CCII) [205, 217, 218] for the current excitation. In all cases, the load driven by the output current can be either grounded or floating.

The implementation of HCPs is usually simple and can be done with commercially available active components (operational amplifiers-Opamps), while the implementation of differential-difference and current-mode topologies necessitates transistor-level fabrication. Thus, although the latter topologies may offer better performance in terms of the main VCCS evaluation characteristics (large and stable transconductance, large output impedance, large bandwidth, and low Total Harmonic Distortion-THD), the availability of discrete active components, makes the HCPs preferable for the implementation of prototype bioimpedance measurement circuits [204].

The basic HCP topology was introduced in 1963 [212]. However, many improvements have been proposed and applied since then. Most of them present topologies based on the Enhanced HCP [219], with ground or floating loads and single-ended or mirrored topologies [205, 208, 220, 221] (see Figure 5.3).

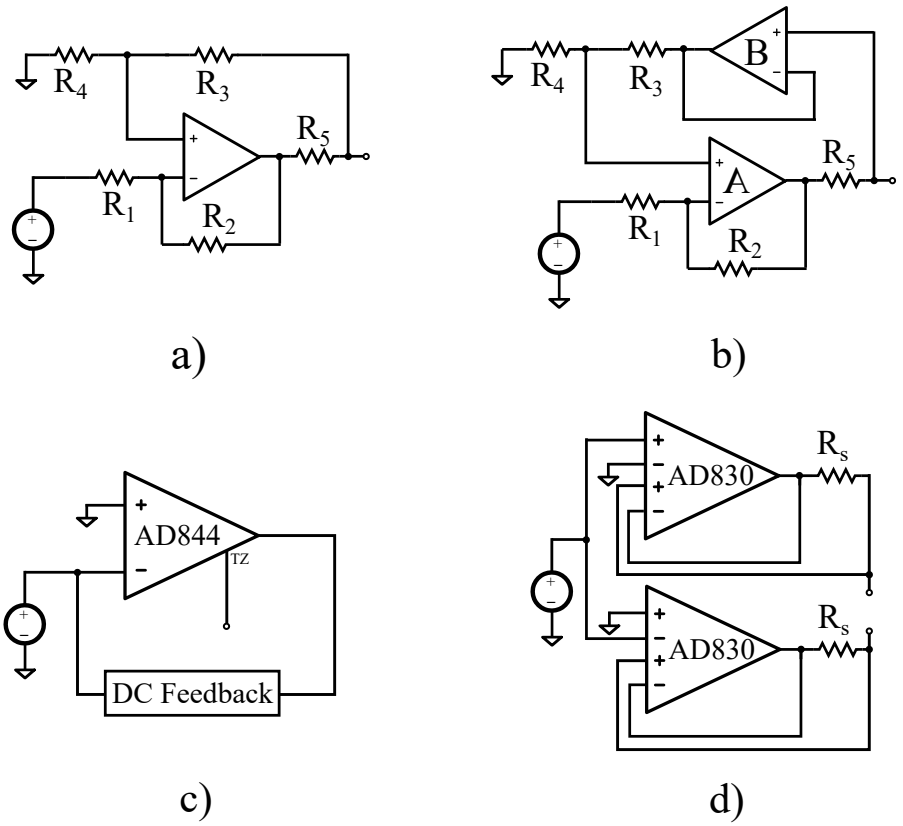

Figure 5.3: Discrete component current source configurations. (**a**) The Enhanced HCP (single-ended). (**b**) The modified buffered HCP (single-ended). (**c**) Current Conveyor based on the AD844 (Bragos CCII). (**d**) Current Source based on the AD830 differential difference-amplifier (Analog Devices, mirrored).

Further improvements, such as buffered positive feedback [222], as in Figure 5.3, lead-lag compensation [223, 224, 225], HCP followed by load-in-the-loop topology stage [224], and bridge topologies [226].

The HCP's bandwidth often suffers from degradation at even medium frequencies due to the components' and cables' parasitic effects. Specifically, despite the fact that most of the proposed topologies offer wide-band current excitation, in practice, their performance is critically limited by the parasitic capacitances of the electrodes' lead wires. Some techniques have been applied to eliminate their effect. These include the usage of triaxial or shielded cables with buffers [227, 228], the usage of negative impedance circuits (usually implemented with generalized impedance converters-GICs) [156, 228, 229], or the usage of active electrodes, where either the VCCS, the 1st stage of the voltage readout, or both, are implemented very close to the electrode [20, 21, 171, 228, 230]. The first solution is expensive, especially for multi-channel systems, and does not compensate for the buffers' input capacitances [228]. The second one cancels the VCCS' output capacitances; however, it might lead to instability due to overcompensation [228]. The active electrode has the advantage of avoiding the cables' and multiplexers' (in multi-channel systems) stray capacitances. The use of active electrodes apart from the VCCS' actual bandwidth, also improves the performance of the voltage readout part, since possible channel impedance imbalances before the 1st readout stage are critically decreased [230]. However, this technique is expen-

sive, since it requires numerous power-consuming active components placed in a small area near each electrode [228].

The mentioned active electrode's drawbacks still make their design process somewhat challenging, despite their potential advantages. Actually, only partially-active electrode configurations have been implemented for multi-channel bioimpedance measurement systems (such as EIT) that exclusively use commercially available active components [171, 230]. The partially-active electrode systems implement only the voltage readout stage near each electrode, while the VCCS is implemented on the system's core. This leads to the development of stray capacitances on the VCCS output, due to the cables and the multiplexer switches, drastically reducing the actual advantages of the active electrodes. Fully-active electrodes, which include both the VCCS and the 1st voltage readout stage, have actually been designed and implemented at integrated chip level [20, 21, 231]. However, they require transistor level application-specific integrated circuit (ASIC) fabrication, making them costly and their applicability still limited. For the passive, partially-active, and fully-active electrode measurement configuration schematics, see Figure 5.4.

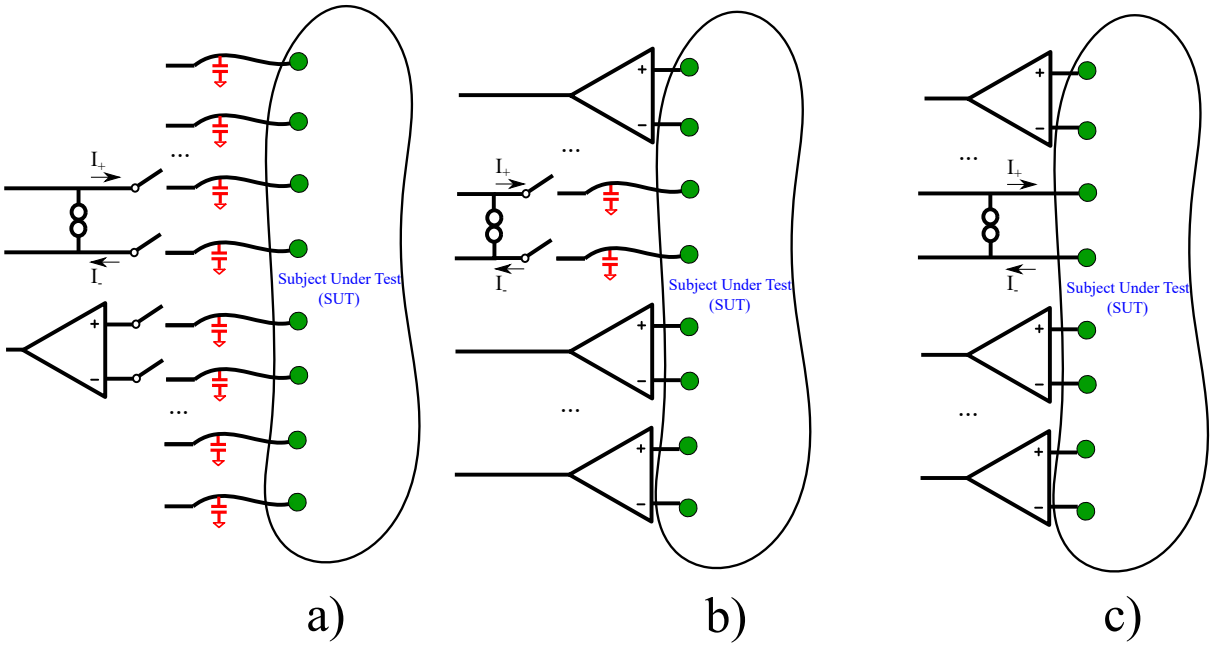

Figure 5.4: Simplified schematics of three bioimpedance measurement configurations. (**a**) Passive electrode configuration. (**b**) Partially-active electrode configuration. (**c**) Fully-active electrode configuration (this work). The cables'/ switches' parasitic capacitances are indicated with red color.

An extensive review of fabricated CMOS level integrated OTA-based current sources for EIT, EIS and other relevant biomedical applications is written in [232]. The fully differential current driver, shown in Fig. 5.5 and presented in [233], employed four current sources in an H-bridge configuration. The output impedance is approximated by: $Z_o = g_{mo}r_{o0}r_{o1}(A_7 + 1)g_{m9}r_{o10}(A_3 + 1)$ where g_{mi} is the transconductance and roi is the drain to source resistance of the i^{th} transistor (see Fig. 5.5). Simulations yield a high output impedance of approximately 10.2 $M\Omega$ at 1 MHz and a THD of 1% at 10 MHz for

an output current of 107 µAp-p [233]. The system operates in open loop configuration, and the output current accuracy is directly affected by internal parameters of the system.

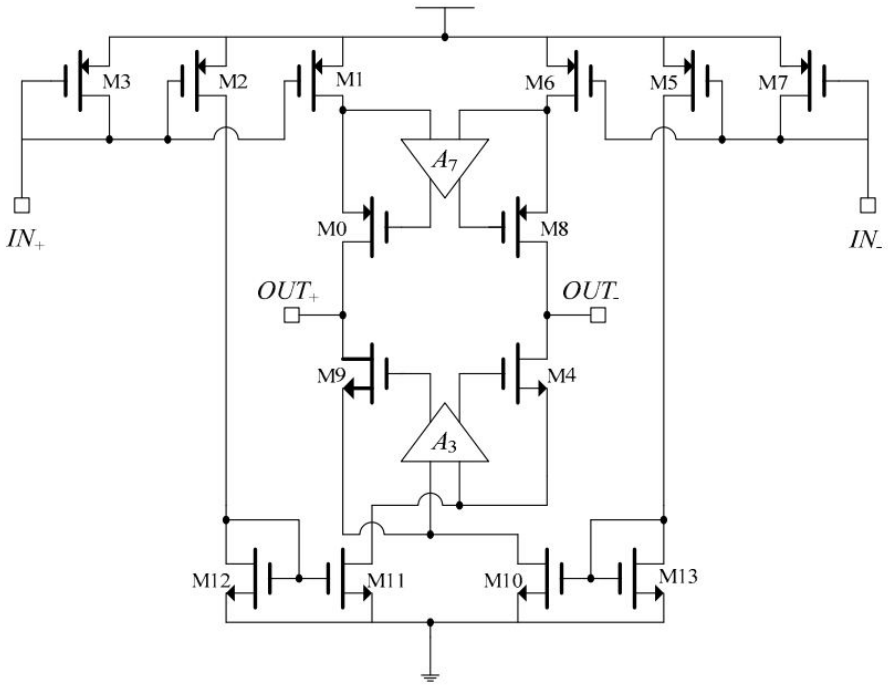

Figure 5.5: Integrated current driver in H-bridge configuration [233].

The current driver in Fig. 5.6 is composed of two fully differential amplifiers (FDA1 and FDA2) with an RC frequency selective network that produces an input sinusoidal voltage, followed by a VCCS, formed by transistors M3 and M4 and resistor R_1 [234]. The FDA is a two-stage folded cascode with source followers at the output stage in order to achieve low output impedance to effectively drive the frequency selective RC bridge network [234]. The RC frequency selective network generated a 90 kHz balanced sinusoidal voltage signal V_{SW^+} and V_{SW^-}. The 2 bit-DAC output adjusts the gate voltages of transistors M3 and M4 that results in variable sinusoidal voltage of $0.22 - 0.78\ V_{p-p}$. The output current is defined as:

$$I_{out} = I^+ - I^- = \frac{V_{SW^+} - V_{SW^-}}{R_1} \tag{5.2}$$

and the output impedance as:

$$Z_o = \frac{1}{gm_3} + \frac{1}{gm_4} + R_1 \tag{5.3}$$

where gm_i is the i^{th} transistor's transconductance.

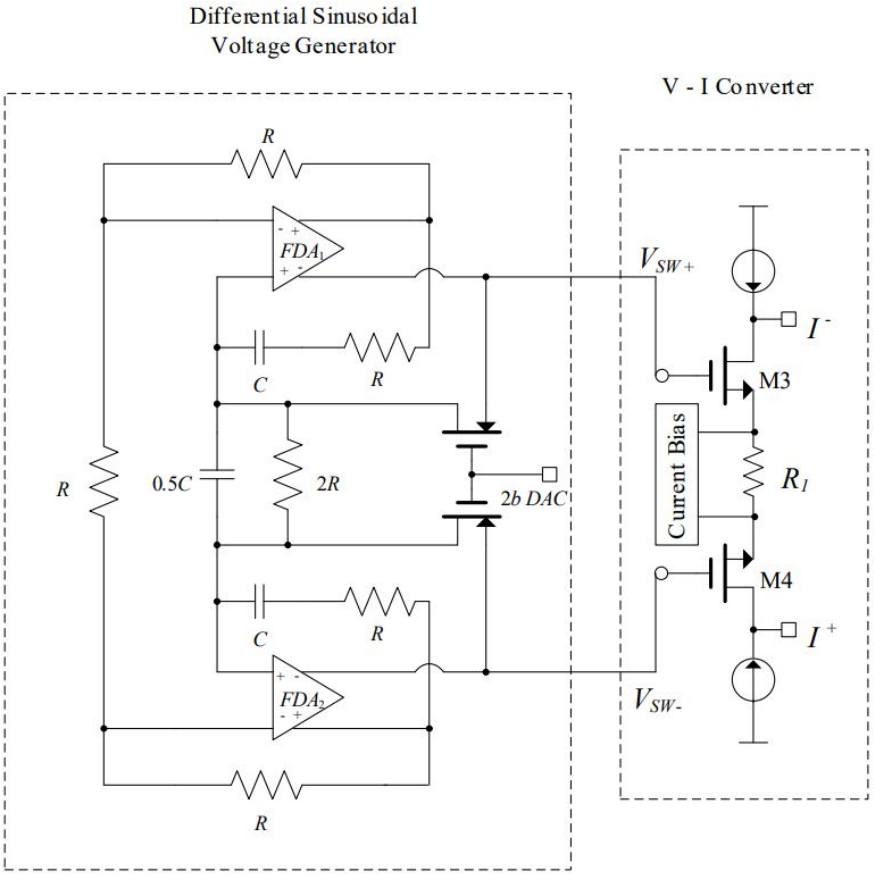

Figure 5.6: Current driver [234].

Other open-loop current driver topologies can be found in [235], [236] and [206].

A number of closed-loop current source implementations have also been presented in the recent literature. In [237], an OTA-based linear feedback current driver topology was presented (Fig. 5.7).

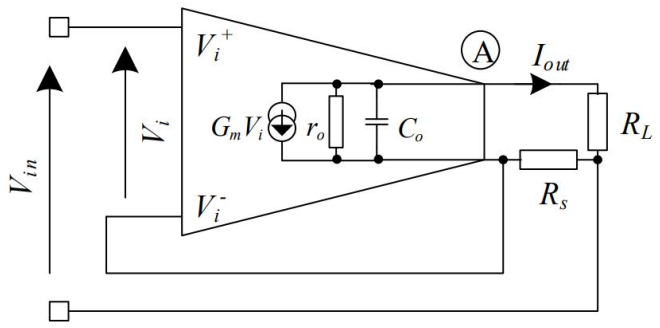

Figure 5.7: Basic linear feedback current driver [237].

Its output current is estimated as follows:

$$I_{out} = \frac{V_{in}}{R_s} \frac{1}{1 + \frac{1}{G_m R_s}\left(1 + \frac{R_s + R_L}{r_o}\right)} \tag{5.4}$$

with the variables as denoted in Fig. 5.7. Correspondingly, the output impedance is given by the following expression:

$$Z_o = r_o + (G_m r_o + 1) R_s \tag{5.5}$$

Although the negative feedback offers a wide frequency bandwidth to the current driver, the circuit suffers of common-mode voltages occurred from the voltage imbalance on the load (see 5.2.1). Furthermore, floating input voltages need to be acted in this circuit, something which isolates the load from any direct path to instrument ground [232]. The overall transconductance of the OTA is given by: $G_m = G_{m1} ro1 Gm2$.

A two cascaded OTAs topology is also implemented in [237] (Fig. 5.8).

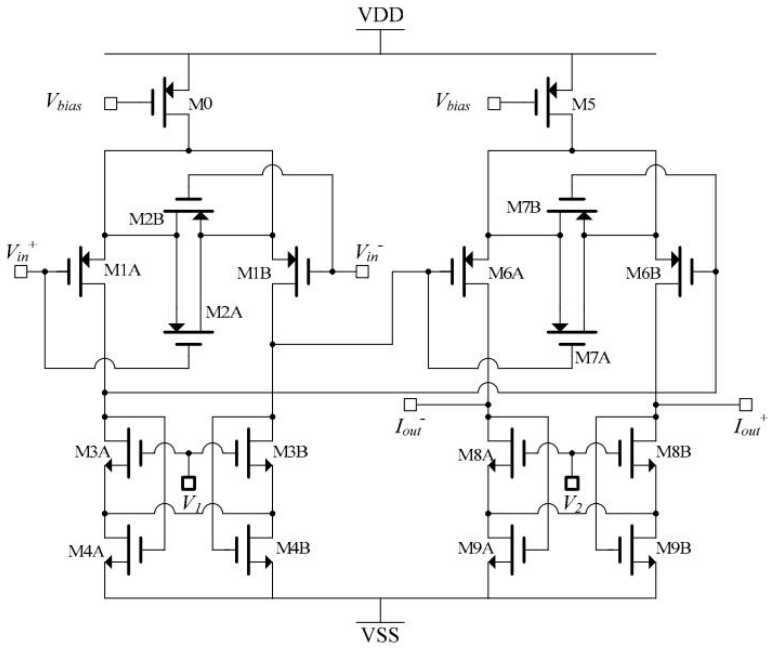

Figure 5.8: A two cascaded OTAs current driver [237].

To overcome the drawbacks of the topologies in [237], a high power current driver was presented in [213]. It employs two identical differential feedback current drivers, operating in a balanced mode, in order to eliminate common mode voltage errors across the load impedance. Furthermore, two voltage buffers are utilized to isolate the load from the input signal, dealing with the floating input drawback [232]. However, stability issues offer occur when using this topology.

Based on the [213] topology, a ± 2.5 V supply voltage current driver, employing a pre-amplification stage by utilizing a differential difference transconductance amplifier (DDTA) before the tranconductance

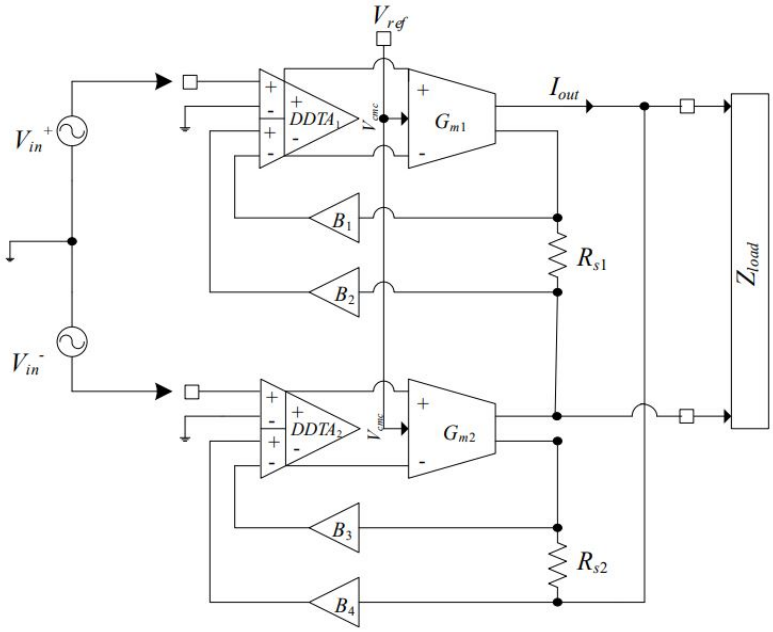

Figure 5.9: Current driver topology implemented in [214].

stage in a mirrored topology, was implemented in [214]. The system-level architecture of the current driver is depicted in Fig. 5.9.

The proposed current driver in [20] and [203] is inspired from [214] and is embedded in a real-time lung monitoring EIT system, implemented in [20]. The output impedance is kept above 614 kΩ at frequencies up to 1 MHz, while the transconductance is given by the following formula:

$$G_m = \frac{A_{loop}}{R_f + R_L + A_{loop} R_f} \tag{5.6}$$

which is almost proportional to $1/R_f$. With R_f is denoted the sense resistor, A_{loop} the total current driver open-loop gain and R_L the load resistance. The output impedance is estimated as follows:

$$Z_o = r_{o,OTA} + R_f[A_{DDTA} G_{m,OTA} r_{o,OTA} + 1] \tag{5.7}$$

where $r_{o,OTA}$ is the output impedance Iout and A_{DDTA} is the open loop gain of the DDTA. The circuit architecture of the DDTA and the OTA are shown in Fig. 5.10.

The current driver implemented in [216] and used in [238] includes a build-in common signal reduction module (Fig. 5.11). It operates at ± 1.65 V. The master circuitry parts includes a DDTA followed by an OTA to achieve a stable transconductance. The slave part consists of a slave voltage receiver (DVR) to provide common-mode feedback.

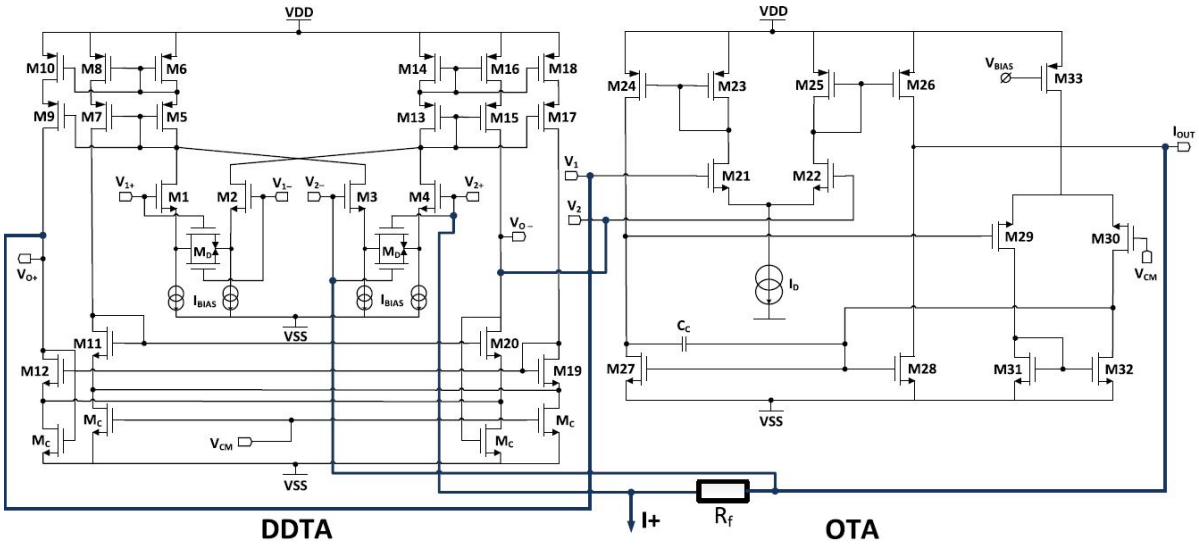

Figure 5.10: Current driver topology implemented in [20].

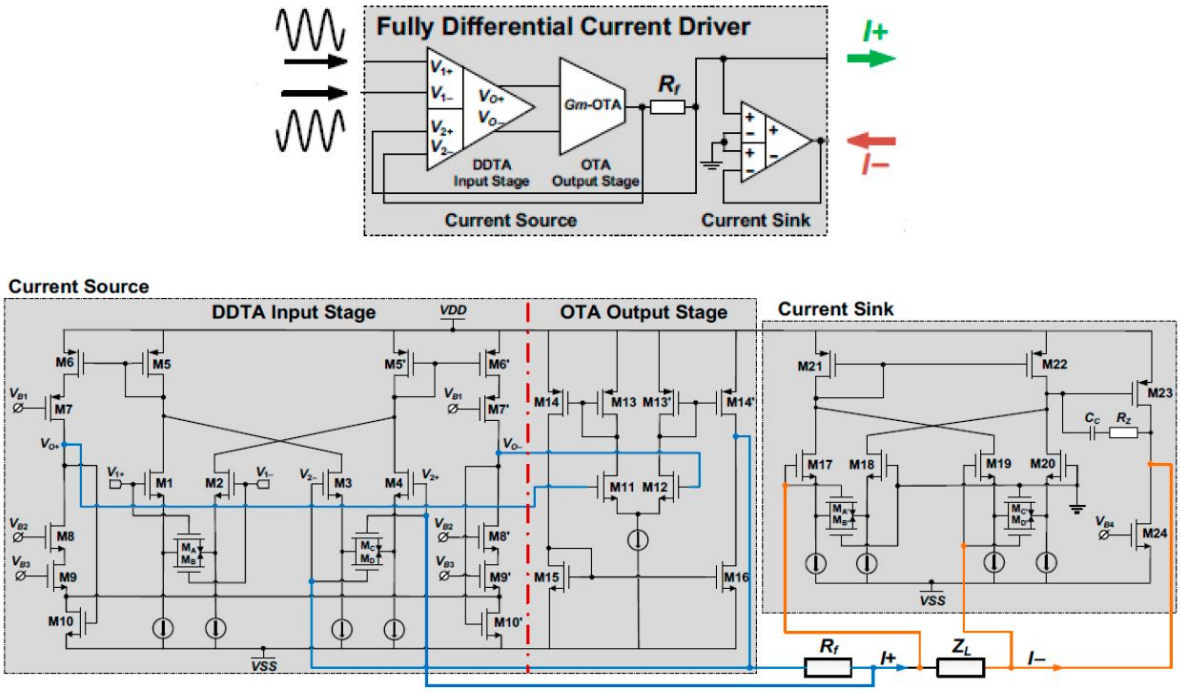

Figure 5.11: Current driver topology implemented in [238].

A CCII-based current driver, employing a DC-servo loop for the common mode feedback, as well as a gain enhanced cascode structure to maintain sufficiently high output impedance is presented in[158]. It can produce sinusoidal currents from 500Hz to 1MHz and of amplitude up to $1mA_{p-p}$. A DDS produces the sinusoidal input signal V_Y, buffered to V_X, an a current $I_X = R_X \cdot V_X$ is generated (see Fig. 5.12). The CCII mirrors this current to the output, $I_Z = I_X$, driving it through a DC-blocking capacitor, C_{block}

(which blocks DC currents to the patient) into the SUT. The output current exhibits a THD of 0.15% for a 1MHz, $1mA_{p-p}$ output. The servo loop maintains an appropriate DC bias voltage at the current driver's output. It includes an OTA, which holds the output node fixed at V_{CM}. Finally, the current driver has a gain-boosted cascode output stage, providing an output impedance of $100k\Omega$ at 1 MHz.

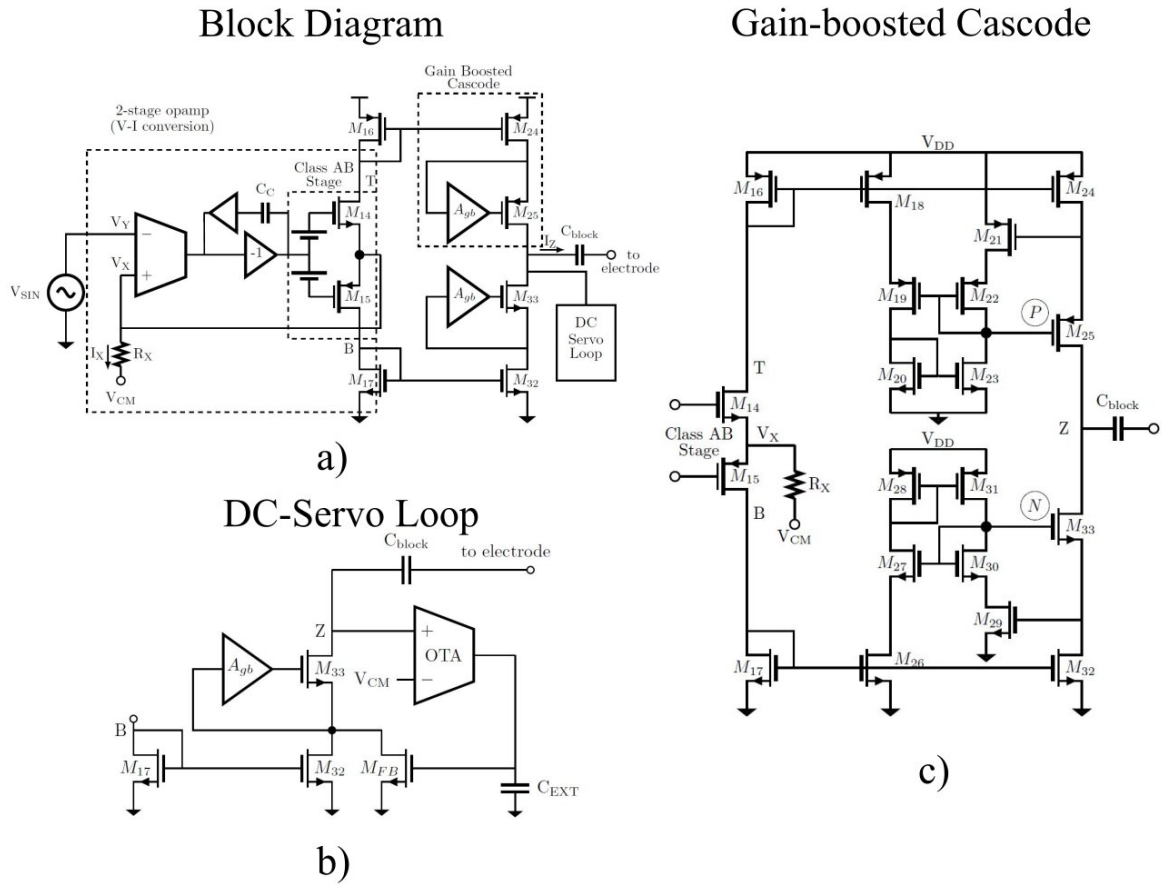

Figure 5.12: Current driver topology implemented in [158]. a) General block-diagram. b) DC servo-loop architecture. c) Output enhanced-gain cascode stage.

Finally, a closed loop non-linear feedback integrated current driver has been implemented in [239] and [240]. It operates at ± 2.5 V, while the system's dominant pole is not affecting its high frequency operation at a cost of longer transient response, due to the low frequency dominant pole of the lowpass filters (see Fig. 5.13).

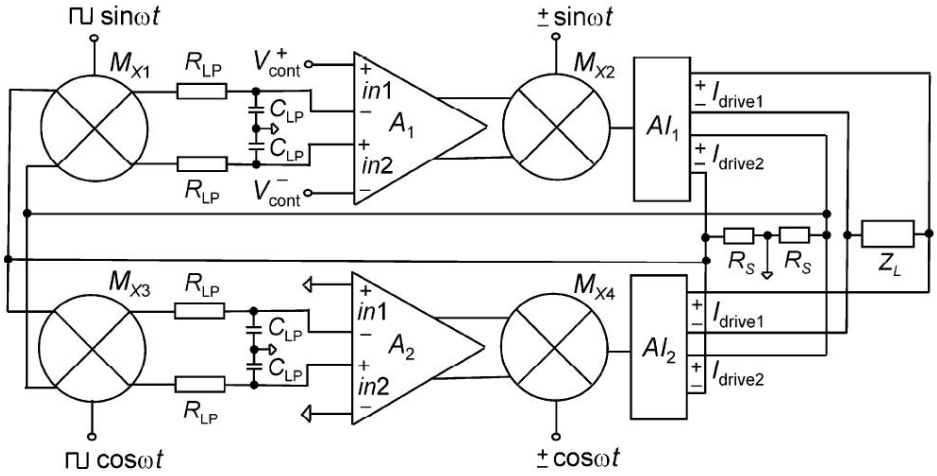

Figure 5.13: Current driver topology implemented in [240].

5.3 Voltage Readout Chain

The voltage recording circuit has the role of measuring the differential voltages on the system's non-current electrodes. Such measurements need to be performed continuously, at all the appropriate voltage measurement channels, according to the measurement pattern selected. The channel voltage acquisition can be performed either in serial or parallel way. In each case, voltage signals collected need to be properly amplified, denoised and driven into an Analog-to-Digital converter (ADC).

5.3.1 General Properties

The voltage readout circuit typically includes an instrumentation amplifier (IA), a programmable gain amplifier (PGA) and an ADC driver. In many cases, one or more buffers and/or band-pass filters may be included. The instrumentation amplifier ideally outputs the difference of the voltages between two selected electrode channels. Since common signal exist due to current source and the channel impedance mismatches, the IA needs to be characterized by a sufficiently high common mode rejection ratio ($CMRR$), to prevent its amplification. The $CMRR$ value is high enough at lower frequencies, however it gradually degrades when frequency increases. This degradation is related with the reduction of the IA input impedance due to stray input capacitance. Hence, the common signal effect may become intense at medium or high frequencies.

Another consideration is the signal noise propagation through the voltage readout chain. The electrode voltage signal includes noise becoming from the injected current and the biological tissues/ subject under test, interference with biological signals, e.t.c. This noise is amplified along with the original signal through the amplification stages, while flicker noise from the active components also contributes to a noisier output signal. The sampling process from the ADC also adds thermal and quantization noise to the signal, further increasing the de-noise filters' requirements.

Two recent general studies for the optimization of SNR in EIT system voltage recording parts have

been presented in the literature. In [169], a mathematical point analysis was conducted to extract an analytic noise model and two approximated noise models: the Continuous Uniform (CU) and the Discrete Uniform (DU). The pure analytical model results in the following expressions for the SNR of the signal amplitude and phase respectively:

$$SNR_A = 10log_{10}\left(A^2\right) - 10log_{10}\left[var\left(V_I\right)\cos^2\phi + var\left(V_Q\right)\sin^2\phi + 2\text{Cov}\left(V_I V_Q\right)\cos\phi\sin\phi\right] \tag{5.8}$$

and

$$SNR_\phi = 10log_{10}\left(A^2\phi^2\right) - 10log_{10}\left[var\left(V_I\right)\cos^2\phi + var\left(V_Q\right)\sin^2\phi - 2\text{Cov}\left(V_I V_Q\right)\cos\phi\sin\phi\right] \tag{5.9}$$

where A denotes the signal amplitude, ϕ the signal's phase in respect to the input current signal, while V_I and V_Q are the demodulated in-phase and quadrature components extracted from a digital matched filter (see 5.3.2). The DU model is described by the following corresponding expressions:

$$SNR_A = 10\log_{10}\left[\frac{A^2\frac{N}{2}}{var\left(d_n^{DU}\right)}\right] \tag{5.10}$$

and

$$SNR_\phi = 10\log_{10}\left[\frac{A^2\frac{N}{2}\phi^2}{var\left(d_n^{DU}\right)}\right] \tag{5.11}$$

where N is the number of matched filter taps per measurement channel. Assuming that the quantization error is described by a random variable with a uniform distribution between -0.5 of the ADC least significant bit voltage range (LSB) and 0.5 LSB, we get:

$$P(d_n^{DU} = mLSB) = \frac{1}{LSB}\int_{-\frac{LSB}{2}}^{+\frac{LSB}{2}} \frac{1}{\sigma_n\sqrt{2\pi}} \int_{\left(m-\frac{1}{2}\right)LSB}^{\left(m+\frac{1}{2}\right)LSB} e^{\frac{-(x-z)^2}{2\sigma_n^2}} dxdz \tag{5.12}$$

where m is an integer,, x is associated with the Gaussian noise u from the analog circuitry that has a std of σ_n^2, and z is associated with the quantization error q [169]. The CU model implies that:

$$var\left(d_n^{CU}\right) = \frac{LSB^2}{12} + \sigma_n^2 \tag{5.13}$$

where

$$LSB = \frac{V_F}{2^b}, \tag{5.14}$$

V_F is the ADC dynamic voltage range and b the ADC resolution in bits.

In [170] a structured methodology to maximize the SNR of an EIT system is analyzed. It is based on the DU model to consider an approach for designing the individual circuit components that meet performance requirements while minimizing power consumption. It also considers the analog matched

filter case, where the amplitude and phase SNR is given by:

$$SNR_A = 10\log_{10}\left[\frac{A^2}{\frac{LSB^2}{12} + 2\sigma_n^2 \cdot \frac{N \cdot BW_F}{BW_n}}\right] \tag{5.15}$$

και

$$SNR_\phi = 10\log_{10}\left[\frac{A^2\phi^2}{\frac{LSB^2}{12} + 2\sigma_n^2 \cdot \frac{N \cdot BW_F}{BW_n}}\right] \tag{5.16}$$

where BW_n is the equivalent noise bandwidth caused by the chain amplifiers' filtering effect and BW_F the analog filter's noise bandwidth. [170] extracts the maximum tolerable Gaussian noise σ_n values regarding the V_F, N, the SNR, and the ADC resolution. Based on this analysis it reveals the minimum ADC resolution and number of filter taps N required.

5.3.2 Impedance Demodulation

The demodulation process is such an important part of the EIT signal acquisition, because not only calculates the signal phase but also filters and synchronizes the signal with the current input. As mentioned above, the most common demodulation is the in-phase/quadrature (IQ demodulation), where the output voltage signal is multiplied with the input signal and its $90-degree$ phase shifted signal. For this purpose, two multipliers and a matched low-pass filter are used. The IQ-demodulation process can be performed either in the analog or the digital domain, as mentioned above. However, the analog approach requires costly high-precision components that make the design concept more challenging [169],[200]. Therefore, in most application designs, the digital matched filter approach is preferred.

For the IQ-demodulation we consider an input signal $V_{in}(t) = V_r \cos(2\pi ft)$ (which is transferred to current for the current stimulation) and an output signal $V_{out}(t) = V_m \cos(2\pi ft + \phi)$ (after the analog voltage recording chain). Then, the following multiplications are performed:

$$\begin{aligned} V_I(t) &= V_{in}(t) \cdot V_{out}(t) = V_r V_m \cos(2\pi ft) \cdot \cos(2\pi ft + \phi) \\ &= \frac{V_r V_m}{2} \cdot [\cos(\phi) + \cos(4\pi ft + \phi)] \end{aligned} \tag{5.17}$$

and

$$\begin{aligned} V_Q(t) &= V_{in}\left(t; \phi - \frac{\pi}{2}\right) \cdot V_{out}(t) = V_r V_m \sin(2\pi ft) \cdot \cos(2\pi ft + \phi) \\ &= \frac{V_r V_m}{2} \cdot [\sin(\phi) + \sin(4\pi ft + \phi)] \end{aligned} . \tag{5.18}$$

Performing low pass filtering we get the DC components of each expression (5.17) and (5.18):

$$I = \frac{V_r V_m}{2}\cos(\phi) \tag{5.19}$$

and

$$Q = \frac{V_r V_m}{2}\sin(\phi) \tag{5.20}$$

that correspond to the in-phase and quadrature components respectively.

Recent approaches recommend three alternative IQ-demodulation schemes [241], [242], [243] [244]. The first advanced demodulation approach considers a sinusoidal current excitation and a n-harmonic square demodulation [241], [242]. Multiplication of the output voltage with the in-phase square signal leads to a result which includes a number of n harmonics. The DC components are collected after acting a low-pass filter. This approach is preferred for CMOS implementations as the multiplier can be merged into the analog front-end in the form of chopper switches while the input signal is often generated using a DDS.

The second approach is to use square excitation and square chopper demodulation. The final dc value after low-pass filtering in the case of in-phase demodulation is expressed as:

$$I_{total} = \frac{8}{\pi^2}\Sigma_{n=1,3,5,...}^{\infty}\frac{A(2\pi n f_o)cos(\theta(2\pi n f_o))}{n^2} \tag{5.21}$$

where f_o is the fundamental frequency, $A(2\pi n f_o)$ is the n^{th} harmonic tissue impedance magnitude at f_o and $\theta(2\pi n f_o))$ is the n^{th} harmonic tissue impedance phase at f_o. Adopting the harmonic error cancellation approach described in [245], only the 1^{st} term is kept ($n = 1$).

The third approach is to induce a pseudo-sine current signal and perform square demodulation. Its performance depends on the number of quantization levels, i.e. the samples used in every pseudo-sine cycle. A pseudosine signal generated using DDS has harmonics in pairs and the frequencies of the harmonic pairs can be expressed as:

$$\omega_h(N \pm 1) = (QN \pm 1)\omega_o \qquad N \in \mathbb{N} \tag{5.22}$$

where ω_h is the harmonic cycle frequency, ω_o the fundamental one, Q the level of quantization and N the harmonic order. The fundamental frequency term's amplitude is given by:

$$C_o = \frac{1}{2}\left|sinc\left(\frac{\pi}{Q}\right)\right| \tag{5.23}$$

while the harmonic terms' amplitudes are given by [200],[246]:

$$C_{h(N\pm1)} = \frac{1}{2}\left|\frac{sinc\left(\frac{\pi}{QN}\right)}{QN \pm 1}\right|, \qquad N \in \mathbb{N} \tag{5.24}$$

Other demodulation techniques employ pulse-width demodulation [247] and time stamp demodulation [248].

5.4 Bioimpedance Measurement Circuits, EIT System Implementations and applications

The basic voltage acquisition circuit parts are mentioned in 5.1 and 5.3.1. However, many implementations have been performed, presenting a variety of modifications at the circuitry in order to maximize the system's performance, according to each specific applications' requirements. The subsection

performs a review of specific implementations presented in the literature, including designs with commercially available components and custom integrated circuit designs. Many of these implementations are part of generic or application targeted EIT systems, while some other can be generally applied for tetrapolar bioimpedance measurement.

The first EIT system hardware was presented in 1978 in [1]. An alternating voltage signal was induced in the electrodes while the output current was collected. The acquisition circuit consisted of a current-to-voltage converter and low pass-filter, two multiplexer arrays and an analog demodulator (see Fig. 5.14). A total number of 100 electrodes were used, as well as a number of 100 corresponding current-to-voltage amplifiers/low-pass filters. The first multiplexer array selects one of the 10 electrodes that will be driven to the corresponding demodulator. A total number of 10 demodulators were implemented (each one for 10 electrodes). Each time, one of the demodulators' outputs is selected from the second multiplexer to get a single output.

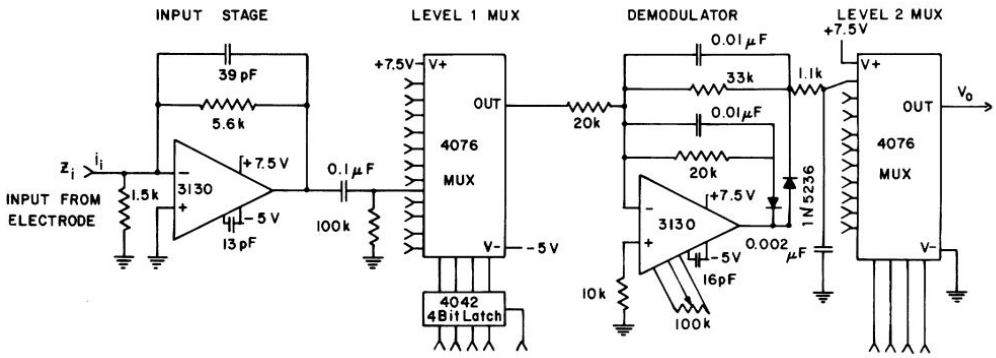

Figure 5.14: The first EIT system voltage acquisition circuit [1].

The Sheffield data collection system [27] (1987), shown in Fig. 5.15, introduced the conventional adjacent current and measurement pattern approach, used in many applications till today. The system induces an alternating current while it collects each electrode pair voltage through multiplexing. Before the multiplexer, one buffer per electrode is employed to reduce the channels' stray capacitances effects (Fig. 5.16).

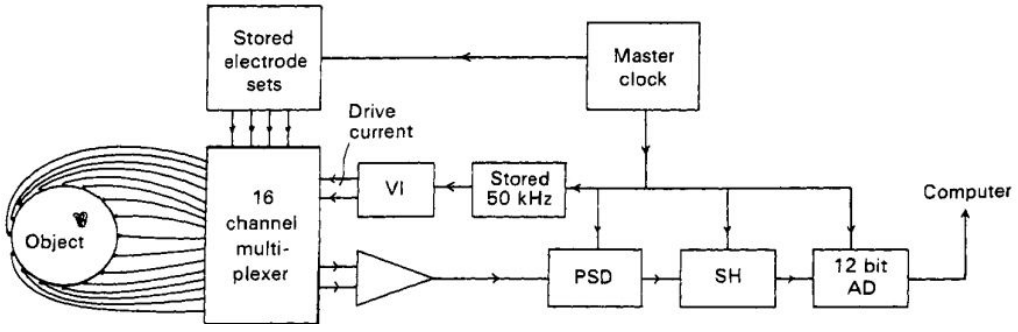

Figure 5.15: The Sheffield data collection system, brief diagram [27].

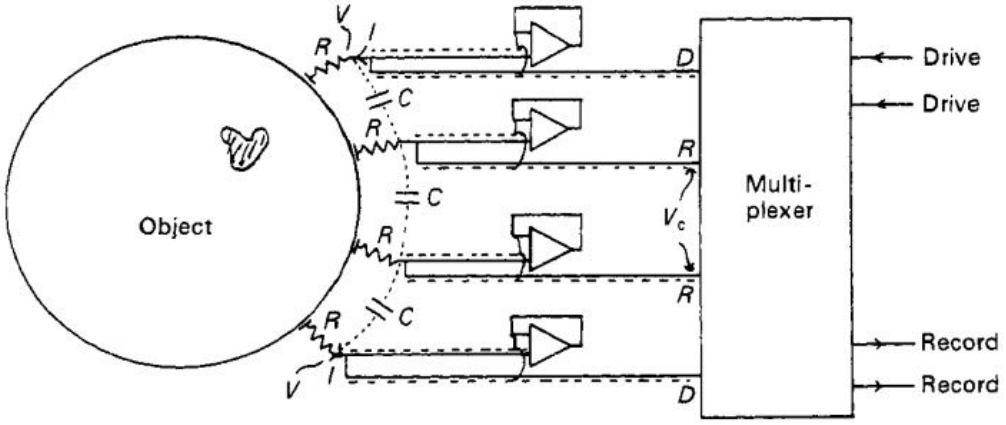

Figure 5.16: Diagram of the Sheffield data collection system circuitry feeding four electrodes [27].

The Sheffield data collection system uses 16 electrodes which are addressed through four multiplexers. A master clock running at 820 kHz is used to generate a 51 kHz sine wave by clocking out 16 values per cycle from an EPROM which feeds a DAC. As everything is controlled by the one clock we can determine both real and imaginary components of the recorded profiles. The 51 kHz sine wave is applied to a VI converter with an output of 5 mA p-p. This current is applied to adjacent electrodes pairs via two of the four multiplexers. Address lines on the two receive multiplexers select adjacent pairs of electrodes and pass the signals to a differential amplifier. These signals are then taken to a phase sensitive detector (PSD) which is set to select in-phase signals. The output of the PSD is taken to a sample and hold circuit prior to a 12 bit ADC.

In [165] (1993) a superheterodyne serial data acquisition system for EIT is introduced. Instead of conventional demodulation, the electrode voltage signal is first translated to an intermediate frequency significantly higher than the carrier frequency. The demodulation is performed at this higher frequency, generating replicas of the spectrum of the multiplexed impedance signals. The high frequency components are then removed by low-order filters, since the distance between them and the desired baseband spectrum is very large.

In [249] (1994), the ACT3 EIT system was presented, making use of 32 current sources and 32 phase-sensitive voltmeters to make a 32-electrode system that is capable of applying arbitrary spatial patterns of current. The instrumentation provided a precision of 16 bit on both the current values and the real and reactive voltage readings and was capable of collecting the data for a single image in 133 ms. It is one of the first EIT implementations that made use of digital demodulation, in an effort to increase the signal SNR levels. The system also provided an automatic trim of the current source output impedance, by employing a negative impedance circuit, as well as a calibration of the VCCS by measuring the current sink output. At both the current and voltage electrodes it employed voltage buffers to reduce the parasitic capacitance effects on the IA input impedance. The voltage readout chain comprised of a switching array and a preamplifier IA. The voltage signal processing proceeded on with an ADC and digital demodulation (see Fig. 5.17).

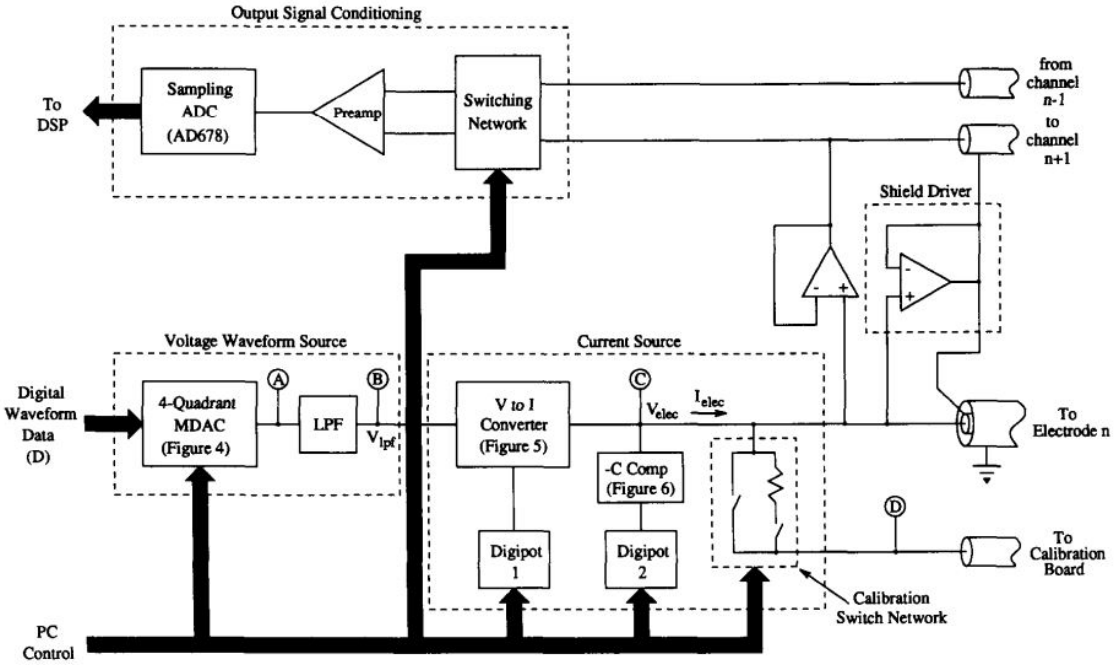

Figure 5.17: Block diagram of the analog circuits for one channel of the ACT3 EIT system, showing the waveform source, current source, shield driver, and output signal conditioner [249].

In [250] (1995) a 32-electrode data collection system for EIT is presented. The demodulator is a multiplexed sample and hold circuit followed by a voltage difference stage. This configuration's difference stage requires very low frequency signals, something that prevents the degradation of $CMRR$. The system employs a 25kHz constant current generator, which consists of four LM13600 operational transconductance amplifiers (OTAs). An AC-to-DC converter, which acts as a differential demodulator, generates a DC output equal to the difference of the real parts of the two sinusoidal signals which appear on the two selected voltage measuring electrodes. A synchronous demodulator implemented using a Sample and Hold circuit is multiplexed to both channels. The multiplexing of a single demodulation stage to two channels is used in order to eliminate any possible discrepancy leading to measurement error due to mismatch of two almost identical stages which otherwise could be used (one for each channel). The circuit architecture as well as further implementation details can be found in [250].

The Mk3.5, an update of the Sheffield EIT system, is presented in [251]. It used 8 electrodes with the adjacent current and voltage measurement protocol and could provide both the real and imaginary part of impedance at 30 discrete frequencies between 2 kHz and 1.6 MHz. The system consisted of eight identical data acquisition boards for the signal generation and the demodulation process (see Figs. 5.18 and 5.19). It included a typical voltage readout circuitry, comprised of a voltage buffer and an IA to lead the output voltage to a 12-bit ADC.

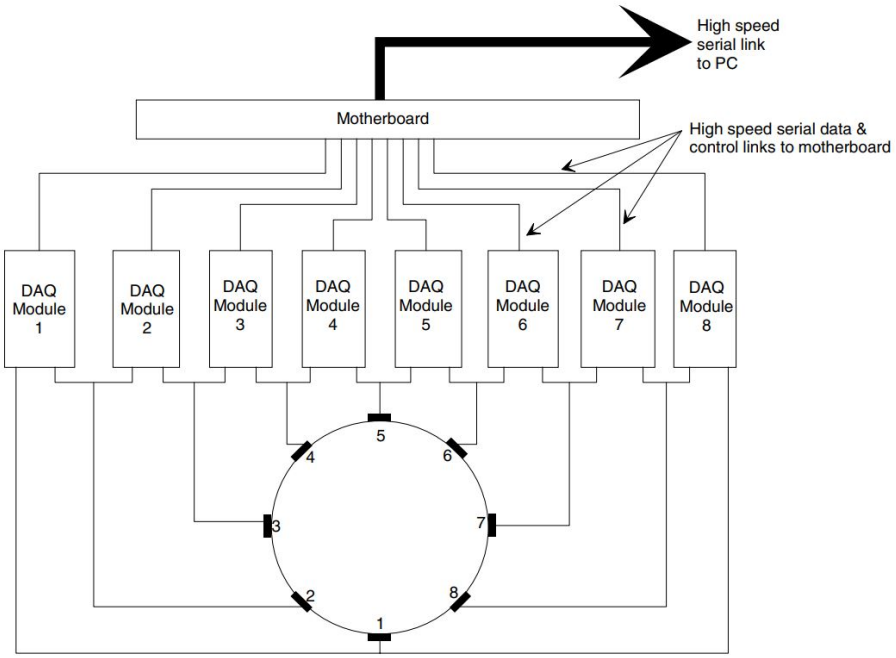

Figure 5.18: Block diagram of Mk3.5 Sheffield EIT system [251].

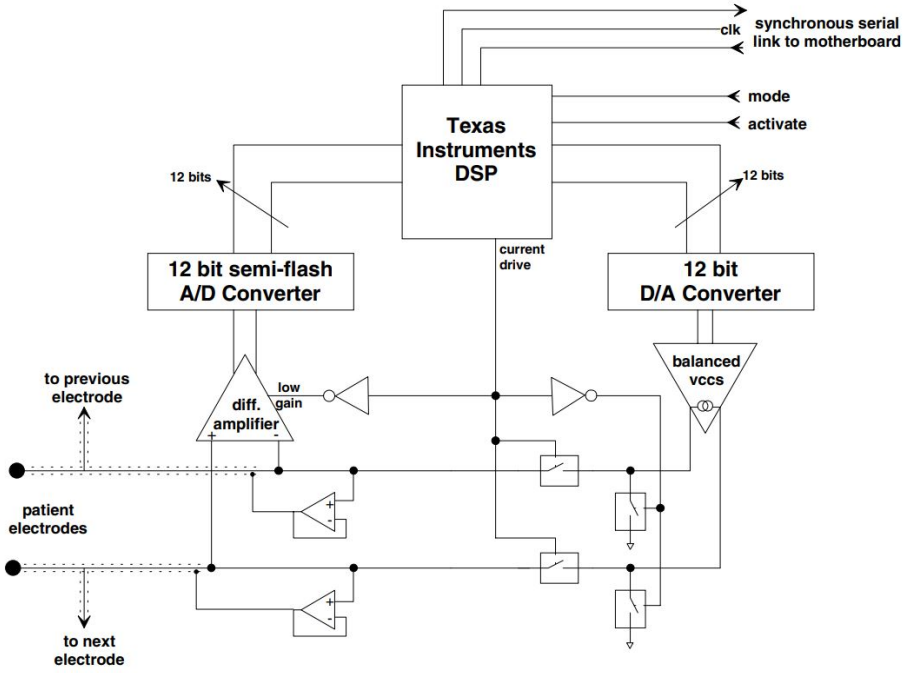

Figure 5.19: Circuitry of each data acquisition module included in the Mk3.5 Sheffield EIT system [251].

An up to 10MHz excitation signal frequency EIT system was developed by the university of Dartmouth in [252], with an update in [9]. The original system included 32 electrodes, while a channel module was employed for each four electrodes, including a DAC, an ADC and the analog circuitry. Each one of

the eight modules was controlled from an FPGA unit for the channel switching, signal generation, acquisition, synchronization and demodulation. In [9] the system was used for breast imaging application, achieving SNR of 94 dB up to 2 MHz current signal frequency, 90 dB up to 7 MHz current signal frequency, and 65 dB at 10 MHz current signal frequency. At the same time, it achieved an impedance magnitude accuracy of 99.7% with small channel-to-channel variations.

In [253], a modular, up to 32 electrodes, adjustable data acquisition system using National Instruments' hardware and software modules, which offer inherent compatibility over generations of hardware and software revisions. This EIT system, which block diagram is shown in Fig. 5.20, can be used to interchangeably apply current or voltage signal, and measure the tissue response in a semi-parallel manner. A 512-point Fast Fourier Transform (FFT) signal averaging algorithm computation block was implemented on an FPGA. FFT output bins were classified as signal or noise. Signal bins constitute a tissue's response to a pure or mixed tone signal. Signal bins' data can be used for traditional applications, as well as synchronous frequency difference imaging. Noise bins were used to compute noise power, which represents a metric of signal quality, and can be used to ensure proper tissue-electrode contact.

The input signal can be selected to be either voltage or current. In the first case, the readout circuit collects a current signal, transferring it to a voltage one before amplification with a PGA. Multiplexing is used for the electrode pair selection.

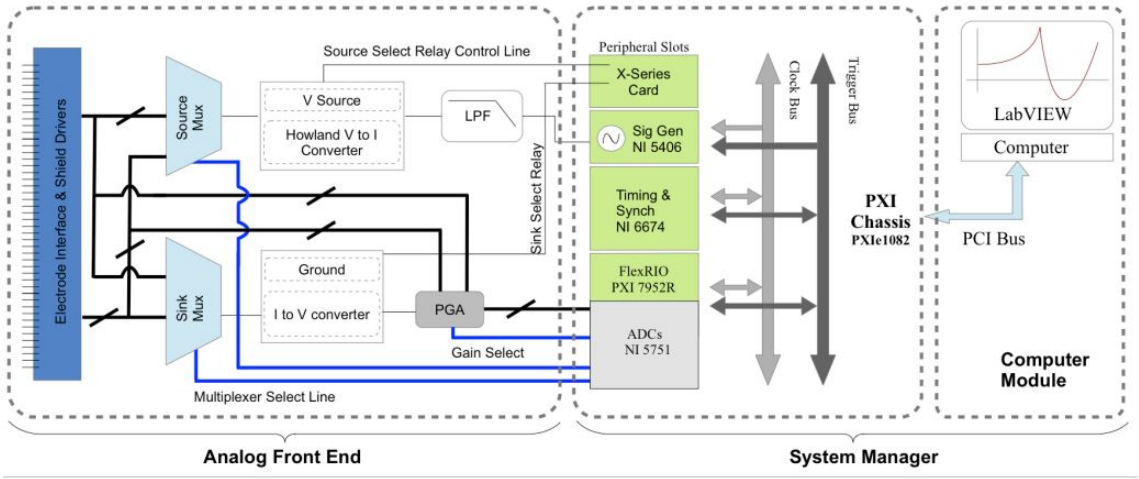

Figure 5.20: Block diagram of the EIT system presented in [253].

In [254], a modular DSP based EIT system was developed. Its block diagram is shown in Fig. 5.21. It supported a number of acquisition and computing modules. Each data acquisition module included a) a VCCS consisted of two mirrored Opamp stages for the DC current restoration followed multiple high slew rate AD844 current-feedback amplifiers (Fig. 5.22), b) An equal-width pulse synthesizer unit and c) a synchronized digital demodulation unit. The computing module included a DSP processor with memory, multichannel buffered serial ports and an IEEE1394 communication interface. Several DSP modules could be pipelined for a series of tasks ranging from measurement control to image reconstruction to flow velocity implementation. The authors of [254] claimed data acquisition speed of 1164 dual-frames per second and a $RMSE$ of less than 0.6% at 80 kHz in static test application. An application in the

measurement of vertical oil-in-water pipe flow was reported.

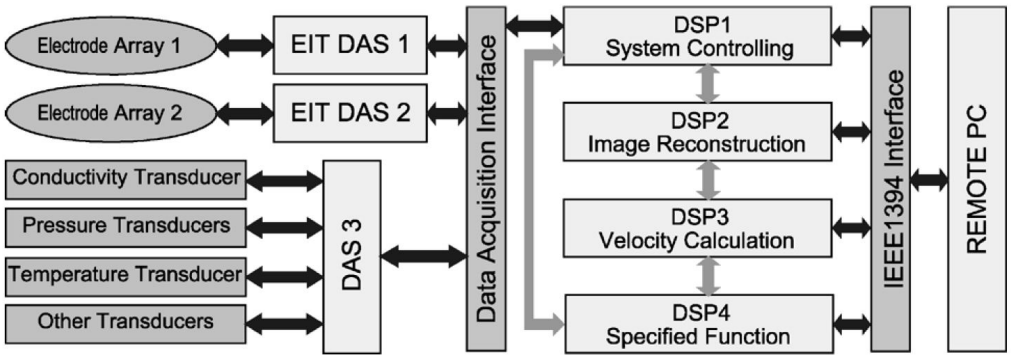

Figure 5.21: Block diagram of the EIT system presented in [254].

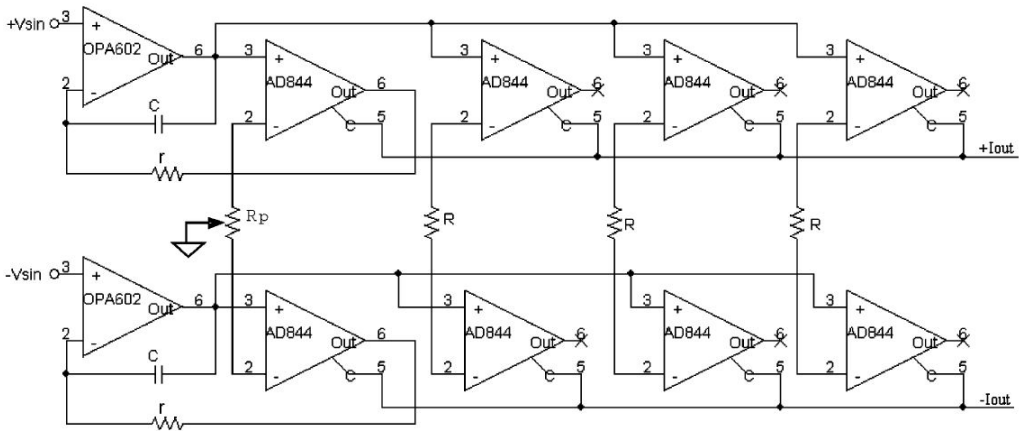

Figure 5.22: VCCS used in the EIT system presented in [254].

The KHU Mark1 EIT system is presented in [255], [256] and [257]. Its analog backplane included a single balanced enhanced Howland VCCS, a generalized impedance converter (GIC) to calibrate and maximize the VCCS output impedance and multiple voltage recording circuits (Figs 5.23, 5.24 and 5.25). It supported current signal frequencies from 10 Hz to 500 kHz and up to 64 voltmeters, that could simultaneously acquire and demodulate voltage signals. Each voltmeter measured a differential voltage between a pair of electrodes and its analog part comprised of multiple amplification stages, as shown in Fig. 5.25. All voltmeters were configured in a radially symmetric architecture in order to optimize the routing of wires and minimize cross-talk. It also employed contact impedance measurements, data overflow detection, spike noise rejection, automatic gain control and programmable data averaging. The multifrequency KHU Mark1 EIT system mainly targeted in brain imaging and was also validated for impedance spectroscopy and time-difference imaging [257].

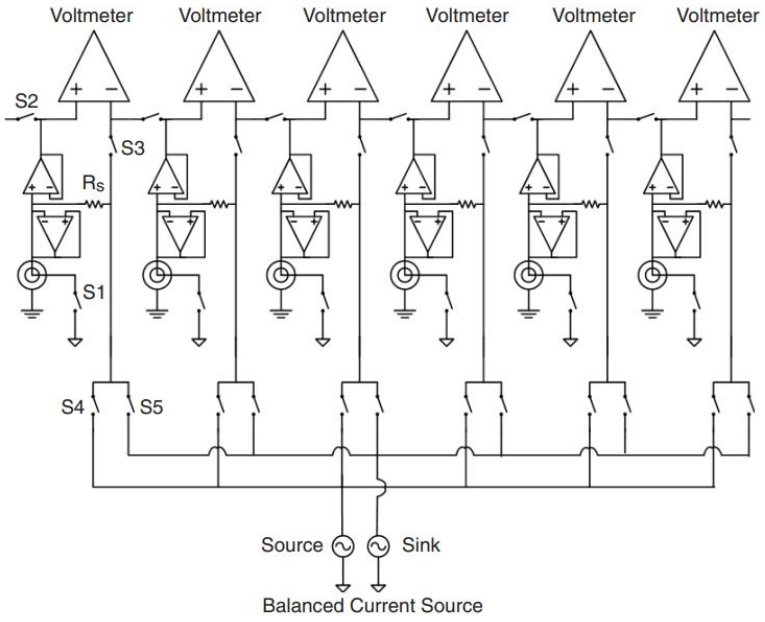

Figure 5.23: Analog backplane of the KHU Mark1 system [255].

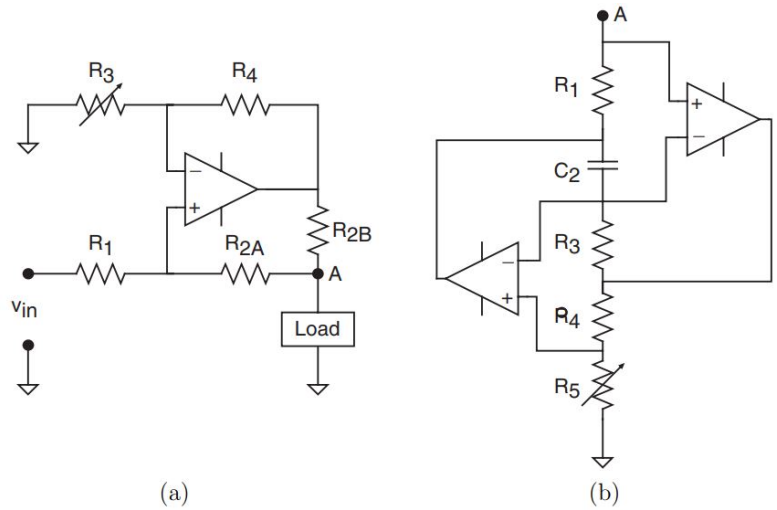

Figure 5.24: The current source circuitry of the KHU Mark1 system [255]. a) Enhanced single-ended Howland VCCS b) Generalized Impedance Converter (GIC) [256].

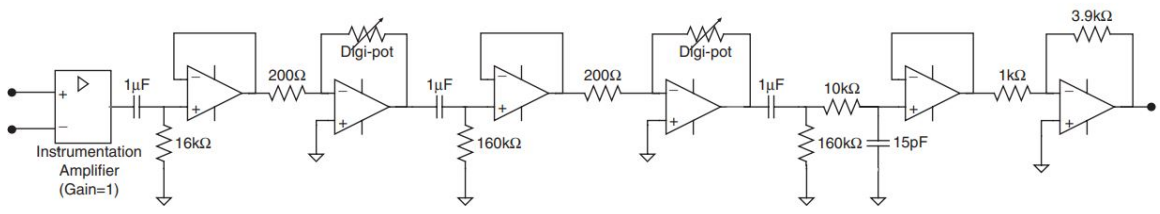

Figure 5.25: Voltage amplifier used in the KHU Mark1 system [256].

The KHU Mark1 system was ascended from the KHU Mark2 [258], which employed an impedance measurement module, including a current source, a voltmeter, a DAC, an ADC and an FPGA control unit on each particular electrode. This offered flexibility, since the hardware could be configured to tailor any electrode configuration needed for a specific application. Furthermore, the KHU Mark2.5 system [156] added automatic self-calibration of the current source via the generalized impedance converter and the FPGA units in order to better support long-term monitoring.

In [259] a prototype of a multi-frequency EIT system was presented (Fig. 5.26). The system used a FPGA as a main controller and was configured to measure at different frequencies simultaneously through a composite waveform. Both real and imaginary components of the data were computed for each frequency and sent to the PC over an ethernet connection, where both time-difference imaging and frequency-difference imaging were reconstructed and visualized.

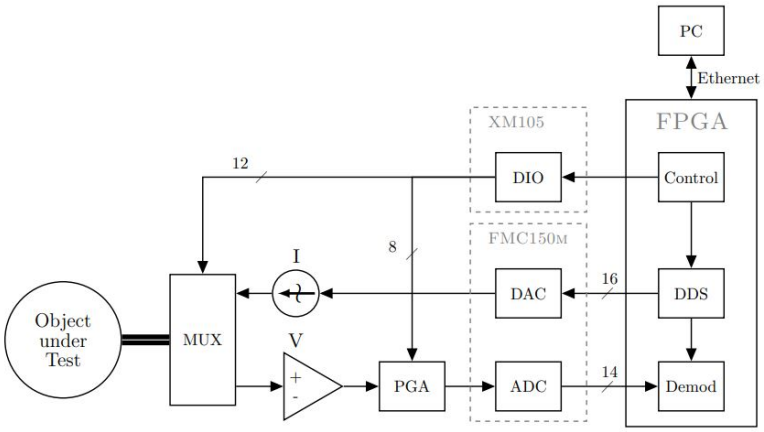

Figure 5.26: Simplified block diagram of the EIT system presented in [259].

In [227], a high precision EIT system was developed, targeting in brain hemorrhage monitoring (Fig. 5.27). A precise digital synthesis method and a digital demodulation technique were applied in order to increase the system's SNR and reduce any errors related to the contact impedance and the skull. Furthermore, a high $CMRR$ voltmeter (Fig. 5.28) and a programmable current source (based on the enhanced Howland one) were designed in order to eliminate the stray capacitance, the shunt and channel mismatch effects. The authors claimed a SNR of more than 83 dB, a high $CMRR$ of 75 dB and a low reciprocity error of 0.125% for frequencies up to 200kHz. The results and the measured values were acquired using a brain physical phantom.

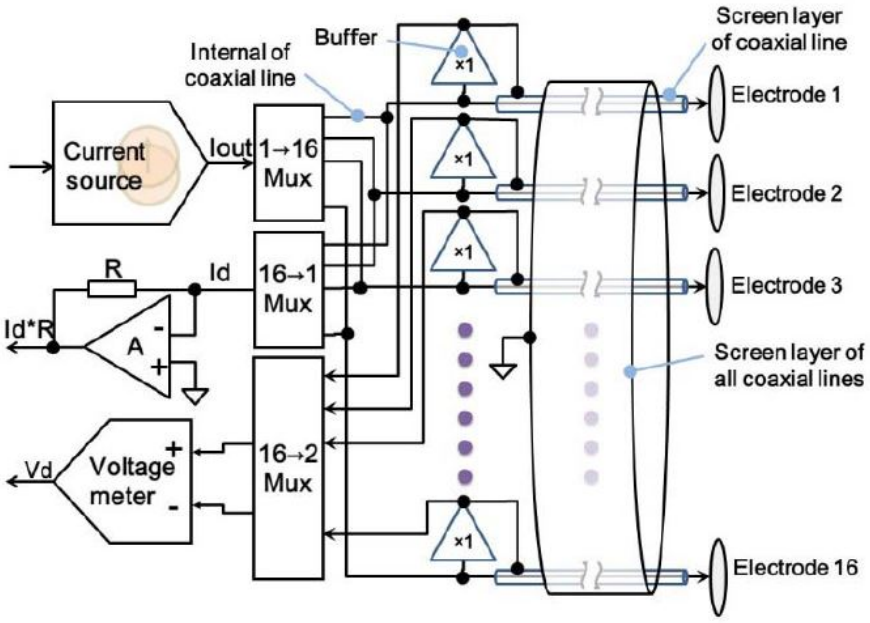

Figure 5.27: Simplified block diagram of the EIT system's analog part presented in [227].

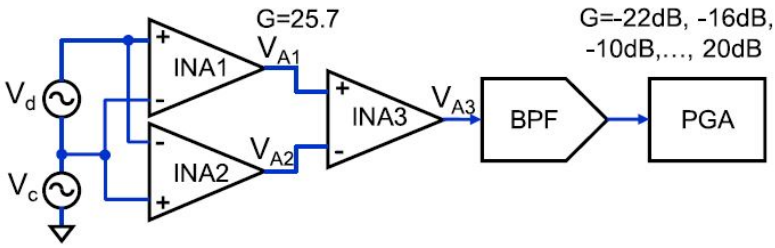

Figure 5.28: Simplified block diagram of the EIT system's voltage recording circuitry presented in [227].

The ACE1 system presented in [171] used a partially active electrode configuration to eliminate the stray capacitance effect, employing a buffer amplifier close to each electrode and a smart switching mode (Fig. 5.29) to efficiently collect both stimulation and non-stimulation electrode voltages. Using this data, the system performed fast digital demodulation to extract the boundary voltage amplitude and phases. The hardware could be modified to support up to 32 electrodes and a variety of current stimulation patterns, achieving SNR levels between 30 and 90 dB. The system was tested for dynamic lung imaging, resulting on frame rates between 16 and 32 fps.

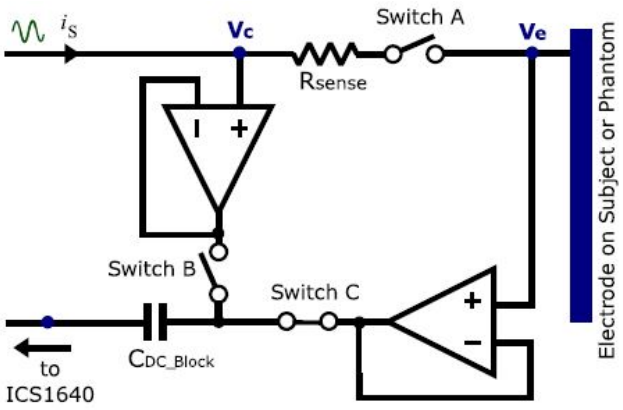

Figure 5.29: Active electrode configuration of the ACE1 system presented in [171].

In [260] a CMOS ($0.18\ \mu m$ technology, 3.3V supply) based analog front end ASIC for cardiac EIT was presented. The ASIC consisted of an integrated current driver, an IA, a variable gain amplifier at the analog front end for voltage readout and an on-chip 10-bit successive approximation register (SAR) serial ADC. Voltage amplitude and phase extraction was performed using a digital matched filter. The readout chain in the ASIC achieved a minimum SNR of 71 dB over the frequency range of 500 Hz–700 kHz, while maintaining an average accuracy of 99.7%. Frame rates of 21 frames per second for a 32 electrode system was feasible, while the ASIC had a power consumption of 11.8 mW. The basic block diagram of the ASIC is demonstrated in Fig. 5.30, while the IA and variable gain amplifiers' CMOS architectures are shown in Fig. 5.31.

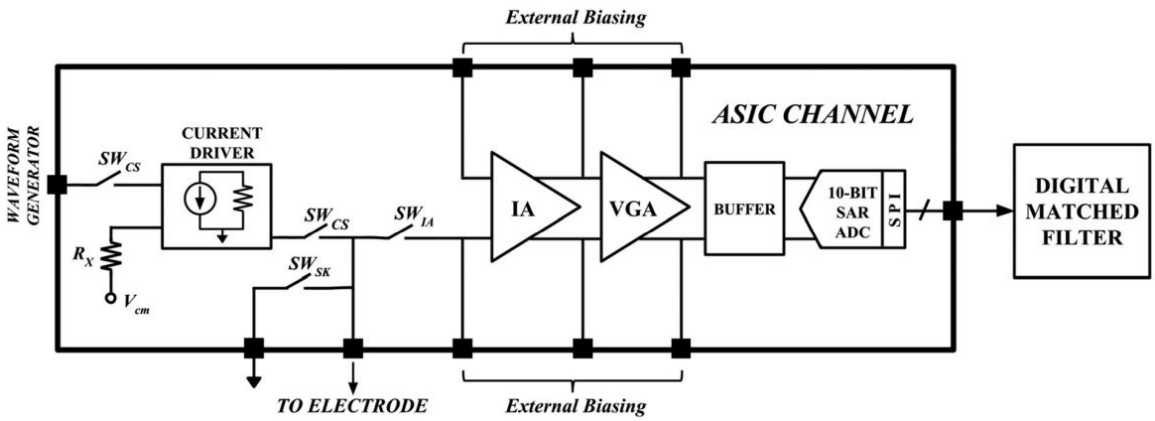

Figure 5.30: Block diagram of the cardiac EIT ASIC presented in [260].

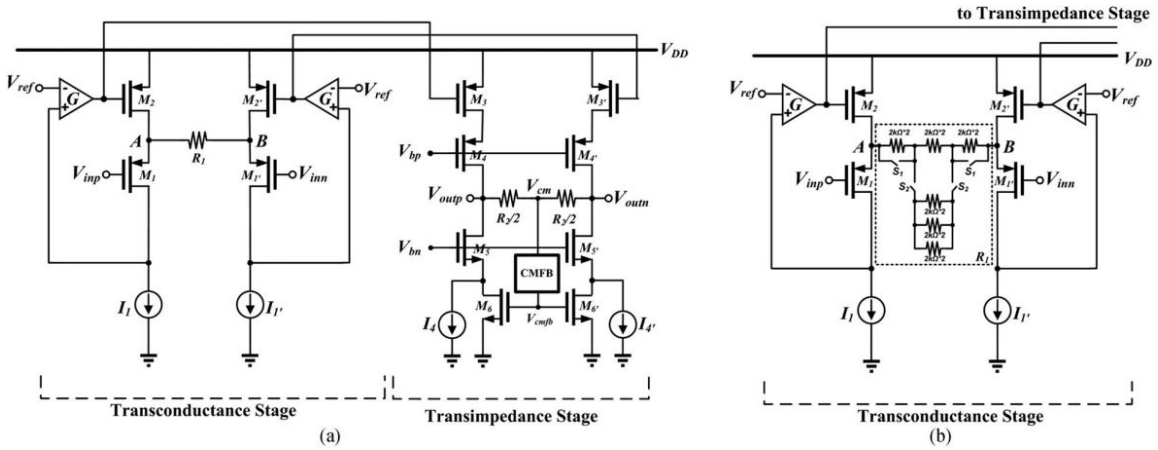

Figure 5.31: a) Current conveyor architecture used for the implementation of the IA. b) The transconductance stage of the variable gain amplifier [260].

In [241] an EIT system based on frequency division multiplexing (FDM) was proposed for real-time lung physiological imaging. This techniques allows the integration of multiple voltage sensing channels by combining data on-chip and sharing of ADC to alleviate area penalty caused by multi-channel. The system was designed in 130nm CMOS technology and includes the following features: 1) Early I/Q demodulation to relax the bandwidth requirement of analog front end and minimize the impact of motion artifacts and DC electrode offset. 2) Eliminates the need of adaptive gain control with constant inverted 'U-shape' gain configuration to compensate amplitude variations across all channels. 3) FDM to combine 13 pairs of I/Q signals into two data streams for quantization using two $\Delta\Sigma$ Modulators. 4) Batch data recovery by Blackman window corrected FFT without any digital filtering involved. A block diagram of this EIT system is demonstrated in Fig. 5.32.

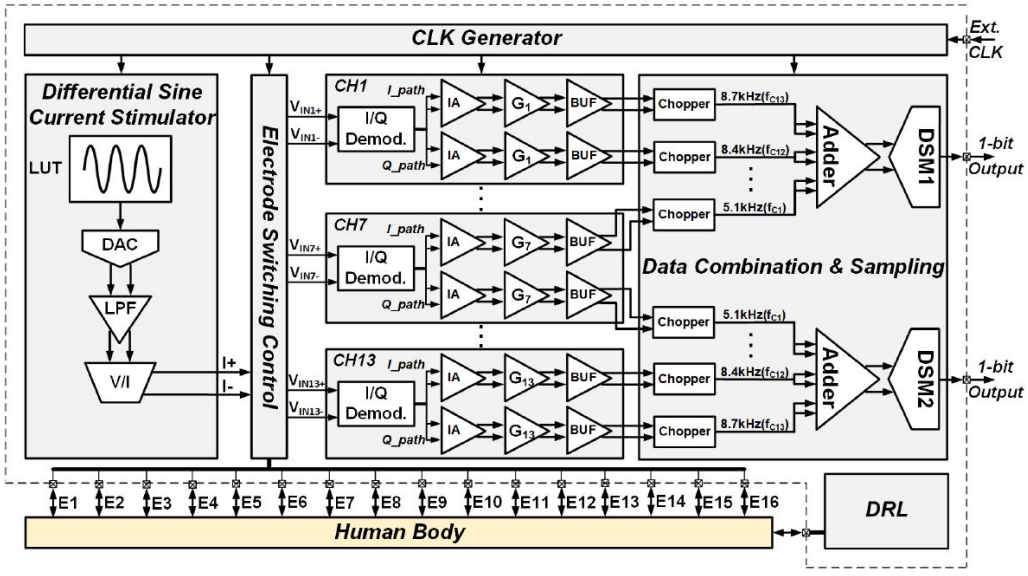

Figure 5.32: Block diagram of the EIT system proposed in [241].

In [261], an active electrode IC ($0.35\mu m$ CMOS process) for continuous monitoring with simultaneous EEG, EIT and electrode-skin contact impedance was proposed (Fig. 5.33). Its main target application is brain imaging, where the contact impedance is a significant modeling error source. The voltage readout circuit is based on a Differential Difference Amplifier and performs single-ended amplification and FDM of the EEG, EIT and contact impedance signals that are sent to the system's back-end. The paper performs an analysis of the mismatches in passive and active components influence on the system's $CMRR$.

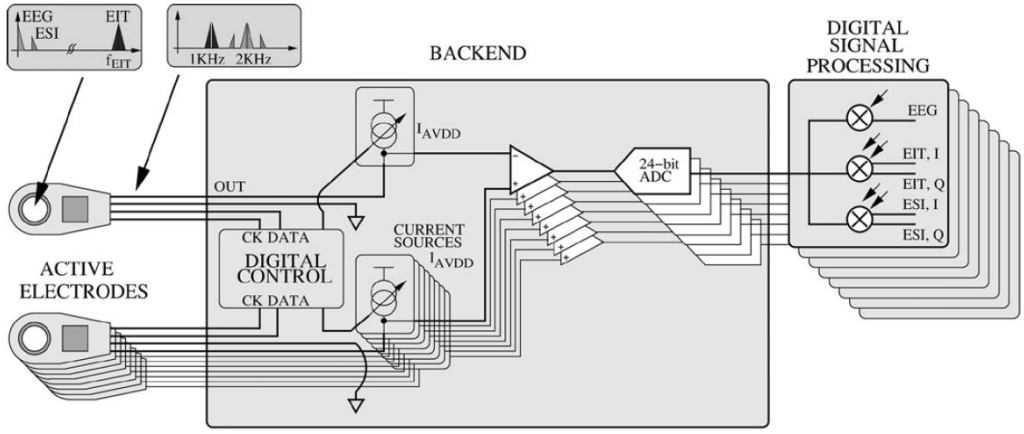

Figure 5.33: Block diagram of the EIT/EEG/contact impedance measurement system proposed in [261].

In [262], a co-integrated with electrodes and optodes (i.e. optical source and detector) ASIC, implemented as an an active sensor to perform EEG, bio-impedance measurement, and near-infrared spectroscopy (NIRS) on scalp is presented. NIRS readout utilizing the near-infrared light could be used to measure the pulse oximetry and blood oxygen saturation (SpO_2). It also allowed the use of silicon photomultipliers (SiPMs) as optical detectors. On circuit level, a SAR-based calibration compensates maximum $40\mu A$ current from ambient light, while digital DC-servo loops reduce the baseline static SiPM current up to $400\ \mu A$, leading to an overall dynamic range of 87 dB. The EEG readout exhibits $720M\Omega$ input impedance at 50 Hz. The BioZ readout presented $3m\Omega/\sqrt{Hz}$ impedance sensitivity by employing dynamic circuit techniques. When EEG, BioZ and NIRS were enabled at the same time, one ASIC consumed $665\mu W$ including the power of LEDs. A brief demonstration of the ASIC sensor is shown in Fig. 5.34.

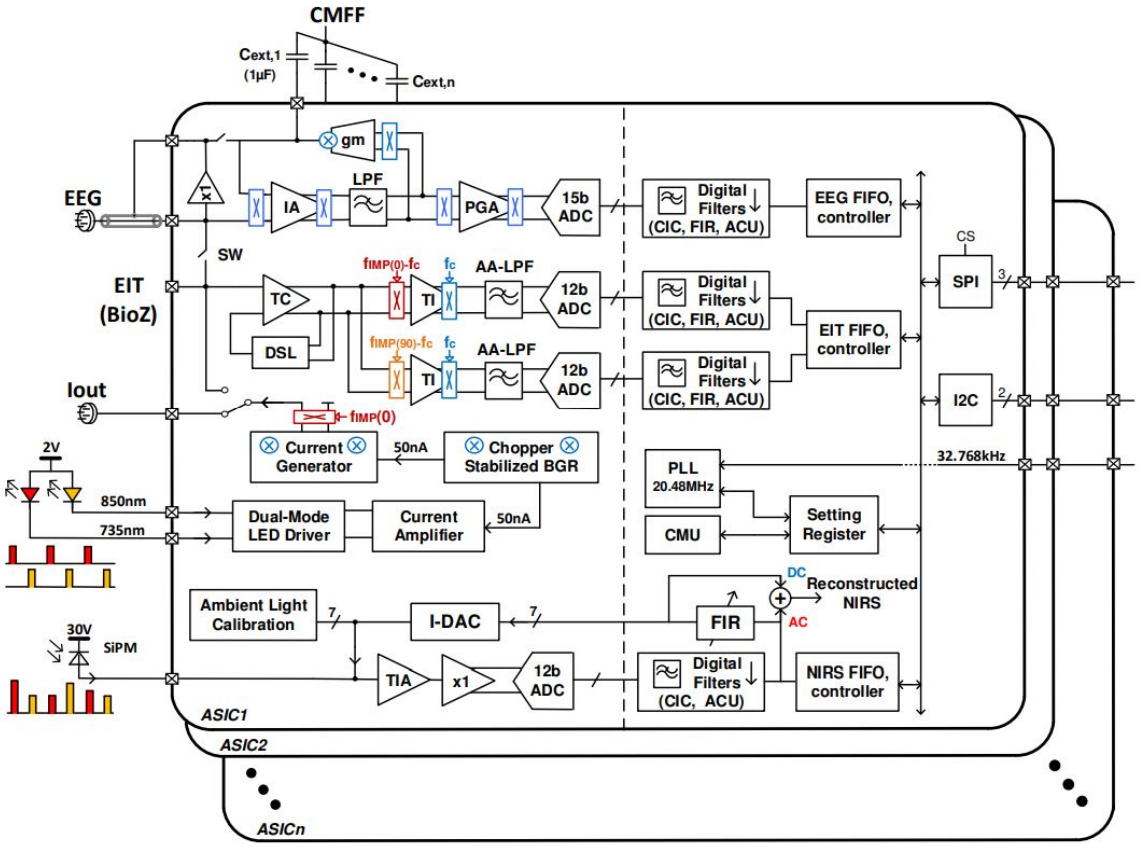

Figure 5.34: Block diagram of active ASIC sensor presented in [262].

A bioimpedance readout IC with frequency sweeping from 1kHz-to-1MHz for EIT is presented in [263]. The IC included a complete readout channel for impedance characterization, an input multiplexer and a programmable digital controller enabling multi-frequency impedance scanning from multiple locations. To relax the bandwidth requirements of the readout channel, pre-demodulation before the IA was employed. A fast channel settling mechanism ($< 1ms$) allowed quick switching between frequencies enabling a fast imaging speed. Dynamic element matching in the current generation and chopping in the readout front-end were adopted to mitigate flicker noise.

In [158], a wideband (up to 1 MHz) EIT system was developed for prostate imaging. Its implementation was based on a 4-channel ASIC (CMOS $0.18\mu m$ technology), which high-level architecture was based on the one in Fig. 5.30. Its current driver was based on a high output impedance current conveyor employing a gain enhanced cascode structure and a servo loop to maintain an appropriate DC bias voltage at the current driver's output (see 5.2.2 and Fig. 5.12). The voltage readout part of the system included a custom IA, a variable gain amplifier and an SPI interface 10-bit SAR ADC. As in [260] the IA and variable gain amplifier architectures are based on a transconductance followed by a transimpedance stage. The system was evaluated using a model transrectal imaging probe immersed into a tank filled with saline and a metal inclusion, maintaining a 66dB to 76dB SNR between 500Hz and 1MHz.

In [20], an up to 100 fps EIT system was developed for dynamic lung imaging, including a number of 32 active electrodes. It employs an ASIC active circuit per electrode, to reduce the channel parasitic ef-

fects. Each ASIC comprises DDTA-based current driver capable of up to $6mA_{p-p}$ output (see 5.2.2, Figs. 5.10 and 5.11), a voltage buffer for EIT and heart rate signal recording as well as contact impedance monitoring and a sensor buffer that provides multi-parameter sensing. For the voltage recording on non-current injected electrodes, the on-chip buffer B_1 (see Fig. 5.35) a first stage, while the rest of amplification and filtering stages as well as the ADC are implemented on a central hub, where all the active electrodes are connected. The digital control of the multiplexer switches (in such a way to define the current injection and voltage measuring strategies), the ADC and the DAC, as well as the signal synchronization demodulation is performed on a FPGA, located on the central hub [20].

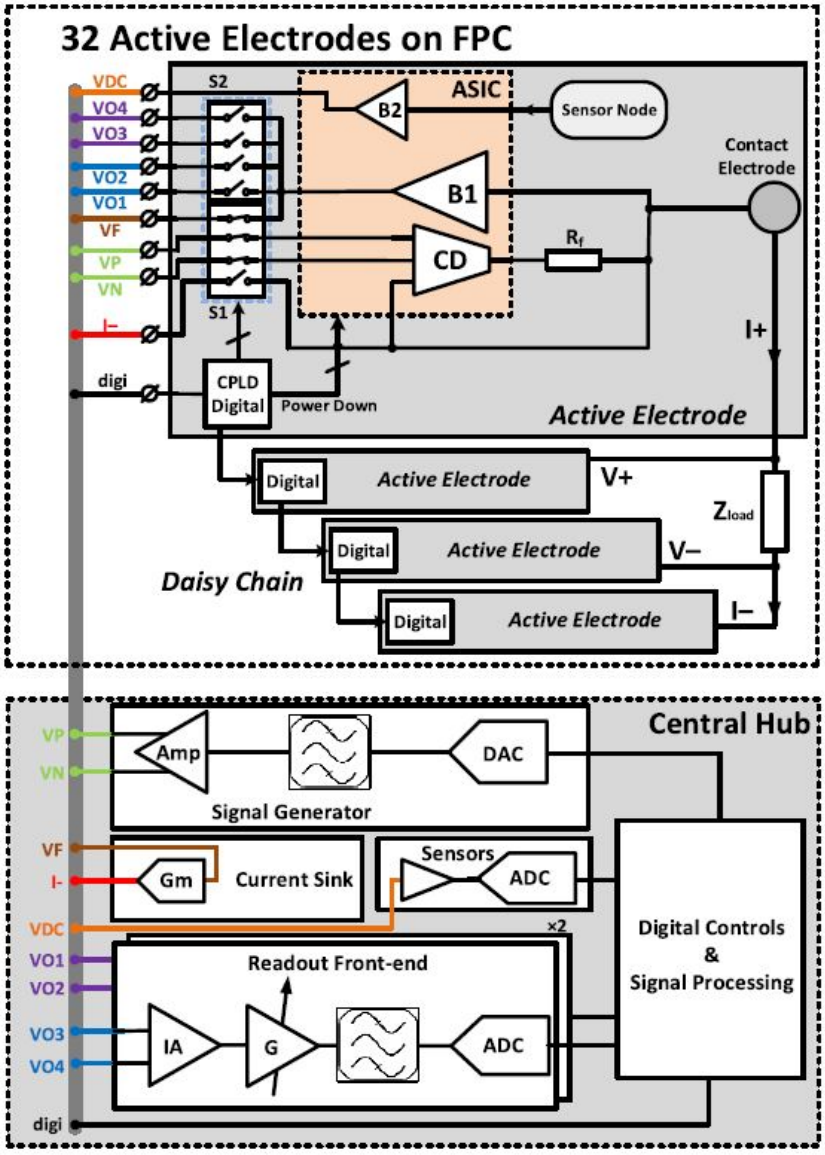

Figure 5.35: Block diagram of active electrode based EIT system presented in [20].

An individual extension of this work, particularly targeted in neonatal lung monitoring, was developed

in [21]. It is worth to mention that neonates do not afford any kind of ionizing radiation, and, therefore the application of EIT for monitoring neonates with respiratory failure during mechanical ventilation. Sixteen active electrodes have been integrated on a belt, with an ASIC connected to each one. Each ASIC consists of a fully-differential DDTA-based wideband current driver, which provides common mode feedback [216], a digital control unit, a switch array and a current feedback IA which measures the differential voltage between two selected electrodes. This system adopts the IA summing topology for the voltage acquisition, which can be applied for every skip voltage measuring pattern. The summing topology has also proven to result at lower noise compared to the buffer one in [20] for low skip numbers (<3). The measurement pattern control, the DDS, the control of the PGAs, the communication with ADC and DAC, the signal demodulation and synchronization is performed from an FPGA. A block diagram of the active electrode tetrapolar measurement configuration is shown in Fig. 5.36, while the IA architecture is depicted in Fig. 5.37.

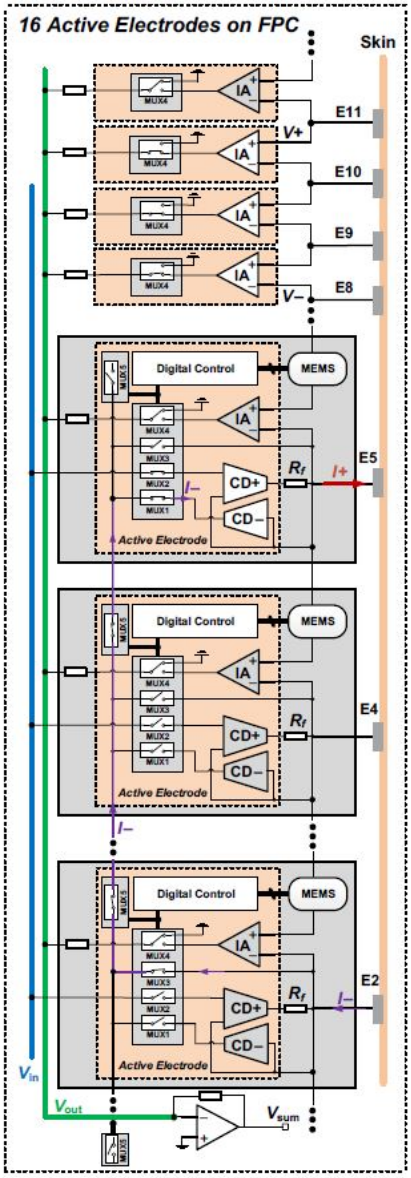

Figure 5.36: Block diagram of active electrode configuration presented in [21].

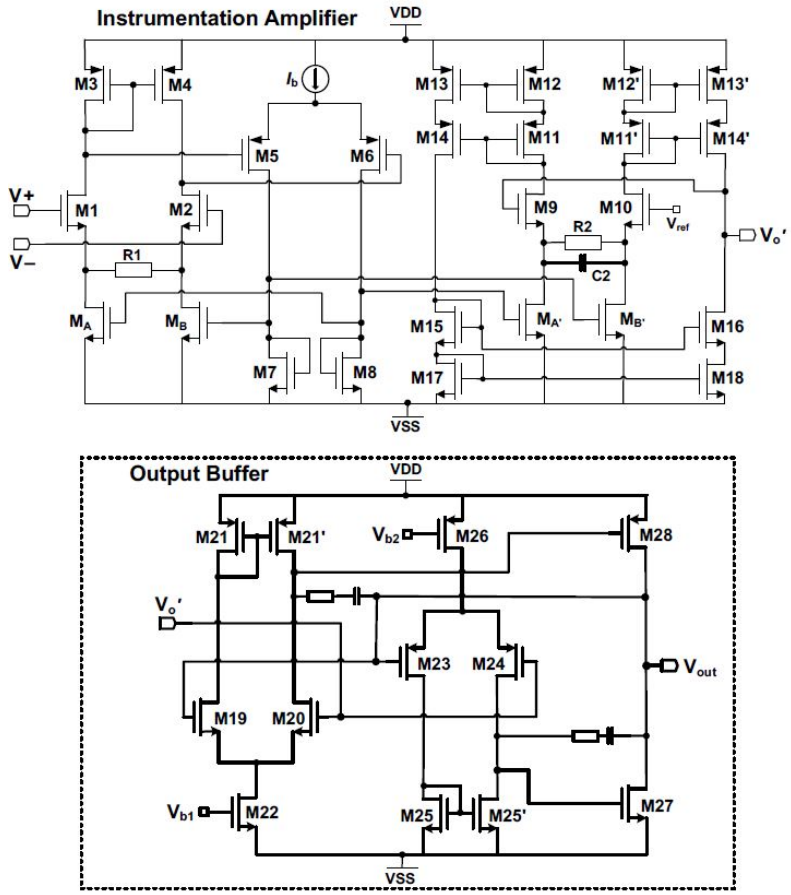

Figure 5.37: Architecture of the current feedback IA designed and used in [21].

6 A simulation interface for Electrical Impedance Tomography hardware

This chapter presents a extended simulation interface for EIT hardware. It comprises of 3 smaller chapters. The first one, which corresponds to [264], presents the general concept of an EIT hardware system SPICE-MATLAB co-simulation, validating its usefulness through circular EIT setups in the presence of modeling errors. The phantom setup's structure is merged in the simulated hardware via equivalent circuit transformations in the forward problem. The second one, which corresponds to [265], has introduced three important features in the simulation method presented: noise analysis, generalized skip current patterns and digital signal demodulation. Finally, in the third sub-chapter [194], the presented interface is applied in $3D$ thoracic equivalent structure cases, where the impact of hardware configurations such as signal noise, electrode contact impedance, ADC resolution, sampling rate and the number of demodulation filter taps is qualitatively and quantitatively examined in the reconstructed images.

6.1 A Parametric EIT System SPICE Simulation with Phantom Equivalent Circuits

Many EIT hardware systems with specific clinical applications have been developed over the last 3 decades, such as the Sheffield MK (v1 1987, v3.5 2001) [251], the Dartmouth breast imaging system (1998, 2001, 2008) [9, 252, 253], the ACT 3 and 4 EIT system (1994, 2005) [249, 266], the Swisstom active electrode system (2012), the KHU Mark 2.5 system (2014) [156] and the ACE1 pulmonary real-time imaging system(2019) [171]. Over the years, many design and configuration improvements have taken place, targeted to the acquired medical images' quality.

The image reconstruction problem of EIT is typically ill-posed and ill-conditioned, which means that even relatively low noise levels at the measurements could lead to significant reconstruction artifacts [36, 267]. Therefore, apart from the essential mathematical modelling of the problem, the measured data need to be as accurate as possible with the minimum noise level. Intrinsic electrical bio-signals and unwanted motion of the electrodes (e.g., breathing or heartbeat) introduce noise in addition to noise due to electronic hardware [171, 268]. Many of these cannot be easily predicted during the hardware design process. This creates the necessity for proper simulation before proceeding to the system design. Although many tools have been used for either the simulation of the tissue's behavior in time and frequency

(MATLAB-EIDORS tool, COMSOL, ANSYS, etc), of the contact impedance's impact [269]; or the simulation of the hardware (SPICE for the current source behavior [205, 270]), there is no complete effort to merge hardware (digital and analog), software and the subject's properties on a single simulation core.

A preliminary parametric study has been presented in [267] where a whole EIT system circuitry has been simulated in LT SPICE, including some 2D phantom equivalent circuits. It has been observed how possible problems such as increased signal noise and large contact impedance variation or more critical issues (electrode disconnections, short-circuits) contribute to imaging errors.

This work extends [267] in the following directions: A) It considers a more detailed model of the current source by including its output impedance, z_{out}, depending on frequency f_{in}. Typically z_{out} decreases in magnitude with f_{in} diverting from the ideal model, B) Digital to Analog Converter's (DAC) quantization noise is included in the analysis, C) Proper analog filtering for antializing is included in the analysis, D) In addition to 2D, 3D Finite Element structures are developed in MATLAB and are imported into LT SPICE as N-port equivalent circuits (N is the number of electrodes used.) to better simulate the EM field effects, and finally, E) The data acquisition system, including both the analog (filters, instrumentation amplifiers, voltage shifting in LT SPICE) and digital (Analog to Digital Converter (ADC), data processing, image reconstruction in MATLAB) parts has been simulated. In addition, the transient effects, current injection and voltage acquisition channels switching times as well as the ADC noise, setting times and sampling rates have been taken into consideration [259].

A parametric study has been performed, modifying properties of the Voltage Controlled Current Source (VCCS), the electrodes, the structure (measuring subject) and the acquisition system within a frequency range of [10, 100] kHz, in an effort to optimize the performance of an EIT system. Although there is difficulty in specifying hardware parameters in such complex systems, the presented simulations can be effective tools for system spec-determination and preliminary design; something that requires increased attention in EIT, since ostensibly small deviations or issues could lead to failure in the image reconstruction.

The section is organized as follows: In subsection 6.1.1 the EIT mathematical model along with the forward and inverse problems are briefly described. In subection 6.1.2, the simulated hardware in LT SPICE is presented, highlighting the signal generation, the current source part, the subject equivalent circuit and the data acquisition process. In subection 6.1.4, EIT simulations are performed for selected VCCS topologies, frequencies, 3D tank phantoms, ADC sampling rates and resolutions, and the corresponding results are presented. The results are compared and discussed in Section 6.1.7.

6.1.1 The EIT Forward and Inverse Problem

The EIT electromagnetic problem is mathematically formulated by a current field diffused into a two- or three-dimensional volume $\Omega \subset \mathbb{R}^d$, $d \in \{2, 3\}$ which implies a Poisson differential equation [4, 36]. The Complete Electrode Model (CEM) is the most popular EIT formulation. It takes into consideration the modelled electrode dimensions and is described by the following equations: [4, 36]

$$\nabla \cdot (\sigma(\boldsymbol{r}) \nabla u(\boldsymbol{r})) = 0, \quad \boldsymbol{r} \in \Omega \tag{6.1}$$

$$u(\boldsymbol{r}) + z_l \sigma(\boldsymbol{r}) \frac{\partial u(\boldsymbol{r})}{\partial n} = U_l, \quad \boldsymbol{r} \in e_l, \quad l = 1, ..., N \tag{6.2}$$

$$\int_{e_l} \sigma(\boldsymbol{r}) \frac{\partial u(\boldsymbol{r})}{\partial n} dS = I_l, \quad l = 1, ..., N \tag{6.3}$$

$$\sigma(\boldsymbol{r}) \frac{\partial u(\boldsymbol{r})}{\partial n} = 0, \quad \boldsymbol{r} \in \partial\Omega \setminus \bigcup_{l=1}^{L} e_l \tag{6.4}$$

Where $u(\boldsymbol{r})$ is the voltage potential, N the number of the electrodes used, $\sigma(\boldsymbol{r})$ is the relative distributed conductivity and z_l the ℓ-th electrode's contact impedance.

Forward Problem

The EIT forward problem assumes a known conductivity distribution σ in Ω and solves for the nodal (or element) voltage potentials. This is usually done using the Finite Element Method (FEM) after converting (6.1) to its weak form for every element and embedding boundary conditions (6.2–6.4). After assembling the local element matrices, the problem results in a sparse (3-diagonal) linear system equation that can be solved with the Cholesky or the Conjugate Gradient algorithms [36].

Inverse Problem

The inverse problem refers to deriving $\sigma(\boldsymbol{r})$ for a known voltage potential distribution $u(r)$ and the voltage measurements on the electrodes $\boldsymbol{U}$. Contrary to the forward problem, this one is severely ill-conditioned and requires special regularization in order to derive a stable solution. The solution given by the generalized Tikhonov regularization is [4, 36]

$$\sigma(\boldsymbol{r}) = \sigma_{ref}(\boldsymbol{r}) + (\boldsymbol{M}^T \boldsymbol{W} \boldsymbol{M} + \lambda^2 \boldsymbol{Q})^{-1} \boldsymbol{M}^T \boldsymbol{W} \boldsymbol{\delta U} \tag{6.5}$$

where $\sigma_{ref}(\boldsymbol{r})$ is a reference conductivity distribution, $\boldsymbol{W}$ is a weighting matrix indicating each measurement's impact, $\boldsymbol{M}$ is the Jacobian matrix representing the sensitivity of each measurement to a conductivity change. In addition, $\boldsymbol{Q}$ is a prior filter matrix, λ is the regularization hyperparameter and $\boldsymbol{\delta U}$ is the difference between measurements acquired for $\sigma_{ref}(\boldsymbol{r})$ and $\sigma(\boldsymbol{r})$ respectively [4, 36, 174]. Although this is a direct one-step solution, many iterative approaches have also been developed, e.g., Gauss–Newton algorithm. However, in terms of this study, the NOSER prior one-step algorithm [36] is used with $\boldsymbol{Q} = diag(\boldsymbol{M}^T \boldsymbol{W})$, since parametric hardware tests are performed and NOSER is a simple, easy to implement reconstruction algorithm in order to check the effectiveness of an EIT hardware. Of course, similar comparison results with small variations are expected if the reconstruction is performed with any other one step inverse algorithm (0th order Tihkonov, Laplace, Gaussian High Pass Filter, D-Bar) or an iterational one (Gauss-Newton). The size of variations between the hardware simulations depends on the inverse algorithm's noise robustness, therefore, in order to get clearer comparisons we did not select a high performance reconstruction algorithm.

6.1.2 EIT Hardware

It has been shown that the tetrapolar measurement technique is the most suitable for EIT especially in bio-impedance instrumentation [4]. To implement is, a sinusoidal (or bi-frequency) current source (up to 1 mA, 10 kHz–100 kHz) is needed, followed by a multiplexing array to drive and sink the current from an electrode pair and take differential measurements from all electrode pairs. More details about the complete system architecture can be found in [267].

Here, we focus on (a) the current source topology and its properties, and, the their impact on the measurements and image reconstruction quality, on (b) the development of an electrical equivalent model of a typical phantom used for evaluating the performance of EIT image reconstruction algorithms, and on (c) the impact of the data converters properties on the image reconstruction quality.

The Current Source

The current source circuitry part described here includes the (voltage) signal generation, the filtering stage and the Voltage Controlled Current Source (VCCS).

A. Signal Generation

For signal generation, a Direct Digital Synthesis (DDS) block is usually a suitable solution. This includes a DAC driven by a sinusoidal or more complex waveform, typically stored in a Look-Up-Table (LUT). The analog output signal-to-noise ratio (SNR), considering only the quantization noise, of an L-bit DAC is [267]

$$SNR(dB) = (6.02L + 1.72)dB + 10log_{10}OSR \tag{6.6}$$

where OSR is the oversampling ratio. In this study, we simulated a 16 bit DAC (14 bit ENOB) with a sampling frequency of 16 times the desired signal frequency (f_{in}), i.e., with $OSR = 8$. Data were written on a text file (.txt) which was used as a PWL LT SPICE voltage source.

The DAC's output is filtered by an analog low-pass or band-pass filter. In our case, we use a 2nd order multiple feedback active band-pass filter with a central frequency of f_{in} and quality factor of $Q = 5$ [271]. The filter (shown in Figure 6.1a) was simulated using the ADA4625 Opamp (analog devices).

B. Voltage-to-Current Conversion

The design of an appropriate VCCS is one of the most challenging parts in an EIT system design, since the specifications must satisfy high output impedance z_{out}, Common Mode Rejection Ratio (CMRR) and sufficient current amplitude (low enough for the patients' safety and high enough to avoid notable noise rates) for as high frequency range as possible. In this study the topologies simulated are based on the modified Howland current source, described in [205, 208, 219]. Specifically, two main approaches have been tested: (a) the grounded load and (b) the mirrored modified Howland VCCS [208]. Their topologies are shown in Figure 6.1b and Figure 6.1c correspondingly. The mirrored VCCS is driven from a THS4130 fully differential amplifier, which follows the analog filter and offers low noise levels ($1.3nV/\sqrt{Hz}$) and an acceptable slew rate ($51V/\mu s$). The Common Mode Voltage V_{CM} was connected to ground. All ICs were supplied with +/- 15 Volts. In addition, since the mirrored VCCS needs to be symmetric, the corresponding resistors are of the same value ($R_4 - R_8$ in Figure 6.1c). In order to be able to measure

the input current to the load, an instrumentation amplifier (AD8421) stage has been added with a fixed sense resistor R_{sense} between its inputs and a configurable gain R_G resistor [272].

The output impedance z_{out} of Howland current sources depends on the balance of the resistors $R_4 - R_8$ which is extremely sensitive. Therefore the resistors above need to be characterized by very low tolerance ($\delta R/R \leq 1\%$). Furthermore, they are affected by the open loop gain of the Opamp (A), which is exposed to factors such as frequency and temperature. Those dependencies can be expressed at an approximate way by the following equations for the grounded load case:[208]

$$Z_{out,min} = \frac{R_8 R_6}{\delta R_4} \tag{6.7}$$

$$Z_{out} = \frac{R_4 R_8 (R_7 + R_6) A + R_8 (R_7 + R_6)(R_4 + R_5)}{[R_4 (R_7 + R_8) - R_5 R_6] A + (R_4 + R_5)(R_6 + R_7 + R_8)} \tag{6.8}$$

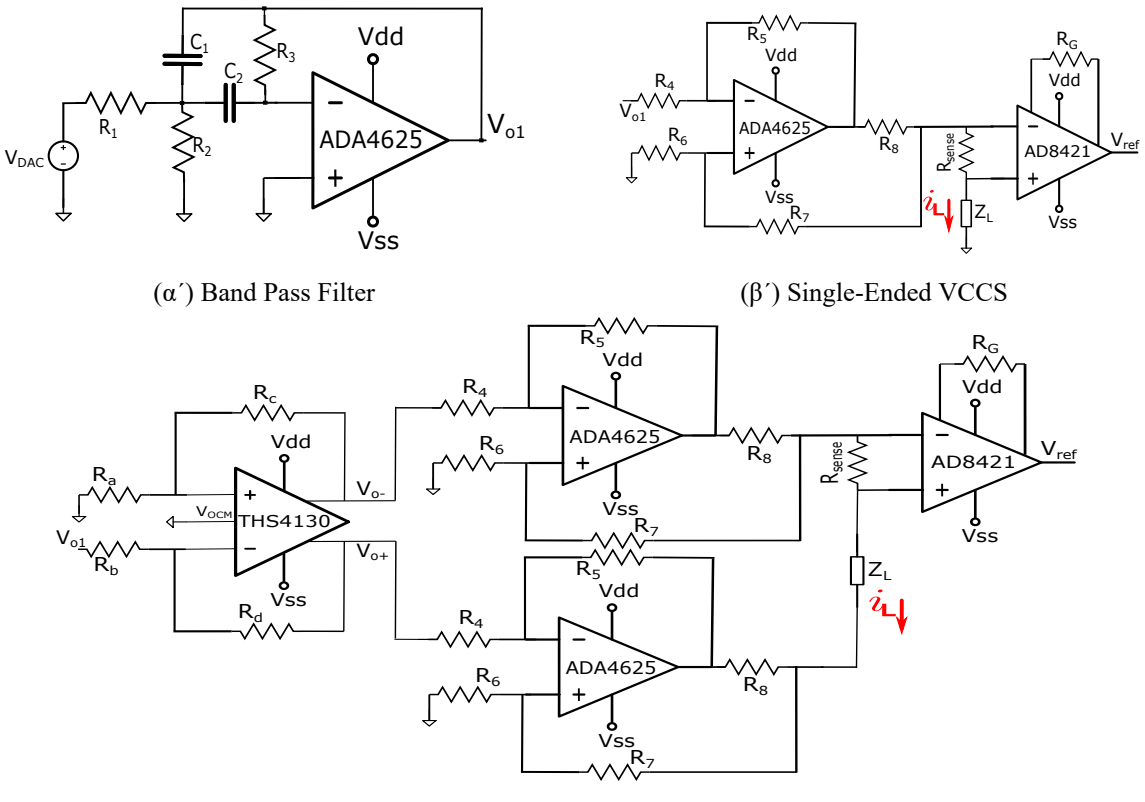

(α′) Band Pass Filter

(β′) Single-Ended VCCS

(γ′) Differential VCCS

Figure 6.1: Schematics of the current source topologies used for the simulations: (**a**) The multiple feedback 2nd order band-pass filter. (**b**) Grounded load modified Howland Voltage Controlled Current Source (VCCS). (**c**) Mirrored modified Howland VCCS, with the THS4130 fully differential amplifier at the previous stages that drives the input voltage.

From the equations above it is concluded that small perturbations of the resistor-coefficients not only could result in a much smaller than expected z_{out} but also to unstable oscillations (since the Opamp already has a positive feedback) [208]. Another important issue occurs from the parasitic impedances

while f_{in} increases, that lead to a severely decreased z_{out} and intense changes of the phase shift. The phase shift can be easily estimated from simulation and circuit testing and be added as a parameter when necessary in the acquisition part. Nevertheless, $|z_{out}|$ can hardly be kept above 200 kΩ for $fin \geq 100$ kHz, which leads to a large percentage of current steer before the load. Simulations performed show that increasing R_8, optimises the condition for the larger frequencies at the cost of current amplitude reduction that results in lower measurement SNR due to white noise and lower resolution.

The mirrored Howland VCCS improves on these issues, since it has larger z_{out} which arises from the sum of the two single ended circuits z_{out} [208]. The current amplitude is also larger and can be adjusted from the THS4310's gain (setting R_c and R_d to proper values). In Figure 6.2, simulations show the z_{out} and the current amplitudes for the two topologies, using the ADA4625 and OPAx210 Opamps. Additionally, a transient simulation that includes the DAC, filter and VCCS output for parametric R_8 resistor is displayed. A 300 Ω resistor in series with a 0.1 uF capacitor were used as load. The resistor values and tolerances selected are shown in Table 6.1.

From the simulation displayed, it is shown that with a mirrored VCCS z_{out} can reach 400 kΩ using the ADA4625 Opamp and even 700 kΩ using the OPAx210 Opamp with $R_8 \geq 4$ kΩ. The load current amplitudes are also kept at levels around 500 uA which are appropriate levels. In reality, the corresponding real z_{out} values have some randomness and may differ, however those simulations demonstrate the order of their magnitude [208], which is an important factor to be taken into consideration during EIT designing.

Table 6.1: Fixed values and tolerances of the components in Figure 6.1 used for the current source simulations at LT SPICE. For all cases R_{sense} and R_G were set to 100 Ω and 500 Ω correspondingly.

Component	R_1	R_2	R_3	R_4	R_5	R_6	R_7
Value	5.11 kΩ	221 kΩ	121 kΩ	97.6 kΩ	97.6 kΩ	100 kΩ	97.6 kΩ
Tolerance (%)	1.00	1.00	1.00	0.10	0.10	0.10	0.10
Component	R_8	R_a	R_b	R_c	R_d	C_1	C_2
Value	2.25 kΩ−6 kΩ	374 Ω	374 Ω	1.5k Ω	1.5 kΩ	1.5 nF	68 pF
Tolerance (%)	1.00	1.00	1.00	1.00	1.00	-	-

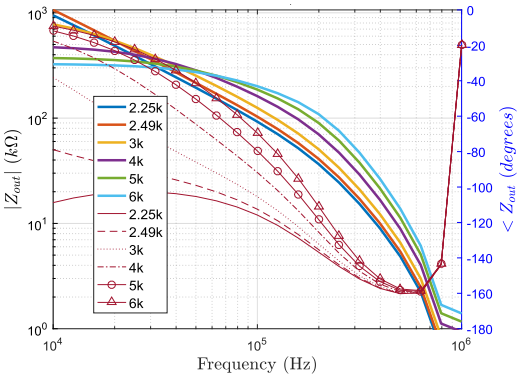

(α′) Single-ended/ADA4625

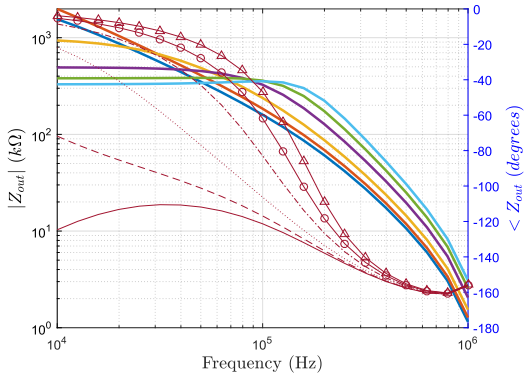

(β′) Single-ended/OPAx210

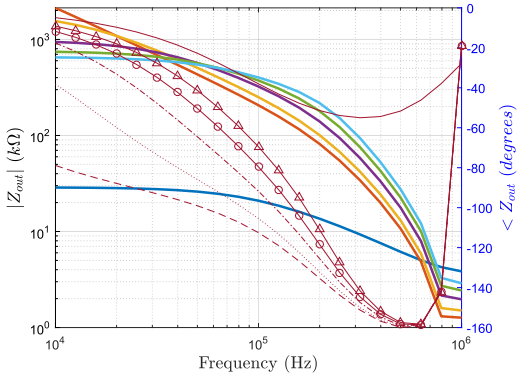

(γ′) Mirrored/ADA4625

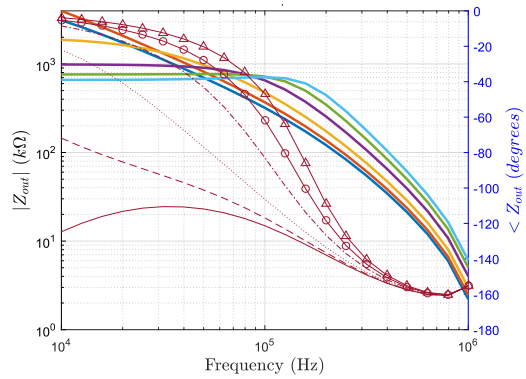

(δ′) Mirrored/OPAx210

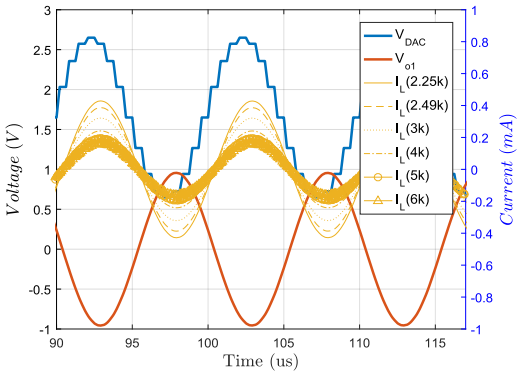

(ε′) Transient, Single-ended/OPAx210

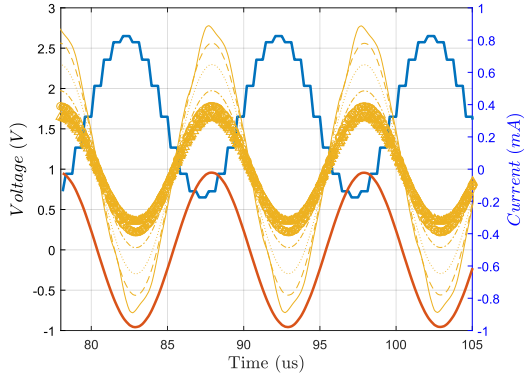

(ς′) Transient, Mirrored/ADA4625

Figure 6.2: Simulated performance (LT SPICE) of the Howland VCCS for selected values of R_8: (**a**)–(**d**): Magnitude and Phase (red thin lines) of z_{out} for Single-ended and Mirrored modified VCCS, using ADA4625/ OPAx210. (**e**)–(**f**): Transient simulations ($f_{in} = 100$ kHz) of the DAC output (produced with MATLAB code), the filter output (V_{o1}) and the load currents for parametric values of R_8.

In the literature, the first EIT systems developed in the late 1980s–early 1990s used single-ended current sources [27, 251]. Due to the degradation caused by the relatively low output impedance, combined with parasitic capacitances, calibration stages (negative impedances at first and Generalized Impedance Converters (GICs) later in the mid-2000 s) were used for the cancellation of stray capacitances and max-

imization of the $|z_{out}|$ [9, 156, 249, 252, 253, 266, 273]. This approach assisted on achieving superior output impedance values (up to 2 MΩ at 100 kHz [156]), allowing proper operation at frequencies up to1 MHz [9, 252, 253]. Small modifications have also been performed on the Howland VCCSs in order to prevent oscillations (capacitors parallel to the negative feedback [156]).Some other implementations included the mirrored VCCS [171, 274] or other approaches (Bragos) [217, 227]. In [227] the current imbalance between source and sink is addressed by measuring the current and adjusting its amplitude. Most of those systems are characterized by z_{out} from a hundred to several hundreds of kΩ at [10,100] kHz.

However, negative impedance circuits might suffer instability due to overcompensation of stray capacitance, [228]. Furthermore GICs need continuous calibration and are incapable of performing over large frequency spans simultaneously (limited bandwidth) [156]. Thus, often multiple GICs are essential, where each one covers a small specific frequency range. On the other hand, differential VCCSs need precise resistor matching with very low tolerances and cause higher white noise levels due to the large number (and values) of resistors used [274]. In each case, the designer has to estimate the pros and cons of his choice, taking into consideration the application targeted and its standards.

Equivalent Circuits

The subject circuit equivalent can be formed by transforming the FEM mesh along with its element admittance values to a N-electrode port RLC circuit. Nevertheless, apart from the examined volume's properties, it is important to include the effect of the electrode properties which contain: (a) their displacement and area, which affects the order of the measured impedance and (b) their contact impedances that need to be balanced and depend on the electrode material. The CEM described in Section 6.1.1, assists to this direction, since it considers about the electrode geometry and $z_{contact}$. However, in terms of this study, we included only the displacement in the FEM mesh; whereas the electrode equivalent circuit was simulated separately at LT SPICE before the N-port inputs, in order to observe each individual component's effect at the measurements, and not just the $z_{contact}$ value's one.

A. Electrode Equivalent

Briefly, the simplest electrode equivalent circuit model consists of a parallel combination of a resistor R_{ct} and an interface capacitance C_{cp} (actually a constant phase component), in series with a solution resistor R_s which indicates the impedance between electrode and subject's surface (skin) [267, 275]. More detailed electrode equivalent models can be found in [275, 276, 277]. In this particular study, simulations are reduced to 3D salted water tanks, therefore very small R_s values have been chosen (<2 Ω). In addition, crosstalk capacitances of less than 100 pF have also been included (see Fig. 6.3), representing the electrode lead wire capacitive effects as well as the multiplexer's stray capacitances. The parasitic effects caused by the electrodes, switches and lead wires can be greatly reduced with the usage of active electrodes [21, 171, 278]. However, an active electrode system implementation can highly increase the total hardware cost.

Subject Equivalent

Let as consider the simulated FEM system equation, which gives the nodal voltages U_i, for $i \in \{1, ..., n\}$ nodes:

$$\begin{bmatrix} \boldsymbol{A_m} + \boldsymbol{A_z} & \boldsymbol{A_v} \\ \boldsymbol{A_v^*} & \boldsymbol{A_D} \end{bmatrix} \begin{bmatrix} \boldsymbol{U} \\ \boldsymbol{V_l} \end{bmatrix} = \begin{bmatrix} \boldsymbol{0} \\ \boldsymbol{I^d} \end{bmatrix} \tag{6.9}$$

where $\boldsymbol{A_m} \in \mathbb{R}^{nXn}$ has resulted from the local element matrices assembling, $\boldsymbol{A_z} \in \mathbb{R}^{nXn}$ and $A_v \in \mathbb{R}^{nXN}$ from the boundary conditions (6.2)–(6.4) and $\boldsymbol{A_d} \in \mathbb{R}^{NXN}$ refers only to the nodes where the measurements are taken [36]. $\boldsymbol{V_l} \in \mathbb{R}^N$ indicate the measurements and $\boldsymbol{I^d}$ the current injected. Let us write $\boldsymbol{A_k} = \boldsymbol{A_m} + \boldsymbol{A_z}$. Then, by expanding the system (6.9):

$$\boldsymbol{A_k U} + \boldsymbol{A_v V_l} = \boldsymbol{0} \tag{6.10}$$

$$\boldsymbol{A_v^* U} + \boldsymbol{A_d V_l} = \boldsymbol{I_d} \tag{6.11}$$

Solving for the nodal potentials and the measurements we get:

$$\boldsymbol{U} = -\boldsymbol{A_k^{-1} A_v V_l} \tag{6.12}$$

$$\boldsymbol{V_l} = \boldsymbol{A_d^{-1} I_d} + \boldsymbol{A_d^{-1} A_v^* A_k^{-1} A_v V_l} \tag{6.13}$$

The last equation is written:

$$(\boldsymbol{I_{N \times N}} - \boldsymbol{A_d^{-1} A_v^* A_k^{-1} A_v})\boldsymbol{V_l} = \boldsymbol{A_d^{-1} I_d} \tag{6.14}$$

Therefore

$$(\boldsymbol{A_d} - \boldsymbol{A_v^* A_k^{-1} A_v})\boldsymbol{V_l} = \boldsymbol{I_d} \tag{6.15}$$

$\boldsymbol{F(\sigma)} = \boldsymbol{A_d} - \boldsymbol{A_v^* A_k^{-1} A_v}$ corresponds to the sparse and almost symmetric conductivity matrix considering each measuring point as a node [279]. Thus, the result is a N-port system, where each impedance between two nodes i and j is computed as: $Z_{ij} = -1/F(\sigma)_{ij}$ [280].

6.1.3 Data Acquisition

In order to get an EIT image frame, when using a current skip-i pattern and a voltage skip-j pattern [281], $N(N-3)$ measurements are conventionally needed if $i = j$ or $N(N-4)$ else. Each measurement is traditionally taken for a particular set up of current source, sink and voltage measuring electrodes. Between each couple of measurements, a transient effect takes place due to the analog multiplexer switching, the network's parasitic behavior and subject's admittance behavior. After those effects ceased the output signal comes to Steady-State (SS) and an integer number of periods has to be properly sampled by an ADC (as shown in Fig. 6.4).

SPICE EIT transient simulation is set as follows: the multiplexers' digital inputs are defined by PWL sources. The pulse rising times t_r have also been considered, according to the multiplexer's specifications

(ADG426). After each multiplexer's change, a t_{tr} time is inserted as the needed time to reach the SS. During t_{tr} the ADC can be initialized or send the previous samples to a DSP/MCU and set to the proper state to sample. t_{tr} usually lasts about 200–300 us and can be extended if the essential configurations have not already finished.

When t_{tr} ends, the corresponding T_{start} time point is written at a .txt file by MATLAB. Then follows the t_{sample} (conversion time) which is the time ADC needs to sample the output signal when at SS. It is recommended to be an integer number k (5 to 10) of the signal's period $T_{in} = 1/f_{in}$. After the sampling is finished, T_{stop} time point is written to the text file. t_c time (in the order of ns) is then needed for the multiplexers to get the order and change their state. For each measurement we have $T_{stop} - T_{start} = t_{sample}$ and the total time needed for the acquisition of a single measurement is:

$$t_{meas} = t_r + t_{tr} + t_{sample} + t_c \tag{6.16}$$

If a particular measurement is taken after a current source position change this duration is increased as follows:

$$t_{meas} = 2t_r + 2t_{tr} + t_{sample} + t_c \tag{6.17}$$

The total time when using pairwise injection protocol (adjacent/ skip-0) is:

$$t_{frame} = N^2(t_r + t_{tr} + kT_{in} + t_c) - N(2t_r + 2t_{tr} + 3kT_{in} + 3t_c) \tag{6.18}$$

t_{frame} obviously depends on the electrode number N, the input signal frequency f_{in} and the ability of the ADC to send the samples quickly to the MCU. It is assumed that any post-acquisition signal processing is performed after the acquisition process has been completed.

The output voltage signal V_{out} is sent to MATLAB after the SPICE transient simulation has ended. Then sampling is performed between each T_{start} and T_{stop} time point, using a cost minimization function between the desired and the actual sampling times, since SPICE simulators do not use constant time steps. Only the first 14 Most Significant Bits (MSB) out of 16 bits of the simulated ADC are used (ENOB), since the two Least Significant Bits (LSBs) are considered as noisy and distorted.

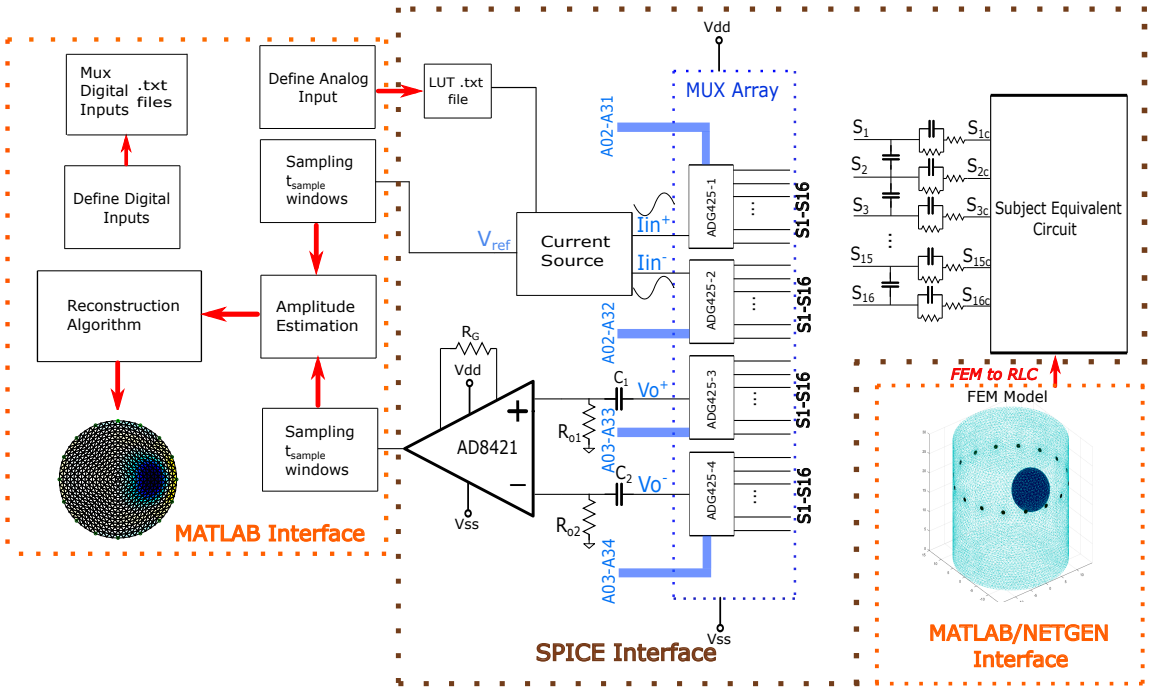

Figure 6.3: Complete EIT process from phantom to imaging.

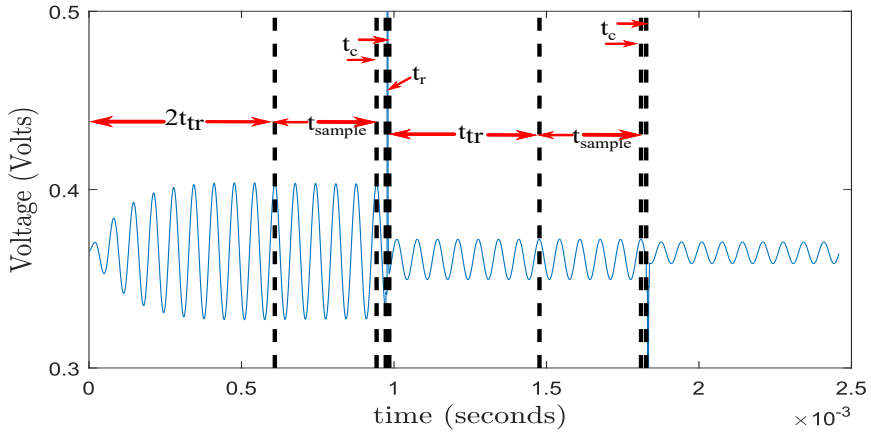

Figure 6.4: Explanatory graph of the acquisition times pipeline.

For each measuring window $m \in \{1, ..., N(N-3)\}$ an amplitude is obtained by the difference of the medians between the five maximum and the five minimum voltage values from the ADC sampled voltage values $V_{o,new}$. The amplitude values are stored in the $Amplitudes(m)$ vector, which is usually normalized, by setting its maximum value to 1. $Amplitudes(m)$ vector is then utilized as raw data for the image reconstruction. In order to get a reliable result from the process described above, it is strongly recommended that $f_s << f_{SPICE\_min}$, where f_{SPICE_min} is the minimum SPICE sampling frequency,

which is defined as the inverse of the maximum SPICE time step.

6.1.4 EIT Simulations and Results

Structures

In this work, a 3D cylindrical tank FEM model attached around with 16 electrodes has been used as an input for the subject equivalent circuit. Each image frame occurs from the measurement difference between two cases (differential EIT, used for either time differential (td-EIT) and frequency differential (fd-EIT)): (a) the reference, which in this case is taken on an almost homogeneous water-salt tank and (b) the inhomogeneous or final, where a plastic -non conductive- object has been inserted in the tank. Furthermore, the FEM model has the following characteristics: height of h = 30 cm, radius R = 15 cm and circular electrodes of r_{el} = 0.5 cm radius attached at $z = h_{el}$ = 20 cm. The model contains a total of 48080 nodes and 254,475 elements and was constructed in MATLAB with the NETGEN mesh tool. The plastic spherical object's centre was put at C_{sphere} = (6.5, 0, 15) cm and its radius was selected to be r_{sphere} = 5 cm.

The conductivity value set to each element in the sphere was $\sigma = 10^{-4} S/m$. For the water with sodium chloride conductivity 2 cases have been introduced: (a) a low salt concentration where each out-of-sphere element has a σ with follows a normal distribution of $\mu = 0.08$ and $var = 16 \times 10^{-4}$. (b) A moderate salt concentration where the normal distribution of σ has $\mu = 0.2$ and $var = 4 \times 10^{-3}$. The values were chosen based on the fact that drinking water has $\sigma < 0.05 S/m$ and sodium-chloride natural and sea water conductivity measurements under constant temperature (approx. $25^o C$) have a variability range of $2 - 5\%$ [282, 283, 284]. Figure 6.5 b,c show the conductivity defined at each element for both cases, when plastic object is inserted.

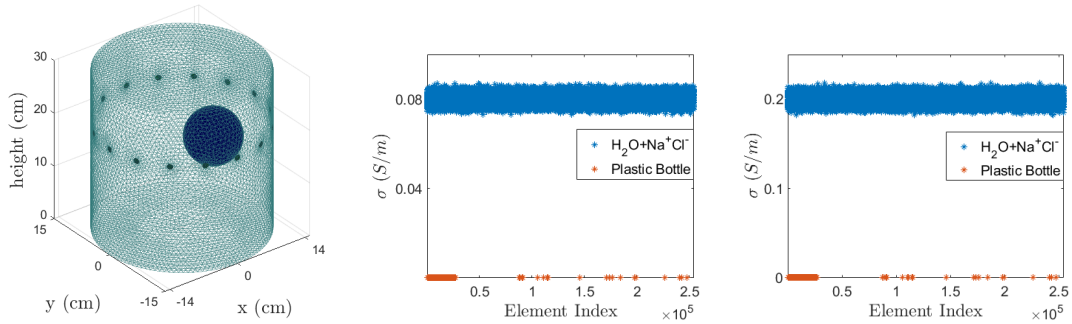

(α′) Finite Element Model (β′) Low Salt σ distribution (γ′) High Salt σ distribution

Figure 6.5: (**a**) 3D Phantom FEM structure model (**b**) Low salt conductivity distribution (**c**) Moderate salt conductivity distribution per element.

6.1.5 Test Cases

At all the test cases (T1–T4), the adjacent skip-0 current pattern [281] was used, along with the NOSER one-step reconstruction algorithm, with a heuristically selected hyperparameter $\lambda = 0.3$. For

the inverse model (where the image reconstruction is performed), a circular point electrode model which includes 1024 equal sized triangular elements was selected. The input signal frequency was $f_{in} = 15$ kHz and $f_{in} = 100$ kHz. The DAC was simulated with $L = 16$ bits (ENOB 14) and $f_s = 16 f_{in}$.

FEM Simulation (T1a-b): Firstly, an EM measurement simulation was performed with the EIDORS library tool in MATLAB [72], by directly solving the forward model of the two structures described before. The simulated measurements were used as inputs to the inverse problem. This test shows the imaging algorithm's performance and demonstrates the measurements behaviour assuming optimal hardware functionality. Therefore, its results (T1a for low Na^+Cl^- concentration and T1b for moderate Na^+Cl^- concentration), shown in Figure 6.6a–b, are used as a reference for the following test cases.

Single-Ended Current Source (T2a–d): A hardware simulation test was performed for the 2 Na^+Cl^- concentrations at $f_{in} = 15$ kHz using the grounded load modified Howland VCCs described in Section 6.1.2. For the acquisition the ADC was assumed to operate at $L = 16$ bits, $V_{ADC} = 3.3$ V with $f_s = 240$ ksps and $f_s = 1$ Msps. The corresponding images are displayed in Figure 6.6c–f.

Mirrored Current Source (T3a-h): These simulations were also executed for the 2 structures described in Section 6.1.4, for $f_{in} = 15$ kHz (T3a-d) with the same ADC properties as in (T2) and for $f_{in} = 100$ kHz (T3e–h), with ADC simulated at $L = 16$ bits with $f_s = 1$ Msps and $f_s = 2$ Msps. Although the Na^+Cl^- properties do not significantly change in the frequency range of [10,100] kHz (something that does not apply to soft human tissues), the currents source's z_{out} is significantly reduced as shown in Section 6.1.2. Therefore, more errors are expected to be introduced at the measurements. The results are shown in Figure 6.6g–n.

Disconnected electrode, imbalanced $z_{contacts}$ (T4a-b): A final Spice simulation was performed for the case of disconnection at the 10th electrode (R_s was set to 1.5 MΩ) and increased solution resistances at 3rd and 5th electrodes (about 10 times the other electrodes' R_s). f_{in} was set to 15 kHz, the mirrored VCCS topology was acted and the 16 bit simulated ADC was sampling at $f_s = 240$ ksps.

At each testcase T2–T4, a -55 dB SNR white noise was directly added to Spice output signals before the ADC acquisition.

6.1.6 Error Estimation

Since the purpose is to estimate the error introduced exclusively from EIT hardware, the measurements simulated and the images produced for the T1 test case are utilized as the desired values. At this point it is important to note that in order to perform a valid comparison, all cases have to be treated with the same reconstruction algorithm parameters, defined in Section 6.1.5. It is also necessary to have all values normalized. The Mean Absolute Percentage Error (MAPE) is defined as:

$$MAPE_{Meas} = \frac{1}{M} \sum_{i=1}^{M} \left| \frac{V_{di} - V_{ei}}{V_{di}} \right| \cdot 100\% \tag{6.19}$$

Where V_d is the measurement vector from the direct FEM simulation (case T1) and V_e the measurements from the hardware simulations after the acquisition process (cases T2–T4). In addition, M is the total number of measurement values per frame (i.e., $M = 208$).

The corresponding $MAPE$ for the reconstructed images is defined by the following equation:

$$MAPE_{Imag} = \frac{1}{K}\sum_{i=1}^{K}\left|\frac{\sigma_{di} - \sigma_{ei}}{\sigma_{di}}\right| \cdot 100\% \tag{6.20}$$

Where σ_d is the normalized σ (for absolute imaging) or difference σ vector (for difference imaging) resulted from the FEM simulated measurements (case T1) and σ_e is the corresponding vector resulted from the hardware parametric simulations (cases T2–T4). K is the number of elements used in the inverse model (i.e., $K = 1024$). Both MAPE errors are shown in Table 6.2.

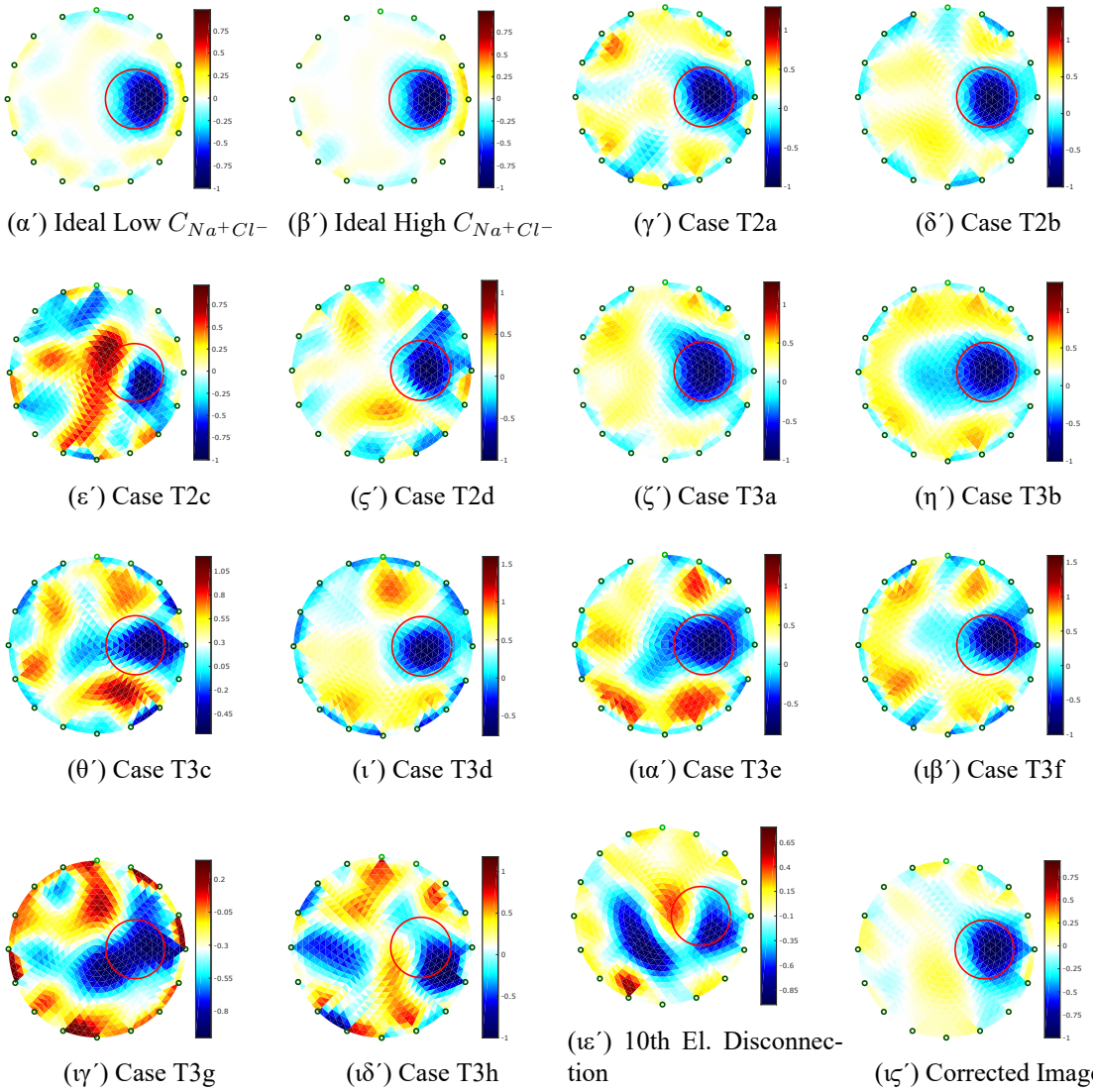

Figure 6.6: EIT image reconstructions. (**a**)–(**b**): Ideal cases (from FEM simulated measurements-Case T1). a): Low salt concentration, b): Moderate salt concentration. (**c**)–(**f**): Single-Ended VCCS for $f_{in} =$ 15 kHz (cases T2a–T2d).(**g**)–(**j**): Mirrored VCCS for $f_{in} = 15$ kHz (cases T3a–T3d). (**k**)–(**n**): Mirrored VCCS for $f_{in} = 100$ kHz (cases T3e–T3h). (**o**)–(**p**): Corrupted image due to 10th electrode disconnection (o) and modified image (p). The target object is indicated with a red circle.

Table 6.2: Simulation parameters and Mean Absolute Percentage Errors (MAPEs) measured for cases T2–T4. In the VCCS cell, "SE" means Single-Ended and "M" Mirrored.

$Case$	$T2a$	$T2b$	$T2c$	$T2d$	$T3a$	$T3b$	$T3c$
$C_{Na^+Cl^-}$ (Low/High)	Low	Low	High	High	Low	Low	High
VCCS (SE/M)	SE	SE	SE	SE	M	M	M
f_{in} (kHz)	15	15	15	15	15	15	15
f_s (kSps)	240	1000	240	1000	240	1000	240
$MAPE_{Meas}$ (%)	12.94	11.62	53.37	33.77	9.31	7.03	25.14
$MAPE_{Imag}$ (%)	219.66	163.70	845	337	234.83	145.47	190.45
$Case$	$T3d$	$T3e$	$T3f$	$T3g$	$T3h$	$T4a$	$T4b$
$C_{Na^+Cl^-}$ (Low/High)	High	Low	Low	High	High	Low	Low
VCCS (SE/M)	M	M	M	M	M	M	M
f_{in} (kHz)	15	100	100	100	100	15	15
f_s (kSps)	1000	1000	2000	1000	2000	1000	1000
$MAPE_{Meas}$ (%)	18.46	19.76	17.60	55.03	48.67	200.86	94.55
$MAPE_{Imag}$ (%)	196.24	437	242.11	328	284.86	325	221.02

We also introduce the Reciprocity Error (RE) for each homogeneous measurement set:

$$RE = \left| \frac{u(i,j)_{I(m,n)} - u(m,n)_{I(i,j)}}{u(i,j)_{I(m,n)}} \right| \cdot 100\% \tag{6.21}$$

where $u(i,j)_{I(m,n)}$ is the voltage difference between electrodes i and j when current is injected from electrodes m and n [156, 226].

Image Correction

In case the measurements are corrupted due to issues that are correlated with bad electrode contacts, disconnections or ever short-circuited lead wires, it is possible to correct the output image, provided there is knowledge of the erroneous electrodes. Then, the weight matrix W (see Section 6.1.1) can be properly corrected so that the inverse problem will not take into account any measurement correlated with those electrodes [285, 286].

Results

The (normalized) difference conductivity distributions $\delta\sigma$ estimated for each particular case described in the previous section are displayed in Figure 6.6. The structures used for the simulations were described in Section 6.1.4. For the filter and the VCCS parts of the hardware the ADA4625 Opamp was finally selected, since the utilization of numerous OPAx210 Opamp models simultaneously with the whole circuitry caused instability to Spice simulations. Due to each testcase's various parameters, each of them is indi-

cated at Table 6.2 for clarity, along with the corresponding $MAPE$ errors estimations. In Figure 6.7 the (normalized) inhomogeneous amplitude measurements for the 1st structure cases (low salt concentration) are also displayed, along with the Diametric Conductivity Plot (DCP) for both $Na^{+}Cl^{-}$ concentrations [287]. Figure 6.8 displays the reciprocity percentage errors estimated for each testcase T2a–d and T3a–h. All results are discussed in the next section.

6.1.7 Discussion

From the simulations described, it is observed that both the reconstructed image artifacts and the measurement and imaging errors along with RE are potentially decreased in cases when high-z_{out} VCCS and high-f_s ADC are combined. Specifically, the minimum errors are obtained in test case T3b (Figure 6.6h shows the object completely in the red circle), where we used a mirrored Modified Howland VCCS with a z_{out} estimated just over than 1 MΩ at $f_{in} = 15$ kHz according to the results in Section 6.1.2. Furthermore, the f_s is 1 MSps which is over 64 times the input signal frequency f_{in}. The corresponding RE was estimated at 0.81% (pointed with a green triangle in Figure 6.8). That satisfies the EIT literature hardware standards ($RE < 2\%$ for typical performance, $RE < 1\%$ for high performance) [9, 156, 226].

When the input signal frequency (f_{in}) is increased to 100 kHz and measurements are taken at the same structure, the mirrored VCCS z_{out} is decreased to 400 kΩ, causing current distortion. Moreover, the sampling rates of 1 MSps and 2 MSps cannot be characterized as oversampling when $f_{in} = 100$ kHz. This results in larger measurement errors (case T3f in Figure 6.6l where the case of $f_{in} = 100$ kHz exhibits greater error than case T3b in Figure 6.6d where $f_{in} = 15$ kHz, while both tests use Mirrored VCCS; same happens with cases T3d and T3g). Overall, increasing the input frequency from 10 kHz to 100 kHz causes a measurement SNR reduction from 5 dB [253] to 20 dB [156] at implemented hardware EIT systems, resulting in a corresponding image quality reduction[156].

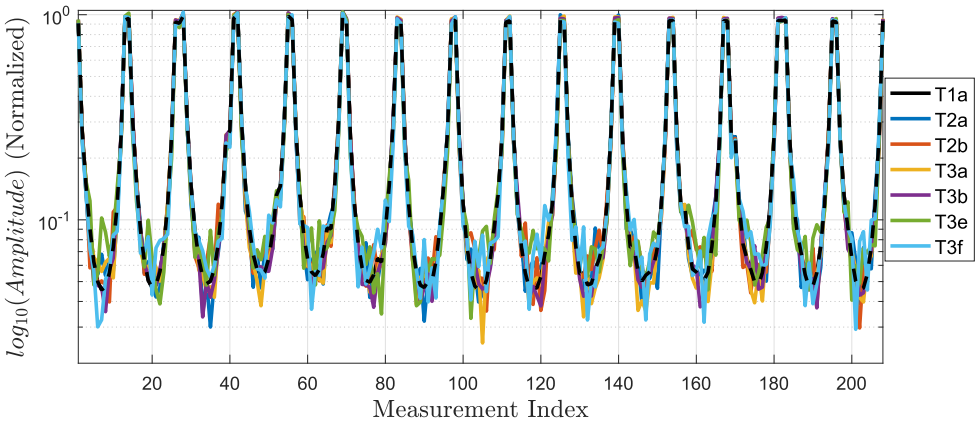

(α′) Low salt concentration background inhomogeneous measurement sets.

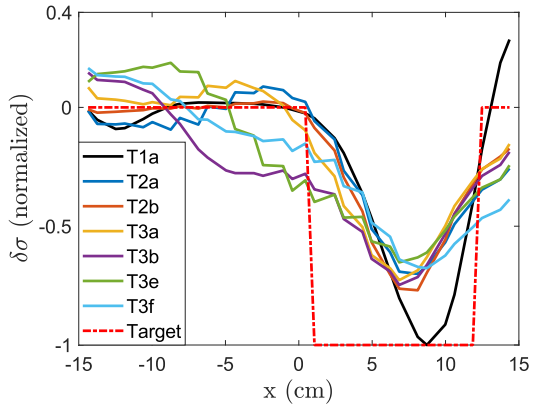

(β′) DCP for low salt concentration

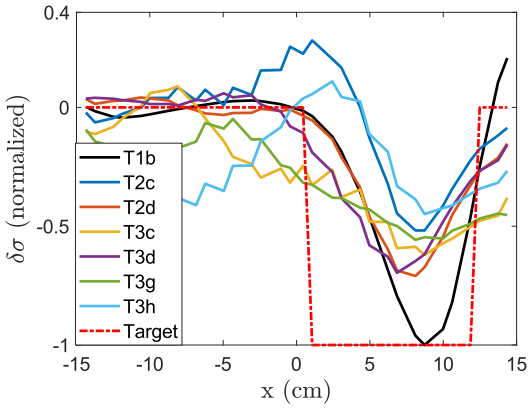

(γ′) DCP for high salt concentration

Figure 6.7: (**a**): Logarithmic values of the measurement ($M = 208$) amplitudes for the low sodium chloride concentrations test cases. (**b**)–(**c**): Diametric Conductivity Plots (DCP) for the 2 sodium chloride concentrations and the corresponding test cases. The target corresponds to the object's circle's (Figure 6.6) diameter.

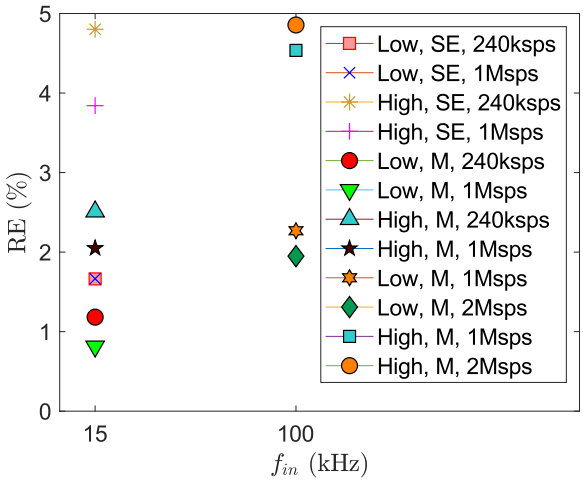

Figure 6.8: Average Reciprocity Errors for cases T2a-d (SE) and T3a-h (M).

In addition, when increasing $Na^{+}Cl^{-}$ concentration in the water, the mean value and range of the background's σ is increased (see Figure 6.5b and c). This results in lower impedance values between each electrode channel and thus very small measuring amplitudes. Even with a $54\ dB$-gain instrumentation amplifier (an AD8421 with R_G = 20 Ω), the measured amplitudes barely reach the value of 1mV when the measure is performed far from the current injected electrodes. Taking into account the signal's noise and the ADC's capabilities, the raw voltage input to the reconstruction algorithm suffers from very low SNR. This has an obvious impact on the $MAPE_{Meas}$ and $MAPE_{Imag}$ values as shown in Table 6.2 and the imaging precision and quality as shown in Figure 6.6: Low $C_{Na^{+}Cl^{-}}$ cases (T2a, T2b, T3a, T3b, T3e, T3f) have been reconstructed with greater success than the high $C_{Na^{+}Cl^{-}}$ ones: (T2c, T2d, T3c, T3d, T3g, T3h); the results are independent of the hardware specifications used in the simulations. Since the measurement accuracy has been reduced, the RE has increased accordingly, reaching the unacceptable for typical EIT design levels of $4-5\%$ (see the 4 highest values in Figure 6.8). However, in the literature RE is measured at homogeneous saline tanks of $\sigma = 0.05S/m$ to $0.1S/m$ [9, 156, 226]; a value much lower than the current value of $0.2S/m$. Therefore, the low salt concentration RE levels are more representative for the hardware's performance. It is also confirmed that higher measurement errors generally lead to higher imaging errors. However, this relation is not proportional; it is rather characterized by a non-linearity which is correlated to the inverse problem's non-linear nature.

The Diametric Conductivity Plots (DCP, Figure 6.7b–c) show that most cases detect the decreased conductivity in the red circle area. However, the reconstruction algorithm is not able to properly centralize the minimum conductivity point of the target (which occurs at x = 6.5 cm), even at the EM simulation (test case T1). This can be explained by the 3D nature of our set-up; the target object is located some centimeters down from the electrode slice (z-layer). Therefore, the currents streamlines go through longer distance in the field until they come across the plastic object and change direction. This results in a deviation between the object's detected position and the actual horizontal position. Moreover, artifacts occur for $x < 0$ cm, where the actual conductivity change $\delta\sigma$ is negligible. The $\delta\sigma$ in most cases follows the corresponding $MAPE_{Meas}$ and $MAPE_{Imag}$, since (as referred earlier) larger deviations in measurements

lead to further imaging artifacts. A hard exception occurs for the T3b case (Mirrored VCCS, low salt concentration, $f_{in} = 15$ kHz, $f_s = 1$ MSps), where despite featuring the least erroneous measurements and the minimum $MAPE_{Imag}$, it has a modest DCP error. However, an observation of the corresponding image reconstruction (Figure 6.6h) shows that the total image artifacts are less intense than most other cases where f_{in} is larger and f_s smaller. Besides, the red circle area identifies the low conductive blue one.

Examining the test case T4, it is shown (Figure 6.6o) that due to an electrode disconnection the reconstruction completely fails: the target object cannot even be distinguished. However, a-priori knowledge of the structure's behavior (a non-conductive object is supposed to appear near the red circle), combined with careful examination of the image leads to the hypothesis that there is a major error near the electrodes 9–10. Properly modifying the measurement weight $\boldsymbol{W}$ matrix, we get a new measurement set, fully uncorrelated with electrode 10, which contains 156 measurements instead of the initial set of 208 measurements. The improvement in Figure 6.6p is significant, since the majority of artifacts has been erased. For case T4b, the $MAPE_{meas}$ was estimated using only the 156 valid measurements. Thus, the RE was not estimated for this test case.

In general, the design of an EIT hardware system is a process where numerous parameters have to be taken into consideration and the specifications are deeply depended on its application field. For instance, a real-time thoracic-imaging EIT system needs to be characterized by very high framing speed [21, 171]; this requires higher current signal frequencies, in order to accelerate the acquisition pipeline described in Section 6.1.2. This leads to the necessity of designing a high-z_{out} VCCS over a large frequency range; moreover, the designer must combine the high-performance VCCS with an ADC with high throughput rates. Another example is a brain-imaging EIT system, where lower frequencies are utilized; however, due to the skull's very large impedance the $z_{contact}$ dramatically increases and the current source should be capable of driving much higher impedances [228].

In all cases, the use of single-ended Howland current pumps without any negative impedance calibration or calibration via current amplitude measurement should be avoided. On the other hand, if the designer chooses a mirrored Howland architecture he must consider carefully the resistors matching and the amount of Johnson noise (trade-off between balance succeeded with high valued, low tolerance resistors and low noise achieved by low value resistors). Furthermore, the ADC sampling rates are strongly recommended to exceed the signal's frequency over 10 times, a condition that has been adopted by most EIT systems [4, 21, 171, 226, 253]. Both factors (high z_{out}, acquisition rates) have a significant impact on the measurements quality.

6.2 SPICE and MATLAB simulation and evaluation of Electrical Impedance Tomography readout chain using phantom equivalents

In this subchapter, a fastidious EIT simulation model which is evaluated in SPICE and MATLAB softwares is presented. This model merges the analog circuitry stages, a subject resistive equivalent acquired from a Finite Element (F.E.) mesh and the digital readout chain interface. Transient simulation values

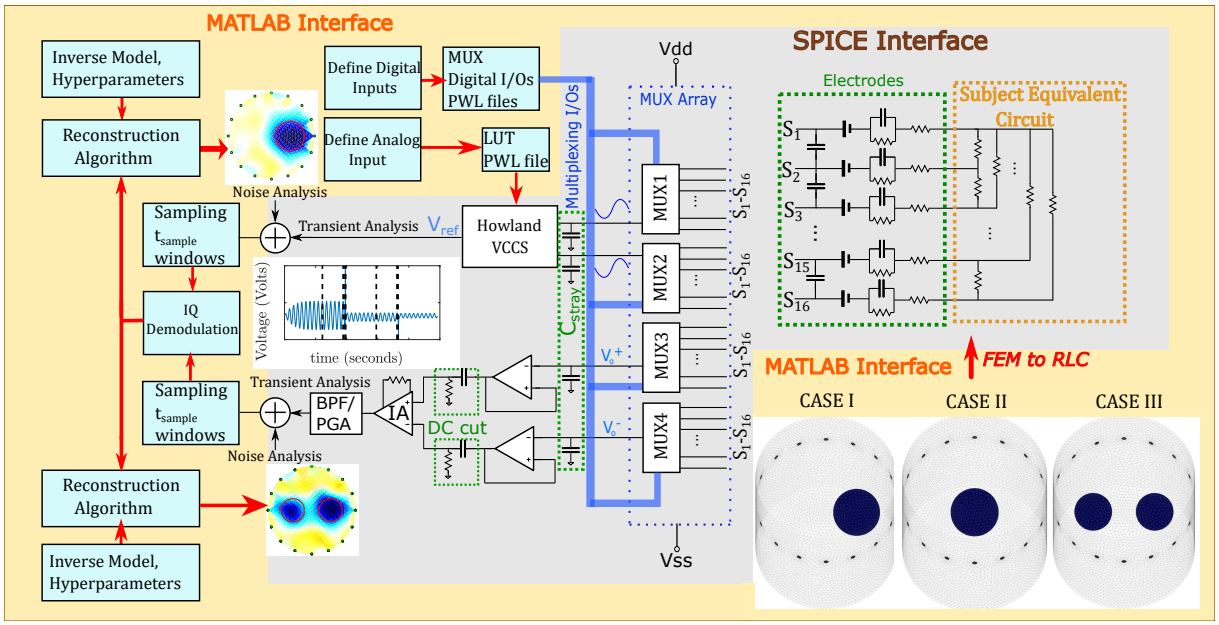

Figure 6.9: Explanatory schematic of the EIT system simulation model described.

are transfered to MATLAB, which simulates the ADC and DSP function and performs the image reconstructions. Preliminary descriptions of this model are presented in [267] and [264]. This work extends these previous studies to three directions: A) the skip-3 measuring pattern is simulated in addition to the adjacent that is exclusively acted in the prior work, B) IQ demodulation in the digital domain is included instead of the highly erroneous amplitude estimation and C) Total analog circuitry noise is calculated via SPICE and added to the transient signal, instead of setting an arbitrary signal SNR that corresponds to the majority of EIT systems. Such simulations can be proved as a useful tool for the evaluation of both EIT design parameters and inverse reconstructing algorithms.

6.3 EIT System Simulation Model

The EIT simulation model is implemented in LT SPICE, while the digital signal processing and imaging is performed via MATLAB software. The analog circuitry includes a Howland Current Pump (HCP), which drives an ac current to the electrodes through a $4-to-16$ multiplexer array. The voltage recording part includes a differential signal path, containing buffers in series with DC cut high-pass filters and an instrumentation amplifier. The properly amplified signal is sent to MATLAB for processing. The SPICE model also includes RC electrode models in order to simulate the contact impedances. The circuitry is described in detail in [264]. In this paper, a differential, 0.1% tolerance resistor HCP is utilized, however, the Spice interface allows to test alternative topologies for both the HCP and the voltmeter, without loss of generality.

In addition to the analog circuitry, a subject N-port equivalent resistive circuit is added and connected to the N electrodes (16 for this work). This comes from the transformation of the forward F.E. model that simulates the phantom [264].

6.4 Digital Signal Processing

The analog circuit inputs and outputs are handled by MATLAB in order to simulate the sampling and imaging process.

6.4.1 Digital Inputs

A 16-bit, 240kSps Digital-to-Analog Converter (DAC) is simulated in MATLAB and a PWL file that contains the sinusoidal signal is loaded from LT Spice. The multiplexers' digital signals are also created in MATLAB, according to the measuring pattern and the estimated simulation time [264].

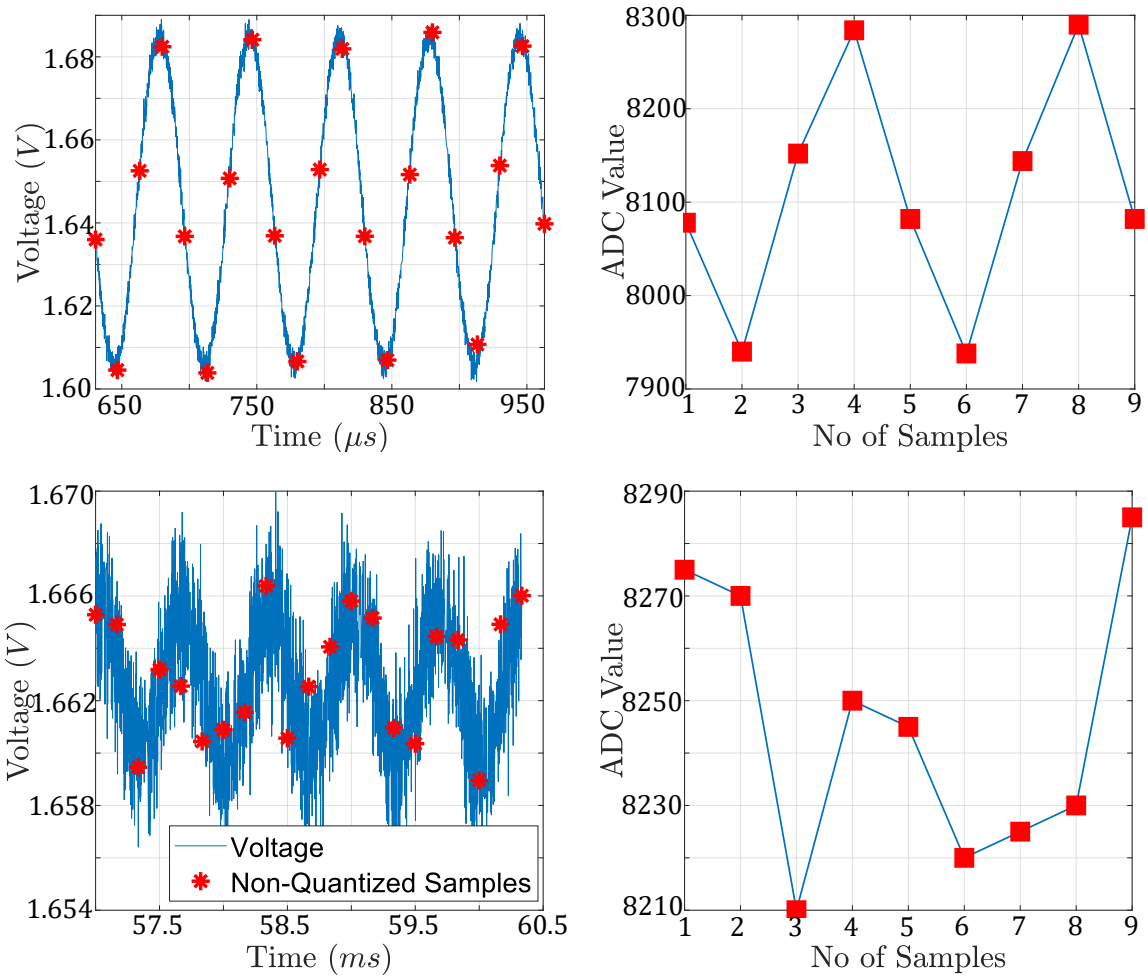

Figure 6.10: SPICE transient signal example with noise included (left column). Current is injected from electrodes 1 and 2. The quantized signal for the first two periods is demonstrated at the right column. The first row shows a measurement taken from electrodes 2 and 3, while the second row displays a measurement from electrodes 8 and 9, furthest away from the current source. Therefore, the second signal's amplitude is much smaller, while it suffers from the same noise amplitude and thus presents a reduced SNR.

6.4.2 ADC Sampling

The SPICE transient output .txt file is transferred to MATLAB and noise is added to it by integrating the PSD simulated in Spice. The ADC function is then simulated in MATLAB as follows. Sinusoidal steady state sampling windows are defined after each transient effect due to switching. A total of $N(N-3)$ measurement windows per frame are needed for the adjacent current pattern or $N(N-4)$ for other skip protocols [26]. Since the SPICE signal is actually discrete, with non-constant time steps, optimal Spice output sampling points are selected at each window, according to the sampling frequency f_s [264]. Then the samples are properly quantized (Fig. 6.10). An integer number N_T of periods is sampled every time, hence f_s needs to be an integer multiplier of the signal's frequency. The simulated ADC is assumed to be 16 bit (14 bit ENOB).

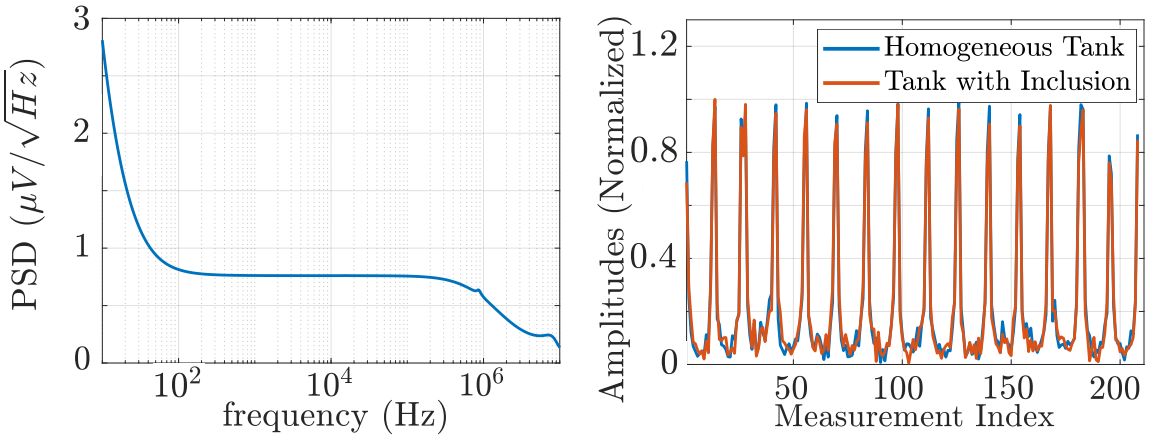

Figure 6.11: Left: Power Spectral Density (PSD) SPICE noise simulation of the analog circuitry, for 1mA current and 46dB instrumentation amplifier (IA) gain, at the IA output. Right: Homogeneous and inhomogeneous voltage amplitude measurements for adjacent pattern, $f_s = 4f_{max}$ and two sampling periods (averaging) per measurement.

6.4.3 IQ Demodulation

The most applicable EIT systems use IQ demodulation in order to isolate the signal's amplitude and phase and reconstruct more reliable images. It has been proved that IQ leads to more accurate results when performed at the digital domain with matched low-pass filters [170]. In this paper, this feature is added to the simulation model presented in [264]. The sampled voltage output and input Spice signals are quadratically interpolated and elementwisely multiplied. From the input signal, which is recorded by measuring the voltage across a sensing resistor in series with the HCP, a 90^o shifted digital signal is obtained at each measuring window and also multiplied elementwisely with the corresponding output. In order to acquire the dc components ($cos\phi$ and $sin\phi$) of these multiplications, 10th order matched low-pass filters characterized by an $L = \frac{N_T \cdot f_s}{f}$ samples length Kaiser window and a cutoff frequency $f_c = 100$Hz are utilized. A group delay is calculated for each window and the mean of the rest of the samples is recorded as an IQ measurement. All the process is performed in MATLAB, with the sampled

signals acquired from the previous DSP function.

6.4.4 Simulations and Results

In order to test the simulation interface described, as well as to compare some measuring parameters' performance in imaging, 3 phantom testcases are specified. For all the testcases, a cylindrical F.E.M. simulation tank with a $h = 30$ cm height and $R = 15$ cm radius is used, attached perimetrically with $N = 16$ electrodes of $r_{el} = 0.5$ cm radius at layer $z_{el} = 20$ cm. The tank is filled with salty water of $\sigma = 0.08$ S/m mean conductivity and 2% std (standard deviation) [264].

In the first case, a $\sigma = 0.1$ mS/m, $r = 5$ cm radius non-conductive sphere is placed in the tank. The sphere's centre is located at $(x, y, z) = (6.5, 0, 17.5)$ cm. In the second case, the same sphere is placed at the tank's centre, located in $(x, y, z) = (0, 0, 17.5)$ cm. Finally, in the third case, two 4 cm non-conductive spheres ($\sigma = 0.1$ mS/m) are placed at $(x_1, y_1, z_1) = (-6.5, 0, 17.5)$ cm and $(x_2, y_2, z_2) = (6.5, 0, 17.5)$ cm respectively. The purpose of these placements, displayed in Fig. 6.9, is to observe single object cases at the boundary and the centre, as well as two symmetric object cases.

All 3 cases are tested for adjacent (current injected at neighboring electrodes) and skip-3 (3-electrodes gap between the current injecting electrodes) current protocols [26]. Voltages are differentially measured between adjacent electrodes. The current frequency is selected at $f = 15$ kHz, while the ADC samples at $f_s = 60$ kHz (OSR=4) or $f_s = 240$ kHz (OSR=16). Furthermore, the sampling windows' lengths per measurement (between two multiplexing switches) are selected at $N_T = 2$ periods and $N_T = 4$ periods. Therefore we examine a total of 24 image reconstructions. It has been shown that the acquired signal amplitude SNR, when performing averaging is: [169]

$$SNR = 10log_{10}\left(\frac{A^2(L/2)}{\frac{V_{ref}^2}{12\cdot 2^{2b}} + \sigma_n^2}\right) \tag{6.22}$$

where A is the mean signal amplitude, L the number of matched filter taps, V_{ref} the ADC voltage range (3.3 V simulated here), b the ADC resolution (bits) and σ_n the circuit noise std. The estimated SNR values from homogeneous tank measurements are shown in Table 7.15. It is shown that increasing either f_s or L gives a significant boost to the SNR. Furthermore, when the skip-3 current pattern is adopted, the SNR is slightly better due to the higher amplitude signals acquired relatively to the adjacent pattern, while both thermal and flicker noise do not change.

Table 6.3: Calculated SNR values (dB) for each measuring parameter case, according to (6.42).

f_s	N_T	skip-0	skip-3
$4f$	2	30.0	37.5
$4f$	4	33.0	40.5
$16f$	2	36.0	39.0
$16f$	4	43.5	46.5

The difference image reconstruction is performed using a single-step Gauss-Newton reconstruction

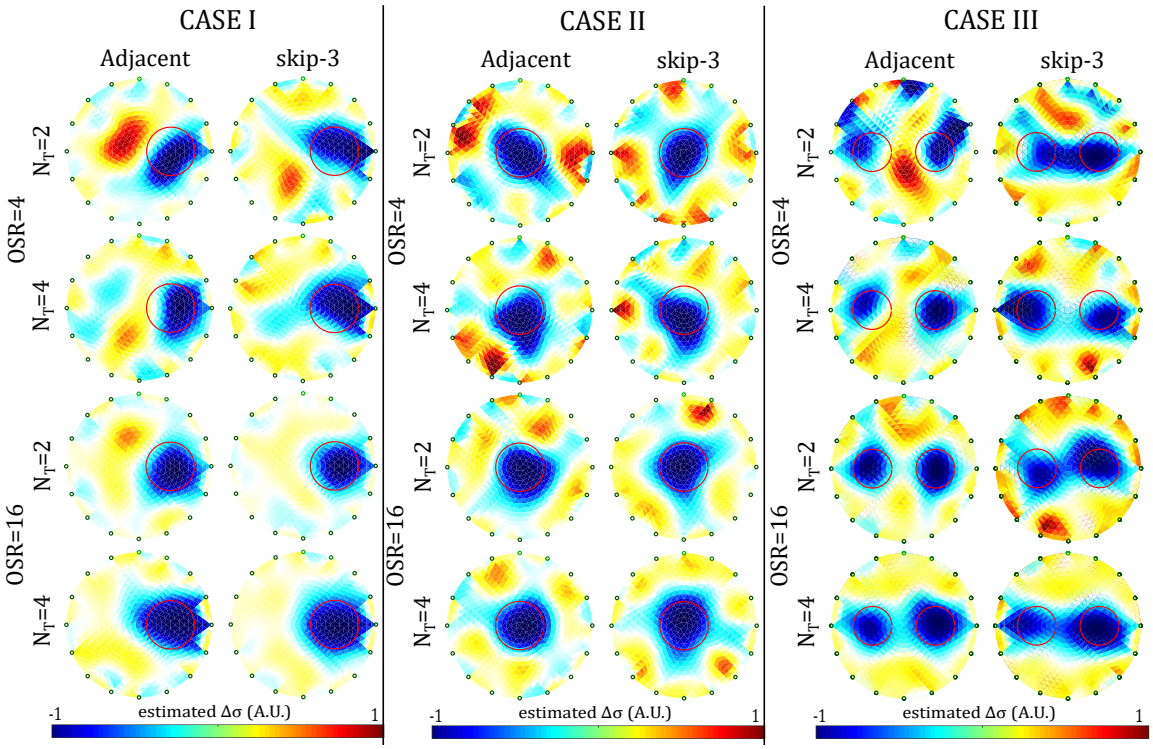

Figure 6.12: Reconstructed EIT images for the 3 cases and the measuring parameters described.

algorithm, that uses a Laplace prior and a heuristically selected hyperparameter of $\lambda = 0.3$ that regularizes the inverse problem's least squares term [151]. Without loss of generality, other reconstruction algorithms could be used as well, such as iterative Gauss-Newton, D-Bar or other priors (Tikhonov, NOSER, Total Variation), however the point is to test the conditions under a common approach. The reconstruction domain is a circular F.E. mesh, containing 545 nodes and 1024 elements. All reconstructed images are displayed in Fig. 6.12.

A quantitative evaluation of the resulting images is achieved by using the Correlation Coefficient (CC), expressed as [288]:

$$CC = \frac{Cov(\sigma_{true}, \hat{\sigma})}{\sigma_{\sigma_{true}} \sigma_{\hat{\sigma}}} \tag{6.23}$$

where σ_{true} is the real conductivity, $\hat{\sigma}$ is the estimated conductivity, Cov the covariance between true and estimated values and σ the values std. CC is 1 when no artifacts take place and is presented for all cases in Table 6.7.

The reconstructed images show that the inclusions are properly detected, except from the 1st raw cases ($N_T = 2, OSR = 4$). Increasing f_s and N_T overall lead to better imaging results qualitatively and quantitatively for both tested current patterns. An exception occurs for the Case III between $N_T = 2$ and $N_T = 4$ conditions when $f_s = 4f$ and adjacent protocol is utilized, which can be attributed to the noise randomization. Although the skip-3 current pattern offers less measurements (192) than the adjacent one (208), it is more effective in cases I and II, since it leads to higher SNR and larger field sensitivity near

the domain's centre. In addition, the extracted CCs in general terms follow the corresponding SNR values (Table 6.3) for each f_s and N_T combination. We note that taking advantage of a larger fraction of the ADC's dynamic range (by further amplifying the signal), as well as taking more samples per measurement (i.e. increasing N_T, which however would critically reduce the fps rate for real-time applications) can lead to significantly better images. However, in this particular study we are focusing on simulating the behavior of generic EIT systems, including the analog, digital and subject domains, either than performance optimization.

Table 6.4: CC of the EIT images, demonstrated in Fig. 6.12.

f_s	N_T	CASE I skip-0	CASE I skip-3	CASE II skip-0	CASE II skip-3	CASE III skip-0	CASE III skip-3
$4f$	2	0.61	0.63	0.65	0.69	0.40	0.55
$4f$	4	0.60	0.66	0.61	0.63	0.62	0.58
$16f$	2	0.75	0.73	0.70	0.75	0.76	0.58
$16f$	4	0.81	0.78	0.77	0.73	0.70	0.63

6.5 Evaluation of Thoracic Equivalent Multiport Circuits Using an Electrical Impedance Tomography Hardware Simulation Interface

Electrical impedance tomography (EIT) is a low-cost imaging technique which applies a 1 kHz–1 MHz frequency low amplitude electrical current to a subject under test (SUT) and collects the measured voltages from an electrode cluster [4, 5]. Then, an estimation of the SUT internal conductivity distribution is performed through a set of inverse algorithms [174]. Although EIT is characterized by critically low spatial resolution compared to X-ray, CT, and MRI, it has the advantages of the absence of ionizing radiation, patient safety, low hardware cost (20 to 100 times compared to a CT scanner), and high speed. High frame rates lead to significant temporal resolution, which makes EIT suitable for applications that need real-time monitoring, such as thoracic and ventilation imaging [21, 174, 200].

EIT's spatial resolution, however, might be further limited by signal noise, since the EIT inverse problem is ill-posed and ill-conditioned [155]. Image artefacts that appear are also related to common signal effects, usually caused from mismatches in the current source and between the electrode channels, combined with limited common mode rejection ratio ($CMRR$) at the voltage recording circuitry [200, 227]. In addition, signal degradation due to the channels' or IC's stray capacitances is a factor that reduces the image quality, especially at frequencies above 100 kHz.

In the case of real-time (dynamic) thoracic imaging, these effects are more intense, since higher signal frequencies are required to achieve a sufficient frame rate and thus temporal resolution in order to extract useful clinical information related to the patient's lung functionality. We note that for perfusion (cardiac-related impedance changes) imaging, even higher frequencies and voltage SNR levels are essential [260, 289]. Furthermore, the effect of thoracic boundary change during each breath cycle, as well as the fact that the accurate boundary shape is unknown, leads to the presence of artefacts. Two related studies

demonstrated that a mismatch of more than 4% between the actual thoracic boundary shape and the EIT reconstruction domain boundary has major effect in the image quality [172, 176].

Considering the many possible sources of imaging errors, the design and implementation of a good performance EIT hardware which is capable of high signal quality excitation is the first essential step for successful EIT imaging. Many different EIT systems have been implemented over time, both generic and application-targeted. Such general purpose EIT systems are the Sheffield MK (v1 1987, v3.5 20021) [251], the ACT 3 and ACT 4 EIT systems [249, 266], and the KHU Mark 2.5 system (2014) [156]. In addition, some EIT systems have been developed specifically for dynamic thoracic imaging, such as the Swisstom AG (2012), the ACE1 [171], and the systems presented in [20, 21]. These EIT systems make use of active electrodes [230, 261] in order to reduce the effect of stray capacitances. Although there has been such improvement in the performance of EIT systems during the last decade, their design and implementation still remains a challenging concept and an open research topic.

Some research has been performed on how to set the proper requirements and design an EIT system. Ref. [169] performs an SNR analysis for the voltage acquisition part of custom EIT systems, deriving a specific model to calculate it. Ref. [170] presents a structured design methodology to achieve a high SNR in EIT systems, focusing on the choice of the instrumentation amplifier at the voltage acquisition part and the analogue-to-digital converter's (ADC) specifications. Similar analysis has been performed in [290], where a low-power readout front-end is also designed, and in [20, 21, 158], with integrated circuit designs.

Although research has been done in system design optimization, it mainly focuses on noise compensation. However, the design of an EIT system faces many other challenges, such as common signal effects due to contact impedances and parasitic effects [200]. Hence, a simulation approach which includes these effects could actually assist in examining their possible impact in imaging quality.

Simulation approaches to EIT hardware and impedance modelling have already been presented. In [291], a general 2D SPICE multiresolution impedance method for low frequencies is presented, where a resistor network mesh is created. In [279], a MATLAB interface which transfers a finite element (F.E.) mesh with assigned impedance or conductivity values to each element to a resistive multiport equivalent was presented. This interface is part of the EIDORS library tool, which is commonly used for EIT image reconstructions [72]. A preliminary integration of 2D F.E. mesh circuit equivalents to basic EIT circuitry for SPICE simulation and image reconstruction was presented in [267], where the impact of electrode short-circuit or disconnection was simulated. This approach was extended in [264] where simulations on 3D saline tank equivalents were performed under single ended and mirrored Howland current pumps. The DAC and ADC functions were also simulated in MATLAB, and results were acquired and compared for 2 current signal frequencies and 2 ADC sampling rates. A minor extension was presented in [265], where the thermal, flicker, and quantization signal noise effects, as well as the demodulation part, were added to the previous interface.

In this paper, the SPICE-MATLAB EIT simulation interface described in [264, 265] is applied to three-dimensional thoracic structures. In specific, two fine F.E. thoracic structures are extracted, based on CT images and representing the deflated (full-exhalation) and inflated (full-inhalation) states respectively. Each tissue's relative conductivity and permittivity are loaded from a web database using Python,

according to the current signal selected frequency. Both structures are transferred to 16-port RLC networks and added in the SPICE EIT circuitry for transient simulations, resulting in two corresponding measurement frames. Signal noise is included, and the sampling and digital processing are simulated in MATLAB, in order to acquire the expected image reconstructions. Simulations are carried out assuming 2 electrode sizes and various ADC specifications and number of taps per voltage channel measurement. It is noted that instead of the previously presented interface which uses only resistive equivalent networks, in this work, both SUT conductivity and permittivity are considered, leading to a frequency-dependent RLC multiport equivalent network. Thus, a standard in-phase and quadrature (IQ) demodulation technique is also simulated in MATLAB. Finally, qualitative and quantitative evaluation of the reconstructed images is performed in order to compare the corresponding image results of each simulated configuration.

The remainder of this paper is written as follows. In subsection 6.5.1, the EIT measurement principle is briefly described. In subsection 6.5.2, the thoracic structures evaluated in this study as well as the tissues admittance data are presented. Subsection 6.5.3 synopsizes the SPICE-MATLAB interface used for the simulations. Furthermore, in subsection 6.5.4, the reconstruction domain used, the algorithm with its parameters, and the image evaluation method are described. In subsection 6.6.1, the hardware and electrode configurations are presented, while presentation and comparison of the results are performed.

6.5.1 EIT Principle

In EIT, a low or medium frequency AC current (usually up to 1 MHz, depending on the application) of a small amplitude (up to $9mA_{p-p}$) is injected to the SUT through 2 selected electrodes from an electrode array attached on its surface. At the same time, differential voltages are acquired through other electrode pairs, rendering a set of tetrapolar measurements. The process is repeated for a number of current electrode pairs. The final set of tetrapolar measurements acquired consists of a measurement frame $\boldsymbol{V}$. In time-difference EIT (td-EIT) imaging, which is usually used for real-time thoracic imaging, two measurement frames are needed to reconstruct an image. Their difference $\boldsymbol{\delta V}$ is used as data in the reconstruction algorithm.

Although many measurement patterns have been used in EIT, the most commonly utilized in lung imaging is the adjacent pattern [292, 293]. It is characterized by the current excitation of two neighbouring electrodes and voltage measurement between two other neighbouring electrodes at each time [31]. Although the adjacent pattern presents low field sensitivity to the current injected near the centre of the SUT, it is often preferred due to the fact that it offers more independent measurements compared to other patterns [31, 281]. In terms of this work, we make use of the adjacent current pattern. However, the simulation interface can be easily modified in order to include other measurement patterns (as in [265], where the skip-3 current pattern is also activated [26]).

The basic EIT circuitry consists of a voltage controlled current source (VCCS) of sufficient transconductance and large output impedance in the largest possible frequency range [200, 228]. The signal waveform (usually sinusoidal, but sometimes pulse signal as superposition of multifrequency signals is used) can be digitally produced from a digital-to-analogue converter (DAC), controlled by a direct digital synthesizer (DDS). The voltages are acquired by an analogue front-end (AFE) which usually in-

cludes one or more instrumentation amplifiers (IA), filters, programmable gain amplifiers (PGA), and an ADC driver [4, 170, 200]. Both the current source and the voltage recording parts are connected through switching multiplexers to an electrode array which is attached on the SUT surface. The analogue voltages are sampled from an ADC (usually successive-approximation, SAR), and the samples are sent to a processing unit (MCU, DSP, or FPGA), which performs the synchronization with the input signal, the demodulation, and the switch control. Finally, the processed measurements are sent to a PC for the image reconstruction. A brief schematic of the description above is presented in Figure 6.13. It is noted that this is a basic EIT configuration principle and not necessarily the unique or optimal one. For example, some systems use active electrodes [20, 21], placing the multiplexers before the VCCS (current source) and after the first IA. Other systems drive multiple electrode pairs with more than one current frequency [274] (these systems apply frequency-difference EIT usually used in brain imaging applications). Moreover, some systems perform simultaneous measurements at the voltage recording front-end [171], while many systems enact analogue demodulation before the ADC part [294, 295].

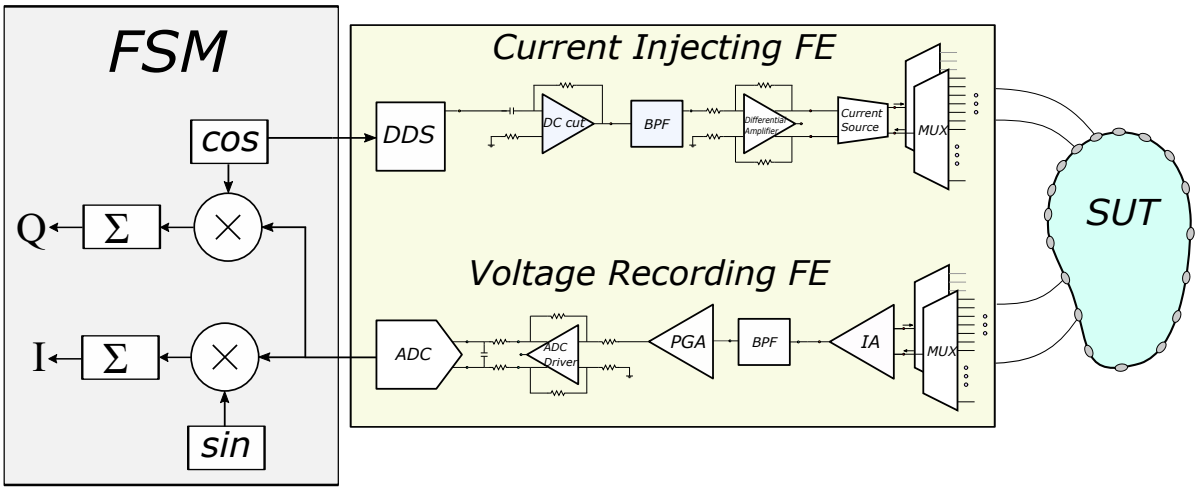

Figure 6.13: Basic EIT hardware concept. The SUT, current injecting front-end (FE), voltage recording FE, and the finite state machine (FSM) are included.

6.5.2 Thoracic Structures

The thoracic SUT was simulated by implementing two fine (dense) 3D F.E. models, representing the full-exhalation (deflated) and the full-inhalation (inflated) lung states respectively (Fig. 6.14). Both models were implemented in MATLAB using the NETGEN tool [186]. Each model includes the following tissues: *left lung, right lung, heart, vertebra, skin,* and the (*muscle-plasma*) background. Each tissue's conductivity σ and permittivity ϵ were loaded from a database demonstrated in [187, 188, 189], according to the current signal frequency selection (i.e., the frequency of the current signal produced from the VCCS). The corresponding conductivities and permittivities per frequency between 1 kHz and 1 MHz are demonstrated in Figure 6.15. In this particular work, we have examined measurement (current signal) frequencies of 15 kHz (low frequency case) and 100 kHz (medium frequency case). For each one of

these two frequencies, we assigned the corresponding σ and ϵ values to each 3D F.E. model's element, according to which one of the mentioned tissues corresponds. To take into consideration possible inhomogeneity in each particular tissue, a standard deviation (std) of 2% for the muscle-plasma background and the heart, 3% for the lungs, and 1% for the skin and bones were assumed. The nominal values assigned to each tissue along with the std are shown in Table 6.5.

The deflated (i.e., state where the lungs are empty) 3D F.E. model's geometry and tissues' boundaries have been taken from a CT-scan of a healthy adult male at the 4th intercostal muscle height. The CT boundary and the corresponding $3D$ model are available online in the EIDORS library tool [72]. The F.E. model uses this geometry as a cross-section to create a $3D$ fine structure, with the x-axis normalized between -1 and 1, and the height set to 1.

For the inflated 3D F.E. thoracic model (i.e., state where the lungs are air-filled), we assumed a chest boundary movement of 10% and a lung cross-section area increase of 15% (see Figure 6.14a)). These values fall into the ranges described in [151]. The 3D F.E. model was created accordingly, as shown in Figure 6.14c). In both models, we have assumed two different electrode placements. In the first, $N_{el} = 16$ electrodes were accurately placed on the 4th intercostal height (i.e., in the middle of each F.E. model's total height, $z = 1/2$). In the second one, an electrode position error has been added, assuming that the electrodes present a 5% height std and a 3% angle std around their nominal values used in the first configuration. Furthermore, for both placements, circular electrodes of radius 0.05 (arbitrary unit—AU) and 0.03 AU are considered. These configurations were added in order to examine the effect of electrodes' placement error and their size in the signal and the reconstructed images' quality. The numbers of nodes and elements per model and electrode configuration are shown in Table 6.6.

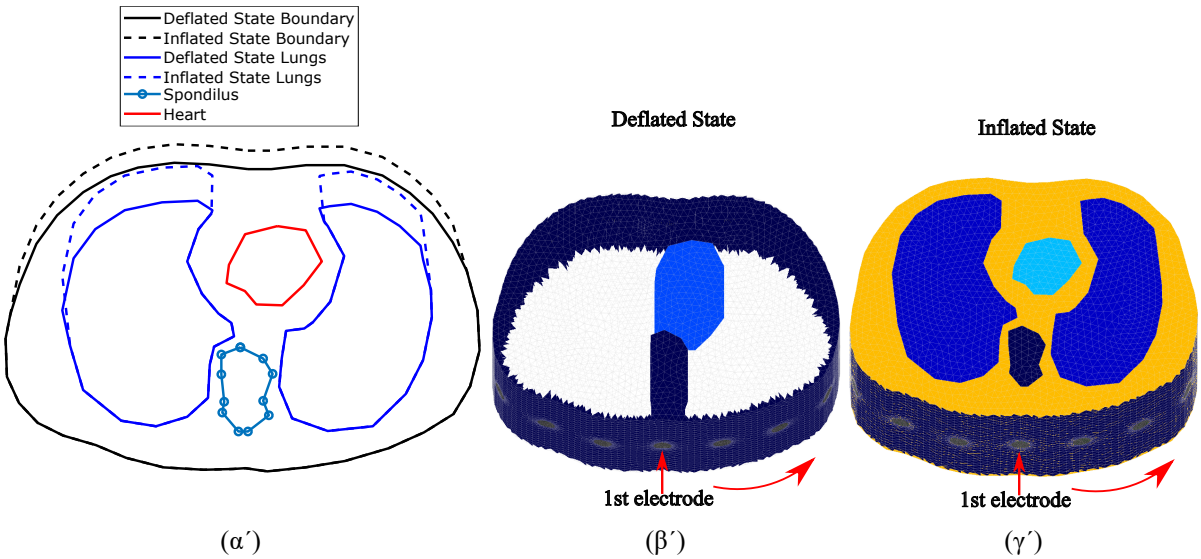

Figure 6.14: (**a**) Cross-section of the F.E. thoracic model boundaries and tissues simulated for the deflated and inflated states. (The deflated state is based on an adult male CT image.) (**b**) Fine thoracic F.E. model for the deflated case (the lungs are not visible since their conductivity is similar to the background's one). (**c**) Fine thoracic F.E. model for the inflated case. The lungs' conductivity is significantly lower than the background's one. In both (**b**,**c**) cases, the skin has been included.

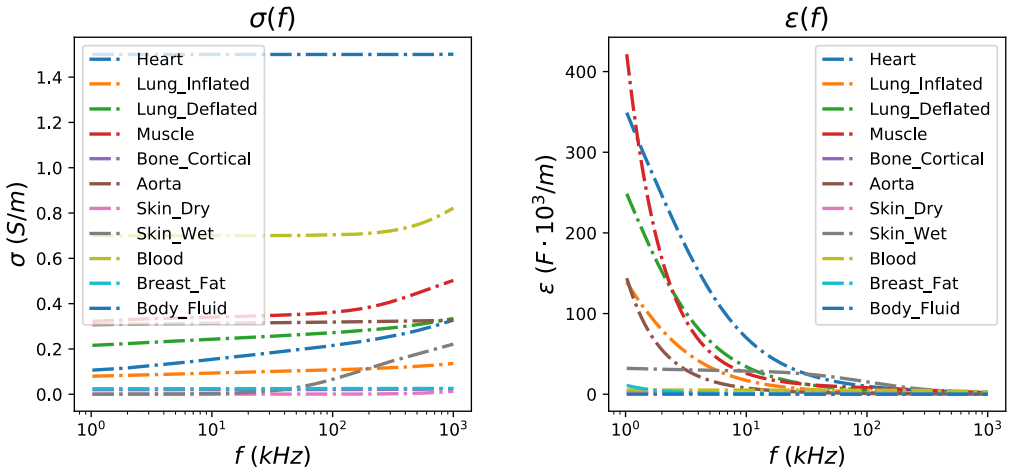

Figure 6.15: Left: Relative conductivity per thoracic tissue in the frequency range between 1 kHz and 1 MHz. Right: Relative permittivity per thoracic tissue in the frequency range between 1 kHz and 1 MHz.

Table 6.5: Assigned conductivity and permittivity values to the thoracic models' tissues for $f = 15$ kHz and $f = 100$ kHz. The admittance is estimated as $\gamma = \sigma + j\omega\epsilon\epsilon_o$. For the skin and fat case, the average values of wet skin and breast fat admittances (see Figure 6.15) were used.

Tissue	σ at 15 kHz (S/m)	$\omega\epsilon\epsilon_o$ at 15 kHz (F·Hz/m)	σ at 100 kHz (S/m)	$\omega\epsilon\epsilon_o$ at 100 kHz (F·Hz/m)
Heart	0.164 ± 0.003	0.041 ± 0.001	0.215 ± 0.004	0.0548 ± 0.001
Inflated Lung	0.095 ± 0.003	0.010 ± 0.000	0.107 ± 0.002	0.014 ± 0.000
Deflated Lung	0.247 ± 0.007	0.020 ± 0.001	0.272 ± 0.003	0.029 ± 0.001
Bones	0.021 ± 0.000	0.000 ± 0.000	0.021 ± 0.000	0.001 ± 0.000
Skin and Fat	0.015 ± 0.000	0.012 ± 0.000	0.045 ± 0.000	0.043 ± 0.000
Muscle and Plasma	0.350 ± 0.007	0.017 ± 0.001	0.380 ± 0.008	0.024 ± 0.001

Table 6.6: Number of tetrahedral elements and nodes of each 3D model case.

Model	No of Elements (L_e)	No of Nodes (n_e)
Inflated, Uniform Electrodes, $R_{el} = 0.05$	145,900	29,507
Inflated, Uniform Electrodes, $R_{el} = 0.03$	133,756	26,861
Inflated, Non-Uniform Electrodes, $R_{el} = 0.05$	146,000	29,542
Inflated, Non-Uniform Electrodes, $R_{el} = 0.03$	135,330	27,120
Deflated, Uniform Electrodes, $R_{el} = 0.05$	134,200	27,460
Deflated, Uniform Electrodes, $R_{el} = 0.03$	133,756	24,849
Deflated, Non-Uniform Electrodes, $R_{el} = 0.05$	133,529	27,328
Deflated, Non-Uniform Electrodes, $R_{el} = 0.03$	119,654	23,965

6.5.3 Simulation Interface

In this section, we briefly describe the simulation approach used for this work. The interface used includes a MATLAB part which creates (with the assistance of NETGEN) the 3D models and assigns

the tissue admittance values, loaded via Python from the database [189] to each element. MATLAB also uses the EIDORS library tool [72] with minor modifications to transfer the 3D thoracic models to RLC 16-port equivalent networks. These networks are integrated in LT SPICE with the whole EIT analogue circuitry, where transient simulations are executed. The transient measurements are imported in MATLAB, where the expected white noise is added and sampling and digital processing are simulated. From the final measurements acquired, the image reconstruction process is performed with the EIDORS tool. The overall process is described in [264, 265]; however, for clarification, we synopsize the main parts. Furthermore, emphasis is given in the active electrode configuration, which was not simulated in previous works.

F.E.M. to RLC Equivalent Circuit Transformation

Considering the 3D thoracic F.E. model, we obtain the following system equation:

$$\begin{bmatrix} \boldsymbol{A_m} + \boldsymbol{A_z} & \boldsymbol{A_v} \\ \boldsymbol{A_v^*} & \boldsymbol{A_D} \end{bmatrix} \begin{bmatrix} \boldsymbol{U} \\ \boldsymbol{V_l} \end{bmatrix} = \begin{bmatrix} \boldsymbol{0} \\ \boldsymbol{I^d} \end{bmatrix} \tag{6.24}$$

where $\boldsymbol{U} = [U_i]_{i=1}^{n_e}$ are the nodal potentials for the corresponding model, $\boldsymbol{A_m} \in \mathbb{R}^{n_e \times n_e}$ is the element-assembled matrix, $\boldsymbol{A_z} \in \mathbb{R}^{n_e \times n_e}$ and $\boldsymbol{A_v} \in \mathbb{R}^{n_e \times N_{el}}$ express the complete electrode model (CEM) boundary conditions [296], and $\boldsymbol{A_d} \in \mathbb{R}^{N_{el} \times N_{el}}$ refers to the nodes where the measurements are taken [37]. Furthermore, $\boldsymbol{V_l} \in N_{el}$ is the voltage measurement vector, and $\boldsymbol{I^d}$ is the current injected per electrode. By writing $\boldsymbol{A_k} = \boldsymbol{A_m} + \boldsymbol{A_z}$, it can be proved that [264, 279]

$$(\boldsymbol{A_d} - \boldsymbol{A_v^*} \boldsymbol{A_k^{-1}} \boldsymbol{A_v}) \boldsymbol{V_l} = \boldsymbol{I_d} \tag{6.25}$$

By setting $\boldsymbol{F(\sigma)} = \boldsymbol{A_d} - \boldsymbol{A_v^*} \boldsymbol{A_k^{-1}} \boldsymbol{A_v}$, we obtain a sparse, almost symmetric conductivity (or admittance) matrix. Therefore, the impedance between two nodes i and j (where voltage measurements are taken) is computed as [264, 279, 280]

$$Z_{ij} = -1/F(\sigma)_{ij} \tag{6.26}$$

In the case where admittances are considered, $\boldsymbol{Z} \in \mathbb{C}^{N_{el} \times N_{el}}$. Thus, each impedance Z_{ij} can be implemented by a parallel combination of a resistor and either a capacitor or an inductor. In this way, we compose an RLC equivalent circuit, where each terminal corresponds to an EIT electrode.

EIT SPICE Circuitry

The SPICE EIT circuitry used for the simulations is mainly based on the basic structure presented in Section 6.5.1. It is implemented according to the passive electrode configuration (i.e., the analogue circuitry is connected to the electrode channels via cables and switches with parasitic capacitors) and the partially active electrode configuration (i.e., the first voltage readout stage—usually a buffer—is placed on each particular electrode, significantly reducing the parasitic effects).

The input signal is created in MATLAB in discretized (vector) form, demonstrating a $L_{DAC} = 16$-bit

DAC look-up-table (LUT) [264]. LUTs for 15 kHz and 100 kHz sinusoidal waveforms are considered, while the DAC sampling rate is simulated at 16 times higher than the corresponding input signal's frequency. Each input waveform is stored in a PWL file, which is transferred to LT SPICE. In addition, the multiplexer digital inputs, according to the measurement pattern adopted, are also stored in PWL files, read by LT SPICE.

The analogue SPICE circuitry current injecting front-end consists of a second-order multiple feedback wideband band pass filter (BPF), a fully differential voltage output driver (THS413-Texas Instruments), and an enhanced mirrored Howland current pump (HCP) which acts as a VCCS. The voltage recording front-end is implemented as a partially active electrode, exclusively in the 100 kHz input signal case, and as a typical passive electrode for both the 15 kHz and 100 kHz input signal cases. In the active electrode configuration, each electrode is directly connected to a buffer (which is placed very close to the electrode). Then, each buffer's output is connected to the IA through analogue (bi-directional) multiplexer switches (ADG426 analogue devices) and two first-order high-pass RC filters (one per IA input channel). In the passive electrode configuration, each electrode is directly connected to two ADG426 analogue multiplexers, one for each differential measurement channel. Each ADG426 output is connected to a buffer and each buffer's output is driven to the corresponding input of the AD8421 IA through a first-order high-pass RC filter. The mirrored HPC VCCS is connected to the electrodes through two ADG426 multiplexers (one for the source and one for the sink electrode) in both the active and passive electrode configurations. The multiplexer switches on resistors are included in the ADG426 SPICE model, while parasitic capacitances (randomly chosen in the range of 100–200 pF) between the electrode channels have been manually added in SPICE, in order to simulate parasitic effects. Furthermore, to include channel imbalance effects at the output (i.e., common signal effects), unequal resistors (20–60 Ω) have been introduced to each measurement channel. Finally, the electrodes are modelled as in [264], according to the descriptions in [275, 276, 277] (assuming AgCl electrodes). A brief schematic of both configurations, including the parasitic effects and channel impedances, is presented in Figure 6.16.

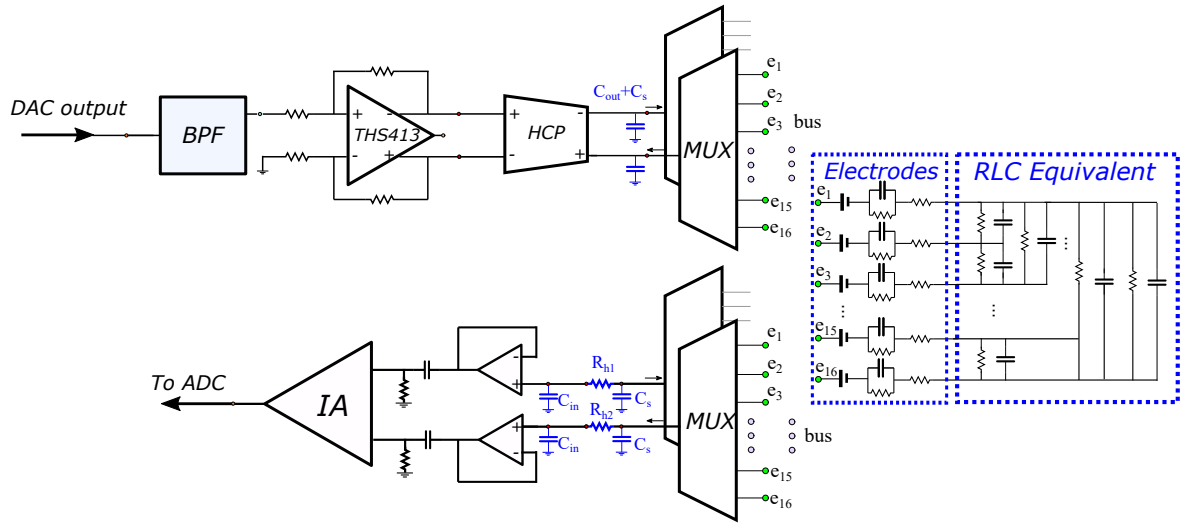

a) Passive Electrode

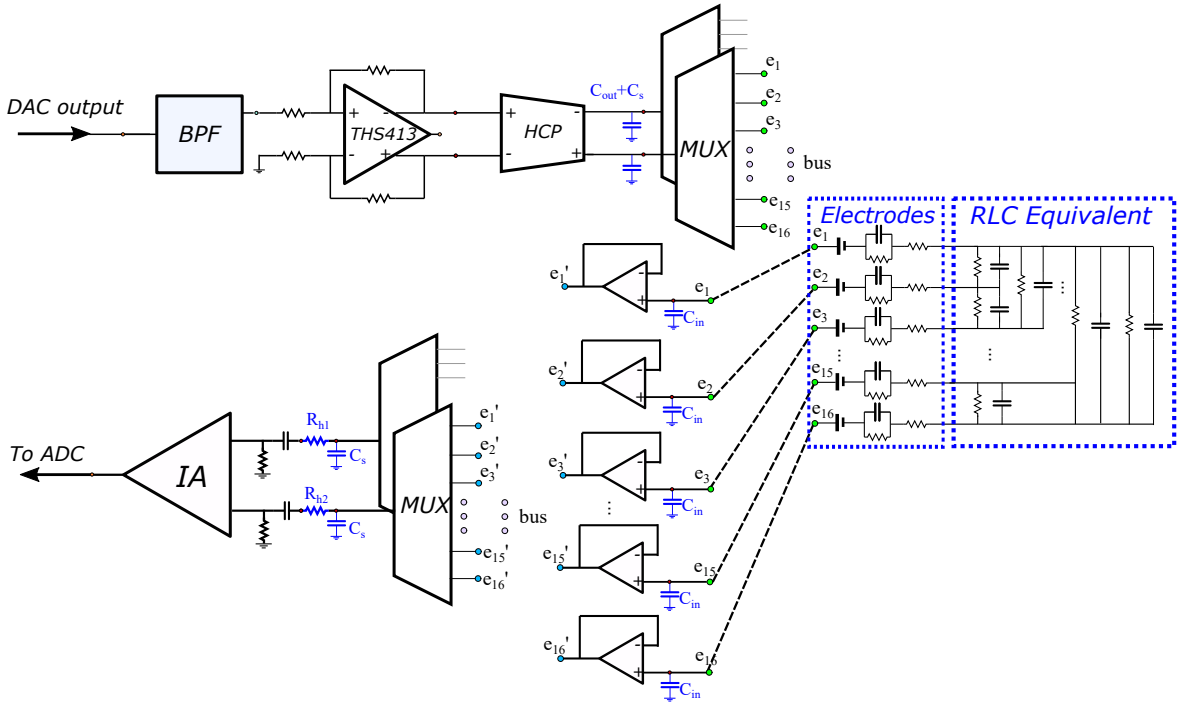

b) Partially-Active Electrode

Figure 6.16: LT SPICE analogue circuitry configurations for (**a**) passive electrodes (cables and switches between the readout front-end circuit and the electrode) and (**b**) partially active electrodes (the first stage of the readout circuit is implemented directly on each particular electrode). Blue-coloured components indicate the parasitic capacitors and channel resistors added to simulate their effect.

Sampling and Digital Signal Processing

A transient simulation is performed in LT SPICE for each image frame. Its total duration depends on the input signal's frequency as well as the selected time between two particular differential voltage measurements. The simulation stops when all the measurements defined by the selected pattern (adjacent) have been acquired. The transient results are written on a text file and sent to MATLAB for processing. The input reference signal is also measured from an IA and sent to MATLAB, in order to sample it and demodulate it with the output signal. Finally, a noise simulation at the SPICE circuit produces a power spectral density diagram (PSD). The total amount of noise, resulting from the integration of PSD, is added to the IA signal output in MATLAB [265].

A MATLAB software program simulates the ADC function in the following way. First, the number of bits L_{ADC} and the sampling frequency f_s are selected. Assuming negligible conversion times, the time points where the signal must be sampled are defined for each measurement window (time space between two switch changes) [264]. Then, for each defined time point, the nearest corresponding SPICE time value is found and the corresponding transient voltage value is sampled (note that the longest timestep in LT SPICE simulations is set to 100 ns, many times smaller than the ADC sampling period which is 625 ns at maximum). The sampling process is explained in detail in [264].

The sampled values from the input and output signals are stored in binary form (dropping the two LSBs which are assumed as noisy), and IQ demodulation is performed (see Figure 6.13). The multiplication results are driven to an adder, which actually acts as a digital low pass filter (LPF). From the in-phase and quadrature results, the signal amplitude of each measurement window is estimated. The final set of amplitudes is then used as data for the difference image reconstruction.

The whole simulation interface is shown in Figure 6.17. It includes the MATLAB/NETGEN modelling interface, where the tissues' electrical properties are loaded from the mentioned database to the two 3D simulation structures (deflated and inflated). These structures are transformed to an RLC equivalent circuit, which is simulated at LT SPICE, along with the whole analogue EIT circuitry, which is shown in a "white box". Any noise, parasitic effects, channel mismatches, and components' non-idealities are added in the SPICE circuitry. The SPICE transient measurements are transferred in MATLAB to be processed as described before, and the reconstruction is performed with the EIDORS tool.

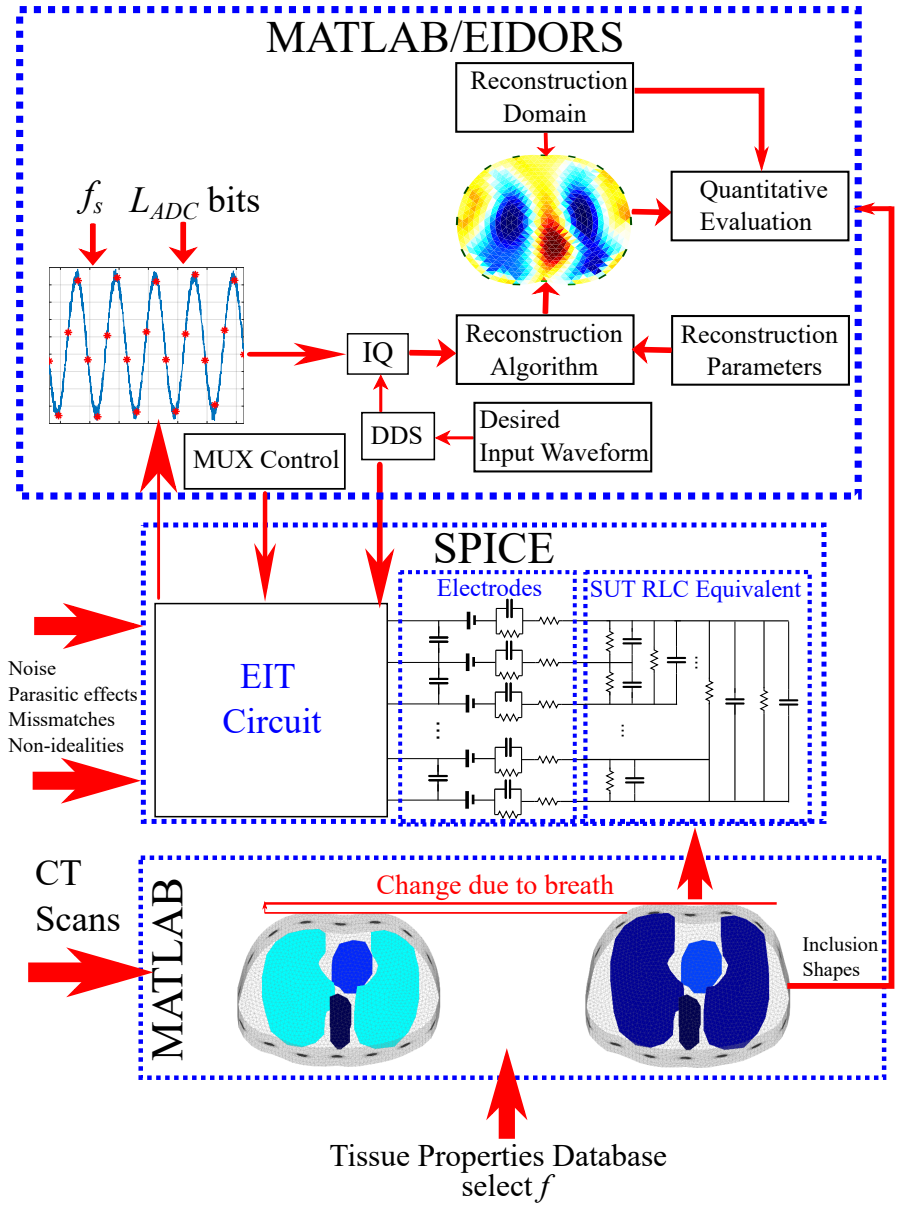

Figure 6.17: Brief diagram of the proposed thoracic EIT simulation interface.

It is important to note that both the simulated analogue circuitry and the digital part are not optimal and are not necessarily recommended for novel EIT system designs, since this is beyond the scope of this work. Instead, the simulations presented compare the expected performance of state-of-the-art EIT hardware designs at different configurations in lung imaging. However, the simulation interface proposed can be easily modified to simulate the performance of new hardware designs.

6.5.4 Reconstruction and Evaluation Method

In this section, a description of the image reconstruction approach is written, presenting the selected algorithm and its parameters. Furthermore, a method for quantitative evaluation of the produced images

is presented, in order to perform a more considered comparison.

Image Reconstruction

Assume that $\boldsymbol{\delta V}$ is the difference voltage data, acquired from two continuous measurement frames (e.g., from a thoracic deflated and inflated state, respectively). We also assume a 2D EIT coarse-element reconstruction domain Ω, consisting of L_c triangular elements. This domain's elliptic boundary $\partial\Omega$ differs from the 3D thoracic F.E. (both deflated and inflated states) boundaries since (A) the SUT boundary is not accurately known in real EIT lung imaging applications, and (B) to obtain a robust reconstruction result, we need to avoid the well-known *inverse crime* [155]. Then, the conventional difference-EIT reconstruction is considered as an optimization problem, where we have to find the optimal $\boldsymbol{\delta\gamma}$ (admittance change) distribution that minimizes the following quantity [54]:

$$\boldsymbol{\delta\gamma_*} = \underset{\boldsymbol{\gamma}\in C^{L_c}}{\operatorname{argmin}}\Big\{F(\boldsymbol{\delta\gamma})\Big\} \tag{6.27}$$

where

$$F(\boldsymbol{\gamma}) = \|\boldsymbol{U_2}(\boldsymbol{\gamma_o}+\boldsymbol{\delta\gamma}) - \boldsymbol{U_1}(\boldsymbol{\gamma_o}) - \boldsymbol{\delta V}\|^2_{\boldsymbol{W}} + \lambda^2 P(\boldsymbol{\delta\gamma}). \tag{6.28}$$

In the expression above, $\boldsymbol{U_1}(\boldsymbol{\gamma_o})$ and $\boldsymbol{U_2}(\boldsymbol{\gamma_o}+\boldsymbol{\delta\gamma})$ are the simulated electrode voltage vectors at the two states (assuming admittance distributions $\boldsymbol{\gamma_o}$ and $\boldsymbol{\gamma_o}+\boldsymbol{\delta\gamma}$ in Ω, respectively), $\boldsymbol{W}$ is a weighting matrix, λ is the regularization hyperparameter, and $P(\boldsymbol{\delta\gamma})$ is the regularization term [4, 54, 174]. We note that regularization is essential, since the EIT reconstruction problem is both ill-posed and ill-conditioned [4, 155]. It is also a heavily non-linear problem.

For this particular work, we use the linearized difference-EIT reconstruction with a smooth regularization term. This is the most common approach in dynamic thoracic imaging, since it enacts only one reconstruction step, allowing real-time imaging. However, it often suffers from accuracy, since the admittance changes during the breath cycle are usually significant [151]. The linearized difference-EIT reconstruction assumes small admittance changes near $\boldsymbol{\gamma_o}$; hence, $\boldsymbol{J\delta\gamma} \simeq \boldsymbol{U_2}(\boldsymbol{\gamma_o}+\boldsymbol{\delta\gamma}) - \boldsymbol{U_1}(\boldsymbol{\gamma_o})$, where

$$\boldsymbol{J} = \frac{\partial\Big(\boldsymbol{U_2}(\boldsymbol{\gamma_o}+\boldsymbol{\delta\gamma}) - \boldsymbol{U_1}(\boldsymbol{\gamma_o})\Big)}{\partial\boldsymbol{\delta\gamma}} \tag{6.29}$$

is the Jacobian matrix. The optimization problem (6.27)–(6.28) then becomes

$$F(\boldsymbol{\gamma}) = \|\boldsymbol{J\delta\gamma} - \boldsymbol{\delta V}\|^2_{\boldsymbol{W}} + \lambda^2\,\|\boldsymbol{\delta\gamma}\|^2_{\boldsymbol{Q}}\,. \tag{6.30}$$

where $\boldsymbol{Q}$ is the prior regularization matrix [54]. We enact generalized Tikhonov regularization, obtaining the following single-step solution [54, 174]:

$$\boldsymbol{\delta\gamma} = \big(\boldsymbol{J^T W J} + \lambda^2\boldsymbol{Q}\big)^{-1}\big(\boldsymbol{J^T W \delta V}\big) \tag{6.31}$$

In terms of this work, the Laplace smoothness prior is used for the reconstruction [54]. However,

other priors, such as the NOSER, standard Tikhnonov, or Gaussian could be also used to obtain the EIT images without loss of generality. The hyperparameter has been heuristically selected to $\lambda = 0.1$ for all the cases. We note that the selection of single-step generalized Tikhonov regularization is indicative, and more recent approaches, such as learning approaches [118, 142, 145], could also be applied and can be considered for future work.

The reconstruction domain Ω is a $L_c = 1024$ triangular element 2D thoracic shape mesh, shown in Figure 6.18a. The gap electrode model has been applied in this domain to model the electrodes [22, 23]. Shape mismatch between the true (cross-section 3D) boundary and the reconstruction domain's boundary ($\partial\Omega$, Figure 6.18b) introduces a minor modelling error. However, the exact thoracic shape is never accurately known, and it also changes during the breath cycle [21, 176].

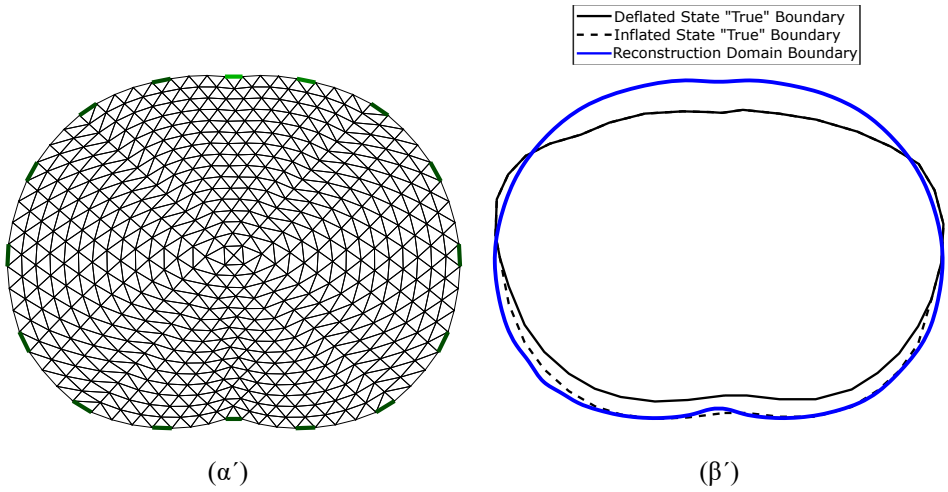

Figure 6.18: (**a**) 2D reconstruction thoracic domain (Ω). (**b**) Shape mismatch between the "true" cross-section model and Ω.

Image Evaluation Method

To evaluate the reconstructed images, we have to set a reference image for the comparisons on the same domain Ω. $\partial\Omega$, however, differs from both the 3D models' boundary shapes. As a result, it is necessary to primarily set a "true boundary" 2D reference, based on the cross-section of the 3D models. At this point, we take into consideration that (A) the 3D model's shape is not constant, and (B) we perform difference-EIT imaging; thus, we reconstruct a single EIT image which represents the conductivity (and permittivity) differences between the two states. To this end, we assume two "true boundary" cross-section 2D references, one for the deflated and one for the inflated case. Then, the Ω domain reference image is created in the following way. First, we scale the Ω and each "true boundary" domain in the y-axis, matching them as shown in Figure 6.18b. Their horizontal limits are also normalized between -1 and 1. Secondly, we assume A_i to be the Ω domain's ith-element area ($i = \{1, 2, \ldots, L_e\}$). For each element i, we find the following weight vector:

$$\boldsymbol{w_d^i} = [w_{j,d}^i]_{j=1}^6 \in R^{6\times 1} \tag{6.32}$$

which represents the percentage of A_i which is included in the following corresponding six tissue curves of the deflated state "true" domain: left lung, right lung, vertebra, heart, skin, and muscle-plasma. The corresponding vector which represents the tissues' (mean) admittances at the deflated state is defined by

$$\boldsymbol{\gamma_{t,d}} = [\gamma_{j,d}]_{j=1}^{6} \in C^{1\times 6} \tag{6.33}$$

Then, we compute the corresponding reference admittance as (see Figure 6.19a)

$$\gamma_{r,d,i} = \boldsymbol{\gamma_{t,d}} \cdot \boldsymbol{w_d^i} \in C \tag{6.34}$$

In the same way, we compute each i element's reference admittance for the inflated state:

$$\gamma_{r,f,i} = \boldsymbol{\gamma_{t,f}} \cdot \boldsymbol{w_f^i} \in C \tag{6.35}$$

where

$$\boldsymbol{w_f^i} = [w_{j,f}^i]_{j=1}^{6} \in C^{6\times 1} \tag{6.36}$$

is the ith element's weight vector at the inflated state and

$$\boldsymbol{\gamma_{t,f}} = [\gamma_{j,f}]_{j=1}^{6} \in C^{1\times 6} \tag{6.37}$$

the vector which represents the tissues' (mean) admittances at the inflated state. We set the deflated and inflated state reference admittances for the domain Ω:

$$\begin{aligned} \boldsymbol{\gamma_{r,d}} &= [\gamma_{r,d,i}]_{i=1}^{L_e} \in C^{L_c\times 1} \\ \boldsymbol{\gamma_{r,f}} &= [\gamma_{r,f,i}]_{i=1}^{L_e} \in C^{L_c\times 1} \end{aligned} \tag{6.38}$$

The final Ω domain reference has the following admittance difference values:

$$\boldsymbol{\gamma_r} = \boldsymbol{\gamma_{r,f}} - \boldsymbol{\gamma_{r,d}} \tag{6.39}$$

where $\boldsymbol{\gamma_r} \in C^{L_e\times 1}$. The reference image obtained is shown in Figure 6.19b.

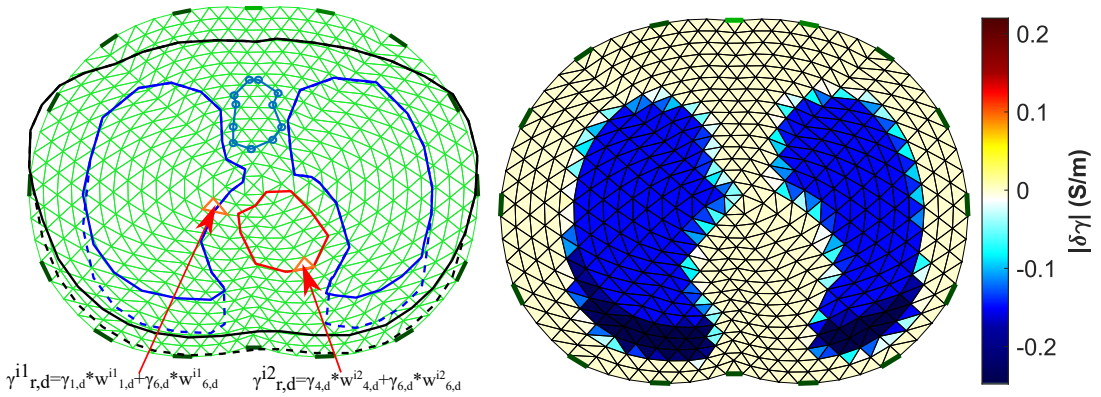

(α′) (β′)

Figure 6.19: (**a**) Visualization of the process to obtain the Ω domain reference image. (**b**) The Ω domain reference image (15 kHz case).

At both the reference and the reconstructed images, the $\boldsymbol{\delta s} = [\|\delta\gamma_i\|]_{i=1}^{L_c} \in R^{L_c \times 1}$ (amplitude) term is demonstrated. For the quantitative evaluation and comparisons, the correlation coefficient CC metric has been considered, defined as follows:

$$CC = \frac{\text{Cov}(\boldsymbol{\delta s_r}, \hat{\boldsymbol{\delta s}})}{\text{Std}(\boldsymbol{\delta s_r})\text{Std}(\hat{\boldsymbol{\delta s}})} \tag{6.40}$$

where $\boldsymbol{\delta s_r}$ is the ground truth admittance amplitude, $\hat{\boldsymbol{\delta s}}$ is the admittance amplitude distribution estimated from the image reconstruction, and Cov is the covariance between reference and estimated values. The value of CC ranges between 0 and 1, and higher CC indicates more similarity between the reference and the reconstructed image.

In addition, to enhance the quantitative evaluation, the relative reconstruction error RRE metric has also been used, defined as follows [142, 145]:

$$RRE = \frac{\left\| \boldsymbol{\delta s_r} - \hat{\boldsymbol{\delta s}} \right\|_2}{\|\boldsymbol{\delta s_r}\|_2} \tag{6.41}$$

We note that for the calculation of RRE, both $\boldsymbol{\delta s_r}$ and $\hat{\boldsymbol{\delta s}}$ were normalized between -1 and 1. Higher RRE indicates a larger error between the reference and the reconstructed image.

6.6 Results and Discussion

In this section, the simulation cases are firstly defined, based on the electrodes' properties, dimensions, and deviation and the digital acquisition part's configurations. The theoretically expected SNRs are also computed for each ADC configuration case. In addition, the obtained images per case are presented, as well as the resulting CC metrics. Furthermore, both qualitative and quantitative results are discussed.

Simulation Cases

For the simulations, we consider two input sinusoidal frequencies: $f = 15$ kHz and $f = 100$ kHz (see Section 6.5.3). For the $f = 15$ kHz case, SPICE simulations are carried out using the passive electrode configuration, while for the $f = 100$ kHz, both passive and active electrode configurations are considered. This is because parasitic effects are much more significant at $f = 100$ kHz than at $f = 15$ kHz. Furthermore, for each of the previous three cases, we examine (A) accurate electrode placement on the 4th intercostal height, (B) electrode deviation (5% height and 3% angle), (C) circular electrodes of 0.03 (A.U.) radius, and (D) circular electrodes of 0.05 (A.U.) radius (for further details, see Section 6.5.2). Moreover, we simulate the following ADC cases: (A) resolution of $L_{ADC} = 12$ bits and sampling rate of $f_s = 4f$, (B) $L_{ADC} = 16$ bits and sampling rate of $f_s = 4f$, (C) $L_{ADC} = 12$ bits and sampling rate of $f_s = 16f$, and (D) $L_{ADC} = 16$ bits and sampling rate of $f_s = 16f$. Finally, we also consider $N_T = 2$ and $N_T = 4$ sine periods to be sampled per voltage channel measurement (see [265] and Fig. 6.20). Hence, we obtain a total of 96 sub-cases for imaging, evaluation, and comparison.

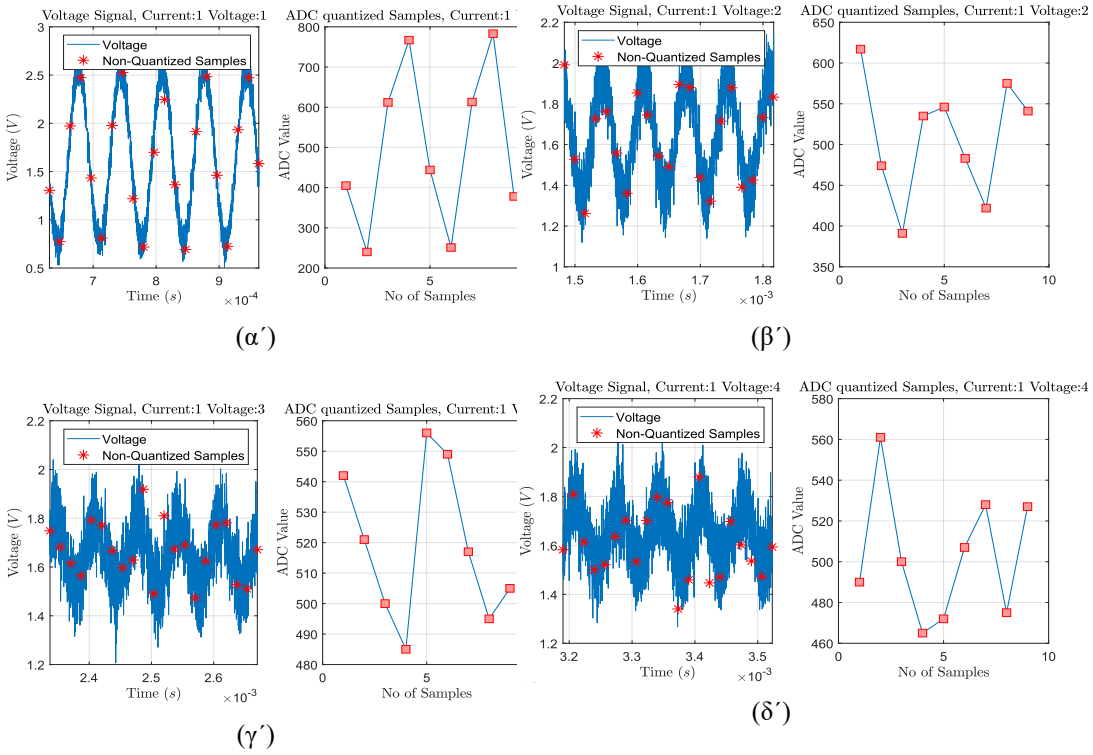

Figure 6.20: Transient plus noise simulations and ADC sampling process for some particular voltage channel measurements, when at deflated state, acting at 15 kHz, $2mA_{p-p}$ current signal, and considering 0.05 radius passive electrodes without position deviation. Sampling and quantization is performed for 2 sine periods, as shown in each right part. Current is injected from the 1st and the 2nd electrodes (adjacent current protocol). The ADC resolution is considered at 12-bit (10-bit ENOB) with a 3.3 V reference voltage. (**a**) Adjacent voltage measuring between the 3rd and the 4th electrodes. (**b**) Adjacent voltage measuring between the 4th and the 5th electrodes. (**c**) Adjacent voltage measuring between the 5th and the 6th electrodes. (**d**) Adjacent voltage measuring between the 6th and the 7th electrodes. As the voltage measuring electrode pair becomes far from the current injecting pair, the noise effect becomes more significant, due to the signal's amplitude decrease.

The expected voltage amplitude SNR can be computed according to the following formula [169]:

$$SNR = 10log_{10}\left(\frac{A^2(K/2)}{\frac{V_{ref}^2}{12{\cdot}2^{2L_{ADC}}} + \sigma_n^2}\right) \tag{6.42}$$

where A is the mean acquired voltage signal amplitude, K the number of matched digital LPF filter taps (samples) at the IQ demodulation part, V_{ref} the ADC voltage reference (3.3 V in the simulated cases), L_{ADC} the ADC resolution (bits), and σ_n the circuit noise std. The ratio $V_{ref}/2^{L_{ADC}}$ denotes the LSB voltage range. Furthermore, the number of taps per measurement is defined by $K = N_T \cdot f_s/f$. As voltage signal amplitude A, we take the mean amplitude between all the channel measurements (208 for the adjacent pattern when 16 electrodes are attached [4, 27]). For the SNR estimation, we also assume that it is not considerably affected by the electrode configurations or the patient's state. However, if we consider different topologies than in Figure 6.16, possible changes in noise levels between active and passive

electrode configuration should be considered (see [21]). Moreover, an increase in signal frequency has a substantial role in SNR reduction, firstly due to the need for higher sampling frequencies f_s and secondly due to the lower voltages acquired, resulting from the increased tissue admittances (see Figure 6.15 and Table 6.5). Therefore, we examine 16 different SNR cases, as demonstrated in Table 6.7. A σ_n value of $4.2mV_{p-p}$ was extracted from LT SPICE noise simulations. This value strongly depends on the input current amplitude and the instrumentation amplifier's gain (set as $2mA_{p-p}$ and 200 V/V, respectively, for these particular simulations). Table 6.7 shows the calculated voltage amplitude SNR per case.

Table 6.7: Calculated mean SNR values (dB) for each measuring parameter case, according to (6.42).

f (kHz)	L_{ADC} (bits)	f_s	N_T	SNR (dB)
15	12	$4f$	2	27.5
15	12	$4f$	4	30.5
15	12	$16f$	2	33.5
15	12	$16f$	4	36.5
15	16	$4f$	2	27.5
15	16	$4f$	4	30.5
15	16	$16f$	2	33.5
15	16	$16f$	4	36.6
100	12	$4f$	2	20.8
100	12	$4f$	4	23.8
100	12	$16f$	2	26.8
100	12	$16f$	4	29.8
100	16	$4f$	2	20.8
100	16	$4f$	4	23.8
100	16	$16f$	2	26.8
100	16	$16f$	4	29.9

As demonstrated, the expected voltage SNR is reduced as the input signal frequency increases from 15 kHz to 100 kHz. At the same time, increasing the sampling frequency from 4 to 16 times the signal frequency and the sampled periods from 2 to 4 (i.e., the number of taps/samples per measurement) leads to improved SNR values. In addition, an increase in the ADC resolution did not have a noticeable effect on SNR in the cases tested. This can be explained by observing (6.42) denominator term. It is demonstrated that if noise level σ_n^2 from the analogue circuitry is significantly higher than the first term, then the ADC resolution does not have a substantial role in the SNR. Nonetheless, this noise can be filtered from the digital LPF by increasing the samples per measurement (K).

We note that these SNRs are the mean ones per each particular measurement frame. In fact, there is a large variation between the voltage channels' measurement SNRs, due to the wide voltage amplitude range. For example, voltage electrode pairs close to the current electrode pair drive significantly higher voltages than the voltage electrode pairs on the other side of the setup, resulting in higher SNR levels. It is also noted that the selected hardware circuitry, as well as the ratio between the voltages acquired and V_{ref}, is not optimized in this particular work. However, the simulation interface presented can be an

effective tool for this direction.

6.6.1 Simulation Results

The images obtained for $f = 15$ kHz and passive electrode configuration are shown in Figure 6.21. The corresponding CC and RRE values are shown for each subcase. In almost all the images, the admittance reduction due to the change between the end-inspiration (deflated) and end-expiration (inflated) states is visible. However, some artefacts are present, including a ringing effect between the lungs (which is often misinterpreted as "heart" [71]) or near the boundary. Furthermore, in some cases (especially when sampling with lower rates), the lung-related admittance change regions appear very close to the reconstruction domain's centre.

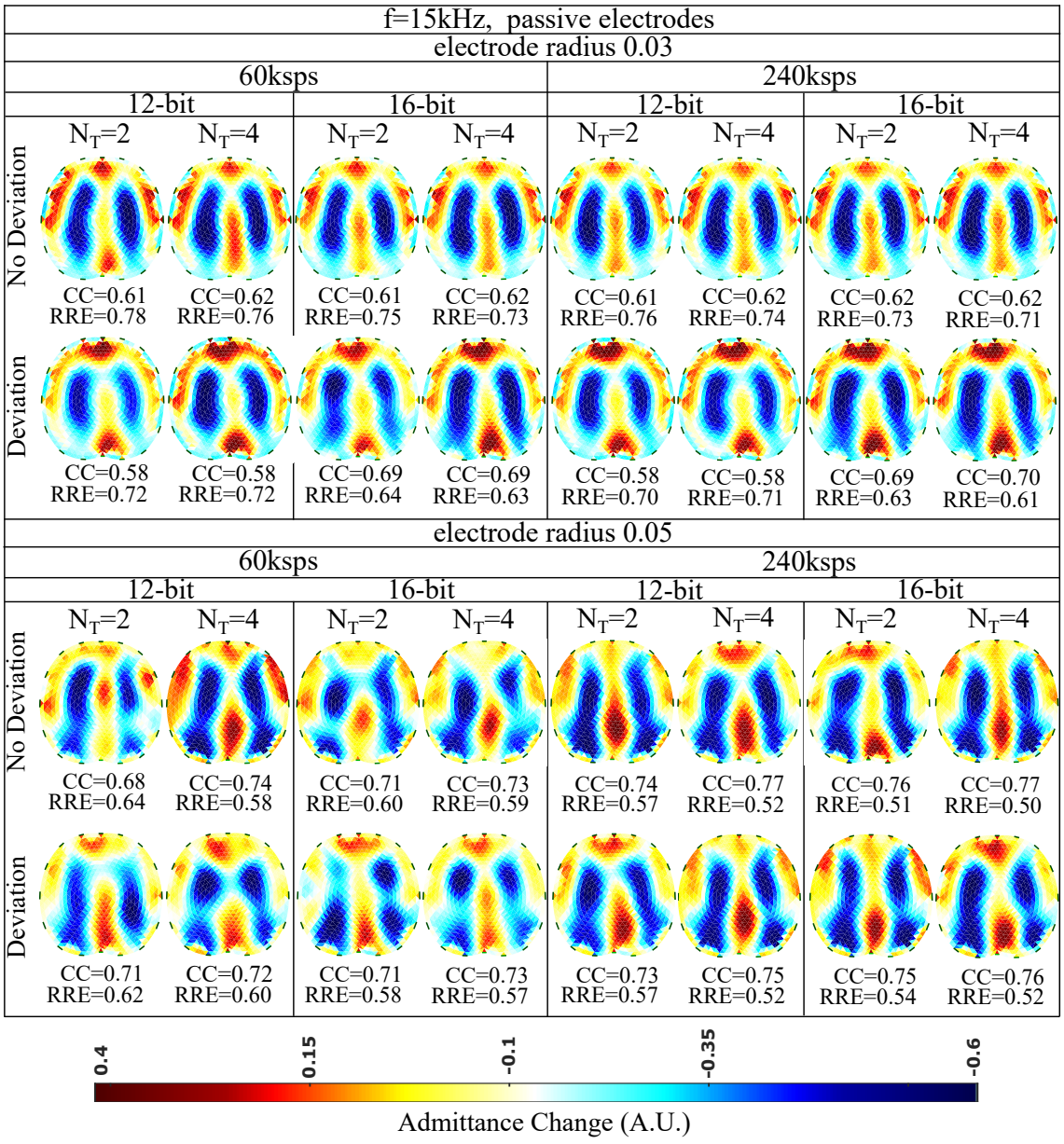

Figure 6.21: Simulation results for 15 kHz input signal and passive electrode configuration. All further hardware configurations, as well as the corresponding CCs and RREs, are noted in the figure.

The presence of artefacts is a result of hardware noise and issues (electrode's contact impedances, common signals between the channels, etc.), boundary and tissues' motion, and the ill-posed and ill-conditioned nature of the inverse problem (low noise levels can lead to strong artefacts) [113, 155, 200]. When lower sampling rates f_s or when a lower number of sampling periods (N_T) is set, the intense change of the lungs' admittance near the chest is often not properly detected. This is verified quantitatively, where for $f_s = 60$ ksps and $N_T = 2$, we obtain a CC between 0.58 and 0.71, while for $f_s = 240$ ksps and $N_T = 4$, CC takes values between 0.58 and 0.77. The electrode's surface area seems to be an important factor, since smaller surfaces lead to higher contact impedances. The contact impedance effect is more intense at lower frequencies [297, 298]. Mismatches between the channels' contact impedances may lead to common signals, especially at the voltage recording circuitry part. This can explain the improved performance (CC of 0.68–0.77 and RRE of 0.50–0.64) observed for an electrode radius of 0.05 compared to this for the 0.03 radius electrode configuration (CC of 0.58–0.70 and RRE of 0.61–0.78). Furthermore, a small electrode position deviation overall leads to minor additional image artefacts, assuming the same gap electrode model for each reconstruction. This is anticipated, since we enact difference-EIT imaging, where minor modelling errors are compensated [175]. Finally, as expected, an increase in the ADC resolution L_{ADC} for 12 to 16 bits does not lead to significant reconstruction improvement with the presence of relatively high white noise levels (see Section 6.6 and Table 6.7).

Overall, for the 15 kHz passive electrode case and high white noise levels, we conclude that the electrode radius and the total number of taps per measurement (proportional to f_s and N_T) are two key factors for the image reconstruction performance. In addition, according to (6.42), for lower analogue circuitry noise levels, the ADC resolution is also expected to boost the performance. However, such a case has not been simulated in this particular work.

The reconstructed images for $f = 100$ kHz and passive electrode configuration are demonstrated in Figure 6.22. First of all, it is observed that the overall spatial resolution and image quality are reduced, compared to the corresponding 15 kHz case. Although the electrodes appear to have reduced contact impedances at this frequency, the parasitic effects taking place between the channel cables become more critical. These effects, combined with the reduced VCCS output impedance and instrumentation amplifier's CMRR, lead to image quality degradation [200, 227]. However, due to the low contact impedances, the electrodes' surface does not significantly affect the performance (CC between 0.54 and 0.74, RRE between 0.54 and 0.74 for the 0.03 radius cases and CC between 0.51 and 0.76, RRE between 0.54 and 0.71 for the 0.05 radius cases). As in the 15 kHz cases, the electrodes' position deviation has a small impact on the images' quality. The best results are obtained by increasing the number of taps per measurement (maximum CC is observed for $f_s = 1.6$ Msps and $N_T = 4$ sampling sine periods. A small improvement is observed when increasing the ADC resolution from 12 to 16 bits.

The EIT images for $f = 100$ kHz and the active (on the voltage recording part) electrode configuration are finally shown in Figure 6.23. A slight improvement of the image quality is detected, mainly due to the reduction of cable parasitic effects at the voltage measurement channels. The maximum CC of 0.77 (corresponding minimum RRE of 0.52) is achieved for non-deviated, 0.05 radius electrodes, when a 16 bit resolution ADC is utilized, sampling at 1.6 Msps for $N_T = 4$ sine periods. As in the passive electrode cases, the performance is less affected by the electrode deviation and the ADC resolution and

mostly affected by the total number of taps per measurement channel. In addition, the electrode surface has minor effect on the performance, due to the lower contact impedances presented at $f = 100$ kHz.

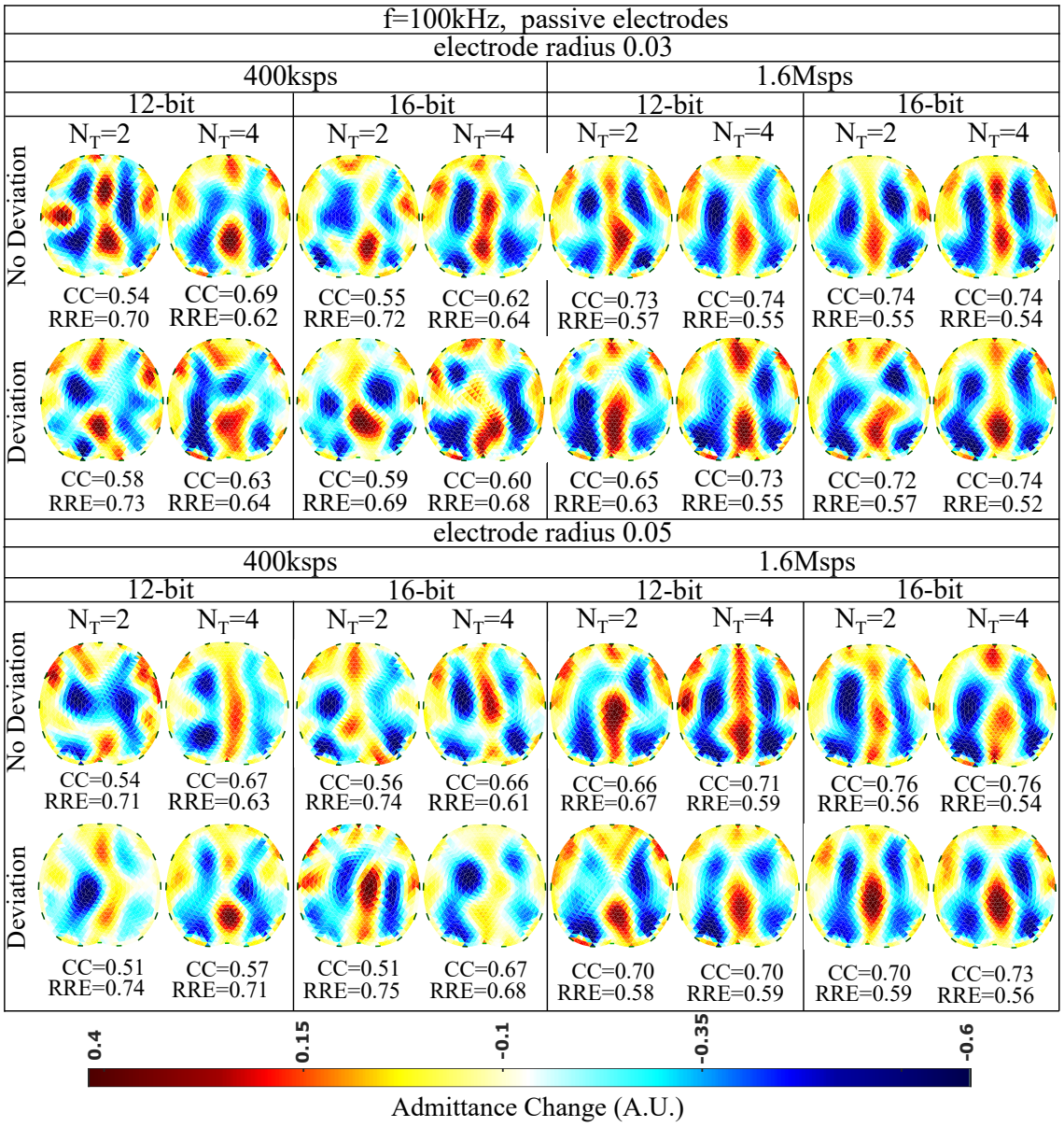

Figure 6.22: Simulation results for 100 kHz input signal and passive electrode configuration. All further hardware configurations, as well as the corresponding CCs and RREs, are noted in the Figure.

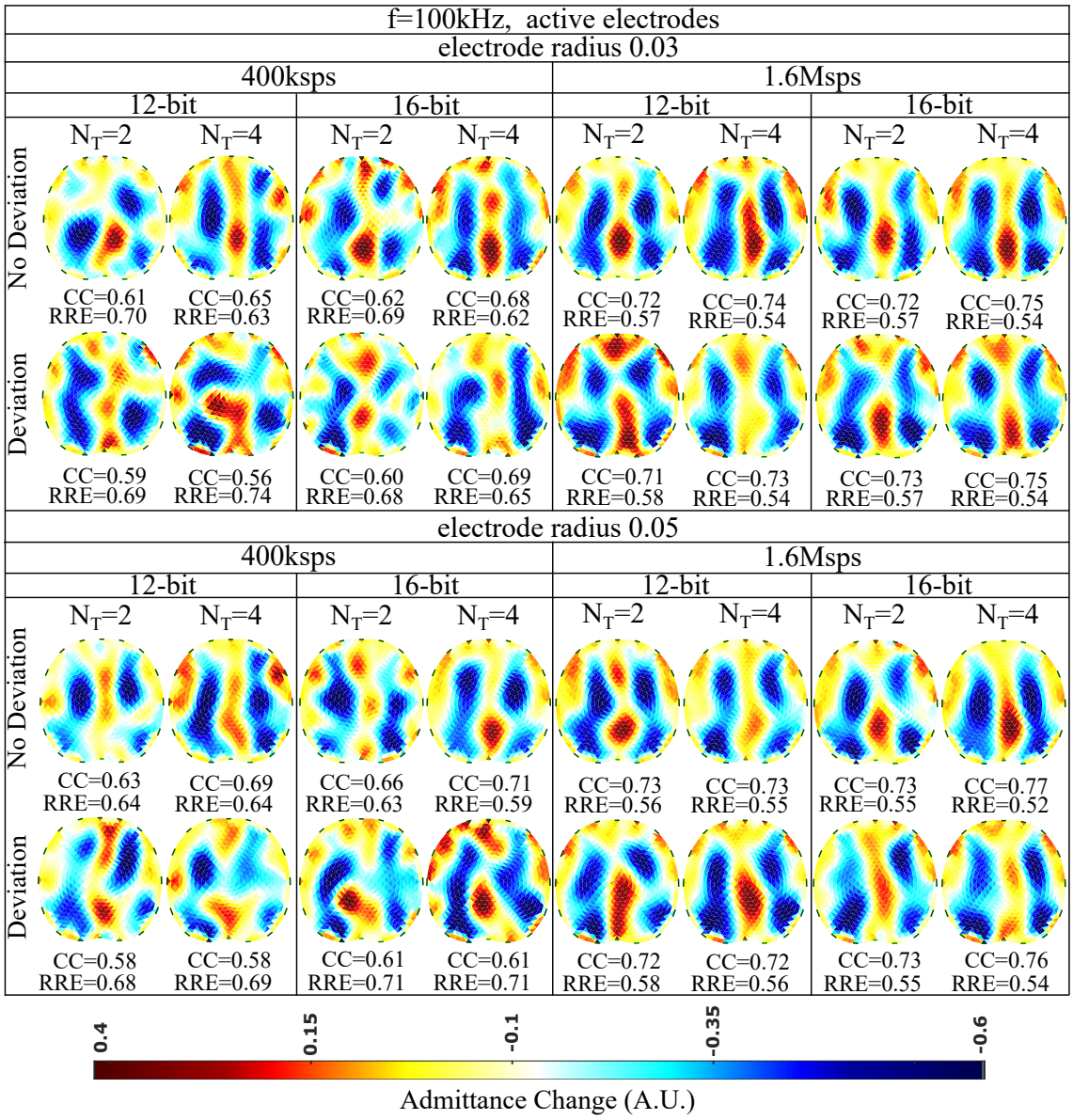

Figure 6.23: Simulation results for 100 kHz input signal and active electrode configuration. All further hardware configurations, as well as the corresponding CCs and RREs, are noted in the Figure.

Discussion

From the results presented above, we can observe the effects of contact impedances, parasitic effects, noise, and shape mismatch under different hardware configurations and measurement frequencies. Specifically, the contact impedance effect becomes more intense at lower frequencies. However, the absence of capacitive effects and attenuation allows a moderate to good performance with a passive electrode configuration, which is achieved at 15 kHz (see Figure 6.21).

At higher input sinusoidal signal frequencies, the use of an active electrode configuration is essential for achieving a sufficient image quality by reducing the capacitive effects. Such systems have been

already implemented in [21, 171, 230]. Fully active electrode EIT systems that implement the current source near each corresponding electrode pair have shown even better performance, since apart from the voltage channels' parasitic effects, they compensate for the current channels' ones. In [21], a comparison between passive and fully active electrode configurations on a lung-imaging EIT system has shown superior performance for the second case over a high frequency span. Hence, higher signal frequency spans can be achieved with active electrodes that allow higher temporal analysis which is essential for real-time lung imaging applications.

Furthermore, high noise levels from the circuitry can be taken care of by increasing the ADC sampling frequency f_s and the number of sine periods N_T that are sampled per measurement window. This leads to the increase of the number of taps K per measurement and benefits the SNR values, according to (6.42). In this way, the matched LPFs' performance is improved (after IQ demodulation) by actually performing signal averaging. Some systems, such as [171], use a high K per measurement window and achieve good voltage SNR levels. However, increasing N_T also increases the total time needed to take a measurement frame. As a result, lower image frame rates are obtained, significantly reducing the imaging temporal resolution. Therefore, lung imaging has to be performed at frequency rates above 100 kHz and relatively high sampling rates f_s. In addition, these frequency ranges usually include valuable information about the thoracic tissues' electrical behavior [21]. Nonetheless, there is always a trade-off between signal noise and frame speed. Refs. [20, 21], for example, achieve an imaging speed of more than 100 frames per second (fps) at a 1 MHz signal frequency; however, the SNR rates fairly drop between 125 kHz and 1 MHz. On the other hand, ref. [171], which, as mentioned, uses a large number of filter taps, keeps a high SNR by dropping the speed to lower than 20 fps. Moreover, another way to increase the SNR is by enacting higher amplitude current signals. However, apart from the patients' safety consideration, this solution demands higher power supplies and thus power consumption, which would be impractical in the case of active electrodes. The usage of a programmable gain amplifier (PGA), which amplifies the voltage signals collected from electrodes that are far from the current source pair, could also improve signal resistance to noise [158, 227]. Finally, the effect of enacting different current patterns instead of the adjacent one to SNR has been partially studied in [265]. Skip current patterns might increase the signal amplitude; however, sometimes they have a negative effect at the imaging reconstruction process, since they lead to a more ill-posed problem than the adjacent pattern. This happens due to the reduced number of electrode boundary measurements and the reduced number of independent measurements [26].

Finally, the shape mismatch between the chest (surface attached by electrode array) boundary and the reconstruction domain, as well as the boundary motion, leads to further image artefacts. Boundary tracking methods, such as the use of accelerometers, have recently been proposed to overcome this effect [21, 176]. Although these methods can improve the image quality, they are often more expensive, due to the extra hardware needed. Furthermore, since the boundary motion due to the breath (or even the subject's movement) is continuous, artefacts will be still present due to the fact that the reconstruction domain does not change through the imaging frames. Until now, such change in real-time thoracic EIT imaging applications is not applicable due to the complexity and time the mesh refinement needs. Therefore, compensation of motion-related imaging errors in EIT imaging applications is still a field under research.

A prior code implementation of the proposed interface can be found online on the following website:

https://github.com/chdim100/SPICE-MATLAB-Interface-for-Electrical-Impedance-Tomography-Simulation-SPICEIT-
(accessed on August, 7, 2021).

7 Miscellaneous Modeling and Simulation works and considerations

This chapter includes the content from 3 research works, related with miscellaneous modeling and simulation approaches, applications and considerations. In the first section, a parametric tunable two-dimensional time-variant thoracic model is presented. The work's purpose, which is published in [192] is to search the effect of tissues boundaries' movement during the measurement process on the image reconstruction quality. In the second section, which corresponds to [297], the tetrapolar impedance setup skin-electrode contact impedance is modeled using Cole models in an active element analog circuitry implementation. Finally, in the third section, which corresponds to [303], an analogue realization of fractional-order healthy and cancerous lung cell models for Electrical Impedance Spectroscopy (EIS) is presented.

7.1 A highly tunable dynamic thoracic model for Electrical Impedance Tomography

A time-dependent, flexible, 2-dimensional fine thoracic Finite-Element model for continuous lung Electrical Impedance Tomography (EIT) imaging is presented. It can be used as a tool to identify lung EIT hardware specifications, such as minimum frame rate, number of electrodes and noise requirements, as well as for prior evaluation of EIT reconstruction algorithms, before applying in-vivo data. The model is parameterized with respect to electrodes' characteristics, the measuring protocol, structural and temporal properties of the thoracic tissues. It is implemented in FEMM using a script generated by MATLAB code, while the measurements are acquired also by MATLAB. The electrodes' contact impedances, as well as the changes in electrical and geometric properties of the thoracic tissues due to breathing and perfusion, during each particular measuring frame, are taken into account.

7.1.1 Introduction

Electrical Impedance Tomography (EIT) is a radiation-free, non-invasive and fast medical imaging technique, in which a small amplitude, medium frequency (kHz) and safety-standard current is applied through an electrode array in the under examination domain. From the raw voltages acquired, a conductiv-

ity distribution map of the subject's interior is estimated. EIT is safer, faster and cheaper than Computed Tomography (CT) or Magnetic Resonance Imaging (MRI), while offering portability and exceptional temporal resolution. This makes EIT sufficient for continuous monitoring applications, such as real-time lung imaging of patients with respiratory failure, that require mechanical ventilation, or neonates that should never be subjected to any ionizing radiation [21],[174].

Despite its remarkable capabilities in applications that require sufficient temporal resolution, EIT lacks adequate spatial resolution and robustness in noisy measurements. Therefore, carefully designed and high quality performance hardware systems are deployed in order to achieve high SNR level bio-signals. Over the last 40 years of EIT development, important steps have been accomplished to this direction, with the implementation of high performance academic and commercially available, generic and application targeted systems [21], [156], [171]. Moreover, significant research has been performed in the image reconstruction problem formulation and post-processing algorithms [151],[174]. However, EIT has not yet become widely applicable in medical equipment.

As a result, there is a lack of available EIT in-vivo data, relative to other imaging techniques, which is essential for the validation of reconstruction algorithms, the determination of system standards, comparisons and even training Machine Learning structures that are currently gaining popularity in EIT applications [118], [127]. Recently, some notable efforts have been made for the classification of open-source EIT data; however, there is still a large field for new investigations [72].

Absence of medical data makes the usage of accurate simulation models necessary for the evaluation and testing of reconstruction approaches. Although numerous accurate F.E.M. structures have been utilized for many applications, in ventilation Time-Difference EIT (Td-EIT) imaging, most of them are actually reduced to two extreme states: full-inhalation and full-exhalation of the lungs ignoring all in-between instances [293], or changes during an individual frame measurement [151]. Furthermore, many of them do not consider the shape-changes of both the boundary (and hence the exact electrode positions) and the tissues during breathing. What actually happens in lung EIT monitoring is that each measuring frame needs a time interval to be recorded. During this space, both electrical and geometric properties are continuously changing. Therefore, for modest frame rates (< 30fps), each set of measurements per frame can not be considered as an EIT "snapshot".

Hence, a thoracic-EIT simulation model which includes numerous shape, conductivity and permittivity states is essential for observing EIT images' behavior through various frame rates, correlated with other parameters such as the electrode number, bio-signal noise levels and measurement pattern. This view can lead to useful conclusions for both the design and the functional parameters of a ventilation-monitoring EIT system.

In this section, a highly tunable, two-dimensional dynamic thoracic F.E.M. model is presented, which includes the following tissues: skin and fat, bones, lungs, muscle and heart. The electrodes' number and characteristics, structure geometry, breathing times and Heart Beat Rate (HR) as well as the Frames Per Second (FPS) and measuring strategy (skip protocol [26]) can be initially defined. Collapsing regions can also be defined. The time-variant model is implemented based on CT images by using MATLAB and FEMM software tools in the following way: a .lua script is created by a MATLAB code and executed in the FEMM software, where a particular shape, conductivity and permittivity state of the thorax

is sketched at each time step. The shape and position states of all tissues except heart, are determined by the corresponding ventilation cycle states, while conductivity and permittivity are specified by the superposition of ventilation and blood circulation cycles.

This paper is organized as follows. In subsection 7.1.2 the EIT measurement principle is described. In subsection 7.2 the model's parameters and properties are extensively described. In subsection 7.2.1, the process performed for the model's execution and measurement collection is presented. Furthermore, in subsection 7.2.2, time evolution simulation results are displayed and compared for selected initial parameters.

7.1.2 EIT measurement principles

Although different types of measuring techniques have been developed, the most conventionally used is the current skip-m, voltage skip-n protocol [26]. In a N-electrode EIT system, a bipolar AC current source is applied to two electrodes with a gap of m electrodes between them, while differential voltages are acquired from two other electrodes, at a distance of n electrodes between each other (tetrapolar measurement). After the voltage measurements are taken, the bipolar source is shifted to the next electrode pair and potentials are collected in a serial or parallel way. The process described above continues for all N current electrode pairs and is briefly demonstrated in Fig. 2.1.

For each current electrode pair injection, $h = N-3$ voltage measurements are acquired when $m = n$ or $h = N-4$, in case $m \neq n$. Therefore, for all current source positions, a total number of $N \cdot h$ voltage measurements is taken, which together create a single EIT measurement frame and are utilized in order to extract a static image through an inverse reconstruction algorithm. If f_r denotes the imaging frames per second (fps), then the total time needed for a frame is $t_{fr} = f_r^{-1}$. For our model, we assume that the time interval between two continuous current electrode-pair position changes is a discrete time step $t_{step} = t_{fr}/N$.

However, to compensate for modeling errors, differential frame imaging in time or frequency domains (Td-EIT or Fd-EIT) is extensively adopted [174], where an initial frame is utilized as reference. ventilation monitoring is one of the most widespread applications of Td-EIT, where L measurement frames are needed for the reconstruction of $L-1$ images. Since the reference is usually the first frame, lung Td-EIT does not reveal the absolute conductivity distribution of the examined thoracic domain. Instead, it illustrates an estimation of the conductivity variations, compared to the first frame each time. This can provide temporal information for pulmonary operation over time which in these applications is more important than real conductivity values. The latter can be later approximated by applying appropriate a-priori data about the corresponding tissue conductivities.

7.2 Model Structure and Parameters

The two-dimensional thoracic model implemented represents a specific cross-section of the thorax. Although the actual thoracic geometry is three-dimensional and many 3D models have been utilized for EIT reconstruction algorithm evaluation [151], no models that include temporal tissue boundary and

admittance behavior during particular frames exist in the literature. The development of a high temporal resolution model needs to be primarily in 2D due to the large numerical complexity of the problem, caused by continuous reshaping and re-meshing.

Tissue Movement

The model described has a dynamic behavior during each EIT simulation. The boundaries of the skin and lung tissue, as well as the position of the chest-placed electrodes and bones (ribs and vertebra) are assumed to synchronously and gradually change between two initially defined constant states, due to the breathing process. The first one indicates the deflated (minimum air in lungs) condition while the second one denotes the fully inflated case (maximum air). The boundary deviation of the lungs is set larger than in the case of the ribs and electrodes' positions, while the number of discrete steps (total positions) between inhalation and exhalation is expressed by:

$$P = \frac{N \cdot t_{br} \cdot f_r}{2} \tag{7.1}$$

where t_{br} is the time needed for a single breath cycle.

Each model which describes tissue (except the heart), skin or electrode boundary consists of a time-variant n-polygon, represented by a point sequence $B_n(t) = [b_i(t)]$, where $i = \{1, 2, ..., n\}$ corresponds to the ith point. We consider that $B_n^{inh} = [b_i^{inh}]$ and $B_n^{exh} = [b_i^{exh}]$ are the initially defined boundary point positions at the exact times of inhalation and exhalation respectively. Each point $b_i(t) = (x_{bi}(t), y_{bi}(t))$ has a total deviation of $Dx_i = \left\| b_i^{inh} - b_i^{exh} \right\|$, and the corresponding space step during t_{step} is calculated by:

$$dx_i = \frac{Dx_i}{P} \tag{7.2}$$

which for the sake of simplicity is assumed to be time-proportional. Hence, dx_i denotes the shift $b_i(t_{j+1}) - b_i(t_j)$, with $t_{step} = t_{j+1} - t_j$ of a polygon's point b_i during the time that current is injected from a single electrode pair.

The heart tissue boundary can be described by a polygon point sequence $H_n(t) = [h_i(t)]$, where $i = \{1, 2, ..., n\}$ also corresponds to the ith point. At the diastolic and systolic-end states the heart boundary polygon gets the following sequence values: $H_n^d = [h_i^d]$ and $H_n^s = [h_i^s]$. For each heart boundary polygon point, the total deviation is $Dh_i = \left\| h_i^d - h_i^s \right\|$ and the space step during t_{step} is given by:

$$dh_i = \frac{2Dh_i}{N \cdot t_{pulse} \cdot f_r} \tag{7.3}$$

where t_{pulse} is the duration of a single heart beat. The total positions of the heart boundary points can be calculated in the following way:

$$Q = \frac{N \cdot t_{pulse} \cdot f_r}{2} \tag{7.4}$$

It is noted that the heart tissues' deviation should be chosen relatively smaller than the lung tissues' one.

Admittance temporal behavior

During the pulmonary and cardiac cycles, apart from the tissues' shapes and positions, significant changes are also detected at most of the admittances.

The most intense variations take place in the lungs, where conductivity σ and permittivity ϵ depend on their volume and their air content. A less important change in both σ and ϵ is caused by blood flow in lungs. Thus, their admittance can be expressed as a function of the pulmonary and circulation cycle states each time.

To set the pulmonary-cycle related lung's admittance, we first assumed that each lung's relative volume F changes piecewise linearly with timesteps $1 \leq i \leq 2P$ during a single breathing period ($t_1 \leq t_i \leq t_{2P}$):

$$F_i = \left\{ \begin{array}{ll} \frac{3}{P+1}i + \frac{3}{P-1} + 4, & \text{if} \quad 1 \leq i \leq P \\ -\frac{3}{P+1}i - \frac{6P+3}{P+1} + 4, & \text{if} \quad P \leq i \leq 2P \end{array} \right\}$$

This piecewise linear function here has been defined for simplicity, since the true dependence of air volume F from time is obviously more complex and might depend on each particular breath's characteristics. The air-related conductivity of a lung as a function of its air volume can be approximated by [193]:

$$\sigma_{l,air} = K_1 \left(\frac{0.85 s_b}{w} + 0.03 s_i \right) \frac{32F + 4.5}{(32F + 9)^2} + K_2 \tag{7.5}$$

Where s_b, w and s_i are parameters related with morphological lung properties [193] and are selected as $s_b = 0.5$, $w = 1.5$ and $s_i = 2$ (mean values). K_1 and K_2 are frequency related parameters and are properly chosen in order to scale $\sigma_{l,air}$ between the absolute inflated ($\sigma_{l,air}(f, F_{max})$) and deflated ($\sigma_{l,air}(f, F_{min})$) lung conductivity values for the used measuring frequency f, as given from [188], [189]. In case of the air-related lung permittivity, the following approximation has been performed [193]:

$$\epsilon_{l,air} = L_1 \left(\frac{0.85 e_{rb}}{w} + 780 F^{1/3} e_{rm} \right) \frac{32F + 4.5}{(32F + 9)^2} + L_2 \tag{7.6}$$

Where e_{rb} and e_{rm} are also morphological lung parameters, selected as 10000 and 10, respectively [193]. L_1, L_2 scale the permittivity between the corresponding inflated and deflated values at the chosen frequency, defined in [188], [189]. The air-related lung admittance value is:

$$\gamma_{l,air} = \sigma_{l,air}(f, F) + j 2\pi f \epsilon_{l,air}(f, F) \tag{7.7}$$

The lungs admittance variation due to blood circulation is assumed to be a piecewise linear function for $t_1 \leq t_j \leq t_{pulse}$:

$$\delta\sigma^j_{l,blood} = \left\{ \begin{array}{ll} \frac{\Delta\sigma_{bo}}{Q} j, & \text{if} \quad 1 \leq j \leq Q \\ \\ -\frac{\Delta\sigma_{bo}}{Q} j + \Delta\sigma_{bo}, & \text{if} \quad Q \leq j \leq 2Q \end{array} \right\}$$

Where $\Delta\sigma_{bo}$ refers to the initially defined total lung conductivity variation due to blood circulation (10 -

20 times lower than air-related changes, 0.005 - 0.01 S/m [293]). The corresponding relative permittivity change is defined as:

$$\delta\epsilon^{j}_{l,blood} = \left\{ \begin{array}{ll} \frac{\Delta\epsilon_{bo}}{Q} j, & \text{if} \quad 1 \leq j \leq Q \\ \\ -\frac{\Delta\epsilon_{bo}}{Q} j + 2\Delta\epsilon_{bo}, & \text{if} \quad Q \leq j \leq 2Q \end{array} \right\}$$

$\Delta\epsilon_{bo}$ refers to the initially defined total lung permittivity variation due to blood circulation (200 - 500 F/m [293]).

While pulmonary cycle is at state i, $1 \leq i \leq 2P$ and cardiac cycle at state j, $1 \leq j \leq 2Q$, we write the total admittance of each lung:

$$\gamma^{i,j}_{l} = \gamma^{i}_{l,air} + \delta\gamma^{j}_{l,blood} = \sigma^{i}_{l,air} + \delta\sigma^{j}_{l,blood} + j2\pi f(\epsilon^{i}_{l,air} + \delta\epsilon^{j}_{l,blood}) \tag{7.8}$$

The heart admittance is assumed to change periodically and piecewise linearly. Thus:

$$\sigma^{j}_{heart} = \left\{ \begin{array}{ll} \sigma_{ho} - \frac{\Delta\sigma_{ho}}{Q} j + \Delta\sigma_{ho}, & \text{if} \quad 1 \leq j \leq Q \\ \\ \sigma_{ho} + \frac{\Delta\sigma_{ho}}{Q} j - \Delta\sigma_{ho}, & \text{if} \quad Q \leq j \leq 2Q \end{array} \right\}$$

and

$$\epsilon^{j}_{heart} = \left\{ \begin{array}{ll} \epsilon_{ho} - \frac{\Delta\epsilon_{ho}}{Q} j + \Delta\epsilon_{ho}, & \text{if} \quad 1 \leq j \leq Q \\ \\ \epsilon_{ho} + \frac{\Delta\epsilon_{ho}}{Q} j - \Delta\epsilon_{ho}, & \text{if} \quad Q \leq j \leq 2Q \end{array} \right\}$$

where σ_{ho} and ϵ_{ho} are the base inner heart conductivity and permittivity (approximately 0.4-0.5 S/m and $5 \cdot 10^4$ F/m respectively [188], [189]), while $\Delta\sigma_{ho}$ and $\Delta\epsilon_{ho}$ refer to the conductivity and permittivity changes of the heart due to blood presence (fixed to 0.025 S/m and 2000 F/m respectively).

Near the heart boundary, the myocardium muscle is defined, which consists of a frequency depended conductivity [304]:

$$\sigma_{mc}(f) = 9 \cdot 10^{-8} \cdot f + 0.168 \tag{7.9}$$

and a permittivity of [304]:

$$\epsilon_{mc}(f) = 2.29 \cdot 10^{5} \cdot (10^{-3} f)^{-0.95} \tag{7.10}$$

It is noted that due to blood circulation, when $|\delta\gamma_{l,blood}|$ is maximized, $|\delta\gamma_{heart}|$ is minimized. Furthermore, piecewise constant functions were selected instead of harmonic ones, because the actual admittivity spectrums exhibit more complex behavior than a single harmonic. The model's accuracy can be further improved using proper regression models, which is not a part of this work.

The muscle tissue, which exists between bones and lungs has a permittivity set in a similar way to γ_{heart} above. Nonetheless, 180^o phase shift has been added, due to the circulation cycle behavior. Moreover, we defined $\delta\sigma_m = 0.01$, $\sigma_{mo} = 0.28$ (S/m), $\delta\epsilon_m = 900$ (F/m) and $\epsilon_{mo} = 13 \cdot 10^3$ (F/m) [188].

The skin-fat (a thin inner layer near the boundary) admittance is assumed to be constant at very small

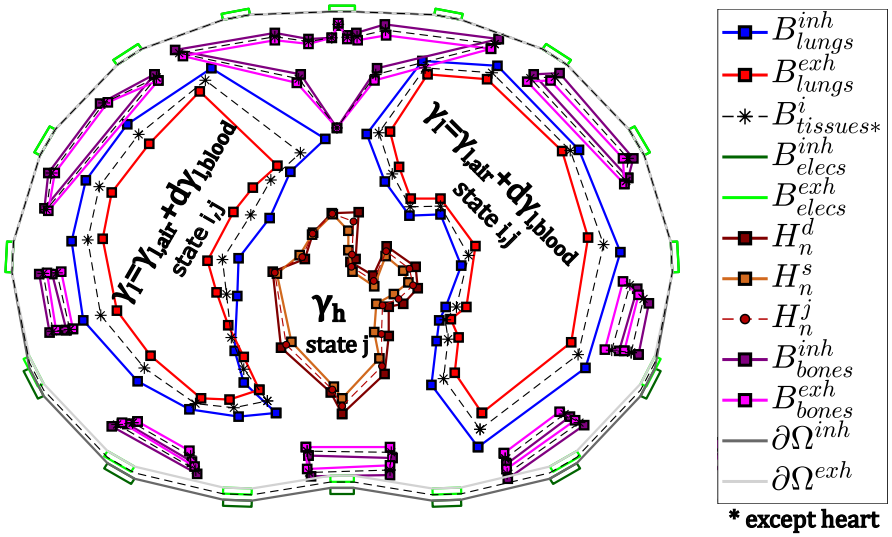

Figure 7.1: Simplified sketch of the dynamic thoracic model. The inhalation and exhalation end, as well as the heart's systolic and diastolic end are noted. The shape boundaries are indicative, since they can be properly tuned. No collapsed areas and skin/fat are included for clarity.

values (i.e. less than 0.03 S/m) [188], [189].

Silent spaces and collapsed areas

At the end of each breath, after the exhalation-end, a small silent time-space usually follows, where no breath activity is recorded. This space is included in the dynamic model's behavior and can be defined between 0.3 and 1.5 seconds. When each silent space ends, a new breath cycle begins with the inhalation process.

Chronic clinical conditions of lungs, such as acute respiratory distress syndrome (ARDS) may cause inflammatory edema that induces regional collapses [168]. This practically means that lungs do not homogeneously function, with some areas not inducing sufficient air volume. This is modeled by inducing 4 possible collapse cases (proportional to the area of collapse) at the left lung and 3 possible cases for the right lung. The selected collapsed area's admittance is not affected by the ventilation cycle state, contrary to the rest of the corresponding lung.

Electrode modeling

The electrodes are modeled as rectangular 2D shapes, with an adjustable width d_{elec}. Their contact impedance relative to area, is approximated by the following formula:

$$\rho_{elec} = Z_{elec}\frac{S}{d_{elec}} \tag{7.11}$$

where Z_{elec} is the electrode's contact impedance and S the corresponding surface area.

Table 7.1: 2-D Thoracic Model Parameters

Parameter	Description
$\partial\Omega^{inh}$	domain's boundary at inhalation
$\partial\Omega^{exh}$	domain's boundary at exhalation
$B_n^{inh}, B \neq heart$	tissue/electrode polygons at inhalation-end
$B_n^{exh}, B \neq heart$	tissue/electrode polygons at exhalation-end
H_n^d	heart shape at end-diastolic phase
H_n^s	heart shape at end-systolic phase
t_{pulse}	pulse duration (secs)
t_{br}	breath duration (secs)
z_{elec}	electrode contact impedances (Ω)
d_{elec}	electrode width (cm)
γ_l	standard lung admittance (σ_l, ϵ_l)
$\Delta\gamma_{l,air}$	total lung admittance variation due to the breath ($\delta\sigma_{l,air}, \delta\epsilon_{l,air}$)
$\Delta\gamma_{l,blood}$	total lung admittance variation due to the HR ($\delta\sigma_{l,blood}, \delta\epsilon_{l,blood}$)
γ_{ho}	standard heart admittance ($\sigma_{ho}, \epsilon_{ho}$)
$\Delta\gamma_{ho}$	total heart admittance variation due to the HR ($\Delta\sigma_{ho}, \Delta\epsilon_{ho}$)

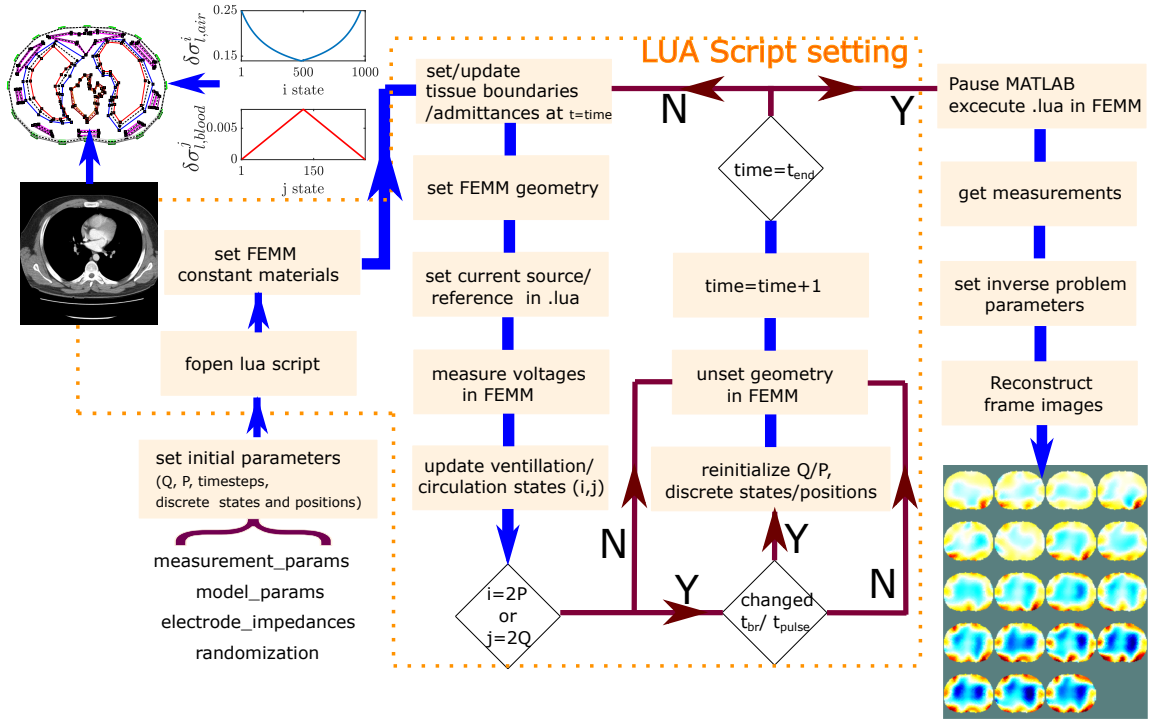

Figure 7.2: Explanatory diagram of the process performed for the temporal thoracic model execution in FEMM and the measurement collection from MATLAB.

7.2.1 Execution Process

The process begins with the initialization of the total tissue and electrode positions, as well as their admittance properties in the time domain, according to the model and measurement input parameters. A .lua script is opened and processed via MATLAB and time-constant properties (bone conductivity and permittivity, collapsed areas, e.t.c.) are set. It is also noted, that the input domain's boundary ($\partial\Omega^{inh}$ and $\partial\Omega^{exh}$), as well as the tissues' respiratory end boundaries (B_n^{inh} and B_n^{exh}) are derived from a CT scan [305], considering a lung volume change of 15% and chest movement of 1 cm (5% vertical change) [151]. The user can also choose to randomize all boundaries, with a standard deviation of 5%. Both initial ventilation and circulation states can also be randomly selected.

For each discrete time step (i.e. current injection, see section II), the tissue current positions and admittances are updated according to the pre-defined sequence (see 1st step). FEMM is instructed to construct the corresponding structure and perform voltage measurements on the electrodes. Furthermore, both ventilation and circulation states are checked. When a breathing cycle ends, a silent space begins that lasts up to 1 second. If a silent space has ended, a new breath cycle begins, with a duration that differs from the previous one at a maximum of 20%. Then, P is recomputed and the tissues' discrete positions and temporal admittances are redefined according to equations (7.1), (7.2) and (7.7). In addition, every 3 circulation cycles, HR changes randomly at a maximum of 2% (assuming calm patient state). In this case, Q, heart tissue discrete positions and each tissue's blood-cycle related admittance variation in time are redefined according to (7.3), (7.4) and the piecewise linear functions defined in section II. The updates and checks described are repeated until the final time step simulation t_{end} is reached.

When the loop is exited, a .lua script is created and MATLAB pauses in order to execute the script using the FEMM software. The latter automatically follows the steps written in the .lua file, efficiently recreating and remeshing the structure at each time step. Electrode potential measurements are written in text files, which are then parsed and assembled by MATLAB according to the selected measuring pattern. Finally, measurements are utilized as inputs to an inverse reconstruction algorithm, where proper hyperparameters are selected.

The process flow is demonstrated in Fig. 7.2 and the previously selected measurement parameters are presented in Table II. The code written for this development is available under an open-source license at `https://github.com/chdim100/Dynamic-Thoracic-Model-for-EIT` .

7.2.2 Simulations and Results

To evaluate the proposed simulation model, a number of simulation cases were derived. In particular, $N = 16$ and $N = 32$ electrodes are selected for simulation test cases of 6 second duration. Imaging is performed at 5, 10 and 30 fps for a current frequency of $200kHz$. During each frame, the shape and admittance properties of each tissue are dynamically changing, as described in previous sections. The current $skip - 2$ measuring protocol is used in the 16-electrode simulations, while for the 32-electrode cases we selected the current $skip - 4$ pattern. In both electrode cases, differential voltages are measured from adjacent electrode pairs (voltage $skip - 0$).

The model parameters are initialized as follows: the inspiration and expiration end positions are de-

Table 7.2: Measurement Parameters

Parameter	Description
N	Number of electrodes
f	Current signal frequency (Hz)
I	Current signal amplitude (mA)
m	Current skip-pattern
n	Voltage skip-pattern
n	Voltage skip-pattern
n	Voltage skip-pattern
t_{fr}	Time needed for each frame (fps^{-1})
t_{end}	Total simulation time ($secs$)

fined according to a specific CT scan (where boundaries are used as mid-points) [305]. The shapes are not further processed via randomization. In order to get clear comparisons, initial breath time is set to 3 seconds, while silent space is set to 0.3 seconds (non-random). Within the 4th second of the simulation, a 2nd breath cycle begins, which has a duration of 3.6 seconds (increased by 20%) and is not completed until the simulation ends. The HR is 75 bpm for the first 3 beats, and then increases to 77.25 bpm ($+3\%$ increment). The right lung is assumed to be healthy, while a lung collapse that corresponds to the 20% of the total left lung's modeled area is inserted. The whole time-evolution of each dynamic tissue's impedance is demonstrated in Fig. 7.3.

The electrodes are assumed to have a width of $d = 0.5$ cm and relative conductivities with a mean value of 0.02 (S/m) and 15% standard deviation, since in real EIT cases, contact impedances always have a variation [306]. The values above are computed using (7.11), assuming $E[z_{elec}] = 1k\Omega$ (dry electrode at 200 kHz for long-term monitoring [307]).

The FEMM time-variant F.E. model includes $\sim 7000 - 7500$ nodes and $\sim 12000 - 14500$ elements, dependent on the number of the electrodes and the boundaries state. Re-meshing is performed at each discrete time step (which as referred corresponds to a bipolar current source position).

For the time-differential image reconstructions, the Gauss-Newton iterative algorithm has been evaluated. The relative conductivity (or admittance) estimation problem can be described as minimization of the following expression [174]:

$$\underset{\delta\sigma}{argmin}\{\|J\delta\sigma - \delta V\|_W^2 + \lambda^2 \|\delta\sigma\|_Q^2\} \tag{7.12}$$

Where $\delta\sigma$ is the conductivity change under estimation, δV the electrode-measured differential potentials, J the Jacobian matrix around a linearization point $\sigma = \sigma_o$, which actually indicates the potential field's sensitivity to conductivity changes. W is a weight matrix, used for calibrating the imbalanced electrode contacts, λ a regularization hyperparameter and Q a prior filter matrix [174]. The function under minimization includes a least-square term and a penalizing regularization term ($\|\delta\sigma\|_Q^2$), in order to encounter the problem's ill-posedness and ill-conditioning [174].

The imaging process is performed in MATLAB using the EIDORS library tool [72]. Reconstructions take place on a default EIDORS static thorax-shape F.E. model, which contains 1024 elements. The

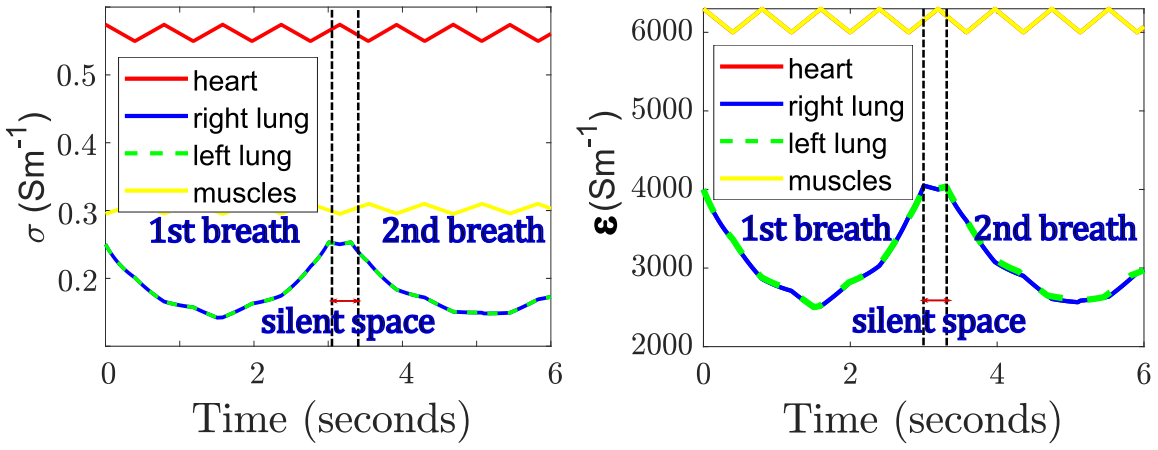

Figure 7.3: Temporal tissues admittances defined for the simulation (200 kHz). Heart and muscle tissue permittivities are almost equal.

hyperparameter is heuristically selected $\lambda = 0.25$ for the 16-electrode cases and $\lambda = 0.03$ for the 32-electrode cases. In addition, Gaussian noise has been added so that the simulated measurements for all cases have a 50 dB SNR which is a moderate noise level for ventilation EIT measurements [127]. It is noted that for high frame rate levels, averaging which increases the signal's SNR is not possible, hence reducing the frame rate level is often preferred for SNR optimization [171]. However, lower fps levels obscure significant temporal information about both ventilation and cardiac-related functions. In order to examine the way lower noise reduces spatial imaging artifacts, a 65 dB SNR signal case has been added for the lower frame rate test cases (5 and 10 fps).

The time evolution of the reconstructed images for 16 and 32 electrodes and each frame rate and noise testcase is shown if Fig. 7.4. Furthermore, to get quantitative information and a clearer comparison of the images' temporal behaviors, we have segmented 3 constant Regions of Interest (ROIs) in the inverse reconstruction model (Fig. 7.5 VI). The first two regions correspond to the areas considered as lungs while the third demonstrates the heart tissue's area. For each ROI, the mean estimated conductivity values over its elements are computed and displayed in the time domain in Fig. 7.5 (I-V).

In all cases, the breathing activity is successfully detected, since two large conductivity curve "valleys" appear in ROIs I and II (Fig. 7.5). Their behavior follows the lung admittance evolution shown in Fig. 7.3. In both the 16 and 32 electrodes configurations, when imaging at low fps (5 - 10) the contribution of the SNR's increase from 50 to 65 dB is observable, since the images' artifacts are descreased, and the curves in Fig. 7.5(I-IV) are smoother, appearing less intense random variations. Increasing the fps rate, leads to aqcuiring more information about some details that can be utilized for further functional analysis [6], [308]. In addition, higher frame sampling gives a more reliable data for each breath's exact depth (i.e. in this example the two breaths are equal, however this is detectable only for $f_{fr} > 10$ fps, as observed in Fig. 7.5). At 30 fps, the imaging quality difference between 16 and 32 electrodes is clear, where in the latter, the left lung's collapsed area is detected without any post image processing (the left lung's impedance change area size is significantly lower that the right ones). The lung, muscle and heart's temporal behaviors due to the blood cycle are still not noticeable without further time and frequency do-

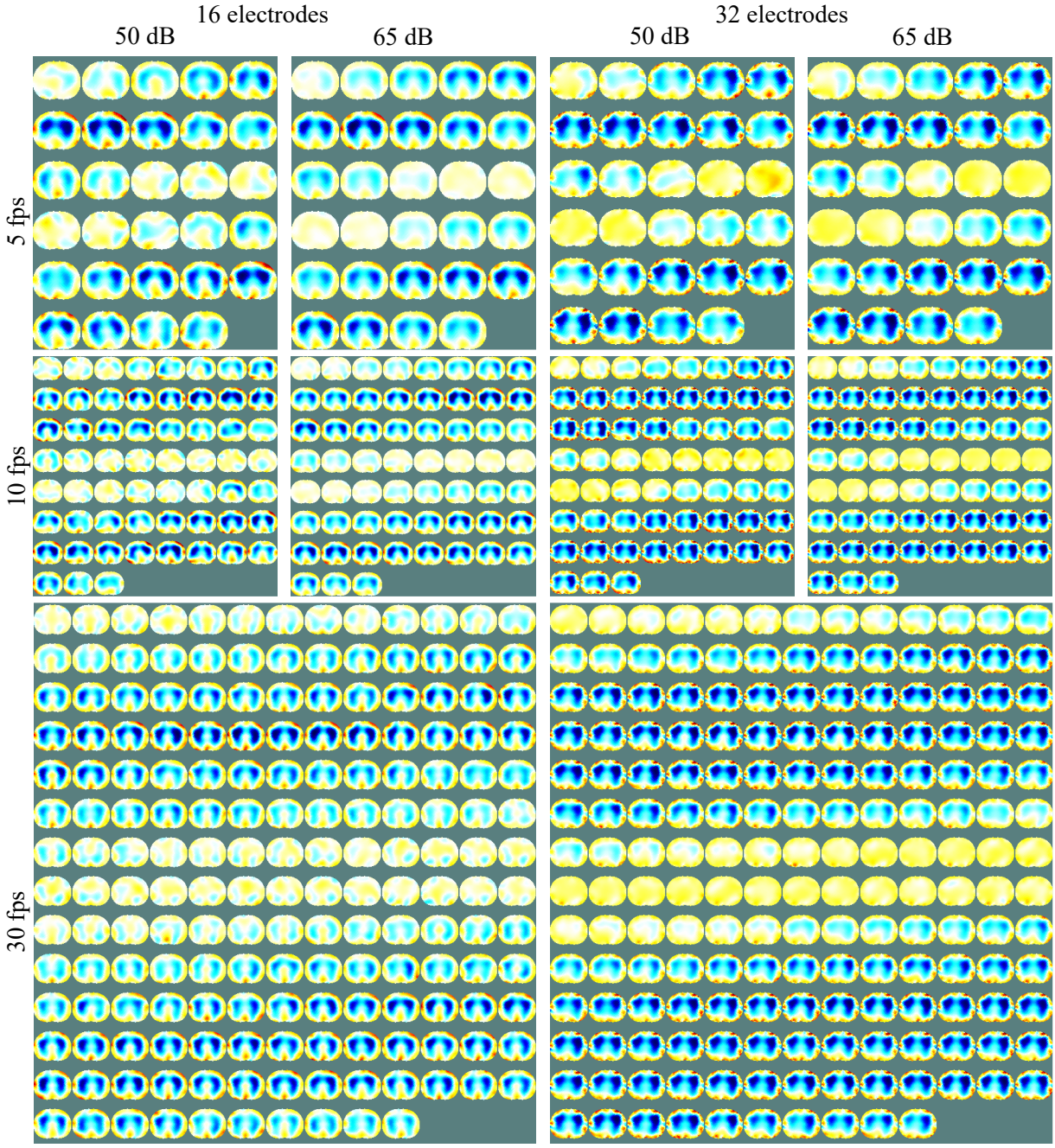

Figure 7.4: EIT image reconstruction of 2 breath cycles of the simulated dynamic model. The first column shows the 16-electrode configuration images, while the second column depicts the 32-electrode case. Each sub-case is displayed in a particular gray frame. When the lungs are in deflated state, the impedance changes are very low, since at all the performed simulations, the reference frame corresponds to full-exhalation end. While the exhalation process takes place, the lung area's impedance gradually decreases (darker blue colors), until it reaches the full-inflated state. From this point the lung impedance begins to increase again and the exhalation part takes place. In order to distinguish the differences between the cases temporal resolution, all the frames are figured.

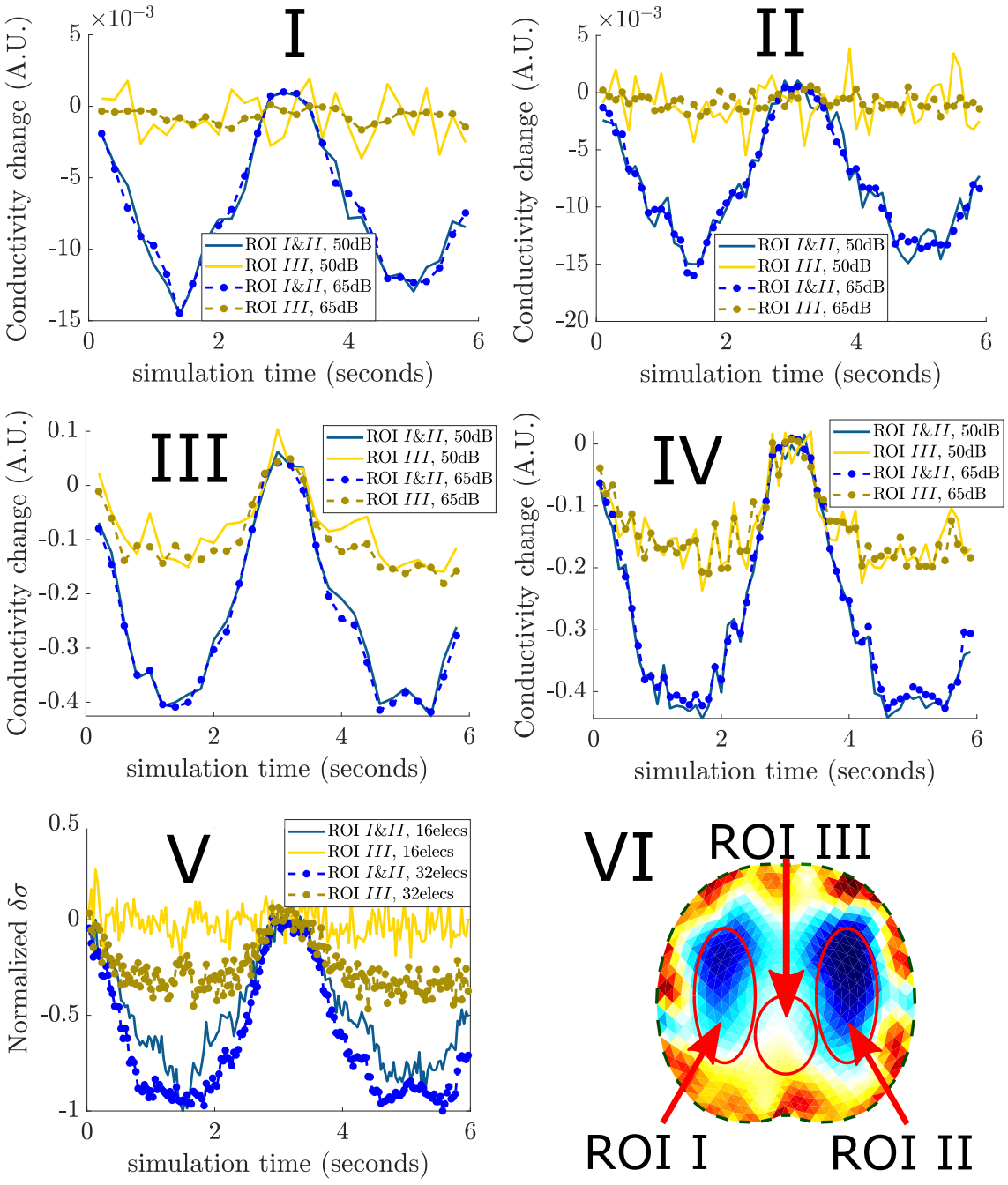

Figure 7.5: Mean estimated (arbitrary) values of each ROI over the time. Case I: 16 electrodes, 5fps. Case II: 32 electrodes, 5fps. Case III: 16 electrodes, 10 fps. Case IV: 32 electrodes, 10 fps. Case V: 16 and 32 electrodes while imaging at 30fps. VI: the 3 ROI areas, related to the inverse reconstruction model.

main analysis, however, for 30 fps some higher frequency periodicity in ROI III can be slightly observed in Fig. 7.5 V.

7.3 Analogue Realization of Fractional-Order Skin-Electrode Model for Tetrapolar Bio-impedance Measurements

This work compares two design methodologies, emulating both AgCl electrode and skin tissue Cole models for testing and verification of electrical bio-impedance circuits and systems. The models are based on fractional-order elements, implemented with active components, and capture bio-impedance behaviors up to $10kHz$. Contrary to passive-elements realizations, both architectures using analog filters coupled with adjustable transconductors offer tunability of the fractional capacitors' parameters. The main objective is to build a tunable active integrated circuitry block that is able to approximate the models' behavior and can be utilized as a Subject Under Test (SUT) and electrode equivalent in bio-impedance measurement applications. A tetrapolar impedance setup, typical in bio-impedance measurements, is used to demonstrate the performance and accuracy of the presented architectures via Spectre Monte-Carlo simulation. Circuit and post-layout simulations are carried out in $90nm$ CMOS process, using the Cadence IC suite.

7.3.1 Introduction

The electrical properties of tissues are strongly related to their structural characteristics and their functional properties [187], [188], [189]. Bio-impedance measurements for example provide valuable information about the structural characteristics of a tissue, such as its hardness, as well as about many biological parameters including Blood Pressure (BP), Pulse Transit Time (PPT), Heart Rate (HR) and blood glucose levels [309], [310]. In addition, bioimpedance measurements make use of complex, non-invasive, radiation-free diagnostic tools like Electrical Impedance Tomography (EIT) and Electrical Impedance Spectroscopy (EIS), in applications such as ventilation monitoring, brain ischemic hemorrhage detection, neuroimaging and tumor detection [171], [174].

The most common way to perform bio-impedance measurements is by applying a small amplitude alternating current through a pair of conductive electrodes, attached on the patient's skin and then measuring the generated potential. The frequency of the injected current can reach up to several hundreds of kHz, while its amplitude is selected to meet safety standards [309]. The hardware-electrode setup for a single impedance measurement can be bipolar (2 electrodes for both current injection and voltage measurement) or tetrapolar (2 separate electrode pairs for current injection and voltage measurement-also called four-terminal) as depicted in Fig. 7.6 [228], [302], [311], [312]. Measuring bio-impedance is a challenging process requiring properly designed instrumentation electronics and measurement methodology. The main design challenges are the sensitivity to strong polarization effects caused by the common injection and measuring path (as is the case in the Bipolar measurement setup) [299] as well as the highly unstable contact impedance of the electrodes which varies with electrode size [313], pressure, humidity and skin surface condition [276], [314], [315]. To address these issues, most bio-impedance measurement systems use the more robust tetrapolar measurement setup (Fig. 7.6 right) [302], [316], [317].

However, the tetrapolar bio-impedance measurement setup also faces some challenges. The most important is the unpredictable sensitivity distribution near the measuring area [316], [318]. The sensitivity

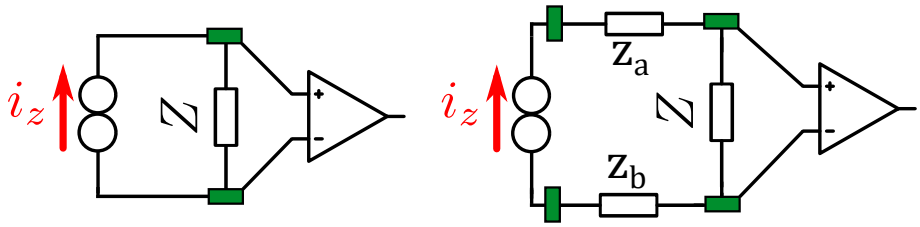

Figure 7.6: Brief schematic of a Bipolar measurement setup (left) and a Tetrapolar measurement setup (right). Green rectangles indicate the electrodes placed. Z refers to the impedance under measure, while z_a and z_b refer to the bio-impedances between injection and measurement electrodes. The schematics are based on the description in [228], assuming infinite current source output impedance, infinite instrumentation amplifier input impedance and negligible electrode impedances.

values can get locally negative [319], while the phase can be erroneously measured positive on capacitive and resistive domains [316]. Furthermore, common signals in differential measurements usually cause problems, especially if stray capacitances are present and the voltage recording circuitry instrumentation has low Common Mode Rejection Ratio (CMRR). [227], [316].

Proper modeling of the tissues' under test electrical characteristics is a crucial step during the design process of bio-impedance measurement systems. To this end, designers simulate and employ equivalent circuits of the SUT [21],[227], [264], [265], usually implemented using lumped passive elements (capacitors and resistors). By utilizing different values of resistors and capacitors, they can simulate different measurement scenarios and setups in order to both determine the measurement system's specifications and simulate its performance. However, the actual impedance behavior of most tissues is described by Cole or Debye models [320], [321], [322] that present large variations at their parameters [315], [321].

Hence, a major limitation of tissue models implemented using passive elements is that they cannot be used for evaluation and calibration of real-world systems as they offer no tunability. Bio-impedance measurement systems often require several months or even years of testing and calibration to provide accurate measurements. To this end human or animal test subjects are typically employed significantly increasing the complexity and cost of the development procedure.

In this work we propose an active, easily tunable circuit implementation of the Cole's skin and electrode models. The design is based on applications from fractional-calculus, since fractional-order models offer more degrees of freedom in comparison with integer-order realizations [323], [324], [325]. To this end, based on the non-integer exponent parameter of the Cole's equation [320], we propose two tunable fractional-order capacitor implementations, implemented as analog filters (voltage output) with a transfer function H(s). The filters can be transferred to impedances (current output) if a Voltage-to-Current Converter (V/I) is connected at the output stage. By utilizing the actively implemented fractional-order capacitors along with an operational transconductance amplifier (OTA) based tunable resistor, we implement the Cole's model in transistor level. The proposed circuit architecture is intended to be used as an analog front-end and along with the required digital circuits to shape an application-specific integrated circuit (ASIC) for evaluation and calibration of bioimpedance measurement systems. The circuit is designed, laid out and simulated in Cadence using TSMC 90nm CMOS process.

Both electrode and skin Cole IC-design models are validated and compared to the RC - approximations (magnitude and phase) for the models' mean parameter values. Moreover, we examine the proposed circuits' adaptability on major variations of the models' parameters. In addition, some tetrapolar measuring setups that include the implemented models are simulated, testing the measured impedance values in various conditions (target's impedance order, shunt resistors' imbalance).

The remainder of this paper is organized as follows. Subsection 7.3.2 describes the electrode and skin Cole theoretical models adopted for this design and the particular selection reasons. The implementation and the behavior of the involved models is presented in subsection 7.3.3, in TSMC 90nm CMOS process. Furthermore, in subsection 7.3.4, validation is performed via simulated tetrapolar measurements on specific target impedances.

7.3.2 Skin and Electrode Cole models

In this section, the skin and electrode Cole models utilized for the integrated circuit implementation are briefly presented. The skin cell and electrode material and contact equivalent circuitry models exhibit major similarities: contact "shunt" impedances in series with an RC parallel impedance. In both cases, the capacitor acts as a Constant Phase Element (CPE), which introduces strong Cole characteristics to the equivalent circuit.

Skin Model

For the representation of the skin tissue complex impedance, many models have been proposed [326],[327], [328]. However, since we focus on bioimpedance measurement for specific tissue function detection, the distances between the recording electrodes have to be relatively small, usually 2-4 centimeters. Furthermore, we aim at a frequency range that covers a variety of bio-signal types; from ECG to EIT injected signals.

Taking into consideration the above factors, we have selected the simplified Cole model described in [326]. The Cole equation that expresses the total skin impedance, including contact is:

$$z_{skin}(\omega) = R_{\infty,s} + \frac{R_{0,s} - R_{\infty,s}}{1 + (j\omega)^{a_1} \cdot (R_{0,s} - R_{\infty,s})C_s} \tag{7.13}$$

Where $R_{\infty,s}$ is the contact (gap) Ohmic impedance, towards which the total impedance converges for higher frequencies, $R_{o,s}$ denotes a low frequency resistor, a_1 is the fractional CPE order, ω is the signal's angular frequency and C the CPE's (fractional order) capacitance. The relation between the capacitance and the characteristic time constant τ_s is shown in the following expression

$$\tau_s = \sqrt[a_1]{(R_{0,s} - R_{\infty,s})C_s} \tag{7.14}$$

The CPE's complex impedance is expressed as in [326], [327], [328]

$$z_{CPE} = \frac{1}{(j\omega)^{a_1} C_s} \tag{7.15}$$

For a frequency range of $1Hz$ to $10kHz$, the corresponding parameters (mean values), as estimated in [326] are shown in Table 7.15. In Table 7.4, the indicated variations of R_o, a and C are summarized, according to [326], [327], [328]. The corresponding equivalent RC-network model is shown in Fig. 7.7 (left subfigure).

Table 7.3: Skin and Electrode Cole parameter mean values [315], [326]

Parameter	R_∞ ($k\Omega$)	R_o (MΩ)	τ (s)	a	C (nF/sec^{1-a})
Skin	1.86	1.39	0.53	0.749	447
Electrode	0.21	1.08	1.41	0.942	1.92

Table 7.4: Skin and Electrode Cole parameter indicated variations [315], [326], [327], [328], [329]

Parameter	R_o (MΩ)	a	C (nF/sec^{1-a})
Skin	0.64-1.46	0.63-0.86	61.2-1042.1
Electrode	0.65-2.09	0.8-0.99	1.39-2.09

It is noted that in terms of this paper, we are limited in frequencies between $1Hz$ and $10kHz$, which are within the range of HR, PPT, BR, neuroimaging and skin impedance measurement applications [11],[309]. However this range does not cover all the bioimpedance measurement applications (e.g. lung EIT monitoring is acted at more than $100kHz$, while cancer tissue detection with EIS is performed at the region around $1MHz$ [21], [158]). The extension of the frequency span can be studied as a future work.

Electrode Model

The electrode model is demonstrated in many previous studies, focusing on various sizes and electrode materials [276],[314], [329]. However, in bioimpedance and ECG measurements $AgCl$-type electrodes are mostly utilized, since they offer smaller material and contact impedance [276]. Although conductive-gel electrodes are more efficient for low contact impedance bio-signal measuring, they are not effective for long-term monitoring which is essential for recording the evolution of any bio-signal's state [314]. Therefore, the electrodes are assumed as dry, circular with a diameter of 25mm. The electrode Cole model

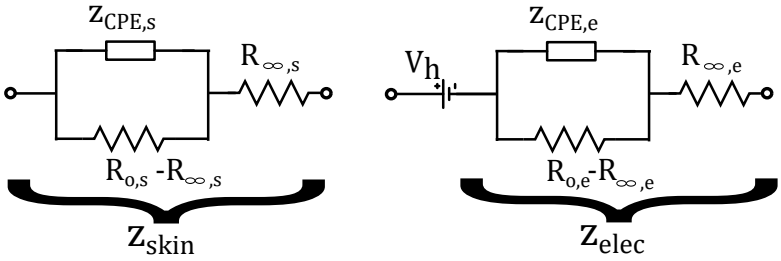

Figure 7.7: Cole models of the skin (left) and electrode (right).

implemented in this paper, is described in [315]. The total impedance is expressed by:

$$z_{el}(\omega) = R_{\infty,e} + \frac{R_{0,e} - R_{\infty,e}}{1 + (j\omega)^{a_2} \cdot (R_{0,e} - R_{\infty,e})C_e} \tag{7.16}$$

Where $R_{\infty,e}$ is the gap high frequency impedance, $R_{o,e}$ the low frequency resistor, a_2 the fractional CPE order, ω the signal's angular frequency and C the fractional capacitance. The time constant τ_e and the complex impedance of the CPE z_{CPE} are computed similarly to the skin's Cole model from (7.14) and (7.41).

The circuit equivalent is schematically identical to the skin's one, however a dc half-cell potential is added here, in series with the RC parallel fractional impedance. This potential value is approximately $230 - 250mV$ [329]. The model's parameter mean values (range $1Hz - 10kHz$) are shown in Table 7.15, the R_o, a and C ranges in Table 7.4 [315], [329] and a simplified RC schematic in Fig. 7.7 (right subfigure).

7.3.3 Circuit Realization of the Cole Electrode and Skin models

There are many different designs and methods for the implementation of fractional-order elements's behavior [330, 331, 332, 333, 334, 335, 336, 337, 338, 339] In this section, we present, evaluate and compare two methods for active implementation of the fractional-order capacitors. The first one is called "Versatile" design methodology [330], while the second one adopts the "Inverse Follow the Leader Feedback (IFLF)" methodology [331, 332, 333, 334, 335]. The low-frequency resistor ($R_o - R_\infty \simeq R_o$, appropriate values in Table 7.15) is achieved also actively with an operational transconductance amplifier (OTA). Hence, in Fig. 7.7 the z_{CPE} and R_o parallel combination is fully active and tunable. The shunt (high frequency) resistor R_∞, is demonstrated with passive potentiometers, since their values are much smaller and sensitive to the contact's characteristics. All approaches are compared with the corresponding theoretical predicted models and the RC-network equivalents.

Fractional Order Capacitor RC-network approximation

Due to the fact that fractional-order elements are not yet commercially available, their behavior is approximated by means of the continue fraction expansion (CPE) method [331, 332, 333, 334, 335, 336], or by modeling them using an RC-network [338],[339], which is depicted in Fig. 7.43. The RC simulation is carried out considering the mean Cole parameter values (Table 7.15) and zero-tolerance for all passive elements and is utilized as a reference point along with the theoretical results. However, in practice, as mentioned in the introduction, a single RC-network lacks tunability, hence it cannot be possibly utilized when the model's parameters need to be changed.

The generalized expression of the RC-network impedance is given by:

$$Y_{tot}(s) = sC_p + \frac{1}{R_p} + \sum_{\kappa=1}^{m} \frac{sC_\kappa}{sR_\kappa C_\kappa + 1} \tag{7.17}$$

In order to calculate the order m and the values of the RC network, we use the appropriate values of

pseudo-capacitance C_{pseudo} and order λ of the element, the phase error $\Delta\phi$ and the frequency range $[f_{low}, f_{high}]$ [338],[339]. The first branch has two elements R_1 and C_1 which can be expressed by:

$$f_{low} = \frac{1}{2\pi R_1 C_1}, \quad f_{high} = \frac{f_{low}}{(ab)^{m-1}} \tag{7.18}$$

The number of the necessary sections m can be calculated by the expression:

$$m = 1 - \frac{\log(\frac{f_{high}}{f_{low}})}{\log ab} \tag{7.19}$$

The values of passive elements are derived through the formula:

$$R_\kappa = R_1 a^{\kappa-1},\ C_\kappa = C_1 b^{\kappa-1} \tag{7.20}$$

$$C_p = C_1 \frac{b^m}{1-b},\ R_p = R_1 \frac{1-a}{a} \tag{7.21}$$

The factors $0 < \alpha, b < 1$ are calculated through the expressions:

$$phase = 90^o \cdot\ \lambda = 90^o \cdot\ \frac{log(\alpha)}{log(\alpha b)} \tag{7.22}$$

$$\alpha b = \frac{0.24}{1+\Delta\phi} \tag{7.23}$$

where λ is the order of the fractional-order capacitor. Since the practical frequency of interest is between $1Hz$ and $10kHz$, the center frequency is $f_o = 100Hz$ and the appropriate order of the RC-network is $m = 5$ (in order to achieve at least 1.5^o accuracy). The values of the elements are summarized in Table 7.5 for both models. The center frequency, the order m of the RC-network and the values of passive elements are derived using MATLAB code [338],[339].

Versatile Active Fractional Capacitor Emulator

In our case, the desired RC-network's behavior is described by active elements instead of passive ones, in order to achieve electronic tuning of the characteristics [330]. For this purpose (tunability of

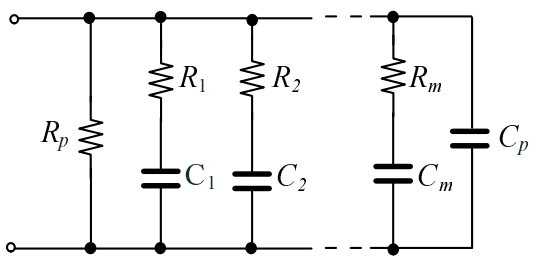

Figure 7.8: RC-network for approximating the behavior of fractional-order capacitors [338].

Table 7.5: Passive element values for approximating the fractional-order capacitors.

Electrode Element	Value	Skin Element	Value
C_1	$232.78pF$	C_1	$146.63nF$
C_2	$203.19pF$	C_2	$81.24nF$
C_3	$177.37pF$	C_3	$45.01nF$
C_4	$154.83pF$	C_4	$29.94nF$
C_5	$135.15pF$	C_5	$13.82nF$
C_p	$928.34pF$	C_p	$17.16nF$
R_1	$683.7M\Omega$	R_1	$1.1M\Omega$
R_2	$75.2M\Omega$	R_2	$188.1k\Omega$
R_3	$8.3M\Omega$	R_3	32.6Ω
R_4	$909.4k\Omega$	R_4	$5.6k\Omega$
R_5	$100k\Omega$	R_5	978.5Ω
R_p	$5.53G\Omega$	R_p	$5.2M\Omega$

both element's impedance and order), OTAs and current conveyors (CCIIs) are utilized to describe the behavior of fractional-order elements. Both fractional-order capacitors for skin and electrode models are designed using cascading filters, connected with a multiple-output OTA, which acts as a Voltage-to-Current (V/I) converter [330, 331, 332, 333, 334, 335]. The cascading filters have transfer functions $H_1(s)$ and $H_2(s)$ respectively. The complete architecture is shown in Fig. 7.44, and the total transfer function, $H(s)$, is given by $H(s) = H_1(s)H_2(s)$. The impedance of both fractional-order capacitors is:

$$Y_{cap}(s) = \frac{1}{g_{mvi}H(s)} \tag{7.24}$$

where g_{mvi} is the transconductance of the V/I converter.

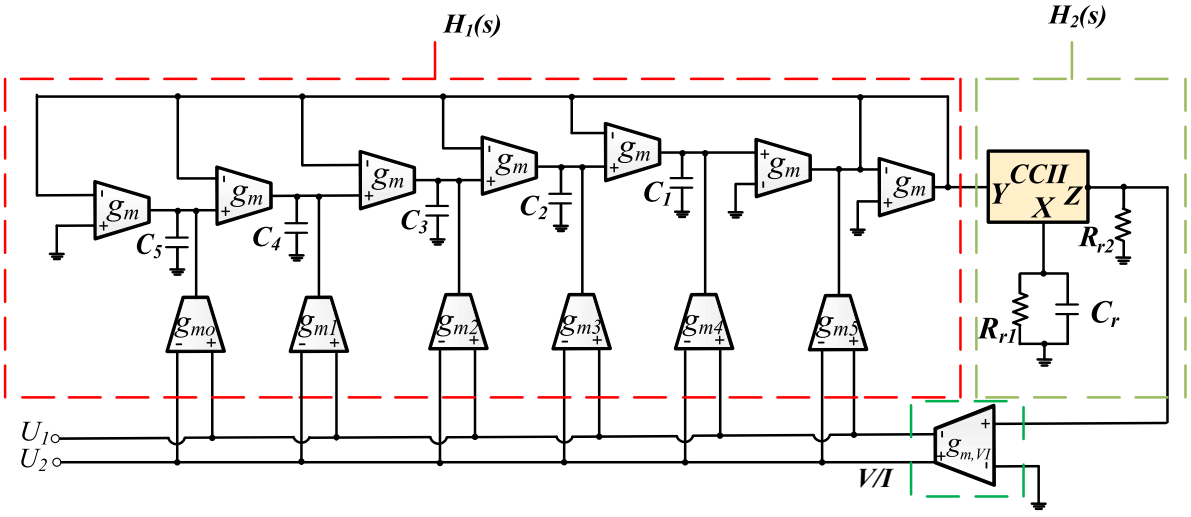

Figure 7.9: Realization of fractional-order capacitor emulator (Versatile Methodology) [330].

The transfer function $H_1(s)$ is that of a 5$^{\text{th}}$ order all-pass filter, given by:

$$H_1(s) = \frac{A(s)}{B(s)}, \tag{7.25}$$

where $A(s)$ is expressed by:

$$A(s) = G_5 s^5 + \frac{G_4 s^4}{\tau_1} + \frac{G_3 s^3}{\tau_1\tau_2} + \frac{G_2 s^2}{\tau_1\tau_2\tau_3} + \frac{G_1 s}{\tau_1\tau_2\tau_3\tau_4} + \frac{G_o}{\tau_1\tau_2\tau_3\tau_4\tau_5} \tag{7.26}$$

and $B(s)$ is described by:

$$B(s) = s^5 + \frac{s^4}{\tau_1} + \frac{s^3}{\tau_1\tau_2} + \frac{s^2}{\tau_1\tau_2\tau_3} + \frac{s}{\tau_1\tau_2\tau_3\tau_4} + \frac{1}{\tau_1\tau_2\tau_3\tau_4\tau_5} \tag{7.27}$$

while the transfer function $H_2(s)$ is that of a lossy differentiator:

$$H_2(s) = R_{r2}C_r s + \frac{R_{r2}}{R_{r1}}. \tag{7.28}$$

The corresponding CCII schematic which is used for the implementation of $H_2(s)$ is depicted in Fig. 7.46 and the employed OTA schematic is demonstrated in Fig. 7.11 [330], [336].

The impedance of the equivalent RC-network (derived using the MATLAB code) [338],[339], which approximates the fractional-order capacitor $Y_\alpha = 1/(C_\alpha s^\alpha)$ is described by:

$$Y_\alpha(s) = \frac{a_5 s^5 + a_4 s^4 + a_3 s^3 + a_2 s^2 + a_1 s + a_o}{b_6 s^6 + b_5 s^5 + b_4 s^4 + b_3 s^3 + b_2 s^2 + b_1 s + b_o} \tag{7.29}$$

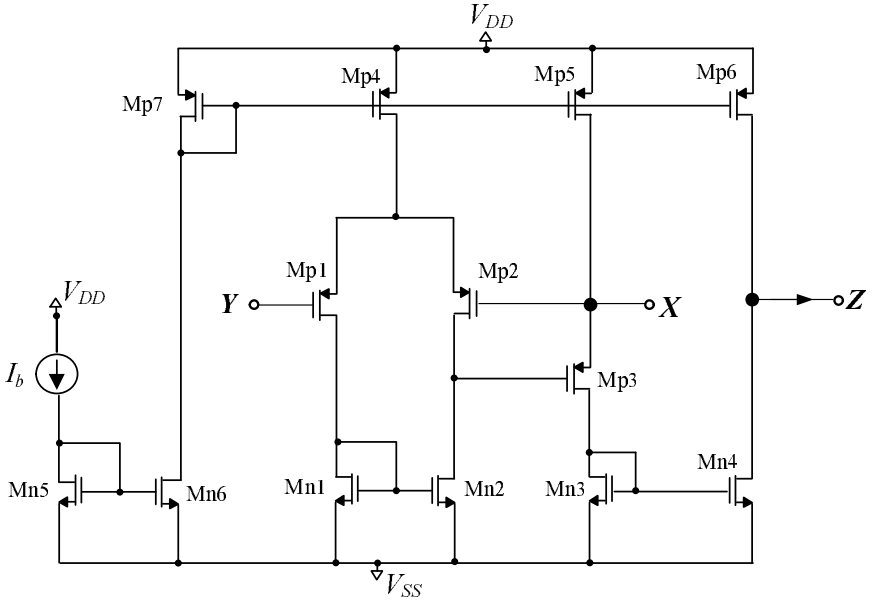

Figure 7.10: Employed CCII [330].

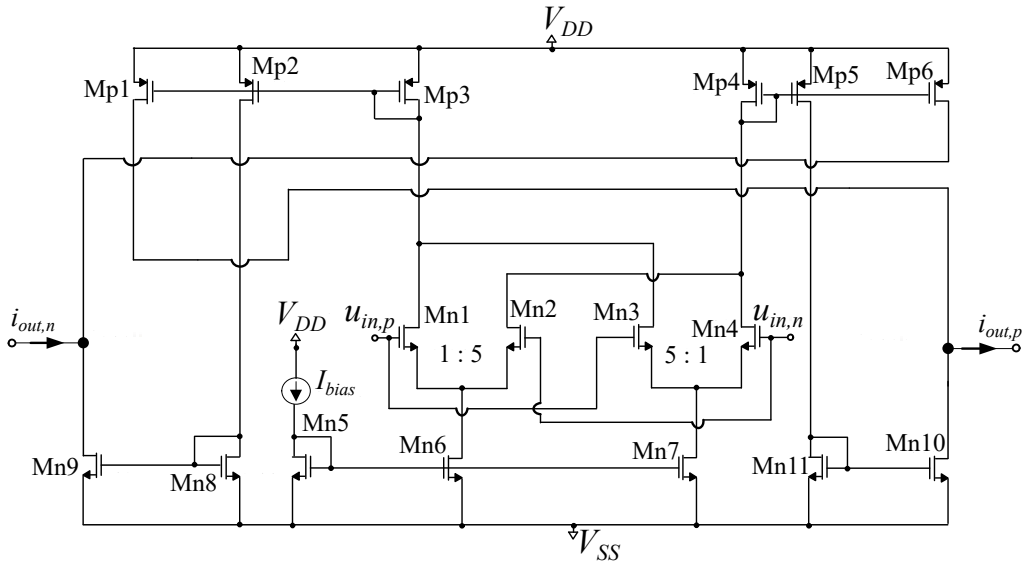

Figure 7.11: Employed OTA [330], [336].

In order to implement the fractional-order models, we compare (7.29) with (7.24) and choose the value of the transcoductance $g_{m,vi}$ to be $100nS$ for both models (electrode and skin). All the parameters are summarized in Table 7.6 (derived according to the C and a values in Table 7.15). The resulting $H(s)$ is expressed by:

$$H(s) = \frac{c_6 s^6 + c_5 s^5 + c_4 s^4 + c_3 s^3 + c_2 s^2 + c_1 s + c_o}{d_5 s^5 + d_4 s^4 + d_3 s^3 + d_2 s^2 + d_1 s + d_o}. \tag{7.30}$$

Table 7.6: Parameters for the implementation of expression H(s) (7.30).

Electrode Parameter	Value	Skin Parameter	Value
c_6	1.0	c_6	6.1
c_5	$9.393 \cdot 10^4$	c_5	$9.388 \cdot 10^5$
c_4	$7.715 \cdot 10^8$	c_4	$1.221 \cdot 10^{10}$
c_3	$6.024 \cdot 10^{11}$	c_3	$1.504 \cdot 10^{13}$
c_2	$4.464 \cdot 10^{13}$	c_2	$1.762 \cdot 10^{15}$
c_1	$2.824 \cdot 10^{14}$	c_1	$1.836 \cdot 10^{16}$
c_o	$1.76 \cdot 10^{14}$	c_o	$1.102 \cdot 10^{16}$
d_5	100.0	d_5	33.33
d_4	$8.184 \cdot 10^6$	d_4	$2.728 \cdot 10^6$
d_3	$5.866 \cdot 10^{10}$	d_3	$1.955 \cdot 10^{10}$
d_2	$3.999 \cdot 10^{13}$	d_2	$1.333 \cdot 10^{13}$
d_1	$2.593 \cdot 10^{15}$	d_1	$8.645 \cdot 10^{14}$
d_o	$1.473 \cdot 10^{16}$	d_o	$4.910 \cdot 10^{15}$

The presented architecture has been designed in TSMC $90nm$ CMOS process, using the Cadence IC design suite. The power supply rails are set to $V_{DD} = -V_{SS} = 0.75V$, and all transistors operate in the

sub-threshold region. The transconductance of the corresponding OTA is given by:

$$g_m = \frac{5I_{bias}}{9nV_T} \tag{7.31}$$

where $1 < n < 2$, and $V_T = 26mV$. Also, the dimensions of the MOS transistors of the OTA and CCII are summarized in Table 7.7. The missing dimensions for the OTA transistors can be easily calculated using current mirrors' properties. In addition, the aspect ratio between transistors $M_{n1} - M_{n2}$ and $M_{n3} - M_{n4}$ is equal to 5. We use this multiplicity in order to increase the linearity of the differential amplifiers' pairs and decrease the transconductance value for the same bias current, compared to an OTA with the same dimensions for the corresponding transistors [340].

Table 7.7: MOS Transistors Dimensions – OTA & CCII.

OTA	W/L $(\mu m/\mu m)$	CCII	W/L $(\mu m/\mu m)$
M_{n2},M_{n3}	$2/1$	M_{p1},M_{p2},M_{p4}	$1.6/0.4$
M_{n8}	$1/2$	M_{p5},M_{p6}	$3.2/0.4$
M_{n5}	$0.5/4$	M_{p3}	$6.4/0.4$
M_{n11}	$1/2$	M_{n1}-M_{n6}	$0.8/0.4$
M_{p3},M_{p4}	$10/5$	M_{p7}	$1.6/0.4$

In order to calculate the values of scaling factors $G_j = g_{mj}/g_m$, where $j = \{0, 1, 2, 3, 4, 5\}$ and time-constants τ_i, where $i = \{1, 2, 3, 4, 5\}$, we compare (7.30) with (7.25) and (7.28). The value of the transconductance is $g_m = 100nS$; as a result, the values of capacitors are calculated by $C_i = \tau_i g_m$ and are summarized in Table 7.8 for both models. The values of resistors are $R_{r1} = 142.8M\Omega$ ($I_{r1} = 61pA$) and $R_{r2} = 1.0M\Omega$ ($I_{r2} = 52.1nA$) for electrode model and $R_{r1} = 156.4M\Omega$ ($I_{r1} = 53pA$) and $R_{r2} = 18.3M\Omega$ ($I_{r2} = 2.8nA$) for skin model.

Bias current for the implementation of the corresponding transconductance $g_{m,vi} = g_m$ is I_{bias}, which is calculated by using the expression $I_{bias} = \frac{9}{5}nV_T g_m$. The current value for a transconductance of $g_{mj} = G_j g_m$ can be calculated by $I_{bias,j} = G_j I_{bias}$, where $j = \{0, 1, 2, 3, 4, 5\}$ and $I_{bias} = 404pA$. The electronic capability of the bias current provides us with the opportunity to achieve different values for both impedance and order of the element. The bias current of CCII is $I_b = 20nA$. The values of the resulting scaling factors are summarized in Table 7.9 for both models.

Table 7.8: Values of Capacitors of Figure 7.44.

Element	Value	Element	Value
C_1	$1.22pF$	C_2	$13.95pF$
C_3	$146.67pF$	C_4	$1.54nF$
C_5	$17.60nF$	C_r	$10.0nF$

Table 7.9: Values of Scaling Factors G_j.

Electrode Model Scaling Factor	Value	Skin Model Scaling Factor	Value
G_o	1.707	G_o	19.188
G_1	1.705	G_1	11.080
G_2	1.505	G_2	6.167
G_3	1.315	G_3	3.418
G_4	1.148	G_4	1.881
G_5	1.000	G_5	1.000

Inverse Follow The Leader Feedback Fractional Capacitor Emulator

In this subsection, we present a typical IFLF architecture for the implementation of fractional-order capacitor. Owing to the fact that the frequency span is from $1Hz$ to $10kHz$ the employment of the 5^{th}-order Continued Fraction Expansion (CFE) approximation is a satisfactory solution in order to achieve the appropriate results [331, 332, 333, 334, 335, 336, 337, 338, 339, 336]. The expression of the 5^{th}-order CFE approximation is described by

$$(\tau s)^{\alpha} \approx \frac{a_5 s^5 + a_4 s^4 + a_3 s^3 + a_2 s^2 + a_1 s + a_o}{b_5 s^5 + b_4 s^4 + b_3 s^3 + b_2 s^2 + b_1 s + b_o} \tag{7.32}$$

where: $\alpha_5 = b_o = -\alpha^5 - 15\alpha^4 - 85\alpha^3 - 225\alpha^2 - 274\alpha - 120$,
$\alpha_4 = b_1 = 5\alpha^5 + 45\alpha^4 + 5\alpha^3 - 1005\alpha^2 - 3250\alpha - 3000$,
$\alpha_3 = b_2 = -10\alpha^5 - 30\alpha^4 + 410\alpha^3 + 1230\alpha^2 - 4000\alpha - 12000$,
$\alpha_2 = b_3 = 10\alpha^5 - 30\alpha^4 - 410\alpha^3 + 1230\alpha^2 + 4000\alpha - 12000$,
$\alpha_1 = b_4 = -5\alpha^5 + 45\alpha^4 + 5\alpha^3 - 1005\alpha^2 + 3250\alpha - 3000$,
$\alpha_o = b_5 = \alpha^5 - 15\alpha^4 + 85\alpha^3 - 225\alpha^2 + 274\alpha - 120$,
and α is the order of fractional-order differentiator (all-pass filter) [331, 332, 333, 334, 335, 336, 337, 338, 339, 336].

In order to obtain the tunability of both impedance and order of the element, operational transconductance amplifiers (OTAs) are utilized to describe fractional-order capacitors. Fractional-order capacitor is designed using an all-pass filter, connected with a multiple-output OTA, which acts as a Voltage-to-Current (V/I) converter [330, 331, 332, 333, 334, 335]. The all-pass filter has a transfer function $H(s)$. The complete architecture is shown in Fig. 7.12. The impedance of fractional-order capacitor is given by:

$$Y_{cap}(s) = \frac{1}{g_{mvi} H(s)} \tag{7.33}$$

where g_{mvi} is the transconductance of the V/I converter.

The transfer function $H(s)$ is that of a 5$^{\text{th}}$ order all-pass filter, given by:

$$H(s) = \frac{A(s)}{B(s)} \tag{7.34}$$

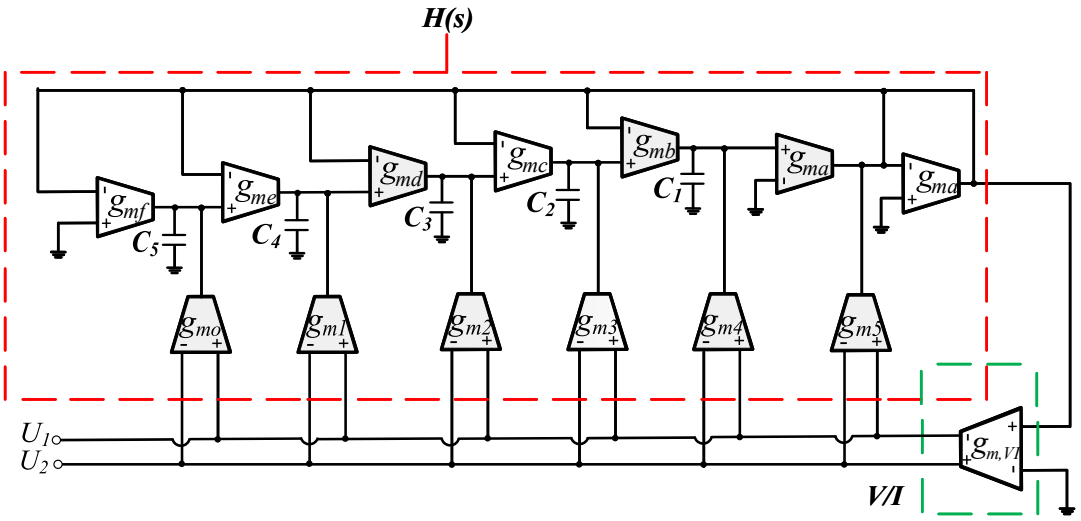

Figure 7.12: Realization of fractional-order capacitor emulator (IFLF Methodology).

where $A(s)$ is expressed by:

$$A(s) = G_5 s^5 + \frac{G_4 s^4}{\tau_1} + \frac{G_3 s^3}{\tau_1 \tau_2} + \frac{G_2 s^2}{\tau_1 \tau_2 \tau_3} + \frac{G_1 s}{\tau_1 \tau_2 \tau_3 \tau_4} + \frac{G_o}{\tau_1 \tau_2 \tau_3 \tau_4 \tau_5} \tag{7.35}$$

and $B(s)$ is described by:

$$B(s) = s^5 + \frac{s^4}{\tau_1} + \frac{s^3}{\tau_1 \tau_2} + \frac{s^2}{\tau_1 \tau_2 \tau_3} + \frac{s}{\tau_1 \tau_2 \tau_3 \tau_4} + \frac{1}{\tau_1 \tau_2 \tau_3 \tau_4 \tau_5} \tag{7.36}$$

The IFLF architecture has been also designed in TSMC $90nm$ CMOS process, using the Cadence IC design suite. The power supply rails are set to $V_{DD} = -V_{SS} = 0.75V$, and all transistors operate in the sub-threshold region. The dimensions of the OTA's MOS transistors are summarized in Table 7.7 also (we use the same OTA as in Versatile design methodology).

In order to calculate the values of scaling factors $G_j = g_{mj}/g_{mx}$, where $j = \{0, 1, 2, 3, 4, 5\}$, $x = \{a, b, c, d, e, f\}$ and time-constants τ_i, we compare (7.34) with (7.32). The value of the transconductance of electrode's fractional-order capacitor is $g_{mvi} = g_{mx} = 830.2nS$; for all x. As a result, the values of capacitors are calculated by $C_i = \tau_i g_m$ and are summarized in Table 7.10 for both models. The values of the transconductances for skin's fractional-order capacitor are summarized in Table 7.11. The resulting scaling factors' values are summarized in Table 7.12 for both models. It is noted that, likewise in the Versatile implementation, these values are derived according to the mean pseudo-capacitor values shown in Table 7.15.

Cole Model Tunable Resistor R_o Realization

In order to achieve tunability of the resistor R_o demonstrated in Fig. 7.7, we use the same multiple OTA (with the same dimensions as shown in Table 7.7) utilized in the previously presented CPE's design methodologies (Fig. 7.11), since we can achieve the desired transconductance by selecting applicable dc

Table 7.10: Values of Capacitors of Figure 7.12.

Element	Value	Element	Value
C_1	$2.58pF$	C_2	$141.43pF$
C_3	$689.82pF$	C_4	$2.75nF$
C_5	$13.80nF$	-	-

Table 7.11: Values of transcoductance for skin model of Figure 7.12.

Parameter	Value	Parameter	Value
g_{ma}	$184.84nS$	g_{mb}	$674.02nS$
g_{mc}	$721.35nS$	g_{md}	$729.19nS$
g_{me}	$713.18nS$	g_{mf}	$564.15nS$
g_{mvi}	$55.37\mu S$	-	-

Table 7.12: Values of Scaling Factors G_j.

Electrode Model Scaling Factor	Value	Skin Model Scaling Factor	Value
G_o	0.002	G_o	0.02
G_1	0.12	G_1	0.19
G_2	0.52	G_2	0.600
G_3	1.92	G_3	1.66
G_4	8.61	G_4	5.33
G_5	422.02	G_5	50.01

bias currents' values. The configuration of the programmable OTA as resistor is depicted in Fig. 7.13 [330], [336].

All transistors are biased in the sub-threshold region, and so the impedance of the effective resistance is given by:

$$R_o = \frac{1}{g_{mo}} \tag{7.37}$$

where g_{mo} is obtained by (7.31).

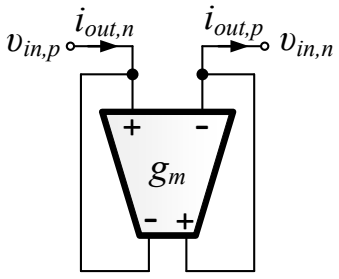

Figure 7.13: Implementation of tunable resistor emulator [330], [336].

Due to the relatively small values of R_∞ for both skin and electrode models and regarding that the impedance of the employed OTA cannot practically achieve values less than $400k\Omega$, we have replaced the R_∞s with passive tunable resistors (potentiometers). However, in the future, research can be done in order to achieve lower value, tunable, active resistors. We also note that all the remaining resistors (R_o, R_{r1}, R_{r2}) used below, are implemented exclusively by programmable OTAs. Therefore, all the model's parameters are implemented actively in IC design except from the resistors R_∞.

Cole Model Circuit Realization Simulation Results

The layout design of the fractional-order skin and electrode models using IFLF design methodology is demonstrated in Fig. 7.14, where the area is 78X278. The layout design of the fractional-order skin and electrode models using Versatile design methodology is demonstrated in Fig. 7.15, where the area is 78X329. Both layouts include all elements except capacitors C_i, where $i = \{1, 2, 3, 4, 5\}$ and resistor R_∞ (potentiometer resistor). All the simulations are achieved from the average variance extracted (ave) circuit (post-layout simulations).

The magnitude and phase response for all design methodologies along with the ideal RC approximation and the theoretically predicted ones, are plotted in Fig. 7.16 for fractional-order electrode model's

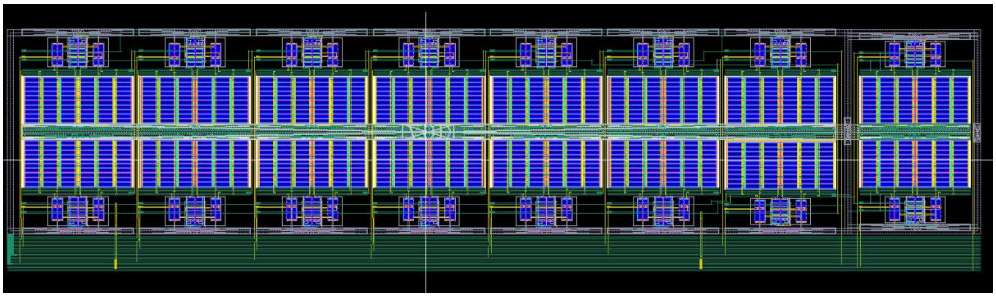

Figure 7.14: Layout design of the implemented fractional-order skin and electrode models (IFLF Methodology).

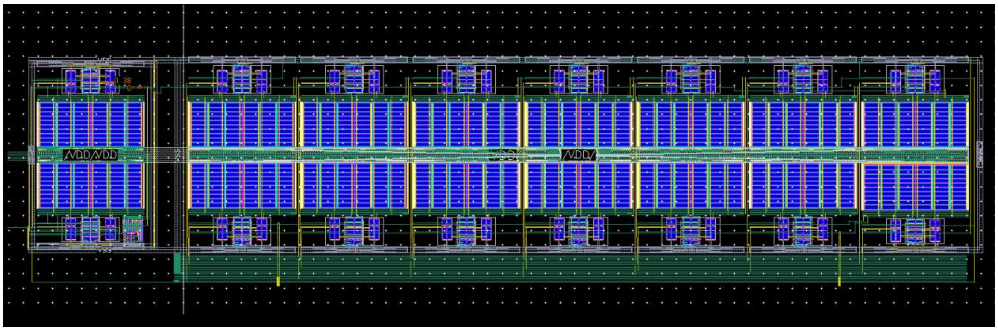

Figure 7.15: Layout design of the implemented fractional-order skin and electrode models (Versatile Methodology).

capacitor. The magnitude values are in fine agreement with the theoretical ones. The phase response, which is very important for the simulation of the fractional-order capacitor, is also close to the ideal value of -84.78^o, for a big part of the frequency band. However, the IFLF approach has an error up to 4.5^o at the span's boundaries ($1Hz$ and $10kHz$), while the maximum error of the Versatile methodology is at 1.5^o.

The corresponding responses for the fractional-order skin model's capacitor are shown in Fig. 7.17. As in the electrode's CPE case, the magnitude response shows very low error, especially for the Versatile approach (the IFLF values have a maximum error of $25k\Omega$ at $1Hz$, however this is minimized at higher frequencies). The phase response, for the case of skin's CPE, shows also minimum error in the middle frequencies (ideal phase is -67.41^o), while IFLF methodology shows critical phase errors in the frequency range's limits. At the same time, the Versatile methodology provides almost the same results as the ideal RC-network simulation.

The obtained impedance responses for the electrode and skin model along with the theoretically predicted ones and the ideal RC-network approximation are provided in Fig. 7.18 and 7.19 respectively. It is observed that both approaches result to successful approximations with low average errors. In specific, superior accuracy is obtained in the skin's and electrode's impedance magnitude (for both the capacitor and the whole Cole models), as shown in Figs. 7.16, 7.17, 7.18 and 7.19 (Left subfigures). In addition, the models realized with the IFLF topology, present almost minimum phase error between $10Hz$ and $1kHz$ but it deviates near the frequency range's limits. However, the IFLF mean and maximum phase errors are lower than in the corresponding CPE model. In contrast, the Versatile design methodology implemented models have better accuracy near the $1Hz - 10Hz$ and $1kHz - 10kHz$, however they present minor error in the middle frequencies.

As mentioned before, the two design methodologies (Versatile and IFLF) approximate the behavior of the fractional order elements. The errors between these two techniques and the theoretical values arise from the approximation's order (CFE and RC approximation). In order to minimize them, the complexity (order) of the whole topology needs to be increased. This is not desirable. Nevertheless, both methodologies are characterized not only by tunability of impedance and order, but also capability to change the central frequency, which can contribute to minimize the errors at the boundaries, if performed properly (by tuning bias current).

Cole Models Parameters Variation and Circuit Emulator Trimming

In previous subsection, we presented the simulation results of RC approximation, Versatile and IFLF design methodologies for both fractional-order skin and electrode models. The parameter values utilized for the models refer to the mean values according to [315] and [326]. However, these parameters exhibit great variations across different human subjects and are affected by situations such as humidity, pressure and temperature at the skin-electrode's surface [315], [321], [326]. In order to implement these possible cases, we have to use a realization methodology which provides tunability and high performance. The RC network provides high performance for a single case, as shown in previous subsection, but it is not appropriate for examining multiple conditions. The main reason of this drawback is the absence of passive

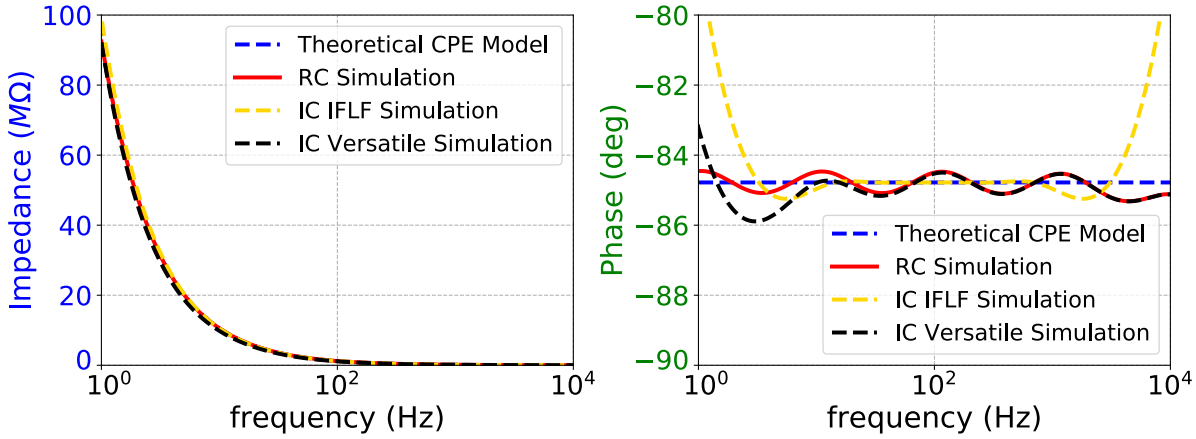

Figure 7.16: Impedance (a) magnitude and (b) phase response of the fractional-order capacitor for the case of electrode model.

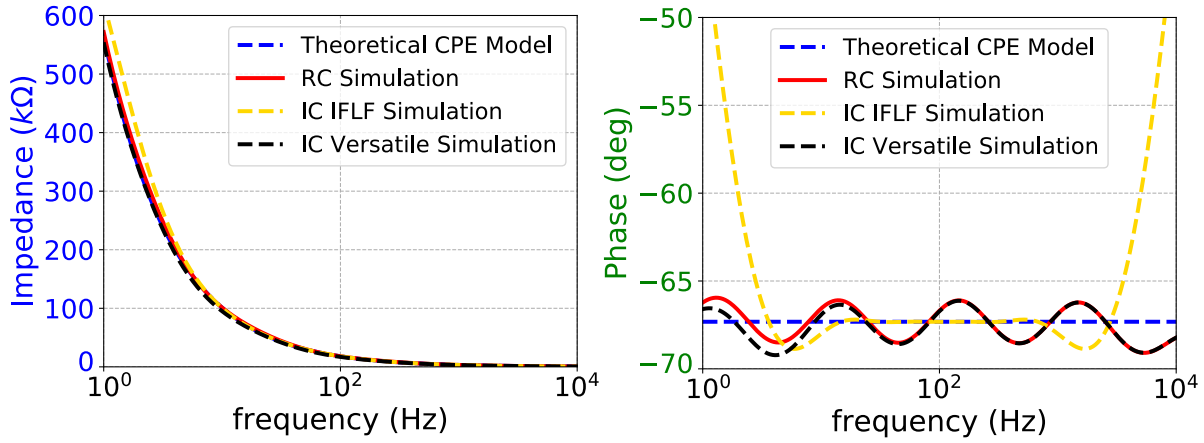

Figure 7.17: Impedance (a) magnitude and (b) phase response of the fractional-order capacitor for the case of skin model.

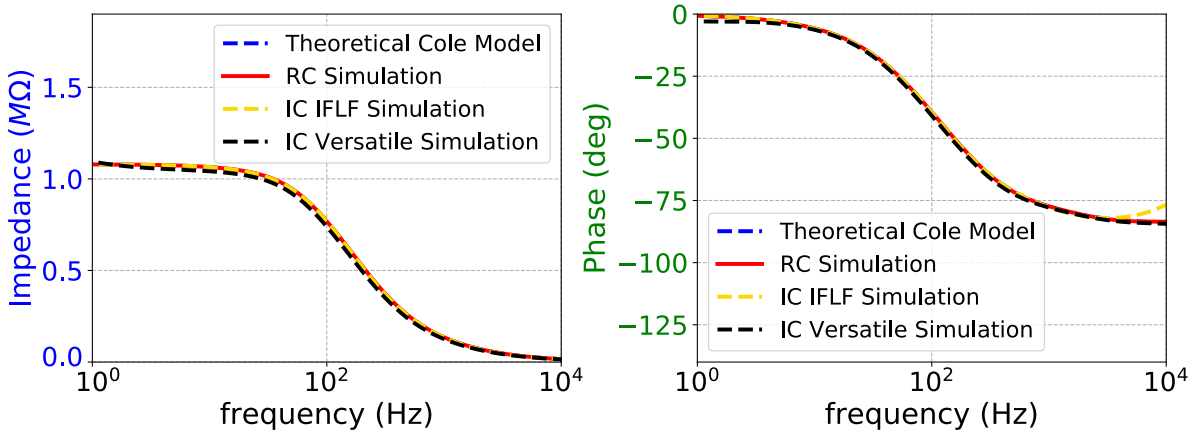

Figure 7.18: Impedance (a) magnitude and (b) phase response of fractional-order electrode model.

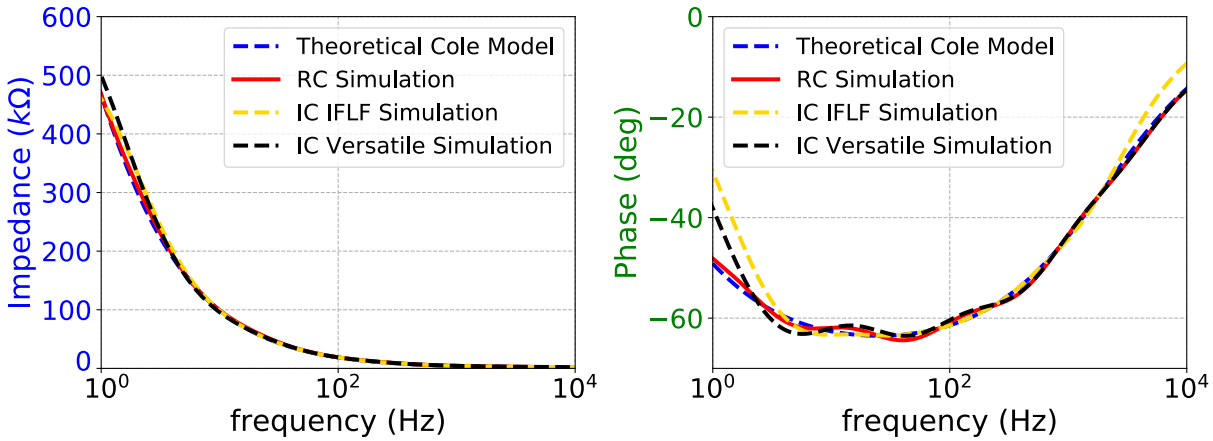

Figure 7.19: Impedance (a) magnitude and (b) phase response of fractional-order skin model.

elements' tunability (in order to achieve different cases we have to continuously change the RC values of the network in Fig. 7.43).

On the other hand, the IC design methodologies offer the possibility to achieve different parameter values. Hence both architectures (Versatile and IFLF) can describe the behavior of both electrode and skin models, under various situations, by using a single core. In this subsection, we evaluate the performance and accuracy of the presented design techniques in describing different conditions.

Electrode Model parameter Variation

In this part, we examine the discussed IC methodologies' accuracy for 8 different model cases. The C (CPE) and R_o (low frequency resistor) parameter variations were extracted from trials over human subjects (experimental results) under two conditions (pressure and removing pressure) in [315]. The order of the CPE is assumed $a = 0.942$ for all the cases. The selection of the appropriate values was derived by adjusting the observed variations around the mean values in Table 7.15 and they are summarized in Table 7.13. The minimum and maximum values for the fractional-order capacitor were computed at $1.39nF/sec^{1-a}$ and $2.09nF/sec^{1-a}$ respectively, while the corresponding values for R_o are $650k\Omega$ and $2.09M\Omega$. The high frequency resistor (R_∞) values are kept constant at 210Ω. The cases described are obtained by controlling the transconductance g_{mvi} of the V/I converter and the g_{mo} of the R_o effective resistor. According to (7.31), the desired g_{mvi} and g_{mo} can achieved just by tuning dc bias current (I_{bias}).

The corresponding results for the two IC methodologies are depicted in Figs. 7.20-7.27. Both architectures provide high accuracy in all the cases, with the exception of the IFLF phase error near $10kHz$ (as in the previous section). This performance cannot be possibly achieved by a single RC-network, since it lacks of tunability.

Skin Model parameter Variation

For the fractional-order skin model, we derived four different cases where C and order a of the CPE

Table 7.13: Electrode Cole parameters values for different cases, $a = 0.942$

Case/ Parameter	R_o $(M\Omega)$	C (nF/sec^{1-a})
Case I	1.08	1.75
Case II	2.09	1.39
Case III	0.65	1.92
Case IV	1.51	1.92
Case V	0.65	1.75
Case VI	1.51	1.75
Case VII	0.65	2.09
Case VIII	1.51	2.09

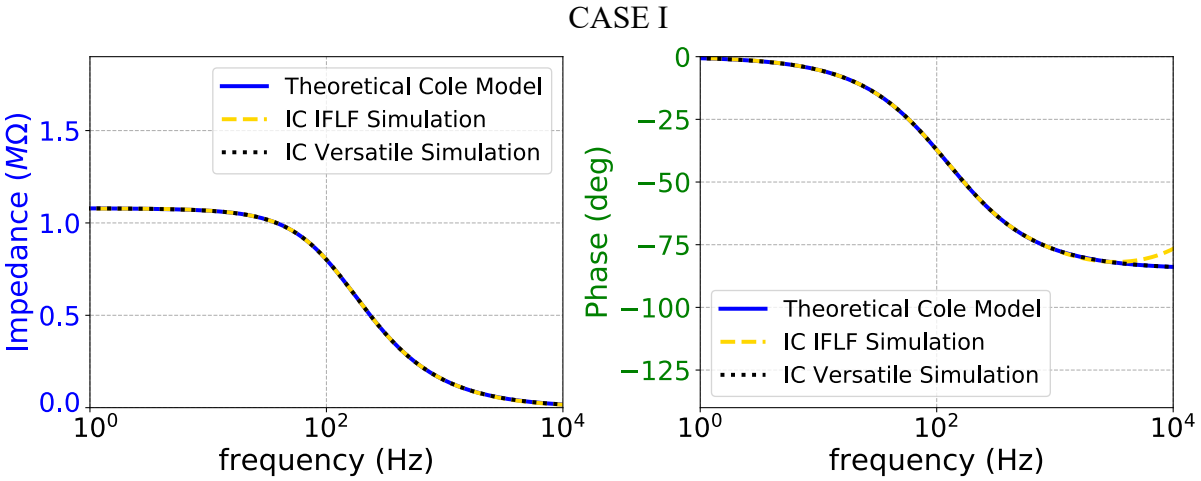

Figure 7.20: Impedance (a) magnitude and (b) phase response of the CASE I fractional-order electrode model.

were tuned, according to the values in [321]. The R_o value was kept constant at $1.39M\Omega$, and R_∞ at $1.86k\Omega$ (Table 7.15). The extracted C and a values are summarized in Table 7.14. All above cases are achieved and performed just by adjusting the appropriate dc bias currents (electroning tuning capability). According to (7.31), we can control the transconductances' values g_m, while, the values of the capacitors in Fig. 7.44 and Fig. 7.12, as in Tables 7.8 and 7.10 are kept constant.

Table 7.14: Skin Cole parameters values for different cases, $R_o = 1.39M\Omega$

Case/ Parameter	a	C (nF/sec^{1-a})
Case I	0.86	65.2
Case II	0.81	61.2
Case III	0.82	88.9
Case IV	0.78	73.1

The corresponding results are demonstrated in Figs. 7.28-7.31, where we approve that the presented

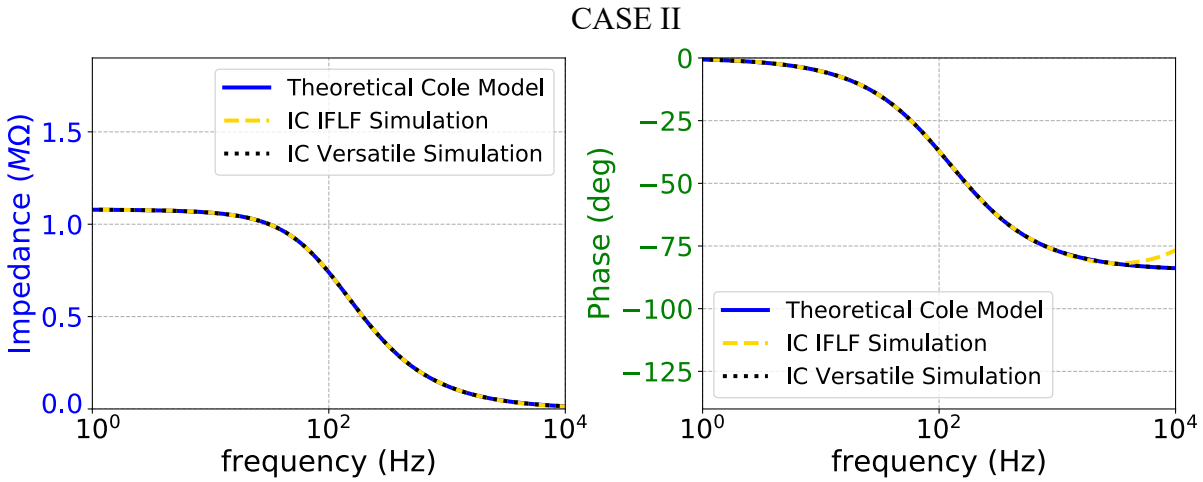

Figure 7.21: Impedance (a) magnitude and (b) phase response of the CASE II fractional-order electrode model.

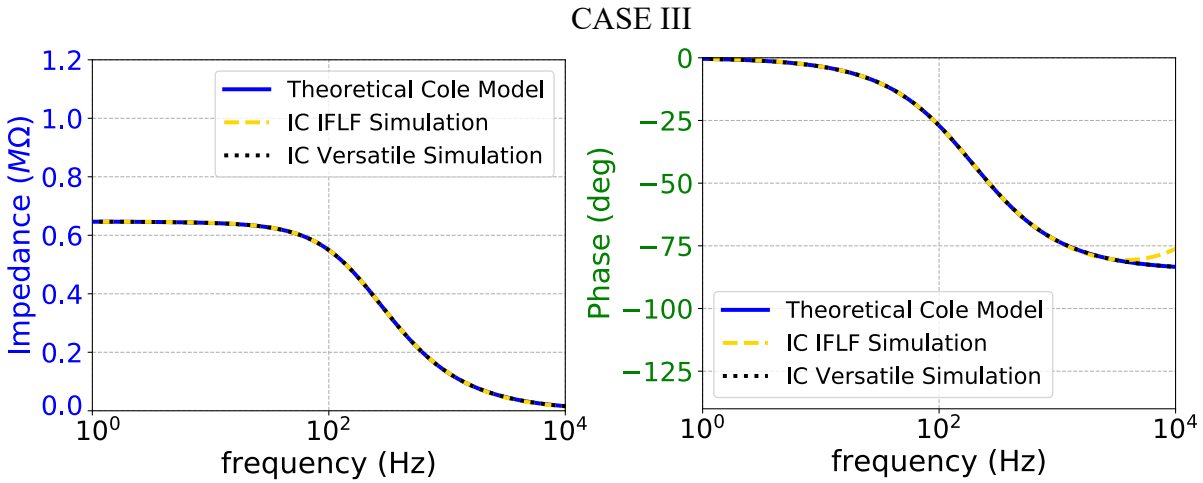

Figure 7.22: Impedance (a) magnitude and (b) phase response of the CASE III fractional-order electrode model.

architectures provide sufficient accuracy. The results are in fine agreement with the case shown in Fig. 7.19, where the the IFLF phase shows maximum error near the frequency span's limits. It is noted that both designs except from pseudo-capacitance C, can also achieve order a tuning.

7.3.4 Tetrapolar Model simulation results

The models implemented above are utilized in simplified tetrapolar setup test cases, in order to observe the impact of electrode and skin impedances at particular bioimpedance measurements. The setup adopted for the tetrapolar ac simulations is shown in Fig. 7.32, assuming 4 vertically placed dry AgCl $2.54cm$ $(1inch)$ diameter electrodes, at a distance of $3cm$ between each other. We note here that this setup is just indicative; a more realistic representation requires a fine Finite Element (F.E.) forward model,

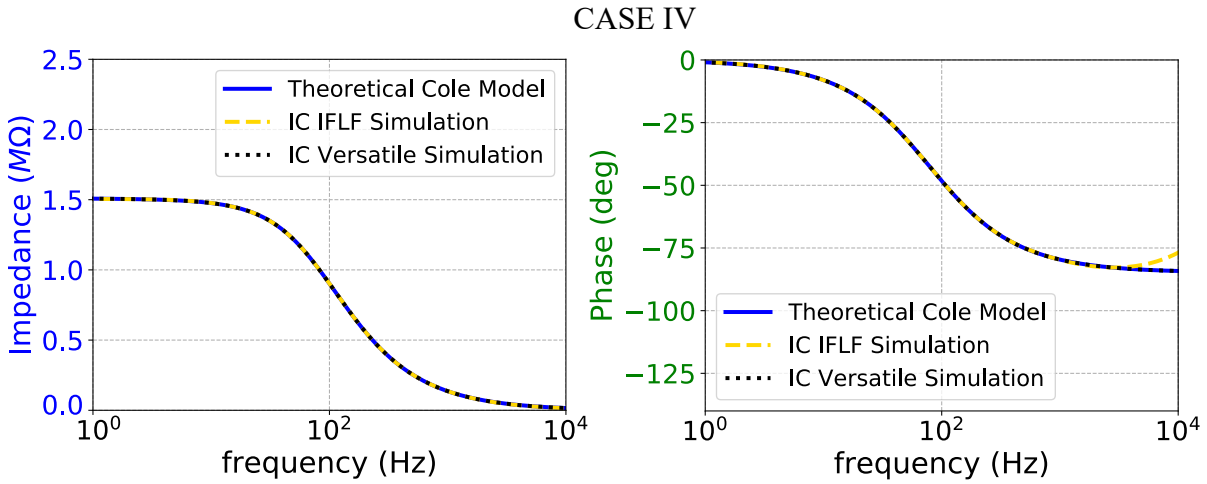

Figure 7.23: Impedance (a) magnitude and (b) phase response of the CASE IV fractional-order electrode model.

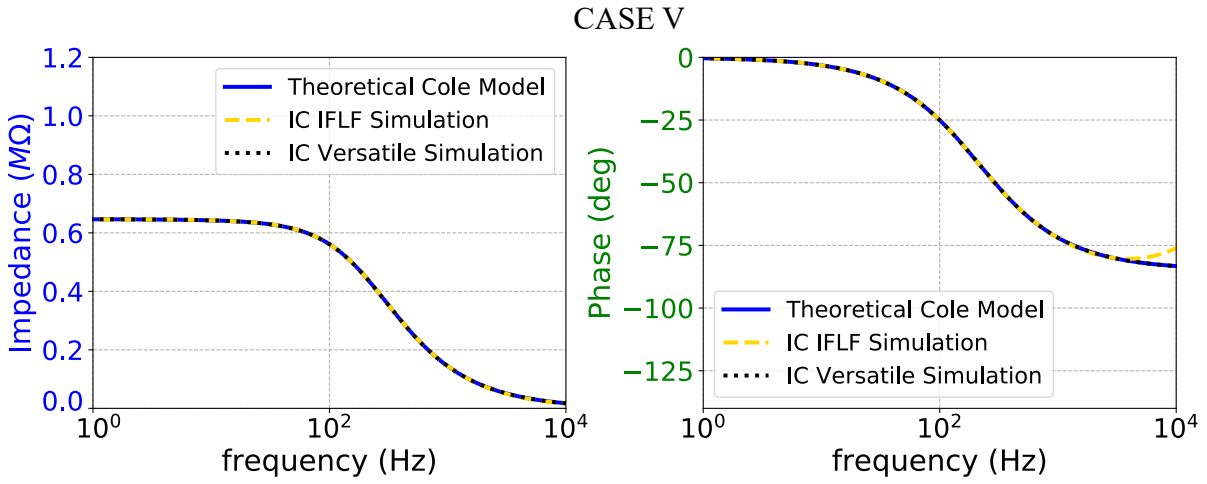

Figure 7.24: Impedance (a) magnitude and (b) phase response of the CASE V fractional-order electrode model.

which has to be properly transferred to a complex setup, consisted of blocks based on the presented models.

The two opposite (upper and lower) electrodes inject a $1mA$ ac current of frequency between $1Hz$ and $10kHz$, while the two middle electrodes perform the differential voltage measurement. The electrode material and skin RC equivalent subcircuits are replaced by the fractional integrated IC models, while the extremely sensitive shunt impedances of electrodes and skin models (R_∞) are merged in one resistor at each contact, which is manually modified in the simulation. A target impedance, R_b is placed between the two voltage measurement electodes, in parallel with a skin model's RC impedance. R_b is the resistance to be measured in each case. Finally, two $20pF$ parasitic capacitors are included for both voltage output traces to include any possible stray capacitive effects [227],[264].

All simulated ac measurements demonstrate the difference $V_+ - V_-$ as shown in Fig. 7.32 and their

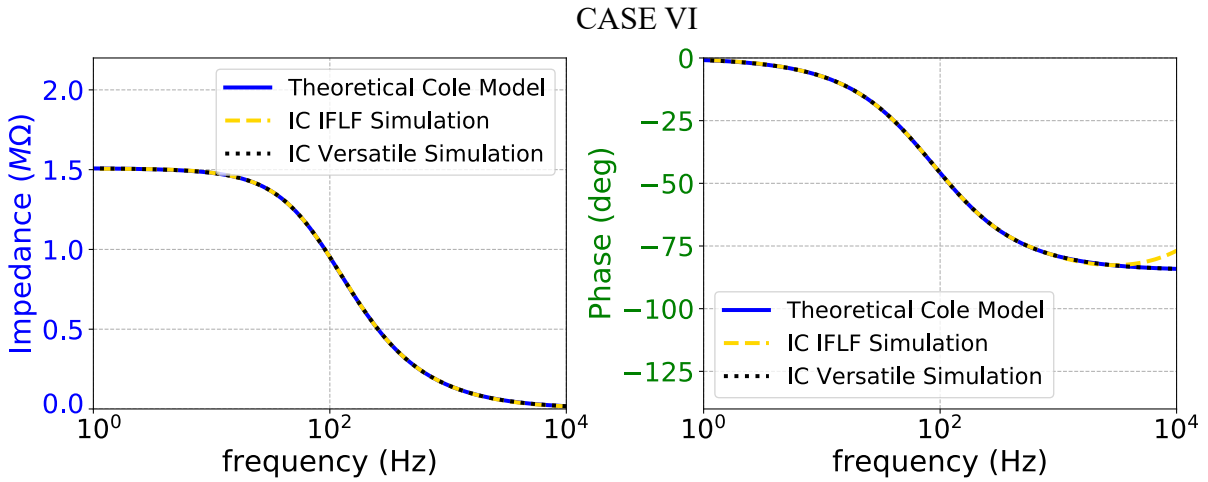

Figure 7.25: Impedance (a) magnitude and (b) phase response of the CASE VI fractional-order electrode model.

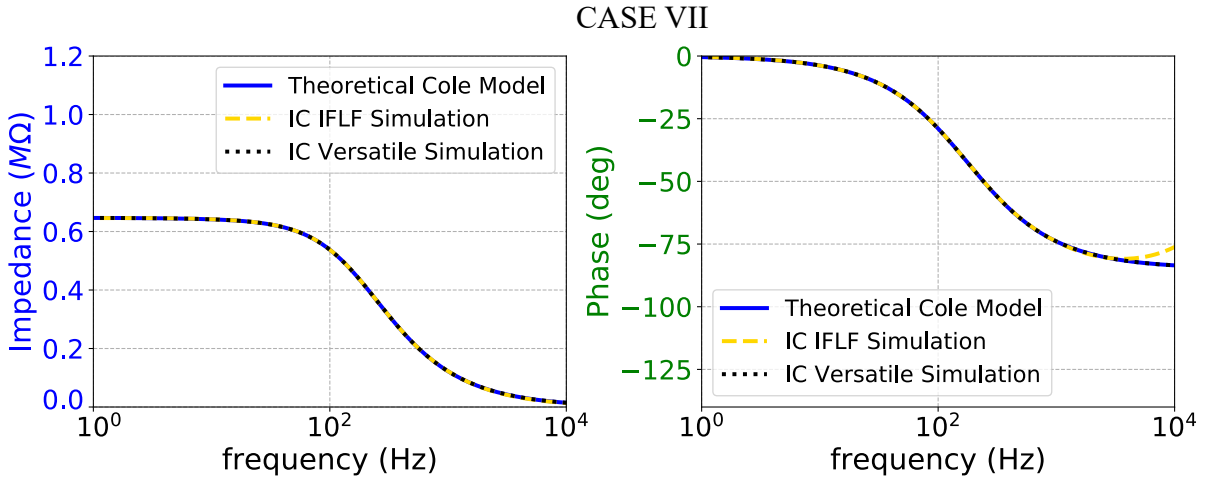

Figure 7.26: Impedance (a) magnitude and (b) phase response of the CASE VII fractional-order electrode model.

magnitude and phase are plotted at a frequency range between $1Hz$ and $10kHz$. The layout design of the fractional-order skin and electrode models using IFLF design methodology is demonstrated in Fig. 7.33, where the area is $351X614$. The layout design of the fractional-order skin and electrode models using Versatile design methodology is demonstrated in Fig. 7.34, where the area is $351X714$. The simulation results of the tetrapolar bioimpedance measurements are post-layout, because we achieved them via ave circuits (extracted).

Case I: Balanced contact impedances

In this case, all shunt impedances are kept at $R_\infty = 1.5k\Omega$, which is a usual medium frequency contact value [307],[341]. The target impedance is set to $R_b = 100\Omega$, $1k\Omega$ and $10k\Omega$ respectively, so as

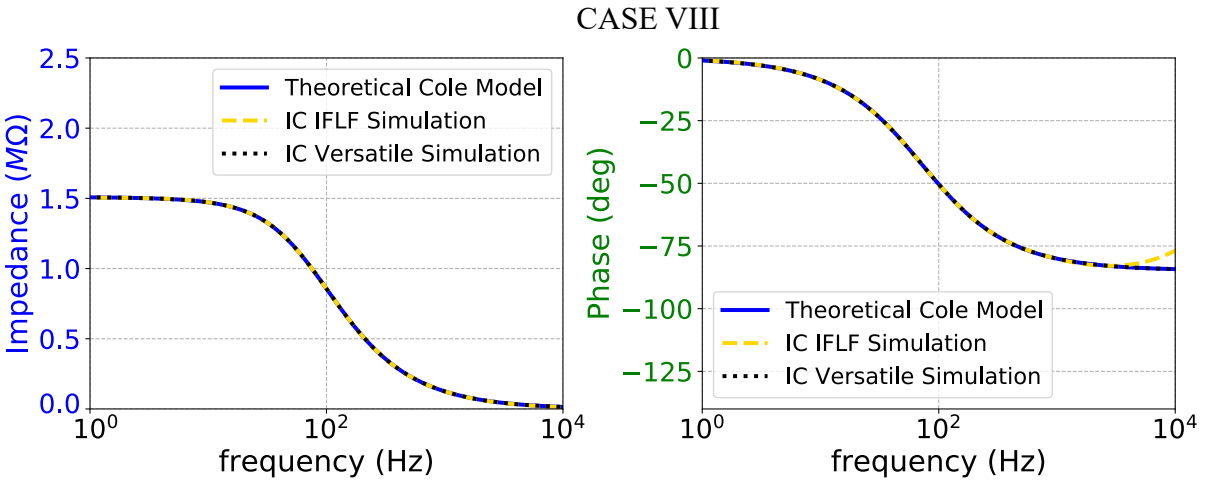

Figure 7.27: Impedance (a) magnitude and (b) phase response of the CASE VIII fractional-order electrode model.

to model the measurement effect at different orders of magnitude. The 3 subcases are compared with the approximation RC-network cases, that correspond to a completely passive model.

The results in Fig. 7.35 indicate a maximum magnitude error of 200Ω and 2^o (for the $10k\Omega$ target case), for both IFLF and Versatile methodologies, when compared with the RC network approximation. In addition, it seems that lower absolute impedances (that are usual when measuring with electrodes placed near to each other) can be accurately measured at frequencies near $10kHz$, while higher valued tissue impedance measurements, such as bones, are strongly affected by the presence of skin. The latter therefore, need either invasive techniques or compensation and proper mathematical processing along with the estimated neighboring skin tissue's impedance to be measured at higher frequencies.

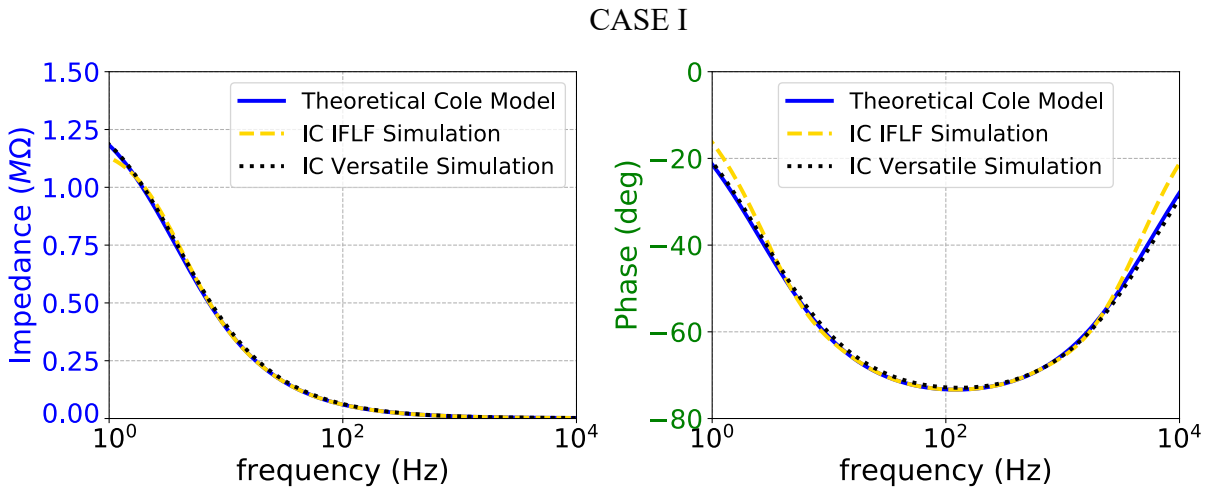

Figure 7.28: Impedance (a) magnitude and (b) phase response of the CASE I fractional-order skin model.

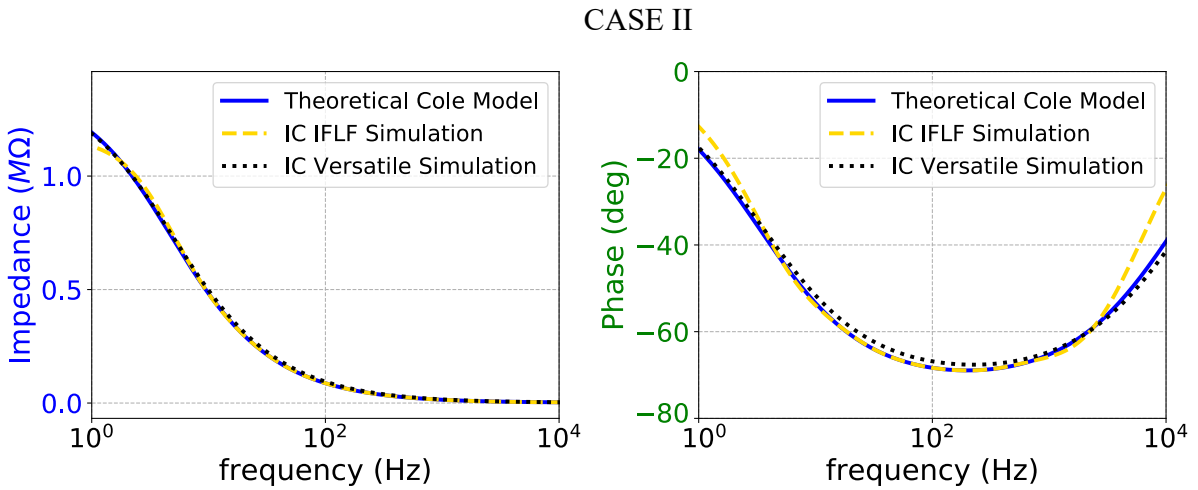

Figure 7.29: Impedance (a) magnitude and (b) phase response of the CASE II fractional-order skin model.

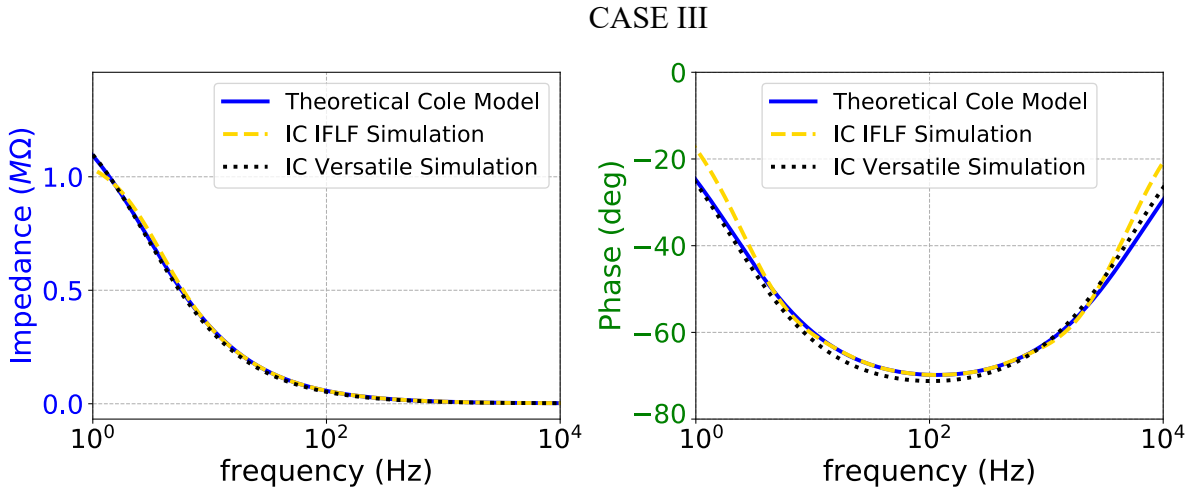

Figure 7.30: Impedance (a) magnitude and (b) phase response of the CASE III fractional-order skin model.

Case II: Imbalanced contact impedances

In bio-impedance measuring setups that include multiple electrodes, deviations between the electrode contact impedances is a usual case. These imbalances might be caused by different pressure on each electrode, local differences of the skin surface smoothness or other external factors, that in extreme conditions might lead even to electrode disconnections.

To examine this effect here, we assume 3 fixed electrode contact impedances of $R_{\infty} = 1.5k\Omega$, while one of them (in series with the positive voltage acquisition electrode) deviates between the following values: $R_{re} = \{500\Omega, 1k\Omega, 1.5k\Omega\ 2.5k\Omega\}$. The target impedance is kept at $R_b = 1k\Omega$. The magnitude and phase results are shown in Fig. 7.36 for Versatile design methodology and in Fig. 7.37 for IFLF design methodology. It is shown that for deviations up to $1k\Omega$ in the contact impedance, we get a maximum magnitude error of 40Ω and less than 1^o of phase error. The choice of IC design methodology does not show to affect the contact impedance's deviation effect in the measurements.

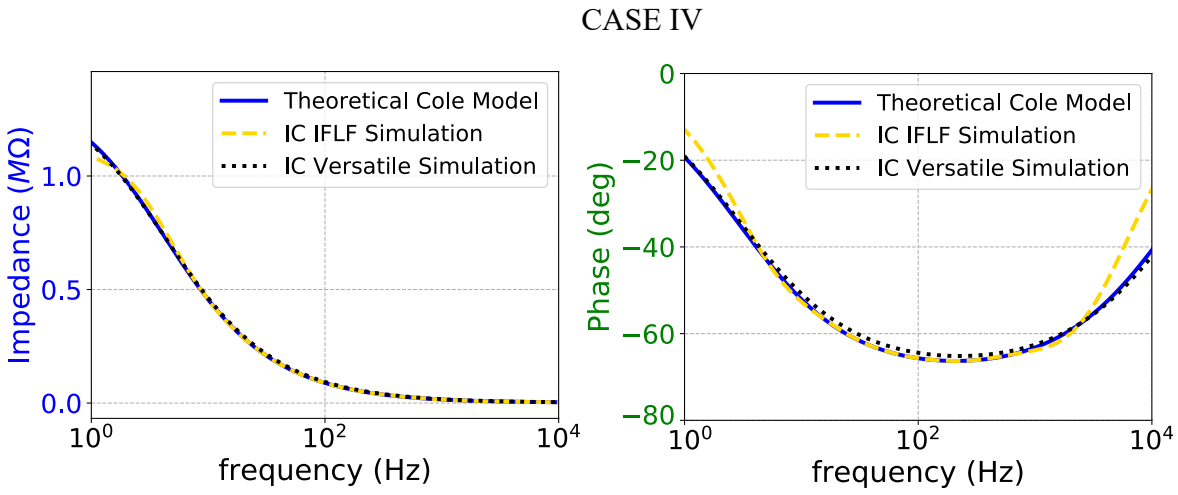

Figure 7.31: Impedance (a) magnitude and (b) phase response of the CASE IV fractional-order skin model.

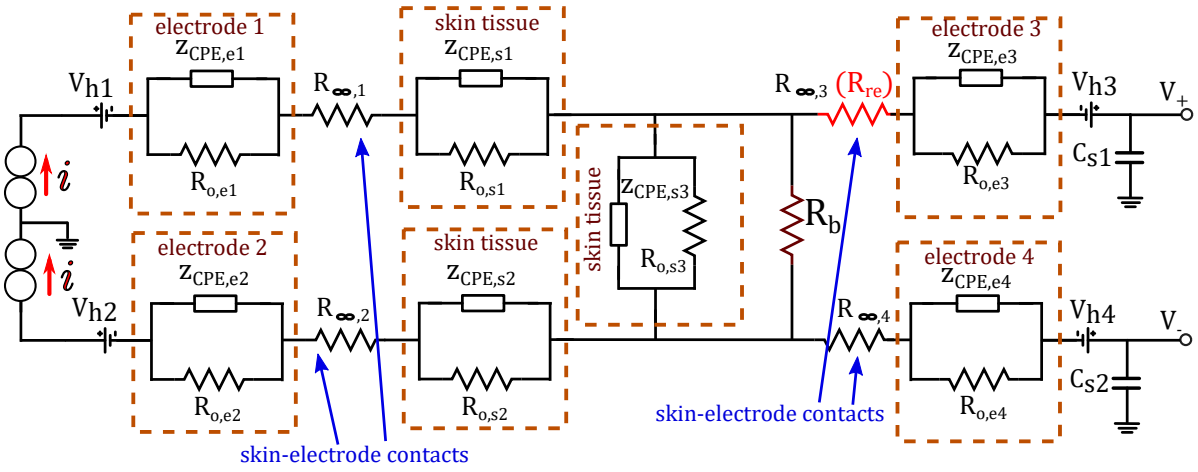

Figure 7.32: Tetrapolar setup cases.

The sensitivity behavior has been evaluated using the Monte-Carlo analysis tool for $N = 100$ runs. The corresponding histograms for impedance and phase for target impedance $R_b = 100\Omega$ are demonstrated in Fig. 7.38 for Versatile design methodology and in Fig. 7.39 for IFLF design methodology , respectively. The mean value of the magnitude and phase for Versatile design methodology is $M_{mean} = 95.82\Omega$ and $P_{mean} = -1.93^o$ and the standard deviation is $\sigma_m = 1.54\Omega$ and $\sigma_P = 0.53^o$ at $f_o = 1kHz$, respectively. The mean value of the magnitude and phase for IFLF design methodology is $M_{mean} = 95.69\Omega$ and $P_{mean} = -1.96^o$ and the standard deviation is $\sigma_m = 1.47\Omega$ and $\sigma_P = 0.47^o$ at $f_o = 1kHz$, respectively.

The sensitivity behavior has been evaluated using the Monte-Carlo analysis tool for $N = 100$ runs. The corresponding histograms for impedance and phase for target impedance $R_b = 10k\Omega$ are demonstrated in Fig. 7.40 for Versatile design methodology and in Fig. 7.41 for IFLF design methodology , respectively. The mean value of the magnitude and phase for Versatile design methodology is

$M_{mean} = 9.72k\Omega$ and $P_{mean} = -5.52^o$ and the standard deviation is $\sigma_m = 0.51k\Omega$ and $\sigma_P = 0.71^o$ at $f_o = 10Hz$, respectively. The mean value of the magnitude and phase for IFLF design methodology is $M_{mean} = 9.81k\Omega$ and $P_{mean} = -5.64^o$ and the standard deviation is $\sigma_m = 0.58k\Omega$ and $\sigma_P = 0.61^o$ at $f_o = 10Hz$, respectively.

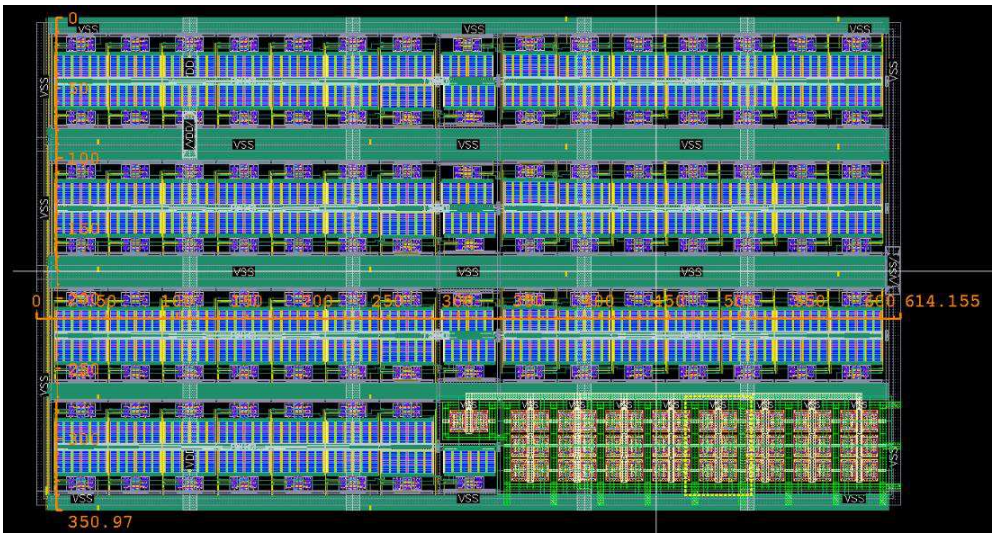

Figure 7.33: Layout design of the implemented tetrapolar bioimpedance measurement.

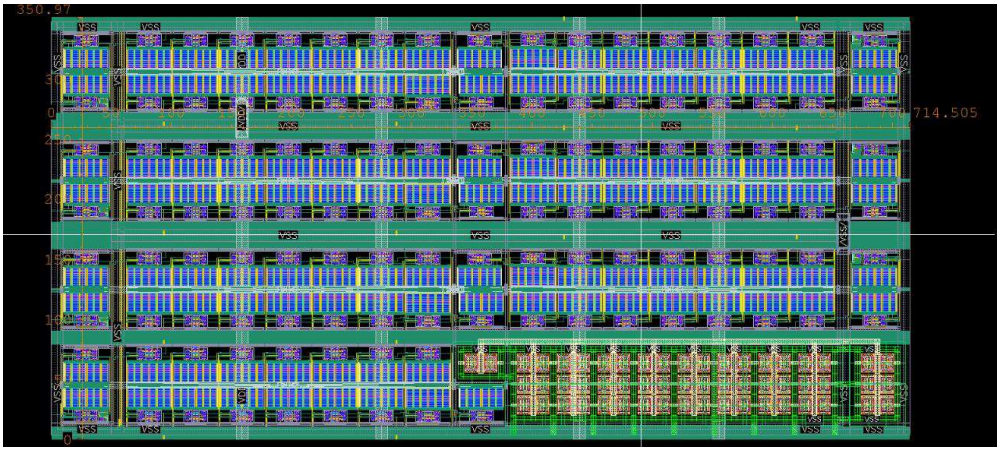

Figure 7.34: Layout design of the implemented tetrapolar bioimpedance measurement.

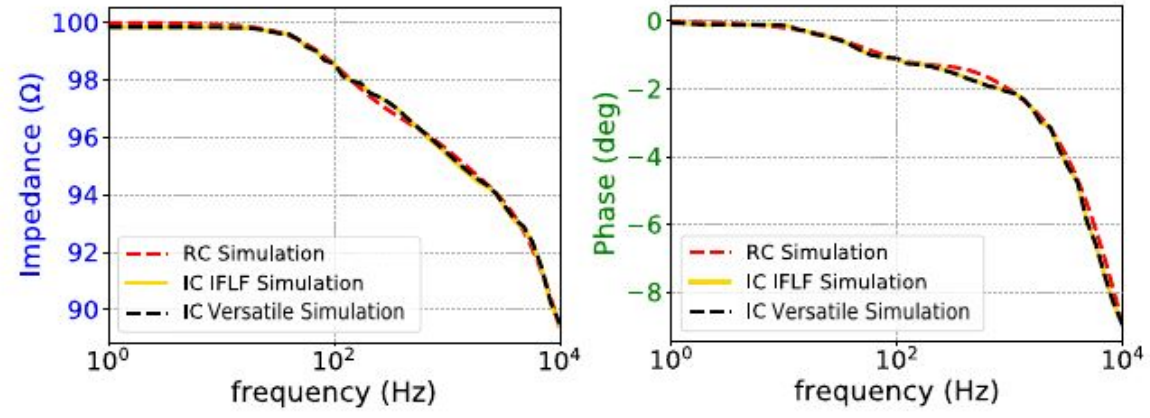

(α') $R_b = 100\Omega$

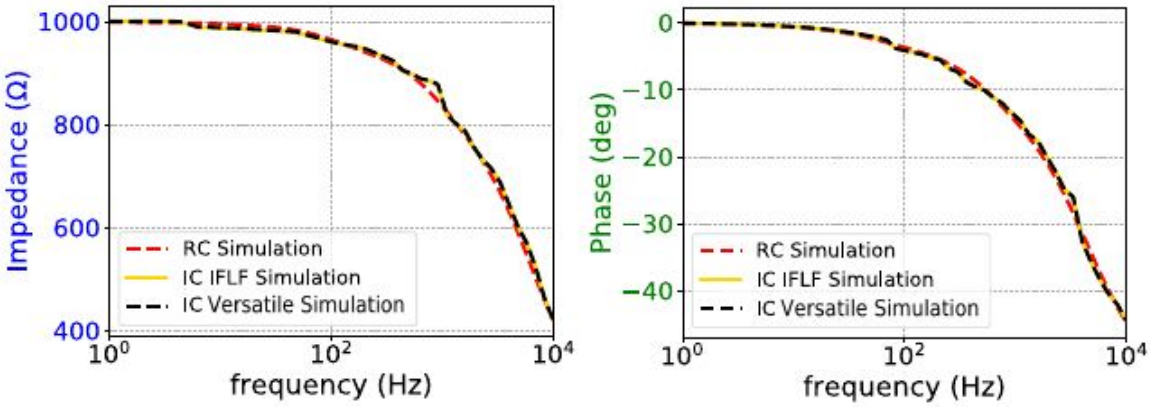

(β') $R_b = 1k\Omega$

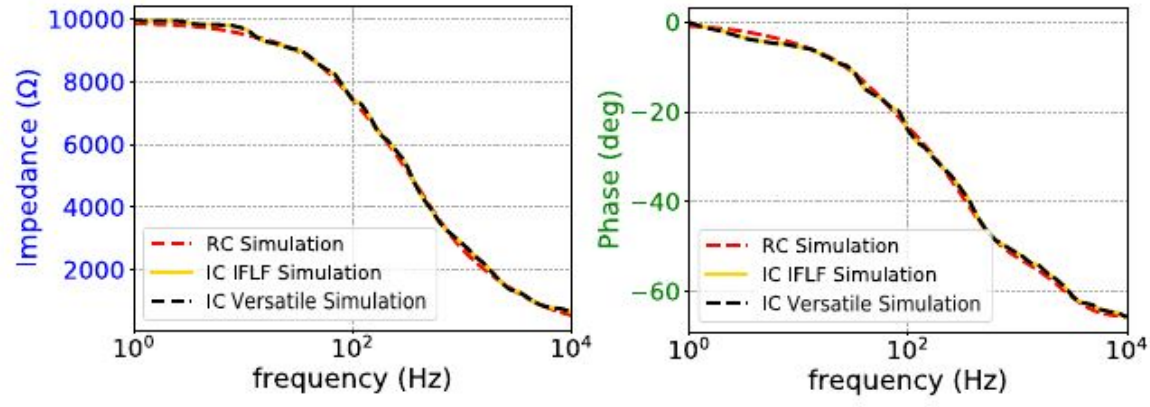

(γ') $R_b = 10k\Omega$

Figure 7.35: Ac magnitude and phase impedance measurements for (a) $R_b = 100\Omega$, (b) $R_b = 1k\Omega$ and (c) $R_b = 10k\Omega$. All electrode and contact impedances are equal ($R_\infty = 1.5k\Omega$). The corresponding RC-network approximations are included for comparison.

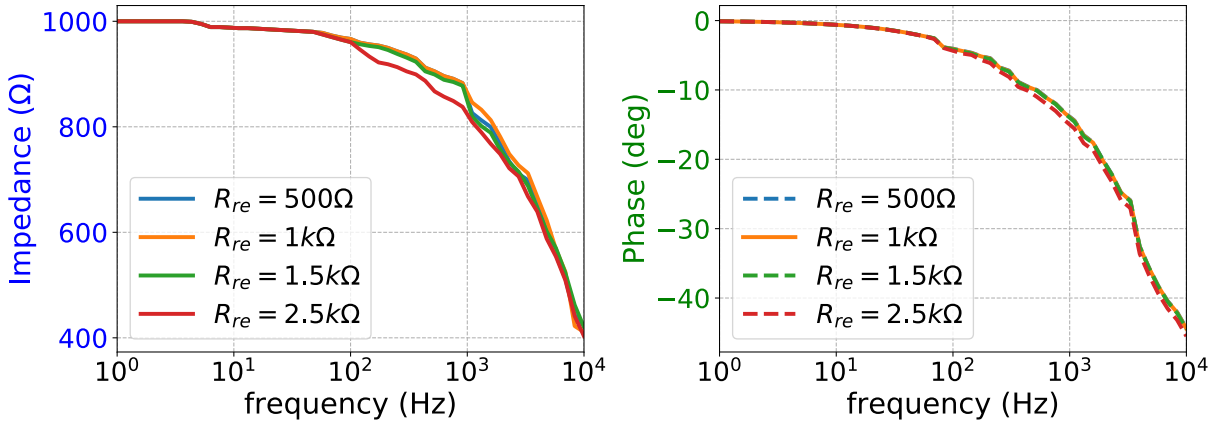

Figure 7.36: Ac magnitude (upper) and phase (down) impedance measurements for deviated shunt impedance of the positive voltage electrode (Versatile design).

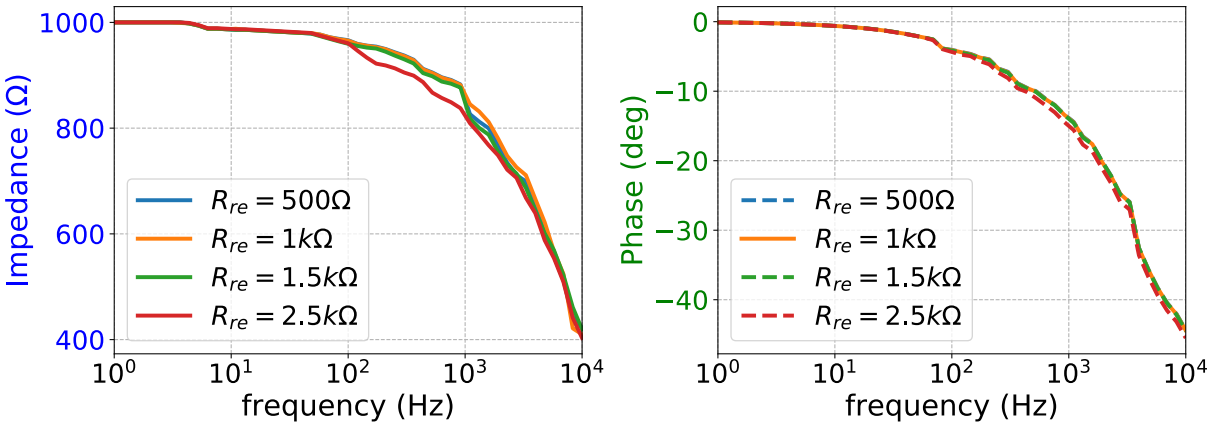

Figure 7.37: Ac magnitude (upper) and phase (down) impedance measurements for deviated shunt impedance of the positive voltage electrode (IFLF design).

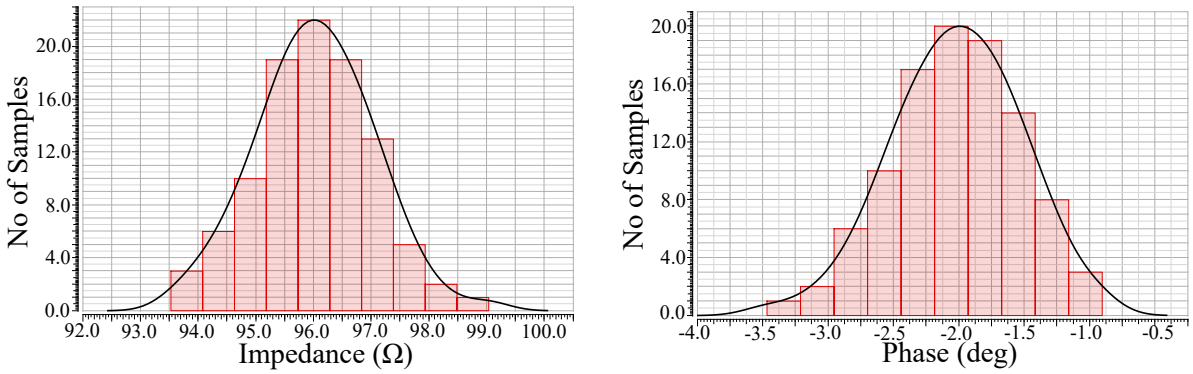

Figure 7.38: Sensitivity performance of magnitude for target impedance $R_b = 100\Omega$ using Monte-Carlo analysis (Versatile design).

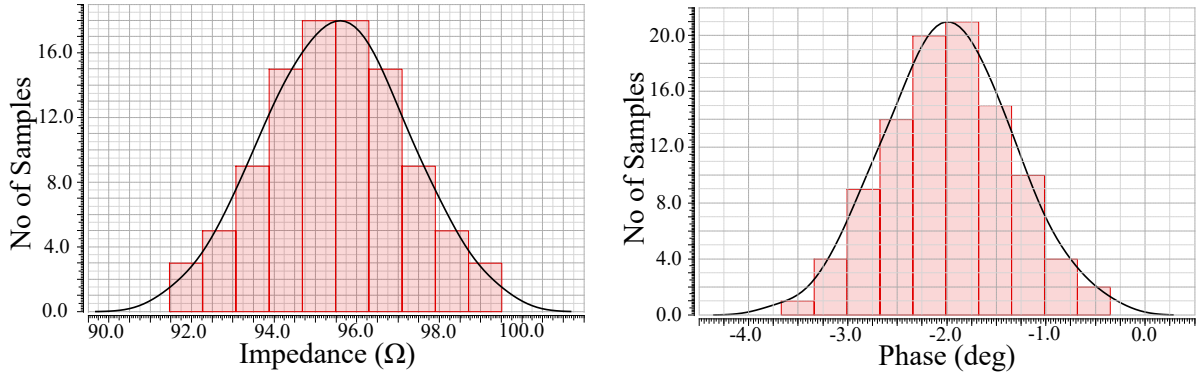

Figure 7.39: Sensitivity performance of magnitude for target impedance $R_b = 100\Omega$ using Monte-Carlo analysis (IFLF design).

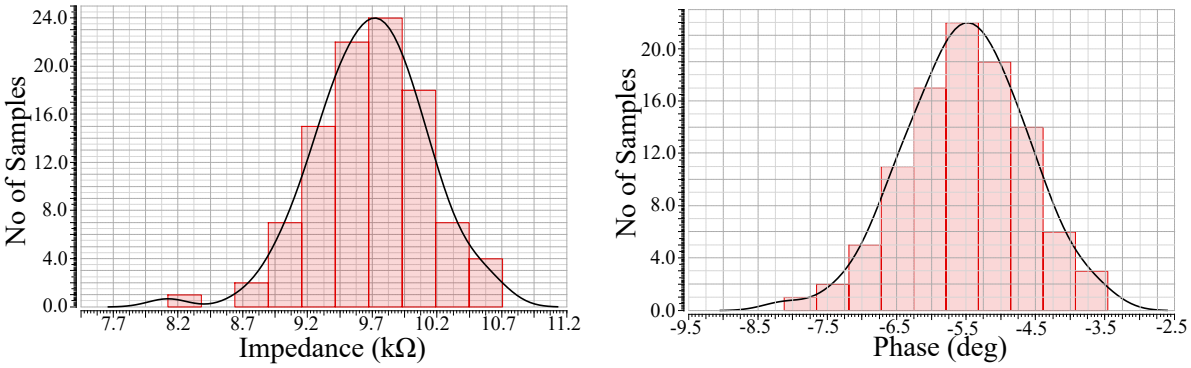

Figure 7.40: Sensitivity performance of magnitude for target impedance $R_b = 10k\Omega$ using Monte-Carlo analysis (Versatile design).

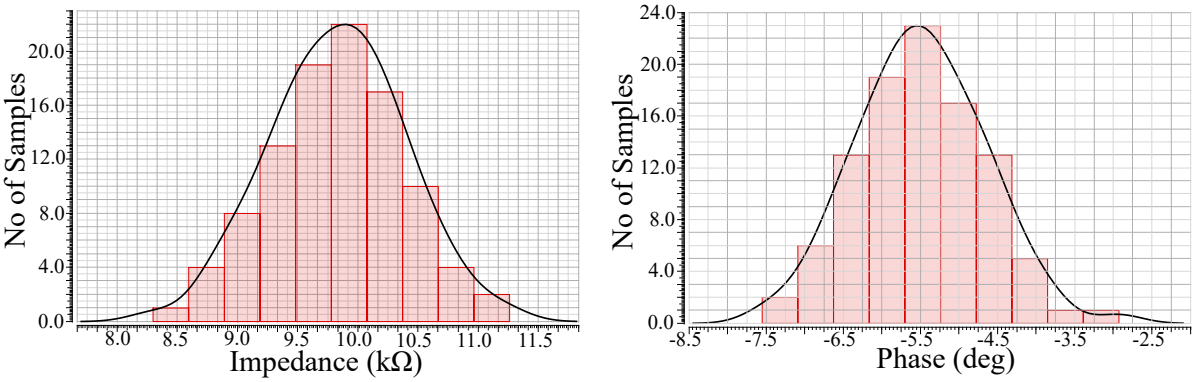

Figure 7.41: Sensitivity performance of phase for target impedance $R_b = 10k\Omega$ using Monte-Carlo analysis (Versatile design).

7.4 Analogue implementation of Fractional-Order healthy and cancerous lung cell model for Electrical Impedance Spectroscopy

This work proposes an integrated-circuit architecture emulating healthy and cancerous lung cell behaviors, approximated by Cole-Cole models and is suitable for calibration and phantom experimental testing of electrical bioimpedance circuits and systems. The architecture is based on fractional-order elements implemented with both active and passive components, offering an accurate transfer function behavior between 10kHz and 1MHz. The high-level architecture includes an analog all-pass filter coupled with a current conveyor. Performance and accuracy of the proposed architecture is confirmed via Monte- Carlo simulation. The proposed circuitry has been designed in TSMC 90nm CMOS process and simulated using the Cadence IC suite.

7.4.1 Introduction

The human tissues are characterized by specific electrical properties that reveal important information about their physical structure and function over space, time and frequency. Therefore, bioimpedance measurements, such as simple tetrapolar measurement, Electrical Impedance Tomography (EIT) and Electrical Impedance Spectroscopy (EIS) are recently becoming widespread methods that can assist the diagnostic process, avoiding invasive or continuous ionizing radiation exhibition procedures. In biompedance measuring methods, a small amplitude alternating current that meets the patient safety standards is acted via an electrode pair, attached on the patient skin surface [21].

Since bioimpedance measuring approaches are still developing both in hardware and software terms, accurate simulations and calibration experiments that include the subject electrical equivalent are immensely desired. This requirement introduces some challenges, since the electrical behavior of most human tissues is very complex and non-linear over the frequency domain. They usually follow a Cole-Cole frequency dispersion sequence. Moreover, the measurements often need to be taken at a wide frequency range, since each frequency region reveals specific tissue properties that might not be detectable at other regions [228].

Hence, high accuracy and large spectrum models are developed in order to replicate the human tissues' cells behavior. Due to their Cole-Cole nature, fractional-order models are essential to achieve the desired accuracy. Many mathematical fractional-order models have been established for biological applications. However, there is a noticeable lack of circuit modeling realization, which is necessary for the simulation of bioimpedance measuring system and the calibration with prior experiments using phantom circuitries. This absence is presented due to the fact that Cole-Cole models are impossible to be implemented using linear RC circuit equivalents. EIT and EIS are widely utilized at the thoracic imaging, for the examination of the lung's structural and functional characteristics. Due to the lung's dynamic behavior over the time domain, thoracic tomographic images are usually obtained at frequencies between 10kHz and 1MHz [21]. Moreover, any maligant tissue regions are more detectable at higher frequencies. Therefore, fractional-order models are needed to be applied at this frequency span.

In this work, an analogue implementation of fractionalorder models, emulating normal and cancer-

ous lung tissue cells from 10kHz-1MHz, is presented. Since fractional-order models offer more degrees of freedom, in comparison with integer-order, they are more accurate and sophisticated for real-world system description [323], [324]. The implementation of the models is based on analog filters. In order to transform the voltage (filter output) to impedance, we add a voltage to current (V/I) converter. The whole architecture describes the behavior of a fractional-order element.

The remainder of this work is organized as follows. In subsection 7.4.2, a brief presentation of the mathematical fractional-order model for the healthy and the cancerous lung tissue is written. In subsection 7.4.3, the analogue implementation is described and in subsection 7.4.4, simulations performed in Cadence IC suite and the corresponding results are demonstrated and discussed.

7.4.2 Lung Cole-Cole model

Many studies related with the lungs' electrical properties over various frequency ranges are found in the literature. Extensive studies for Cole-Cole parameter fitting at a large variety of human tissues are found in [188], [189]. General Cole-Cole modelling studies targetted in EIS are also presented in [342] and [343]. Specific work on the lung tissue cell electrical behavior from 1 MHz to 20GHz is found in [344], while [193] searches an accurate correlation between the air content and the admittance.

In this particular work, we implement the Cole-Cole model described in [345], since it covers a the frequency spectrum of interest (10 kHz to 1MHz) for EIS applications, and separates the model behavior between benign and maligant lung tissue cells.

Each cell can be modeled using a parallel combination of a Constant Phase Element (CPE) and a resistor, in series with a shunt impedance (Fig. 7.42). The Cole-Cole equation that expresses the healthy lung cell is [345]

$$z_b(\omega) = R_{\infty,b} + \frac{R_{0,b} - R_{\infty,b}}{1 + (j\omega)^{a_b} \cdot (R_{0,b} - R_{\infty,b})C_b} \tag{7.38}$$

while the equation that expresses the cancerous cell is [345]

$$z_m(\omega) = R_{\infty,m} + \frac{R_{0,m} - R_{\infty,m}}{1 + (j\omega)^{a_m} \cdot (R_{0,m} - R_{\infty,m})C_m} \tag{7.39}$$

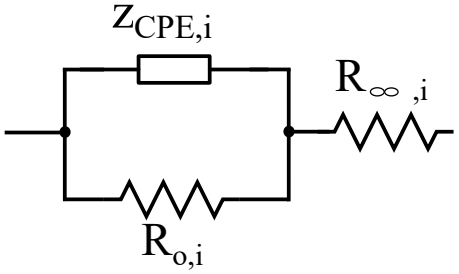

Figure 7.42: Cole-Cole model for a lung cell, where $i = \{b, m\}$.

Where $R_{\infty,i}$ is the shunt Ohmic impedance, towards which the cell's impedance converges while frequency tends to infinity, $R_{o,i}$ is the low frequency resistor, a_i is the fractional CPE order, ω is the

Table 7.15: Normal and cancerous lung cell Cole-Cole parameters

Parameter	R_∞ (Ω)	R_o (Ω)	a	τ ($\cdot 10^{-7} s$)	C ($\mu F/sec^{1-a}$)
Normal	153 ± 69	1280 ± 421	0.66 ± 0.06	5.70 ± 3.71	0.067
Cancerous	76 ± 80	558 ± 143	0.64 ± 0.08	6.82 ± 0.12	0.235

angular frequency and C_i the CPE's (pseudo)capacitance. The characteristic time constant τ_i is expressed by

$$\tau_i = \sqrt[a_i]{(R_{0,i} - R_{\infty,i})C_i} \tag{7.40}$$

The CPE's impedance is computed with the following expression

$$z_{CPE} = \frac{1}{C_i(j\omega)^{a_i}} \tag{7.41}$$

It is noted that $i = \{b, m\}$, where b denotes a healthy lung cell and m a maligant one. The Cole-Cole parameter values for both cases are demonstrated in Table 7.15, where the CPEs values have been estimated from (7.40) using the mean parameter values.

It is obvious that there is a large variation at the parameters' values, mainly due to the lung's air content. A lung can be at any state between the full inhalation (inflated state) and the full exhalation (deflated state). Nevertheless, in this work we are focusing on EIS applications for cancerous cell detection. Since between 10kHz and 1MHz the electrical conductivities and permittivities of a normal and a cancerous cell do not overlap [345], our analogue circuitry model is based on the mean parameter values.

7.4.3 Model Implementation

Implementation of the behavior of fractional-order elements is based on two types of approximation techniques due to the fact that they are not yet available for massive production. The first technique is RC-network approximation which provides easy implementation but it does not have the capability of electronic tuning on the element's characteristics (order or impedance) [338], [339].

The second one is integer order expression and the behavior of the element is approximated for example by means of the continue fraction expansion (CPE) method, round a center frequency $\omega_o = 1/\tau$. This is achieved via electronic parts such as operational transcoductance amplifies (OTAs) [346], current mirrors [336] and current feedback operation amplifiers (CFOAs) [347]. This provides new high-level architectures and new building blocks for the design of more complex and accurate systems.

RC-network approximation

A typical network for approximating the behavior of fractional-order capacitor is depicted in Fig. 7.43. It is consists of two correction factors R_p and C_p and m parallel resistors and capacitors branches.

The generalized expression of the RC-network impedance is given by:

$$Z_{tot}(s) = sC_p + \frac{1}{R_p} + \sum_{\kappa=1}^{m} \frac{sC_\kappa}{sR_\kappa C_\kappa + 1} \tag{7.42}$$

Since the practical frequency of interest is between 10kHz and 1MHz, the center frequency is $f_o = 100$kHz and the appropriate order of the RC-network is $m = 3$ (in order to achieve at least 1.5^o accuracy). Elements' values are summarized in Table 7.16 for both lung cells. The center frequency, the order m of the RC-network and the values of passive elements are derived using MATLAB code [338, 339].

Table 7.16: Passive element values for approximating the fractional-order capacitors of Fig. 2.

Normal Lung		Cancerous Lung	
Element	Value	Element	Value
C_1	1.0nF	C_1	2.90nF
C_2	451.40pF	C_2	1.25nF
C_3	203.48pF	C_3	535.77pF
C_p	167.02pF	C_p	404.42pF
R_1	15.9kΩ	R_1	5.5kΩ
R_2	3.4kΩ	R_2	1.2kΩ
R_3	720Ω	R_3	274Ω
R_p	58.7kΩ	R_p	19.1kΩ

CFE approximation

The behavior of fractional-order capacitor is described by a fractional-order differentiator connected with a double-output Current Conveyor (DO-CCII) which acts as Voltage to Current (V/I) converter. Fractional-order differentiator is approximated by an all-pass filter, which is implemented by utilizing Current Feedback Operational Amplifiers (CFOAs) as active elements.

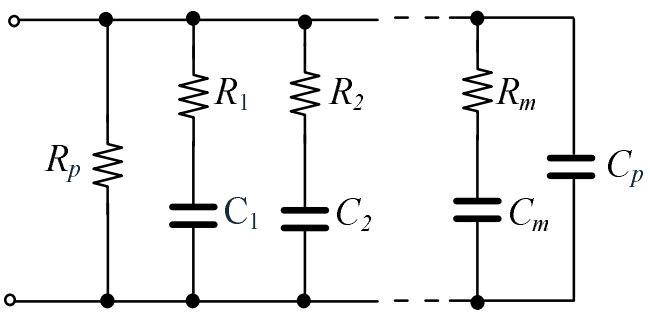

Figure 7.43: Valsa-Vlach RC-network.

The frequency range is set to be from 10kHz to 1MHz for our model and we choose 3^{rd}-order CFE approximation round a center frequency $\omega_o = 1/\tau$ [336, 337, 347, 348]. The expression of the 3^{rd}-order CFE approximation is described by:

$$(\tau s)^{\alpha} \approx \frac{a_3 s^3 + a_2 s^2 + a_1 s + a_o}{b_3 s^3 + b_2 s^2 + b_1 s + b_o} \tag{7.43}$$

where:
$\alpha_3 = b_o = \alpha^3 + 6\alpha^2 + 11\alpha + 6$,
$\alpha_2 = b_1 = -3\alpha^3 - 6\alpha^2 + 27\alpha + 54$,
$\alpha_1 = b_2 = 3\alpha^3 - 6\alpha^2 - 27\alpha + 54$,
$\alpha_o = b_3 = -\alpha^3 + 6\alpha^2 - 11\alpha + 6$
and α is the order of the differentiator (all pass filter) [336, 337, 347, 348]. The complete design of proposed architecture is depicted in Fig. 7.44 and parameters are summarized in Table 7.17. In Fig. 3 the resistors' and capacitors' values can be easily calculated using the corresponding parameters based on (7.43). The transfer function of the fractional-order differentiator, which is based on a 3^{rd}-order all pass filter is given by:

$$H(s) = (\tau s)^{\alpha} = \frac{a_3 s^3 + a_2 s^2 + a_1 s + a_o}{b_3 s^3 + b_2 s^2 + b_1 s + b_o} \tag{7.44}$$

The impedance of the fractional-order capacitor is given by:

$$Z_{cap}(s) = \frac{R_{vi}}{H(s)} \tag{7.45}$$

where R_{vi} is the appropriate resistor of the V/I converter and $H(s)$ is the expression of the filter.

Table 7.17: Parameter of the circuit in Fig. 7.44.

Parameter	Value	Parameter	Value
b_3	1	b_2	$\frac{1}{R_1 C_1}$
b_1	$\frac{b_2}{R_2 C_2}$	b_o	$\frac{b_1}{R_3 C_3}$
α_3	$\frac{R_6 R_8}{R_1(R_6+R_8)}$	α_2	$\frac{\alpha_3}{RC} + \frac{b_2 R_8 R_6}{RC(R_6+R_8)}$
α_o	$\frac{b_1 R_8}{R_7(R_6+R_8)}$	α_1	$RC\alpha_o + \frac{b_2 R_8 R_6}{RCR_5(R_6+R_8)}$

7.4.4 Simulations and Results

The proposed lung cell has been designed in TSMC 90nm CMOS process, using the Cadence IC design suite. The schematic of the corresponding CFOA is shown in Fig. 7.45 and the schematic of the appropriate V/I converter is depicted in Fig. 7.46, according to [337]. The power supply rails are set to $V_{DD} = -V_{SS} = 0.75$V, $I_b = 200nA$, $I_{bias} = 3nA$ and all transistors operate in the sub-threshold region. The dimensions of the MOS transistors of the CFOA and the DO-CCII are summarized in Table

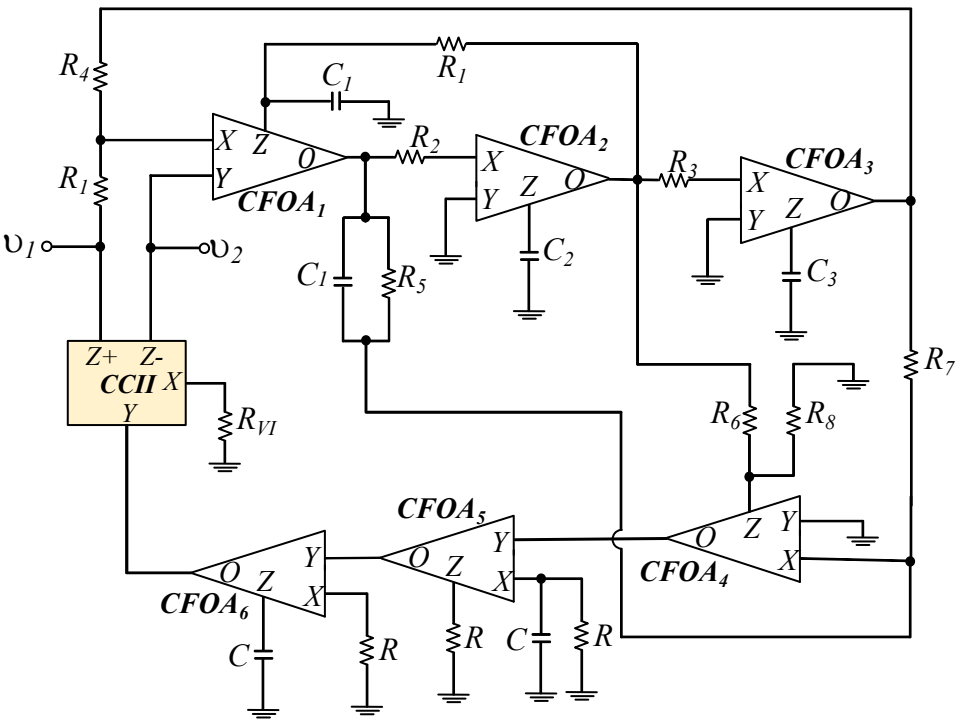

Figure 7.44: Implementation of fractional-order capacitor emulator.

7.18.

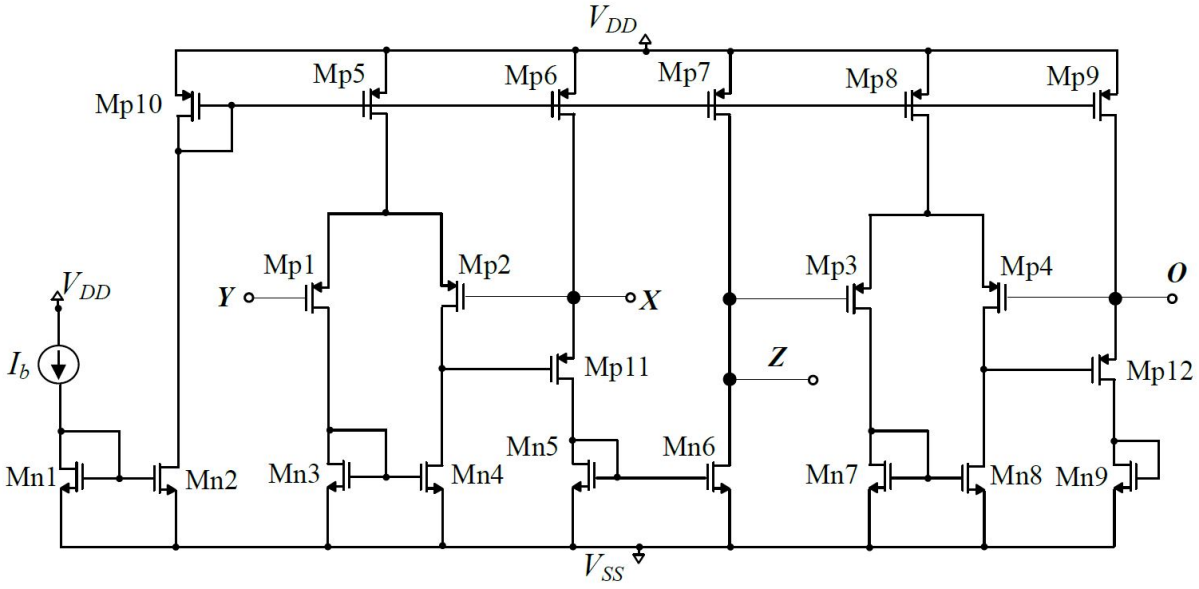

Figure 7.45: Employed CFOA.

The obtained magnitude and phase responses in comparison with both RC-network and theoretically predicted ones confirm the behavior of the fractional-order healthy and cancerous lung cell model as

shown in Fig. 7.47. The results of the proposed impedance models are in fine agreement with the theoretical ones and confirm the proper operation, performance and accuracy of the proposed topology.

The sensitivity behavior has been evaluated using the Monte-Carlo analysis tool for $N = 100$ runs for impedance and phase for health lung. The mean value of the impedance and phase is $I_{mean} = 1.06\text{k}\Omega$ and $P_{mean} = -18.28^o$ and the standard deviation is $\sigma_I = 0.07\text{k}\Omega$ and $\sigma_P = 1.36^o$ at $f_o = 100\text{kHz}$, respectively. The Monte-Carlo analysis demonstrates the performance and accuracy of the proposed architecture.

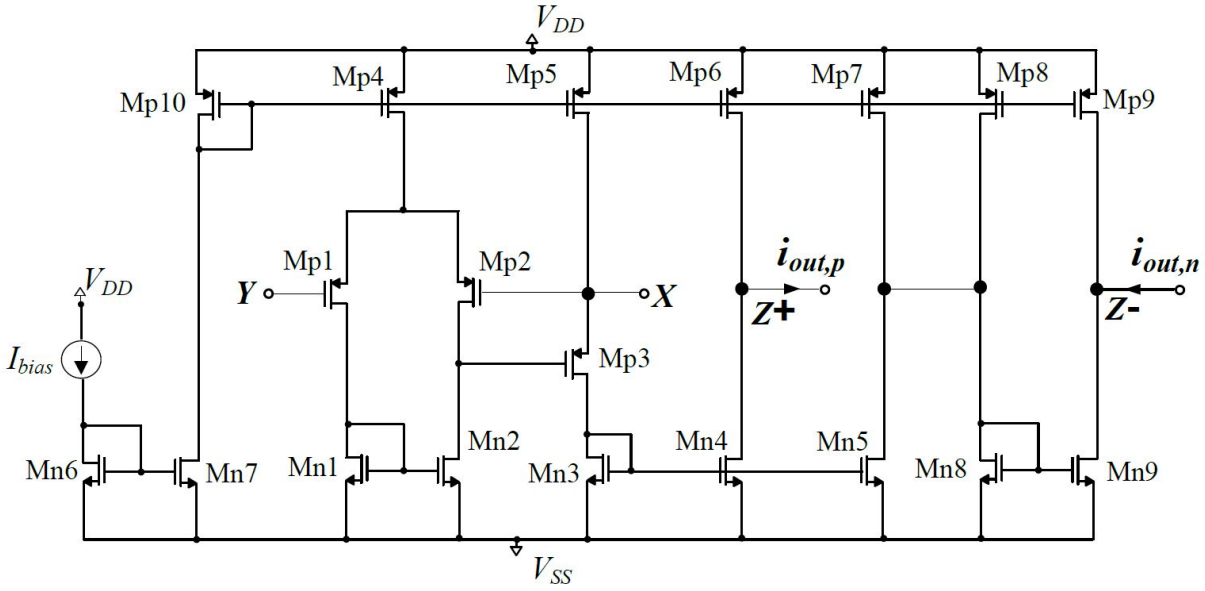

Figure 7.46: Employed DO-CCII for the implementation of V/I converter.

Table 7.18: MOS Transistors Dimensions – CFOA & DO-CCII.

CFOA	W/L $(\mu m/\mu m)$	DO-CCII	W/L $(\mu m/\mu m)$
M_{n1}-M_{n9}	13/0.5	M_{n1}-M_{n9}	13/0.5
M_{p5}-M_{p10}	50/0.5	M_{p4}-M_{p10}	50/0.5
M_{p11},M_{p12}	100/0.5	M_{p3}	100/0.5
M_{p1}-M_{p4}	20/0.4	M_{p1},M_{p2}	20/0.4

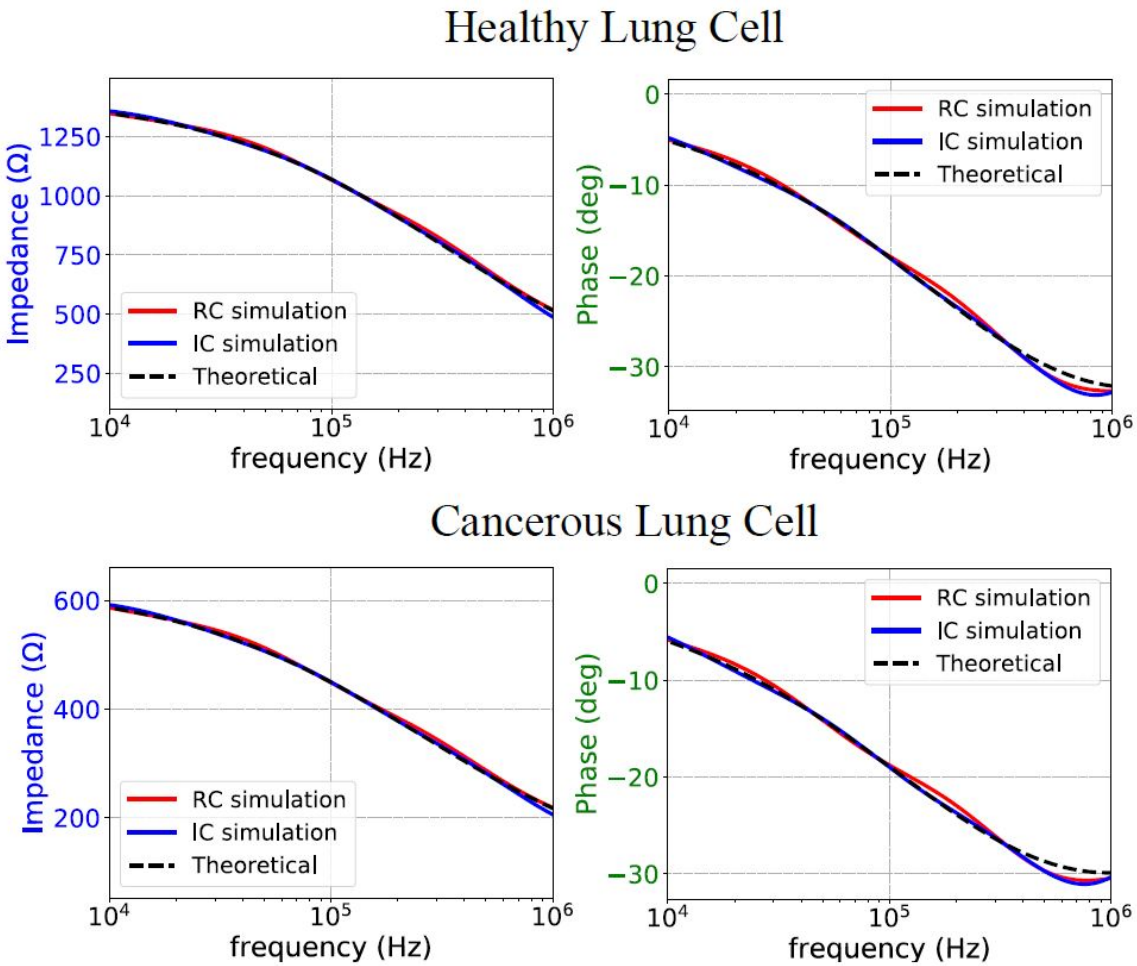

Figure 7.47: Frequency responses of fractional-order lung cell model.

8 Conclusions

This chapter draws some important conclusions about the results from the research conducted in this PhD thesis. It focuses on the results and the contribution of Chapters 3, 4, 6 and 7.

In the third chapter (Chapter 3) of this PhD thesis, an integral equation based Point-Matching Method-of-Moment for difference-EIT imaging, employing Green's functions and expressing the conductivity logarithm as RBFs superposition was presented. It was evaluated via 2D simulation, experimental and medical-data-based cases as well as with 3D cylindrical-cavity simulations. The results indicate that the conductivity inclusions were successfully detected with a small number of iterations. SVD analysis, simulations with noisy signals and experimental data demonstrate that the proposed method is more robust to noise than conventional F.E.M. imaging approaches. The method can be used with any pairwise measurement pattern, for serial or simultaneous voltage measurement, making it an efficient one for time-difference EIT. It can also be extended to work with multiple current source schemes used for frequency-difference EIT.

In the fourth chapter (Chapter 4), the method-of-moment EIT reconstruction approach is combined with an SBL method and applied to dynamic EIT lung imaging. In this study, 3D CT-based F.E. thoracic cavities considering 5 breath cycle states and the basic thoracic tissues were developed to simulate the measuring process. Quantitative evaluation was performed using a variety of metrics, and an extensive comparison with other reconstruction approaches took place. In vivo imaging using online available data was also carried out. The results show that the proposed (PM-MoM SBL) approach appears to improve spatial resolution in the reconstructed EIT images. Furthermore, despite the method's high time complexity, the lack of necessity for hyperparameter selection reduces the effects of this disadvantage. Future research must be performed in the following directions: A) Optimization of the SBL algorithm in terms of imaging quality and time complexity; and B) Application in 3D multi-layer EIT imaging.

In chapter 6, an EIT simulation interface which makes use of Python, MATLAB, and LT SPICE software is applied in order to evaluate the impact of modeling, parasitic, and noise effects in phantom cylindrical cases and in thoracic imaging. Each SUT is modeled as a fine F.E. structure, which is transformed to a multiport RLC circuitry block and merged in the analogue SPICE EIT circuitry. Transient and noise simulations are carried out in LT SPICE, while MATLAB creates the input data (input sinusoidal waveform and digital signals for the multiplexers' control) and handles the output SPICE transient data

to simulate the digital EIT hardware part. Configurations of the electrodes and the signal sampling are considered, and comparison of the results is performed. Simulations showed the significant effect of the channels' impedances at low frequencies and passive-electrode configurations in reconstructions as well as the effect of the parasitic channels' capacitors at higher frequencies. The active electrode configuration can compensate for these effects, while increasing the demodulation filter taps can increase the acquired signal SNR and, as a result, the reconstructed image quality. This interface can be used as a valuable tool in EIT system design for prior estimation of custom EIT system performance under different analogue and digital part characteristics.

In chapter 7, the results of three individual research works are discussed. In 7.1 a high temporal resolution multiparameter thoracic simulation model for EIT is described. The simulations are executed in MATLAB and FEMM software. The effect of ventilation (breathing) and circulation (blood) cycles on tissue movement and admittances was taken into account during each frame measurement. For each frame, the bipolar current source is shifted N times between the electrodes and each one is considered as a discrete simulation time step, giving a resolution of N time steps per frame. The simulation model's tunability can be further improved, with the randomization of more thoracic sections and chest-types initial boundaries. Extensive functional analysis and post processing needs to be performed on the images, in order to acquire valid medical data.

In 7.3 skin and electrode Cole models we implemented, using two design methodologies, in fractional order integrated form using OTAs and CCIIs as structural elements. Simulations showed very low magnitude and phase errors, while tetrapolar setup simulations revealed possible bio-impedance measuring issues related to the electrode and adjacent skin tissues up to 10 kHz. The ICs and layouts implemented can be used in more complex circuitry setups for calibration and phantom experimental testing much more effectively than simple resistor or RC networks that are currently utilized, since they offer sufficient tunability over all frequencies of interest and model parameter variations.

In 7.4 the healthy and cancerous lung cells (Cole model) were implemented in fractional order integrated form using CFOAs and CCIIs as active elements. Simulations showed very low impedance and phase errors for fractionalorder model and also confirming the accuracy and the performance of the proposed architecture, in system level. The ICs implemented can be used in more complex circuitry setups for calibration and phantom experimental testing, much more effectively than simple resistor or RC networks.

Overall, the research conducted, the methodologies adopted and the results acquired through this PhD dissertation makes a scientific contribution in the field of biomedical engineering, medical imaging, medical electronics and especially Electrical Impedance Tomography. Furthermore, I hope that it will provide the scientific community with some useful knowledge and tools for future accomplishments in the field that will lead to wider clinical application of Electrical Impedance Tomography. A possible future related research direction could be found in the field of Machine Learning, where both supervised deep learning and non-supervised learning approaches could potentially improve the image reconstructions' spatial resolution. Another research direction is the implementation of a wide-band EIT system that can be adapted to a range of medical applications, such as real-time lung monitoring, cancerous cell detection and tracking, as well as brain EIT and neuroimaging.

9 Appendix A: MATLAB-EIDORS code

9.1 Code for the Regularized and GREIT reconstructions in Chapter 2

```
%%%%Run eidors
%%%run path_to_eidors\startup.m
%%%%define measurement pattern
skipcurr=0;
skipvolt=0;
%%%%define electrode number
N=16;
elecs=N;
%%%%cylindrical setup dimensions
height=1;
radius=1.5;
%%%%grid density (NETGEN parameter)
maxh=0.1;
electrode_z=0.6;
%%%%DEFINE signal SNR
SNR1=60;
SNR2=40;

%%%%%homogeneous model
%%%%call NETGEN
fmdl = ng_mk_cyl_models([height,radius,maxh],[elecs,electrode_z],0.1);
[stim,els] = mk_stim_patterns(N,1,[0,skipcurr+1],[0,skipvolt+1],{},0.001);
FWD_image = mk_image(fmdl,1);
FWD_image.fwd_model.stimulation = stim;
FWD_image.fwd_solve.get_all_meas = 1;
vh=fwd_solve(FWD_image);

%%%%%inhomogeneous model
%%%create spherical inclusion
object={'ball','solid ball = sphere(0,0.5,0.5;0.35);'};
%%%%call NETGEN
fmdl2 = ng_mk_cyl_models([height,radius,maxh],[elecs,electrode_z],0.05,object);
FWD_image2= mk_image(fmdl2,1);
FWD_image2.elem_data(fmdl2.mat_idx{2})=0.1;
FWD_image2.fwd_model.stimulation = stim;
FWD_image2.fwd_solve.get_all_meas = 1;
vi=fwd_solve(FWD_image2);

%%%%image simulation model with inclusion

figure
H1=show_fem(FWD_image2,1);
axis tight
axis off
colormap jet
set(H1, 'edgecolor', [0.5 0.5 0.5]);
set(H1, 'edgealpha', 0.25);
hold on
plot3(1.5*cos(0:0.01:2*pi),1.5*sin(0:0.01:2*pi),(1+0.01)*ones(length(0:0.01:2*pi),1),'--b','LineWidth',2)
```

```
hold on
plot3(1.5*cos(0:0.01:2*pi),1.5*sin(0:0.01:2*pi),zeros(length(0:0.01:2*pi),1),'--r','LineWidth',2)
zlim([0 1.02])
view([0 40])
axis off
co = colorbar;

co.TickLabelInterpreter='Latex';
co.FontSize=13;
co.Label.String = 'Conductivity ($S/m$)';
co.Label.Interpreter='Latex';
co.Label.FontSize=16;

%%%%show voltage distribution

figure
img_v1 = rmfield(FWD_image2, 'elem_data');
img_v1.node_data = vi.volt(:,1);
show_slices(img_v1,[0.2;0.3;0.4]*[inf,inf,1])

figure
img_v2 = rmfield(FWD_image2, 'elem_data');
img_v2.node_data = vi.volt(:,6);
show_slices(img_v2,[0.2;0.3;0.4]*[inf,inf,1])

%%%%%%%%%%%%%%%%%%show measurements (noise-free)

figure
Mmax=max(max(real(vh.meas)),max(real(vi.meas)));
plot(real(vh.meas)/Mmax,'b','LineWidth',2)
hold on
plot(real(vi.meas)/Mmax,'r','LineWidth',2)
grid on
XL=xlabel('Measurement Index','Interpreter','Latex');
XL.FontSize=16;
YL=ylabel('Normalized Voltage (Noise-free)','Interpreter','Latex');
YL.FontSize=16;
a = get(gca,'XTickLabel');
set(gca,'XTickLabel',a,'fontsize',16)
set(gca,'TickLabelInterpreter', 'latex');
xlim([0 210])
ylim([0 1.3])
Leg=legend({'Homogeneous','With Inclusion'},'Interpreter','Latex');

%%%%%%%%%%%%%%%
%%%% add noise to measurements
vh1n1 = awgn(vh.meas,SNR1,'measured');
vh2n1 = awgn(vi.meas,SNR1,'measured');

vh1n2 = awgn(vh.meas,SNR2,'measured');
vh2n2 = awgn(vi.meas,SNR2,'measured');

%%%%%%Default hyperparamter values
lambdaSTR1=1e-06;
lambdaSTR2=1e-05;
%
lambdaLaplace1=1e-06;
lambdaLaplace2=1e-05;
%
lambdaNoser1=0.002;
lambdaNoser2=0.02;
%
lambdaGauss1=1e-06;
lambdaGauss2=1e-05;
%
lambdaTV1=1e-12;
lambdaTV2=1e-10;


%%%%%%%%%Set inverse (2D reconstruction) model

invmodel=mk_common_model('d2c3',N);
invmodel.fwd_model.stimulation = stim;
invmodel.fwd_model.meas_select=els;
invmodel.fwd_solve.get_all_meas = 1;

%%%%%Gauss-Newton Reconstruction
```

```
eidors_msg('Difference GN-Recostruction');
invmodelGN=invmodel;
invmodelGN.solve=@inv_solve_gn;
invmodelGN.inv_solve_gn.max_iterations = 20;

%%%%Standard Tikhonov Reg
invmodelSTR=invmodelGN;
invmodelSTR.RtR_prior = @prior_tikhonov;
%%%%SNR1
invmodelSTR.hyperparameter.value=lambdaSTR1;
imagesSTR1=inv_solve(invmodelSTR,vh1n1,vh2n1);
%%%%SNR2
invmodelSTR.hyperparameter.value=lambdaSTR2;
imagesSTR2=inv_solve(invmodelSTR,vh1n2,vh2n2);

%%%%Laplace Reg
invmodelLaplace=invmodelGN;
invmodelLaplace.RtR_prior = @prior_laplace;
%%%%SNR1
invmodelLaplace.hyperparameter.value=lambdaLaplace1;
imagesLaplace1=inv_solve(invmodelLaplace,vh1n1,vh2n1);
%%%%SNR2
invmodelLaplace.hyperparameter.value=lambdaLaplace2;
imagesLaplace2=inv_solve(invmodelLaplace,vh1n2,vh2n2);

%%%%NOSER Reg
invmodelNOSER=invmodelGN;
invmodelNOSER.RtR_prior = @prior_noser;
%%%%SNR1
invmodelNOSER.hyperparameter.value=lambdaNoser1;
imagesNOSER1=inv_solve(invmodelNOSER,vh1n1,vh2n1);
%%%%SNR2
invmodelNOSER.hyperparameter.value=lambdaNoser2;
imagesNOSER2=inv_solve(invmodelNOSER,vh1n2,vh2n2);

%%%%Gauss Reg
invmodelGauss=invmodelGN;
invmodelGauss.RtR_prior = @prior_gaussian_HPF;
%%%%SNR1
invmodelGauss.hyperparameter.value=lambdaGauss1;
imagesGauss1=inv_solve(invmodelGauss,vh1n1,vh2n1);
%%%%SNR2
invmodelGauss.hyperparameter.value=lambdaGauss2;
imagesGauss2=inv_solve(invmodelGauss,vh1n2,vh2n2);

%%%%TV Reconstruction
eidors_msg('Difference TV-Recostruction');
invmodelTV=invmodel;
invmodelTV.solve=@inv_solve_TV_pdipm;
invmodelTV.parameters.term_tolerance= 1e-3;
invmodelTV.parameters.keep_iterations= 0;
invmodelTV.R_prior = @prior_TV;
%%%%SNR1
invmodelTV.hyperparameter.value=lambdaTV1;
imagesTV1=inv_solve(invmodelTV,vh1n1,vh2n1);
%%%%SNR2
invmodelGauss.hyperparameter.value=lambdaTV2;
imagesTV2=inv_solve(invmodelTV,vh1n2,vh2n2);

%%%%GREIT
eidors_msg('GREIT 2.5D Recostruction');
%%%%set NF
opt.noise_figure = 0.5;
%%%%%Set training model
LB=size(invmodel.fwd_model.boundary,1);
boundary=zeros(LB,2);
li=1;
for ll=1:LB
boundary(ll,:)=[invmodel.fwd_model.nodes(invmodel.fwd_model.boundary(li,1),1)...
invmodel.fwd_model.nodes(invmodel.fwd_model.boundary(li,1),2)];
boundary(ll+1,:)=[invmodel.fwd_model.nodes(invmodel.fwd_model.boundary(li,2),1)...
invmodel.fwd_model.nodes(invmodel.fwd_model.boundary(li,2),2)];
li=li+1;
end
boundary(LB+1,:)=[];
%boundary=boundary/100;
for electrode=1:N
```

```
elec_x(electrode)=invmodel.fwd_model.nodes(invmodel.fwd_model.electrode(electrode).nodes(1),1);
elec_y(electrode)=invmodel.fwd_model.nodes(invmodel.fwd_model.electrode(electrode).nodes(1),2);
end
elec_pos=[360*(atan2(elec_y,elec_x)/(2*pi))' 0.5*ones(N,1)];
elec_shape = [0.05,0,0.01];
%
invmodel3D=ng_mk_extruded_model({1, boundary, [2 12], 0.2}, elec_pos, elec_shape);
invmodel3D.stimulation = stim;
invmodel3D.meas_select=els;
invmodel3D.fwd_solve.get_all_meas = 1;
%%%%create reconstruction model
s_size=[35 35];
opt.imgsz=s_size;
imdlgr = mk_GREIT_model(invmodel3D,0.2,[],opt);
%%%%SNR1
imagesGREIT1=inv_solve(imdlgr,vh1n1,vh2n1);
%%%%SNR2
imagesGREIT2=inv_solve(imdlgr,vh1n2,vh2n2);



figure
subplot(1,2,1)
H2=show_fem(imagesSTR1);
set(H2,'edgecolor', [0.5 0.5 0.5]);
set(H2,'edgealpha', 0.25);
axis off
axis tight
colormap jet
subplot(1,2,2)
H3=show_fem(imagesSTR2);
set(H3,'edgecolor', [0.5 0.5 0.5]);
set(H3,'edgealpha', 0.25);
axis off
axis tight
colormap jet


figure
subplot(1,2,1)
H4=show_fem(imagesLaplace1);
set(H4,'edgecolor', [0.5 0.5 0.5]);
set(H4,'edgealpha', 0.25);
axis off
axis tight
colormap jet
subplot(1,2,2)
H5=show_fem(imagesLaplace2);
set(H5,'edgecolor', [0.5 0.5 0.5]);
set(H5,'edgealpha', 0.25);
axis off
axis tight
colormap jet


figure
subplot(1,2,1)
H6=show_fem(imagesNOSER1);
set(H6,'edgecolor', [0.5 0.5 0.5]);
set(H6,'edgealpha', 0.25);
axis off
axis tight
colormap jet
subplot(1,2,2)
H7=show_fem(imagesNOSER2);
set(H7,'edgecolor', [0.5 0.5 0.5]);
set(H7,'edgealpha', 0.25);
axis off
axis tight
colormap jet

figure
subplot(1,2,1)
H8=show_fem(imagesGauss1);
set(H8,'edgecolor', [0.5 0.5 0.5]);
set(H8,'edgealpha', 0.25);
```

```
axis off
axis tight
colormap jet
subplot(1,2,2)
H9=show_fem(imagesGauss2);
set(H9,'edgecolor', [0.5 0.5 0.5]);
set(H9,'edgealpha', 0.25);
axis off
axis tight
colormap jet


figure
subplot(1,2,1)
H10=show_fem(imagesTV1);
set(H10,'edgecolor', [0.5 0.5 0.5]);
set(H10,'edgealpha', 0.25);
axis off
axis tight
colormap jet
subplot(1,2,2)
H11=show_fem(imagesTV2);
set(H11,'edgecolor', [0.5 0.5 0.5]);
set(H11,'edgealpha', 0.25);
axis off
axis tight
colormap jet

figure
subplot(1,2,1)
H12=show_fem(imagesGREIT1);
set(H12,'edgecolor', [0.5 0.5 0.5]);
set(H12,'edgealpha', 0.25);
axis off
axis tight
colormap jet
subplot(1,2,2)
H13=show_fem(imagesGREIT2);
set(H13,'edgecolor', [0.5 0.5 0.5]);
set(H13,'edgealpha', 0.25);
axis off
axis tight
colormap jet
```

9.2 Code for SPICE-MATLAB hardware simulation interface

This code has been used in the SPICEIT project:

`https://github.com/chdim100/SPICE-MATLAB-Interface-for-Electrical-Impedance-Tomography-Simulation-SPICEIT-`

to obtain the simulation results in [264], [265] and [194].

```
        %%%testbench_Tank.m
%%%%%%%%%
%%%%SPICEIT Phantom Tank testbench
%%%%%%%%%
%%%path to eidors ('...\eidors-v3.9-ng\eidors\')
path2EID='C:path_to_eidors';
%%%start EIDORS
startpath=[path2EID 'startup'];
run(startpath)

%%%path to SPICEIT
path2SPICEIT='D:\EIT\SPICEIT\';
%%%%path to measurement files (...'LT_SPICE\Measurements\')
deskpath=[path2SPICEIT 'LT_SPICE\Measurements\'];

%%%No of electrodes
N=16;

%%%%measurement pattern (skip-0, skip-0 for both 15k and 100k freqs
%%%% or skip-3, skip-0 for only 15kHz freqs)
%%%skip-current
skipcurr=0;
%%%skip-voltage
```

```
skipvolt=0;

%%%%electrode configuration (ONLY 'Passive')
Circuit_Electrodes='Passive';

%%%electrode deviation (ONLY 'Symmetric' (no deviation))
electrode_deviation='Symmetric';

%%%electrode size (ONLY '005')
electrode_size='005';

%%%sinusoidal signal frequency (15000 or 100000 in Hz). %%%NOTE THAT 100KHz
%%%are not available for current skip-3, voltage skip-0 pattern
sig_frequency=15000;
%sig_frequency=100000;

%%%ADC sampling rate (MSPS)
fs=1e+05;

%%%ADC resolution
Lbits=16;

%%%Number of periods sampled per measurement (1-4)
NofSinePeriods=4;

%%%ADC Voltage Reference
Vref=3.3;

%%%white noise resulting from LT SPICE simulation (Vrms)
Noise=1e-03;

%%%reconstruction algorithm================================================

%%%-Algorithm: 'direct' or 'one_step' for single-step approach,
%%% 'TV' or 'Total_Variation' or 'Pdipm' or 'pdipm' or 'PDIPM'
%%% for Total Variation
%%% 'iterationalGN' or 'mulistepGN' or 'iterationGN' or 'GN2' for iterative
%%% (non-linear) Gauss-Newton approach

Algorithm='direct';

%%%reconstruction prior====================================================

%%%-prior: 1,'NOSER','Noser' or 'noser' for NOSER,
%%% 2,'LAPLACE','Laplace' or'laplace' for Laplace
%%% 3,'Gaussian','Gauss','GAUSSIAN' or 'gaussian' for Gaussian HPF
%%% 4,'TV' or 'Total_Variation' for Total Variation
%%% lambda: hyperparameter of the inverse problem

prior='Noser';

%%%%reconstruction hyperparameter
lambda=0.1;

%%%%%calculate SNR
getcell=1;

situation1='Homo';
situation2='inhomo';
%%%%
%%%tank case 1-3
tankcase=2;

measdest_homo=['Tank1Homo_Skip' num2str(skipcurr)];
measdest_inhomo=['Tank' num2str(tankcase) 'inhomo_Skip' num2str(skipcurr)];

%%%%deflated case measurements
[Amplitudeshomo,Realhomo,Imagehomo,Phaseshomo,VoltageCell1]=Get_Spice_Measurements(N,skipcurr,...
skipvolt,sig_frequency,Lbits,fs,measdest_homo,electrode_deviation,...
Circuit_Electrodes,electrode_size,deskpath,Vref,Noise,NofSinePeriods,Vref,'Tank',getcell,1);
%%%%inflated case measurements
[Amplitudesinh,Realinh,Imaginh,Phasesinh,VoltageCell2]=Get_Spice_Measurements(N,skipcurr,...
skipvolt,sig_frequency,Lbits,fs,measdest_inhomo,electrode_deviation,...
Circuit_Electrodes,electrode_size,deskpath,Vref,Noise,NofSinePeriods,Vref,'Tank',getcell,0);

%%%%set reconstruction model
target='d2c2';
```

```
IMDL=set_inverse_model(N, skipcurr, skipvolt, Algorithm, prior, lambda, target);

Imreal=inv_solve(IMDL, Realhomo/max(Realhomo), Realinh/max(Realhomo));
Maxscale=max(real(Imreal.elem_data));
%Minscale=min(real(Imreal.elem_data));
Imreal.elem_data=(Imreal.elem_data)/Maxscale*0.3;
im=Imreal;
figure
H1=show_fem(Imreal,1);
axis off
set(H1, 'edgecolor', 'none');
axis square
figure
plot(Amplitudeshomo/max(Amplitudeshomo),'LineWidth',2)
hold on
plot(Amplitudesinh/max(Amplitudesinh),'LineWidth',2)
L=legend({'Homogeneous','Inhomogeneous'},'interpreter','latex');
L.FontSize=12;
XL1=xlabel('Measurement Index','interpreter','latex');
XL1.FontSize=14;
YL1=ylabel('Amplitudes (Normalized)','interpreter','latex');
YL1.FontSize=14;
xlim([0 210])
ylim([0 1.3])

        %%%testbench_Thorax.m
        close all
        %%%%%%%%%
        %%%%SPICEIT_Thorax testbench
        %%%%%%%%%
        %%%path to eidors ('...\eidors-v3.9-ng\eidors\')
        path2EID='C:path_to_eidors';
        %%%start EIDORS
        startpath=[path2EID 'startup'];
        run(startpath)

        %%%path to SPICEIT
        path2SPICEIT='D:\EIT\SPICEIT\';
        %%%%path to measurement files (...'LT_SPICE\Measurements\')
        deskpath=[path2SPICEIT 'LT_SPICE\Measurements\'];

        %%%No of electrodes
        N=16;

        %%%%measurement pattern (only adjacent, i.e. skip-0, skip-0 is supported
        %%%%for the thorax for the time)
        %%%skip-current
        skipcurr=0;
        %%%skip-voltage
        skipvolt=0;

        %%%%electrode configuration ('Passive' or 'Active_Rec')
        Circuit_Electrodes='Passive';
        %Circuit_Electrodes='Active_Rec';

        %%%electrode deviation ('Symmetric' or 'Asymmetric')
        electrode_deviation='Symmetric';
        %electrode_deviation='Asymmetric';

        %%%electrode size ('005' or '003')
        electrode_size='003';
        %electrode_size='005';

        %%%sinusoidal signal frequency (15000 or 100000 in Hz)
        %sig_frequency=15000;
        sig_frequency=100000;

        %%%ADC sampling rate (SPS)
        fs=1176470.5882352941176;
        % fs=240000;
        %fs=400000;
        %fs=1600000;

        %%%ADC resolution
        Lbits=16;

        %%%Number of periods sampled per measurement (1-4)
```

```
NofSinePeriods=4;

%%%ADC reference (V)
Vref=3.3;

%%%white noise resulting from LT SPICE simulation (Vrms)
Noise=6e-03;

%%%reconstruction algorithm================================================

%%%-Algorithm: 'direct' or 'one_step' for single-step approach,
%%% 'TV' or 'Total_Variation' or 'Pdipm' or 'pdipm' or 'PDIPM'
%%% for Total Variation
%%% 'iterationalGN' or 'mulistepGN' or 'iterationGN' or 'GN2' for iterative
%%% (non-linear) Gauss-Newton approach

Algorithm='direct';

%%%reconstruction prior=====================================================

%%%-prior: 1,'NOSER','Noser' or 'noser' for NOSER,
%%% 2,'LAPLACE','Laplace' or'laplace' for Laplace
%%% 3,'Gaussian','Gauss','GAUSSIAN' or 'gaussian' for Gaussian HPF
%%% 4,'TV' or 'Total_Variation' for Total Variation
%%% lambda: hyperparameter of the inverse problem

prior='Noser';

%%%%reconstruction hyperparameter
lambda=0.1;

%%%%getSNR
getcell=1;


%%%%image reconstruction
[im,SNR]=Thoracic_image_with_SPICEIT(path,deskpath,N,skipcurr,skipvolt,...
Circuit_Electrodes,electrode_deviation,electrode_size,sig_frequency,fs,...
Lbits,NofSinePeriods,Vref,Noise,Algorithm,prior,lambda,getcell);

%%%%%load reference image for the corresponding frequency
load(['inv_ref_' num2str(round(sig_frequency/1000)) 'kHz.mat'])
%%%% compute image CC (R^2)
CCmat=corrcoef(inv_reference.elem_data,im.elem_data);
CC=CCmat(1,2);
normalized_reference=normalize_meas(inv_reference.elem_data);
normalized_measurements=normalize_meas(im.elem_data);
RRE=norm(normalized_reference-normalized_measurements)/norm(normalized_reference);

SNR
CC
RRE

%%%=========================================================
function [im,SNR]=Thoracic_image_with_SPICEIT(path,deskpath,N,skipcurr,skipvolt,...
Circuit_Electrodes,electrode_deviation,electrode_size,sig_frequency,fs,...
Lbits,NofSinePeriods,Vref,Noise,Algorithm,prior,lambda,getcell)
%%%%%%acquire thoracic images
%%% Inputs:
%%%-path: the path to EIDORS
%%%-deskpath: the path to the transient SPICE measurement files (folder
%%%Measurements)
%%%-N: the number of electrodes used for the measurements
%%%-skipcurr: current-skip protocol (if available)
%%%-skipvolt: voltage-skip protocol (if available)
%%%-Circuit_Electrodes: 'Passive' for passive electrode configuration,
%%%'Active_Rec' for active electrode configuration
%%%-electrode_deviation: 'Symmetric' for no electrode deviation,
%%%'Asymmetric' for minor electrode deviation
%%%-electrode_size: '005' or '003' (5 or 3cm) radius circular electrodes
%%%-sig_frequency: input signal frequency 15000 or 100000 (in Hz)
%%%-fs: ADC sampling frequency (in Hz)
%%%-Lbits: ADC resolution
%%%-NofSinePeriods: No of periods to be sampled (integer, 1-4)
%%%-Noise: white noise signal (in Volts), as computed from SPICE simulation
%%%-Algorithm: 'direct' or 'one_step' for single-step approach,
%%% 'TV' or 'Total_Variation' or 'Pdipm' or 'pdipm' or 'PDIPM'
```

```
%%% for Total Variation
%%% 'iterationalGN' or 'mulistepGN' or 'iterationGN' or 'GN2' for iterative
%%% (non-linear) Gauss-Newton approach
%%% prior: 1,'NOSER','Noser' or 'noser' for NOSER,
%%% 2,'LAPLACE','Laplace' or 'laplace' for Laplace
%%% 3,'Gaussian','Gauss','GAUSSIAN' or 'gaussian' for Gaussian HPF
%%% 4,'TV' or 'Total_Variation' for Total Variation
%%% lambda: hyperparameter of the inverse problem

%%%Outputs:
%%% im: reconstructed image struct (EIDORS format)

%%%=========================================================================
%%%=========================================================================
situation1='deflated';
situation2='inflated';
if skipvolt==0&&skipcurr==0
skip='';
else
skip=['skip',num2str(skipcurr),'_',num2str(skipvolt),'_'];
end

measdest_deflated=['EIT_2019_',num2str(round(sig_frequency/1000)),...
'k_',skip,'Mirrored_Current_Pt_Bright_VAR' situation1];
measdest_inflated=['EIT_2019_',num2str(round(sig_frequency/1000)),...
'k_',skip,'Mirrored_Current_Pt_Bright_VAR' situation2];

%%%%deflated case measurements
[Amplitudesdef,Realdef,Imagdef,Phasesdef,VoltageCell1]=Get_Spice_Measurements(N,skipcurr,...
skipvolt,sig_frequency,Lbits,fs,measdest_deflated,electrode_deviation,...
Circuit_Electrodes,electrode_size,deskpath,Noise,NofSinePeriods,Vref,'Thoracic',getcell,0);
%%%%inflated case measurements
[Amplitudesinf,Realinf,Imaginf,Phasesinf,VoltageCell2]=Get_Spice_Measurements(N,skipcurr,...
skipvolt,sig_frequency,Lbits,fs,measdest_inflated,electrode_deviation,...
Circuit_Electrodes,electrode_size,deskpath,Noise,NofSinePeriods,Vref,'Thoracic',getcell,0);
%%%%set reconstruction model
target='d2T3';
IMDL=set_inverse_model(N,skipcurr,skipvolt,Algorithm,prior,lambda,target);
IMDL.fwd_model.electrode([9:-1:1,16:-1:10])=IMDL.fwd_model.electrode;

Imreal=inv_solve(IMDL,Realinf/max(Amplitudesdef),Realdef/max(Amplitudesdef));
Maxscale=max(real(Imreal.elem_data));
%Minscale=min(real(Imreal.elem_data));
Imreal.elem_data=(Imreal.elem_data)/Maxscale*0.3;
im=Imreal;

if getcell==1
%%%%%%Calculate mean signal SNR
SNRmean1=Calculate_SNR(VoltageCell1,Lbits,Vref,NofSinePeriods,sig_frequency,fs,Noise);
SNRmean2=Calculate_SNR(VoltageCell2,Lbits,Vref,NofSinePeriods,sig_frequency,fs,Noise);
SNR=(SNRmean1+SNRmean2)/2;
else
SNR=[];
end

figure
H1=show_fem(Imreal,1);
axis off
set(H1, 'edgecolor', 'none');
axis square
figure
plot(Amplitudesdef/max(Amplitudesdef),'LineWidth',2)
hold on
plot(Amplitudesinf/max(Amplitudesinf),'LineWidth',2)
L=legend({'Deflated Lungs','Inflated Lungs'},'interpreter','latex');
L.FontSize=12;
XL1=xlabel('Measurement Index','interpreter','latex');
XL1.FontSize=14;
YL1=ylabel('Amplitudes (Normalized)','interpreter','latex');
YL1.FontSize=14;
xlim([0 210])
ylim([0 1.3])


end

        %%%%%%=========================================
```

```
function thorax_model=Set_Thorax(path,state,freq,electrode_deviation,Rel,conductivity_values)
clc
%%% Creates 3D F.E.M. and SPICE Netgen Thorax models
%%%Inputs:
%%%-path: path to EIDORS folder (...\eidors-v3.9-ng\eidors\)
%%%-state: Inflated or Deflated
%%%-freq: Signal Frequency (15000 or 100000 Hz)
%%%-electrode_deviation: set electrode deviation. 'Symmetric' or
%%%'Assymetric'
%%%-Rel: '003' or '005' (normalized circular electrode radius)
%%%-conductivity_values: 'constant' for constant conductivity in each
%%%tissue, 'variational' for std conductivities
%%%

%%%Outputs:
%%%-thorax_model: F.E.M. thorax 3D model extracted

%thorax_model=Set_Thorax('Inflated',15000,'Symmetric',0.05,'variational');

switch Rel
case 0.05
electrode_size='Large_AgCl';
otherwise
electrode_size='Small_AgCl';
end
%%%set geometry
initial_struct=['Thorax_' state '_' electrode_deviation '_Rel=' num2str(Rel)];
structure_path=[path 'Structures\Thoracic_New\'];
structure_geometry=[structure_path initial_struct '.mat'];
if exist(structure_geometry,'file')~=2
[img,elec_pos]=create_thorax_geometry(structure_geometry,state,electrode_deviation,Rel,path);
else
load(structure_geometry)
end
%%%set element conductivities
thorax_model=set_elem_conducts(img,state,freq,conductivity_values,path);
%img.fwd_model.nodes=12*img.fwd_model.nodes;

%%%create the equivalent N-port circuit .cir file
name=['Thorax2020_' state '_' electrode_deviation '_' num2str(round(freq/1000)) 'k'];
element_path=[structure_path 'freq_elements\'];
element_data=thorax_model.elem_data;
elem_file_name=[element_path name '_Rel=' num2str(Rel) '.mat'];
save(elem_file_name,'element_data')
eit_spiceRLC(thorax_model,name,freq,'Thorax',Device,electrode_size);
end

function [img,elec_pos]=create_thorax_geometry(structure_geometry,state,symmetry,Rel,path)

thorax = shape_library('get','adult_male','boundary');
rlung  = shape_library('get','adult_male','right_lung');
llung  = shape_library('get','adult_male','left_lung');
%%%DEFAULT MODEL IS CONSIDERATED AS DEFLATED CASE
%WE BUILD THE INFLATED CASE
thoraxinf=thorax;
thoraxinf(1:8,2)=thoraxinf(1:8,2)+0.08;
thoraxinf(end-7:end,2)=thoraxinf(end-7:end,2)+0.08;
rlunginf=rlung;
rlunginf(end-6:end,2)=rlunginf(end-6:end,2)+0.15;
llunginf=llung;
llunginf(2:8,2)=llunginf(2:8,2)+0.14;
% one could also run:
% shape_library('get','adult_male');
% to get all the info at once in a struct
load([path '\Boundaries\Spondilus1.mat'])
load([path '\Boundaries\NewHeart.mat'])
% show the library image
shape_library('show','adult_male');
hold on
plot([spondilus(:,1); spondilus(1,1)],[spondilus(:,2); spondilus(1,2)],'-o','LineWidth',2)
hold on
plot([newheart(:,1); newheart(1,1)], [newheart(:,2); newheart(1,2)],'-o','LineWidth',2)
figure
switch state
case 'Deflated'
o=[];
case 'Inflated'
```

```
thorax=thoraxinf;
llung=llunginf;
rlung=rlunginf;
end

objects={thorax, rlung, llung, flipud(spondilus), newheart};

if strcmp(symmetry,'Asymmetric')
load([path 'Structures\elec_pos_dev1.mat'])
[img,elec_pos]=create_Forw_model(16, objects,symmetry,Rel,elec_pos);
else
[img,elec_pos]=create_Forw_model(16, objects,symmetry,Rel);
end

save(structure_geometry,'img')
fprintf('saved new structure geometry: %s\n',structure_geometry)

end

function thorax_model=set_elem_conducts(img,state,freq,conductivity_values,path)

%clear all previous values
img.elem_data(:)=1;
%select tissuelist depended on the state
switch state
case 'Deflated'
listofinterest=[1 3 4 5 8, 10];
case 'Inflated'
listofinterest=[1 2 4 5 8, 10];
end

%load Tissues_admittance!
checktissuefile=[path 'Tissue_Properties\Thorax\Tissues_',num2str(round(freq/1000)),'kHz.mat'];
while exist(checktissuefile,'file')~=2
fprintf('RUN Python script for f=%4.0f Hz!\n',freq)
fprintf('Then press enter\n')
pause()
end
load(checktissuefile)

%set admittances to elements
img.elem_data(:)=Tissues_admittance(listofinterest(3),1);
img.elem_data(img.fwd_model.mat_idx{2})= ...
Tissues_admittance(listofinterest(2),1)+...
1i*Tissues_admittance(listofinterest(2),2); % rlung
img.elem_data(img.fwd_model.mat_idx{3})= ...
Tissues_admittance(listofinterest(2),1)+...
1i*Tissues_admittance(listofinterest(2),2); % llung
img.elem_data(img.fwd_model.mat_idx{4})=...
Tissues_admittance(listofinterest(4),1)+...
1i*Tissues_admittance(listofinterest(4),2); % spondilus
img.elem_data(img.fwd_model.mat_idx{5})= ...
Tissues_admittance(listofinterest(1),1)+...
1i*Tissues_admittance(listofinterest(1),2); % heart
% skin
[srf, idx] = find_boundary(img.fwd_model.elems);
bound_nodes_coords1=img.fwd_model.nodes(srf(:,1),:);
bound_nodes_coords2=img.fwd_model.nodes(srf(:,2),:);
bound_nodes_coords3=img.fwd_model.nodes(srf(:,3),:);
bound_element_coords(:,1)=(bound_nodes_coords1(:,1)+bound_nodes_coords2(:,1)+bound_nodes_coords3(:,1))/3;
bound_element_coords(:,2)=(bound_nodes_coords1(:,2)+bound_nodes_coords2(:,2)+bound_nodes_coords3(:,2))/3;
bound_element_coords(:,3)=(bound_nodes_coords1(:,3)+bound_nodes_coords2(:,3)+bound_nodes_coords3(:,3))/3;

bound_peripheral_local_ind=find(bound_element_coords(:,3)<=0.98&bound_element_coords(:,3)>=0.02);
bound_peripheral_global_ind=idx(bound_peripheral_local_ind);
img.elem_data(bound_peripheral_global_ind)=(Tissues_admittance(listofinterest(6),1)+...
1i*Tissues_admittance(listofinterest(6),2)+Tissues_admittance(listofinterest(5),1)+...
1i*Tissues_admittance(listofinterest(5),2))/2;
figure
show_fem(img); view(0,70);

switch conductivity_values
case 'constant'
%do nothing!
case 'variational'
%muscle
L1=length(img.elem_data(img.fwd_model.mat_idx{1}));
```

```
img.elem_data(img.fwd_model.mat_idx{1})= ...
img.elem_data(img.fwd_model.mat_idx{1}).*(1+randn(L1,1)*0.02);
%right lung
L2=length(img.elem_data(img.fwd_model.mat_idx{2}));
img.elem_data(img.fwd_model.mat_idx{2})= ...
img.elem_data(img.fwd_model.mat_idx{2}).*(1+randn(L2,1)*0.03);
%left lung
L3=length(img.elem_data(img.fwd_model.mat_idx{3}));
img.elem_data(img.fwd_model.mat_idx{3})= ...
img.elem_data(img.fwd_model.mat_idx{3}).*(1+randn(L3,1)*0.03);
%spondilus
L4=length(img.elem_data(img.fwd_model.mat_idx{4}));
img.elem_data(img.fwd_model.mat_idx{4})= ...
img.elem_data(img.fwd_model.mat_idx{4}).*(1+randn(L4,1)*0.01);
%heart
L5=length(img.elem_data(img.fwd_model.mat_idx{5}));
img.elem_data(img.fwd_model.mat_idx{5})= ...
img.elem_data(img.fwd_model.mat_idx{5}).*(1+randn(L5,1)*0.02);
end
figure
plot(abs(img.elem_data),'*')
hold on
thorax_model=img;
end

%%%%%%==================================================
function IMDL=set_inverse_model(N,skipcurr,skipvolt,algorithm,filt,lambda,target)
%sets the inverse model where the reconstruction is taking place
%target='d2c2';
%target='d2t3';

imdl2= mk_common_model(target,N);
% Calculate a stimulation pattern
[stim,els] = mk_stim_patterns(N,1,[0,skipcurr+1],[0,skipvolt+1],{},1);
% Solve all voltage patterns
imdl2.fwd_model.stimulation = stim;
imdl2.fwd_model.meas_select=els;
imdl2.fwd_solve.get_all_meas = 1;
%set algorithm parameters
imdl2.hyperparameter.value = lambda;
switch algorithm
case{1,'direct','one_step'}
imdl2.solve=@inv_solve_diff_GN_one_step;
case{2,'iterational','mulistep','iteration','GN'}
imdl2.solve=@inv_solve_abs_GN;
imdl2.inv_solve_gn.max_iterations = 20;
case{3,'TV','Total_Variation','Pdipm','pdipm','PDIPM'}
imdl2.solve=@inv_solve_TV_pdipm;
imdl2.R_prior=      @prior_TV;
imdl2.parameters.term_tolerance= 1e-3;
imdl2.parameters.max_iterations=25;
imdl2.parameters.keep_iterations= 25;
case{4,'Back-Projection','Back-projection','BP'}
imdl2.solve= @inv_solve_backproj;
imdl2.inv_solve_backproj.type='simple_filter';
case{5,'iterationalGN','mulistepGN','iterationGN','GN2'}
imdl2.solve=@inv_solve_gn;
imdl2.inv_solve_gn.max_iterations = 20;
imdl2.inv_solve_gn.return_working_variables = 1;
otherwise
error('under construction')
end
if algorithm~=4
switch filt
case {1,'NOSER','Noser','noser'}
imdl2.RtR_prior= @prior_noser;
case{2,'LAPLACE','Laplace','laplace'}
imdl2.RtR_prior= @prior_laplace;
case{3,'Gaussian','Gauss','GAUSSIAN','gaussian'}
imdl2.RtR_prior = @prior_gaussian_HPF;
case{4,'TV','Total_Variation'}
imdl2.RtR_prior=@prior_TV;
otherwise
error('under construction')
end
end
imdl2.jacobian_bkgnd.value= 1;
```

```
IMDL=imdl2;
end

%%%%%%============================================================
function spice = eit_spiceRLC(img,path2lib,name,f,tissue_type,electrode_size)
%function spice = eit_spice(img, [name])
% Converts an EIT FEM model with assigned conductivities (an EIDORS "img") to a
% model reduced, fully connected mesh of resistors in SPICE format.
% If the FEM model has complex valued conductivities, the mesh will be an RLC
% mesh network.
%
% An optional subcircuit 'name' can be provided.
%
% DONE! complex value support (DIMAS 2020)
% TODO fix electrode ordering for mixed PEM/CEM electrodes
%
% CITATION_REQUEST:
% AUTHOR: A Boyle and A Adler
% TITLE: Integrating Circuit Simulation with EIT FEM Models
% JOURNAL: 19th International Conference on Biomedical Applications of Electrical Impedance Tomography, Edinburgh, UK
% YEAR: 2018
%

% (C) 2018 A. Boyle, License: GPL version 2 or version 3

%%%%%Inputs:
%%%-img: 3D FEM model
%%%-path2lib: path to SPICE library (where Netgen .cir models are stored)
%%%-name: 'name of the model'
%%%-f: input signal frequency (Hz)
%%%-tissue_type: 'Thorax' for thorax, 'Head' for head structure
%%%-electrode_size: '003' or '005' (normalized circular electrode radius)

if ischar(img) & strcmp(img, 'UNIT_TEST') unit_test(); end

if nargin == 1
name = ['eit_',num2str(f),'Hz'];
end

Dprime = model_reduce(img);
% disp(full(1./Dprime))
% disp(full(-1./(Dprime - tril(Dprime))));
spice = netlist(Dprime,name,f);

if nargout == 0
if strcmp(tissue_type,'Head')
folder=[path2lib 'Structures\New_Structs_2020\' tissue_type '\'];
else
folder=[path2lib 'Structures\New_Structs_2020\' tissue_type '\' electrode_size '\'];
end
filename = [folder name '.cir' ];
ind=1;
while exist(filename,'file')==2
ind=ind+1;
filename = [folder name '_' num2str(ind) '.cir' ];
end
FILE = fopen(filename, 'w');
fprintf(FILE,'%s\n',spice{:});
fclose(FILE);
eidors_msg(['saved SPICE netlist to ' filename]);
return
end
end

function Dprime = model_reduce(img)
Y = calc_system_mat(img); Y= Y.E;
nn= num_nodes(img);
% Decompose into blocks; assumes that the nn+1:end nodes are CEM electrodes
rm = 1:nn; % nodes to fold
kp = nn+1:size(Y,1); % nodes to keep
% Now handle PEM electrodes, by transferring nodes between the rm and el sets
for i = 1:length(img.fwd_model.electrode)
el = img.fwd_model.electrode(i);
if length(el.nodes) == 1 %if electrodes are just points
rm(rm == el.nodes) = []; %remove those points from rm
kp(end+1) = el.nodes; %and add them to the electrode part
end
```

```
end
% Note: C = B' ... we don't need to calculate it for symmetric matrices
A = Y(rm,rm); B= Y(rm,kp); D = Y(kp,kp);
%Dprime  = D - B'*inv(A)*B;
Dprime  = D - B'/A*B;
o=[];
end

function out = netlist(Dprime, name,f)
nn = size(Dprime,1);
ndr = floor(log10(nn*(nn-1)/2))+1; % number of digits for resistors
nde = floor(log10(nn))+1; % number of digits for electrodes
str = ['.subckt ' name ];
for ii = 1:nn
str = [ str sprintf([' %' num2str(nde) 'd'], ii) ];
end
out = { str };
%str = ['R%' num2str(ndr) 'd %' num2str(nde) 'd %' num2str(nde) 'd %s'];
strR = ['R%d %' num2str(nde) 'd %' num2str(nde) 'd %s'];
strC = ['C%d %' num2str(nde) 'd %' num2str(nde) 'd %s'];
strL = ['L%d %' num2str(nde) 'd %' num2str(nde) 'd %s'];
rr=1;
cc=1;
ll=1;
for ii = 1:nn
for jj = (ii+1):nn
%          R=real(-1/Dprime(ii,jj));
R=1/real(-Dprime(ii,jj));
valR = sprintf('%3.12g',R);
out(end+1,1) = { strrep(sprintf(strR,rr,ii,jj,valR),'+','') }; % we strip '+'
rr = rr +1;
%          CN=imag(-1/Dprime(ii,jj))/(2*pi*f);
CN=1/(1/imag(-Dprime(ii,jj)));
if CN>=0
%              C=CN;
C=CN/(2*pi*f);
valC = sprintf('%3.12g',C);
out(end+1,1) = { strrep(sprintf(strC,cc,ii,jj,valC),'+','') }; % we strip '+'
cc=cc+1;
else
%              L=-CN;
L=-1/(CN*2*pi*f);
valL = sprintf('%3.12g',L);
out(end+1,1) = { strrep(sprintf(strL,ll,ii,jj,valL),'+','') }; % we strip '+'
ll=ll+1;
end
end
end
out(end+1,1) = { '.ends' };
end

function unit_test()
fmdl = mk_common_model('a2s',8);
img = mk_image(fmdl,1);
eit_spiceRC(img,'eit2')
end

%%%%=========================================
function [img,elec_pos]=create_Forw_model(N, objects,symmetry,Rel,elec_pos)
%Rel=0.05;
if strcmp(symmetry,'Asymmetric')
if nargin<5
height=randn(1)*0.1+1;
for i=1:length(objects)
ox=objects{i}(:,1);
oy=objects{i}(:,2);
mx=mean(ox);
my=mean(oy);
oxm=ox-mx;
oym=oy-my;
oxmn=oxm*(0.1*randn(1)+1);
oymn=oym*(0.1*randn(1)+1);
oxmnm=oxmn+mx;
oymnm=oymn+my;
objectsnew{i}=[oxmnm oymnm];
angles=90:-360/N:-270;
neg=find(angles<0);
```

```
angles(neg)=angles(neg)+360;
angles=angles(1:end-1);
angles_dev=angles.*(0.03*(rand(1,N)-0.5)+1);
elec_z_dev=0.5*(0.05*randn(1,N)+1)+zeros(1,length(angles));
elec_pos=[angles_dev; elec_z_dev]';
end
else
height=1;
objectsnew=objects;
fprintf('electrode positions defined as input\n')
end

else
height=1;
objectsnew=objects;
elec_pos = [ N,                % number of elecs per plane
1,                  % equidistant spacing
0.5]';
end
shape = { height,                      % height
        objectsnew, % contours
        %normally [4,50],
        [4,50],                % perform smoothing with 50 points
        %1,
        0.04};                 % small maxh (fine mesh)
%normally: maxh==0.04
% elec_pos = [ N,                  % number of elecs per plane
%              1,                   % equidistant spacing
%              0.5]';               % a single z-plane


elec_shape = [Rel,                % radius
0,                 % circular electrode
0.01 ]';             % maxh (electrode refinement)
%normally: maxh==0.01
fmdl = ng_mk_extruded_model(shape, elec_pos, elec_shape);
% this similar model is also available as:
% fmdl = mk_library_model('adult_male_16el_lungs');

[stim,meas_sel] = mk_stim_patterns(N,1,[0,1],[0,1],{'no_meas_current'}, 1);
fmdl.stimulation = stim;

img=mk_image(fmdl,1);
% img.elem_data(:)=0.35;
% img.elem_data(img.fwd_model.mat_idx{2})= 0.1812 + 0.0101i; % rlung
% img.elem_data(img.fwd_model.mat_idx{3})= 0.1812 + 0.0101i; % llung
% img.elem_data(img.fwd_model.mat_idx{4})= 0.1+0.002i; % spondilus
% img.elem_data(img.fwd_model.mat_idx{5})= 0.5+0.0025i; % heart

show_fem(img); view(0,70);
o=[];
end

%%%==============================================
function [Amplitudes,Real,Imag,Phases,VoltageCell]=Get_Spice_Measurements(N,skipcurr,skipvolt,f,RESADC,fSample,subjectfile,Electrode_po

switch casetest
case 'Thoracic'
%confirm electrode size chars
switch electrode_size
case '005'
sizel='';
otherwise
sizel='_Rel=003';
end
filemeas=[deskpath num2str(f/1000),'k\Pt_Bright\',Circuit_Electrodes,'\',subjectfile,...
'_',Electrode_pos,'_',Circuit_Electrodes,'_','NonBalancedCaps','_with_skin',sizel,'.txt'];
case 'Tank'
filemeas=[deskpath 'TankConf\' subjectfile '.txt'];
otherwise
error('Under Update')
end
%=========================================================================
%1. Get Spice Data
%open Times and Transient Spice files
fileTimes=[deskpath 'Times\Times_',num2str(N),'_skip-',...
num2str(skipcurr),'_skip-',num2str(skipvolt),'_',num2str(f/1000),'kHz.txt'];
```

```
Times=dlmread(fileTimes,'\t',0,0);

Values=dlmread(filemeas,'\t',1,0);
%Spice Transient Points
Spice_Transient_Voutput=Values(:,2);
Spice_Transient_Ioutput=Values(:,3);
Spice_Transient_Timepoints=Values(:,1);

%=========================================================================
%2. Initialize DAQ and some other specs
%2A. DAQ Specs
%ADC Voltage Swing
% VADC=3.3;
%LEAST SIGNIFICANT BITS
LSB=0;
%ADC ENOB
ACTUALRESADC=RESADC-LSB;
%Number of periods per window used for IQ
NT=NofSinePeriods;

%2B. Set the number of voltage measurements per current source electrode
%position
if skipcurr==skipvolt
meas=N-3;
else
meas=N-4;
end

%=========================================================================
%3.Place the Spice transient points in the corresponding measurement window
%3A. Initialize the Spice transient points per measurement matrices
point_per_measurement=round(fSample*(5/f))+1;
Vout_samples_permeasurement=zeros(N*meas,point_per_measurement);
Iout_samples_permeasurement=zeros(N*meas,point_per_measurement);

%run loop in measurements to propely complete those matrices
%set a counter (ii)
ii=1;
VoltageCell={};
for currentsource=1:N
for voltagemeasurement=1:meas
%the Times matrix is precomputed and indicates when to start and
%stop each measuring window (avoiding transient effects)
%Times is different for each frequency and measuring pattern

%3.B. Set the start and stop times for this measuring window
%(iith): When to start and stop getting Spice transient points
%to complete the ith measure
Tstart=Times(2*ii-1,1);
Tstop=Times(2*ii,1);

%3.C. find the corresponding indices of spice timepoints that are
%included in the integral [Tstart, Tstop]
indices_of_spicepoints=find(Spice_Transient_Timepoints>=Tstart&Spice_Transient_Timepoints<=Tstop);
%add a last indice, +1 from the previous last
last=indices_of_spicepoints(end);
indices_of_spicepoints=[indices_of_spicepoints; last+1];

%3.D.Get the corresponding values of Voltage (and current) outputs from
%the Spice transients that are in [Tstart, Tstop]. Do same for
%Spice transient Timepoints

Voltage_Spice_transient_Window=Spice_Transient_Voutput(indices_of_spicepoints);
Current_Spice_transient_Window=Spice_Transient_Ioutput(indices_of_spicepoints);
Spice_Timepoints_Window=Spice_Transient_Timepoints(indices_of_spicepoints);

%3.E. Add the precomputed noise to them:
%Noise to the Voltage output
Noisesignal=add_white_noise(length(Voltage_Spice_transient_Window),Noise);
if getcell==1
VoltageCell{end+1}=Voltage_Spice_transient_Window;
end
Noisy_Voltage_Spice_transient_Window=Voltage_Spice_transient_Window+Noisesignal;
%Noise to the Current output (here we just add awgn of 70-90dB)
Noisy_Current_Spice_transient_Window=awgn(Current_Spice_transient_Window,70);
select_inj=[1,2,3,4,5,6,7,8];
plottransient=1;
```

```
%         for ils=1:length(select_inj)
%         %Plot the window if selected so:
%         if plottransient&&ii==select_inj(ils)
%             currentsourceplotted=currentsource;
%             voltagemeasurementplotted=voltagemeasurement;
%             figure
%             subplot(1,2,1)
%             plot(Spice_Timepoints_Window,Noisy_Voltage_Spice_transient_Window)
%             Title=title(['Voltage Transient Signal, Current:' num2str(currentsource) ...
%                 ' Voltage:' num2str(voltagemeasurement)],'Interpreter','Latex');
%             Title.FontSize=16;
%             hold on
%         end
%         end

%ADC

%3.F. Since the LT Spice timeline does not have a constant step
%we find the nearest LTspice timepoints to the timepoints we sample!
%ideal ADC Samplepoints
Ideal_ADCSample_Window_timepoints=Tstart:1/fSample:(point_per_measurement-1)/fSample+Tstart;
%REPMAT ideal ADC Samplepoints and Spice Timepoints of this Window
%in order to be able to compare them
A = repmat(Ideal_ADCSample_Window_timepoints',[1 length(Spice_Timepoints_Window)]);
B=repmat(Spice_Timepoints_Window,[1 length(Ideal_ADCSample_Window_timepoints)]);
%find the indices of Spice Window Timepoints that are closest to ideal ADC Samplepoints
[minValue,closestIndex] = min(abs(A'-B));
%get the corresponding Spice Window Timepoints (Values in sec):
closest_Spice_timepoint_Value=Spice_Timepoints_Window(closestIndex);
%closestValue is the Spice Window timepoints we actually sample!!!!
%closestIndex is the indices of Spice timepoints we sample!!!
%so...

%3.G. Get the Voltage and Current values that are to be sampled
Noisy_Voltage_Spice_transient_Window=(10+0.05*randn(1))*(Noisy_Voltage_Spice_transient_Window-mean(Noisy_Voltage_Spice_transient_Windov
Vout_samples_permeasurement(ii,:)=Noisy_Voltage_Spice_transient_Window(closestIndex);
Iout_samples_permeasurement(ii,:)=Noisy_Current_Spice_transient_Window(closestIndex);
%and we got the samples!!!
%plot them on the transient scheme if selected
hh =  findobj('type','figure');
nn = length(hh);
if show_transient==1
for ils=1:length(select_inj)
if plottransient&&ii==select_inj(ils)
currentsourceplotted(ils)=currentsource;
voltagemeasurementplotted(ils)=voltagemeasurement;
figure(nn+1)
nno=nn+1;
subplot(1,2,1)
plot(Spice_Timepoints_Window,Noisy_Voltage_Spice_transient_Window)
Title=title(['Voltage Signal, Current:' num2str(currentsource) ...
' Voltage:' num2str(voltagemeasurement)],'Interpreter','Latex');
Title.FontSize=16;
hold on
plot(closest_Spice_timepoint_Value,Vout_samples_permeasurement(ii,:),'r*','MarkerSize',10)
hold on
xlim([min(Spice_Timepoints_Window) max(Spice_Timepoints_Window)]);
YL1=ylabel('Voltage ($V$)','Interpreter','Latex');
YL1.FontSize=14;
XL1=xlabel('Time ($s$)','Interpreter','Latex');
XL1.FontSize=14;
LL=legend({'Voltage','Non-Quantized Samples'});
LL.FontSize=12;
grid on
att = gca;
att.FontSize = 12;
end
end
end
ii=ii+1;
end
end

%=========================================================================
%4. ADC Sample and quantization
```

```
%4A. set each Voltage output window in the ADC voltage swing range
%(this can be done with the filter and the ADC driver)
% Vout_samples_permeasurement_ranged=((Vout_samples_permeasurement -...
%      mean(mean(Vout_samples_permeasurement))))*VADC+VADC/2;
Vout_samples_permeasurement_ranged=Vout_samples_permeasurement;
%check and rerange if any voltage is <0 (out of ADC's range):
while ~isempty(Vout_samples_permeasurement_ranged(Vout_samples_permeasurement_ranged<=0))
Vout_samples_permeasurement_ranged=0.8*Vout_samples_permeasurement_ranged+0.3;
end
%current measurements are already in ADC voltage swing range!

%4.B. quantize sampled values
Vout_samples_permeasurement_quantized=round(Vout_samples_permeasurement_ranged/VADC*(2^RESADC-1));
Iout_samples_permeasurement_quantized=round(Iout_samples_permeasurement/VADC*(2^RESADC-1));

%4.C. create the sin input signal (plus 90 degrees)
Iout_sinus_samples_permeasurement_quantized=Iout_samples_permeasurement_quantized(:,round(fSample/f/4)+1:end);

%4.D. take the sampled and quantized signals to binary form
Vout_samples_permeasurement_quantized_binary=dec2bin(Vout_samples_permeasurement_quantized);
Iout_samples_permeasurement_quantized_binary=dec2bin(Iout_samples_permeasurement_quantized);
Iout_sinus_samples_permeasurement_quantized_binary=dec2bin(Iout_sinus_samples_permeasurement_quantized);

%4.E. throw out noisy LSB
Vout_samples_permeasurement_quantized_binary_reduced=Vout_samples_permeasurement_quantized_binary(:,1:end-LSB);
Iout_samples_permeasurement_quantized_binary_reduced=Iout_samples_permeasurement_quantized_binary(:,1:end-LSB);
Iout_sinus_samples_permeasurement_quantized_binary_reduced=Iout_sinus_samples_permeasurement_quantized_binary(:,1:end-LSB);

%4.G. take the signals in decimal form
%output voltage
Vout_samples_permeasurement_quantized_decimal_reduced=...
reshape(bin2dec(Vout_samples_permeasurement_quantized_binary_reduced),...
[N*meas size(Vout_samples_permeasurement_ranged,2)]);
%output current cos
Iout_samples_permeasurement_quantized_decimal_reduced=...
reshape(bin2dec(Iout_samples_permeasurement_quantized_binary_reduced),...
[N*meas size(Iout_samples_permeasurement_quantized,2)]);
%output current sin
Iout_sinus_samples_permeasurement_quantized_decimal_reduced=...
reshape(bin2dec(Iout_sinus_samples_permeasurement_quantized_binary_reduced),...
[N*meas size(Iout_sinus_samples_permeasurement_quantized,2)]);

%4.H. take the integer number of periods selected ([1,4])
Vout_samples_quantized_final=Vout_samples_permeasurement_quantized_decimal_reduced(:,1:round(NT*fSample/f)+1);
Iout_samples_quantized_final=Iout_samples_permeasurement_quantized_decimal_reduced(:,1:round(NT*fSample/f)+1);
Iout_sinus_samples_quantized_final=Iout_sinus_samples_permeasurement_quantized_decimal_reduced(:,1:round(NT*fSample/f)+1);

%plot if desired
if show_transient==1
if plottransient
for ils=1:length(select_inj)
figure(nno-length(select_inj)+ils)
subplot(1,2,2)
plot(Vout_samples_quantized_final(select_inj(ils),:),'-s','MarkerSize',10,...
'MarkerEdgeColor','red',...
'MarkerFaceColor',[1 .6 .6])
Title2=title(['ADC quantized Samples, Current:' num2str(currentsourceplotted(ils)) ...
' Voltage:' num2str(voltagemeasurementplotted(ils))],'Interpreter','Latex');
Title2.FontSize=16;
YL1=ylabel('ADC Value','Interpreter','Latex');
YL1.FontSize=14;
XL1=xlabel('No of Samples','Interpreter','Latex');
XL1.FontSize=14;
grid on
att = gca;
att.FontSize = 12;
end

end
end


%4.I. write samples at voltage form
Vout_samples_final=Vout_samples_quantized_final*VADC/(2^ACTUALRESADC-1);
Iout_samples_final=Iout_samples_quantized_final*VADC/(2^ACTUALRESADC-1);
Iout_sinus_samples_final=Iout_sinus_samples_quantized_final*VADC/(2^ACTUALRESADC-1);
```

```
%=========================================================================

%5. Interpolation and Multiplication
NN=1;
for mm=1:N*meas
%for each measuring Window:

%5.A. upsampling NN points
if NN>1
X=1:length(Vout_samples_final(1,:));
NY1n=upsampling(Vout_samples_final(mm,:),X,NN);
NY2n=upsampling(Iout_samples_final(mm,:),X,NN);
NY3n=upsampling(Iout_sinus_samples_final(mm,:),X,NN);
else
NY1n=Vout_samples_final(mm,:);
NY2n=Iout_samples_final(mm,:);
NY3n=Iout_sinus_samples_final(mm,:);
end

%5.B. Multiply elementwise
Cosf_expanded(mm,:)=(NY1n-mean(NY1n)).*(NY2n-mean(NY2n));
Sinf_expanded(mm,:)=(NY1n-mean(NY1n)).*(NY3n-mean(NY2n));
end

%=========================================================================

%6. Act Lowpass matched digital filter, GET IQ

%6.A. Act matched filters

% [Cosfiltered,b]=act_lowpass_filt(Cosf_expanded,fSample,min(950,length(Cosf_expanded(1,:))),10);
% [Sinfiltered,b]=act_lowpass_filt(Sinf_expanded,fSample,min(950,length(Sinf_expanded(1,:))),10);

%6.B. Get IQ components
Cosf=mean(Cosf_expanded,2);
Sinf=mean(Sinf_expanded,2);
Amplitudes=sqrt(Cosf.^2+Sinf.^2);
Real=Cosf;
Imag=Sinf;
Phases=atan2(Sinf,Cosf);
end


%%%%=================================
function normalized_values=normalize_meas(measurements)
%%%%normalizes the measurements between -1 and 1
DMAX = max(abs(measurements));
normalized_values = (measurements+DMAX)*2/(2*DMAX)-1;
end


%%%%=================================
function [yf,b]=act_lowpass_filt(y,Fs,Windowlength,Order)

L=size(y,2);
K=size(y,1);
% t=linspace(0,L/Fs,L);
fc = 100;
Wn = (2/Fs)*fc;
b = fir1(Windowlength,Wn,'low',kaiser(Windowlength+1,Order));
delay=mean(grpdelay(b,Order,Fs));
% fvtool(b,1,'Fs',Fs)
% tt = t(1:end-round(delay*1.5));
%
for k=1:K
y1(k,:) = filter(b,1,y(k,:));
%yf(k,:) = y1(k,round(delay)+1:end);
yf(k,:) = y1(k,end-50:end);
end
end


%%%%=================================
function Rand=add_white_noise(L,Arms)
Rand=Arms*sqrt(2)*randn(L,1);
end


%%%%=================================
```

```
function SNRmean=Calculate_SNR(VoltageCell,Lbits,Vref,NT,f,fs,Noise)
%%computes DU model SNR
%%%Inputs:
%%%-VoltageCell: a cell array consisted of SPICE transient voltage measurements results
%%%-Lbits: ADC Resolution
%%%-Vref: ADC reference
%%%-NT: sine periods sampled
%%%-f: input signal frequency
%%%-fs: sampling frequency
%%%-Noise: Noise signal amplitude

%%%Outputs:
%%%-SNRmean: Mean signal SNR of the measurement frame
LM=length(VoltageCell);
A=zeros(LM,1);
for ii=1:LM
A(ii)=max(VoltageCell{ii})-min(VoltageCell{ii});
end
LSB=Vref/(2^Lbits);
sn=Noise/sqrt(2);
N=NT*fs/f;
SNR=10*log10((mean(A).^2*N/2)/(LSB^2/12+sn^2));
SNRmean=mean(SNR);
end
```

9.3 Code for two-dimensional time-variant thoracic modeling with FEMM

This code for [192] can be found in:
`https://github.com/chdim100/Dynamic-Thoracic-Model-for-EIT`.

```
%Test_Dynamic_model_script.m
%%==============================
path='C:path_to_folder';
path2eidors='C:path_to_eidors';
paths={path, path2eidors};

%%%%Measurement Parameters

%No of electrodes
N=16;
%current skip-m
skipcurr=0;
%voltage skip-n
skipvolt=0;
%ac current frequency (Hz), f=200kHz
f=200000;
%total simulated image frames
total_frames=30;
%frames per second
fps=10;
%ac current amplitude
Current_Amplitude=0.001; %Amperes
%pack measurement parameters
Measurement_params=[N skipcurr skipvolt f total_frames fps Current_Amplitude];

%%%%Model Parameters

breath_time=3; %seconds
Zelectrodes(:,1)=0.02*(randn(N,1)*0.1+1);
Zelectrodes(:,2)=300*(randn(N,1)*0.3+1);
delec=0.5; %electrode_width (cm)
random_start=0;
random_state=0;
%deflated lung conductivity at 200kHz ~0.25S/m []
%inflated lung conductivity at 200kHz ~0.1S/m []
slairmax=0.25; %(S/m)
end_Admittances(1)=slairmax;
slairmin=0.1; %(S/m)
end_Admittances(2)=slairmin;
%blood cycle-related conductivity variance in lungs ~0.008S/m (10-20 times
%less than air-related [])
dslblood=0.008; %(S/m)
```

```
end_Admittances(3)=dslblood;

%deflated lung permittivity at 200kHz ~4000F/m []
%inflated lung permittivity at 200kHz ~2000F/m []
elairmax=4000; %(S/m)
end_Admittances(4)=elairmax;
elairmin=2000; %(S/m)
end_Admittances(5)=elairmin;
%blood cycle-related permittivity variance in lungs ~100 F/m (10-20 times
%less than air-related [])
delblood=100;
end_Admittances(6)=delblood;

%base heart (champers, aorta, no-myocardium) conductivity ~0.55 S/m at
%200kHz
Sheart=0.55; %(S/m)
end_Admittances(7)=Sheart;
%base heart (champers, aorta, no-myocardium) conductivity variation ~0.025 S/m at
%200kHz (~15-20%)[]
dSheart=0.025;
end_Admittances(8)=dSheart;

%base heart (champers, aorta, no-myocardium) conductivity ~6000 F/m at
%200kHz
Eheart=6000;
end_Admittances(9)=Eheart;
%base heart (champers, aorta, no-myocardium) permittivity variation ~300 S/m at
%200kHz (~15-20%)[]
dEheart=300;
end_Admittances(10)=dEheart;

%HR
bpm=75;
%Collapsions states for Left and Right lung. From 1, which denotes an 20%
%lung collapsion to 4 which denotes a healthy lung.
Collapse_LL=1;
Collapse_RL=3;

Collapse_LL=4;
Collapse_RL=4;
%pack model parameters
Model_params=[end_Admittances breath_time delec bpm Collapse_LL Collapse_RL];

%%% call the model constructor
[M,Gr,Patient_labeled_data]=Dynamic_Thorax_Imaging(Measurement_params,...
Model_params,Zelectrodes,random_start,random_state,paths);


%%%%References

%%%%=================================================
function [M,Gr,Patient_labeled_data]=Dynamic_Thorax_Imaging(Measurement_params,Model_params,Zelectrodes,randomstart,randomcond,paths)
%%%Implementation of the Dynamic Thoracic Model for EIT
%%%Creates a .lua script, to be executed in FEMM
%%%Automatically pauses, until FEMM performs the EM simulation ordered for
%%%the .lua
%%%Collects the EIT potential measurements

%Inputs:
%Measurement_params: parameters that define the measuring properties:
%-N: the number of electrodes (single layer)
%-currentskip: skip-m current protocol
%-voltageskip: skip-n voltage measurement protocol
%-frequency: injected ac current frequency (in Hz)
%-total_frames: total image frames to be simulated
%-fps: measurement frames per second
%-Current: Injected ac current's Amplitude

%Model_params: parameters that define the measuring properties:
%1. end_Admittances: includes the inspiration/expiration-end
%conductivities and permittivities of each tissue
%-deflated lung conductivity (S/m)  end_Admittances(1)
%-inflated lung conductivity (S/m)  end_Admittances(2)
%-blood cycle-related conductivity variance in lungs (S/m) end_Admittances(3)
%-deflated lung permittivity (F/m)  end_Admittances(4)
%-inflated lung permittivity (F/m)  end_Admittances(5)
%-blood cycle-related permittivity variance in lungs (F/m)  end_Admittances(6)
```

```
%-base heart (champers, aorta, no-myocardium) conductivity (S/m) end_Admittances(7)
%-base heart (champers, aorta, no-myocardium) conductivity variation
%(S/m) end_Admittances(8)
%-base heart (champers, aorta, no-myocardium) conductivity (S/m) end_Admittances(9)
%-base heart (champers, aorta, no-myocardium) permittivity variation
%(F/m) end_Admittances(10)
%2. breath_time (seconds), Initial Breathing Time
%3. delec (cm), the electrodes width
%4. bpm, Initial Heart Rate
%5. Collapse_LL, Left Lung Collapsion state (1-4)
%6. Collapse_RL, Right Lung Collapsion state (1-4)

%Zelectrodes: A 2XN matrix. The first raw contains each electrode's contact
%relative conductivity. The second raw contains each electrode's contact
%relative permittivity.

%random_start: 0 if simulation starts from pulmonary and cardiac states 1
%(full exhalation and start of heartbeat). 1 if simulation starts from
%random states at both cycles.

%randomcond: if 1: breathing times and HR are randomly changed every cycle and 3
%cycles respectively. Else if 0: initial breathing time is 3 seconds,
%silent space is 0.3seconds and next breath lasts +20%. Initial heart beat
%rate is 75bpm and increases by 3% every 3 beats.

%paths: A cell array. paths{1} denotes the directory to the Bio-lungs
%folder ('C:\.....\Bio-lungs\')
%paths{2} denotes the directory to the Eidors library
%('C:\.....\eidors-v3.9-ng\eidors\')

%%%%%%%%%%%%

%Outputs:
%M: The final, noise-free potential measurements. Automatically saved in
%C:\....\Bio-lungs\Dynamic_Thorax_Model\Cardio-Pulmonary

%Gr: Simulated admittances graph. A matrix called Input_set_date() is automatically
%saved in C:\....\Bio-lungs\Dynamic_Thorax_Model\Cardio-Pulmonary



%%%% unpack Measurement_params

N=Measurement_params(1); currentskip=Measurement_params(2);
voltageskip=Measurement_params(3);
frequency=Measurement_params(4);
total_frames=Measurement_params(5);
fps=Measurement_params(6);
Current=Measurement_params(7);

%%%% unpack Model_params
end_Admittances=Model_params(1:10);
breath_time=Model_params(11);
delec=Model_params(12);
bpm=Model_params(13);
Collapse_LL=Model_params(14);
Collapse_RL=Model_params(15);

%%%% unpack Paths
path=paths{1};
path2EIDORS=paths{2};
path2save=paths{1};

%start EIDORS
run ([path2EIDORS 'startup.m'])

[initial_times, initial_total_positions, Collapsion_areas, electrodes, Tissues, Ventilation, Circulation, Graph, Silences, r, k]=...
set_initial_parameters(N, fps, total_frames, frequency, breath_time, delec, bpm, Collapse_LL, Collapse_RL, end_Admittances, randomstart, randomcond);
clc
%% lua
%%%
[fileID, d, folds]=open_script(frequency, path);
set_materials_in_lua(fileID, Current, Tissues, Zelectrodes);
[Graph, timesteps, total_time_est, History_of_Tissues]=...
frame_loop(N, currentskip, initial_times, initial_total_positions, ...
Collapsion_areas, electrodes, Silences, fileID, Graph, Circulation, ...
Ventilation, Tissues, d, r, k, frequency, end_Admittances, folds, randomcond);
```

```
[letterplus,Gr]=configure_graph(Graph,total_frames,fps,total_time_est,path2save);
M=configure_measurements(N,letterplus,currentskip,voltageskip,timesteps,d,path2save,path);
%imageC=thorax_GN_v3(32,4,1,0.02,Measurements',0,2,2,2,1,[]);
Patient_labeled_data=complete_patient_labeled_data(Graph,Collapsion_areas,History_of_Tissues);
end

function [initial_times,initial_total_positions,Collapsion_areas,electrodes,Tissues,Ventilation,Circulation,Graph,Silences,r,k]=...
set_initial_parameters(N,fps,total_frames,f,breath_time,delec,bpm,Collapse_LL,Collapse_RL,end_Admittances,randomstart,randomcond)
%defines the initial parameters (time, step, collapsions,electrodes,tissue_configuration,all possible positions, initial cycle states)
initial_times=define_times(N,fps,total_frames,breath_time,bpm,randomcond);
initial_total_positions=define_total_positions(N,1,initial_times.tim,initial_times.tbr); %Dy=1
[Collapsion_areas.collapsions,Collapsion_areas.cross_points]=define_collapse_areas(Collapse_LL,Collapse_RL,randomcond);
initial_times.pulse_dur=(2*(initial_total_positions.total_positions-1)+1)*(initial_times.tbr/initial_times.Tpulse)^(-1);
if randomcond
k=0.95 + (1.05-0.95)*randn(1,1);
else
k=1;
end
[electrodes.electrode_average,electrodes.electrode_possible,...
electrodes.delec]=electrodes_preset(N,1,initial_total_positions.dy,delec,k); %Dy=1
if randomcond
r=0.95 + (1.05-0.95)*randn(1,1);
else
r=1;
end
[Tissues.Left_lung,Tissues.Right_lung,Tissues.Heart,Tissues.Muscles,Tissues.Bones,r,k]=...
define_tissues(r,k,initial_times,initial_total_positions,0,f,end_Admittances,randomcond);
%returns the initial states of breathing and cardiac cycles
%pulmocycle and cardio_cycle indicate the positions of lungs and heart
%pulmcounter and cardcounter indicate whether they are increasing or
%decreasing
%plot(Tissues.Bones.Bone3.shape.full(:,1),Tissues.Bones.Bone3.shape.full(:,2))
%hold on
%plot(electrodes.electrode_average.x(1,:),electrodes.electrode_average.y(1,:),'o')
[Ventilation.pulmocycle,Circulation.cardio_cycle,Ventilation.pulmcounter,Circulation.cardcounter,Circulation.pulse_dur]=...
randomize(initial_times,initial_total_positions,randomstart); %randomstart==1
Graph=initialize_graph();
Silences=initialize_silences();
end

function initial_times=define_times(N,fps,total_frames,breath_time,bpm,randomcond)
%sets simulation times, breathing and blood cycle periods (all time
%parameters)
initial_times.tim=define_frame_time(N,fps);
initial_times.tbr=define_breath_time(breath_time,randomcond);
initial_times.total_time_est=estimate_total_simulation_time(initial_times.tim,total_frames);
initial_times.Tpulse=define_cardiac_cycle_time(bpm,randomcond);
end

function tim=define_frame_time(N,fps)
%estimates required time for a frame (in seconds)
if N==16||N==32
tim=1/fps; %total time for a measurement cycle
elseif N==64
tim=2; %when using 64 electrodes system is too slow to perform tdEIT
end
end

function tbr=define_breath_time(breath_time,randomcond)
%defined unitial breath period (randomly between 2 and 6 seconds)
%uniform distribution selection
if randomcond
tbr=rand(1)*6;
while tbr<2
tbr=rand(1)*6; %re-defined breath period until passes 2 seconds
end
else
tbr=breath_time;
end
end

function total_time_est=estimate_total_simulation_time(tim,total_frames)
%estimates total simulation time, that will NOT change!
total_time_est=tim*total_frames;
end

function Tpulse=define_cardiac_cycle_time(bpm,randomcond)
```

```
%defines the initial cardiac frequency
if randomcond
bpm=55+rand(1)*55;  %initial Bpm
else
%bpm=75;
end
fpulse=bpm/60;
Tpulse=1/fpulse;
end

function initial_total_positions=define_total_positions(N,Dy,tim,tbr)
%initializes electrode movement step and total possible positions,
%according to the initialized breathing time
initial_total_positions.dy=2*Dy*tim/(N*tbr); %initializes electrode movement step
%total possible positions for tissues
initial_total_positions.total_positions=floor(Dy/initial_total_positions.dy+1);
end

function [collapsions,cross_points]=define_collapse_areas(Collapse_LL,Collapse_RL,randomcond)
if randomcond
%randomize collapsing area for left lung
Collapse_cases.left_lung=randi([1 4]);
%randomize collapsing area for right lung
Collapse_cases.right_lung=randi([1 4]);
%degree of collaspion on left_lung
collapsions.collapsion_left_lung=randi(5)-1;
%degree of collaspion on right_lung
collapsions.collapsion_right_lung=randi(4)-1;
else
collapsions.collapsion_left_lung=Collapse_LL;
collapsions.collapsion_right_lung=Collapse_RL;
%     collapsions.collapsion_left_lung=1;
%     collapsions.collapsion_right_lung=3;
end
switch collapsions.collapsion_left_lung
case 1
cross_points.left_lung=[4 14];
case 2
cross_points.left_lung=[3 14];
case 3
cross_points.left_lung=[3 15];
case 4
cross_points.left_lung=[2 16];
otherwise
cross_points.left_lung=[1 16];
end
switch collapsions.collapsion_right_lung
case 1
cross_points.right_lung=[2 12];
case 2
cross_points.right_lung=[2 14];
case 3
cross_points.right_lung=[1 14];
otherwise
cross_points.right_lung=[1 15];
end
end

function [electrode_average,electrode_possible,delec]=electrodes_preset(N,Dy,dy,delec,k)
if N==16
F5=mk_common_model('d2T3',16);
AAAx=zeros(1,14);
BBBx=AAAx;
AAAy=zeros(1,14);
BBBy=AAAx;
for iii=1:14
AAAx(1,iii)=F5.fwd_model.nodes(486+4*iii,1);
BBBx(1,iii)=F5.fwd_model.nodes(487+4*iii,1);
end
for iii=15:16
AAAx(1,iii)=F5.fwd_model.nodes(478+4*(iii-14),1);
BBBx(1,iii)=F5.fwd_model.nodes(479+4*(iii-14),1);
end

electrode_average.x=[AAAx;BBBx]/5.8;
for iii=1:14
AAAy(1,iii)=F5.fwd_model.nodes(486+4*iii,2);
```

```
BBBy(1,iii)=F5.fwd_model.nodes(487+4*iii,2);
end
for iii=15:16
AAAy(1,iii)=F5.fwd_model.nodes(478+4*(iii-14),2);
BBBy(1,iii)=F5.fwd_model.nodes(479+4*(iii-14),2);
end
electrode_average.y=[AAAy;BBBy]/5.8;
dimension1=floor(Dy/dy+1);
electrode_possible.y1=zeros(dimension1,7); electrode_possible.y2=zeros(dimension1,7);
for el=6:12
%          electrode_possible.y1(:,el-5)=electrode_average.y(1,el)+Dy/2:-dy:electrode_average.y(1,el)-Dy/2;
%          electrode_possible.y2(:,el-5)=electrode_average.y(2,el)+Dy/2:-dy:electrode_average.y(2,el)-Dy/2;
electrode_possible.y1(:,el-5)=flip(linspace(electrode_average.y(1,el)-Dy/2,electrode_average.y(1,el)+Dy/2,dimension1));
electrode_possible.y2(:,el-5)=flip(linspace(electrode_average.y(2,el)-Dy/2,electrode_average.y(2,el)+Dy/2,dimension1));
end
%     plot(electrode_average.x(1,9)*ones(dimension1,1),electrode_possible.y1(:,4),'o')
%     hold on
%     plot(electrode_average.x(2,9)*ones(dimension1,1),electrode_possible.y2(:,4),'o')
o=[];


elseif N==32
F5=mk_common_model('d2T3',32);
AAAx=zeros(1,14);
BBBx=AAAx;
AAAy=zeros(1,14);
BBBy=AAAx;
for iii=1:28
AAAx(1,iii)=F5.fwd_model.nodes(488+2*iii,1);
BBBx(1,iii)=F5.fwd_model.nodes(489+2*iii,1);
end
for iii=29:32
AAAx(1,iii)=F5.fwd_model.nodes(480+2*(iii-28),1);
BBBx(1,iii)=F5.fwd_model.nodes(481+2*(iii-28),1);
end

electrode_average.x=[AAAx;BBBx]/5.8;
for iii=1:28
AAAy(1,iii)=F5.fwd_model.nodes(488+2*iii,2);
BBBy(1,iii)=F5.fwd_model.nodes(489+2*iii,2);
end
for iii=29:32
AAAy(1,iii)=F5.fwd_model.nodes(480+2*(iii-28),2);
BBBy(1,iii)=F5.fwd_model.nodes(481+2*(iii-28),2);
end
electrode_average.y=[AAAy;BBBy]/5.8;
dimension1=floor(Dy/dy+1);
electrode_possible.y1=zeros(dimension1,15); electrode_possible.y2=zeros(dimension1,15);
for el=10:24
%electrode_possible.y1(:,el-9)=electrode_average.y(1,el)+Dy/2:-dy:electrode_average.y(1,el)-Dy/2;
%electrode_possible.y2(:,el-9)=electrode_average.y(2,el)+Dy/2:-dy:electrode_average.y(2,el)-Dy/2;
electrode_possible.y1(:,el-9)=flip(linspace(electrode_average.y(1,el)-Dy/2,electrode_average.y(1,el)+Dy/2,dimension1));
electrode_possible.y2(:,el-9)=flip(linspace(electrode_average.y(2,el)-Dy/2,electrode_average.y(2,el)+Dy/2,dimension1));
end
end
electrode_average.x=k*electrode_average.x;
electrode_average.y=k*electrode_average.y;
electrode_possible.y1=k*electrode_possible.y1;
electrode_possible.y2=k*electrode_possible.y2;
o=[];
end

function [Left_lung,Right_lung,Heart,Muscles,Bones,r,k]=...
define_tissues(r,k,times,discrete_points,firsttime,f,end_Admittances,randomcond,Tissues)
%defines tissues properties
if exist('Tissues')~=0 %tissues exist but need to be updated (end of cycle)
%in order to be updated we have to temporarily store their positions
Left_lung=Tissues.Left_lung;
pos1=Left_lung.position;
Right_lung=Tissues.Right_lung;
pos2=Right_lung.position;
Exterior=Tissues.Heart.exterior;
pos3a=Exterior.position;
Interior=Tissues.Heart.interior;
pos3b=Interior.position;
Muscles=Tissues.Muscles;
Bones=Tissues.Bones;
```

```
pos4=Bones.Bone1.position;
pos5=Bones.Bone2.position;
pos6=Bones.Bone3.position;
pos7=Bones.Bone4.position;
pos8=Bones.Bone5.position;
pos9=Bones.Bone6.position;
pos10=Bones.Bone7.position;
pos11=Bones.Bone8.position;
end
%%%% unpack end_Admittances
slairmax=end_Admittances(1);
slairmin=end_Admittances(2);
dslblood=end_Admittances(3);
elairmax=end_Admittances(4);
elairmin=end_Admittances(5);
delblood=end_Admittances(6);
Sheart=end_Admittances(7);
dSheart=end_Admittances(8);
Eheart=end_Admittances(9);
dEheart=end_Admittances(10);

Left_lung=define_lung_properties(times,discrete_points,slairmax,slairmin,dslblood,elairmax,elairmin,delblood);
Right_lung=define_lung_properties(times,discrete_points,slairmax,slairmin,dslblood,elairmax,elairmin,delblood);
Heart=define_heart_properties(f,times,Sheart,dSheart,Eheart,dEheart);
Muscles=define_muscles_properties(times);
Bones=define_bones_properties();

if exist('Tissues')~=0 %tissues exist but need to be updated (end of cycle)
Left_lung.position=pos1;
Right_lung.position=pos2;
Heart.exterior.position=pos3a;
Heart.interior.position=pos3b;
Bones.Bone1.position=pos4;
Bones.Bone2.position=pos5;
Bones.Bone3.position=pos6;
Bones.Bone4.position=pos7;
Bones.Bone5.position=pos8;
Bones.Bone6.position=pos9;
Bones.Bone7.position=pos10;
Bones.Bone8.position=pos11;
end

[Left_lung,Right_lung,Heart,Bones,r,k]=...
define_tissues_movement(r,k,Left_lung,Right_lung,Heart,Bones,times,discrete_points,firsttime,randomcond);
end


function Lung=define_lung_properties(times,discrete_points,slairmax,slairmin,dslblood,elairmax,elairmin,delblood)
Lung.props.Volume=set_Volume(discrete_points.total_positions);
Lung.props.Conductivity=set_lung_Conductivity(times,Lung.props.Volume,slairmax,slairmin,dslblood);
Lung.props.permittivity=set_lung_permittivity(times,Lung.props.Volume,elairmax,elairmin,delblood);
end


function Heart=define_heart_properties(f,times,Sheart,dSheart,Eheart,dEheart)
Heart.interior.props.Conductivity=set_heart_Conductivity(times,Sheart,dSheart);
Heart.interior.props.permittivity=set_heart_permittivity(times,Eheart,dEheart);
Heart.exterior.props.Conductivity=set_myocardium_Conductivity(f);
Heart.exterior.props.permittivity=set_myocardium_permittivity(f);
end

function Volume=set_Volume(total_positions)
%during the breath, each tissue and the electrodes, pass from each
%possible position twice
i2=total_positions:1:2*total_positions+1; %time samples of exhalation
i1=1:1:(total_positions-1); %time samples of inhalation
F2=-3/(total_positions-1)*i1+3/(total_positions-1)+4; %lungs volume during inhalation
F1=3/(total_positions+1)*i2+4-3*(2*total_positions+1)/(total_positions+1); %lungs volume during exhalation
i=[i1 i2]; %combine the two continuous time windows
Volume=[F1 F2]; %combine the two continuous volume functions
end

function S=set_lung_Conductivity(times,Volume,slairmax,slairmin,dslblood)
%lungs parameters
w=1.5;
sb=0.5;
si=2;
```

```
% conductivity changes during breath cycle due to air flow
s10lungs=18*(32*Volume+4.5)./(32*Volume+9).^2*((0.85/w*sb+0.03*si));
%scaling (K1, K2)
s1lungs=(slairmax+slairmin)/2+(slairmax-(slairmax+slairmin)/2)*(s10lungs-mean(s10lungs))/(max(s10lungs-mean(s10lungs)));
pulse_dur=times.pulse_dur;
%dslblood=0.008; %ds in lungs due to blood cycle
j1=1:1:pulse_dur/2;
j2=pulse_dur/2:1:pulse_dur;
%conductivity changes during blood cycle due to blood flow
sklungs=dslblood*2/pulse_dur*j1;
sllungs=-dslblood*2/pulse_dur*j2+2*dslblood;
j=[j1 j2];
s2lungs=[sklungs sllungs];
S.air=s1lungs;
S.blood=s2lungs;
end

function E=set_lung_permittivity(times,Volume,elairmax,elairmin,delblood)
erb=10000;
erm=10;
b=0.325;
w=1.5;
% permittivity changes during breath cycle due to air flow
er10lungs=18*(32*Volume+4.5)./(32*Volume+9).^2.*((0.85/w*erb+2400*b*Volume.^(1/3)*erm));
%scaling (L1, L2)
er1lungs=(elairmax+elairmin)/2+(elairmax-(elairmax+elairmin)/2)*(er10lungs-mean(er10lungs))/(max(er10lungs-mean(er10lungs)));
pulse_dur=times.pulse_dur;
dElungs=delblood;
%dElungs=500; %ÄE in lungs due to blood cycle
j1=1:1:pulse_dur/2;
j2=pulse_dur/2:1:pulse_dur;
j=[j1 j2];
% permittivity changes during blood cycle due to blood flow
er2klungs=dElungs*2/pulse_dur*j1-2*dElungs/pulse_dur;
er2llungs=-dElungs*2/pulse_dur*j2+2*dElungs;
er2lungs=[er2klungs er2llungs];
E.air=er1lungs;
E.blood=er2lungs;
end

function S=set_heart_Conductivity(times,Sinheart,dSheart)
pulse_dur=times.pulse_dur;
j1=1:1:pulse_dur/2;
j2=pulse_dur/2:1:pulse_dur;
j=[j1 j2];
%heart parameters
%dSheart=0.025; %conductivity change of heart during cardio cycle
%Sinheart=0.5; %sigma heart~0.5, around is ~0.2
sheart1=-2*dSheart/pulse_dur*j1+dSheart+Sinheart;
sheart2=2*dSheart/pulse_dur*j2-dSheart+Sinheart;
S=[sheart1 sheart2];
o=[];
end

function E=set_heart_permittivity(times,Eheartin,dEheart)
pulse_dur=times.pulse_dur;
j1=1:1:pulse_dur/2;
j2=pulse_dur/2:1:pulse_dur;
j=[j1 j2];
% dEheart=300;
% Eheartin=6000;
er1heart=-dEheart*2/pulse_dur*j1+dEheart+Eheartin;
er2heart=dEheart*2/pulse_dur*j2-dEheart+Eheartin;
E=[er1heart er2heart];
end

function S=set_myocardium_Conductivity(f)
S=9*10^(-5)*f/1000+0.168;
end

function E=set_myocardium_permittivity(f)
E=2.29*10^5*(f/1000)^(-0.95);
end


function Muscles=define_muscles_properties(times)
Muscles.props.Conductivity=define_muscle_conductivity(times);
```

```
Muscles.props.permittivity=define_muscle_permittivity(times);

end

function S=define_muscle_conductivity(times)
%soft_tissues parameters
pulse_dur=times.pulse_dur;
j1=1:1:pulse_dur/2;
j2=pulse_dur/2:1:pulse_dur;
dSsoft=0.015; %muscle-plasma conductivity change due to blood flow
Sinsoft=0.28; %average muscle-plasma-gap conductivity
ssoft1=2*dSsoft/times.pulse_dur*j1+dSsoft+Sinsoft-2*dSsoft/times.pulse_dur;
ssoft2=-2*dSsoft/times.pulse_dur*j2+dSsoft+Sinsoft+2*dSsoft;
S=[ssoft1 ssoft2];
end

function E=define_muscle_permittivity(times)
%soft_tissues parameters
pulse_dur=times.pulse_dur;
j1=1:1:pulse_dur/2;
j2=pulse_dur/2:1:pulse_dur;
dEsoft=300;
Esoftin=6000;
er1soft=-dEsoft*2/pulse_dur*j1+dEsoft+Esoftin+2*dEsoft/pulse_dur;
er2soft=dEsoft*2/pulse_dur*j2+dEsoft+Esoftin-2*dEsoft;
E=[er1soft er2soft];
end

function Bones=define_bones_properties()
%assuming constant conductivity and permittivity
Bones.props.Conductivity=0.07;
Bones.props.permittivity=250;
end

function [Left_lung,Right_lung,Heart,Bones,r,ks]=...
define_tissues_movement(r,ks,Left_lung,Right_lung,Heart,Bones,times,discrete_points,firsttime,randomcond)
%Defines:
%initially the minimum and maximum shapes of the tissues (assuming they
%have constant limits)
%at every new blood or breath cycle the steps of each tissue's boundary
%change
%r = H + (H-L)*rand(DIM,1)
%Left Lung
Left_lung.shape.full=r*[-5.1 -7.6 -8.3 -8.1 -8 -5.6 -4 -1.3 -10.1 -16.6 -19.8 -20.9 -20 -15.8 -11.8...
 -8; -12.8 -10.3 -7.7 -3.2 -0.1 3.2 7 9.7 15.5 10.9 6.3 1.3 -5.2 -10.2 -12.5 -13.1]';
Left_lung.shape.empty=r*[-6.4 -7.6 -8.8 -9.7 -10.4 -8.4 -6.9 -5 -11 -14.9 -17.8 -18.5 -17.4 -14.8...
 -10.9 -8.7;-10.9 -8.2 -5.6 -2.9 -0.3 3.7 5.7 7.5 13.6 9.3 5.3 1.5 -4.4 -8.1 -11.6 -11.7]';
Left_lung.shape.step=define_steps(Left_lung,discrete_points.total_positions);
%Right lung
Right_lung.shape.full=r*[10.5 18.8 21.5 18.3 12 6.2 1.9 3.3 5.2 7.6 9.2 8 7.5 7.3 6.9; -15.6 -9.1...
 0.4 8.8 15.7 16.1 10.1 6.2 3.4 3.5 -0.7 -4.1 -5.2 -6.9 -10.5]';
Right_lung.shape.empty=r*[10.8 17.7 19 17 11.2 6.6 3.7 4.4 5.3 7.6 10.3 9.6 8.4 9 8.7;-12.8 -7 1.6...
 8.7 14.6 15 10.3 7.4 4.8 4.8 0.9 -4.1 -5.1 -6.6 -9.5]';
Right_lung.shape.step=define_steps(Right_lung,discrete_points.total_positions);
%Heart exterior
Heart.exterior.shape.full=[0 4.1 4.5 4.5 5.9 7.3 7.1 4.3 3 0.8 1.3 1.6 -1 -2.8 -3.6 -6.7 -5.9...
 -1.1;-14.6 -10.5 -6.6 -3.6 -3.3 -1.7 0.5 2.6 -0.4 1 1.3 6.1 6 4 1.3 0 -7.8 -12.4]';
Heart.exterior.shape.empty=[0 3.6 3.1 3.3 5 6.4 5.9 4.2 3.1 1 0.6 0.6 -0.9 -2.9 -4.1 -6.3 -4.9...
 -0.8;-13 -8.9 -6.2 -3.3 -2.3 -1.1 0.1 1.6 -1.5 0 2.2 4.2 5.9 3.8 1.7 -0.2 -7.2 -11.8]';

Heart.exterior.shape.full(:,2)=Heart.exterior.shape.full(:,2)+1;
Heart.exterior.shape.empty(:,2)=Heart.exterior.shape.empty(:,2)+1;

Heart.exterior.shape.full=0.8*r*Heart.exterior.shape.full;
Heart.exterior.shape.empty=0.8*r*Heart.exterior.shape.empty;

%Heart interior
aa=[1 2 4 9 15 17];
Heart.interior.shape.full=0.65*Heart.exterior.shape.full(aa,:);
Heart.interior.shape.empty=0.65*Heart.exterior.shape.empty(aa,:);

%heart exterior shifting
Heart.exterior.shape.full(:,2)=Heart.exterior.shape.full(:,2)-2;
Heart.exterior.shape.empty(:,2)=Heart.exterior.shape.empty(:,2)-2;

Heart.exterior.shape.step=define_steps(Heart.exterior,discrete_points.total_positions*times.tbr/times.Tpulse);
```

```
%Heart interior shifting
Heart.interior.shape.full(:,2)=Heart.interior.shape.full(:,2)-2.5;
Heart.interior.shape.empty(:,2)=Heart.interior.shape.empty(:,2)-2.5;

Heart.interior.shape.step=define_steps(Heart.interior,discrete_points.total_positions*times.tbr/times.Tpulse);



%Bones
Bones.Bone1.shape.empty=ks*[21.8 22.9 21.7 20.3; -7.7 -3.1 -2 -7.6]';
Bones.Bone2.shape.empty=ks*[21.8 21.7 16.1 14.3; 6 8.1 14.5 14.4]';
%Spondilus
Bones.Bone3.shape.empty=ks*[11.5 3.4 1.2 0.4 -0.3 -0.8 -2.6 -5.2 -12.3 -3.5 -0.4 2.5; 17.1 18.2 17.8...
 17.9 19.2 18 17.5 17.8 16.5 14.3 10.6 14.5]';
Bones.Bone4.shape.empty=ks*[-14.2 -18.1 -22.2 -22.7;14.5 12.7 6.9 3.8]';
Bones.Bone5.shape.empty=ks*[-20.8 -21.7 -22.8 -22.1;-5.9 -1.2 -1.3 -6]';
Bones.Bone6.shape.empty=ks*[-15.8 -17 -11.4 -11.8; -13.5 -13.6 -17.2 -15.9]';
Bones.Bone7.shape.empty=ks*[-2.8 -2.7 3.7 3.7;-15.6 -17.4 -17.1 -15.6]';
Bones.Bone8.shape.empty=ks*[12.5 12.7 18 16.8;-16.1 -17.4 -13.4 -12.7]';
Bones.Bone1.shape.full=ks*[22.9 23.7 22.8 21.4; -8 -3.8 -2.6 -7.7]';
Bones.Bone2.shape.full=ks*[22.1 22.5 16.8 14.8; 6.5 8.1 15.1 15]';
%Spondilus
Bones.Bone3.shape.full=ks*[12.1 3.3 1.1 0.4 -0.3 -0.8 -2.6 -5.2 -12.9 -3.2 -0.4 2.7; 17.9 19.1 18.4...
 18.2 19 18 17.9 18.4 17 15 10.6 15.5]';
Bones.Bone4.shape.full=ks*[-14.5 -18.7 -22.7 -23; 15 12.6 6.9 4]';
Bones.Bone5.shape.full=ks*[-21.3 -22.4 -23.4 -22.6; -6 -1.4 -1.4 -6.2]';
Bones.Bone6.shape.full=ks*[-16.6 -17.8 -11.2 -11.6;-13.7 -13.9 -17.8 -16.8]';
Bones.Bone7.shape.full=ks*[-2.6 -2.4 3.7 3.9; -16.3 -18 -17.9 -16.5]';
Bones.Bone8.shape.full=ks*[12.7 12.8 18.7 17.6; -17 -18.2 -13.8 -13.1]';
for k=1:8
Bone=eval(['Bones.Bone' num2str(k)]);
eval(['Bones.Bone' num2str(k) '.shape.step=define_steps(Bone,discrete_points.total_positions)'])
end
if firsttime==0&&randomcond==1
while check_intersections(Left_lung,Right_lung,Heart,Bones)==1
%if we have just initialized the tissues and we have intersections
%re-initialize the positions
r=0.95 + (1.05-0.95)*randn(1,1);
ks=0.95 + (1.05-0.95)*randn(1,1);
[Left_lung,Right_lung,Heart,Bones,r,ks]=define_tissues_movement(r,ks,Left_lung,Right_lung,Heart,Bones,times,discrete_points,firsttime,0);
end
end
end

function step=define_steps(Tissue,total_positions)
len=length(Tissue.shape.empty(:,1));
step(1:len,1)=(Tissue.shape.empty(:,1)-Tissue.shape.full(:,1))/total_positions;
step(1:len,2)=(Tissue.shape.empty(:,2)-Tissue.shape.full(:,2))/total_positions;
end

function [fileID,d,folds]=open_script(frequency,path)
d5=1;
folder=[path '\Dynamic_Thorax_Model\LUA_files\'];
prefix_data=['File',num2str(date()),'_',num2str(d5)];
dataformat='.lua';
nol=strcat(folder,prefix_data,dataformat);
while exist(nol)>0
folder=[path '\Dynamic_Thorax_Model\LUA_files\'];
prefix_data=['File',num2str(date()),'_',num2str(d5)];
dataformat='.lua';
nol=strcat(folder,prefix_data,dataformat);
d5=d5+1;
end
%% begin writing on script
fileID=fopen(nol,'w');
%% set parameters of the problem in FEMM
fprintf(fileID,'newdocument(3)\n');
fprintf(fileID,'ci_probdef("centimeters","planar",%4.2f,1.E-8,1,15)\n',frequency);
%% set file for the measurements to be written
d=1;
ex=1;
while ex==1
folder=[path 'Dynamic_Thorax_Model\LUA_files\'];
prefix_data=[num2str(date()),'_test',num2str(d)];
dataformat='.fee';
nl=strcat(folder,prefix_data,dataformat);
if exist(nl)>0
```

```
d=d+1;
%disp('exist')
else
ex=0;
end
end
%% save it
folds=strrep(folder, '\', '\\\\');
folds=[folds 'Temporary\\\\'];
fprintf(fileID,'ci_saveas("%s%s_test%.0f.fee")\n',folds,date(),d);
end

function []=set_materials_in_lua(fileID,Current,Tissues,Zelectrodes)
inhomogeneous_materials_stable(fileID,Tissues,Zelectrodes)
%%set current values
set_currents(fileID,Current)
%%set ground value
set_ground(fileID)
end

function[]=inhomogeneous_materials_stable(fileID,Tissues,Zelectrodes)
%sets some constant values on tissues; only bones will be used
%trabecular bone resistance 2000Ùcm cortical 10000Ùcm at 10kHz
%20 Ùm===>1/20Sm^-1
%10000 Ùcm=0.01Sm^-1
fprintf(fileID,'ci_addmaterial("Lungs",0.1,0.1,5000,5000,"<None>","<None>")\n');
fprintf(fileID,'ci_addmaterial("Bone",0.07,0.07,250,250,"<None>","<None>")\n');
fprintf(fileID,'ci_addmaterial("Heart",0.3,0.3,5000,5000,"<None>","<None>")\n');
fprintf(fileID,'ci_addmaterial("Softer tissues",3,3,5000,5000,"<None>","<None>")\n');
fprintf(fileID,'ci_addmaterial("Near_skin_",0.3,0.3,2000,2000,"<None>","<None>")\n');
Sigmaext=Tissues.Heart.exterior.props.Conductivity;
Eext=Tissues.Heart.exterior.props.permittivity;
fprintf(fileID,'ci_addmaterial("Miocardium",%4.2f,%4.2f,%4.2f,%4.2f,"<None>","<None>")\n',Sigmaext,Sigmaext,Eext,Eext);
fprintf(fileID,'ci_addmaterial("Fat",%4.2f,%4.2f,%4.2f,%4.2f,"<None>","<None>")\n',0.12,0.12,1000,1000);
for electrode=1:length(Zelectrodes(:,1))
fprintf(fileID,'ci_addmaterial("Zelectrode%2.0f",%4.2f,%4.2f,%4.2f,%4.2f,"<None>","<None>")\n',...
electrode,Zelectrodes(electrode,1),Zelectrodes(electrode,1),Zelectrodes(electrode,2),Zelectrodes(electrode,2));
end
end

function[]=set_currents(fileID,Current)
%sets the value of current injection amplitude
fprintf(fileID,'ci_addconductorprop("Iin",0,%1.3f,0)\n',Current);
fprintf(fileID,'ci_addconductorprop("Iout",0,-%1.3f,0)\n',Current);
end

function[]=set_ground(fileID)
%Ground is 0 volts!
fprintf(fileID,'ci_addboundprop("Ground", 0, 0, 0, 0, 0)\n');
end

function [pulmo,card,pulmcounter,cardcounter,pulse_dur]=...
randomize(initial_times,initial_total_positions,random)

%returns the initial states of breathing and cardiac cycles
%pulmo and card indicate the positions of lungs and heart
%pulmcounter and cardcounter indicate whether they are increasing or
%decreasing
tot=initial_total_positions.total_positions;
tbr=initial_times.tbr;
Tpulse=initial_times.Tpulse;
if random==1 %pulmo cycle and cardio cycle are at random points when simulation starts
kappa=tot*rand(1); %random ventilation point
cof1=rand(1); %determine if we have exhalation (-1) or inhalation (+1)
if cof1<0.5
cof=1;
else
cof=-1;
end
cof2=rand(1);
if cof2<0.5
cardio=1;
else
cardio=-1;
end
i=round(kappa);
pulse_dur=tot*(tbr/Tpulse)^(-1);
```

```
kappa1=rand(1)*pulse_dur;
j=round(kappa1);
pulmo=i;
card=j;
pulmcounter=cof;
cardcounter=cardio;
else  %if random is non-one when simulation starts, pulmocycle and cardiocycle
%are set to starting point
pulmo=1;
card=1;
pulmcounter=1;
cardcounter=1;
pulse_dur=tot*(tbr/Tpulse)^(-1);
end
end

function Graph=initialize_graph()
%input conductivities zero defining
Graph.heart.conductivity=[];
Graph.right_lung.conductivity=[];
Graph.left_lung.conductivity=[];
Graph.muscles.conductivity=[];
Graph.heart.permittivity=[];
Graph.right_lung.permittivity=[];
Graph.left_lung.permittivity=[];
Graph.muscles.permittivity=[];
end

function Silences=initialize_silences()
Silences.silence=0; %when starting at a random point, not in silence space
Silences.time_sil_start=-1; %start time (seconds) of the silence space
Silences.relaxing_time=-1; %duration (seconds) of the silence space
Silences.cardiobeats=1;
end
%% loop
function [Graph,timesteps,total_time_est,History_of_Tissues]=...
frame_loop(N,currentskip,initial_times,initial_total_positions,...
Collapsion_areas,electrodes,Silences,fileID,Graph, Circulation,...
Ventilation, Tissues,d,r,k,frequency,end_Admittances,folds,randomcond)
times=initial_times;
tim=initial_times.tim;
total_positions=initial_total_positions;
total_time_est=initial_times.total_time_est;
count=1;
timesteps=1;
History_of_Tissues=initialize_history();
%step is (time required for a frame)/(number of electrodes)
%therefore (time) step is the time we set a current input
fprintf(fileID,'ci_zoom(%d,%d,%d,%d) \n',-30,-30,30,30);
for time=(tim/N):(tim/N):total_time_est
%each iteration has a tim/N duration which corresponds
%to the time the measurements are taken for a single
%current source electrodes position
if mod(count-1,N)==0
count=1;
end
% find  SIGMA and E in (ith) state
Graph=inhomogeneous_materials_var_setting(Graph, Circulation, Ventilation, Tissues, fileID);
%detect positions of each electrode and tissue
%and define the geometry which changes in every time step
%find the electrodes and tissues POSITIONS in (ith) state
electrodes.position=electrode_positions(N,Ventilation,electrodes);
Tissues=tissue_positions(Ventilation,Circulation,Tissues,Collapsion_areas);

%     %%%%time record every boundary and tissue
electrodes.positions(1:N,1:2,1,timesteps)=(electrodes.position.x)';
electrodes.positions(1:N,1:2,2,timesteps)=(electrodes.position.y)';

%       Tissues_times.Left_lung(:,:,timesteps)=Tissues.Left_lung.position;
%       Tissues_times.Right_lung(:,:,timesteps)=Tissues.Right_lung.position;
%       Tissues_times.Heart.interior(:,:,timesteps)=Tissues.Heart.interior.position;
%       Tissues_times.Heart.exterior(:,:,timesteps)=Tissues.Heart.exterior.position;
%       Tissues_times.Bone1=Tissues.Bones.Bone1.position;
```

```
History_of_Tissues=update_history(History_of_Tissues,Tissues);
%set assist temporary points to measure later
[assist_points,electrode_central_points,electrode_exterior_sides]=dynamic_geometry(N,electrodes,Tissues,Collapsion_areas,fileID);
%add labels to each region according to current (ith) state
[LLCC,RLCC,CALCC,CARCC,STCC,Xbone,Ybone,Xfat,Yfat,Xint,Yint,Xext,Yext]=...
addmaterial_labels(Tissues,Ventilation,Circulation,Collapsion_areas,fileID,r,k,electrode_central_points);
%set current source position for the (ith) state
set_current_source(N,currentskip,assist_points,count,fileID,electrode_exterior_sides);
%set reference (arbitrary ground) electrode
set_reference(N,currentskip,assist_points,count,fileID,electrode_exterior_sides);
% save the file
save_process(d,fileID,folds);
% measure the voltages for this state (this current source position)
measure_voltages(N,electrodes.position,d,timesteps,fileID,electrode_exterior_sides,folds);
%update cycle states; then check if any of them has come to an end
%if so, change durations, total positions, properties, e.t.c.
delec=electrodes.delec;
[Ventilation,Circulation,total_positions,times,Silences,Tissues,electrodes,r,k]=...
update_cycle_states(N,Ventilation,Circulation,total_positions,times,Silences,...
Tissues,time,electrodes,r,k,frequency,end_Admittances,delec,randomcond);
display=0;
%       plot(Tissues.Bones.Bone7.position(:,1),Tissues.Bones.Bone7.position(:,2))
%          hold on
%       plot(electrodes.position.x(:,9),electrodes.position.y(:,9),'o')
%       hold on
if isfield(Tissues.Left_lung,'position')==0
o=[];
end
if display==1&&mod(timesteps,15)==0
RTG=display_realtime_graph(N,Graph,Ventilation,Circulation,Tissues,electrodes,time,timesteps,Collapsion_areas,times);
end
%% at the iteration end unset FEMM geometry
%because it's gonna change in the next step/iteration
unset_current_source(N,fileID,currentskip,assist_points,count,electrode_exterior_sides)
unset_reference(N,fileID,currentskip,assist_points,count,electrode_exterior_sides)
undo_dynamic_geometry(Tissues,fileID,electrodes.position,electrode_exterior_sides)
clear_labels(fileID,LLCC,RLCC,CALCC,CARCC,STCC,Xbone,Ybone,Xfat,Yfat,Xint,Yint,Xext,Yext,electrode_central_points)
count=count+1;
timesteps=timesteps+1;
if mod(timesteps,100)==0
fprintf('Loading script %2.0f %%\n',round(100*time/total_time_est))
end
end
o=[];
end
%%
function History_of_Tissues=initialize_history()
History_of_Tissues.Left_lung=[];
History_of_Tissues.Right_lung=[];
History_of_Tissues.Heart.exterior=[];
History_of_Tissues.Heart.interior=[];
for Bone=1:8
B_k=[];
switch Bone
case 1
History_of_Tissues.Bones.Bone1=B_k;
case 2
History_of_Tissues.Bones.Bone2=B_k;
case 3
History_of_Tissues.Bones.Bone3=B_k;
case 4
History_of_Tissues.Bones.Bone4=B_k;
case 5
History_of_Tissues.Bones.Bone5=B_k;
case 6
History_of_Tissues.Bones.Bone6=B_k;
case 7
History_of_Tissues.Bones.Bone7=B_k;
case 8
History_of_Tissues.Bones.Bone8=B_k;
end
end
end

function History_of_Tissues=update_history(History_of_Tissues,Tissues)
History_of_Tissues.Left_lung=[History_of_Tissues.Left_lung Tissues.Left_lung.position];
```

```
History_of_Tissues.Right_lung=[History_of_Tissues.Right_lung Tissues.Right_lung.position];
History_of_Tissues.Heart.exterior=[History_of_Tissues.Heart.exterior Tissues.Heart.exterior.position];
History_of_Tissues.Heart.interior=[History_of_Tissues.Heart.interior Tissues.Heart.interior.position];
for Bone=1:8
B_k=eval(['Tissues.Bones.Bone',num2str(Bone),'.position']);
switch Bone
case 1
History_of_Tissues.Bones.Bone1=[History_of_Tissues.Bones.Bone1 B_k];
case 2
History_of_Tissues.Bones.Bone2=[History_of_Tissues.Bones.Bone2 B_k];
case 3
History_of_Tissues.Bones.Bone3=[History_of_Tissues.Bones.Bone3 B_k];
case 4
History_of_Tissues.Bones.Bone4=[History_of_Tissues.Bones.Bone4 B_k];
case 5
History_of_Tissues.Bones.Bone5=[History_of_Tissues.Bones.Bone5 B_k];
case 6
History_of_Tissues.Bones.Bone6=[History_of_Tissues.Bones.Bone6 B_k];
case 7
History_of_Tissues.Bones.Bone7=[History_of_Tissues.Bones.Bone7 B_k];
case 8
History_of_Tissues.Bones.Bone8=[History_of_Tissues.Bones.Bone8 B_k];
end
end
end
%%
function Graph=inhomogeneous_materials_var_setting(Graph, Circulation, Ventilation, Tissues, fileID)
%Writes the tissues properties of the current state(s) as FEMM materials
%Returns an updated graph
%this is updated at each time step

s1lungs=Tissues.Left_lung.props.Conductivity.air;
s2lungs=Tissues.Left_lung.props.Conductivity.blood;
%fprintf('%2.0f\n',Ventilation.pulmocycle)
if Ventilation.pulmocycle<=0
o=[];
end
left_lung_cond_value=s1lungs(Ventilation.pulmocycle)+s2lungs(Circulation.cardio_cycle);
Graph.left_lung.conductivity=[Graph.left_lung.conductivity left_lung_cond_value];

er1lungs=Tissues.Left_lung.props.permittivity.air;
er2lungs=Tissues.Left_lung.props.permittivity.blood;

left_lung_perm_value=er1lungs(Ventilation.pulmocycle)+er2lungs(Circulation.cardio_cycle);
Graph.left_lung.permittivity=[Graph.left_lung.permittivity left_lung_perm_value];

cheart=Tissues.Heart.interior.props.Conductivity(Circulation.cardio_cycle);
 errheart=Tissues.Heart.interior.props.permittivity(Circulation.cardio_cycle);
Graph.heart.conductivity=[Graph.heart.conductivity cheart];
Graph.heart.permittivity=[Graph.heart.permittivity errheart];

csoft=Tissues.Muscles.props.Conductivity(Circulation.cardio_cycle);
 errsoft=Tissues.Muscles.props.permittivity(Circulation.cardio_cycle);
Graph.muscles.conductivity=[Graph.muscles.conductivity csoft];
Graph.muscles.permittivity=[Graph.muscles.permittivity errsoft];


fprintf(fileID,'ci_addmaterial("Lungs_state_%d_%d",%4.2f,%4.2f,%4.2f,%4.2f,"<None>",...
"<None>")\n',Ventilation.pulmocycle,Circulation.cardio_cycle,...
left_lung_cond_value,left_lung_cond_value,left_lung_perm_value,left_lung_perm_value);
fprintf(fileID,'ci_addmaterial("Heart_state_%d",%4.2f,%4.2f,%4.2f,%4.2f,"<None>","<None>")\n',...
Circulation.cardio_cycle,cheart,cheart,errheart,errheart);
fprintf(fileID,'ci_addmaterial("Soft_tissue_state_%d",%4.2f,%4.2f,%4.2f,%4.2f,"<None>",...
"<None>")\n',Circulation.cardio_cycle,csoft,csoft,errsoft,errsoft);
end

function electrode_position=electrode_positions(N,Ventilation,electrodes)
%Returns this state's electrode positions
electrode_average=electrodes.electrode_average;
electrode_possible=electrodes.electrode_possible;
i=Ventilation.pulmocycle;

if N==16
electrode_position.y(:,1:5)=electrode_average.y(:,1:5);
electrode_position.y(:,12:16)=electrode_average.y(:,12:16);
electrode_position.x=electrode_average.x;
electrode_position.y(1,6:12)=electrode_possible.y1(i,1:7);
```

```
electrode_position.y(2,6:12)=electrode_possible.y2(i,1:7);
elseif N==32
electrode_position.y(:,1:9)=electrode_average.y(:,1:9);
electrode_position.y(:,24:32)=electrode_average.y(:,24:32);
electrode_position.x=electrode_average.x;
electrode_position.y(1,10:24)=electrode_possible.y1(i,1:15);
electrode_position.y(2,10:24)=electrode_possible.y2(i,1:15);
end
end

%%
function Tissues=tissue_positions(Ventilation,Circulation,Tissues,Collapsion_areas)

%Returns each tissue position at current state (time) i
LL=Tissues.Left_lung;
LL.position=[LL.shape.empty(:,1)-LL.shape.step(:,1)*...
Ventilation.pulmocycle,LL.shape.empty(:,2)-LL.shape.step(:,2)*Ventilation.pulmocycle];
switch Collapsion_areas.collapsions.collapsion_left_lung
case 1
%fix collapsed area positions at the middle of empty and full
%positions
LL.position(14:16,1)=1/2*(LL.shape.empty(14:16,1)+LL.shape.full(14:16,1));
LL.position(14:16,2)=1/2*(LL.shape.empty(14:16,2)+LL.shape.full(14:16,2));
LL.position(1:4,1)=1/2*(LL.shape.empty(1:4,1)+LL.shape.full(1:4,1));
LL.position(1:4,2)=1/2*(LL.shape.empty(1:4,2)+LL.shape.full(1:4,2));
case 2
LL.position(14:16,1)=1/2*(LL.shape.empty(14:16,1)+LL.shape.full(14:16,1));
LL.position(14:16,2)=1/2*(LL.shape.empty(14:16,2)+LL.shape.full(14:16,2));
LL.position(1:3,1)=1/2*(LL.shape.empty(1:3,1)+LL.shape.full(1:3,1));
LL.position(1:3,2)=1/2*(LL.shape.empty(1:3,2)+LL.shape.full(1:3,2));
case 3
LL.position(15:16,1)=1/2*(LL.shape.empty(15:16,1)+LL.shape.full(15:16,1));
LL.position(15:16,2)=1/2*(LL.shape.empty(15:16,2)+LL.shape.full(15:16,2));
LL.position(1:3,1)=1/2*(LL.shape.empty(1:3,1)+LL.shape.full(1:3,1));
LL.position(1:3,2)=1/2*(LL.shape.empty(1:3,2)+LL.shape.full(1:3,2));
case 4
LL.position(16,1)=1/2*(LL.shape.empty(16,1)+LL.shape.full(16,1));
LL.position(16,2)=1/2*(LL.shape.empty(16,2)+LL.shape.full(16,2));
LL.position(1:2,1)=1/2*(LL.shape.empty(1:2,1)+LL.shape.full(1:2,1));
LL.position(1:2,2)=1/2*(LL.shape.empty(1:2,2)+LL.shape.full(1:2,2));
otherwise
%do nothing
end
%Substitution
Tissues.Left_lung=LL;

RL=Tissues.Right_lung;
RL.position=[RL.shape.empty(:,1)-RL.shape.step(:,1)*...
Ventilation.pulmocycle,RL.shape.empty(:,2)-RL.shape.step(:,2)*Ventilation.pulmocycle];
switch Collapsion_areas.collapsions.collapsion_right_lung
case 1
RL.position(12:15,1)=1/2*(RL.shape.empty(12:15,1)+RL.shape.full(12:15,1));
RL.position(12:15,2)=1/2*(RL.shape.empty(12:15,2)+RL.shape.full(12:15,2));
RL.position(1:2,1)=1/2*(RL.shape.empty(1:2,1)+RL.shape.full(1:2,1));
RL.position(1:2,2)=1/2*(RL.shape.empty(1:2,2)+RL.shape.full(1:2,2));
case 2
RL.position(14:15,1)=1/2*(RL.shape.empty(14:15,1)+RL.shape.full(14:15,1));
RL.position(14:15,2)=1/2*(RL.shape.empty(14:15,2)+RL.shape.full(14:15,2));
RL.position(1:2,1)=1/2*(RL.shape.empty(1:2,1)+RL.shape.full(1:2,1));
RL.position(1:2,2)=1/2*(RL.shape.empty(1:2,2)+RL.shape.full(1:2,2));
case 3
RL.position(14:15,1)=1/2*(RL.shape.empty(14:15,1)+RL.shape.full(14:15,1));
RL.position(14:15,2)=1/2*(RL.shape.empty(14:15,2)+RL.shape.full(14:15,2));
RL.position(1,1:2)=1/2*(RL.shape.empty(1,1:2)+RL.shape.full(1,1:2));
otherwise
%do nothing
end
%Substitution
Tissues.Right_lung=RL;

H=Tissues.Heart.exterior;
H.position=[H.shape.full(:,1)+H.shape.step(:,1)*...
Circulation.cardio_cycle,H.shape.full(:,2)+H.shape.step(:,2)*Circulation.cardio_cycle];
Tissues.Heart.exterior=H;
Hint=Tissues.Heart.interior;
Hint.position=[Hint.shape.full(:,1)+Hint.shape.step(:,1)*...
Circulation.cardio_cycle,Hint.shape.full(:,2)+Hint.shape.step(:,2)*Circulation.cardio_cycle];
```

```
Tissues.Heart.interior=Hint;

B=Tissues.Bones;
for bone=1:8
B_k=eval(['B.Bone',num2str(bone)]);
B_k.position=[B_k.shape.empty(:,1)-B_k.shape.step(:,1)*...
Ventilation.pulmocycle,B_k.shape.empty(:,2)-B_k.shape.step(:,2)*Ventilation.pulmocycle];
switch bone
case 1
B.Bone1=B_k;
case 2
B.Bone2=B_k;
case 3
B.Bone3=B_k;
case 4
B.Bone4=B_k;
case 5
B.Bone5=B_k;
case 6
B.Bone6=B_k;
case 7
B.Bone7=B_k;
case 8
B.Bone8=B_k;
end
%eval(['B.Bone',num2str(k)])=B_k;
end
Tissues.Bones=B;
end


function [assist_points,electrode_central_points,electrode_exterior_sides]=dynamic_geometry(N,electrodes,Tissues,Collapsion_areas,fileID)
%Takes the current step electrode and Tissue positions
%Generates the LUA code needed to design them in FEMM
%Returns the electode assist points from where the measurements are going
%to be taken later
LL=Tissues.Left_lung;
RL=Tissues.Right_lung;
H=Tissues.Heart;

if N==16 %only if 16 electrodes are used, arcs are needed
%otherwise they only increase the mesh nodes without important reason
angles1=[1 40 10 20 10 20 10 20 10 26 5 26 5 22.5 1 22.5 1];
len=length(angles1);
angles=[angles1 fliplr(angles1(1:len-1))];
end
d=electrodes.delec;
electrode_position=electrodes.position;
len=length(electrode_position.x);
% figure
% plot(electrode_position.x,electrode_position.y,'o')
% hold on
%add the electrode points
%add the electrode points
electrode_central_points=zeros(len,2);
electrode_exterior_sides=zeros(len,4);
extarc=5;
for i=1:len
fprintf(fileID,'ci_addnode(%4.2f,%4.2f)\n',electrode_position.x(1,i),electrode_position.y(1,i));
fprintf(fileID,'ci_addnode(%4.2f,%4.2f)\n',electrode_position.x(2,i),electrode_position.y(2,i));
%%%%
%add the exterior electrode volume points
%d=0.5;
x1=electrode_position.x(1,i);
y1=electrode_position.y(1,i);
x2=electrode_position.x(2,i);
y2=electrode_position.y(2,i);
a=-d*abs(x2-x1)*(y2-y1)/((x2-x1)*sqrt((x2-x1)^2+(y2-y1)^2));
b=d*abs(x2-x1)/sqrt((x2-x1)^2+(y2-y1)^2);
if y2>-3
x3=x1+a; y3=y1+b;
x4=x2+a; y4=y2+b;
else
x3=x1-a; y3=y1-b;
x4=x2-a; y4=y2-b;
end
electrode_central_points(i,:)=[(x1+x4)/2 (y1+y4)/2];
```

```
electrode_exterior_sides(i,:)=[x3 y3 x4 y4];
%      plot(x3,y3,'+')
%      hold on
%      plot(x4,y4,'+')
%      hold on
fprintf(fileID,'ci_addnode(%4.2f,%4.2f)\n',x3,y3);
fprintf(fileID,'ci_addnode(%4.2f,%4.2f)\n',x4,y4);
%connect (x1,y1) with (x3,y3), (x3,y3) with (x4,y4) and (x2,y2) with
%(x4,y4) (give dimensions to the electrodes)
fprintf(fileID,'ci_addsegment(%4.2f,%4.2f,%4.2f,%4.2f)\n',x1,y1,x3,y3);
fprintf(fileID,'ci_addarc(%4.2f,%4.2f,%4.2f,%4.2f,%4.2f,1)\n',x4,y4,x3,y3,extarc);
fprintf(fileID,'ci_addsegment(%4.2f,%4.2f,%4.2f,%4.2f)\n',x2,y2,x4,y4);
%%%%
end
%fprintf('%4.4f,%4.4f\n',electrode_central_points(8,1),electrode_central_points(8,2))

%connect the electrodes with arcs if N=16 or straight if N=32 or 64
for i=1:1:len
inext=i+1;
if i==len
inext=1;
end
if N==16
fprintf(fileID,'ci_addarc(%4.2f,%4.2f,%4.2f,%4.2f,%4.2f,1)\n',electrode_position.x(1,inext),electrode_position.y(1,inext),electrode_position.x(2,i),el
else
fprintf(fileID,'ci_addsegment(%4.2f,%4.2f,%4.2f,%4.2f)\n',electrode_position.x(1,inext),electrode_position.y(1,inext),electrode_position.x(2,i),electro
end
end
%connect the 2 points of each electrode with arcs
if N==16
for i=1:1:len
fprintf(fileID,'ci_addarc(%4.2f,%4.2f,%4.2f,%4.2f,%4.2f,1)\n',electrode_position.x(2,i),electrode_position.y(2,i),electrode_position.x(1,i),electrode_
end
else
for i=1:1:len
fprintf(fileID,'ci_addarc(%4.2f,%4.2f,%4.2f,%4.2f,%4.2f,1)\n',electrode_position.x(2,i),electrode_position.y(2,i),electrode_position.x(1,i),electrode_
end
end

%add the left_lung points and connect them
tissue_marker(fileID,LL.position);
%now add the segment that separates the main lung from the collapse area
%%add the LEFT lung's collapsed area
collapsed_boundary_maker(fileID,LL.position,Collapsion_areas.cross_points.left_lung);

%add the right_lung points and connect them
%add the left_lung points and connect them
tissue_marker(fileID,RL.position);
%%add the right lung's collapsed area
collapsed_boundary_maker(fileID,RL.position,Collapsion_areas.cross_points.right_lung);

%add the Heart's exterior points and connect them
tissue_marker(fileID,H.exterior.position);

%add the Heart's interior points and connect them
tissue_marker(fileID,H.interior.position);

%add each Bone's points and connect them
for k=1:8
B_k=eval(['Tissues.Bones.Bone' num2str(k)]);
tissue_marker(fileID,B_k.position);
end

%connect fat boundary points
B1p=Tissues.Bones.Bone1.position;
B2p=Tissues.Bones.Bone2.position;
%from 3rd point of 1st Bone to 1st point of 2nd Bone
fprintf(fileID,'ci_addsegment(%4.2f,%4.2f,%4.2f,%4.2f)\n',B1p(3,1),B1p(3,2),B2p(1,1),B2p(1,2));
B3p=Tissues.Bones.Bone3.position;
fprintf(fileID,'ci_addsegment(%4.2f,%4.2f,%4.2f,%4.2f)\n',B2p(4,1),B2p(4,2),B3p(1,1),B3p(1,2));
B4p=Tissues.Bones.Bone4.position;
fprintf(fileID,'ci_addsegment(%4.2f,%4.2f,%4.2f,%4.2f)\n',B3p(9,1),B3p(9,2),B4p(1,1),B4p(1,2));
B5p=Tissues.Bones.Bone5.position;
fprintf(fileID,'ci_addsegment(%4.2f,%4.2f,%4.2f,%4.2f)\n',B4p(4,1),B4p(4,2),B5p(2,1),B5p(2,2));
B6p=Tissues.Bones.Bone6.position;
fprintf(fileID,'ci_addsegment(%4.2f,%4.2f,%4.2f,%4.2f)\n',B5p(1,1),B5p(1,2),B6p(1,1),B6p(1,2));
B7p=Tissues.Bones.Bone7.position;
```

```
fprintf(fileID,'ci_addsegment(%4.2f,%4.2f,%4.2f,%4.2f)\n',B6p(4,1),B6p(4,2),B7p(1,1),B7p(1,2));
B8p=Tissues.Bones.Bone8.position;
fprintf(fileID,'ci_addsegment(%4.2f,%4.2f,%4.2f,%4.2f)\n',B7p(4,1),B7p(4,2),B8p(1,1),B8p(1,2));
fprintf(fileID,'ci_addsegment(%4.2f,%4.2f,%4.2f,%4.2f)\n',B8p(4,1),B8p(4,2),B1p(4,1),B1p(4,2));

%derive assist points
len=length(electrode_position.x);
assist_points=zeros(len,2);
for i=1:len
mid1=(electrode_position.x(1,i)+electrode_position.x(2,i))/2;
mid2=(electrode_position.y(1,i)+electrode_position.y(2,i))/2;
assist_points(i,:)=[mid1 mid2];
end
end

function []=tissue_marker(fileID,Positions)
% takes the specific tissue position points at the current time step
% writes the LUA code for the specific tissue design in FEMM
len=length(Positions);
for i=1:len
fprintf(fileID,'ci_addnode(%4.2f,%4.2f)\n',Positions(i,1),Positions(i,2));
if i>1
fprintf(fileID,'ci_addsegment(%4.2f,%4.2f,%4.2f,%4.2f)\n',Positions(i-1,1),Positions(i-1,2),Positions(i,1),Positions(i,2));
end
if i==len
fprintf(fileID,'ci_addsegment(%4.2f,%4.2f,%4.2f,%4.2f)\n',Positions(i,1),Positions(i,2),Positions(1,1),Positions(1,2));
end
end
end

function []=collapsed_boundary_maker(fileID,Position,Cross_points)
% takes the (R or L) lung's tissue position points at the current time step and
% the collapsion area's cross points
% writes the LUA code for the specific collapse area boundary design in FEMM
fprintf(fileID,'ci_addsegment(%4.2f,%4.2f,%4.2f,%4.2f)\n',Position(Cross_points(1),1),...
Position(Cross_points(1),2),Position(Cross_points(2),1),Position(Cross_points(2),2));
end

function[LLCC,RLCC,CALCC,CARCC,STCC,Xbone,Ybone,Xfat,Yfat,Xint,Yint,Xext,Yext]=...
addmaterial_labels(Tissues,Ventilation,Circulation,Collapsion_areas,fileID,r,k,electrode_central_points)
%adds material labels in a point that is in the corresponding tissue area
%(in FEMM)
%each tissue dynamic shape centroid is selected for the corresponding
%material label
%Left Lung Properties
[LLccx,LLccy]=find_centroid(Tissues.Left_lung.position);
fprintf(fileID,'ci_addblocklabel(%4.2f,%4.2f)\n',LLccx,LLccy);
fprintf(fileID,'ci_selectlabel(%4.2f,%4.2f)\n',LLccx, LLccy);
fprintf(fileID,'ci_setblockprop("Lungs_state_%d_%d",1,"<None>","<None>")\n',Ventilation.pulmocycle,Circulation.cardio_cycle);
fprintf(fileID,'ci_clearselected()\n');
%set left lung collapsion area
if Collapsion_areas.collapsions.collapsion_left_lung~=0
CACCL=Collapsion_areas.cross_points.left_lung;
CAL=[Tissues.Left_lung.position(CACCL(2):1:length(Tissues.Left_lung.position(:,1)),:); Tissues.Left_lung.position(1:CACCL(1),:)];
[CALccx,CALccy]=find_centroid(CAL);
CALCC=[CALccx CALccy];
fprintf(fileID,'ci_addblocklabel(%4.2f,%4.2f)\n',CALccx,CALccy);
fprintf(fileID,'ci_selectlabel(%4.2f,%4.2f)\n',CALccx,CALccy);
fprintf(fileID,'ci_setblockprop("Lungs",1,"<None>","<None>")\n');
fprintf(fileID,'ci_clearselected()\n');
else
CALCC=[];
end
%Right Lung Properties
[RLccx,RLccy]=find_centroid(Tissues.Right_lung.position);
fprintf(fileID,'ci_addblocklabel(%4.2f,%4.2f)\n',RLccx,RLccy);
fprintf(fileID,'ci_selectlabel(%4.2f,%4.2f)\n',RLccx,RLccy);
fprintf(fileID,'ci_setblockprop("Lungs_state_%d_%d",1,"<None>","<None>")\n',Ventilation.pulmocycle,Circulation.cardio_cycle);
fprintf(fileID,'ci_clearselected()\n');
if Collapsion_areas.collapsions.collapsion_right_lung~=0
%set right lung collapsion area
CACCR=Collapsion_areas.cross_points.right_lung;
CAR=[Tissues.Right_lung.position(CACCR(2):1:length(Tissues.Right_lung.position(:,1)),:); Tissues.Right_lung.position(1:CACCR(1),:)];
[CARccx,CARccy]=find_centroid(CAR);
CARCC=[CARccx CARccy];
fprintf(fileID,'ci_addblocklabel(%4.2f,%4.2f)\n',CARccx,CARccy);
fprintf(fileID,'ci_selectlabel(%4.2f,%4.2f)\n',CARccx,CARccy);
```

```
fprintf(fileID,'ci_setblockprop("Lungs",1,"<None>","<None>")\n');
fprintf(fileID,'ci_clearselected()\n');
else
CARCC=[];
end

%Internal Heart Properties
IntPos=Tissues.Heart.interior.position;
Xint=(IntPos(1,1)+IntPos(5,1))/2;
Yint=(IntPos(1,2)+IntPos(5,2))/2;

fprintf(fileID,'ci_addblocklabel(%4.2f,%4.2f)\n',Xint,Yint);
fprintf(fileID,'ci_selectlabel(%4.2f,%4.2f)\n',Xint,Yint);
fprintf(fileID,'ci_setblockprop("Heart_state_%d",1,"<None>","<None>")\n',Circulation.cardio_cycle);
fprintf(fileID,'ci_clearselected()\n');

%External Heart Properties
ExPose=Tissues.Heart.exterior.position;
Xext=(ExPose(4,1)+ExPose(9,1))/2;
Yext=(ExPose(4,2)+ExPose(9,2))/2;

fprintf(fileID,'ci_addblocklabel(%4.2f,%4.2f)\n',Xext,Yext);
fprintf(fileID,'ci_selectlabel(%4.2f,%4.2f)\n',Xext,Yext);
fprintf(fileID,'ci_setblockprop("Miocardium",1,"<None>","<None>")\n');
fprintf(fileID,'ci_clearselected()\n');


%Bone properties
%Bone 7 (down)
Bonepos7=Tissues.Bones.Bone7.position;
[Xbone7,Ybone7]=find_centroid(Bonepos7);
fprintf(fileID,'ci_addblocklabel(%4.2f,%4.2f)\n',Xbone7,Ybone7);
fprintf(fileID,'ci_selectlabel(%4.2f,%4.2f)\n',Xbone7,Ybone7);
fprintf(fileID,'ci_setblockprop("Bone",1,"<None>","<None>")\n');
fprintf(fileID,'ci_clearselected()\n');

%Bone 6
Bonepos6=Tissues.Bones.Bone6.position;
[Xbone6,Ybone6]=find_centroid(Bonepos6);
fprintf(fileID,'ci_addblocklabel(%4.2f,%4.2f)\n',Xbone6,Ybone6);
fprintf(fileID,'ci_selectlabel(%4.2f,%4.2f)\n',Xbone6,Ybone6);
fprintf(fileID,'ci_setblockprop("Bone",1,"<None>","<None>")\n');
fprintf(fileID,'ci_clearselected()\n');

%Bone 5
Bonepos5=Tissues.Bones.Bone5.position;
[Xbone5,Ybone5]=find_centroid(Bonepos5);
fprintf(fileID,'ci_addblocklabel(%4.2f,%4.2f)\n',Xbone5,Ybone5);
fprintf(fileID,'ci_selectlabel(%4.2f,%4.2f)\n',Xbone5,Ybone5);
fprintf(fileID,'ci_setblockprop("Bone",1,"<None>","<None>")\n');
fprintf(fileID,'ci_clearselected()\n');

%Bone 4
Bonepos4=Tissues.Bones.Bone4.position;
[Xbone4,Ybone4]=find_centroid(Bonepos4);
fprintf(fileID,'ci_addblocklabel(%4.2f,%4.2f)\n',Xbone4,Ybone4);
fprintf(fileID,'ci_selectlabel(%4.2f,%4.2f)\n',Xbone4,Ybone4);
fprintf(fileID,'ci_setblockprop("Bone",1,"<None>","<None>")\n');
fprintf(fileID,'ci_clearselected()\n');

%Bone 3
Bonepos3=Tissues.Bones.Bone3.position;
[Xbone3,Ybone3]=find_centroid(Bonepos3);
fprintf(fileID,'ci_addblocklabel(%4.2f,%4.2f)\n',Xbone3,Ybone3);
fprintf(fileID,'ci_selectlabel(%4.2f,%4.2f)\n',Xbone3,Ybone3);
fprintf(fileID,'ci_setblockprop("Bone",1,"<None>","<None>")\n');
fprintf(fileID,'ci_clearselected()\n');

%Bone 2
Bonepos2=Tissues.Bones.Bone2.position;
[Xbone2,Ybone2]=find_centroid(Bonepos2);
fprintf(fileID,'ci_addblocklabel(%4.2f,%4.2f)\n',Xbone2,Ybone2);
fprintf(fileID,'ci_selectlabel(%4.2f,%4.2f)\n',Xbone2,Ybone2);
fprintf(fileID,'ci_setblockprop("Bone",1,"<None>","<None>")\n');
fprintf(fileID,'ci_clearselected()\n');

%Bone 1
```

```
Bonepos1=Tissues.Bones.Bone1.position;
[Xbone1,Ybone1]=find_centroid(Bonepos1);
fprintf(fileID,'ci_addblocklabel(%4.2f,%4.2f)\n',Xbone1,Ybone1);
fprintf(fileID,'ci_selectlabel(%4.2f,%4.2f)\n',Xbone1,Ybone1);
fprintf(fileID,'ci_setblockprop("Bone",1,"<None>","<None>")\n');
fprintf(fileID,'ci_clearselected()\n');

%Bone 8
Bonepos8=Tissues.Bones.Bone8.position;
[Xbone8,Ybone8]=find_centroid(Bonepos8);
fprintf(fileID,'ci_addblocklabel(%4.2f,%4.2f)\n',Xbone8,Ybone8);
fprintf(fileID,'ci_selectlabel(%4.2f,%4.2f)\n',Xbone8,Ybone8);
fprintf(fileID,'ci_setblockprop("Bone",1,"<None>","<None>")\n');
fprintf(fileID,'ci_clearselected()\n');

Xbone=[Xbone1 Xbone2 Xbone3 Xbone4 Xbone5 Xbone6 Xbone7 Xbone8];
Ybone=[Ybone1 Ybone2 Ybone3 Ybone4 Ybone5 Ybone6 Ybone7 Ybone8];

% STccx=-k*6.7;
% STccy=-k*15.5;
STccx=(Xbone(6)+Tissues.Left_lung.position(15,1))/2;
STccy=(Ybone(6)+Tissues.Left_lung.position(15,2))/2;
fprintf(fileID,'ci_addblocklabel(%4.2f,%4.2f)\n',STccx,STccy);
fprintf(fileID,'ci_selectlabel(%4.2f,%4.2f)\n',STccx,STccy);
fprintf(fileID,'ci_setblockprop("Soft_tissue_state_%d",1,"<None>","<None>")\n',Circulation.cardio_cycle);
fprintf(fileID,'ci_clearselected()\n');
STCC=[STccx STccy];

Xfat=(Bonepos6(3,1)+Bonepos7(2,1))/2;
Yfat=(Bonepos6(3,2)+Bonepos7(2,2))/2;
%fat properties
fprintf(fileID,'ci_addblocklabel(%4.2f,%4.2f)\n',Xfat,Yfat);
fprintf(fileID,'ci_selectlabel(%4.2f,%4.2f)\n',Xfat,Yfat);
fprintf(fileID,'ci_setblockprop("Fat",1,"<None>","<None>")\n');
fprintf(fileID,'ci_clearselected()\n');

%%%electrodes
for electrode=1:length(electrode_central_points(:,1))
fprintf(fileID,'ci_addblocklabel(%4.2f,%4.2f)\n',...
electrode_central_points(electrode,1),electrode_central_points(electrode,2));
fprintf(fileID,'ci_selectlabel(%4.2f,%4.2f)\n',...
electrode_central_points(electrode,1),electrode_central_points(electrode,2));
fprintf(fileID,'ci_setblockprop("Zelectrode%2.0f",1,"<None>","<None>")\n',electrode);
fprintf(fileID,'ci_clearselected()\n');
end

LLCC=[LLccx LLccy];
RLCC=[RLccx RLccy];

end

function [ccx,ccy]=find_centroid(Shape)
polyShape=polyshape([Shape(:,1); Shape(1,1)],[Shape(:,2); Shape(1,2)]);
[ccx,ccy]=centroid(polyShape);
end

function set_current_source(N,skipcurr,assist_points,count,fileID,electrode_exterior_sides)
k=skipcurr+1;
%set input current electrode
% fprintf(fileID,'ci_selectarcsegment(%4.2f,%4.2f)\n',assist_points(count,1),assist_points(count,2));
% fprintf(fileID,'ci_setarcsegmentprop(4,"<None>",0,"<None>","Iin")\n');
% fprintf(fileID,'ci_clearselected()\n');
fprintf(fileID,'ci_selectarcsegment(%4.2f,%4.2f)\n',(electrode_exterior_sides(count,1)+electrode_exterior_sides(count,3))/2,...
(electrode_exterior_sides(count,2)+electrode_exterior_sides(count,4))/2);
fprintf(fileID,'ci_setarcsegmentprop(4,"<None>",0,"<None>","Iin")\n');
fprintf(fileID,'ci_clearselected()\n');
% fprintf(fileID,'ci_selectsegment(%4.2f,%4.2f)\n',(electrode_exterior_sides(count,1)+electrode_exterior_sides(count,3))/2,...
%     (electrode_exterior_sides(count,2)+electrode_exterior_sides(count,4))/2);
% fprintf(fileID,'ci_setsegmentprop(4,"<None>",0,"<None>","Iin")\n');
% fprintf(fileID,'ci_clearselected()\n');
if count+k<=N
next=count+k;
else
next=count+k-N;
end
%set output current electrode
% fprintf(fileID,'ci_selectarcsegment(%4.2f,%4.2f)\n',assist_points(next,1),assist_points(next,2));
```

```
% fprintf(fileID,'ci_setarcsegmentprop(4,"<None>",0,"<None>","Iout")\n');
% fprintf(fileID,'ci_clearselected()\n');
fprintf(fileID,'ci_selectarcsegment(%4.2f,%4.2f)\n',(electrode_exterior_sides(next,1)+electrode_exterior_sides(next,3))/2,...
(electrode_exterior_sides(next,2)+electrode_exterior_sides(next,4))/2);
fprintf(fileID,'ci_setarcsegmentprop(4,"<None>",0,"<None>","Iin")\n');
fprintf(fileID,'ci_clearselected()\n');
% fprintf(fileID,'ci_selectsegment(%4.2f,%4.2f)\n',(electrode_exterior_sides(next,1)+electrode_exterior_sides(next,3))/2,...
%     (electrode_exterior_sides(next,2)+electrode_exterior_sides(next,4))/2);
% fprintf(fileID,'ci_setsegmentprop(4,"<None>",0,"<None>","Iout")\n');
% fprintf(fileID,'ci_clearselected()\n');
end

function set_reference(N,skipcurr,assist_points,count,fileID,electrode_exterior_sides)
k=skipcurr+1;
%set a ground reference
if count+k+1<=N
ref=count+k+1;
else
ref=count+k+1-N;
end
% fprintf(fileID,'ci_selectarcsegment(%4.2f,%4.2f)\n',assist_points(ref,1),assist_points(ref,2));
% fprintf(fileID,'ci_setarcsegmentprop(4,"Ground",0,"<None>","<None>")\n');
% fprintf(fileID,'ci_clearselected()\n');
fprintf(fileID,'ci_selectarcsegment(%4.2f,%4.2f)\n',(electrode_exterior_sides(ref,1)+electrode_exterior_sides(ref,3))/2,...
(electrode_exterior_sides(ref,2)+electrode_exterior_sides(ref,4))/2);
fprintf(fileID,'ci_setarcsegmentprop(4,"Ground",0,"<None>","<None>")\n');
fprintf(fileID,'ci_clearselected()\n');
% fprintf(fileID,'ci_selectsegment(%4.2f,%4.2f)\n',(electrode_exterior_sides(ref,1)+electrode_exterior_sides(ref,3))/2,...
%     (electrode_exterior_sides(ref,2)+electrode_exterior_sides(ref,4))/2);
% fprintf(fileID,'ci_setsegmentprop(4,"Ground",0,"<None>","<None>")\n');
% fprintf(fileID,'ci_clearselected()\n');
end

function []=save_process(d,fileID,folds)
fprintf(fileID,'ci_saveas("%s%s_test%.0f.fee")\n',folds,date(),d);
fprintf(fileID,'ci_createmesh()\n');
fprintf(fileID,'ci_saveas("%s%s_test%.0f.fee")\n',folds,date(),d);
fprintf(fileID,'ci_saveas("%s%s_test%.0f.fec")\n',folds,date(),d);
fprintf(fileID,'ci_analyze(0)\n');
fprintf(fileID,'ci_loadsolution()\n');
end

function measure_voltages(N,electrode_position,d,timestep,fileID,electrode_exterior_sides,folds)
%writes LUA commands in order to measure the electrode voltages
o=[];
for i=1:N
fprintf(fileID,'co_addcontour(%4.2f,%4.2f)\n',electrode_exterior_sides(i,1),electrode_exterior_sides(i,2));
fprintf(fileID,'co_addcontour(%4.2f,%4.2f)\n',electrode_exterior_sides(i,3),electrode_exterior_sides(i,4));
fprintf(fileID,'co_makeplot(0,10,0)\n');
fprintf(fileID,'co_makeplot(0,%.0f,"%s%s_test%.0f_Voltages%d_%d.txt",0)\n',N,folds,date(),d,timestep,i);
fprintf(fileID,'co_clearcontour()\n');
end
fprintf(fileID,'co_close()\n');
fprintf(fileID,'ci_purgemesh()\n');
pause(0.1)
end

function [Ventilation,Circulation,total_positions,times,Silences,Tissues,electrodes,r,k]=...
update_cycle_states(N,Ventilation,Circulation,...
total_positions,times,Silences,Tissues,time,electrodes,r,k,frequency,end_Admittances,delec,randomcond)
%updates breath and cardiac cycle indicators
%updates breath and cardiac cycle durations and tissues discrete positions
%after the end of a correspoding cycle
%called in each for loop iteration

Ventilation.pulmocycle=Ventilation.pulmocycle+Ventilation.pulmcounter;
Circulation.cardio_cycle=Circulation.cardio_cycle+Circulation.cardcounter;

% plot(time,Ventilation.pulmocycle,'b*')
% hold on
% plot(time,Circulation.cardio_cycle,'r*')
% hold on
% if pulmonary cycle reaches left/right limit, change the indicator
if Ventilation.pulmocycle>total_positions.total_positions-1
Ventilation.pulmcounter=-Ventilation.pulmcounter;
end
% if pulmonary cycle is at 1 and breath pausing has not started
```

```
% start the pause duration
if (Ventilation.pulmocycle<2)&&(Silences.silence==0)
%relaxing time between 0 and 1 seconds
if randomcond==1
Silences.relaxing_time=rand(1);
else
Silences.relaxing_time=0.3;
end
%pause breathing
Silences.silence=1;
%store the time point pause started
Silences.time_sil_start=time;
% zero the indicator during relaxing time
Ventilation.pulmcounter=0;
end
% if relaxing time has come to an end
% stop pausing and redefine breathig time
if (Silences.time_sil_start+Silences.relaxing_time<=time)&&(Silences.silence==1)
%breath period will change up to 20% at upcoming cycle
if randomcond==1
times.tbr=times.tbr+0.2*2*(round(rand(1,1))-1)*rand(1)*times.tbr;
else
times.tbr=1.2*times.tbr;
end
%%positive pulmonary cycle indicator
%to start the upcoming breath cycle
Ventilation.pulmcounter=1;
%stop pausing
Silences.silence=0;
%no more relax!
Silences.time_sil_start=-1;
Silences.relaxing_time=-1;
%new position step for tissues
total_positions.dy=2*1*times.tim/(N*times.tbr); %DY=1
%which changes total possible positions
%not their boundaries
%but their possible positions!
total_positions.total_positions=1/total_positions.dy+1; %Dy=1
%this either changes the possible tissue conductivities states!!
%and either the tissue possible positions!!
%(lungs and front bones)
[Tissues.Left_lung,Tissues.Right_lung,Tissues.Heart,Tissues.Muscles,Tissues.Bones,r,k]=...
define_tissues(r,k,times,total_positions,1,frequency,end_Admittances,randomcond,Tissues);
fprintf('Positions have been redefined!\n');
%either the possible (but not the limits) of the electrode
%positions!
[electrodes.electrode_average,electrodes.electrode_possible]=electrodes_preset(N,1,total_positions.dy,delec,k); %Dy=1
%and either the tissue possible positions!!
%(lungs and front bones)
end
%if cardio cycle reaches left/right limit
%change the indicator
if Circulation.cardio_cycle>times.pulse_dur-1
Circulation.cardcounter=-Circulation.cardcounter;
end
if Circulation.cardio_cycle<2
%if left limit reached
%change the indicator
Circulation.cardcounter=-Circulation.cardcounter;
%and add one cardio beat!
Silences.cardiobeats=Silences.cardiobeats+1;
fpulse=1/times.Tpulse;
if mod(Silences.cardiobeats,3)==0 %heart rythm change up to 3% each 3 beats
%define new heart rythm every start after 3 cardio beats
if randomcond==1
fpulse=fpulse+0.03*2*(round(rand(1,1))-1)*rand(1)*fpulse;
else
fpulse=fpulse*1.03;
end
times.Tpulse=1/fpulse;
%redefining the cardio frequency
%ALSO leads to redefine the possible tissue conductivity
%states!
%and positions! (of the heart)
%but not any change at limits!
%increasing frequency leads to less positions
%they have less time to come across the limits
```

```
%thus they have to "jump" more
%this increases the step!
%and decreases the kwantized positions
fprintf('Cardio has been redefined!\n');
times.pulse_dur=2*total_positions.total_positions*(times.tbr/times.Tpulse)^(-1);
[Tissues.Left_lung,Tissues.Right_lung,Tissues.Heart,Tissues.Muscles,Tissues.Bones,r,k]=...
define_tissues(r,k,times,total_positions,1,frequency,end_Admittances,randomcond,Tissues);
end
end
end

function []=unset_current_source(N,fileID,k,assist_points,count,electrode_exterior_sides)
%unset input current electrode
% fprintf(fileID,'ci_selectarcsegment(%4.2f,%4.2f)\n',assist_points(count,1),assist_points(count,2));
% fprintf(fileID,'ci_setarcsegmentprop(4,"<None>",0,"<None>","<None>")\n');
% fprintf(fileID,'ci_clearselected()\n');
fprintf(fileID,'ci_selectarcsegment(%4.2f,%4.2f)\n',(electrode_exterior_sides(count,1)+electrode_exterior_sides(count,3))/2,...
(electrode_exterior_sides(count,2)+electrode_exterior_sides(count,4))/2);
fprintf(fileID,'ci_setarcsegmentprop(4,"<None>",0,"<None>","None")\n');
fprintf(fileID,'ci_clearselected()\n');
if count+k<=N
next=count+k;
else
next=count+k-N;
end
%unset output current electrode
% fprintf(fileID,'ci_selectarcsegment(%4.2f,%4.2f)\n',assist_points(next,1),assist_points(next,2));
% fprintf(fileID,'ci_setarcsegmentprop(4,"<None>",0,"<None>","<None>")\n');
% fprintf(fileID,'ci_clearselected()\n');
fprintf(fileID,'ci_selectarcsegment(%4.2f,%4.2f)\n',(electrode_exterior_sides(next,1)+electrode_exterior_sides(next,3))/2,...
(electrode_exterior_sides(next,2)+electrode_exterior_sides(next,4))/2);
fprintf(fileID,'ci_setarcsegmentprop(4,"<None>",0,"<None>","None")\n');
fprintf(fileID,'ci_clearselected()\n');
end

function unset_reference(N,fileID,k,assist_points,count,electrode_exterior_sides)
%unset  ground reference
if count+k+1<=N
ref=count+k+1;
else
ref=count+k+1-N;
end
% fprintf(fileID,'ci_selectarcsegment(%4.2f,%4.2f)\n',assist_points(ref,1),assist_points(ref,2));
% fprintf(fileID,'ci_setarcsegmentprop(4,"<None>",0,"<None>","<None>")\n');
% fprintf(fileID,'ci_clearselected()\n');
fprintf(fileID,'ci_selectarcsegment(%4.2f,%4.2f)\n',(electrode_exterior_sides(ref,1)+electrode_exterior_sides(ref,3))/2,...
(electrode_exterior_sides(ref,2)+electrode_exterior_sides(ref,4))/2);
fprintf(fileID,'ci_setarcsegmentprop(4,"<None>",0,"<None>","None")\n');
fprintf(fileID,'ci_clearselected()\n');
end

function []=undo_dynamic_geometry(Tissues,fileID,electrode_position,electrode_exterior_sides)
len=length(electrode_position.x);
LL=Tissues.Left_lung.position;
RL=Tissues.Right_lung.position;
H=Tissues.Heart.exterior.position;
Hint=Tissues.Heart.interior.position;
B=Tissues.Bones;
%select the electrode points
for i=1:len
fprintf(fileID,'ci_selectnode(%4.2f,%4.2f)\n',electrode_position.x(1,i),electrode_position.y(1,i));
fprintf(fileID,'ci_selectnode(%4.2f,%4.2f)\n',electrode_position.x(2,i),electrode_position.y(2,i));
end
%select the left_lung points
len=length(LL);
for i=1:len
fprintf(fileID,'ci_selectnode(%4.2f,%4.2f)\n',LL(i,1),LL(i,2));
end
%select the right_lung points
len=length(RL);
for i=1:len
fprintf(fileID,'ci_selectnode(%4.2f,%4.2f)\n',RL(i,1),RL(i,2));
end
%select the Heart's points
len=length(H);
for i=1:len
fprintf(fileID,'ci_selectnode(%4.2f,%4.2f)\n',H(i,1),H(i,2));
```

```
end
len=length(Hint);
for i=1:len
fprintf(fileID,'ci_selectnode(%4.2f,%4.2f)\n',Hint(i,1),Hint(i,2));
end
%select each Bone's points
for k=1:8
len=length(eval(['B.Bone' num2str(k) '.position(:,1)']));
for i=1:len
fprintf(fileID,'ci_selectnode(%4.2f,%4.2f)\n',eval(['B.Bone' num2str(k) '.position(i,1)']),eval(['B.Bone' num2str(k) '.position(i,2)']));
end
end
%%%select electrode external points
for electrode=1:length(electrode_exterior_sides(:,1))
fprintf(fileID,'ci_selectnode(%4.2f,%4.2f)\n',...
electrode_exterior_sides(electrode,1),electrode_exterior_sides(electrode,2));
fprintf(fileID,'ci_selectnode(%4.2f,%4.2f)\n',...
electrode_exterior_sides(electrode,3),electrode_exterior_sides(electrode,4));
end
%delete all selected nodes (with their segments and arcs)
fprintf(fileID,'ci_deleteselectednodes()\n');
end

function []=clear_labels(fileID,LLCC,RLCC,CALCC,CARCC,STCC,Xbone,Ybone,...
Xfat,Yfat,Xint,Yint,Xext,Yext,electrode_central_points)
fprintf(fileID,'ci_selectlabel(%4.2f,%4.2f)\n',LLCC(1), LLCC(2));
fprintf(fileID,'ci_selectlabel(%4.2f,%4.2f)\n',RLCC(1), RLCC(2));
fprintf(fileID,'ci_selectlabel(%4.2f,%4.2f)\n',Xint,Yint);
fprintf(fileID,'ci_selectlabel(%4.2f,%4.2f)\n',Xext,Yext);
fprintf(fileID,'ci_selectlabel(%4.2f,%4.2f)\n',Xbone(1),Ybone(1));
fprintf(fileID,'ci_selectlabel(%4.2f,%4.2f)\n',Xbone(2),Ybone(2));
fprintf(fileID,'ci_selectlabel(%4.2f,%4.2f)\n',Xbone(3),Ybone(3));
fprintf(fileID,'ci_selectlabel(%4.2f,%4.2f)\n',Xbone(4),Ybone(4));
fprintf(fileID,'ci_selectlabel(%4.2f,%4.2f)\n',Xbone(5),Ybone(5));
fprintf(fileID,'ci_selectlabel(%4.2f,%4.2f)\n',Xbone(6),Ybone(6));
fprintf(fileID,'ci_selectlabel(%4.2f,%4.2f)\n',Xbone(7),Ybone(7));
fprintf(fileID,'ci_selectlabel(%4.2f,%4.2f)\n',Xbone(8),Ybone(8));
if ~isempty(CALCC)
fprintf(fileID,'ci_selectlabel(%4.2f,%4.2f)\n',CALCC(1),CALCC(2));
end
if ~isempty(CARCC)
fprintf(fileID,'ci_selectlabel(%4.2f,%4.2f)\n',CARCC(1),CARCC(2));
end
fprintf(fileID,'ci_selectlabel(%4.2f,%4.2f)\n',STCC(1),STCC(2));
fprintf(fileID,'ci_selectlabel(%4.2f,%4.2f)\n',-6,-11.85);
fprintf(fileID,'ci_selectlabel(%4.2f,%4.2f)\n',Xfat,Yfat);
for electrode=1:length(electrode_central_points(:,1))
fprintf(fileID,'ci_selectlabel(%4.4f,%4.4f)\n',...
electrode_central_points(electrode,1),electrode_central_points(electrode,2));
end
%fprintf('%4.4f,%4.4f\n',electrode_central_points(8,1),electrode_central_points(8,2))
fprintf(fileID,'ci_deleteselectedlabels()\n');
end

function [letterplus,Gr]=configure_graph(Graph,frames,fps,total_time_est,path2save)
[Gr,time]=plot_graph(Graph,frames,fps,total_time_est);
letterplus=save_graph(Graph,time,path2save);
fprintf('Please open a FEMM project!\n')
fprintf('Then load the corresponding LUA file and press enter\n')
pause()
end

function [Gr,time]=plot_graph(Graph,frames,fps,total_time_est)
Gr=figure(1);
subplot(2,1,1)
time=linspace(0, total_time_est,length(Graph.heart.conductivity));
plot(time,Graph.heart.conductivity,'r','LineWidth',2)
hold on
Graph.right_lung.conductivity=Graph.left_lung.conductivity;
plot(time,Graph.right_lung.conductivity,'b','LineWidth',2)
hold on
plot(time,Graph.left_lung.conductivity,'g--','LineWidth',2)
hold on
plot(time,Graph.muscles.conductivity(1:end),'y','LineWidth',2)
hold on
TGr=title('Tissues conductivity (S/m)');
TGr.FontSize=16;
```

```
legend('\sigma_{heart}','\sigma_{right lung}','\sigma_{left lung}','\sigma_{muscles}')
ylabel('\sigma (Sm^-^1)','Fontsize',14)
xlabel('Time (seconds)','Fontsize',14)
subplot(2,1,2)
plot(time,Graph.heart.permittivity,'r','LineWidth',2)
hold on
Graph.right_lung.permittivity=Graph.left_lung.permittivity;
plot(time,Graph.right_lung.permittivity,'b','LineWidth',2)
hold on
plot(time,Graph.left_lung.permittivity,'b','LineWidth',2)
hold on
plot(time,Graph.muscles.permittivity(1:end),'y','LineWidth',2)
TGr=title('Tissues permittivity (F/m)');
TGr.FontSize=16;
legend('\epsilon_{heart}','\epsilon_{right lung}','\epsilon_{left lung}','\epsilon_{muscles}')
ylabel('\epsilon (Fm^-^1)','Fontsize',14)
xlabel('Time (seconds)','Fontsize',14)
end


function [letterplus]=save_graph(Graph,time,path2save)
letterplus='a';
for letter='a':'z'
filetosearch=[path2save 'Cardio-Pulmonary\Input_set_',num2str(date()),'_',num2str(letter),'.mat'];
if exist(filetosearch)
letterplus=char(letter+1);
end
end
Inputs_dat.Graph=Graph;
Inputs_dat.time=time;
save([path2save 'Dynamic_Thorax_Model\Cardio-Pulmonary\Input_set_',num2str(date()),'_',num2str(letterplus),'.mat'],'Inputs_dat');
end

function [Measurements]=configure_measurements(N,letterplus,currentskip,voltageskip,timesteps,d,path2save,path)
%% press everything to get the measurements!
% get the measurements from the files written during the timer loop
Measurements=get_measurements(N,voltageskip,d,timesteps,path);
l1=length(Measurements);
%disp(l1)
nk=mod(l1,N*N);
%hold integer cycles
Measurements=Measurements(1:end-nk);
%and save them
save([path2save 'Dynamic_Thorax_Model\Cardio-Pulmonary\Measurement_set_',num2str(date()),'_',num2str(letterplus),'.mat'],'Measurements');
end

function M=get_measurements(N,voltageskip,d,timestep,path)
M=[];
voltageskip=voltageskip+1;
for j=1:timestep-1
M1=[];
modulo=mod(j,N);
if modulo==0
modulo=N;
end
for i=1:N
folder=[path '\Dynamic_Thorax_Model\LUA_files\Temporary\'];
prefix_data=[date(),'_test',num2str(d),'_Voltages',num2str(j),'_',num2str(i)];
dataformat='.txt';
filetoread=strcat(folder,prefix_data,dataformat);
while exist(filetoread)==0
fprintf('ERROR! Measurements File missing!:')
filetoread
fprintf('\nPress anything to continue!')
pause()
end
T1=dlmread(filetoread,'\t',4,0);
delete(filetoread);
N1=T1(:,2);
meas=mean(N1(2:end-1));
meas1=N1(length(N1)/2);
meas=max(meas,meas1);
%bad electrode!
%if badelectrodes(i)==1||badelectrodes(modulo)==1
%    meas=meas*2*rand(1,1);
%end
M1=[M1 meas];
```

```
end
if voltageskip==1
M1=[-diff(M1) M1(N)-M1(1)];
else
M2=zeros(1,N);
for i=1:N
if i+voltageskip<=N
M2(i)=M1(i)-M1(i+voltageskip);
else
M2(i)=M1(i)-M1(N-i+voltageskip);
end
end
M1=M2;
end
M=[M M1];
end
oo=[];
end

function Patient_labeled_data=complete_patient_labeled_data(Graph,Collapsion_areas,History_of_tissues)

Patient_labeled_data=1;
end

%%%=======================================
function[imageC]=Gauss_Newton_Reconstruction(N,skipcurr,skipvolt,hyperparameter,H,meascur,geometry,recons,solver,prior,Vref)
%%%Performs Gauss-Newton EIT Reconstruction. Requires the EIDORS library
%%%tool
%%%%Inputs:
%N: Electrode Number
%skipcurr: Current skip-m protocol
%skipvolt: Voltage skip-n protocol
%hyperparameter: regularization hyperparameter (lambda)
%H: measurement frame, a N^2X1 collumn vector
%measucur: if set to 0: only tetrapolar measurements. If set to 1:
%Tetrapolar and bipolar measurements, including current source electrodes
%geometry: reconstruction model geometry. If 1: circular disk. If 2:
%thoracic boundary
%recons: Nodal/element reconstruction. 1 for one step nodal solver with Laplace prior
%2 for element-wise solvers.
% prior: reconstruction algorithm/ prior. Works only with elementwise
% reconstruction here. 1 for Gauss-Newton iterative approach. 2 for
% One-Step NOSER prior approach. 3 for Total Variation iterative approach
%solver: 1 for 'absolute', 2 for 'differential'
%Vref: reference measurement frame, a N^2X1 collumn vector


if meascur==1
opt={'meas_current'};
else
opt={'no_meas_current'};
end
if geometry==1
imdl = mk_common_model ('d2d1c',N);
elseif geometry==2
if N==16
imdl=mk_common_model('d2T3',N);
elseif N==32
imdl=mk_common_model('d2T3',32);
elseif N==64
imdl=mk_common_model('h2T3',64);
end
end
if N==32
[st, els]= mk_stim_patterns (N,1,[0 skipcurr+1],[0 skipvolt+1;],opt,0.185);
else
[st, els]= mk_stim_patterns (N,1,[0 skipcurr+1],[0 skipvolt+1;],opt,10);
end

imdl.fwd_model.stimulation= st;
imdl.fwd_model.meas_select= els;
if solver==1
imdl.reconst_type = 'absolute';
elseif solver==2
imdl.reconst_type = 'difference';
img = mk_image(imdl, 1);
if isempty(Vref)
```

```
vh = fwd_solve(img);
Hl=vh.meas;
else
vh=Vref;
Hl=vh;
end
end
if N~=16
H=H(find(imdl.fwd_model.meas_select~=0));

end
imdl.hyperparameter.value = hyperparameter;
if recons==1
imdl.solve=@nodal_solve;
imdl.RtR_prior = @prior_laplace;
elseif recons==2
if prior==1
imdl.solve = @inv_solve_abs_GN;
imdl.RtR_prior = @prior_laplace;
imdl.inv_solve_gn.max_iterations = 120;
elseif prior==2
imdl.solve=@inv_solve_diff_GN_one_step;
imdl.RtR_prior= @prior_noser;
imdl.jacobian_bkgnd.value= 1;
elseif prior==3
imdl.solve=       @inv_solve_TV_pdipm;
imdl.R_prior=     @prior_TV;
imdl.parameters.term_tolerance= 1e-3;
imdl.parameters.keep_iterations= 0;
else
while prior~=1&&prior~=2&&prior~=3
fprintf('Press:\n')
fprintf('1 for Iterative Gauss Newton\n')
fprintf('2 for NOSER reconstruction\n')
fprintf('3 for Total Variation\n')
msg='Selection: ';
prior=input(msg);
end
end
end
if solver==1
imageC = inv_solve(imdl,H);
else
imageC = inv_solve(imdl,H,Hl);
end
show=0;
if show==1
show_fem(imageC,1)
caxis([-0.275 0.275])
axis off
end
end
```

```
%%%%reconstruction_and_functional_analysis.m
%%==============================
%%%%load the measurements%%%%
N=16;
clear rawimagedata RLimagedata RRimagedata Himagedata MRLimagedata MRRimagedata MHimagedata
clear imageCN
%%%%skip-m current pattern
skipcurr=2;
%%%%skip-n voltage pattern
skipvolt=0;
if exist('Measurements')~=1
error('please import/load the Measurements!')
end
%%%%%set directory to the EIDORS library:
%%%%%%% path2eidors='C:\.....\eidors-v3.9-ng\eidors\';

if exist('path2eidors')~=1
error('please set a directory to the EIDORS library')
else
run ([path2eidors 'startup.m'])
end

%%%% add some Gaussian noise to the measurements
noise = randn(size(Measurements))*norm(Measurements)/10^(90/20);
```

```
Measurementsn=Measurements+noise;
clc
%%%%calculate their SNR, manually redefine noise until desired SNR is
%%%%reached
fprintf('SNR:\n')
20*log10(norm(Measurements)/norm(noise))
if N==16
%heuristically selected values for the 50-60dB SNR levels
lambda=0.25;
elseif N==32
%%%% the large difference in hyperparameters has to do with the Jacobian's norms,
%%%% not the  problems' ill-conditioning
lambda=0.01;
end
for i=1:length(Measurements)/N^2-1
%%%%Differential iterative Gauss-Newton Reconstruction Algorithm
%%%%for more choices, see function
[imageCN(i)]=Gauss_Newton_Reconstruction(N,skipcurr,skipvolt,lambda,Measurementsn(i*N^2+1:(i+1)*N^2)',0,2,2,2,1,Measurementsn(1:N^2)')
end
figure
%%%%show the temporal conductivity behavior
show_slices(imageCN)
%%%%%%%%%%%%%%%%%%%%%%%%%%%%%%%%%%%%%

%%%% Define and plot ROIs
model=imageCN(1);
elements=model.fwd_model.elems;
L=length(elements);
elementcentre=zeros(L,2);
for element=1:L
nodes=[model.fwd_model.elems(element,1) model.fwd_model.elems(element,2) model.fwd_model.elems(element,3)];
elementcentre(element,1)=(model.fwd_model.nodes(nodes(1),1)+model.fwd_model.nodes(nodes(2),1)+model.fwd_model.nodes(nodes(3),1))/3;
elementcentre(element,2)=(model.fwd_model.nodes(nodes(1),2)+model.fwd_model.nodes(nodes(2),2)+model.fwd_model.nodes(nodes(3),2))/3;
end

figure
clf
H1=show_fem(imageCN(9));
set(H1, 'edgecolor', 'none');
axis off
hold on
a=35; % horizontal radius
b=60; % vertical radius
x0=-70; % x0,y0 ellipse centre coordinates
y0=0;
t=-pi:0.01:pi;
x=x0+a*cos(t);
y=y0+b*sin(t);
plot(x,y,'r','LineWidth',3)
axis square
hold on
a1=35; % horizontal radius
b1=60; % vertical radius
x01=70; % x0,y0 ellipse centre coordinates
y01=0;
t=-pi:0.01:pi;
x1=x01+a1*cos(t);
y1=y01+b1*sin(t);
plot(x1,y1,'r','LineWidth',3)
axis square
hold on
a2=35; % horizontal radius
b2=35; % vertical radius
x02=0; % x0,y0 ellipse centre coordinates
y02=-35;
t=-pi:0.01:pi;
x2=x02+a2*cos(t);
y2=y02+b2*sin(t);
plot(x2,y2,'r','LineWidth',3)
axis square

XX=elementcentre(:,1); YY=elementcentre(:,2);
RLROI=find((XX-x0).^2/a^2+(YY-y0).^2/b^2<1);
RRROI=find((XX-x01).^2/a1^2+(YY-y01).^2/b1^2<1);
HROI=find((XX-x02).^2/a2^2+(YY-y02).^2/b2^2<1);

for frame=1:length(imageCN)
```

```
rawimagedata(frame,:)=imageCN(frame).elem_data;
RLimagedata(frame,:)=rawimagedata(frame,RLROI);
RRimagedata(frame,:)=rawimagedata(frame,RRROI);
Himagedata(frame,:)=rawimagedata(frame,HROI);
MRLimagedata(frame)=mean(RLimagedata(frame,:));
MRRimagedata(frame)=mean(RRimagedata(frame,:));
MHimagedata(frame)=mean(Himagedata(frame,:));
end
%%%%%%%%%%%%%%%%%%%%%%%%%%%%%
%%%%plot mean ROI element values
figure
plot(MRLimagedata,'--*b','LineWidth',2)
hold on
plot(MRRimagedata,'--*r','LineWidth',2)
hold on
plot(MHimagedata,'--*','color',[255,215,0]/256,'LineWidth',2)
hold on
```

10 Appendix B: Mathematical Proofs

10.1 Proof of the EIT's Green integral equation ((3.9) in Chapter 3)

From the EIT governing equation (3.1) we have

$$\begin{aligned}\nabla^2 U(\boldsymbol{r};\boldsymbol{r}_+,\boldsymbol{r}_-) = \frac{kI}{\sigma(\boldsymbol{r})}\big(\delta(\boldsymbol{r}-\boldsymbol{r}_+)-\delta(\boldsymbol{r}-\boldsymbol{r}_-)\big)\\ -\nabla \ln\sigma(\boldsymbol{r})\cdot\nabla U(\boldsymbol{r};\boldsymbol{r}_+,\boldsymbol{r}_-)\end{aligned} \tag{10.1}$$

which is simplified following our assumption in 3.1.1, for the conductivity σ_o near the electrodes, giving

$$\begin{aligned}\nabla^2 U(\boldsymbol{r};\boldsymbol{r}_+,\boldsymbol{r_P}-) = \frac{kI}{\sigma_o}\big(\delta(\boldsymbol{r}-\boldsymbol{r}_+)-\delta(\boldsymbol{r}-\boldsymbol{r}_-)\big)\\ -\nabla \ln\sigma(\boldsymbol{r})\cdot\nabla U(\boldsymbol{r};\boldsymbol{r}_+,\boldsymbol{r}_-)\end{aligned} \tag{10.2}$$

Substituting (3.4), (3.6), and (3.6) into (3.5) results in

$$\begin{aligned}\int_\Omega G(\boldsymbol{r},\boldsymbol{r'})\left[\frac{kI}{\sigma_o}\big(\delta(\boldsymbol{r'}-\boldsymbol{r}_+)-\delta(\boldsymbol{r'}-\boldsymbol{r}_-)\big)-\nabla\ln\sigma(\boldsymbol{r'})\cdot\nabla U(\boldsymbol{r'};\boldsymbol{r}_+,\boldsymbol{r}_-)\right]dA\\ +\int_\Omega U(\boldsymbol{r'};\boldsymbol{r}_+,\boldsymbol{r}_-)\delta(\boldsymbol{r}-\boldsymbol{r'})dA = C(\boldsymbol{r}_+,\boldsymbol{r}_-)\end{aligned} \tag{10.3}$$

where function $C(\boldsymbol{r}_+,\boldsymbol{r}_-)$ is defined in (3.8). Using Dirac function's integration property we derive (3.9) where $U_o(\boldsymbol{r};\boldsymbol{r}_+,\boldsymbol{r}_-)$ is defined in (3.10).

10.2 Proof of the 2D circular Green's function solution ((3.54) in Chapter 3)

Let Ω is a 2D circular disk with a radius R_o. The Green function PDE problem becomes

$$\nabla^2 G(\boldsymbol{r}, \boldsymbol{r'}) = -\delta(\boldsymbol{r} - \boldsymbol{r'}) \tag{10.4}$$

$$\frac{\partial G(\boldsymbol{r}, \boldsymbol{r'})}{\partial \boldsymbol{n}} = -\frac{1}{2\pi R_o} \tag{10.5}$$

The free space solution is easily acquired

$$G_o(\boldsymbol{r}, \boldsymbol{r'}) = -\frac{1}{2\pi} \ln |\boldsymbol{r} - \boldsymbol{r'}| \tag{10.6}$$

The correction term $G_1(\boldsymbol{r}, \boldsymbol{r'})$ is written as

$$G_1(\boldsymbol{r}, \boldsymbol{r'}) = \sum_{n=1}^{\infty} \Big[A'_n \cos(n\phi) + B'_n \sin(n\phi) \Big] r^n \tag{10.7}$$

For $r = R_o$ in (10.5) we get

$$\begin{aligned} &\frac{1}{2\pi} \frac{R_o - r' \cos(\phi - \phi')}{R_o^2 + r'^2 - 2R_o r' \cos(\phi - \phi')} \\ &= \sum_{n=1}^{\infty} \Big[A'_n \cos(n\phi) + B'_n \sin(n\phi) \Big] n R_o^{n-1} + \frac{1}{2\pi R_o} \end{aligned} \tag{10.8}$$

Substituting $\bar{\phi} \iff \phi - \phi'$, (10.8) is written

$$\begin{aligned} &\frac{1}{2\pi} \frac{R_o - r' \cos(\bar{\phi})}{R_o^2 + r'^2 - 2R_o r' \cos(\bar{\phi})} - \frac{1}{2\pi R_o} \\ &= \sum_{n=1}^{\infty} \Big[A'_n \cos(n(\bar{\phi} + \phi')) + B'_n \sin(n(\bar{\phi} + \phi')) \Big] n R_o^{n-1} \end{aligned} \tag{10.9}$$

The left part of (10.9) is an even and periodic function $f(\bar{\phi})$ with period $T = 2\pi$. Therefore

$$\begin{aligned} &A'_n \cos(n\bar{\phi}) + B'_n \sin(n\bar{\phi}) \\ &= -\frac{1}{2\pi^2 n R_o^{n-1}} \int_0^{2\pi} \frac{R_o - r' \cos(\bar{\phi})}{R_o^2 + r'^2 - 2R_o r' \cos(\bar{\phi})} \cos(n\bar{\phi}) d\bar{\phi} \end{aligned} \tag{10.10}$$

and

$$A'_n \cos(n\bar{\phi}) - B'_n \sin(n\bar{\phi}) = 0 \tag{10.11}$$

Setting $\rho = r' R_o^{-1}$, the integral in (10.10) can be written as

$$\begin{aligned} I_n &= \frac{1}{R_o}\int_0^{2\pi} \frac{1-\rho\cos(\bar{\phi})}{1+\rho^2-2\rho\cos(\bar{\phi})}\cos(n\bar{\phi})d\bar{\phi} \\ &= \frac{1}{R_o}\int_0^{\pi} \frac{1-\rho\cos(\bar{\phi})}{1+\rho^2-2\rho\cos(\bar{\phi})}\cos(n\bar{\phi})[1+(-1)^n]d\bar{\phi} \end{aligned} \tag{10.12}$$

Since $\rho < 1$, it is found that

$$\int_0^{\pi} \frac{1-\rho\cos(\bar{\phi})}{1+\rho^2-2\rho\cos(\bar{\phi})}\cos(n\bar{\phi})d\bar{\phi} = \frac{\pi\rho^n}{2} \tag{10.13}$$

Therefore, from (10.12) and (10.13)

$$I_n = \frac{\pi\rho^n}{R_o} \tag{10.14}$$

Replacing (10.14) in (10.10) gives

$$A'_n\cos(n\bar{\phi}) + B'_n\sin(n\bar{\phi}) = -\frac{\rho^n}{2\pi n R_o^{n-2}} = z(\rho,n) \tag{10.15}$$

From (10.11) and (10.15), we get

$$A'_n = z(\rho,n)\cdot\cos(n\phi') \tag{10.16}$$

$$B'_n = z(\rho,n)\cdot\sin(n\phi') \tag{10.17}$$

From (10.16) and (10.17), the summary in (10.7) becomes

$$\begin{aligned} G_1(\boldsymbol{r},\boldsymbol{r'}) = \sum_{n=1}^{\infty} \Big[& z(\rho,n)\cdot\cos(n\phi')\cos(n\phi) \\ & + z(\rho,n)\cdot\sin(n\phi')\sin(n\phi)\Big] r^n \end{aligned} \tag{10.18}$$

From known trigonometric identity this is furtherly written

$$\begin{aligned} G_1(\boldsymbol{r},\boldsymbol{r'}) &= \sum_{n=1}^{\infty}\Big[z(\rho,n)\cdot\cos(n(\phi-\phi'))\Big] r^n \\ &= -\frac{1}{2\pi}\sum_{n=1}^{\infty}\Big[\frac{1}{n}\left(\frac{\rho}{R_o}\right)^n\cdot\cos\big(n(\phi-\phi')\big)\Big] r^n \end{aligned} \tag{10.19}$$

Recalling $\sum_{n=1}^{\infty}\frac{1}{n}a^n\cos(nx) = -\frac{1}{2}\ln(1-2a\cos x + a^2)$, for $\quad |a|<1$, we acquire the final solution

$$G(\boldsymbol{r},\boldsymbol{r'}) = -\frac{1}{2\pi}\ln|\boldsymbol{r}-\boldsymbol{r'}| \\ -\frac{1}{2\pi}\ln\sqrt{1+\frac{(r\cdot r')^2}{R_o^4}-2\frac{r\cdot r'}{R_o^2}\cos(\phi-\phi')} \tag{10.20}$$

It is important to note here that due to the Neumman's boundary condition, an arbitrary DC potential term appears in addition to the previous solution. However, since the voltage is taken as a difference between the Green's functions over a single observation point (see 3.1.1, this term does not have any substantial role at the voltage distribution.

References

[1] Ross P Henderson and John G Webster. “An impedance camera for spatially specific measurements of the thorax”. In: *IEEE Transactions on Biomedical Engineering* 3 (1978), pp. 250–254.

[2] Robert WM Smith, Ian Leslie Freeston, and Brian Hilton Brown. “A real-time electrical impedance tomography system for clinical use-design and preliminary results”. In: *IEEE Transactions on Biomedical Engineering* 42.2 (1995), pp. 133–140.

[3] A Adler et al. “Monitoring changes in lung air and liquid volumes with Electrical Impedance Tomography”. In: *Journal of Applied Physiology* 83.5 (1997), pp. 1762–1767.

[4] D. S. Holder. *Electrical Impedance Tomography: Methods, History and Applications*. First. Institute of Physics, Series in Medical Physics and Biomed. Eng., 2004.

[5] Marc Bodenstein, Matthias David, and Klaus Markstaller. “Principles of electrical impedance tomography and its clinical application”. In: *Critical care medicine* 37.2 (2009), pp. 713–724.

[6] Inéz Frerichs et al. “Chest Electrical Impedance Tomography examination, data analysis, terminology, clinical use and recommendations: consensus statement of the TRanslational EIT developmeNt stuDy group”. In: *Thorax* 72.1 (2017), pp. 83–93.

[7] Haipeng Liu, John Allen, Dingchang Zheng, and Fei Chen. “Recent development of respiratory rate measurement technologies”. In: *Physiological measurement* 40.7 (2019), 07TR01.

[8] Shuo-Yao Qu, Meng Dai, Shuo Wu, Zhi-Rang Lv, Xin-Yu Ti, and Feng Fu. “System introduction and evaluation of the first Chinese chest EIT device for ICU applications”. In: *Scientific Reports* 11.1 (2021), pp. 1–7.

[9] Ryan J Halter et al. “A broadband high-frequency Electrical Impedance Tomography system for breast imaging”. In: *IEEE Trans. on Biomed. Eng.* 55.2 (2008), pp. 650–659.

[10] Kirill Y Aristovich et al. “Imaging fast electrical activity in the brain with EIT”. In: *NeuroImage* 124 (2016), pp. 204–213.

[11] Nir Goren et al. “Multi-frequency Electrical Impedance Tomography and neuroimaging data in stroke patients”. In: *Scientific data* 5.1 (2018), pp. 1–10.

[12] YD Jiang and Manuchehr Soleimani. “Capacitively coupled electrical impedance tomography for brain imaging”. In: *IEEE transactions on medical imaging* 38.9 (2019), pp. 2104–2113.

[13] Artur J Jaworski and Tomasz Dyakowski. “Application of electrical capacitance tomography for measurement of gas-solids flow characteristics in a pneumatic conveying system”. In: *Measurement Science and Technology* 12.8 (2001), p. 1109.

[14] J. Porzuczek. “Assessment of the Spatial Distribution of Moisture Content in Granular Material Using Electrical Impedance Tomography”. In: *MDPI Sensors* 19.12 (2019), pp. 2807–2822.

[15] Kent Wei et al. “Super-sensing technology: Industrial applications and future challenges of Electrical Tomography”. In: *Philosophical Trans. of the Royal Society A: Mathematical, Phys. and Eng. Sciences* 374.2070 (2016), p. 20150328.

[16] Carl Tholin-Chittenden and Manuchehr Soleimani. “Planar array capacitive imaging sensor design optimization”. In: *IEEE Sensors Journal* 17.24 (2017), pp. 8059–8071.

[17] Yandan Jiang and Manuchehr Soleimani. “Capacitively coupled phase-based dielectric spectroscopy tomography”. In: *Scientific reports* 8.1 (2018), pp. 1–10.

[18] WQ Yang and Lihui Peng. “Image reconstruction algorithms for electrical capacitance tomography”. In: *Measurement science and technology* 14.1 (2002), R1.

[19] Swisstom AG. *Swisstom BB2 Product Information*. 2013. URL: `http://www.swisstom.com/en/products/swisstombb2_en/`.

[20] Yu Wu, Dai Jiang, Andy Bardill, Serena De Gelidi, Richard Bayford, and Andreas Demosthenous. “A high frame rate wearable EIT system using active electrode ASICs for lung respiration and heart rate monitoring”. In: *IEEE Transactions on Circuits and Systems I: Regular Papers* 65.11 (2018), pp. 3810–3820.

[21] Yu Wu, Dai Jiang, Andy Bardill, Richard Bayford, and Andreas Demosthenous. “A 122 fps, 1 MHz bandwidth multi-frequency wearable EIT belt featuring novel active electrode architecture for neonatal thorax vital sign monitoring”. In: *IEEE transactions on biomedical circuits and systems* 13.5 (2019), pp. 927–937.

[22] Kuo-Sheng Cheng, David Isaacson, JC Newell, and David G Gisser. “Electrode models for electric current computed tomography”. In: *IEEE Transactions on Biomedical Engineering* 36.9 (1989), pp. 918–924.

[23] Erkki Somersalo, Margaret Cheney, and David Isaacson. “Existence and uniqueness for electrode models for Electric Current Computed Tomography”. In: *SIAM Journal on Applied Mathematics* 52.4 (1992), pp. 1023–1040.

[24] Martin Hanke, Bastian Harrach, and Nuutti Hyvönen. “Justification of point electrode models in Electrical Impedance Tomography”. In: *Mathematical Models and Methods in Applied Sciences* 21.06 (2011), pp. 1395–1413.

[25] Z. Wei and X. Chen. “Induced-Current Learning Method for Nonlinear Reconstructions in Electrical Impedance Tomography”. In: *IEEE Trans. on Med. Imag.* to appear.to appear (2019), to appear.

[26] O. L. Silva et al. “Influence of current injection pattern and electric potential measurement strategies in Electrical Impedance Tomography”. In: *Control Engineering Practice* 58 (2017), pp. 276–286.

[27] Brian H Brown and Andrew D Seagar. “The Sheffield data collection system”. In: *Clinical Physics and Physiological Measurement* 8.4A (1987), p. 91.

[28] Ping Hua et al. “Iterative reconstruction methods using regularization and optimal current patterns in Electrical Impedance Tomography”. In: *IEEE Trans. on Med. Imag.* 10.4 (1991), pp. 621–628.

[29] DG Gisser, D Isaacson, and JC Newell. “Current topics in impedance imaging”. In: *Clinical Physics and Physiological Measurement* 8.4A (1987), p. 39.

[30] Margaret Cheney et al. “NOSER: An algorithm for solving the inverse conductivity problem”. In: *International Journal of Imaging systems and technology* 2.2 (1990), pp. 66–75.

[31] V Kolehmainen, M Vauhkonen, PA Karjalainen, and JP Kaipio. “Assessment of errors in static electrical impedance tomography with adjacent and trigonometric current patterns”. In: *Physiological measurement* 18.4 (1997), p. 289.

[32] Eugene Demidenko, Alex Hartov, Nirmal Soni, and Keith D Paulsen. “On optimal current patterns for electrical impedance tomography”. In: *IEEE Transactions on Biomedical Engineering* 52.2 (2005), pp. 238–248.

[33] Thomas Yorkey. “Electrical Impedance Tomography with piecewise polynomial conductivities”. In: *J. of comp. phys.* 91.2 (1990), pp. 344–360.

[34] EJ Woo et al. “Finite-Element method in Electrical Impedance Tomography”. In: *Med. and Biol. Eng. and Comp.* 32.5 (1994), pp. 530–536.

[35] Alberto P Calderón. “On an inverse boundary value problem”. In: *Comput. Appl. Math* (2006), pp. 2–3.

[36] Nicholas Polydorides. “Image reconstruction algorithms for soft-field tomography”. In: *PhD Thesis, UMIST* (2002).

[37] Nick Polydorides and William RB Lionheart. “A MATLAB toolkit for three-dimensional Electrical Impedance Tomography: a contribution to the Electrical Impedance and Diffuse Optical Reconstruction Software project”. In: *Meas. science and technology* 13.12 (2002), p. 1871.

[38] Martin Hanke. “Iterative regularization techniques in image reconstruction”. In: *Surveys on solution methods for inverse problems*. Springer, 2000, pp. 35–52.

[39] MG Crabb. “Convergence study of 2 D forward problem of electrical impedance tomography with high-order finite elements”. In: *Inverse Problems in Science and Engineering* 25.10 (2017), pp. 1397–1422.

[40] T. J. C. Faes J. C. de Munck and R. M. Heethaar. “The Boundary Element Method in the Forward and Inverse Problem of Electrical Impedance Tomography”. In: *IEEE Trans. on Biomed. Eng.* 47.6 (2000), pp. 792–800.

[41] G. L.Chahine R. Duraiswami and K Sarkar. “Boundary element techniques for efficient 2-D and 3-D Electrical Impedance Tomography”. In: *Elsevier, Chemical Eng. Science* 52.13 (1997), pp. 2185–2196.

[42] G. L.Chahine R. Duraiswami and K Sarkar. “Efficient 2D and 3D Electrical Impedance Tomography using dual reciprocity boundary element techniques”. In: *Elsevier, Engineering with Boundary Elements* 22.1 (1998), pp. 13–31.

[43] Muhammad Mushtaq, Nawazish Ali Shah, and Ghulam Muhammad. “Advantages and disadvantages of boundary element methods for compressible fluid flow problems”. In: *J. Am. Sci* 6.1 (2010), pp. 162–165.

[44] Robert V Kohn and Michael Vogelius. “Determining conductivity by boundary measurements II. Interior results”. In: *Communications on Pure and Applied Mathematics* 38.5 (1985), pp. 643–667.

[45] John Sylvester and Gunther Uhlmann. “A global uniqueness theorem for an inverse boundary value problem”. In: *Annals of mathematics* (1987), pp. 153–169.

[46] Adrian I Nachman. “Global uniqueness for a two-dimensional inverse boundary value problem”. In: *Annals of Mathematics* (1996), pp. 71–96.

[47] Yougmin Kim, JOhn Webster, and Willis Tompkins. “Electrical impedance imaging of the thorax”. In: *Journal of microwave Power* 18.3 (1983), pp. 245–257.

[48] Thomas J Yorkey, John G Webster, and Willis J Tompkins. “Comparing reconstruction algorithms for electrical impedance tomography”. In: *IEEE Transactions on Biomedical Engineering* 11 (1987), pp. 843–852.

[49] Robert Guardo, Christian Boulay, Bruno Murray, and Michel Bertrand. “An experimental study in electrical impedance tomography using backprojection reconstruction”. In: *IEEE transactions on biomedical engineering* 38.7 (1991), pp. 617–627.

[50] DC Barber, BH Brown, and NJ Avis. “Image reconstruction in electrical impedance tomography using filtered back-projection”. In: *1992 14th Annual International Conference of the IEEE Engineering in Medicine and Biology Society*. Vol. 5. IEEE. 1992, pp. 1691–1692.

[51] Anders H Andersen and Avinash C Kak. “Simultaneous algebraic reconstruction technique (SART): a superior implementation of the ART algorithm”. In: *Ultrasonic imaging* 6.1 (1984), pp. 81–94.

[52] Taoran Li, Tzu-Jen Kao, David Isaacson, Jonathan C Newell, and Gary J Saulnier. “Adaptive Kaczmarz method for image reconstruction in electrical impedance tomography”. In: *Physiological measurement* 34.6 (2013), p. 595.

[53] Per Christian Hansen. *Rank-deficient and discrete ill-posed problems: numerical aspects of linear inversion*. SIAM, 1998.

[54] M. Vauhkonen et al. “Tikhonov Regularization and Prior Information in EIT”. In: *IEEE Trans. on Med. Imag.* 17.2 (1998), pp. 285–293.

[55] Andy Adler and Robert Guardo. “Electrical Impedance Tomography: regularized imaging and contrast detection”. In: *IEEE Trans. on Med. Imag.* 15.2 (1996), pp. 170–179.

[56] Kenneth Levenberg. “A method for the solution of certain non-linear problems in least squares”. In: *Quarterly of applied mathematics* 2.2 (1944), pp. 164–168.

[57] Donald W Marquardt. “An algorithm for least-squares estimation of nonlinear parameters”. In: *Journal of the society for Industrial and Applied Mathematics* 11.2 (1963), pp. 431–441.

[58] Changyou Li, Mirza Karamehmedović, Ekaterina Sherina, and Kim Knudsen. “Levenberg–Marquardt Algorithm for Acousto-Electric Tomography based on the Complete Electrode Model”. In: *Journal of Mathematical Imaging and Vision* 63.4 (2021), pp. 492–502.

[59] Andrea Borsic, Brad M Graham, Andy Adler, and William RB Lionheart. “Total variation regularization in Electrical Impedance Tomography”. In: (2007).

[60] Andrea Borsic et al. “In vivo impedance imaging with total variation regularization”. In: *IEEE Trans. on Med. Imag.* 29.1 (2009), pp. 44–54.

[61] Zhou Zhou et al. “Comparison of total variation algorithms for Electrical Impedance Tomography”. In: *Physiol. meas.* 36.6 (2015), p. 1193.

[62] Youzuo Lin and Lianjie Huang. “Acoustic-and elastic-waveform inversion using a modified total-variation regularization scheme”. In: *Geophysical Journal International* 200.1 (2014), pp. 489–502.

[63] Qi Wang, Jianming Wang, Xiuyan Li, Xiaojie Duan, Ronghua Zhang, Hong Zhang, Yanhe Ma, Huaxiang Wang, and Jiabin Jia. “Exploring Respiratory Motion Tracking through Electrical Impedance Tomography (EIT)”. In: *IEEE Transactions on Instrumentation and Measurement* (2021).

[64] Yoon Mo Jung and Sangwoon Yun. “Impedance imaging with first-order TV regularization”. In: *IEEE transactions on medical imaging* 34.1 (2014), pp. 193–202.

[65] Knud D Andersen et al. “An efficient primal-dual interior-point method for minimizing a sum of Euclidean norms”. In: *SIAM Journal on Scientific Computing* 22.1 (2000), pp. 243–262.

[66] Tom Goldstein and Stanley Osher. “The split Bregman method for L1-regularized problems”. In: *SIAM journal on imaging sciences* 2.2 (2009), pp. 323–343.

[67] Stanley Osher, Martin Burger, Donald Goldfarb, Jinjun Xu, and Wotao Yin. “An iterative regularization method for total variation-based image restoration”. In: *Multiscale Modeling & Simulation* 4.2 (2005), pp. 460–489.

[68] Fang Li, Juan FPJ Abascal, Manuel Desco, and Manuchehr Soleimani. “Total variation regularization with split Bregman-based method in magnetic induction tomography using experimental data”. In: *IEEE Sensors Journal* 17.4 (2016), pp. 976–985.

[69] Chenning Wu and Manuchehr Soleimani. “Frequency difference EIT with localization: A potential medical imaging tool during cancer treatment”. In: *IEEE Access* 7 (2019), pp. 21870–21878.

[70] Murat Belge, Misha E Kilmer, and Eric L Miller. “Simultaneous multiple regularization parameter selection by means of the L-hypersurface with applications to linear inverse problems posed in the wavelet transform domain”. In: *Bayesian Inference for Inverse Problems*. Vol. 3459. International Society for Optics and Photonics. 1998, pp. 328–336.

[71] Andy Adler, John H Arnold, Richard Bayford, Andrea Borsic, Brian Brown, Paul Dixon, Theo JC Faes, Inéz Frerichs, Hervé Gagnon, Yvo Gärber, et al. “GREIT: a unified approach to 2D linear EIT reconstruction of lung images”. In: *Physiological measurement* 30.6 (2009), S35.

[72] A. Adler and W. Lionheart. “Uses and abuses of EIDORS: An extensible software base for EIT”. In: *Phys. Meas* 27.5 (2006).

[73] David Isaacson, Jennifer L Mueller, Jonathan C Newell, and Samuli Siltanen. “Reconstructions of chest phantoms by the D-bar method for electrical impedance tomography”. In: *IEEE Transactions on medical imaging* 23.7 (2004), pp. 821–828.

[74] Kim Knudsen, Matti Lassas, Jennifer L Mueller, and Samuli Siltanen. “Regularized D-bar method for the inverse conductivity problem”. In: *Inverse Problems & Imaging* 3.4 (2009), p. 599.

[75] Jennifer L Mueller and Samuli Siltanen. *Linear and nonlinear inverse problems with practical applications*. SIAM, 2012.

[76] Claudia NL Herrera, Miguel FM Vallejo, Jennifer L Mueller, and Raul G Lima. “Direct 2-D reconstructions of conductivity and permittivity from EIT data on a human chest”. In: *IEEE transactions on medical imaging* 34.1 (2014), pp. 267–274.

[77] Jennifer L Mueller and Samuli Siltanen. “The D-bar method for electrical impedance tomography—demystified”. In: *Inverse problems* 36.9 (2020), p. 093001.

[78] Giovanni Alessandrini. “Stable determination of conductivity by boundary measurements”. In: *Applicable Analysis* 27.1-3 (1988), pp. 153–172.

[79] Ethan K Murphy and Jennifer L Mueller. “Effect of domain shape modeling and measurement errors on the 2-D D-bar method for EIT”. In: *IEEE transactions on medical imaging* 28.10 (2009), pp. 1576–1584.

[80] Sarah J Hamilton, WRB Lionheart, and A Adler. “Comparing D-bar and common regularization-based methods for electrical impedance tomography”. In: *Physiological measurement* 40.4 (2019), p. 044004.

[81] Stanley Osher and James A Sethian. “Fronts propagating with curvature-dependent speed: Algorithms based on Hamilton-Jacobi formulations”. In: *Journal of computational physics* 79.1 (1988), pp. 12–49.

[82] Eric T Chung, Tony F Chan, and Xue-Cheng Tai. “Electrical impedance tomography using level set representation and total variational regularization”. In: *Journal of computational physics* 205.1 (2005), pp. 357–372.

[83] Manuchehr Soleimani, Oliver Dorn, and William RB Lionheart. “A narrow-band level set method applied to EIT in brain for cryosurgery monitoring”. In: *IEEE transactions on biomedical engineering* 53.11 (2006), pp. 2257–2264.

[84] M Soleimani, WRB Lionheart, and O Dorn. “Level set reconstruction of conductivity and permittivity from boundary electrical measurements using experimental data”. In: *Inverse problems in science and engineering* 14.2 (2006), pp. 193–210.

[85] Dong Liu, Anil Kumar Khambampati, Sin Kim, and Kyung Youn Kim. “Multi-phase flow monitoring with electrical impedance tomography using level set based method”. In: *Nuclear Engineering and Design* 289 (2015), pp. 108–116.

[86] Hong-Kai Zhao, Tony Chan, Barry Merriman, and Stanley Osher. “A variational level set approach to multiphase motion”. In: *Journal of computational physics* 127.1 (1996), pp. 179–195.

[87] Dong Liu, Anil Kumar Khambampati, and Jiangfeng Du. “A parametric level set method for electrical impedance tomography”. In: *IEEE transactions on medical imaging* 37.2 (2017), pp. 451–460.

[88] Dong Liu, Danny Smyl, and Jiangfeng Du. “A parametric level set-based approach to difference imaging in electrical impedance tomography”. In: *IEEE transactions on medical imaging* 38.1 (2018), pp. 145–155.

[89] Dong Liu, Yuxi Zhao, Anil Kumar Khambampati, Aku Seppänen, and Jiangfeng Du. “A parametric level set method for imaging multiphase conductivity using electrical impedance tomography”. In: *IEEE Transactions on Computational Imaging* 4.4 (2018), pp. 552–561.

[90] Shangjie Ren, Yu Wang, Guanghui Liang, and Feng Dong. “A robust inclusion boundary reconstructor for electrical impedance tomography with geometric constraints”. In: *IEEE Transactions on Instrumentation and Measurement* 68.3 (2018), pp. 762–773.

[91] Michael Kass, Andrew Witkin, and Demetri Terzopoulos. “Snakes: Active contour models”. In: *International journal of computer vision* 1.4 (1988), pp. 321–331.

[92] Ricard Delgado-Gonzalo, Virginie Uhlmann, Daniel Schmitter, and Michael Unser. “Snakes on a plane: A perfect snap for bioimage analysis”. In: *IEEE Signal Processing Magazine* 32.1 (2014), pp. 41–48.

[93] Shangjie Ren, Kai Sun, Dong Liu, and Feng Dong. “A statistical shape-constrained reconstruction framework for electrical impedance tomography”. In: *IEEE transactions on medical imaging* 38.10 (2019), pp. 2400–2410.

[94] Dong Liu and Jiangfeng Du. “A moving morphable components based shape reconstruction framework for electrical impedance tomography”. In: *IEEE transactions on medical imaging* 38.12 (2019), pp. 2937–2948.

[95] Xu Guo, Weisheng Zhang, Jian Zhang, and Jie Yuan. “Explicit structural topology optimization based on moving morphable components (MMC) with curved skeletons”. In: *Computer methods in applied mechanics and engineering* 310 (2016), pp. 711–748.

[96] Weisheng Zhang, Jishun Chen, Xuefeng Zhu, Jianhua Zhou, Dingchuan Xue, Xin Lei, and Xu Guo. “Explicit three dimensional topology optimization via Moving Morphable Void (MMV) approach”. In: *Computer Methods in Applied Mechanics and Engineering* 322 (2017), pp. 590–614.

[97] Dong Liu et al. “Shape-driven reconstruction using Fourier representations”. In: *IEEE Trans. on Med. Imag.* (2020).

[98] Dong Liu, Danping Gu, Danny Smyl, Jiansong Deng, and Jiangfeng Du. “B-spline level set method for shape reconstruction in electrical impedance tomography”. In: *IEEE transactions on medical imaging* 39.6 (2019), pp. 1917–1929.

[99] Dong Liu, Danping Gu, Danny Smyl, Jiansong Deng, and Jiangfeng Du. “Shape reconstruction using Boolean operations in electrical impedance tomography”. In: *IEEE transactions on medical imaging* 39.9 (2020), pp. 2954–2964.

[100] Dong Liu, Danping Gu, Danny Smyl, Anil Kumar Khambampati, Jiansong Deng, and Jiangfeng Du. “Shape-driven EIT reconstruction using Fourier representations”. In: *IEEE Transactions on Medical Imaging* 40.2 (2020), pp. 481–490.

[101] Andy Adler and Robert Guardo. “A neural network image reconstruction technique for electrical impedance tomography”. In: *IEEE Transactions on Medical Imaging* 13.4 (1994), pp. 594–600.

[102] E Ratajewicz-Mikolajczak, GH Shirkoohi, and J Sikora. “Two ANN reconstruction methods for electrical impedance tomography”. In: *IEEE transactions on magnetics* 34.5 (1998), pp. 2964–2967.

[103] Magdalena Stasiak, Jan Sikora, Stefan F Filipowicz, and Konrad Nita. “Principal component analysis and artificial neural network approach to electrical impedance tomography problems approximated by multi-region boundary element method”. In: *Engineering Analysis with Boundary Elements* 31.8 (2007), pp. 713–720.

[104] Jianwei Li, Xiaoguang Yang, Youhua Wang, and Ruzheng Pan. “An image reconstruction algorithm based on RBF neural network for electrical capacitance tomography”. In: *2012 Sixth International Conference on Electromagnetic Field Problems and Applications*. IEEE. 2012, pp. 1–4.

[105] Luca Brillante, Benjamin Bois, Olivier Mathieu, and Jean Lévêque. “Electrical imaging of soil water availability to grapevine: a benchmark experiment of several machine-learning techniques”. In: *Precision agriculture* 17.6 (2016), pp. 637–658.

[106] Tomasz Rymarczyk and Edward Kozłowski. “Using statistical algorithms for image reconstruction in EIT”. In: *MATEC Web of Conferences*. Vol. 210. EDP Sciences. 2018, p. 02017.

[107] J Nasehi Tehrani, Alistair McEwan, Craig Jin, and A Van Schaik. “L1 regularization method in electrical impedance tomography by using the L1-curve (Pareto frontier curve)”. In: *Applied Mathematical Modelling* 36.3 (2012), pp. 1095–1105.

[108] Chao Tan, Shuhua Lv, Feng Dong, and Masahiro Takei. “Image reconstruction based on convolutional neural network for electrical resistance tomography”. In: *IEEE Sensors Journal* 19.1 (2018), pp. 196–204.

[109] Tomasz Rymarczyk, Grzegorz Kłosowski, Edward Kozłowski, and Paweł Tchórzewski. “Comparison of selected machine learning algorithms for industrial electrical tomography”. In: *Sensors* 19.7 (2019), p. 1521.

[110] Kyong Hwan Jin, Michael T McCann, Emmanuel Froustey, and Michael Unser. “Deep convolutional neural network for inverse problems in imaging”. In: *IEEE Transactions on Image Processing* 26.9 (2017), pp. 4509–4522.

[111] Simon Arridge, Peter Maass, Ozan Öktem, and Carola-Bibiane Schönlieb. “Solving inverse problems using data-driven models”. In: *Acta Numerica* 28 (2019), pp. 1–174.

[112] William Herzberg, Daniel B Rowe, Andreas Hauptmann, and Sarah J Hamilton. “Graph Convolutional Networks for Model-Based Learning in Nonlinear Inverse Problems”. In: *arXiv preprint arXiv:2103.15138* (2021).

[113] Sébastien Martin and Charles TM Choi. “A post-processing method for three-dimensional electrical impedance tomography”. In: *Scientific reports* 7.1 (2017), pp. 1–10.

[114] Patrick Putzky and Max Welling. “Recurrent inference machines for solving inverse problems”. In: *arXiv preprint arXiv:1706.04008* (2017).

[115] Jonas Adler and Ozan Öktem. “Solving ill-posed inverse problems using iterative deep neural networks”. In: *Inverse Problems* 33.12 (2017), p. 124007.

[116] Bo Zhu, Jeremiah Z Liu, Stephen F Cauley, Bruce R Rosen, and Matthew S Rosen. “Image reconstruction by domain-transform manifold learning”. In: *Nature* 555.7697 (2018), pp. 487–492.

[117] Olaf Ronneberger, Philipp Fischer, and Thomas Brox. “U-net: Convolutional networks for biomedical image segmentation”. In: *International Conference on Medical image computing and computer-assisted intervention*. Springer. 2015, pp. 234–241.

[118] Sarah Jane Hamilton and Andreas Hauptmann. “Deep D-bar: Real-time Electrical Impedance Tomography imaging with deep neural networks”. In: *IEEE Trans. on Medical Imaging* 37.10 (2018), pp. 2367–2377.

[119] Sarah J Hamilton, Asko Hänninen, Andreas Hauptmann, and Ville Kolehmainen. “Beltrami-net: domain-independent deep D-bar learning for absolute imaging with electrical impedance tomography (a-EIT)”. In: *Physiological measurement* 40.7 (2019), p. 074002.

[120] Zhun Wei, Dong Liu, and Xudong Chen. “Dominant-current deep learning scheme for electrical impedance tomography”. In: *IEEE Transactions on Biomedical Engineering* 66.9 (2019), pp. 2546–2555.

[121] Xudong Chen. “Subspace-based optimization method for solving inverse-scattering problems”. In: *IEEE Transactions on Geoscience and Remote Sensing* 48.1 (2009), pp. 42–49.

[122] Xi Duan, Sebastien Taurand, and Manuchehr Soleimani. “Artificial skin through super-sensing method and electrical impedance data from conductive fabric with aid of deep learning”. In: *Scientific reports* 9.1 (2019), pp. 1–11.

[123] Zhou Chen, Yunjie Yang, Jiabin Jia, and Pierre Bagnaninchi. “Deep Learning Based Cell Imaging with Electrical Impedance Tomography”. In: *2020 IEEE International Instrumentation and Measurement Technology Conference (I2MTC)*. IEEE. 2020, pp. 1–6.

[124] Zhou Chen, Yunjie Yang, and Pierre-Olivier Bagnaninchi. “Hybrid Learning-Based Cell Aggregate Imaging With Miniature Electrical Impedance Tomography”. In: *IEEE Transactions on Instrumentation and Measurement* 70 (2020), pp. 1–10.

[125] Zhou Chen and Yunjie Yang. “Structure-Aware Dual-Branch Network for Electrical Impedance Tomography in Cell Culture Imaging”. In: *IEEE Transactions on Instrumentation and Measurement* 70 (2021), pp. 1–9.

[126] Zhe Liu, Pierre Bagnaninchi, and Yunjie Yang. “Impedance-optical Dual-modal Cell Culture Imaging with Learning-based Information Fusion”. In: *arXiv preprint arXiv:2106.07985* (2021).

[127] Zhun Wei and Xudong Chen. “Induced-current learning method for nonlinear reconstructions in electrical impedance tomography”. In: *IEEE transactions on medical imaging* 39.5 (2019), pp. 1326–1334.

[128] Jinxi Xiang, Yonggui Dong, and Yunjie Yang. “FISTA-Net: Learning A fast iterative shrinkage thresholding network for inverse problems in imaging”. In: *IEEE Transactions on Medical Imaging* 40.5 (2021), pp. 1329–1339.

[129] Zhou Chen, Jinxi Xiang, Pierre Bagnaninchi, and Yunjie Yang. “MMV-Net: A Multiple Measurement Vector Network for Multi-frequency Electrical Impedance Tomography”. In: *arXiv preprint arXiv:2105.12474* (2021).

[130] Masao Fukushima. “Application of the alternating direction method of multipliers to separable convex programming problems”. In: *Computational Optimization and Applications* 1.1 (1992), pp. 93–111.

[131] Shangjie Ren, Kai Sun, Chao Tan, and Feng Dong. “A two-stage deep learning method for robust shape reconstruction with electrical impedance tomography”. In: *IEEE Transactions on Instrumentation and Measurement* 69.7 (2019), pp. 4887–4897.

[132] Danny Smyl and Dong Liu. “Optimizing Electrode Positions in 2-D Electrical Impedance Tomography Using Deep Learning”. In: *IEEE Transactions on Instrumentation and Measurement* 69.9 (2020), pp. 6030–6044.

[133] Nazri Mohd Nawi, RS Ransing, and MR Ransing. “An improved conjugate gradient based learning algorithm for back propagation neural networks”. In: *International Journal of Computational Intelligence* 4.1 (2007), pp. 46–55.

[134] Lu Yang, Hongtao Wu, Kai Liu, Bai Chen, Wei Han, and Jiafeng Yao. "Image Reconstruction Improvement with Optimal Driven-measurement Pattern Selection for Electrical Impedance Tomography". In: *IEEE Sensors Journal* (2021).

[135] Zeying Wang, Shihong Yue, Kai Song, Xiaoyuan Liu, and Huaxiang Wang. "An unsupervised method for evaluating electrical impedance tomography images". In: *IEEE Transactions on Instrumentation and Measurement* 67.12 (2018), pp. 2796–2803.

[136] Zeying Wang, Shihong Yue, Qi Li, Xiaoyuan Liu, Huaxiang Wang, and Alistair McEwan. "Unsupervised Evaluation and Optimization for Electrical Impedance Tomography". In: *IEEE Transactions on Instrumentation and Measurement* 70 (2021), pp. 1–12.

[137] Xudong Chen, Zhun Wei, Maokun Li, and Paolo Rocca. "A review of deep learning approaches for inverse scattering problems (invited review)". In: *Progress In Electromagnetics Research* 167 (2020), pp. 67–81.

[138] Zhilin Zhang and Bhaskar D Rao. "Extension of SBL algorithms for the recovery of block sparse signals with intra-block correlation". In: *IEEE Transactions on Signal Processing* 61.8 (2013), pp. 2009–2015.

[139] Jun Fang, Yanning Shen, Hongbin Li, and Pu Wang. "Pattern-coupled sparse Bayesian learning for recovery of block-sparse signals". In: *IEEE Transactions on Signal Processing* 63.2 (2014), pp. 360–372.

[140] Qisong Wu, Yimin D Zhang, Moeness G Amin, and Braham Himed. "Multi-task Bayesian compressive sensing exploiting intra-task dependency". In: *IEEE Signal Processing Letters* 22.4 (2014), pp. 430–434.

[141] Shengheng Liu, Yimin D Zhang, Tao Shan, Si Qin, and Moeness G Amin. "Structure-aware Bayesian compressive sensing for frequency-hopping spectrum estimation". In: *Compressive Sensing V: From Diverse Modalities to Big Data Analytics*. Vol. 9857. International Society for Optics and Photonics. 2016, 98570N.

[142] Shengheng Liu et al. "Image reconstruction in Electrical Impedance Tomography based on structure-aware sparse Bayesian learning". In: *IEEE Trans. on Med. Imag.* 37.9 (2018), pp. 2090–2102.

[143] Shengheng Liu, Hancong Wu, Yongming Huang, Yunjie Yang, and Jiabin Jia. "Accelerated structure-aware sparse Bayesian learning for three-dimensional electrical impedance tomography". In: *IEEE Transactions on Industrial Informatics* 15.9 (2019), pp. 5033–5041.

[144] Jiang Zhu, Lin Han, and Xiangming Meng. "An AMP-based low complexity generalized sparse Bayesian learning algorithm". In: *IEEE Access* 7 (2018), pp. 7965–7976.

[145] Shengheng Liu, Ruisong Cao, Yongming Huang, Taweechai Ouypornkochagorn, and Jiabin Jia. "Time sequence learning for electrical impedance tomography using Bayesian spatiotemporal priors". In: *IEEE Transactions on Instrumentation and Measurement* 69.9 (2020), pp. 6045–6057.

[146] Shengheng Liu, Yongming Huang, Hancong Wu, Chao Tan, and Jiabin Jia. “Efficient multitask structure-aware sparse Bayesian learning for frequency-difference electrical impedance tomography”. In: *IEEE Transactions on Industrial Informatics* 17.1 (2020), pp. 463–472.

[147] Andy Adler et al. “Impedance imaging of lung ventilation: do we need to account for chest expansion?” In: *IEEE Trans. on Biomed. Eng.* 43.4 (1996), pp. 414–420.

[148] D. G. Duffy. *Green's functions with applications*. First. Chapman-Hall, 2001.

[149] Jennifer L Mueller et al. “A reconstruction algorithm for Electrical Impedance Tomography data collected on rectangular electrode arrays”. In: *IEEE Trans. on Biomed. Eng.* 46.11 (1999), pp. 1379–1386.

[150] Robert Reams. “Hadamard inverses, square roots and products of almost semidefinite matrices”. In: *Linear Algebra and its Applications* 288 (1999), pp. 35–43.

[151] Dong Liu et al. “Nonlinear difference imaging approach to three-dimensional Electrical Impedance Tomography in the presence of geometric modeling errors”. In: *IEEE Trans. on Biomed. Eng.* 63.9 (2015), pp. 1956–1965.

[152] Leonid I Rudin et al. “Nonlinear total variation based noise removal algorithms”. In: *Physica D: nonlinear phenomena* 60.1-4 (1992), pp. 259–268.

[153] A Borsic et al. “Electrical impedance tomography reconstruction for three-dimensional imaging of the prostate”. In: *Physiol. meas.* 31.8 (2010), S1.

[154] Dominique Brunet et al. “On the mathematical properties of the structural similarity index”. In: *IEEE Trans. on Image Processing* 21.4 (2011), pp. 1488–1499.

[155] William Lionheart. “EIT reconstruction algorithms: pitfalls, challenges and recent developments”. In: *Physiol. meas.* 25.1 (2004), p. 125. ISSN: 1361-6579. DOI: 10.1088/0967-3334/25/1/021.

[156] Hun Wi et al. “Multi-frequency Electrical Impedance Tomography system with automatic self-calibration for long-term monitoring”. In: *IEEE Trans. on Biomed. Circ. and Sys.* 8.1 (2013), pp. 119–128.

[157] J. Kourunen et al. “Suitability of a PXI platform for an EIT system”. In: *Meas. Scien. and Tech.* 20.1 (2008).

[158] Arun Rao et al. “A 1 MHz Miniaturized Electrical Impedance Tomography System for Prostate Imaging”. In: *IEEE Trans. on Biom. Circ. and S.* (2020).

[159] Taoran Li et al. “Adaptive techniques in Electrical Impedance Tomography reconstruction”. In: *Physiol. meas.* 35.6 (2014), p. 1111.

[160] Robert J Renka. “Mesh improvement by minimizing a weighted sum of squared element volumes”. In: *International Journal for Numerical Methods in Engineering* 101.11 (2015), pp. 870–886.

[161] V. Kolehmainen A. Hauptmann and S. Siltanen. “Open 2d Electrical Impedance Tomography data archive”. In: *arXiv:1704.01178* (2017).

[162] Sadayuki Murashima. “Analyses of Some Potential Problems in Cylindrical Coordinates in Connection with Four-Point Probe Technique”. In: *Japanese Journal of Applied Physics* 12.8 (1973), p. 1244.

[163] William W Hager. “Updating the inverse of a matrix”. In: *SIAM review* 31.2 (1989), pp. 221–239.

[164] G. Savoie. “Applications de la tomographie d’impédance électrique à l’étude de phénomènes physiologiques”. PhD thesis. École Polytechnique de Montréal, Canada, 1994.

[165] V. Guardo et al. “A superheterodyne serial Data Acquisition System forElectrical Impedance Tomography”. In: *Proc. 15th Ann. Int. Conf. IEEE Eng. in Med. Biol. Soc.* San Diego, CA, USA, 1993.

[166] David G Tingay et al. “Electrical Impedance Tomography can identify ventilation and perfusion defects: a neonatal case”. In: *American journal of resp. and critical care medicine* 199.3 (2019), pp. 384–386.

[167] O Brabant, B Crivellari, G Hosgood, A Raisis, AD Waldmann, U Auer, A Adler, L Smart, M Laurence, and M Mosing. “Effects of PEEP on the relationship between tidal volume and total impedance change measured via electrical impedance tomography (EIT)”. In: *Journal of Clinical Monitoring and Computing* (2021), pp. 1–10.

[168] M Consuelo Bachmann, Caio Morais, Guillermo Bugedo, Alejandro Bruhn, Arturo Morales, João B Borges, Eduardo Costa, and Jaime Retamal. “Electrical Impedance Tomography in acute respiratory distress syndrome”. In: *Critical Care* 22.1 (2018), pp. 1–11.

[169] Ethan K Murphy, Mohammad Takhti, Joseph Skinner, Ryan J Halter, and Kofi Odame. “Signal-to-noise ratio analysis of a phase-sensitive voltmeter for electrical impedance tomography”. In: *IEEE transactions on biomedical circuits and systems* 11.2 (2016), pp. 360–369.

[170] Mohammad Takhti and Kofi Odame. “Structured design methodology to achieve a high SNR Electrical Impedance Tomography”. In: *IEEE Trans. on Biomed. Circ. and Sys.* 13.2 (2019), pp. 364–375.

[171] Michelle M Mellenthin, Jennifer L Mueller, Erick Dario León Bueno de Camargo, Fernando Silva de Moura, Talles Batista Rattis Santos, Raul Gonzalez Lima, Sarah J Hamilton, Peter A Muller, and Melody Alsaker. “The ACE1 electrical impedance tomography system for thoracic imaging”. In: *IEEE transactions on instrumentation and measurement* 68.9 (2018), pp. 3137–3150.

[172] Bartłomiej Grychtol, William RB Lionheart, Marc Bodenstein, Gerhard K Wolf, and Andy Adler. “Impact of model shape mismatch on reconstruction quality in electrical impedance tomography”. In: *IEEE transactions on medical imaging* 31.9 (2012), pp. 1754–1760.

[173] Bartłomiej Grychtol and Andy Adler. “Uniform background assumption produces misleading lung EIT images”. In: *Physiological measurement* 34.6 (2013), p. 579.

[174] Andy Adler and Alistair Boyle. “Electrical impedance tomography: Tissue properties to image measures”. In: *IEEE Transactions on Biomedical Engineering* 64.11 (2017), pp. 2494–2504.

[175] Manuchehr Soleimani, Camille Gómez-Laberge, and Andy Adler. “Imaging of conductivity changes and electrode movement in EIT”. In: *Physiological measurement* 27.5 (2006), S103.

[176] Ander Biguri, Bartlomij Grychtol, Andy Adler, and Manuchehr Soleimani. “Tracking boundary movement and exterior shape modelling in lung EIT imaging”. In: *Physiological measurement* 36.6 (2015), p. 1119.

[177] Y. Wu and W. Shi. “On Calibration of Three-Axis Magnetometer”. In: *IEEE Sensors Journal* 15.11 (2015), pp. 6424–6431. ISSN: 1530-437X. DOI: 10.1109/JSEN.2015.2459767.

[178] Shengheng Liu, Jiabin Jia, and Yunjie Yang. “Image reconstruction algorithm for electrical impedance tomography based on block sparse Bayesian learning”. In: *2017 IEEE International Conference on Imaging Systems and Techniques (IST)*. IEEE. 2017, pp. 1–5.

[179] Christos Dimas, Nikolaos Uzunoglu, and Paul Sotiriadis. “An efficient Point-Matching Method-of-Moments for 2D and 3D Electrical Impedance Tomography Using Radial Basis functions”. In: *IEEE Transactions on Biomedical Engineering* (2021).

[180] N. Polydorides. “Image Reconstruction Algorithms for Soft-Field Tomography”. PhD thesis. University of Manchester, 2002.

[181] TN Tallman, S Gungor, KW Wang, and Charles E Bakis. “Damage detection and conductivity evolution in carbon nanofiber epoxy via electrical impedance tomography”. In: *Smart Materials and Structures* 23.4 (2014), p. 045034.

[182] K. Knudsen et al. “D-Bar Method for EIT with Discontinuous Conductivities”. In: *SIAM J. of Appl. Math.* 67.3 (2007), pp. 893–913.

[183] S. J. Hamilton. “EIT Imaging of admittivities with a D-bar method and spatial prior: experimental results for absolute and difference imaging”. In: *Physiol. Meas.* 38.6 (2017), pp. 1176–1192.

[184] Petre Stoica and Prabhu Babu. “SPICE and LIKES: Two hyperparameter-free methods for sparse-parameter estimation”. In: *Signal Processing* 92.7 (2012), pp. 1580–1590.

[185] Anthony P Reeves, Alberto M Biancardi, D Yankelevitz, S Fotin, Brad M Keller, Artit Jirapatnakul, and Jaesung Lee. “A public image database to support research in computer aided diagnosis”. In: *2009 Annual International Conference of the IEEE Engineering in Medicine and Biology Society*. IEEE. 2009, pp. 3715–3718.

[186] Joachim Schöberl. “NETGEN An advancing front 2D/3D-mesh generator based on abstract rules”. In: *Computing and visualization in science* 1.1 (1997), pp. 41–52.

[187] Camelia Gabriel, Sami Gabriel, and y E Corthout. “The dielectric properties of biological tissues: I. Literature survey”. In: *Physics in medicine & biology* 41.11 (1996), p. 2231.

[188] Sami Gabriel et al. “The dielectric properties of biological tissues: II. Measurements in the frequency range 10 Hz to 20 GHz”. In: *Physics in medicine & biology* 41.11 (1996), p. 2251.

[189] Sami Gabriel, RW Lau, and Camelia Gabriel. “The dielectric properties of biological tissues: III. Parametric models for the dielectric spectrum of tissues”. In: *Physics in medicine & biology* 41.11 (1996), p. 2271.

[190] Dräger Manufacturer. *Dräger Manufacturer Brochure. Technical Datasheet: Dräger Pulmovista 500*. 2010. URL: http://www.draeger.com/sites/assets/PublishingImages/Products/rsp_pulmovista500/Attachments/rsp_pulmovista_500_pi_9066475_en.pdf.

[191] Swisstom AG Manufacturer. *Swisstom AG Manufacturer Brochure. Swisstom BB2 Product Information 2st100–112, Rev.000.* 2012. URL: http://www.swisstom.com/wp-content/uploads/BB2_Brochure_2ST100-112_Rev.000_EIT_inside.pdf.

[192] Christos Dimas, Konstantinos Asimakopoulos, and Paul P Sotiriadis. "A highly tunable dynamic thoracic model for Electrical Impedance Tomography". In: *2020 IEEE 20th International Conference on Bioinformatics and Bioengineering (BIBE)*. IEEE. 2020, pp. 961–968.

[193] P Nopp, E Rapp, H Pfutzner, H Nakesch, and C Rusham. "Dielectric properties of lung tissue as a function of air content". In: *Physics in Medicine & Biology* 38.6 (1993), p. 699.

[194] Christos Dimas, Vassilis Alimisis, Ioannis Georgakopoulos, Nikolaos Voudoukis, Nikolaos Uzunoglu, and Paul P Sotiriadis. "Evaluation of Thoracic Equivalent Multiport Circuits Using an Electrical Impedance Tomography Hardware Simulation Interface". In: *Technologies* 9.3 (2021), p. 58.

[195] Yu Wu, Dai Jiang, Rebecca Yerworth, and Andreas Demosthenous. "An Imaged Based Method for Universal Performance Evaluation of Electrical Impedance Tomography Systems". In: *IEEE Transactions on Biomedical Circuits and Systems* 15.3 (2021), pp. 464–473.

[196] R Guardo, C Boulay, G Savoie, and A Adier. "A superheterodyne serial data acquisition system for electrical impedance tomography". In: *Proceedings of the 15th Annual International Conference of the IEEE Engineering in Medicine and Biology Societ*. IEEE. 1993, pp. 86–87.

[197] BM Graham and Andy Adler. "Objective selection of hyperparameter for EIT". In: *Physiological measurement* 27.5 (2006), S65.

[198] Marion Darbas, Jérémy Heleine, Renier Mendoza, and Arrianne Crystal Velasco. "Sensitivity analysis of the complete electrode model for electrical impedance tomography". In: *AIMS Mathematics* 6.7 (2021), pp. 7333–7366.

[199] Jouko Vankka, Kari AI Halonen, and Kari Halonen. *Direct digital synthesizers: Theory, design and applications*. Vol. 614. Springer Science & Business Media, 2001.

[200] Yu Wu, Farnaz Fahimi Hanzaee, Dai Jiang, Richard H Bayford, and Andreas Demosthenous. "Electrical Impedance Tomography for Biomedical Applications: Circuits and Systems Review". In: *IEEE Open Journal of Circuits and Systems* 2 (2021), pp. 380–397.

[201] GD Hammond, CC Speake, and M Stiff. "Noise analysis of a Howland current source". In: *International journal of electronics* 95.4 (2008), pp. 351–359.

[202] Xu Bai and Jiangtao Sun. "Noise analysis of a driven chain with an improved Howland current source for electrical impedance tomography". In: *Measurement Science and Technology* 32.9 (2021), p. 095903.

[203] Yu Wu, Peter Langlois, Richard Bayford, and Andreas Demosthenous. “Design of a CMOS active electrode IC for wearable electrical impedance tomography systems”. In: *2016 IEEE International Symposium on Circuits and Systems (ISCAS)*. IEEE. 2016, pp. 846–849.

[204] Dhouha Bouchaala, Olfa Kanoun, and Nabil Derbel. “High accurate and wideband current excitation for bioimpedance health monitoring systems”. In: *Measurement* 79 (2016), pp. 339–348.

[205] P Bertemes-Filho, BH Brown, and AJ Wilson. “A comparison of modified Howland circuits as current generators with current mirror type circuits”. In: *Physiological measurement* 21.1 (2000), p. 1.

[206] Hongwei Hong, Mohamad Rahal, Andreas Demosthenous, and Richard H Bayford. “Comparison of a new integrated current source with the modified Howland circuit for EIT applications”. In: *Physiological measurement* 30.10 (2009), p. 999.

[207] Pedro Bertemes-Filho, Volney Coelho Vincence, Marcio S Santos, and Ilson Xavier Zanatta. “Low power current sources for bioimpedance measurements: A comparison between Howland and integrated CMOS OTA circuits”. In: *Journal of Electrical Bioimpedance* 3.1 (2012), pp. 66–73.

[208] Pedro Bertemes-Filho, Alexandre Felipe, Volney C Vincence, et al. “High accurate Howland current source: Output constraints analysis”. In: *Circuits and Systems* 4.07 (2013), p. 451.

[209] Daniel S Batista, Guilherme B Silva, Francisco Granziera, Marcelo C Tosin, Décio L Gazzoni Filho, and Leonimer F Melo. “Howland current source applied to magnetic field generation in a tri-axial helmholtz coil”. In: *IEEE Access* 7 (2019), pp. 125649–125661.

[210] Dhouha Bouchaala, Qinghai Shi, Xinyue Chen, Olfa Kanoun, and Nabil Derbel. “Comparative study of voltage controlled current sources for biompedance measurements”. In: *International Multi-Conference on Systems, Signals & Devices*. IEEE. 2012, pp. 1–6.

[211] Fernando Seoane, Ramon Bragós, and Kaj Lindecrantz. “Current source for multifrequency broadband electrical bioimpedance spectroscopy systems. A novel approach”. In: *2006 International Conference of the IEEE Engineering in Medicine and Biology Society*. IEEE. 2006, pp. 5121–5125.

[212] Fu Zhang, Zhaosheng Teng, Haowen Zhong, Yuxiang Yang, Jianmin Li, and Jiangyan Sang. “Wideband mirrored current source design based on differential difference amplifier for electrical bioimpedance spectroscopy”. In: *Biomedical Physics & Engineering Express* 4.2 (2018), p. 025032.

[213] Loucas Constantinou, Iasonas F Triantis, Richard Bayford, and Andreas Demosthenous. “High-power CMOS current driver with accurate transconductance for electrical impedance tomography”. In: *IEEE Transactions on Biomedical Circuits and Systems* 8.4 (2014), pp. 575–583.

[214] Loucas Constantinou, Richard Bayford, and Andreas Demosthenous. “A wideband low-distortion CMOS current driver for tissue impedance analysis”. In: *IEEE Transactions on Circuits and Systems II: Express Briefs* 62.2 (2015), pp. 154–158.

[215] Hongwei Hong, Mohamad Rahal, Andreas Demosthenous, and Richard H Bayford. “Floating voltage-controlled current sources for electrical impedance tomography”. In: *2007 18th European Conference on Circuit Theory and Design*. IEEE. 2007, pp. 208–211.

[216] Yu Wu, Dai Jiang, Peter Langlois, Richard Bayford, and Andreas Demosthenous. “A CMOS current driver with built-in common-mode signal reduction capability for EIT”. In: *ESSCIRC 2017-43rd IEEE European Solid State Circuits Conference*. IEEE. 2017, pp. 227–230.

[217] Ramon Bragos, Javier Rosell, and Pere Riu. “A wide-band AC-coupled current source for electrical impedance tomography”. In: *Physiological measurement* 15.2A (1994), A91.

[218] AJ Rao, EK Murphy, M Shahghasemi, and KM Odame. “Current-conveyor-based wide-band current driver for electrical impedance tomography”. In: *Physiological measurement* 40.3 (2019), p. 034005.

[219] Texas Instruments. “An-1515 a comprehensive study of the Howland current pump”. In: *Application report SNOA474A* (2008).

[220] Pedro Bertemes Filho. “Tissue characterisation using an impedance spectrosopy probe”. PhD thesis. 2002.

[221] Hanen Nouri, Emna Ben Ayed, Dhouha Bouchaala, Houda Ben-Jmeaa Derbel, and Olfa Kanoun. “Comparative Study of Howland Current Source Configurations for Accurate Biomedical Devices”. In: *2019 5th International Conference on Nanotechnology for Instrumentation and Measurement (NanofIM)*. IEEE. 2019, pp. 1–8.

[222] Amin Mahnam, Hassan Yazdanian, and Mohsen Mosayebi Samani. “Comprehensive study of Howland circuit with non-ideal components to design high performance current pumps”. In: *Measurement* 82 (2016), pp. 94–104.

[223] Aaron S Tucker, Robert M Fox, and Rosalind J Sadleir. “Biocompatible, high precision, wide-band, improved Howland current source with lead-lag compensation”. In: *IEEE Transactions on Biomedical Circuits and Systems* 7.1 (2012), pp. 63–70.

[224] KF Morcelles, VG Sirtoli, P Bertemes-Filho, and VC Vincence. “Howland current source for high impedance load applications”. In: *Review of Scientific Instruments* 88.11 (2017), p. 114705.

[225] Jinzhen Liu, Xiaoyan Qiao, Mengjun Wang, Weibo Zhang, Gang Li, and Ling Lin. “The differential Howland current source with high signal to noise ratio for bioimpedance measurement system”. In: *Review of Scientific Instruments* 85.5 (2014), p. 055111.

[226] Vinicius G Sirtoli, Kaue F Morcelles, and Volney C Vincence. “Design of current sources for load common mode optimization”. In: *Journal of Electrical Bioimpedance* 9.1 (2018), p. 59.

[227] Xuetao Shi, Weichen Li, Fusheng You, Xuyang Huo, Canhua Xu, Zhenyu Ji, Ruigang Liu, Benyuan Liu, Yandong Li, Feng Fu, et al. “High-precision electrical impedance tomography data acquisition system for brain imaging”. In: *IEEE Sensors Journal* 18.14 (2018), pp. 5974–5984.

[228] Franco Simini and Pedro Bertemes-Filho. *Bioimpedance in biomedical applications and research*. Springer, 2018.

[229] Ali Zarafshani, Thomas Bach, Chris Chatwin, Liangzhong Xiang, and Bin Zheng. “Current source enhancements in Electrical Impedance Spectroscopy (EIS) to cancel unwanted capacitive effects”. In: *Medical Imaging 2017: Biomedical Applications in Molecular, Structural, and Functional Imaging*. Vol. 10137. International Society for Optics and Photonics. 2017, p. 101371X.

[230] Pascal Olivier Gaggero, Andy Adler, Josef Brunner, and Peter Seitz. “Electrical impedance tomography system based on active electrodes”. In: *Physiological measurement* 33.5 (2012), p. 831.

[231] Jiawei Xu, Srinjoy Mitra, Akinori Matsumoto, Shrishail Patki, Chris Van Hoof, Kofi AA Makinwa, and Refet Firat Yazicioglu. “A wearable 8-channel active-electrode EEG/ETI acquisition system for body area networks”. In: *IEEE Journal of Solid-State Circuits* 49.9 (2014), pp. 2005–2016.

[232] Nazanin Neshatvar, Peter Langlois, Richard Bayford, and Andreas Demosthenous. “Analog integrated current drivers for bioimpedance applications: A review”. In: *Sensors* 19.4 (2019), p. 756.

[233] Javad Frounchi, Fahimeh Dehkhoda, and Mohammad Hossein Zarifi. “A low-distortion wideband integrated current source for tomography applications”. In: *European Journal of Scientific Research* 27.1 (2009), pp. 56–65.

[234] Long Yan, Joonsung Bae, Seulki Lee, Taehwan Roh, Kiseok Song, and Hoi-Jun Yoo. “A 3.9 mW 25-electrode reconfigured sensor for wearable cardiac monitoring system”. In: *IEEE Journal of Solid-State Circuits* 46.1 (2010), pp. 353–364.

[235] Kiseok Song, Unsoo Ha, Seongwook Park, Joonsung Bae, and Hoi-Jun Yoo. “An impedance and multi-wavelength near-infrared spectroscopy IC for non-invasive blood glucose estimation”. In: *IEEE Journal of solid-state circuits* 50.4 (2015), pp. 1025–1037.

[236] Hyoungho Ko, Takhyung Lee, Ji-Hoon Kim, Jong-ae Park, and Jong Pal Kim. “Ultralow-power bioimpedance IC with intermediate frequency shifting chopper”. In: *IEEE Transactions on Circuits and Systems II: Express Briefs* 63.3 (2015), pp. 259–263.

[237] Hongwei Hong, Andreas Demosthenous, Iasonas F Triantis, Peter Langlois, and Richard Bayford. “A high output impedance CMOS current driver for bioimpedance measurements”. In: *2010 Biomedical Circuits and Systems Conference (BioCAS)*. IEEE. 2010, pp. 230–233.

[238] Yu Wu, Dai Jiang, Xiao Liu, Richard Bayford, and Andreas Demosthenous. “A human–machine interface using electrical impedance tomography for hand prosthesis control”. In: *IEEE transactions on biomedical circuits and systems* 12.6 (2018), pp. 1322–1333.

[239] Nazanin Neshatvar, Peter Langlois, and Andreas Demosthenous. “An improved wideband CMOS current driver for bioimpedance applications”. In: *2016 IEEE International Symposium on Circuits and Systems (ISCAS)*. IEEE. 2016, pp. 2447–2450.

[240] Nazanin Neshatvar, Peter Langlois, and Andreas Demosthenous. “A non-linear feedback current driver with automatic phase compensation for bioimpedance applications”. In: *IEEE Transactions on Circuits and Systems II: Express Briefs* 65.10 (2018), pp. 1340–1344.

[241] Boxiao Liu, Guoxing Wang, Yongfu Li, Lei Zeng, Hui Li, Yue Gao, Yixin Ma, Yong Lian, and Chun-Huat Heng. "A 13-Channel 1.53-mW 11.28-mm 2 Electrical Impedance Tomography SoC Based on Frequency Division Multiplexing for Lung Physiological Imaging". In: *IEEE transactions on biomedical circuits and systems* 13.5 (2019), pp. 938–949.

[242] Nick Van Helleputte, Sunyoung Kim, Hyejung Kim, Jong Pal Kim, Chris Van Hoof, and Refet Firat Yazicioglu. "A 160uA Biopotential Acquisition IC With Fully Integrated IA and Motion Artifact Suppression". In: *IEEE Transactions on Biomedical Circuits and Systems* 6.6 (2012), pp. 552–561. DOI: 10.1109/TBCAS.2012.2224113.

[243] Long Yan, Julia Pettine, Srinjoy Mitra, Sunyoung Kim, Dong-Woo Jee, Hyejung Kim, Masato Osawa, Yasunari Harada, Kosei Tamiya, Chris Van Hoof, et al. "A 13 μA Analog Signal Processing IC for Accurate Recognition of Multiple Intra-Cardiac Signals". In: *IEEE transactions on biomedical circuits and systems* 7.6 (2013), pp. 785–795.

[244] Nick Van Helleputte, Mario Konijnenburg, Julia Pettine, Dong-Woo Jee, Hyejung Kim, Alonso Morgado, Roland Van Wegberg, Tom Torfs, Rachit Mohan, Arjan Breeschoten, et al. "A 345 μW multi-sensor biomedical SoC with bio-impedance, 3-channel ECG, motion artifact reduction, and integrated DSP". In: *IEEE Journal of Solid-State Circuits* 50.1 (2014), pp. 230–244.

[245] Saqib Subhan and Sohmyung Ha. "A harmonic error cancellation method for accurate clock-based electrochemical impedance spectroscopy". In: *IEEE transactions on biomedical circuits and systems* 13.4 (2019), pp. 710–724.

[246] WA Evans and MS Towers. "Hybrid technique in waveform generation and synthesis". In: *IEE Proceedings G-Electronic Circuits and Systems*. Vol. 127. 3. IET. 1980, pp. 119–128.

[247] Milad Zamani, Yasser Rezaeiyan, Omid Shoaei, and Wouter A Serdijn. "A 1.55 μW bio-impedance measurement system for implantable cardiac pacemakers in 0.18 μm CMOS". In: *IEEE transactions on biomedical circuits and systems* 12.1 (2018), pp. 211–221.

[248] Yu Wu, Dai Jiang, Maryam Habibollahi, Noora Almarri, and Andreas Demosthenous. "Time stamp–a novel time-to-digital demodulation method for bioimpedance implant applications". In: *IEEE Transactions on Biomedical Circuits and Systems* 14.5 (2020), pp. 997–1007.

[249] Raymond Douglas Cook, Gary J Saulnier, David G Gisser, John C Goble, JC Newell, and David Isaacson. "ACT3: a high-speed, high-precision electrical impedance tomograph". In: *IEEE Transactions on Biomedical Engineering* 41.8 (1994), pp. 713–722.

[250] Christos S Koukourlis, George A Kyriacou, and J Sahalos. "A 32-electrode data collection system for electrical impedance tomography". In: *IEEE Transactions on Biomedical Engineering* 42.6 (1995), pp. 632–636.

[251] AJ Wilson, P Milnes, AR Waterworth, RH Smallwood, and BH Brown. "Mk3. 5: a modular, multi-frequency successor to the Mk3a EIS/EIT system". In: *Physiological Measurement* 22.1 (2001), p. 49.

[252] Ryan Halter, Alex Hartov, and Keith D Paulsen. “Design and implementation of a high frequency electrical impedance tomography system”. In: *Physiological measurement* 25.1 (2004), p. 379.

[253] Shadab Khan, Preston Manwaring, Andrea Borsic, and Ryan Halter. “FPGA-based voltage and current dual drive system for high frame rate electrical impedance tomography”. In: *IEEE transactions on medical imaging* 34.4 (2014), pp. 888–901.

[254] Mi Wang, Yixin Ma, Nigel Holliday, Yunfeng Dai, Richard A Williams, and Gary Lucas. “A high-performance EIT system”. In: *IEEE Sensors Journal* 5.2 (2005), pp. 289–299.

[255] Tong In Oh, Eung Je Woo, and David Holder. “Multi-frequency EIT system with radially symmetric architecture: KHU Mark1”. In: *Physiological measurement* 28.7 (2007), S183.

[256] Tong In Oh, Kyung Heon Lee, Sang Min Kim, Hwan Koo, Eung Je Woo, and David Holder. “Calibration methods for a multi-channel multi-frequency EIT system”. In: *Physiological measurement* 28.10 (2007), p. 1175.

[257] Tong In Oh, Hwan Koo, Kyung Heon Lee, Sang Min Kim, Jeehyun Lee, Sung Wan Kim, Jin Keun Seo, and Eung Je Woo. “Validation of a multi-frequency electrical impedance tomography (mfEIT) system KHU Mark1: impedance spectroscopy and time-difference imaging”. In: *Physiological measurement* 29.3 (2008), p. 295.

[258] Tong In Oh, Hun Wi, Do Yub Kim, Pil Joong Yoo, and Eung Je Woo. “A fully parallel multi-frequency EIT system with flexible electrode configuration: KHU Mark2”. In: *Physiological measurement* 32.7 (2011), p. 835.

[259] Susana Aguiar Santos, Anne Robens, Anna Boehm, Steffen Leonhardt, and Daniel Teichmann. “System description and first application of an FPGA-based simultaneous multi-frequency electrical impedance tomography”. In: *Sensors* 16.8 (2016), p. 1158.

[260] Arun Rao, Yueh-Ching Teng, Chris Schaef, Ethan K Murphy, Saaid Arshad, Ryan J Halter, and Kofi Odame. “An analog front end ASIC for cardiac electrical impedance tomography”. In: *IEEE transactions on biomedical circuits and systems* 12.4 (2018), pp. 729–738.

[261] Marco Guermandi, Roberto Cardu, Eleonora Franchi Scarselli, and Roberto Guerrieri. “Active electrode IC for EEG and electrical impedance tomography with continuous monitoring of contact impedance”. In: *IEEE transactions on biomedical circuits and systems* 9.1 (2014), pp. 21–33.

[262] Jiawei Xu, Mario Konijnenburg, Shuang Song, Hyunsoo Ha, Roland Van Wegberg, Massimo Mazzillo, Giorgio Fallica, Chris Van Hoof, Walter De Raedt, and Nick Van Helleputte. “A 665 μW silicon photomultiplier-based NIRS/EEG/EIT monitoring ASIC for wearable functional brain imaging”. In: *IEEE transactions on biomedical circuits and systems* 12.6 (2018), pp. 1267–1277.

[263] Hyunsoo Ha, Mario Konijnenburg, Budi Lukita, Roland Van Wegberg, Jiawei Xu, Richard van den Hoven, Marijn Lemmens, Ronald Thoelen, Chris Van Hoof, and Nick Van Helleputte. “A bio-impedance readout IC with frequency sweeping from 1k-to-1MHz for electrical impedance tomography”. In: *2017 Symposium on VLSI Circuits*. IEEE. 2017, pp. C174–C175.

[264] Christos Dimas, Nikolaos Uzunoglu, and Paul Peter Sotiriadis. “A parametric EIT system spice simulation with phantom equivalent circuits”. In: *Technologies* 8.1 (2020), p. 13.

[265] Christos Dimas, Vassilis Alimisis, and Paul P Sotiriadis. “SPICE and MATLAB simulation and evaluation of Electrical Impedance Tomography readout chain using phantom equivalents”. In: *2020 European Conference on Circuit Theory and Design (ECCTD)*. IEEE. 2020, pp. 1–4.

[266] Ning Liu. *ACT4: A high-precision, multi-frequency electrical impedance tomograph*. Rensselaer Polytechnic Institute, 2007.

[267] Christos Dimas, Nikolaos Uzunoglu, and Paul P Sotiriadis. “Electrical impedance tomography image reconstruction: Impact of hardware noise and errors”. In: *2019 8th International Conference on Modern Circuits and Systems Technologies (MOCAST)*. IEEE. 2019, pp. 1–4.

[268] Martin Proença. *Non-invasive hemodynamic monitoring by electrical impedance tomography*. Tech. rep. EPFL, 2017.

[269] KG Boone and DS Holder. “Effect of skin impedance on image quality and variability in electrical impedance tomography: a model study”. In: *Medical and Biological Engineering and Computing* 34.5 (1996), pp. 351–354.

[270] GJ Saulnier, Ahmed Abdelwahab, and F Maysha. “DSP-based adaptive current source for EIT applications”. In: *20th International Conference on Biomedical Applications of Electrical Impedance Tomography (EIT 2019)*. Vol. 7. 2019.

[271] Thomas Kugelstadt. “Active filter design techniques”. In: *Op amps for everyone*. Elsevier, 2009, pp. 365–438.

[272] Youssoufa Mohamadou, Tong In Oh, Hun Wi, Harsh Sohal, Adnan Farooq, Eung Je Woo, and Alistair Lee McEwan. “Performance evaluation of wideband bio-impedance spectroscopy using constant voltage source and constant current source”. In: *Measurement Science and Technology* 23.10 (2012), p. 105703.

[273] W Wang, M Brien, DW Gu, and J Yang. “A comprehensive study on current source circuits”. In: *13th International Conference on Electrical Bioimpedance and the 8th Conference on Electrical Impedance Tomography*. Springer. 2007, pp. 213–216.

[274] James Avery, Tom Dowrick, Anna Witkowska-Wrobel, Mayo Faulkner, Kirill Aristovich, and David Holder. “Simultaneous EIT and EEG using frequency division multiplexing”. In: *Physiological measurement* 40.3 (2019), p. 034007.

[275] Vera Button. *Principles of Measurement and transduction of biomedical variables*. Academic Press, 2015.

[276] Anas Albulbul. “Evaluating major electrode types for idle biological signal measurements for modern medical technology”. In: *Bioengineering* 3.3 (2016), p. 20.

[277] Wendy Franks, Iwan Schenker, Patrik Schmutz, and Andreas Hierlemann. “Impedance characterization and modeling of electrodes for biomedical applications”. In: *IEEE Transactions on Biomedical Engineering* 52.7 (2005), pp. 1295–1302.

[278] Pascal Olivier Gaggero. “Miniaturization and distinguishability limits of electrical impedence tomography for biomedical application”. PhD thesis. Université de Neuchâtel, 2011.

[279] Alistair Boyle and Andy Adler. “Integrating Circuit Simulation with EIT FEM Models”. In: *ELECTRICAL IMPEDANCE TOMOGRAPHY* (2018), p. 20.

[280] M Proenca. “Resistor Networks and Finite Element Models”. PhD thesis. University of Manchester Manchester, UK, 2011.

[281] Christos Dimas and Paul P Sotiriadis. “Electrical impedance tomography image reconstruction for adjacent and opposite strategy using FEMM and EIDORS simulation models”. In: *2018 7th International Conference on Modern Circuits and Systems Technologies (MOCAST)*. IEEE. 2018, pp. 1–4.

[282] D Hem. “Study and interpretation the chemical of natural of characteristics water”. In: *U. S Geol. Surv. Water-Supply Pap* 2254 (1985).

[283] A Costall, Brett Harris, and JP Pigois. “Electrical resistivity imaging and the saline water interface in high-quality coastal aquifers”. In: *Surveys in geophysics* 39.4 (2018), pp. 753–816.

[284] Lebea N Nthunya, Sebabatso Maifadi, Bhekie B Mamba, Arne R Verliefde, and Sabelo D Mhlanga. “Spectroscopic determination of water salinity in brackish surface water in Nandoni Dam, at Vhembe District, Limpopo Province, South Africa”. In: *Water* 10.8 (2018), p. 990.

[285] Ge Zhang, Meng Dai, Lin Yang, Weichen Li, Haoting Li, Canhua Xu, Xuetao Shi, Xiuzhen Dong, and Feng Fu. “Fast detection and data compensation for electrodes disconnection in long-term monitoring of dynamic brain electrical impedance tomography”. In: *Biomedical engineering online* 16.1 (2017), pp. 1–23.

[286] Alzbeta E Hartinger, Robert Guardo, Andy Adler, and Hervé Gagnon. “Real-time management of faulty electrodes in electrical impedance tomography”. In: *IEEE Transactions on Biomedical Engineering* 56.2 (2008), pp. 369–377.

[287] Tushar Kanti Bera, Samir Kumar Biswas, K Rajan, and J Nagaraju. “Improving image quality in electrical impedance tomography (EIT) using projection error propagation-based regularization (PEPR) technique: a simulation study”. In: *Journal of Electrical Bioimpedance* 2.1 (2011), pp. 2–12.

[288] D. Liu et al. “Shape reconstruction using Boolean operations in electrical impedance tomography”. In: *IEEE Trans. on Med. Imag.* to appear.to appear (2020), to appear.

[289] DT Nguyen, C Jin, A Thiagalingam, and AL McEwan. “A review on electrical impedance tomography for pulmonary perfusion imaging”. In: *Physiological measurement* 33.5 (2012), p. 695.

[290] Mohammad Takhti and Kofi Odame. “A power adaptive, 1.22-pw/hz, 10-mhz read-out front-end for bio-impedance measurement”. In: *IEEE transactions on biomedical circuits and systems* 13.4 (2019), pp. 725–734.

[291] Michael Eberdt, Patrick K Brown, and Gianluca Lazzi. “Two-dimensional SPICE-linked multiresolution impedance method for low-frequency electromagnetic interactions”. In: *IEEE transactions on biomedical engineering* 50.7 (2003), pp. 881–889.

[292] Andy Adler, Pascal Olivier Gaggero, and Yasheng Maimaitijiang. “Adjacent stimulation and measurement patterns considered harmful”. In: *Physiological measurement* 32.7 (2011), p. 731.

[293] Vinko Tomicic and Rodrigo Cornejo. “Lung monitoring with electrical impedance tomography: technical considerations and clinical applications”. In: *Journal of thoracic disease* 11.7 (2019), p. 3122.

[294] Panagiotis Kassanos, Loucas Constantinou, Iasonas F Triantis, and Andreas Demosthenous. “An integrated analog readout for multi-frequency bioimpedance measurements”. In: *IEEE Sensors Journal* 14.8 (2014), pp. 2792–2800.

[295] Sunjoo Hong, Jaehyuk Lee, Joonsung Bae, and Hoi-Jun Yoo. “A 10.4 mW electrical impedance tomography SoC for portable real-time lung ventilation monitoring system”. In: *IEEE Journal of Solid-State Circuits* 50.11 (2015), pp. 2501–2512.

[296] Nuutti Hyvönen. “Complete electrode model of electrical impedance tomography: Approximation properties and characterization of inclusions”. In: *SIAM Journal on Applied Mathematics* 64.3 (2004), pp. 902–931.

[297] Vassilis Alimisis, Christos Dimas, Georgios Pappas, and Paul P Sotiriadis. “Analog Realization of Fractional-Order Skin-Electrode Model for Tetrapolar Bio-Impedance Measurements”. In: *Technologies* 8.4 (2020), p. 61.

[298] Lin Yang, Meng Dai, Canhua Xu, Ge Zhang, Weichen Li, Feng Fu, Xuetao Shi, and Xiuzhen Dong. “The frequency spectral properties of electrode-skin contact impedance on human head and its frequency-dependent effects on frequency-difference EIT in stroke detection from 10Hz to 1MHz”. In: *PloS one* 12.1 (2017), e0170563.

[299] Hanbin Ma, Yang Su, and Arokia Nathan. “Cell constant studies of bipolar and tetrapolar electrode systems for impedance measurement”. In: *Sensors and Actuators B: Chemical* 221 (2015), pp. 1264–1270.

[300] Christos Dimas, Petros Tsampas, Nikolaos Ouzounoglou, and Paul P Sotiriadis. “Development of a modular 64-electrodes electrical impedance tomography system”. In: *2017 6th International Conference on Modern Circuits and Systems Technologies (MOCAST)*. IEEE. 2017, pp. 1–4.

[301] Panagiotis Kassanos, Florent Seichepine, and Guang-Zhong Yang. “A Comparison of Front-End Amplifiers for Tetrapolar Bioimpedance Measurements”. In: *IEEE Transactions on Instrumentation and Measurement* 70 (2020), pp. 1–14.

[302] Panagiotis Kassanos, Henry MD Ip, and Guang-Zhong Yang. “A tetrapolar bio-impedance sensing system for gastrointestinal tract monitoring”. In: *2015 IEEE 12th International Conference on Wearable and Implantable Body Sensor Networks (BSN)*. IEEE. 2015, pp. 1–6.

[303] Vassilis Alimisis, Christos Dimas, and Paul P Sotiriadis. “Analogue Realization of Fractional-Order Healthy and Cancerous Lung Cell Models for Electrical Impedance Spectroscopy”. In: *2020 32nd International Conference on Microelectronics (ICM)*. IEEE. 2020, pp. 1–4.

[304] Karthik Raghavan, John E Porterfield, Anil TG Kottam, Marc D Feldman, Daniel Escobedo, Jonathan W Valvano, and John A Pearce. “Electrical conductivity and permittivity of murine myocardium”. In: *IEEE Transactions on Biomedical Engineering* 56.8 (2009), pp. 2044–2053.

[305] Hiram Madero Orozco, Osslan Osiris Vergara Villegas, Vianey Guadalupe Cruz Sánchez, Humberto de Jesús Ochoa Domínguez, and Manuel de Jesús Nandayapa Alfaro. “Automated system for lung nodules classification based on wavelet feature descriptor and support vector machine”. In: *Biomedical engineering online* 14.1 (2015), p. 9.

[306] Eugene Demidenko, Andrea Borsic, Yuqing Wan, Ryan J Halter, and Alex Hartov. “Statistical estimation of EIT electrode contact impedance using a magic Toeplitz matrix”. In: *IEEE transactions on biomedical engineering* 58.8 (2011), pp. 2194–2201.

[307] Roman Kusche, Steffen Kaufmann, and Martin Ryschka. “Dry electrodes for bioimpedance measurements—design, characterization and comparison”. In: *Biomedical Physics & Engineering Express* 5.1 (2018), p. 015001.

[308] Christian Putensen, Benjamin Hentze, Stefan Muenster, and Thomas Muders. “Electrical Impedance Tomography for cardio-pulmonary monitoring”. In: *Journal of clinical medicine* 8.8 (2019), p. 1176.

[309] Bassem Ibrahim and Roozbeh Jafari. “Cuffless blood pressure monitoring from an array of wrist bio-impedance sensors using subject-specific regression models: Proof of concept”. In: *IEEE transactions on biomedical circuits and systems* 13.6 (2019), pp. 1723–1735.

[310] Bassem Ibrahim, Drew A Hall, and Roozbeh Jafari. “Bio-impedance simulation platform using 3D time-varying impedance grid for arterial pulse wave modeling”. In: *2019 IEEE Biomedical Circuits and Systems Conference (BioCAS)*. IEEE. 2019, pp. 1–4.

[311] AO Ragheb, LA Geddes, JD Bourland, and WA Tacker. “Tetrapolar electrode system for measuring physiological events by impedance”. In: *Medical and Biological Engineering and Computing* 30.1 (1992), pp. 115–117.

[312] BH Brown, AJ Wilson, and P Bertemes-Filho. “Bipolar and tetrapolar transfer impedance measurements from volume conductor”. In: *Electronics Letters* 36.25 (2000), pp. 2060–2062.

[313] Roberto Cardu, Philip HW Leong, Craig T Jin, and Alistair McEwan. “Electrode contact impedance sensitivity to variations in geometry”. In: *Physiological measurement* 33.5 (2012), p. 817.

[314] Yu Mike Chi, Tzyy-Ping Jung, and Gert Cauwenberghs. “Dry-contact and noncontact biopotential electrodes: Methodological review”. In: *IEEE reviews in biomedical engineering* 3 (2010), pp. 106–119.

[315] Bahareh Taji, Adrian DC Chan, and Shervin Shirmohammadi. "Effect of pressure on skin-electrode impedance in wearable biomedical measurement devices". In: *IEEE Transactions on Instrumentation and Measurement* 67.8 (2018), pp. 1900–1912.

[316] Sverre Grimnes and Ørjan G Martinsen. "Sources of error in tetrapolar impedance measurements on biomaterials and other ionic conductors". In: *Journal of Physics D: Applied Physics* 40.1 (2006), p. 9.

[317] Panagiotis Kassanos, Andreas Demosthenous, and Richard H Bayford. "Comparison of tetrapolar injection-measurement techniques for coplanar affinity-based impedimetric immunosensors". In: *2008 IEEE Biomedical Circuits and Systems Conference*. IEEE. 2008, pp. 317–320.

[318] Pasi Kauppinen, Jari Hyttinen, and Jaakko Malmivuo. "Sensitivity distribution visualizations of impedance tomography measurement strategies". In: *International Journal of Bioelectromagnetism* 8.1 (2006), pp. 1–9.

[319] Onic Islam Shuvo and Md Naimul Islam. "Sensitivity analysis of the tetrapolar electrical impedance measurement systems using comsol multiphysics for the non-uniform and inhomogeneous medium". In: *Dhaka University Journal of Science* 64.1 (2016), pp. 7–13.

[320] Kenneth S Cole. "Permeability and impermeability of cell membranes for ions". In: *Cold Spring Harbor symposia on quantitative biology*. Vol. 8. Cold Spring Harbor Laboratory Press. 1940, pp. 110–122.

[321] Sverre Grimnes and Orjan G Martinsen. "Cole electrical impedance model-a critique and an alternative". In: *IEEE transactions on biomedical engineering* 52.1 (2004), pp. 132–135.

[322] Sverre Grimnes and Orjan G Martinsen. *Bioimpedance and bioelectricity basics*. Academic press, 2011.

[323] Richard L Magin. "Fractional calculus in bioengineering, part 1". In: *Critical Reviews™ in Biomedical Engineering* 32.1 (2004).

[324] Ahmed AboBakr, Lobna A Said, Ahmed H Madian, Ahmed S Elwakil, and Ahmed G Radwan. "Experimental comparison of integer/fractional-order electrical models of plant". In: *AEU-International Journal of Electronics and Communications* 80 (2017), pp. 1–9.

[325] Todd J Freeborn. "A survey of fractional-order circuit models for biology and biomedicine". In: *IEEE Journal on emerging and selected topics in circuits and systems* 3.3 (2013), pp. 416–424.

[326] Goran Lazović, Zoran Vosika, Mihailo Lazarević, Jovana Simić-Krstić, and Đuro Koruga. "Modeling of bioimpedance for human skin based on fractional distributed-order modified cole model". In: *FME Transactions* 42.1 (2014), pp. 74–81.

[327] Zoran B Vosika, Goran M Lazovic, Gradimir N Misevic, and Jovana B Simic-Krstic. "Fractional calculus model of electrical impedance applied to human skin". In: *PloS one* 8.4 (2013), e59483.

[328] CS Poon and TT Choy. "Frequency dispersions of human skin dielectrics". In: *Biophysical journal* 34.1 (1981), pp. 135–147.

[329] Brian R Eggins. “Skin contact electrodes for medical applications”. In: *Analyst* 118.4 (1993), pp. 439–442.

[330] Vassilis Alimisis, Georgios Pappas, and Paul P Sotiriadis. “Fractional-order instrumentation amplifier transfer function for control applications”. In: *2020 33rd Symposium on Integrated Circuits and Systems Design (SBCCI)*. IEEE. 2020, pp. 1–6.

[331] Georgia Tsirimokou, Costas Psychalinos, Todd J Freeborn, and Ahmed S Elwakil. “Emulation of current excited fractional-order capacitors and inductors using OTA topologies”. In: *Microelectronics journal* 55 (2016), pp. 70–81.

[332] Costas Vastarouchas, Georgia Tsirimokou, Todd J Freeborn, and Costas Psychalinos. “Emulation of an electrical-analogue of a fractional-order human respiratory mechanical impedance model using OTA topologies”. In: *AEU-International Journal of Electronics and Communications* 78 (2017), pp. 201–208.

[333] Georgia Tsirimokou, Costas Psychalinos, and Ahmed S Elwakil. “Emulation of a constant phase element using operational transconductance amplifiers”. In: *Analog Integrated Circuits and Signal Processing* 85.3 (2015), pp. 413–423.

[334] Georgia Tsirimokou, Aslihan Kartci, Jaroslav Koton, Norbert Herencsar, and Costas Psychalinos. “Comparative study of discrete component realizations of fractional-order capacitor and inductor active emulators”. In: *Journal of Circuits, Systems and Computers* 27.11 (2018), p. 1850170.

[335] Kleoniki Baxevanaki and Costas Psychalinos. “Second-Order Bandpass OTA-C Filter Designs for Extracting Waves from Electroencephalogram”. In: *2019 8th International Conference on Modern Circuits and Systems Technologies (MOCAST)*. IEEE. 2019, pp. 1–4.

[336] Vassilis Alimisis, Panagiotis Bertsias, Costas Psychalinos, and Ahmed S Elwakil. “Electronically tunable implementation of the arterial viscoelasticity model”. In: *2019 42nd International Conference on Telecommunications and Signal Processing (TSP)*. IEEE. 2019, pp. 145–148.

[337] Vassilis Alimisis, Marios Gourdouparis, Christos Dimas, and Paul P Sotiriadis. “Implementation of fractional-order model of nickel-cadmium cell using current feedback operational amplifiers”. In: *2020 European Conference on Circuit Theory and Design (ECCTD)*. IEEE. 2020, pp. 1–4.

[338] Juraj Valsa and Jiri Vlach. “RC models of a constant phase element”. In: *International Journal of Circuit Theory and Applications* 41.1 (2013), pp. 59–67.

[339] Georgia Tsirimokou. “A systematic procedure for deriving RC networks of fractional-order elements emulators using MATLAB”. In: *AEU-International Journal of Electronics and Communications* 78 (2017), pp. 7–14.

[340] Ilias Dimeas, Georgia Tsirimokou, Costas Psychalinos, and Ahmed S Elwakil. “Experimental verification of fractional-order filters using a reconfigurable fractional-order impedance emulator”. In: *Journal of Circuits, Systems and Computers* 26.09 (2017), p. 1750142.

[341] Mehmet Isik, Thomas Lonjaret, Haritz Sardon, Rebeca Marcilla, Thierry Herve, George G Malliaras, Esma Ismailova, and David Mecerreyes. "Cholinium-based ion gels as solid electrolytes for long-term cutaneous electrophysiology". In: *Journal of Materials Chemistry C* 3.34 (2015), pp. 8942–8948.

[342] Rubén Buendía López. "Model Based Enhancement of Bioimpedance Spectroscopy Analysis: Towards Textile Enabled Applications". PhD thesis. KTH Royal Institute of Technology, 2011.

[343] DA Dean, T Ramanathan, D Machado, and R Sundararajan. "Electrical impedance spectroscopy study of biological tissues". In: *Journal of electrostatics* 66.3-4 (2008), pp. 165–177.

[344] Kensuke Sasaki, Kanako Wake, and Soichi Watanabe. "Development of best fit Cole-Cole parameters for measurement data from biological tissues and organs between 1 MHz and 20 GHz". In: *Radio Science* 49.7 (2014), pp. 459–472.

[345] Jie-Ran Wang, Ben-Yuan Sun, Hua-Xiang Wang, Shan Pang, Xiao Xu, and Qing Sun. "Experimental study of dielectric properties of human lung tissue in vitro". In: *Journal of Medical and Biological Engineering* 34.6 (2014), pp. 598–604.

[346] Georgia Tsirimokou, Costas Psychalinos, and Ahmed Elwakil. *Design of CMOS analog integrated fractional-order circuits: applications in medicine and biology*. Springer, 2017.

[347] Ilias Dimeas, Georgia Tsirimokou, Costas Psychalinos, and Ahmed S Elwakil. "Realization of fractional-order capacitor and inductor emulators using current feedback operational amplifiers". In: *aa* 2.8 (2015), p. 2.

[348] Elpida Kaskouta, Stavroula Kapoulea, Costas Psychalinos, and Ahmed S Elwakil. "Implementation of a fractional-order electronically reconfigurable lung impedance emulator of the human respiratory tree". In: *Journal of Low Power Electronics and Applications* 10.2 (2020), p. 18.